Technische Universität München

Fakultät für Chemie

Nanometallurgy in Solution: Synthesis Strategies for Nano-Sized Materials and Investigation on their Catalytic Performance in the Alkyne Semi-Hydrogenation

Lena Staiger

Vollständiger Abdruck der von der Fakultät für Chemie der Technischen Universität München zur Erlangung des akademischen Grades einer

Doktorin der Naturwissenschaften (Dr. rer. nat.)

genehmigten Dissertation.

Vorsitzender:	Prof. Dr. Sebastian Günther
Prüfer der Dissertation:	1. Prof. Dr. Dr. h.c. Roland A. Fischer
	2. Prof. Dr. Ulrich Heiz

Die Dissertation wurde am 08.03.2022 bei der Technischen Universität München eingereicht und durch die Fakultät für Chemie am 19.04.2022 angenommen.

„Nur im Wörterbuch steht der Erfolg vor dem Fleiß“

Vidal Sassoon

„Wer schwankt hat mehr vom Weg“

Songtext von „Dicht und Ergreifend“, bayrische Mundart-Band

Danksagung

Viele Menschen haben mich auf meinem Weg der letzten Jahre begleitet, denen ich auf persönlicher sowie wissenschaftlicher Ebene sehr dankbar bin.

Meiner Prüfungskommission mit **Prof. Sebastian Günther** als Vorsitz und **Prof. Ulrich Heiz** als Zweitprüfer danke ich für die bereitwillige und freundliche Übernahme des Koreferats.

In erster Linie möchte ich meinem Doktorvater **Prof. Roland A. Fischer** für die Chance und Möglichkeit danken, an Ihrem Lehrstuhl meine Doktorarbeit anfertigen zu können. Während dieser Zeit standen mir jegliche Freiheiten, Möglichkeiten sowie die eigene Interpretation meines Themengebietes offen. Ich danke Ihnen für Ihr stetiges Vertrauen in mich. Trotz Laborunfällen und Rückschlägen im Labor haben Sie mich stets unterschützt, gefördert und haben mir den Rücken gestärkt. Insbesondere unsere gemeinsame Reise nach Japan bleibt mir hier in positiver Erinnerung, welche sicherlich ein Highlight meiner Promotion war. Ihr Enthusiasmus für die Forschung mit der einhergehenden Forderung sowie Förderung Ihrer Doktoranden hat mir auf persönlicher Ebene sehr geholfen, mich weiterzuentwickeln.

Mein Dank gilt zudem meinem Betreuer **Dr. Mirza Cokoja**. Durch deine stetige Unterstützung und Ideen sowie den Anspruch, die richtigen und wichtigen Fragen zu beantworten hast du mir gezeigt, wie man wissenschaftlich korrekt arbeitet. Ich bin dir zudem sehr dankbar, dass du auch immer ein offenes Ohr bei jeglichen nicht wissenschaftlichen Problemen für mich hattest und dir immer Zeit für mich genommen hast. Von dir habe ich nicht nur auf wissenschaftlicher Ebene sehr lernen können, sondern auch im Umgang mit Kollegen, Vorgesetzten und Mitarbeitern. Vielen Dank für deine Unterstützung!

Weiterhin möchte ich meinem Kommilitonen **Tim Kratky** meinen herzlichen Dank für die erfolgreiche Zusammenarbeit, den guten Wein, den viel zu starken Kaffee sowie stets einer ehrlichen, kritischen aber auch Mut machenden Meinung aussprechen. Ohne deine Ideen, die guten Gespräche, deine Zeit und deine Unterstützung hätte ich meine Doktorarbeit nicht so gestalten können, wie ich es dank dir konnte.

Further I cordially thank **Janos Mink** for your support over the last four years on all of my projects concerning IR spectroscopy. Beside your exceptional knowledge about every single IR vibrational mode in this world, your ongoing and never stopping interest in science, you are also a role model for me in the way you treat people and your willingness to help.

I want to thank **Juanjuan Huang** from the Chair of Biomedical Physics for the opportunity to measure EXAFS and XANES measurements of my samples. Thank you for your kind support, your ideas, and your time. Furthermore, my thanks go to **Ondrej Tomanek** for the reliable HR-TEM measurements of all my samples. I know this was a lot of work and I really appreciate it. Thank you! I thank **Zhiying Fan** for our collaboration project we did during our time at the

AMC chair. It was a pleasure to work with you, I really enjoyed it. Desweiteren möchte ich **Tabea Groß** sehr herzlich für die Zusammenarbeit und die schnelle und effiziente Durchführung und Auswertung der Daten danken! Zudem danke ich **Ben Hofmann** für sein Interesse an meinem Projekt, seiner Hilfe sowie seine außerordentlichen Expertise, Auswertung und Berechnung sämtlicher EPR Experimente. Ich danke **Jan Berger** für die schnelle und zuverlässige Hilfe bei der Auswertung von BET Daten. **Martin Schellerer** und **Dana Weiß** danke ich für eure Hilfe und Geduld in allen bürokratischen, administrativen und formellen Angelegenheiten. Für die tatkräftige Unterstützung in analytischen Fragestellungen danke ich **Maria Mathews**, **Jürgen Kudermann**, **Ulrike Ammari, Dr. Carsten Peters** und **Dr. Oksana Storcheva**.

Neben der wissenschaftlichen Betreuung ist das Arbeitsumfeld mit das Wichtigste, um die Promotionszeit genießen zu können. Deswegen gilt mein herzlicher Dank der ganzen **AMC Gruppe** für die vielen lustigen Momente, eure Geduld mit meiner impulsiven Art sowie euren lieben Worte, wenn es mir einmal nicht so gut ging. Dank euch konnte ich den Alltag im Labor genießen. Insbesondere möchte ich hierbei **Philip Altmann, David Mayer, Pia Vervoorts, Sebastian Weishäupl, Patricia Weishäupl, Kathrin Kollmannsberger** sowie **Philip Stanley** danken. Ihr habt es möglich gemacht, dass ich nicht nur mit Arbeitskollegen, sondern mit Freunden zusammenarbeiten durfte. Wenn auch etwas spät dazu gestoßen, möchte ich weiterhin **Tom Calmus** und **Simon Deger** danken, die mir meine letzte Laborzeit leichter gemacht haben und durch die ich den Spaß im Labor nicht verloren habe. Ich möchte weiterhin **Max Schütz**, **Stefan Burger** und **Franziska Hanusch** für die schnelle Hilfe bei dem Brand in meinem Abzug danken. Zudem möchte ich in besonderem Maße **Maximilian Muhr** für unsere (manchmal etwas holprige, aber doch stets kollegiale) Zusammenarbeit danken. Durch dich und unser gemeinsames Projekt habe ich gelernt, auch in Konfliktsituationen auf Augenhöhe und ehrlich zu kommunizieren und die Sicht des anderen besser zu verstehen. Das Bewältigen dieser anfangs schwierigen Situation hat mich auf persönlicher Ebene sehr stark vorangebracht. Ich danke dir dafür! Neben dem AMC Lehrstuhl möchte ich auch noch dem Lehrstuhl für Makromolekulare Chemie für das Kaffee-Asyl danken. Vielen Dank, dass ihr mich nicht nur akzeptiert, sondern auf stets freundlich aufgenommen habt. Besonders erwähnenswert sind hier **Tom Pehl** sowie **Marc Kloberg**. Danke für die vielen Feierabendbiere, Nachmittagskaffees sowie eure Freundschaft!

Mein besonderer Dank geht an dich, **Karina Hemmer**. Du warst nicht nur die beste Masterandin, die ich mir vorstellen konnte, sondern bist auch zu einer Freundin geworden. Ich bin dir für deine Geduld mit mir, für dein offenes Ohr in allen Hinsichten sowie die ganzen gemeinsamen Erlebnisse dankbar. Mit deiner Ankunft am AMC Lehrstuhl hast du meine Zeit

hier mit am meisten bereichert und ich möchte diese Zeit nicht missen wollen. Weiterhin möchte ich **Silva Kronawitter** danken. Du bist für mich in kürzester Zeit nicht nur eine gute Freundin geworden, sondern auch eine Person, der ich blind vertrauen kann. Ich danke dir für deine Loyalität, die gemeinsamen Abende und den Schlafplatz auf deiner Couch. Du hast es geschafft, dass ich auch in meinem letzten Promotionsjahr noch sehr gerne ins Labor gegangen bin und jeden Tag Spaß bei der Arbeit hatte.

Zusammen gehangen, zusammen gefangen – dieses Motto gilt wohl für **Stefan Burger** und **Fabian Schmidt**. Wir haben fast gleichzeitig hier angefangen und waren von Anfang an ein Team. Ihr habt meine Promotion beeinflusst wie kein anderer. Die gemeinsamen Ausflüge, sei es auf Konzerte oder nach London waren Highlights meiner Zeit hier am Lehrstuhl. **Stefan**, ich danke dir für unsere großartige Freundschaft, deine Unterstützung und die gemeinsame Zeit. Du hast mir die Welt des Gin Tonics näher gebracht sowie meine Leidenschaft für die bayrische Hiphop-Kultur geweckt. **Fabi**, mein herzlichster Dank gilt dir. Wir sind nicht nur das wahre „Team“, sondern uns verbindet auch eine ganz besondere Freundschaft. Ich hätte mir keinen besseren Laborpartner und Subgroup-Partner als dich vorstellen können. Danke für deine ehrliche Meinung, deine Unterstützung im Labor, die gemeinsamen Abende und Reisen. Du hast mir nicht nur gezeigt, wie man chemische Problemstellungen angeht, sondern auch, wie man den verrückten und teils stressigen Arbeitsalltag meistern kann. Ich habe mich dank dir nicht nur fachwissenschaftlich, sondern vor Allem menschlich weiter entwickeln können. Du bist mit das Positivste, was mir hier während meiner Promotion passieren konnte.

Ich möchte auch meiner guten Freundin **Clara Aletsee** für die ganzen gemeinsamen Jahre seit Beginn unseres Studiums danken. Ohne dich hätte ich das Chemiestudium nicht so meistern können und hätte mit Sicherheit auch viel weniger Spaß dabei gehabt. Ich danke dir für unsere tolle Freundschaft, die absolut verlässliche Unterstützung in allen Lebenslagen und deine Loyalität mir gegenüber. In guten wie in schlechten Zeiten – ich denke, dass beschreibt unsere Freundschaft sehr gut.

Zu guter Letzt möchte ich meiner Familie danken. **Mama** und **Papa**, eurer liebevolle, fürsorgevolle und doch manchmal strenge Erziehung hat mich sehr geprägt. Nur durch die bedingungslose, finanzielle sowie mentalen Unterstützung konnte ich mein Studium und Promotion meistern. Zudem konntest du mich, Papa, für die Chemie begeistern und hast mit Sicherheit einen großen Teil dazu beigetragen, dass ich mich für diesen Weg entschieden habe. Meinem Zwillingsbruder **Lukas** möchte ich für deine Unterstützung von Beginn an danken.

Zusammenfassung

Die selektive Hydrierung von Alkinen zu Alkenen stellt einen wichtigen Zwischenschritt in der industriellen Polyethylenherstellung da. Da die Vollhydrierung zum Alkan jedoch thermodynamisch favorisiert ist, wurden verschiedene Katalysatorkonzepte zur Erhöhung der Selektivität gegenüber des Olefins in heterogenen Systemen entwickelt. Sowohl die Nutzung von kleinen organischen Molekülen, welche an die Katalysatoroberfläche binden und somit die elektronischen Eigenschaften des aktiven Zentrums verändern, als auch die Einführung eines zweiten, inaktiven Metalls sind etablierte Methoden, um die Selektivität zugunsten des gewünschten Olefins zu steuern. Obwohl in den letzten Jahrzehnten ein fundiertes Wissen über die Steuerung der Aktivität und Selektivität heterogener Systeme gesammelt werden konnte, gibt bei der Untersuchung kolloidaler und somit quasi-homogener Systeme in Lösung nur wenige Studien über die Steuerung der katalytischen Eigenschaften. Deswegen ist ein tieferes Verständnis über die entscheidenden Parameter für ein hochselektives Katalysatorsystem mit kolloidalen Nanopartikeln als aktive Spezies noch nicht gegeben. Ein entscheidender Vorteil von quasi-homogenen Katalysatoren ist zudem die Möglichkeit der gezielten Untersuchung des Einflusses von Additiven auf die Performance der aktiven Spezies.

Die vorliegende Arbeit befasst sich mit der Syntheseentwicklung kolloidaler Nanopartikel für die Anwendung in der Semihydrierungskatalyse von flüssigen Alkinen. Ziel ist es, ein weitreichendes Verständnis über die entscheidenden Faktoren zu erlangen, welche für die Aktivität, Selektivität und Stabilität entscheidend sind. Der Fokus der Arbeit liegt hierbei nicht nur auf der katalytischen Leistung der hier getesteten Systeme, sondern insbesondere auch auf der Erforschung und Entwicklung von Synthesestrategien für neuartige, bimetallische Kolloide mit besonderem Augenmerk auf den Bildungsmechanismen und die Aufklärung der Partikelstruktur.

Inspiriert von den industriell angewandten Palladium-basierten Katalysatorsystemen fokussiert sich das erste Projekt dieser Arbeit auf monometallische Palladium-Kolloide. Dabei wird der Einfluss von verschiedenen Liganden, welche nach der Partikelsynthese hinzugegeben werden, auf das katalytische Verhalten des Materials evaluiert. Ionisch stabilisierte Nanopartikel wurden hierbei als hochaktives und leicht regulierbares System identifiziert. Nach erfolgreicher Optimierung der Katalysebedingungen wurde der Einfluss von verschiedenen koordinierenden Additiven erforscht. Die Zugabe von NHC-Liganden, ionischen Flüssigkeiten und einer Serie unterschiedlicher Phosphane hat dabei gezeigt, dass sowohl die Aktivität wie auch die Selektivität dieses Systems stark beeinflusst werden kann.

Insbesondere die Gruppe der Phosphane stellte sich hierbei als vielversprechendes Additiv heraus, da durch Zugabe von Liganden mit marginalen Unterschieden bezüglich der elektronischen sowie sterischen Eigenschaften wichtige Parameter für einen Hochleistungskatalysator bestimmt werden konnten.

Das zweite Projekt dieser Thesis adressiert die Entwicklung einer Synthesestrategie für bimetallische Pd/Ga-Nanopartikel in Lösung. Palladium (Pd) wurde dabei als katalytisch aktives Metall gewählt, während Gallium (Ga) als nicht-aktives Metall zur Verdünnung der aktiven Zentren dienen soll. Kolloide mit verschiedenen Pd/Ga Verhältnissen ausgehend von den Metallprecursoren [$Pd_2(dvds)_3$] und GaCp* wurden erfolgreich synthetisiert, vollständig charakterisiert sowie der Bildungsmechanismus aufgeklärt. Zudem konnte bestätigt werden, dass durch die Einführung eines zweiten, inaktiven Metalls die Selektivität in der Semihydrierungskatalyse gezielt gesteuert werden kann. Anschließend wurde der Einfluss von Liganden auf die Partikelstabilität in Bezug auf Temperatur, Wasserstoffatmosphäre sowie Sauerstoff getestet. Durch Zugabe von Carbonsäuren ist es ohne jegliche Zersetzung möglich, luftstabile bimetallische Pd/Ga Partikel zu generieren, welche die gleichen katalytischen Eigenschaften zeigen wie die ursprünglichen, ohne zusätzliche Additive stabilisierten (und Sauerstoff-sensiblen) Partikel.

Das letzte Projekt dieser Arbeit beschäftigt sich mit der Entwicklung einer Synthesestrategie für bimetallische Systeme aus metallorganischen Startmaterialien, welche aus günstigen und nachhaltig verfügbaren Elementen bestehen. Hierbei wurden die Metalle Eisen (Fe) und Aluminium (Al) als maximal kostengünstige Elementkombination gewählt. Durch gezielte Anpassung der Reaktionsparameter gelang es, verschiedene heterogene sowie quasi-homogene (kolloidale) bimetallische Fe/Al Systeme zu erzeugen, welche vollständig charakterisiert und in der Semihydrierungskatalyse von flüssigen Alkinen getestet wurden. Hierbei zeigten die Kolloide eine Reaktivität bei milden Bedingungen, während bei den bimetallischen Feststoffen als Katalysatoren erhöhte Temperaturen und Wasserstoffdrücke nötig waren, um einen Substratumsatz zu erzielen. Neben der Untersuchung der Reaktivität der hier getesteten Materialen lag der Fokus dieses Projektes auch auf der Erforschung des zugrundeliegenden Bildungsmechanismus der Materialien. Es stellte sich heraus, dass das Legieren von Fe mit Al nicht nur die resultierenden Partikelgrößen und katalytischen Leistungen beeinflusst, sondern auch das Fe vor Oxidation schützt.

Abstract

The semi-hydrogenation of alkynes is an important catalytic process in industry. Thus, stopping the hydrogenation of the product at the stage of the alkene and preventing the thermodynamically favoured over-hydrogenation to the respective alkane is challenging. The crucial step for an increased selectivity towards the olefin is to create a controlled preference towards olefin desorption from the catalyst surface instead of a further hydrogenation to the alkane. Several attempts regarding this scientific issue were already reported for heterogeneous systems. The effect of coordinating agents as well as the introduction of a second, inactive metal are well-established strategies for an enhanced selectivity towards the olefin. Even though the scientific community succeeded in the accumulation of a fundamental knowledge concerning the control of activity and selectivity of heterogeneous systems, the investigation of colloidal systems is still in its early stage. Therefore, a deeper understanding of the crucial parameters concerning quasi-homogeneous systems of colloidal nanoparticles is still missing currently limiting any systematic developments in this field.

The present work addresses the development of synthesis strategies for small, colloidal nanoparticles and their application in the semi-hydrogenation of liquid alkynes. Understanding the crucial factors for adjusting the activity, selectivity as well as stability of the herein studied systems is of utmost importance. The focus not only lies on the catalytic performance of the tested systems, but also on the investigation of synthesis strategies for novel, bimetallic colloids with special regard to building mechanisms and particle structure.

Based on industrially applied semi-hydrogenation catalysts, the first project focuses on monometallic Pd colloids, and the influence of various, post-synthetically added agents on the catalytic performance. Starting with the optimization of the nanoparticle (NP) synthesis as well as elucidating and defining the optimal parameters for the catalytic tests, we found Pd NPs stabilized by the ionic surfactant $N(Octyl)_4Br$ to be a highly active and easily tunable system. The addition of NHC ligands, ionic liquids as well as a series of phosphanes lead to a change in both, activity and selectivity, thus providing a deeper understanding of the parameters required for an optimal catalytic performance. In detail, phosphanes turned out to not only increase the particle activity but also strongly influence the selectivity towards the olefin. Testing a series of promising phosphanes with subtle differences in electronics and sterics resulted in the identification of the necessary features for a high-performance, colloidal monometallic semi-hydrogenation catalyst.

The second project addresses the strategy of using Pd-based bimetallic catalysts for the herein studied catalytic reaction. Based on our experience regarding organometallic chemistry, a bottom-up synthesis strategy for Pd/Ga colloids starting from $[Pd_2(dvds)_3]$ and GaCp* as metal precursors by adjusting the synthesis parameters in terms of precursor ratio, temperature, and reaction time was developed. The successful synthesis and full-characterization of a series of Pd/Ga colloids with varying metal ratios not only lead to a better understanding of the formation mechanism of the colloids but also confirms the influence of a second, inactive metal on the semi-hydrogenation selectivity. Further investigation on post-synthetic additives, namely amines and carboxylic acids, resulted in an increased stability of the colloids towards temperature, H_2 pressure and oxygen. Here, the air-stable Pd/Ga colloids stabilized by a carboxylic acid showed the same catalytic performance than the initial, non-stabilized and air-sensitive Pd/Ga NPs.

The last project deals with the development of a bottom-up synthesis of abundant, bimetallic catalyst systems. The combination of Fe and Al as most promising and affordable metal combination was therefore chosen. Starting from the organometallic precursors $[Fe_2(mesityl)_4]$ and $[AlH_3]$–NMe_3, adjusting the synthesis parameters resulted in different heterogeneous (powder) as well as homogeneous (colloidal) bimetallic systems, which were fully characterized and tested in the semi-hydrogenation catalysis of liquid alkynes. While the Fe/Al colloids already showed a good reactivity at mild conditions, the Fe/Al powders required higher temperatures and H_2 pressures to be active in the conversion of liquid alkynes. The alloying of Fe with Al turned out to not only influence the resulting particle sizes and catalytic performances, but also protected the Fe against oxidation.

Table of Contents

List of Abbreviations

Å	Ångström [10^{-10} m]
ATR	Attenuated Total Reflection
a.u.	Atomic Units
BET	Brunauer, Emmett, Teller
btsa	Bis(trimethylsilyl)amide
cod	Cyclooctadiene
Cp*	1,2,3,4,5-Pentamethylcyclopentadienyl
DFT	Density Functional Theory
DLS	Dynamic Light Scattering
dvds	1,3-Divinyl-1,1,3,3-tetramethyldisiloxane
EDX	Energy-dispersive X-Ray analysis
EPR	Electron Paramagnetic Resonance
EXAFS	Extended X-Ray Absorption Fine Structure Analysis
FID	Flame Ionization Detector
FT	Fourier Transformation
GC	Gas Chromatography
h	hour
HAADF	High-Angle Annular Dark-Field
HHDMA	Hexadecyl(2-hydroxyethyl)dimethyl ammonium dihydrogen phosphate
HR-TEM	High-Resolution Transmission Electron Microscopy
ICP MS	Inductively Coupled Plasma Mass Spectrometry
ICP OES	Inductively Coupled Plasma Optical Emission Spectroscopy
IL	Ionic Liquid
IR	Infrared
k	Reaction Constant
K	Kelvin
LIFDI-MS	Liquid Injection Field Desorption Ionization Mass Spectrometry
m/z	Mass to ionization ratio
MHz	Mega Hz
min	Minute

MuCLS	Munich Compact Light Source
MS	Mass Spectrometry
mT	Millitesla
ν	Wavenumber [cm^{-1}]
NHC	N-Heterocyclic Carbene
NMR	Nuclear Magnetic Resonance
NP	Nanoparticle
OMIMBr	1-Octyl-3-Methyl Imidazolium Bromide
PE	Polyethylene
-Ph	Phenyl
ppm	Parts Per Million
PXRD	Powder X-Ray Diffraction
PVP	Poly(vinylpyrrolidone)
PVA	Poly(vinylalcohol)
r	Reaction Rate
RT	Room Temperature
SQUID	Superconducting Quantum Interference Device
T	Temperature [°C or K]
t	time [s, min or h]
*t*Bu-NHC	1,3-Di-tert-butyl-N-heterocyclic Carbene
TGA-MS	Thermogravimetric Analysis coupled with a Mass Spectrometer
TM	Transition Metal
TOF	Turnover Frequency
s	Second
SI	Supporting Information
sccm	Standard Cubic Centimeters per Minute [$cm^3 \cdot min^{-1}$]
XANES	X-Ray Absorption Near Edge Spectroscopy
XPS	X-Ray Photoelectron Spectroscopy

1. Introduction

The selective semi-hydrogenation of alkynes to alkenes has attracted attention particularly for its relevance in the production of polymers and fine chemicals. Most prominently, ethene and also alkenes with longer alkyl chains, namely 2-butene and 1,3-butadiene, are important building blocks in the chemical industry. Focusing on the manufacture of polymer-grade ethene, the semi-hydrogenation reaction represents a crucial step with the aim of completely eliminating alkynes and dienes in the alkene feedstocks.[1] The production of ethene by pyrolysis of saturated C2-C6 hydrocarbons in the petrochemical industry leads to an alkene feed with small amounts of alkyne.[2] These traces of residual acetylene must be removed in ethene-rich streams in order to avoid poisoning of the Ziegler-Natta polymerization catalyst.[3] Therefore, high ethene purities are required. Preventing undesired over-hydrogenation and oligomerization of the substrates is of fundamental relevance, as for industrial interest the loss of ethene by full-hydrogenation should not be higher than 1 %.[3] Raising awareness to the importance of this chemical, the annual growth of the worldwide ethene demand of 3.5 % leads to a production of 120 million tons in 2010 in contrast to the early beginnings of 1950[4] where the ethene production was estimated to 1 million ton per year and 80.5 million tons in 1998.[3] These amount are directly related to the annual need of polyethylene (PE). About 30 % of all plastics used in the in the consumption and manufacturing sectors globally are polyethylene-based products, reflecting this polymer to be the most commonly used plastic worldwide.[5] This high need of PE is related to its characteristics, as the mechanical, thermal and chemical properties can be precisely adjusted depending on the production conditions.[6] In general, the cost-effectiveness, its impermeability to water and high resistance to strong acids and bases enables a wide range of products, e.g. for packaging, medical devices, or automotive applications.[7] The particular type of application depends on the polymer weight, type of branching and density directly influencing important factors like the stability, ductility and crystallinity of the material.

Hence, due to the worldwide need of PE, the production of polymer-grade ethylene represents an important step towards all PE-based products. The targeted removal of acetylene traces in ethene streams to impede the poisoning of the Ziegler-Natta catalyst is crucial for a cost-efficient PE production. The design of a highly selective semi-hydrogenation catalyst based on the understanding of adsorption and desorption processes on the catalyst surface regarding alkyne, alkene and alkane is required. Therefore, the selective semi-hydrogenation of alkynes was intensively studied in the last decades with focus on alkyne adsorption and hydrogenation mechanism. Yet, fully disentangling molecular reaction steps

and understanding the nature of the active sites is crucial to establish structure-performance relationships, which ultimately leads to novel synthesis strategies towards industrially profitable catalysts.

1.1 Semi-hydrogenation catalysis

As demonstrated in numerous reports in literature on the investigation of selective catalysts for the semi-hydrogenation of alkynes and dienes for 74 years, the main challenge is to avoid of the undesired full hydrogenation to alkanes (see Scheme 1).[8,9] Upon adsorption of the alkyne to a catalyst (metal) surface, a two-step hydrogenation, which can be described by a Langmuir-Hinshelwood mechanism, with co-adsorbed molecular hydrogen results in the formation of the (still adsorbed) olefin via a vinyl intermediate. The crucial step for a high selectivity towards the olefin – hence its desorption from the catalyst surface vs. its further hydrogenation - depends on the catalyst characteristics (see Scheme 1, green vs. orange energy difference).[10,11] In addition, under industrial conditions, not only the desorption of the formed olefin in order to avoid full hydrogenation but also a strongly preferred adsorption of the alkyne compared to the olefin is of primary importance due to the high olefin content in the feed which causes a competitive adsorption with the alkyne at the metal surface (see Scheme 1, blue vs. green energy difference). In general, a good catalyst is characterized by showing a high stability of the adsorbed alkyne and a low stability of the alkene adsorbed on the metal surface. The former determines the overall rate of alkyne conversion, whereas the latter determines the selectivity towards the olefin.[12]

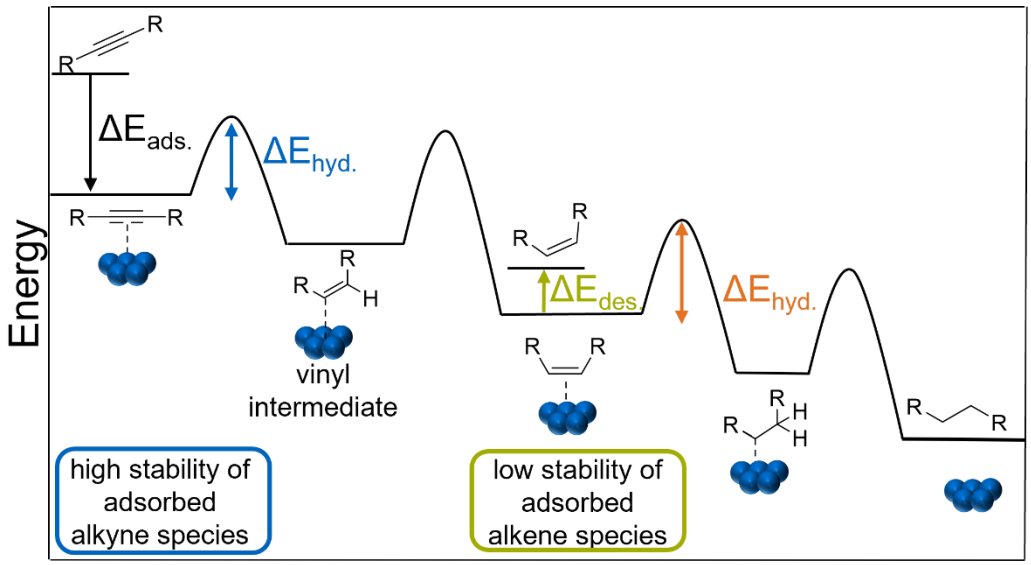

Scheme 1. Schematic energy profile of the catalytic hydrogenation reactions for alkynes with H_2 resulting in either the olefin or the alkane.

Mechanistic studies showed that the alkyne hydrogenation to produce either alkenes or alkanes proceeds *via* different pathways, which were particularly studied for acetylene as substrate (see Scheme 2).[13] The hydrogenation of the alkyne to the olefin (Path **b1**) followed by its desorption and re-adsorption and further hydrogenation (Path **b2**) to the alkane is shown in Path **b** (green). Here, the adsorption of the acetylene molecule proceeds via a π-coordinated intermediate, which is subsequently first transformed into a di-σ-bonded and then into a vinyl species. This vinyl species allows for a step-wise addition of adsorbed hydrogen species on the metal surface following the well-established Horiuti-Polanyi mechanism, resulting in a π-bonded ethylene molecule.[14] As a result of the higher adsorption enthalpy of acetylene compared to ethylene, this π-coordinated species is displaced by an acetylene molecule, inhibiting the full-hydrogenation to ethane. With progressive alkyne conversion, the surface coverage decreases allowing for alkene re-adsorption and its hydrogenation to the alkane (Path **b2**). In contrast, Path **a** (yellow) highlights the reactive adsorption of acetylene to produce multiple bound intermediates such as ethylidyne and ethylidene that are directly hydrogenated to the respective alkane. Additionally, oligomerization processes of the alkyne as well as of the alkene (Path **c**, blue and Path **d**, red) yielding hydrocarbons with carbon numbers ranging from C4 to C32 are reported in particular for small alkynes (e.g. acetylene) with dissociatively adsorbed acetylene and vinylidene intermediates.[3]

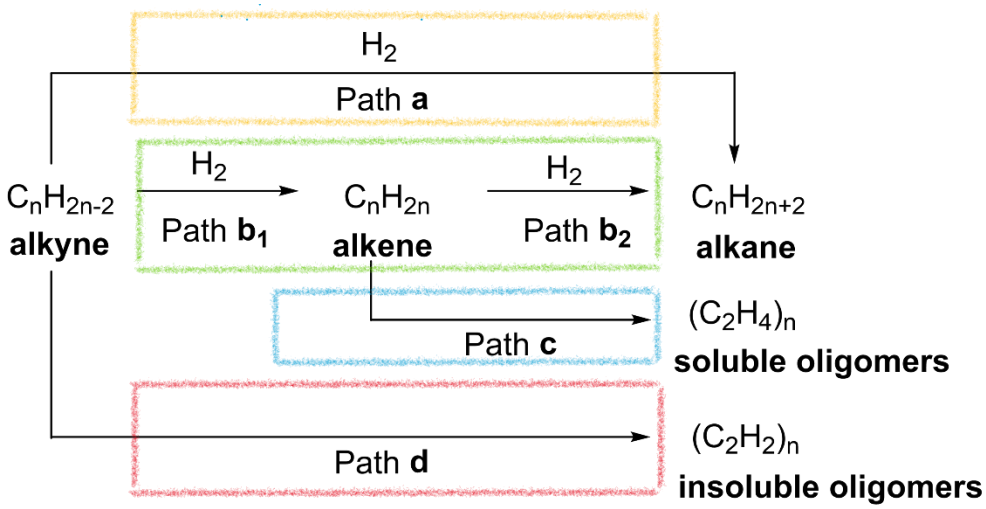

Scheme 2. Mechanistic investigation of the semi-hydrogenation of alkynes showing different reaction pathways by the reaction with H_2.

With increasing substitution of the alkyne, the steric interferences in the C-C bond formation step lead to a decreased oligomer formation of the respective alkene (Path **c**, blue). Nevertheless, studies have reported on 20-40% (undesired) C4 hydrocarbons and higher (soluble) oligomers in the semi-hydrogenation of acetylene, which therefore present a serious

issue regarding the product yield and hence the selectivity towards the alkene.[3],[15],[16] Apart from the undesired oligomerization of the product, also a chain growth reaction of the alkyne can be observed (Path **d**), resulting in insoluble, long-chain hydrocarbon species. Investigations on the mechanism of the formation of such oligomers revealed that the presence of a di-adsorbed free-radical form of the half-hydrogenated state of ethyne $H_2C\text{-}CH^{\bullet}$ adsorbed on a Pd surface leads to an initiation of a free-radical polymerization with an adjacent di-adsorbed σ-coordinated acetylene molecule. This process then continues as long as suitable disposed acetylene molecules are available.[9] The formation of irreversibly adsorbed heavy hydrocarbons on the catalyst surface leads to carbonaceous deposits on the metal surface, depending on the temperature, hydrogen coverage and type of crystallographic surface plane. In detail, C-C bond breaking of the adsorbed hydrocarbons by increasing temperature and subsequent partly hydrogenation of these C_nH_m hydrocarbon layers results in a catalyst deactivation during semi-hydrogenation catalysis, therefore modifying the catalyst´s properties. Depending on the deposited species and amount, the stability, activity and selectivity of the catalyst is either positively or negatively affected. For instance, various studies revealed that a certain amount and species of carbon deposits on the surface enhances the catalyst´s selectivity.[17] In contrast, a high degree of coking induces an undesired catalyst deactivation.

The catalyst performance to the desired alkene can be tuned by the choice of the catalyst and the reaction parameters (e.g. the composition of the feedstock).[18] With special regard to the catalyst, various factors, namely choice of the metal, metal dispersion, carbon deposits, the formation of metal hydrides, promoters and additives play a crucial role.[10],[19],[20] Different scale lengths of the catalyst architecture have been proposed to control the catalytic performance. On the nanoscale, the morphology of the active metal NPs as well as shape and the presence of specific types of active sites affect its performance. With focus on the mesoscale, interactions between the active metal and the intimate environment can be assessed by modification in terms of alloying, the involvement of additives or metal-support interactions. Finally, tailoring the support structure on the macroscale to the particular requirements of the reaction in combination with the development of a suitable chemical reactor can lead to an enhanced catalytic performance.[21]

Concerning heterogeneous metal catalysts for the hydrogenation of C≡C triple bonds, several transition metals have proven to be active (e.g. Fe, Ni, Rh, Pd, Ag, Pt).[22] Among these metals, those with high hydrogen activation capacity such as Ni or Pt present severe selectivity issues due to their strong over-hydrogenation potential. In contrast, high selectivities to the alkene were reported for metals with low reactivity towards H_2 such as Ag or Au but are hardly

competitive with respect to activity.[23] Therefore, Pd-based catalysts have been identified as the most efficient catalysts representing a balance of selectivity and activity, which leads to the development of various supported Pd catalysts. The ability to absorb hydrogen in the bulk phase results in a β-PdH species, which acts as source of reactive surface hydrogen species.[24] Nevertheless, the β-PdH is also discussed to promote full-hydrogenation to the alkane, whereas selective semi-hydrogenation occurs on the metal surface.[25] The superior catalyst performance has been particularly attributed to the stronger adsorption of the alkyne C≡C triple bond relative to the alkene double bond on the Pd surface, thus preventing the over-reduction of the alkene product. Nevertheless, this energetic difference is rather small, evoking a mechanistic investigation and the development of strategies to enhance selectivity.[12] Apart from the nature of the metal itself, the coverage of the above mentioned intermediate species (ethylidene, ethylidyne, di-σ-ethylene) can have a huge impact of the catalyst performance.[26,27] The formation of such less-reactive intermediates blocking the adsorption sites thus limiting the availability of hydrogen can enhance the selectivity. The existence of these species is strongly dependent on the hydrogen pressure, altering the overall performance of the catalyst.[28]

The intrinsic ability of palladium to yield a high alkene selectively can be further improved by the addition of promoters/modifiers, altering electronic and/or geometric properties of palladium and affecting the selectivity by influencing the formation of the β-PdH species. One of the most renowned benchmark catalysts is a quinoline-poisoned Pd@$CaCO_3$ material, also known as *Lindlar* catalyst, with Pd nanoparticles (NPs) as active species supported on $CaCO_3$ and poisoned by lead diacetate and quinoline resulting in a heterogeneous catalyst.[29] Yet, this most famous semi-hydrogenation catalyst lacks robustness and its irreversible deactivation by the deposits of insoluble acetylene-based oligomerization products $(C_2H_2)_n$ hamper the catalyst recycling. Moreover, the presence of toxic lead and the required amine additive are the main drawbacks for industry with regard to health and environmental aspects.[21] Another concept for a high-performance semi-hydrogenation catalyst is the electronic modification of the active metal, in which the spatial isolation of Pd atoms increases the catalyst stability.[24] This is realized in the industrially applied alloying of Al_2O_3-supported Pd NPs with Ag, promoting the selective hydrogenation of the vinyl intermediate to ethylene while suppressing the undesired full-hydrogenation to the ethylidene species (see Scheme 2, Path **a**).[26,27] Additionally, alloying Pd with Ag results in a hindered formation of β-PdH as the number of larger Pd ensemble decreases.[30] In the bimetallic Pd/Ag catalysts, this species is not only minimized but the bulk hydrogen is additionally stronger bound to the Pd resulting in a decreased, (undesired) hydrogen spill-over from the bulk Pd to the catalytically active metal

surface.[3] There is an unbroken interest for the development of catalyst with a higher overall performance. Further research efforts need to be devoted to the understanding of fundamental phenomena such as the nature of the active site or stabilization effects in order to enable the fine-tuning of catalyst performance with respect to selectivity, activity and recyclability.

1.2 Strategies for an enhanced catalyst activity

The decrease in size of active metal particles is a well-known and widely applied strategy to tune activity and selectivity, due to is direct effect on surface to mass ratio of the metal as well as on electronic properties. Therefore, most studies focus on the development of synthesis strategies for a further downsizing of metal NPs yielding a high quantity of heterogeneous and homogeneous systems reported in literature. Nevertheless, not only the diameter but also the size distribution, dispersion as well as the shape of the NPs can play an important role for a high substrate conversion.[20,31] A low metal dispersion and low loading is assumed to achieve high semi-hydrogenation activities.[3] For a deeper understanding of the role of the catalyst structure, it is important to separate the effects of NP size from those of NP shape. With special regard to Pd based catalysts, the NP size becomes crucial not only in terms of increasing the surface area but also for the formation of the β-PdH phase. The relative number of octahedral lattice vacancies, important for hydrogen diffusion into the bulk metal, is highly dependent on the surface atoms and hence the NP size.[32]

Studies with special regard on the catalytic influence of the size effect of Pd NPs is impeded by the challenging synthesis of highly dispersed unimodal metal nanocrystals. Yet, one of the first studies on Pd NPs supported on alumina for the selective acetylene semi-hydrogenation confirmed that the catalyst activity was significantly influenced by small particle sizes.[31] Surprisingly, larger Pd NPs with a size of 8 nm showed a higher activity than particles around 2 nm. The authors explain this effect by the preferential formation of the β-hydride phase for larger NPs, which is required for an active catalytic hydrogenation. The formation of this hydride phase by hydrogen diffusion into the Pd crystallite structure leads to a coverage of available octahedral vacancies in the metal bulk phase. Hence, with smaller particle sizes, the number of bulk Pd atoms (and hence unoccupied octahedral vacancies) with respect to metal surface atoms strongly decreases with a limiting value of about 2.5 nm, where the absorbed hydrogen amount is calculated to be close to zero.[32,33] Additionally, small NPs with sizes less than 2 nm have surface atoms of low coordination number with an electron density deficiency. Upon alkyne addition, the surface atoms are strongly coordinated by the highly unsaturated,

electron-rich substrate leading to a decreased conversion.[21] Interestingly, Mastalir et al. compared Pd NPs with sizes ranging from 1.5 and 3.0 to 6.2 nm and could show that the highest catalytic activity was achieved with 3 nm sized NPs, thus indicating an optimum size for a highly active catalyst.[34a] Also here, the smallest NPs with sizes around 1.5 nm showed a decreased activity, which goes in line with previous reports. A similar effect was reported by the group of Kiwi-Minsker on the semi-hydrogenation of liquid alkynes with colloidal Pd NPs with different sizes from 2.1–9.8 nm.[22] Here, larger particles showed an enhanced activity, which was attributed to modifications regarding the electronic, structural as well as steric features of the catalyst. The increased fraction of Pd_{plane} surfaces in larger Pd NPs improves the alkyne adsorption. Concluding, these investigations indicate that very small metal particles are not suitable for hydrogenation catalysis. An active semi-hydrogenation catalyst requires certain electronic features, strongly influencing the chemisorption behavior of electron-rich substrates such as alkynes, and octahedral vacancies for the adsorption of H_2. Controversy, recent studies focused on atomically dispersed metal atoms on a support, allowing for the semi-hydrogenation of alkynes at a single-atom active site. For instance, $Pd_1@C_3N_4$ was reported to show an increased catalytic performance compared to the industrial Lindlar catalyst in combination with a high coke-resistance.[34b] This strategy can be extended to single-atom alloys, where isolated active metal sites are embedded in a host metal. This approach combines the benefits of a high atom economy and an enhanced activity as well as selectivity by an electronic influence of the second metal.[34c] Theoretical studies have shown that single-site catalysts, without any edges and corner sites (as present in a NP-based catalyst) result in a faster and preferred olefin formation instead a full-hydrogenation to the respective alkane.[34d] Nevertheless, preparation of such catalytic systems as well as the characterization in order to evidence the existence of atomically dispersed metal atoms without any larger agglomerates is highly challenging.

Apart from the particle size, the shape of the NPs has a significant effect on the catalyst performance. Reports on the hydrogenation of alkynols illustrated that the activity depends on the amount of the active site (here: Pd_{111}) and not only on the particle size.[35] More recently, Kiwi-Minsker and co-workers were able to show for a series of Pd nanocrystals with well-defined sizes and shapes, namely cubic, octahedral and cuboctahedral, that two types of active sites are involved in hydrogenation catalysis.[36] The authors found that the semi-hydrogenation preferentially takes place on planes, whereas full-hydrogenation occurs mainly at edges. Nevertheless, the effect of two or more different kinds of active sites has not been thoroughly investigated and discussed yet, bearing a significant potential of catalyst optimization for industrially relevant hydrogenation reactions. Thus, the identification and

characterization of the nature of the active sites is the first step towards the optimization of selective hydrogenation catalysts at the nano level. However, the challenging synthesis of well-defined nanocrystals impedes in-depth studies for a full kinetic description and hence the prediction of shape effect for a maximized catalytic efficiency. The implementation of versatile colloidal synthesis is the most promising strategy for new developments in the nanoscaled architecture of catalysts.

1.3 Strategies for an enhanced selectivity towards the olefin

Beside a high activity, one of the most important performance indicator regarding semi-hydrogenation catalysts is their selectivity towards the desired olefin. External factors such as temperature and hydrogen pressure affect the kinetics of the reaction and thus the alkene selectivity. For example, in the case of Pd based catalysts the partial H_2 pressure is of high relevance. The formation of the β-hydride phase of Pd at high H_2 pressures by the absorption of molecular hydrogen in the bulk of the metal results an highly active but unselective catalyst, as the full-hydrogenation of the alkyne is favored by the subsurface hydrogen species.[1] In order to avoid the formation of this β-hydride phase, the adjustment of the reaction parameters (e.g. a lower H_2 partial pressure) is important.

Apart from external parameters, the nature of the catalyst itself plays an essential role for its selectivity towards the olefin. Several strategies have been developed so far, with systematic testing as well as theoretical studies for a better understanding of the interactions between substrate/intermediate olefin and the catalytic surface. The modification of the electronic or local structure of the active metal is the key point to accomplish high selectivities, as this directly influence the catalyst adsorption behavior. Addition of coordinating (σ-donoring) molecules (also known as surfactants) or alloying the active metal with a second, inactive one, changes the structure of the catalyst and hence directly influences the catalyst binding properties. The effect on the relative adsorption strengths of both the alkyne and the olefin, results in a decreased number of multi-adsorbed species (such as strongly bounded, di-σ-coordinated alkyne or olefin species). This, in turn, can lead to a preferred olefin desorption over its further hydrogenation (see Scheme 3). In addition, the geometrical separation of the active centers, either by a blockage of the coordinating surfactants or the introduction of an inactive metal inhibits full hydrogenation of the olefin due to a decreased hydrogen supply.

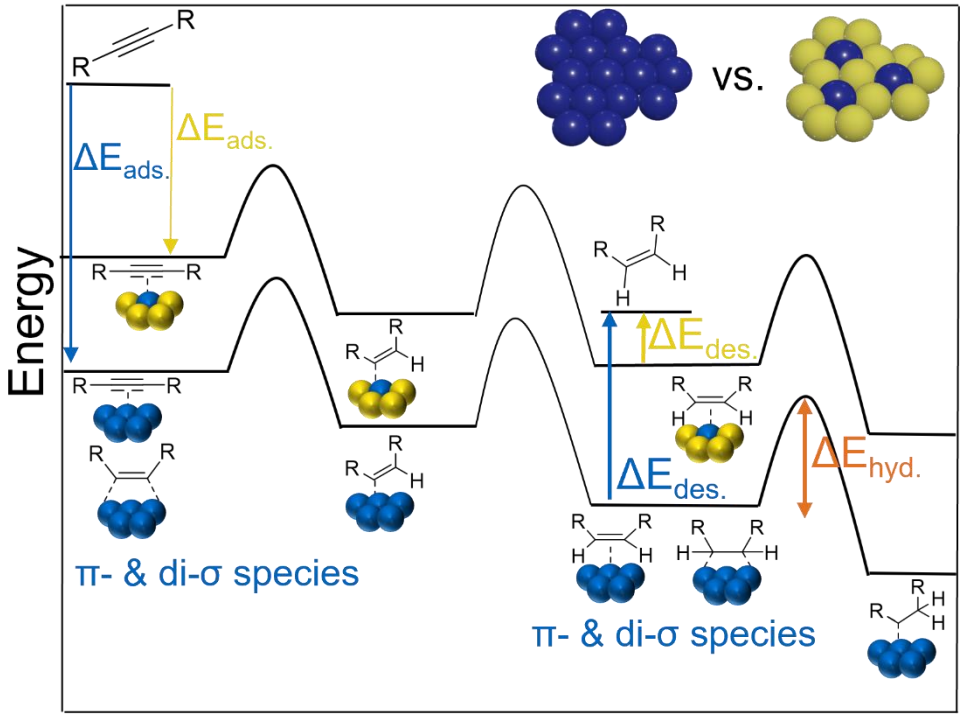

Scheme 3. Schematic energy profile showing the change of the adsorption and hydrogenation behavior by the addition of a coordinating surfactant or a second, inactive metal (blue: unmodified, unselective catalyst; blue-yellow: modified catalyst with a higher selectivity towards the olefin).

1.3.1 Additives as effective modifier of the catalytic performance

Monometallic catalysts are attractive due to their effectiveness and simplicity. However, for an optimized catalyst activity and selectivity, modifications on the catalyst surface have to be undertaken for improvement, which is mostly realized by the use of surfactants.[37,38] The coordinating surfactant molecules, particularly σ-donor type stabilizing agents, bear spatial control of the accessibility as well as influencing the electronic properties of the surface atoms of the colloids, and therefore have an impact on the catalytic activity and selectivity as well.[37,39] The interaction of the surfactant with the particle surface can lead to a preferred alkyne adsorption instead of the competitive olefin coordination and hence improve the selectivity towards the semi-hydrogenation product.[37] Understanding and controlling such effects of organic ligands on the catalytic performance of NPs as well-defined system can open up new possibilities in providing a spatial control of catalyst performance. Perez-Ramirez and co-workers applied this strategy for Pd NPs supported on carbon or TiO_2 by the addition of hexadecyl-(2-hydroxyethyl)dimethyl ammonium dihydrogen phosphate (HHDMA).[40] This heterogeneous catalyst exhibit selectivities comparable to those of the *Lindlar* catalyst in the semi-hydrogenation of a broad range of liquid alkynes, which can be attributed to a rather rigid adsorption of the additive over the Pd surface, thus reducing the

number of active sites (geometric effect) as well as the hydride coverage at the metal surface (electronic effect). With an increasing amount of HHDMA, the material showed an enhanced catalytic performance in terms of activity, whereas the high selectivity could be maintained.[41] This effect was ascribed to a change in the ligand adsorption configuration, as the flat layer of additive at low coverage blocking a large number of metal sites, changes into a three-dimensional configuration at higher additive amounts. This results in a lower fraction of Pd sites blocked by the organic layer. Another example highlighting the outstanding potential of additives as effective catalyst modifier was reported by Glorius and co-workers.[42] Addition of N-heterocyclic carbenes (NHCs) to an otherwise unreactive Pd@Al_2O_3 catalyst for the Buchwald-Hartwig amination of aryl halides resulted in a highly active catalytic system. A detailed structural analysis of the catalyst revealed a chemical binding of the NHC to the surface of the Pd NPs, therefore changing the steric and electronic environment of the supported heterogeneous catalyst. Hence, NHCs with the ability to donate electron density to the active metal, thus lowering the energetic activation barrier of the substrate, represent a promising choice of additives for improving the catalyst performance.

A major drawback of such heterogeneous systems is that the surfactant often loses its dynamics upon removal of solvents, resulting in a blockage of the active sites. Additionally, even though heterogeneous catalysts are well performing in catalysis, the general complexity of elucidating powders along with their high degree of inhomogeneity e.g. metal nanoparticle size, currently limits any further development on the correlation of their structural and electronic properties with performance. An elegant alternative for heterogeneous catalysts to study fundamental phenomena is the use of colloidal NPs, because crucial material properties such as particle size or the ratio of the active metal to the metal are precisely tunable by a concise adjusting of the reaction parameters. Studying the catalytic behavior of such model particles allows for a fundamental understanding of structure-performance relations. Furthermore, surfactants in monometallic colloidal systems still stay flexible and offer a wide spectrum of possible manipulations of the catalyst surface by coordinating agents. Working in solution also enables the application of a variety of analytical methods, such as liquid injection field desorption ionization mass spectrometry (LIFDI-MS) and NMR spectroscopy, identifying active species as well as oligomerization products. Hence, exploiting homogeneous, colloidal systems allows an alternative and innovative studies to disentangle the underlying catalytic mechanisms in contrast to industrially applied heterogeneous systems.

For colloidal NPs, various examples of utilizing different surfactants influencing their catalytic performance are reported in the literature to achieve an enhanced performance as well as

increased catalyst stability and recyclability. The spectrum of investigated additives ranges from NHC ligands, ionic ligands, sulfides to phosphanes. Glorius and co-workers showed that the reactivity regarding the hydrogenation of olefins catalyzed by colloidal Pd NPs can be tuned by the addition of coordinating and stabilizing NHC ligands bearing long alkyl chains at their backbone depending on the steric hindrance of the substrate.[43] Expanding the scope of additives with an NHC moiety, Prechtl et al. demonstrated that the formation of highly monodispersed Pd NPs stabilized by a nitrile-functionalized ionic liquid (IL) shows a high activity as well as selectivity in a multiphase system for a series of liquid alkynes.[44] Dupont and co-workers compared various ionic liquids as surfactants for Pd NPs, which showed an improved catalytic performance in terms of both activity and selectivity by using P- and N-containing ionophilic additives.[45] The authors explain the increased activity by the additional stabilization of the NPs by the functional groups coordinating to the metal surface, therefore preventing agglomeration and the formation of larger particles. Additionally, steric and/or electronic effects promoted by the P- and N-donating moieties favor an alkyne adsorption over the coordination of the alkene resulting in an increased selectivity towards the desired olefin.[46] Summarizing, ionic liquids have proved to be an effective media for the stabilization and solubilization of metal NPs during synthesis and catalysis, due to their coordination to the metal surface. The use of ionophilic ligands has been extensively studied as one effect is the inhibitions of leaching of the catalyst into the organic phase by this kind of ligands. The fixation of the metal NPs in the IL additionally allows for a catalyst recycling without significant loss of activity.[47]

Sulfides as surfactants have the benefit of strongly stabilizing the NPs, therefore resulting in very small and stable colloids. The introduction of either long alkyl chains or polar functional groups can generate colloids, which are either soluble in organic solvents or even in water. This approach offers a large field of possibilities and provides the opportunity to tune a catalytic system in an optimal way for several catalytic applications.[48] A study of colloidal Pt NPs stabilized by thiolate capping agents with varying steric demands emphasized the rather strong interaction of the additive with the metal surface. The authors found that a reduced ligand concentration leads to an increased catalytic activity in the semi-hydrogenation of liquid alkynes in polar solvents, while the particle stability could be maintained.[49] Moreover, a systematic investigation on the relation between the catalytic performance and the surface ligand density of thiolate capped Pd NPs showed a clear coherence between the amount of coordinated surfactants, the resulting diameter of the colloids and the catalytic activity for the isomerization of allyl alcohols.[50] A lower surface ligand coverage resulted in higher activities emphasizing the potential of an easy tunability of colloidal systems by the addition of simple

organic molecules in general. Follow-up investigations on this system also confirmed a high selectivity for the mono-hydrogenation of 1,4-dienes which highlights the versatile catalytic applications of such materials.[51,52]

Besides strongly binding sulfides, phosphanes with a weaker ability to bind to the metal surface have also attracted attention as surfactants for colloidal systems. Their ability to reversible coordinate to the metal surface without poisoning the catalyst surface, as well as the possibility to introduce a stereo- and chemoselectivity are interesting features to investigate. Beller et al. reported on a change of stereoselectivity in the semi-hydrogenation of alkynes from the respective E- to Z-alkenes upon addition of multidentate phosphane ligands using a monometallic Ni catalyst.[53] Mechanistic investigations revealed a fundamental difference of the catalytic mechanisms, as the hydrogenation resulting in the Z-alkene was identified as a heterogeneous process (catalyzed by the colloidal NPs), while the E-alkene was formed by a homogeneous catalytic cycle by the formation of a molecular Ni complex. Upon addition of the phosphane ligands, a homogeneous Ni-phosphane complex is formed, responsible for the high selectivity towards the E-alkene. This study shows the outstanding opportunities for a directed catalytic performance using coordinating surfactants. Beside tuning the catalyst stereoselectivity, also the chemoselectivity can be controlled by adding phosphanes. Yang, Li et al. reported on a highly selective nanoparticular Pd catalyst for hydrogenation reactions. Upon addition of PPh_3, the electron donating effect of the surfactant endowed the NPs with an electron-rich surface, greatly enhancing the hydrogenation of electrophilic substrates and suppressing the conversion of nucleophilic reactants. Therefore, this example nicely demonstrates the effect of small organic molecules such as PPh_3 on the catalytic activity and selectivity.[54] Nevertheless, the study lacks a deeper investigation on a series of similar additives bearing subtle differences regarding spatial and electronic features, which could give rise to new insights into the underlying mechanisms leading to an increased catalyst activity and selectivity. Investigations on the influence of additives require a colloidal system with flexible coordinating surfactants since such conditions enable a post-synthetic addition of various substrates without changing the NP size or synthetic procedure.

In order to elaborate the influence of the post-synthetic addition of a series of coordinating ligands on the catalyst performance, a colloidal NPs with weakly stabilizing, hence reversibly binding surfactants is desirable. Within such a system, the “original” surfactant needed for the colloid stabilization during NP synthesis can be replaced by a stronger binding ligand, which is added to the existing colloidal system. Hence, the use of ionic surfactants for the generation of small colloidal systems provides ideal preconditions for the systematic

investigation of the catalytic effect of additives. Such an easily adjustable colloidal system was reported by Coronado et al., presenting very small Pd colloids without a significant size distribution using tetraoctylammonium bromide $N(Octyl)_4Br$ as capping agent.[55] This system represents a perfect starting point for an evaluation of the influence of small molecules with small differences on the catalytic performance of a colloidal system in the semi-hydrogenation of alkynes.

1.3.2 Bimetallic nanoalloys for an enhanced selectivity

Apart from tuning the electronic properties and the accessibility of the active sites by the addition of a coordinating organic molecule, an alternative strategy is the alloying with a second, inactive metal, resulting in an enhanced selectivity towards the semi-hydrogenated product.[12] This well-known effect is already applied in industrial environment by exploiting the decreased activity of Pd alloyed with up to 80 % Ag for the semi-hydrogenation of residual acetylene in ethene-rich streams resulting in the formation of a solid solution structure.[56] The difference in electronegativities of these metals in combination with the differences regarding the electrons in the d orbital result in a novel electronic structure.[57] DFT calculations reveal that the increased selectivity originates from stability alteration of adsorbed acetylene and ethylene, whereas the activation barriers for hydrogenation was found to be metal-independent.[58] Hence, the tendency to adsorption of the two species are the decisive parameters for the potential activity and selectivity of the catalyst. Moreover, the introduction of an additional metal component leads to an uniform surrounding of the active sites.[59,60] The absence of neighboring active metal sites – the so-called *site isolation* concept – significantly limits the surface hydrogen supply, improving the selectivity towards the olefin. In addition, the isolation of Pd atoms leads to an improved catalyst life time since undesired oligomerization reactions and carbon deposition causing catalyst deactivation are suppressed.[59,60]

The theoretical study of Studt et al. in 2008 shed a new light on this strategy by screening about 70 different bimetallic compounds for methyl binding energies and identified several metal combinations as potential highly selective semi-hydrogenation catalysts (see Scheme 4).[12] Beside Pd-based metal combinations such as Pd/Zn and Pd/Ga, also Fe/Zn and Ni/Zn alloys turned out to be particularly interesting. Yet, further effects such as intrinsic stability, segregation progresses of supported NPs, the resistance to coking and poisoning by other molecules, sintering properties, size distribution and the ability to dissociate

hydrogen are equally important factors for an efficient semi-hydrogenation catalyst. Therefore, not all metal combinations identified by Studt et al. are suitable systems with an outstanding catalytic performance.[12] For example, Cu-based alloys turned out to rapidly deactivate.[61] Thus, catalysis experiments are required to verify the suitability of a given candidate material.

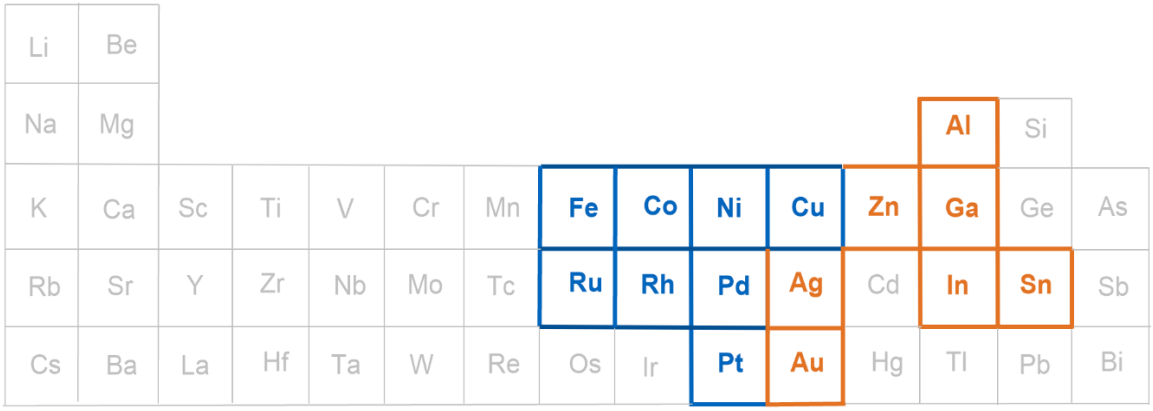

Scheme 4. Periodic system with metals for the semi-hydrogenation catalysis highlighted in blue (active metal) and orange (inactive metal). Metals not applied as semi-hydrogenation catalysts are marked in grey.

As already introduced, different metal alloy combinations may be potential candidates for a high-performance semi-hydrogenation catalyst, highlighted in Scheme 4. These combinations were identified and evaluated in the theoretical study of Studt et al.[12] The site isolation of the active sites (blue, transition metals) by inactive metals (orange, mainly main group metals) results theoretically in an increased selectivity towards the olefin, while the activity is maintained. With focus on Pd-based metal alloys, the industrially applied combination of Pd/Ag (forming a solid solution) and also other combinations like the solid solution of Pd/Zn and Pd/Ga (forming Hume-Rothery phases) showed interesting characteristics in this DFT study. Consistent with this theoretical study, experimental data shows moderate selectivities for monometallic Pd catalysts, while the system of Pd/Ga is outstanding in terms of both activity and selectivity. In general, metal combinations of a transition metal with a main group 13 metal results in the formation of so-called Hume-Rothery phases, which structures are dependent on the valence electron concentration. Continuous alloying of the transition metal with the group 13 metal results in a higher electron concentration and hence in higher occupied energy levels. At a certain electron concentration, a change of the crystal structure into a more energetically preferred one is obtained. This allows for different structures depending on the metal/metal ratio, hence enabling a detailed study on the influence of the electronic and geometric environment of the active metal on the catalytic performance. Studt et al. also identified other, more cost-efficient metal alloys as promising candidates such as the Fe-based combinations Fe/Zn and Fe/Al. In the following

section, current experimental and theoretical studies on the two metal combinations Pd/Ga and Fe/Al will be put in focus.

The bimetallic system of Pd/Ga is one of the promising materials for the acetylene conversion to ethylene, as this metal combination was not only theoretically computed but investigated experimentally and proved to exhibit an exceptional catalytic performance. First studies on the PdGa bulk phase showed that the isolation of the active metal Pd by Ga in combination with a covalent bonding to stabilize the desired geometry under reaction conditions resulted in an enhanced catalytic properties compared to a pure Pd catalyst.[62–64] A direct comparison of the PdGa and Pd_3Ga_7 bulk phase revealed that both catalysts exhibit a higher activity, selectivity as well as long-term stability in the acetylene semi-hydrogenation compared to the industrial $PdAg@Al_2O_3$ catalyst.[65] More precisely, Pd_3Ga_7 possesses a crystal structure where the palladium atoms are exclusively surrounded by Ga atoms. Therefore, the authors suggest that the high selectivity and stability of the tested catalyst can be assigned to the active-site isolation in the crystallographic structure of Pd-Ga intermetallic compounds resulting in weakly π-bonded acetylene molecules on top of isolated Pd atoms. Additionally, this modification of adsorption and desorption properties and the absence of Pd hydrides further provide a high selectivity towards the olefin.[66,67]

To further enhance the catalytic activity of Pd/Ga intermetallic compounds, several approaches for the synthesis of well-defined bimetallic nanoparticles have been investigated. In 2011 Armbrüster et al. reported on single-phase PdGa and Pd_2Ga NPs deposited on Al_2O_3 as support in a two-step synthesis by co-reduction of ionic metal precursors.[68] The initially formed Pd NPs mediate a reduction of Ga(III) on the NP surface during an additional annealing step via Pd-activated hydrogen. Coagulation of the elemental Ga is inhibited by the exclusive formation of Ga(0) on the Pd surface resulting in intermetallic phases. Comparison of the nanoparticular Pd/Ga phases with the respective bulk materials in the semi-hydrogenation catalysis of acetylene shows a multifold increase in activity by downsizing the catalyst to the nano regime, whereas the selectivity towards the olefin is preserved. Changing the Ga(III) precursor from $GaCl_3$ to Ga(III) stearate also results in intermetallic Pd_2Ga NPs but associated with an amorphous network of Ga_2O_3 emphasizing the high influence of the starting materials on the resulting catalytic system.[69] Another bimetallic Pd/Ga based catalyst for the semi-hydrogenation of acetylene was reported by Schlögl and co-workers by using a hydrotalcite-based material as precursor.[70] Co-precipitation of the respective metal nitrates (Pd(II), Mg(II) and Ga(III)) yielded a catalyst precursor with the composition $(Mg_{0.7-x}Pd_x)Ga_{0.3}(OH)_2(CO_3)\cdot m\times H_2O$. In a second step, Pd NPs were obtained under reducing conditions and upon a further increase of temperature, partial reduction of Ga species on the

metallic Pd surface leads to the formation of Pd_2Ga NPs supported on $MgO/MgGa_2O_4$. Due to the high dispersion and structural integrity of the NPs, the catalytic properties in the acetylene semi-hydrogenation were found to be superior in terms of activity compared to a bulk Pd_2Ga sample.[70] Nevertheless, mechanistic studies revealed a dynamic change of the active species during catalysis since a surface metal segregation of the Pd_2Ga NPs into Pd-rich surface species and Ga_2O_3 was observed. Hence, the authors suggest the active state of the final catalyst to be a Pd_2Ga core – $Pd/PdC_x/Ga_2O_3$ shell configuration.[71] This example emphasizes that Pd-based intermetallic hydrogenation catalysts can be prepared in a feasible and controlled manner to give nanostructured materials. However, the well-known catalytic properties of the bulk intermetallic phases can only partly be retained. Instead, surface dynamics in reactive atmospheres result in a great complexity in terms of the structure of the resulting bimetallic material.

Apart from Pd-based semi-hydrogenation catalysts, alternative metal combinations were identified to be promising candidates for this reaction type.[12] In general, replacing noble metals by low-cost substituents has driven scientific and industrial research efforts for many years. With special regard to ubiquitous iron (Fe), catalysts require very high H_2 pressures and temperatures to be active in the hydrogenation of unsaturated C-C bonds, but only show a limited selectivity in the semi-hydrogenation.[72,73] Nevertheless, these drawbacks can be addressed by taking advantage of the site-isolation concept applying structurally well-ordered intermetallic compounds. The dilution of Fe as principally active, abundant and low-cost metal with an inactive metal might result in not only an active and selective semi-hydrogenation catalyst, but also in the possibility to strongly reduce the costs for such bimetallic systems (see Scheme 4). Only very few reports on the application of intermetallic (nano-) Fe/Al phases for the selective semi-hydrogenation of alkynes exist in literature. Guided by this site-isolation concept, the intermetallic compound $Al_{13}Fe_4$ was presented as efficient and selective catalyst for the hydrogenation of acetylene to ethylene.[74] The monoclinic structure of this intermetallic compound includes Fe atoms solely coordinated by Al atoms as well as Fe-Al-Fe species located in the cavities of the three-dimensional Al framework, thus resulting in an encapsulation of the active metal sites (see Figure 1).[75,76]

Comparison of the $Al_{13}Fe_4$ intermetallic phase with a commercial $Pd/Ag@Al_2O_3$ catalyst showed a comparable catalytic performance in acetylene semi-hydrogenation, with a similar activity (20 h time on stream at 200 °C, 95 % vs. 80 %) and only a slightly decreased selectivity (88 % vs. 82 %). This example demonstrates the possibility to tailor the catalytic properties of abundant and cheap 3d transition metals with p-elements by the formation of bimetallic materials.

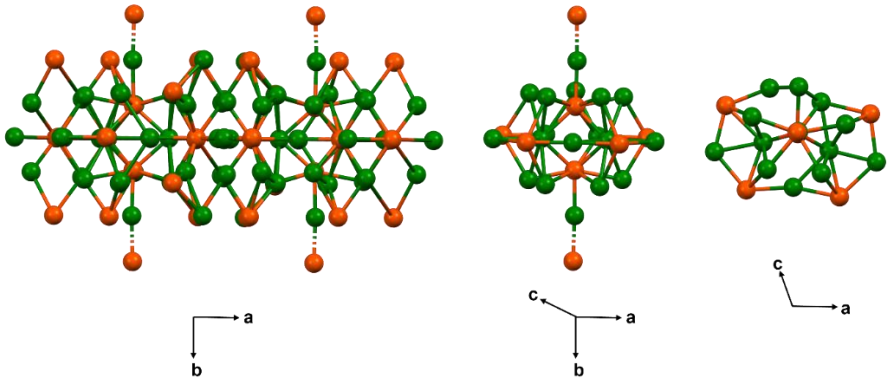

Figure 1. Unit cell (left) and selected parts (middle and right) of $Al_{13}Fe_4$ emphasizing the structurally isolated Fe-Al-Fe units (Al, green; Fe, orange).[74,76]

1.4 Synthesis strategies for colloidal systems

Most studies dealing with the semi-hydrogenation catalysis of alkynes focus on heterogeneous systems as they offer advantages like an easy catalyst preparation and the possibility of recycling. Nevertheless, the co-precipitation of commercial metal salts on a support with subsequent calcination often requires harsh conditions (e.g. high temperatures) in order to obtain metallic (alloy) NPs. This results in rather large particle sizes and size distributions. Hence, milder reaction conditions would be beneficial. Colloidal NPs are an attractive alternative to classical heterogeneous catalysts, as such systems do not require high temperatures leading to less agglomeration processes and therefore often smaller NP sizes. Starting from easily reducible metal precursors, the colloids are formed in a "bottom-up" approach by the growth of nuclei and stabilized in solution by coordinating organic surfactants.[37] The introduction of different electronic and steric features to these ligands can be further used to influence and optimize the NPs´ reactivity. Additionally, keeping the NPs in solution offers novel, solution-based analysis techniques such as mass spectrometry or NMR, thus enabling the study of chemical processes in solution during the particle formation or catalytic runs.

Several examples of mono- and bimetallic colloids for catalytic applications have been reported so far. Various NP structures can be obtained depending on the synthesis methodology. For instance, core-shell structures, nanoalloys as well as mixed phases of the metals can be synthesized.[37] Inspired by the commercial Pd/Ag catalyst, Kiwi-Minsker and co-workers investigated bimetallic Pd/Ag colloids, which were prepared by chemical reduction of the second metal on pre-formed Pd colloids stabilized by a polymer.[77] The NPs showed a Pd-core and Ag-shell structure. With the same synthetic strategy, they also

obtained Pd/Cu nano-sized catalysts, however, resulting in an alloy structure. This emphasizes that the obtained structures are not only dependent on the synthesis procedure but also on the choice of the metals. Both colloids showed a significant increase in the selectivity at full conversion for the selective hydrogenation of unsaturated alcohols. Another preparation of core-shell Pd@Ag NPs is the deposition of Ag on Pd colloids by the reduction of $AgNO_3$ with ascorbic acid which revealed a catalyst system with excellent alkene selectivities in the semi-hydrogenation of 1-octyne under mild conditions.[78] For high Ag contents, over-hydrogenation of the olefin was prevented, whereas Pd-rich NPs showed some degree of alkane formation. This difference in selectivity was attributed to the complementary relation between Pd and Ag derived from the core-shell structure.

Along these lines, it becomes obvious that the synthesis of colloidal mono- and bimetallic systems is a challenge and that each metal system requires unique parameters for successfully obtaining nano-sized and stable colloidal solutions. The choice of metal precursor, reducing agent, solvent, temperature, and stabilizing surfactants determines whether the particles stay in solution or agglomerate, mostly accompanied by undesired particle precipitation. With special regard to bimetallic colloids, a control of the colloidal structure can be obtained by an adjustment of the synthesis parameters, leading to either nanoalloys, core-shell structures or intermetallic nano-phases. Depending on the redox potentials of both metals, the choice of the metal precursors is also of utmost importance. Therefore, in the following section a deeper insight in the possibilities of the synthesis regarding colloidal systems will be given.

1.4.1 Monometallic systems

For the synthesis of monometallic colloidal systems, most reactions proceed via the reduction of the respective metal salt precursor in a bottom-up approach. The choice of reducing agent, solvent and reaction parameters is of utmost importance to obtain a stable colloidal system. These parameters have to be chosen wisely depending on the formation mechanism. It is generally known that colloids are formed by initial nucleation, further growing to NPs by Ostwald ripening.[37] The final size of the colloids is thus determined by the number of nuclei initially formed, which can be influenced by the temperature and the addition of the reducing agent. At some point, the metal precursor is completely consumed. A further undesired particle growth induced agglomeration process can be prevented by the use of stabilizing agents.

Stabilizing agents, most prominently surfactants, are required to prevent agglomeration and precipitation of the NPs in solution.[79] Typical surfactants are alkyl sulfides, polymers, dendrimers, surface-active ionic liquids or carboxylates exhibiting long alkyl chains to stabilize the colloids either sterically or electrostatically.[22,37,49,55,80] Such organic ligands are capable of providing control over the core size of the colloids during the synthesis and improve the stability as well as solubility of the NPs.[81] Coordination of the surfactant and the formation of as layer on the NP surface can not only lead to a stable colloid solution but also can decrease the catalytic activity, depending on the coordination strength between particle and surfactant.[49,82] For instance, such catalyst poisoning is often observed with sulfides forming covalent bonds to the metal surface.[81] This class of surfactants has been the most popular choice for protecting organic monolayers on the NP surface, owing to the high stability of thiolate-capped NPs enabling an isolation with the opportunity to re-dissolve the colloids without any agglomeration.[50,83] Nevertheless, alkanethiols as surfactants are often reported as poisons to metal NP surfaces which can be attributed to the strong affinity of thiols to noble metals.[84] The strong bonding between the RS^- group and the electrophilic NP surface results in a covalently linked surfactant, decreasing the number of surface atoms available for catalysis.[79,85]

One of the most studied types of steric stabilization agents are polymers stabilizing colloids by ligation of the metal surface and physically occupying space around the NPs, thereby sterically inhibiting direct contact between the colloids.[79,86] The most studies report on poly(vinylpyrrolidone) (PVP) and poly(vinylalcohol) (PVA) as surfactant. They only require a critical amount of polymer, whereas the addition of higher amounts does not lead to an improved stabilization.[87] Even though PVP stabilized colloids have been generally shown to be active in several catalytic reactions (e.g. hydrogenations[22,88]), the polymeric coordination often results in steric blocking of the metal surface atoms compromising the catalytic activity.

The catalytic effect of post-synthetic added coordinating agents in colloidal systems can be exploited most efficiently if the surfactants applied in the colloidal synthesis exhibit rather weak and dynamic coordination behavior. Instead of the formation of an irreversible layer on the metal surface (e.g. observed with sulfides or polymers), a flexible and tunable system is advantageous.[79] Hence, small organic ligands are gaining more attention as NP stabilizers, owing to their highly promising potential of forming a well-defined system with spatial control in surrounding environments of reactive surfaces. Tetraalkylammonium salts with long alkyl chains have therefore been identified as promising surfactants for such systems.[55] They stabilize the electrophilic metal surface by coordination of the anion providing an electrostatic stabilization, whereas the sterically demanding cation further contributes to the stability by

expanding the diffuse layer of ions around the NP, and hence increasing the thickness of the protecting layer.[89] Due to the ionic nature of this stabilizing approach, post-synthetic modification by other additives, also coordinating to the metal surface, becomes feasible without a destabilization of the colloids. Therefore, such monometallic, ionically stabilized colloidal systems seem to be a promising starting point for an investigation of the influence of a series of additives with marginal differences regarding spatial and electronic features on the catalytic performance and could give rise to new insights into the underlying mechanisms responsible for catalyst activity and selectivity.

1.4.2 Bimetallic systems

In contrast to widely studied monometallic colloids, the synthesis of bimetallic systems is rather challenging and more complicated. First, there are different possibilities for the formation of bimetallic structures. Depending on the choice of metal and reaction conditions, core-shell structures, nanoalloys or intermetallic phases can be formed.[37] Nevertheless, a direct control over the nature of the bimetallic particles is difficult. Second, keeping both metals in solution is not trivial since metal oxides are easily formed which tend to precipitate. Hence, working under inert conditions to prevent metal oxidation and choosing the right metal precursors is of high relevance. While monometallic systems can easily be synthesized by the reduction of a metal salt in combination with a surfactant, these precursors are mostly not convenient for the formation of bimetallic colloids since the redox potential of both metal precursors have to be similar. If this is not the case, the metals will not form a bimetallic system but rather two monometallic phases.

Many reports deal with the synthesis of bimetallic NPs consisting of metals with similar redox potentials. Therefore, the approach of a co-reduction of both metals is feasible. Kitagawa et al. pursued an interesting approach by mimicking one transition metal by the alloy of its two neighboring metals, leading to so-called “pseudo-elements”.[90,91] Using a bottom-up chemical reduction method, these systems are successfully prepared over the whole composition range resulting in solid-solution NPs. The group reported on three different metal combinations stabilized by PVP, namely Rh_xAg_{1-x} (“pseudo-Pd”),[90] Pd_xRu_{1-x} (“pseudo-Rh”)[92] and Au_xIr_{1-x} (“pseudo-Pt”),[93] which all showed entirely new or superior catalytic properties compared to the corresponding bulk metals. Hence, these bimetallic colloids can rather be interpreted as a composite of both metals than a simple mixture. The solid solution NPs were tested for various applications and compared to the corresponding mimicked transition metal.

With special attention to Rh_xAg_{1-x} as "pseudo-Pd", the hydrogen storage capacity of the NPs among the whole composition range showed a maximum at $Rh_{0.5}Ag_{0.5}$ with an electronic structure similar to Pd.[94] Notably, neither bulk Ag nor Rh exhibit a hydrogen storage ability, highlighting the fascinating material properties resulting from a strong interaction of both metals.

In contrast to the examples of Kitagawa and co-workers, metal combinations with different redox potentials cannot be synthesized by a simple approach of co-precipitation. This applies, for example, for the Pd/Ga system. The difference in redox potentials of Ga(III) and Pd(II) complicates a co-nucleation of both metals. Ga(III) salts as strong Lewis acids tend to form stable complexes with electron donors, hindering the reduction to Ga(0). Starting from the elemental metals themselves, a controlled synthesis of nanostructured materials is challenging due to the low melting point of Ga at 29 °C, as a coagulation of the liquid metal is often observed.[95] For a successful co-reduction of these two metals, the choice of the right reduction temperature as well as reducing agent and solvent is of high importance. Hence, finding optimal reaction conditions for bimetallic NPs requires the development of novel synthesis strategies. Behrens and co-workers reported on the reduction of $Pd(acac)_2$ (acac = acetylacetonate) in the presence of $Ga(butyl)_3$ by transmetalation. This approach resulted in monometallic Pd colloids with an organic Ga(III) matrix.[96] Post-synthetic heterogenization by Al_2O_3 as support with a calcination process at high temperatures resulted in PdGa NPs due to the reduction of the Ga on the Pd surface. Nevertheless, this example emphasizes the difficulties obtaining a truly colloidal bimetallic system. So far, there were no examples reported in literature on colloidal Pd/Ga NPs.

An elegant way for the synthesis of bimetallic colloids was first reported by Fischer et al., where the authors introduced a versatile one-step wet chemical precursor route to nanocrystalline Ni/Al particles in solution. The reaction of $[Ni(cod)_2]$ (cod = cyclooctadiene) with $[(AlCp^*)_4]$ yielded colloidal Ni/Al NPs, where a free variation of the Ni/Al ratio was possible.[97] The use of precursors exhibiting weakly coordinating or "all-hydrocarbon" ligands is favorable as they enable an easy ligand exchange and the formation of bimetallic cluster compounds. Furthermore, the adjustment of the reaction conditions is substantial as the reactivity strongly depends on the precursor ratios, temperature, and solvent. For instance, the use of another Al source, $[AlH_3]—NMe_3$, did not yield in a colloidal system but in a complete precipitation of the respective Ni/Al phase. Hence, mild reagents like $[(AlCp^*)_4]$ slowly co-decompose with the second metal precursor, therefore resulting in a soluble, bimetallic system. This approach was further extended to the Co/Al system. The reaction of $[Co(\eta^4\text{-}C_8H_{12})(\eta^3\text{-}C_8H_{13})]$ with $[(AlCp^*)_4]$ giving intermetallic β-CoAl NPs in solution emphasizes

that the wet-chemical route to bimetallic alloys under mild reaction conditions results in a true alloying of the applied metals.[98] Janiak et al. combined the strategy of organometallic precursors as starting materials with the use of ionic liquids as solvent and stabilization agent. In this study, they reported on the successful synthesis of colloidal Ni/Ga NPs by the targeted decomposition of organometallic precursors.[99] Microwave-induced co-pyrolysis of all-hydrocarbon ligand precursors [$Ni(cod)_2$] and GaCp* (Cp* = pentamethyl cyclopentadienyl) in ILs selectively yielded the intermetallic nano-sized phases NiGa and Ni_3Ga. The intrinsic particle stabilizing properties of ILs are supposed to be responsible for the homogeneous composition, high crystallinity, and small size distribution of the colloids. Depending on the metal sources, solvents and reaction conditions, the authors either observed a mixture of amorphous Ni/Ga phases or single-phase NiGa and Ni_3Ga colloids highlighting the sensitivity of such bimetallic systems. The good catalytic performance of these materials in the semi-hydrogenation of 1-octyne further confirmed the concept of alloying the active metal with an inactive one in order to increase the selectivity.

Up to now, only very few reports on abundant intermetallic nano-sized Fe/Al materials exist in literature. Most studies are based on the investigation of bulk materials, mostly top-down synthesized by a simple ball milling of both metals.[75,100,102,103,104] Literature on nanoscale aluminide powders is mostly based on laser evaporation/condensation techniques.[105] These techniques provide no access to materials with a precise composition, morphology or selected size. First attempts regarding the synthesis of nanoparticular Fe/Al structures by a wet-chemical approach were reported by Dutta et al. for the reduction of $FeCl_2$ with $LiAlH_4$.[106] Fe/Al NPs were synthesized under harsh conditions yielding large particle sizes around 20 nm with a broad size distribution. Using the same metal precursors but under milder reaction conditions and with ionic liquids as reaction medium, Schmitz et al. could show the formation of a crystalline, but not nano-scaled FeAl phase.[107] Nevertheless, by changing the metal precursors to [$LiFe(btsa)_3$] (btsa = bis(trimethylsilyl)amide) and $LiAlH_4$, FeAl NPs with a size of 10 nm were observed. Due to the high sensitivity of Fe/Al towards oxygen, all obtained particles were fully oxidized according to XPS measurements. Using [$Fe(CO)_5$] and [$(AlCp^*)_4$] instead, leads to the formation of nano-sized $FeAl_2O_4$ material. These examples emphasize the challenges for the synthesis of small, colloidal Fe/Al nanoparticles. Not only the choice of the right precursors, but also the reaction medium and reaction conditions are crucial factors. Due to a favored oxidation of iron aluminide NPs upon exposure to only traces of oxygen, preserving the stability of the colloids is also challenging.

2. Goal of this PhD project

In this PhD project, an investigation of selected catalyst systems for the semi-hydrogenation of alkynes is presented. Along the different strategies for an enhanced catalytic selectivity towards the olefin, mono- and bimetallic NPs are examined (see Scheme 5). The evolution a deep understanding of the fundamental mechanism to control the selectivity of colloidal systems by testing various parameters is the goal of this work. Guided by the two approaches of an increased selectivity, namely the additive approach for monometallic systems and the site-isolation principle for bimetallic systems, the aim is to develop synthesis strategies and optimize the parameters in order to obtain NPs with the desired features is pursued. The focus on colloidal systems enables a precise adjustment of the particles' features. Additionally, testing these catalytic systems in the semi-hydrogenation of liquid alkynes is expected to unravel a clear connection between catalyst characteristics and its catalytic performance.

Starting with a monometallic and therefore intrinsically unselective Pd-based system, the influence of several additives on the activity as well as the selectivity will be investigated. The comparison of various σ-donating surfactants bearing subtle differences in terms of sterics and electronics can lead to a better understanding of the required properties of an additive for the desired catalytic features. Hence, choosing the right colloidal system is important. A flexible interaction of surfactant and metal surface is beneficial, enabling a post-synthetic addition of σ-donor agents. Therefore, studying colloidal Pd NPs with the ionic capping agent $N(Octyl)_4Br$ is a good starting point for a deeper investigation on various additives. This colloidal system itself is well-known in literature[55] but was not tested in catalysis so far. Moreover, thiolate stabilized Pd colloids will be investigated as well.[51] Hence, the first chapter of this PhD thesis deals with monometallic Pd-based colloidal systems, with the focus on optimizing the reaction conditions for the semi-hydrogenation catalysis and choosing reasonable additives.

In a second part of this thesis, colloidal Pd-based bimetallic systems are investigated. Going in line with promising literature-reported heterogeneous systems,[62,108,109] Ga as second, inactive metal was chosen. A simple co-reduction of commercial Pd(II) and Ga(III) salts is not expedient, as this requires high temperatures and does lead not to colloidal nanoalloys but to the precipitation of bimetallic powders.[96] Over many years, our group's research program has been focusing on the synthesis of metal-organic mixed metal materials in solution consisting of group 12 and 13 metal species [ECp*] with transition metals. This provides an elegant tool for controlled TM-E bond formation to eventually yield molecular alloys of the general formula $[TM_aE_b](L)_n$ (typically n = b).[110] With special regard to the Pd/Ga system,

studies have shown that by the reaction of $[Pd_2(dvds)_3]$ (dvds = 1,3-divinyl-1,1,3,3-tetramethyldisiloxane) with GaCp*, the product formation strongly depends on the reaction conditions. For instance, depending on the metal precursor ratios and reaction conditions, such as temperature and solvent, the isolation of the dinuclear $[Pd_2(GaCp^*)_2(\mu_2\text{-}GaCp^*)_3]$ and the trinuclear $[Pd_3(GaCp^*)_4(\mu_2\text{-}GaCp^*)_4$ cluster were reported.[111] Therefore, under slightly changed reaction conditions, $[Pd_2(dvds)_3]$ and GaCp* as precursors seem suitable candidates for a well-defined nanoparticle synthesis as they are self-assembling in a broad scope of desired Pd/Ga ratios and decompose upon loss of their organic shell in toluene at elevated temperatures under inert conditions. These simple metal-organic precursors can serve as the starting material for bimetallic colloids by adjusting the reaction parameters precisely.

This colloidal Pd/Ga system will then be further studied upon the post-synthetic addition of various surfactants. Here, the focus is not only on the influence on the catalytic performance but also on the stability of the bimetallic colloids. With special regard to the particle stability at ambient conditions, additives with the ability to prevent colloid decomposition upon exposure to air will be chosen.

Finally, selecting the abundant metals Fe and Al as a bimetallic semi-hydrogenation catalyst alternative will require a pursuing development of suitable synthesis strategies. Apart from literature known top-down synthesis of generating Fe/Al systems by the reaction of Fe and Al powders in a ball mill, only few examples on wet-chemical approaches are reported. According to our approach of using organometallic precursors with labile protecting ligands, we intend to investigate the reaction of $[Fe_2(mesityl)_4]$ with $[AlH_3]{-}NMe_3$ as promising metal precursors at mild conditions. In contrast to the preferential use of [ECp*] precursors as mild reaction agents, e.g. applied for the Ga-based systems, starting with [AlCp*] seems not reasonable due to the high affinity to the formation of stable Fe-Cp* species[112,113], thus not resulting in a bimetallic system. Hence, $[AlH_3]{-}NMe_3$ will be chosen as Al source. Beside the challenging optimization of synthesis parameters, the exceptional high oxophilicity of both metals not only requires adjusted working methods but also significantly complicates a detailed analysis. The obtained material will then not only be intensively studied in terms of materials characteristics but also in the semi-hydrogenation catalysis of liquid alkynes. The herein gained knowledge on bimetallic, abundant catalysts will lead to the development of further optimizations in future studies.

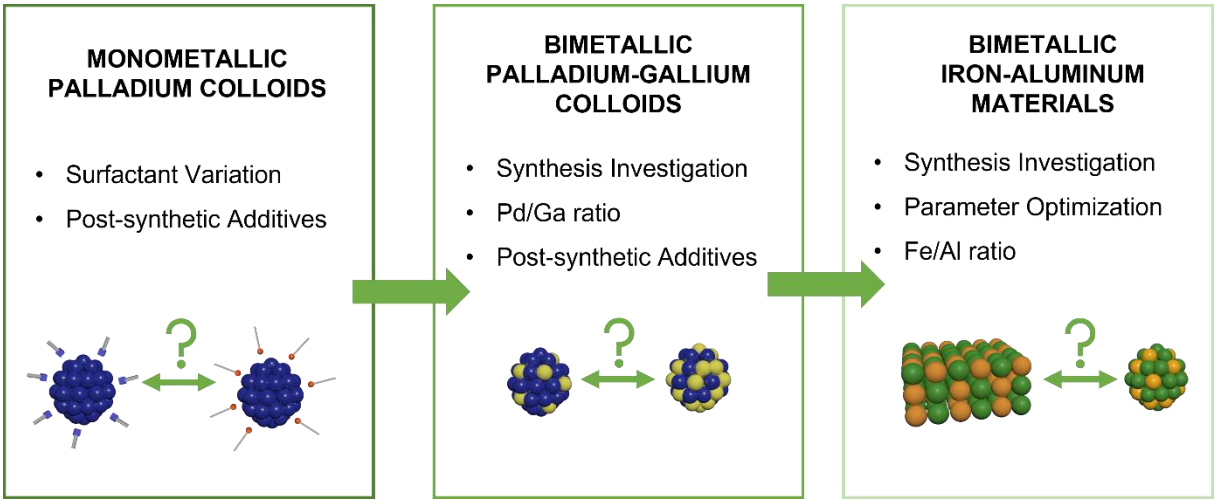

Scheme 5. Outline of this PhD project showing all different projects, starting with the investigation of monometallic Pd colloidal NPs and the influence of post-synthetic additives (left), the development bottom-up synthesis strategies for bimetallic Pd/Ga colloids (middle) and the analysis of Fe/Al materials (right) obtained from an organometallic synthesis approach.

3. Results and Discussion

3.1 Monometallic colloids

Reports on highly selective, un-alloyed heterogeneous metal catalysts are uncommon; in the existing reports additives are used for altering the surface properties of the catalyst. A study of the ligand effect on the surface and hence, on the control over selectivity for this reaction can easier be investigated in solution; for this reason, colloidal metal nanoparticles are convenient case study models. To date, there is only a handful of reports on colloidal, single metal NPs for semi-hydrogenation. The existing examples are isolated cases and thus hardly comparable. There is a need for a systematic study of the parameters, which influence the selectivity of colloidal metal NPs for the abovementioned reaction.

Scientific Issues

In this chapter, the focus is set on (intrinsically unselective) monometallic Pd catalysts and the influence of 1) the adjustment of the reaction conditions and 2) the post-synthetic addition of coordinating surfactants. Therefore, different literature-reported synthesis protocols for Pd colloids as well as various additives are tested. Following questions will be addressed:

a) Thiols as strongly coordinating ligands are known to stabilize colloids in an effective way. Is it possible to take advantage of this stabilization and additionally influence the catalytic performance? Does the organic moiety of the thiol affect the activity and selectivity of the respective catalyst?

b) Does the application of weaker, ionic stabilized Pd colloids in the semi-hydrogenation reaction of alkynes result in a stable catalytic system? Can a monometallic system already obtain good activity and selectivities by a systematic parameter optimization?

c) Do weakly stabilized Pd colloids allow for a systematic investigation of post-synthetic additives on the catalytic performance? If yes, which crucial factors (with special regard to steric demand and σ-donoring ability) are necessary to boost the catalytic performance?

3.1.1 Thiolate-capped Pd colloids

Synthesis and Characterization of thiol stabilized Pd colloids

Inspired by the work of Shon and co-workers[48,51,52,81,114], the synthesis of very small thiol-capped Pd colloids was investigated. The reaction of the precursor $K_2[PdCl_4]$ with aqueous $NaBH_4$ in the presence of two different sodium S-alkyl thiosulfates NaS_2O_3R (R = dodecanoyl, 2-phenylethanyl) in toluene lead to colloidal Pd NPs. These two surfactants were chosen since both prevent particle agglomeration by the formation of a metal-thiol bond but exhibit different steric hindrance and electronic features due to the varied alkyl chains.

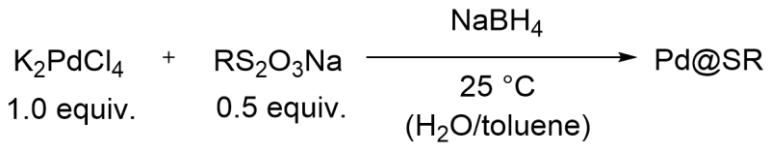

Scheme 6. Reaction of a Pd(II) precursor with $NaBH_4$ as reducing agent and sodium S-alkyl thiosulfate surfactants leading to small thiol-capped Pd colloids.

The particle sizes were analyzed by dynamic light scattering (DLS) measurements (see Figure 2) with sizes of 3.3 ± 0.4 nm for the dodecane thiol-capped and 4.6 ± 0.7 nm for the phenylethane thiol-capped particles, respectively (see Figure 2 and Scheme 6).

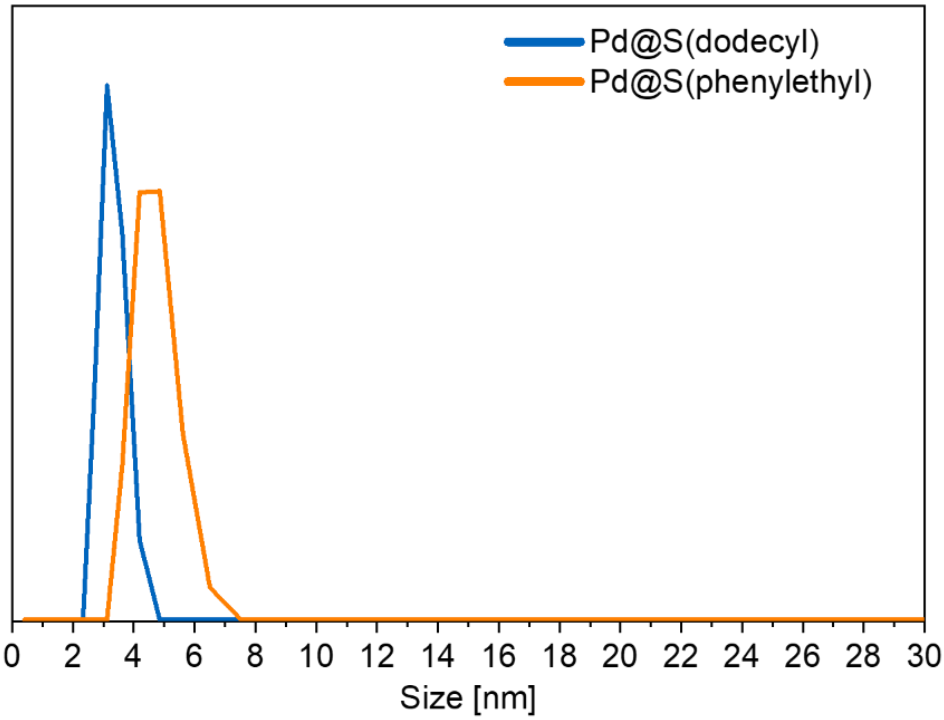

Figure 2. DLS measurements of thiol-capped Pd colloids.

The size determination with this method is based on the intensity fluctuations of the scattered light at the NPs in solution. The hydrodynamic radius of the particles is then calculated by the Einstein-Stokes equation. This method is suitable for a fast and easy size determination and size distribution of the solubilized colloids but does not give any information about the shape of the NPs. Here, transmission electron microscopy (TEM) would be required.

Catalytic performance of thiol-capped Pd colloids in the alkyne semi-hydrogenation

The thiol-stabilized Pd colloids were further tested in the semi-hydrogenation reaction of 1-octyne. Conversion and selectivity of the semi-hydrogenation catalysis with 1-octyne as substrate were quantified by GC-FID analysis. Nevertheless, despite the very small size of the colloids, catalysis experiments with various reaction parameters only showed a minor activity in the semi-hydrogenation reaction of 1-octyne (see Table 1) with the highest conversion of 41 % after 24 h reaction time (see Table 1, Entry 6). All other catalysis runs showed even minor conversions (see Table 1, Entries 1-5). This might be attributed to the strong bond of the surfactant to the metal surface, thus poisoning and therefore inactivating the catalyst.[50]

Comparison with a literature-reported study on thiol-capped Pt colloids in the (semi)-hydrogenation reaction of terminal and internal alkynes under similar, mild conditions (1 bar H_2, 25 °C), shows a similar trend with a strongly decreased catalyst activity.[52] For higher conversion rates, substrates with functional activating groups were required facilitating the coordination to the metal surface by *p*-orbital interaction.

Table 1. Semi-hydrogenation catalysis of 1-octyne in toluene using 1 mol% thiol-capped Pd colloids after 24 h reaction time. The amount of PPh_3 is referred to the Pd amount.

Entry	Catalyst	Temperature [°C]	p(H_2) [bar]	Post-synthetic additive	Conversion [%]	Selectivity [%]
1	Pd@S(dodecyl)	0	0.5	-	5	40
2	Pd@S(dodecyl)	0	0.5	1.0 equiv. PPh_3	4	43
3	Pd@S(dodecyl)	25	0.5	-	16	13
4	Pd@S(phenylethyl)	0	0.5	-	6	83
5	Pd@S(phenylethyl)	25	0.5	-	41	42

Additionally, even at very low conversions and mild conditions, the selectivity towards the olefin is low with a maximum of 83 % (but only a conversion of 6 %, see Table 1, Entry 4). The post-synthetic addition of a σ-donoring additive, namely PPh_3, lead to no change in the

colloid reactivity (see Table 1, Entry 2). This clearly shows that a partial replacement of the thiol by another donor (here PPh_3) is not possible and hence does not influence the catalytic performance of thiol-capped colloids.

Concluding from these experiments, thiol-capped Pd colloids did not show the desired features for an active, selective, and easily tunable catalytic system. In addition, no improvement by a post-synthetic addition of a potentially coordinating additive was achieved. This might be attributed to an inhibited coordination of the additive, as the interaction of the thiol-based surfactant with the metal surface is too strong and provides no space for another substrate to coordinate. This also explains the rather low activity of the colloidal system without any additional ligands, as also here the alkyne might not be able to coordinate to the metal surface in an effective way resulting in a low conversion. Additionally, despite the low activity, mainly the full-hydrogenated substrate is observed, indicating an intrinsically low selectivity. Due to all these findings, no further investigations were performed on these systems.

3.1.2 Weakly stabilized Pd colloids

Preface

In this chapter, the study on Pd-based monometallic colloids in the semi-hydrogenation and the effect of additives on the catalytic performance is continued. Therefore, a colloidal system with a flexible ionic surfactant was chosen, thus allowing other agents to coordinate to the metal surface. Such a flexibility was not given with the thiol-capped NPs, as the rather strong interaction of the surfactant with the colloidal surface inhibits the coordination of other substrates. Hence, the literature-known Pd@N(Octyl)$_4$Br system[55] was selected for systematically testing steric and electronic effects of different coordinating agents in order to learn more about the crucial parameters for controlling the selectivity of the reaction. Additionally, studying the stability of the colloids in solution and the interactions of the ligands with the particle surface are interesting parameters for a comprehensive understanding of the major factors for an active, selective and stable monometallic catalytic system.

Parts of this chapter were published in the Journal *ChemCatChem* the article entitled “Steric and Electronic Effects of Phosphane Additives on the Catalytic Performance of Colloidal Palladium Nanoparticles in the Semi-Hydrogenation of Alkynes”. In a collaboration with the Chair of Physical Chemistry (TU Munich) and the Regional Center of Advanced Technologies and Materials (RCPTM), the catalytic effect of the post-synthetic addition of phosphanes to a catalytic system of colloidal Pd NPs stabilized by the ionic surfactant N(Octyl)$_4$Br was investigated. The XPS data were fully collected and analyzed by Tim Kratky, whereas the HR-TEM images were detected by Ondra Tomanek. The contributors are listed in the reference:

L. Staiger, T. Kratky, S. Günther, O. Tomanek, R. Zboril, R.W. Fischer, R.A. Fischer, M. Cokoja *ChemCatChem* **2021**, *13*, 227-234.

Synthesis and Characterization of Pd@N(Octyl)$_4$Br colloids

Reduction of the precursor $K_2[PdCl_4]$ with an excess of aqueous $NaBH_4$ in the presence of $N(Octyl)_4Br$ surfactant yielded colloidal Pd NPs as a black solution (see Scheme 7).

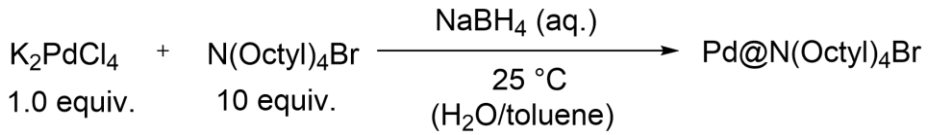

Scheme 7. Reaction of a Pd(II) precursor with $NaBH_4$ as reducing agent and $N(Octyl)_4Br$ as surfactant leading to small ionic-capped Pd colloids soluble in toluene.

Structure and size determination

In good accordance with the literature-reported particles,[55] using $N(Octyl)_4Br$ as weakly coordinating capping agent resulted in the successful formation small colloids. The NPs were stable for months at low temperatures (4 °C). Decreasing the amount of the capping agent $N(Octyl)_4Br$ from 10 equiv. to 5.0 equiv. with respect to palladium results in less stable particles, which agglomerate and precipitate in a shorter amount of time (e.g. after one week). The NPs were analyzed by high-resolution transmission electron microscopy (HR-TEM) and DLS (see Figure 3), both confirming NPs with a small size of 1.9 nm and a narrow size distribution. For HR-TEM analysis, the colloidal solution was dropped on a Cu mesh grid and all volatile compounds (e.g. solvent) were evaporated.

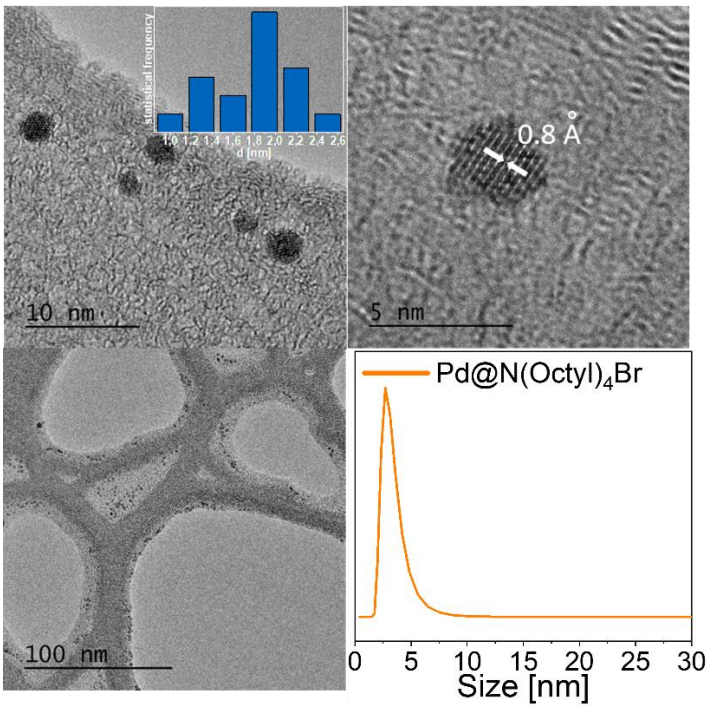

Figure 3. HR-TEM images (above: high magnification, bottom left: low magnification) and DLS measurement (bottom right) of Pd@N(Octyl)$_4$Br colloids.

According to DLS and HR-TEM measurements, no larger agglomerates are formed. Energy-dispersive X-ray (EDX) spectra confirm the sample composition of Pd as well as N, C and Br (originating from the surfactant $N(Octyl)_4Br$). The Cu signal originates from the cupper mesh grid used for these measurements. Additionally, a signal of oxygen indicates a partial oxidation of the metal. Potassium and chlorine residues from the Pd precursor were not detected. Elemental mapping of the colloids shows that the surfactant is distributed homogeneously over the entire sample (see Figure 4).

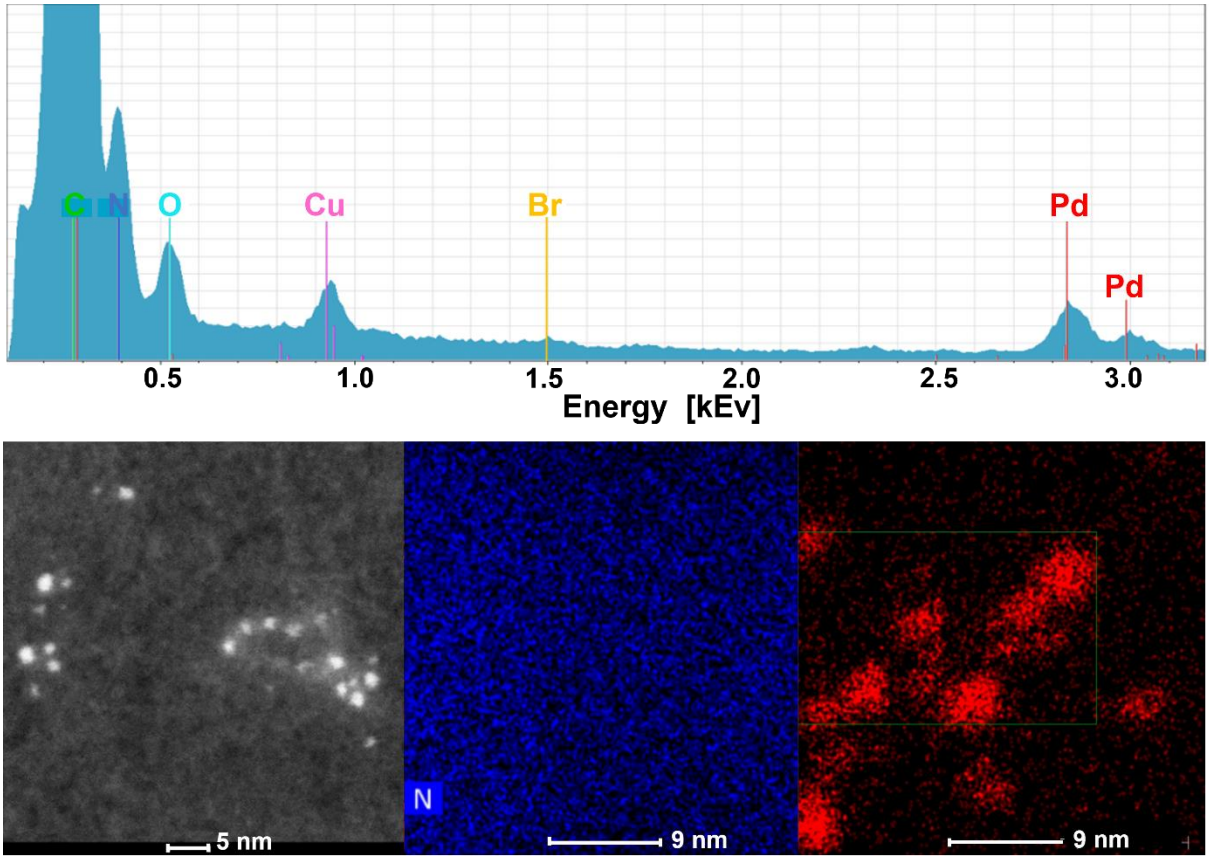

Figure 4. EDX spectrum (above) of $Pd@N(Octyl)_4Br$ colloids, elemental mapping of Pd and N (bottom, left and middle) and HAADF image.

For a further verification of the particle size, powder X-ray diffraction (PXRD) was measured (see Figure 5, left). This technique helped to confirm the small crystallite size of the NPs. Measurement of the colloidal $Pd@N(Octyl)_4$ solution (in toluene) shows that the Pd reflections are very broadened and even hard to identify (see Figure 5, left graph, orange trace). This indicates small crystallite sizes. If the sample is dried to obtain a powder (by evaporation of all volatile compounds), only the reflexes of the intact surfactant are visible.

The oxidation state of the Pd was analyzed by X-ray photoelectron spectroscopy (XPS). For sample preparation, the colloidal solution was dropped on a Si wafer and all volatile compounds were evaporated. The recorded spectrum shows the main signal corresponding

to metallic Pd(0) (see Figure 5). Deconvolution into two pairs of doublets proves the presence of metallic Pd (at 334.1 eV and 339.4 eV) as well as Pd(II) (at 336.2 eV and 341.4 eV). Evaluation of the integrals reveals a fraction of oxidic species (Pd(II)) of 19%. These findings are matching well with the EDX spectra, as also here an oxygen signal was detected. Synthesis approaches under inert conditions avoiding any possible oxygen source resulted in no particle stabilization and lead to a full metal precipitation. These findings suggest that a certain amount of surface oxidation is crucial for the formation of a stable colloidal system. Comparison of these results with literature-known systems of Pd NPs stabilized by an ionic liquid,[44,115] which also showed oxidized surface Pd atoms, lead to the assumption that a thin layer of metal oxide is beneficial for particle stabilization as the polarity of the oxygen atoms facilitates a better interaction with the ionic capping agent.

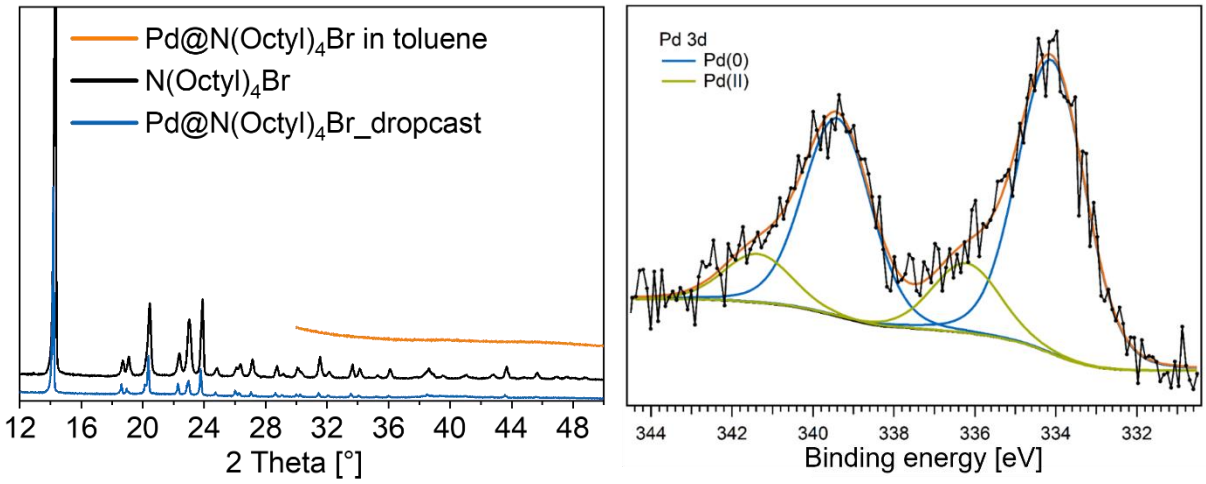

Figure 5. Left: PXRD measurements of Pd@N(Octyl)$_4$Br in solution (green) and dried down (blue) with N(Octyl)$_4$Br as reference (black). Right: Pd 3d photoemission spectra obtained from Pd@N(Octyl)$_4$Br NPs.

Investigation on the colloid stabilization

In order to learn more about the colloid stabilization, Fourier-transform-attenuated-total-reflection-infrared spectroscopy (FT-ATR-IR, see Figure 6) of Pd@N(Octyl)$_4$Br NPs was measured. For a detailed analysis of the NP surface, the colloidal solution was dropped on the IR instrument and all volatile compounds were evaporated prior to measurement. The spectrum shows vibration bands of the surfactant N(Octyl)$_4$Br, which match with those of neat N(Octyl)$_4$Br.

Characteristic $\tilde{\nu}$(C-H,sp^3) absorption bands in a range from 2953 to 2850 cm^{-1} as well as a very weak $\tilde{\nu}$(C-H,sp^2) absorption band at 3004 cm^{-1}originating from residual toluene can be identified. Furthermore, symmetric and antisymmetric $\tilde{\nu}$(C-C/C-Me) vibrations are observed

at 1466 and 1353 cm^{-1}, and at 753 and 720 cm^{-1}, respectively, which is in accordance with a previously reported IR spectrum of neat $N(Octyl)_4Br$.[55] Further analysis by ^1H NMR spectroscopy confirms an intact structure of the capping agent without any impurities, as the recorded spectrum matches with the reference spectra of pure $N(Octyl)_4Br$ (see Supporting Information SI, Figure 77). No shift of the surfactant upon addition of the Pd colloids is observed, indicating (in accordance with the IR spectra) a rather weak coordination of the cation $[N(Octyl)_4]^+$ to the metal surface. This is in good accordance with the literature, as a previously reported study[55b] applying X-ray absorption near edge structure (XANES) measurements on $Pd@N(Octyl)_4Br$ NPs suggests that the anion is present on the inside of the protection shell, located between the Pd NP surface and $[N(Octyl)_4]^+$ groups forming the protection shell. This explains the stabilization of the $Pd@N(Octyl)_4Br$ colloids without any signal shift of the surfactant in the ^1H NMR and IR spectra. The distance between the NP metal surface and the cation caused by the presence of the anion results in no major influence on the electronic environment of the $[N(Octyl)_4]^+$ groups, therefore showing a similar spectroscopic analysis compared to the pure $N(Octyl)_4Br$ molecule.

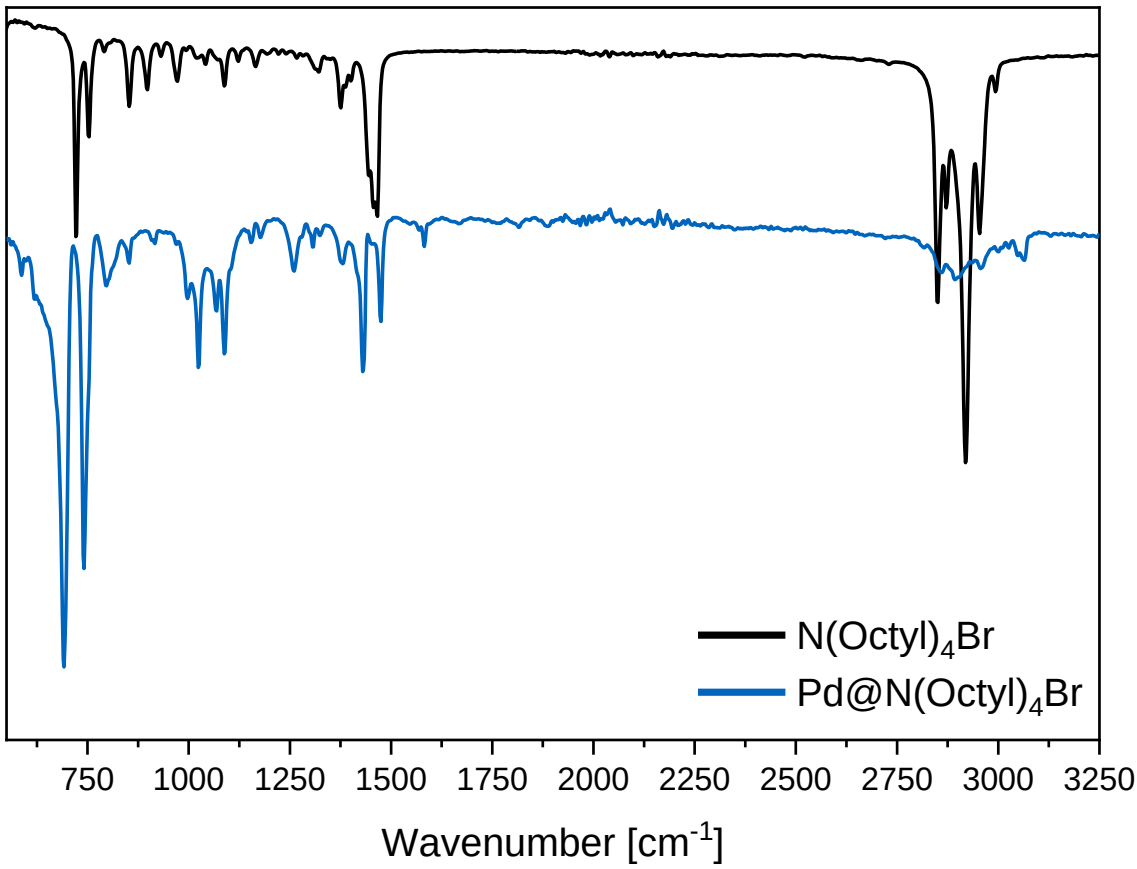

Figure 6. FT-IR spectra (ATR-mode) of $Pd@N(Octyl)_4Br$ and $N(Octyl)_4Br$ showing an intact surfactant upon coordination to the colloids.

Catalytic performance of Pd@N(Octyl)$_4$Br NPs in the alkyne semi-hydrogenation

Parameter optimization

For a systematic investigation of the catalytic activity of Pd@N(Octyl)$_4$Br NPs in the semi-hydrogenation reaction of liquid alkynes, the terminal alkyne 1-octyne was used as model substrate (see Scheme 8).

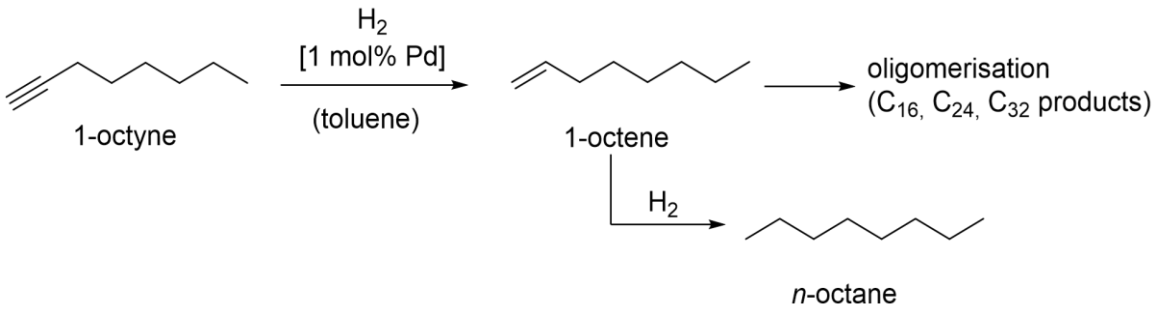

Scheme 8. Reaction scheme of the semi-hydrogenation catalysis using 1 mol% catalyst Pd@N(Octyl)$_4$Br in a H_2 atmosphere.

In order to find the optimal parameters in terms of a high activity as well as, temperature and H_2 pressure were systematically varied and the effect on the substrate conversion and product selectivity was evaluated. Generally, for all catalytic runs, beside the undesired full-hydrogenation to *n*-octane, also oligomerization products can be principally formed and will also be considered for the evaluation of the overall catalytic performance (see Scheme 8). Table 2 shows that a variation of both parameters significantly influences the catalytic activity and selectivity towards the olefin. In general, low temperatures and a relatively low hydrogen partial pressure have a positive influence on the selectivity.

Table 2. Parameter optimization in the semi-hydrogenation of 1-octyne using 1 mol% Pd@N(Octyl)$_4$Br NPs after 3 h reaction time.

Entry	T [°C]	p(H_2) [bar]	Conversion [%]	Selectivity [%]	Oligomerization [%]	TOF [h^{-1}]
1	25	0.5	100	15	31	460
2	0	0.5	45	84	5	210
3	0	1.0	80	80	12	325
4	0	2.0	100	11	24	340

For a better comparison of the different catalysis runs, the turnover frequency (TOF) values were calculated according to following formula:

$$\text{TOF } [h^{-1}] = \frac{\text{conversion (after 1 h)} \times n_0(\text{alkyne})}{n(\text{cat}) \times 1\ \text{h}}$$

where n(cat) = n(all Pd)×0,764 (Pd surface atoms)

Here, the amount of Pd surface atoms was calculated based on the model of magic cluster numbers and a perfect icosahedral NP structure, with a Pd NP diameter of 1.5 nm. In detail, 76% of all Pd atoms are located on the surface.

Starting at room temperature and a H_2 pressure of 0.5 bar, a highly active but unselective system was observed (Table 2, Entry 1). Decreasing the reaction temperature to 0 °C with a hydrogen pressure of 0.5 bar leads to an improved selectivity but decreased activity (Table 1, Entry 2). Increasing the H_2 pressure to 1.0 bar at 0 °C results in a high conversion of 80 % and an enhanced selectivity towards 1-octene of 80 % after 3 h (Table 1, Entry 3). Here, an oligomerization of 1 % and full-hydrogenation to *n*-octane of 8 % was observed with a TOF of 325 h^{-1}. Further increase of the hydrogen pressure at low temperatures does not result in an increased activity, as a similar TOF value of 340 h^{-1} is observed, but in a decreased selectivity due to an increased olefin hydrogenation and as well oligomerization (Table 1, Entry 4). Therefore, it can be concluded that generally, at elevated temperatures and hydrogen pressure, alkane formation and oligomerization are increased. Noteworthy, no particle precipitation is observed independent on the applied catalytic conditions. Variation of the catalyst amount at the optimized reaction conditions of 0 °C and 1.0 bar H_2 revealed a linear correlation of the catalyst amount and the reaction rate, suggesting no influence of the catalyst concentration on its performance (see Figure 7, left).

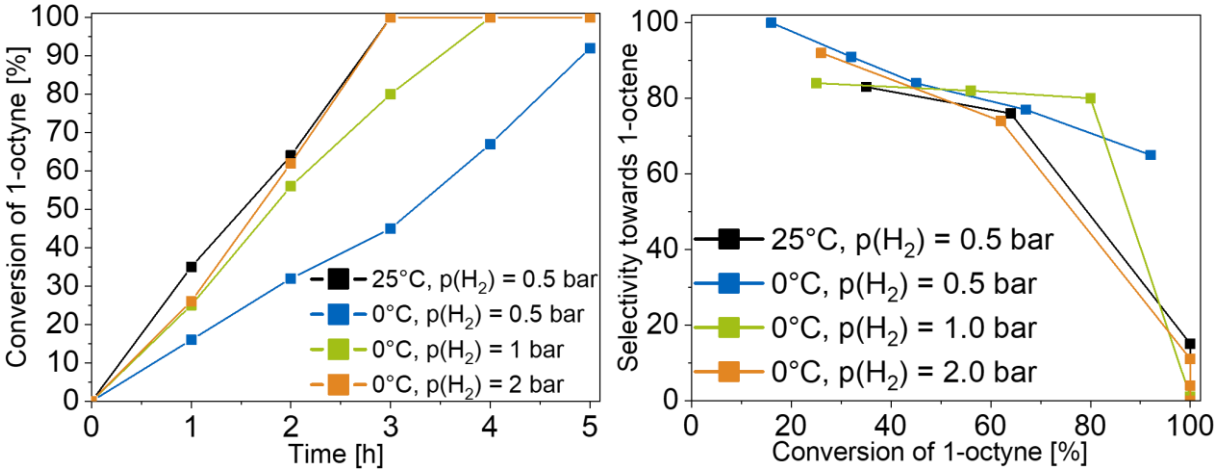

Figure 7. Catalytic performance of Pd@N(Octyl)$_4$Br NPs in the semi-hydrogenation of 1-octyne with varied reaction parameters using 1 mol% catalyst. Left graph: conversion of 1-octyne. Right graph: selectivity towards 1-octene.

Substrate variation

For a better understanding of the herein tested catalytic system, substrates with other electronic and steric features were studied. Hence, 2-octyne as internal alkyne and phenylacetylene as bulky substrate with an aromatic system were tested under the optimized reaction conditions (1 mol % Pd@N(Octyl)$_4$Br, 0 °C, 1.0 bar H_2) and compared to the catalytic data of 1-octyne (see Figure 8, right).

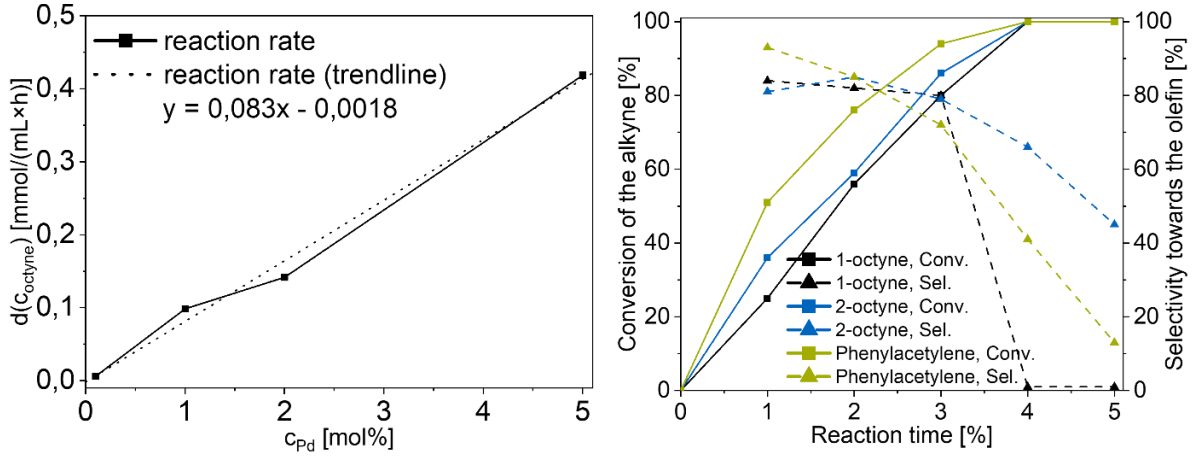

Figure 8. Left: Reaction rate of the catalytic semi-hydrogenation of 1-octyne at 0 °C and 1 bar H_2 with different amounts of catalyst (0.1 mol%, 1.0 mol%, 2.0 mol%, 5.0 mol% Pd) showing a linear correlation. Right: Substrate variation with 1mol % Pd@N(Octyl)$_4$Br NPs as catalyst at 0°C and 1.0 bar H_2.

Comparison of the conversion of the three tested substrates shows an increased conversion of phenylacetylene compared to 1-octyne and 2-octyne. This might be attributed to the aromatic nature of the substrate resulting in an increased reactivity. Additionally, the higher activity observed for 2-octyne and phenylacetylene compared to the terminal alkyne was also previously reported in literature.[39] The selectivities towards the olefin, independent of the substrate, are rather low (80 % for 2-octyne and 73 % for phenylacetylene after 3 h reaction time with conversion of 93 % and 86 %, see Figure 8, left) and full-hydrogenation to the alkane is observed for all substrates.

Table 3. Oligomerization of 1-octyne using 1 mol% Pd@N(Octyl)$_4$Br NPs at different reaction conditions (varied temperature and p(H_2)).

Time [h]	25 °C, 0.5 bar [%]	0 °C, 0.5 bar [%]	0 °C, 1.0 bar [%]	0 °C, 2.0 bar [%]
1	5	0	3	0
2	13	3	8	3
3	31	5	12	42
4	40	11	43	44
5	58	22	45	46

The rather low selectivity of the herein tested substrates was further confirmed by hydrogenation experiments of the respective alkenes, namely 1-octene, 2-octene and styrene. With all substrates, full conversion to the alkane was observed (see SI, Table 36-39), showing principally no intrinsic selectivity towards the semi-hydrogenation product but rather a kinetic dependence on the product distribution.

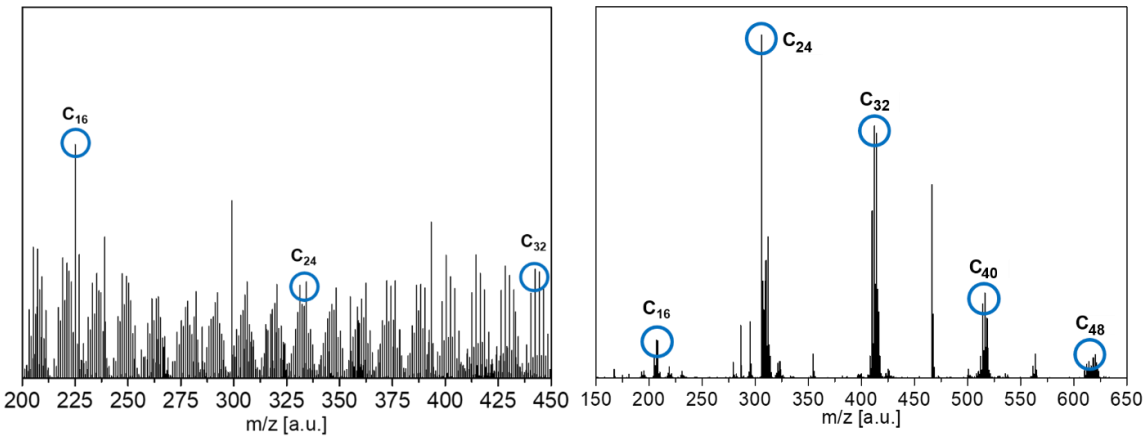

Figure 9. LIFDI-MS spectrum of the reaction mixture after catalysis with 1-octyne or as substrate (left) and phenylacetylene (right) showing oligomerization of 1-octene and styrene with typical mass signals of higher polymers.

Additionally, oligomerization of the olefin to dimers and higher products has been detected in all experiments of this study by LIFDI-MS measurements (see Table 3 and Figure 9). Generally, the oligomerization is increased at higher reaction temperatures and higher H_2 pressures. The oligomerization to dimers and trimers catalyzed by Group 10 metals is well-known since the early works of Keim, Jolly, Wielke and others.[15,16,116,117] Regarding heterogeneous acetylene semi-hydrogenation catalysis, the phenomenon of oligomerization of the product resulting in hydrocarbon deposits on the catalyst surface was reported in literature earlier.[3,17,118]

Particle analysis after catalysis runs

The stability after catalysis of the colloids was analyzed in terms of a structural analysis by DLS and HR-TEM showing a slight particle agglomeration (see Figure 10). This is not surprising, as the colloids are only stabilized by the weak coordinating surfactant $N(Octyl)_4Br$. Nevertheless, no precipitation of the catalyst is observed. Nevertheless, no particle precipitation was observed.

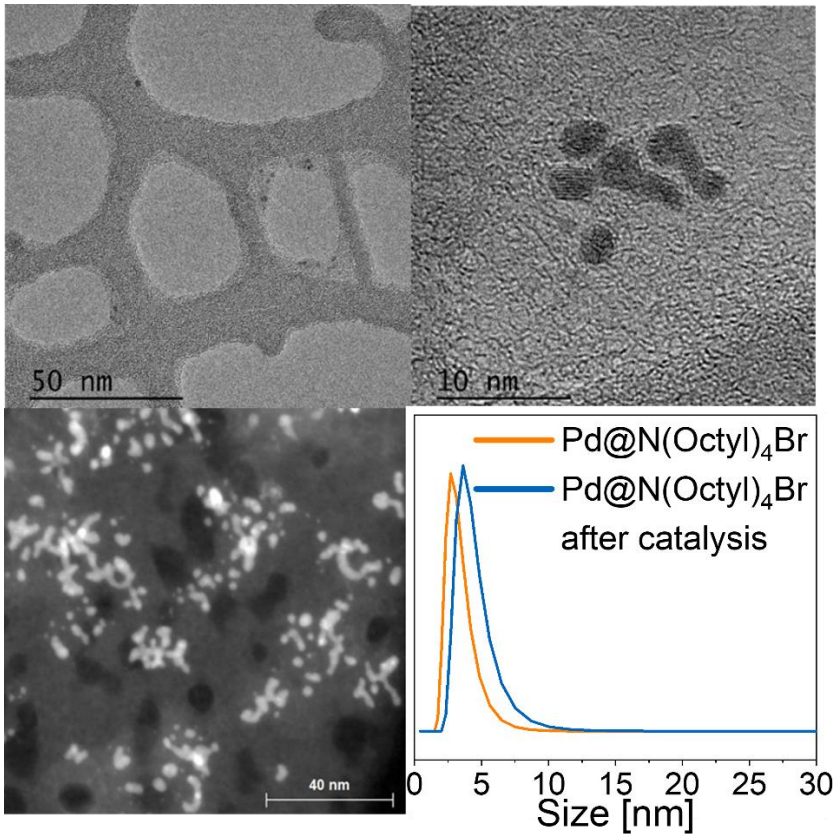

Figure 10. HR-TEM measurements (including HAADF) and DLS measurements after catalysis show a slight agglomeration of Pd@N(Octyl)$_4$Br.

Concluding, the herein shown catalytic experiments reveal a highly active catalytic system at mild conditions (low temperature and low H_2 partial pressure) which presents the perfect starting point for additional investigations on the further catalytic optimization of a monometallic colloidal system. Yet, without any additives, the selectivity towards 1-octene is rather low as the hydrogenation of alkynes is not stopped at the olefins but proceeds further to the alkanes. This might be attributed to the favored olefin hydrogenation over olefin desorption, explaining the observed overreduction.[118] For an anticipated enhancement of the catalytic performance, the post-synthetic addition of various σ-donoring agents was tested and will be presented hereinafter. Going in line with literature-reported systems, NHC ligands as well as ionic liquids and phosphanes were added post-synthetically to the Pd@N(Octyl)$_4$Br colloids. The influence on the stability as well as on the catalytic performance which will be discussed in detail in the following sections.

Influence additives on the catalytic performance of Pd@N(Octyl)$_4$Br NPs

N-heterocyclic carbenes (NHCs) and ionic liquids (ILs) as post-synthetic additives

Inspired by the work of Dupont, Glorius and others, this chapter deals with the post-synthetic addition of both NHC ligands as well as ionic liquids to Pd colloids stabilized by N(Octyl)$_4$Br in toluene. Coordination of the free Arduengo-carbene to the metal surface might change its electronic structure and hence influences the catalytic performance of the catalyst. A NHC ligand bearing two *tert*-butyl groups at the nitrogen wingtip positions (1,3-di-*tert*-butyl-1H-imidazol-3-ium-2-ide = di-*t*Bu-NHC) was chosen due to its easy synthesis, isolation, and high stability. Additionally, the protonated type of a NHC ligand, namely 1-octyl-3-methyl-imidazolium bromide [OMIM]Br, was tested as post-synthetic additive (see Scheme 9).

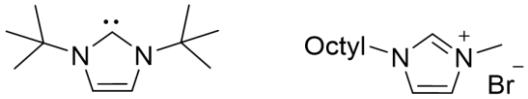

di-*t*Bu-NHC [OMIM]Br

Scheme 9. Chemical structures of the chosen additives di-*t*Bu-NHC (left) and [OMIM]Br (right).

Comparison of this cation with the NHC ligand might lead to a better understanding of the crucial factors for a beneficial influence of additives on the semi-hydrogenation catalyst. In addition, [OMIM]Br as surface-active agent exhibits a similar stabilizing effect compared to N(Octyl)$_4$Br bearing the same anion and could cover the particle surface to a lesser extend due to the single alkyl chain. Therefore, the effect of the alkyl groups of the cations $[N(Octyl)_4]^+$ and $[OMIM]^+$ on the catalytic performance can be compared. The same catalytic conditions were chosen compared to the catalytic runs of pure Pd@N(Octyl)$_4$Br without any additives (1 mol% catalyst in toluene, 0°C, 1bar H_2, 1-octyne as substrate).

Addition of 1.0 equiv. di-*t*Bu-NHC, referred to the Pd amount, resulted in an increased activity. Comparison of the conversion after 3 h reaction time of the colloidal system without any additives and upon addition of di-*t*Bu-NHC showed an increase in activity from 80 % to 90 % (see Table 3, Entry 2).

Table 4. Semi-hydrogenation of 1-octyne using 1 mol% Pd@N(Octyl)$_4$Br NPs with various additives after 3 h reaction time.

Entry	Additive	Conversion [%]	Selectivity [%]	Oligomerization [%]
1	-	80	80	12
2	1.0 equiv. di-*t*Bu-NHC	90	73	13
3	0.1 equiv. di-*t*Bu-NHC	100	21	18
4	1.0 equiv. [OMIM]Br	78	35	57

Nevertheless, the selectivity towards the olefin was decreased upon addition of the NHC ligand to only 73 % from 80 %. Here, it has to be noted that this loss in selectivity is not only referred to full-hydrogenation to *n*-octane but also to an increased formation of oligomerization products (analyzed via LIFDI-MS with similar m/z values as already discussed above). Decreasing the additive amount to 0.1 equiv. based on Pd, the activity can be boosted even further with full-conversion after 2 h but also with a decreased selectivity of only 48 % (see Table 4, Entry 3). These results show that the addition of a σ-donoring agent can influence both the activity and the selectivity of a colloidal system. Nevertheless, tuning these two parameters in an optimal way is challenging and the herein tested additive, di-*t*Bu-NHC, does not lead to the desired features for a highly selective semi-hydrogenation catalyst.

Further investigation on [OMIM]Br as additive did not result in the intended increase of activity and selectivity in the semi-hydrogenation reaction catalyzed by Pd@N(Octyl)$_4$Br colloids (see Table 3, Entry 4). Notable, with the IL as additional ligand, the catalysis was run in THF as solvent as [OMIM]Br is not soluble in toluene, which would result in a biphasic system. Therefore, the Pd@N(Octyl)$_4$Br NPs were first dissolved in THF and afterwards, 1.0 equiv. [OMIM]Br was added. In contrast to the catalytic runs with the NHC as additive, [OMIM]Br did not affect the activity of the catalytic system but strongly increased the formation of oligomerization products, thus decreasing the selectivity towards the olefin. Additionally, also THF as weakly coordinating solvent could have an influence on the catalytic performance.

Concluding from these results, no further catalysis experiments on the system of Pd@N(Octyl)$_4$Br with NHCs and ILs as post-synthetic additives were performed. Both additives did not lead to an increased alkene selectivity. Nevertheless, the observed catalytic data clearly show the effect of additives on the catalytic performance of a monometallic colloidal system, generally confirming the potential of coordinating agents to change the reactivity of colloids in a beneficial way.

Phosphanes as post-synthetic additives: Influence on the colloid stability

Based on the results of NHCs and ILs as additives, the influence of the addition of triorganylphosphanes PR_3 bearing different substituents (R = alkyl, aryl) on the catalytic performance of colloidal Pd NPs for the alkyne semi-hydrogenation was investigated. Colloidal NPs surrounded by a coordinating ligand shell involve a hard-soft matter interface between the metal surface and pendant ligands.[119]

The impact of metal conduction electrons on the ligand nuclei detected by NMR analysis can provide a detailed insight into the ligand shell of the NP. In solution, a fast re-orientation of small molecules results in an isotropic chemical shift and sharp resonance lines. By coordination of the surfactant to the particle, their location changes from solution to an interface between solution and solid, resulting in a line broadening of the resonances and a chemical shift. The interaction of the metal surface with an organic molecule can further lead to an increased relaxation time, as this parameter depends on the Brownian molecular motion.[120] These motions include rotational and translational movements of the NP in solution changing the local environment of the ligand. As a result, the signal intensity of the ligand atomic nucleus closely attached to the metal surface can be decreased or even eliminated. Hence, NMR analysis can be used as a powerful tool to provide an insight into ligand-particle bonding at the hard-soft matter interface.[119]

Starting with the addition of co-catalytic amounts (with respect to the Pd) of PPh_3, a signal shift in the ^{31}P NMR from -5.3 ppm to -5.0 ppm with a signal broadening points to a phosphane coordination to the metal surface (see Figure 11).

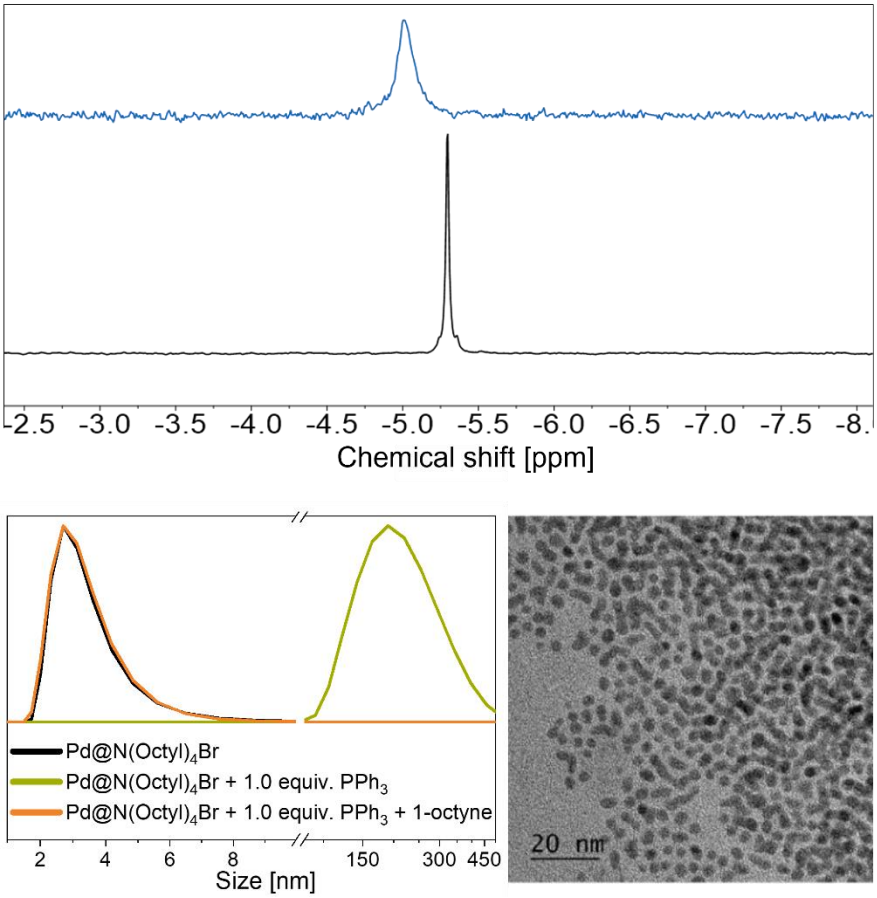

Figure 11. Top: ^{31}P NMR spectra of Pd@N(Octyl)$_4$Br upon addition of 1.0 equiv. PPh_3 (blue trace) and pure PPh_3 (black trace) as reference. Bottom: DLS (left) and HR-TEM (right) measurements of the colloids upon addition of 1.0 equiv. PPh_3 showing a particle agglomeration.

Due to the rather weak stabilization ability of PPh_3, its coordination results in particle agglomeration, as shown by DLS and HR-TEM measurements indicating an insufficient long-term particle stabilization of the colloids. Nevertheless, such particle agglomeration is not observed in the presence of an alkyne, suggesting an additional stabilizing effect upon coordination to the NP surface.

Mechanistic investigation on the influence of phosphanes on the Pd colloids by means of ATR-IR and ^{31}P NMR measurements reveals a partial phosphane oxidation (up to 20 %, see Figure 12).

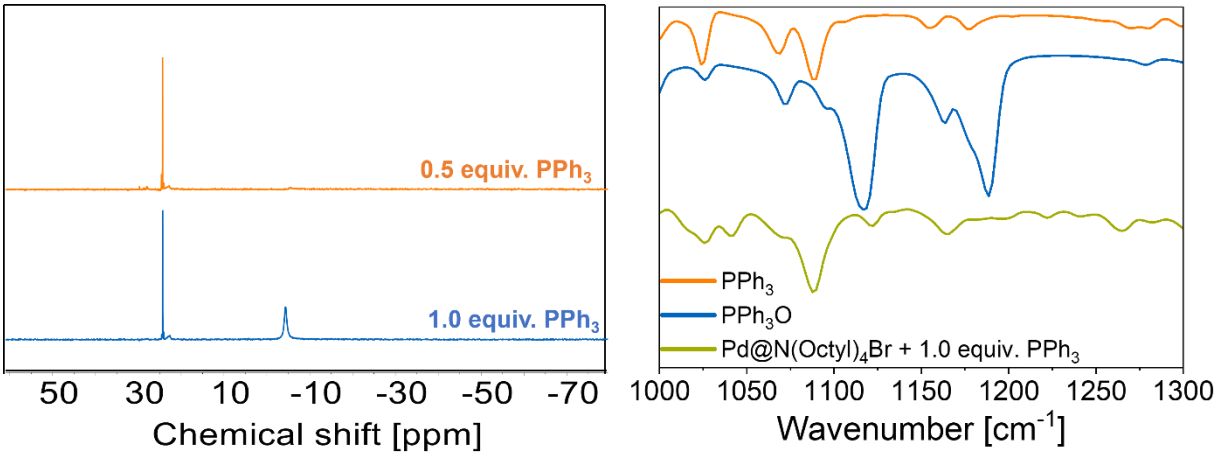

Figure 12. Left: *In situ* ^{31}P-NMR study of PPh_3 (0.5 equiv. and 1 equiv. referred to Pd) addition to a solution of 1 mol% $Pd@N(Octyl)_4Br$ NPs and 1-octyne in dry and degassed toluene-d_8 under inert conditions (without H_2). Right: ATR-IR study of $Pd@N(Octyl)_4Br$ with 1.0 equiv. of PPh_3 (green trace) with PPh_3 (orange trace) and PPh_3O (blue trace) as reference.

As XPS analysis of the pure $Pd@N(Octyl)_4Br$ colloids revealed about 19 % of the Pd being in the oxidized state, the addition of the phosphane might lead to a full reduction of the metal on the particle surface resulting in Pd(0) and phosphane oxide. Decreasing the amount of PPh_3 from 1.0 equiv. to 0.5 equiv. referred to the Pd amount, almost full phosphane oxidation is observed illustrated in the ^{31}P NMR spectrum by the presence of only one signal for PPh_3O at 24.9 ppm (see Figure 12, left). As already mentioned before, colloid synthesis under inert conditions, without any traces of oxygen, lead to a complete particle precipitation. This also explains the colloid agglomeration upon addition of PPh_3, as the required oxygen for a stable colloidal system is removed by phosphane oxidation. Nevertheless, in a catalytic system with the alkyne being present in the solution, the colloids remain stable, as the alkyne probably also has a stabilizing effect on the NPs. The oxygen was further confirmed to originate from the metal surface and not from physically dissolved oxygen in the solvent by ^{31}P NMR studies, as these studies were performed both under air and under argon. Phosphane oxidation is in fact enhanced by using solvents containing residual H_2O but is also present under inert

conditions, thus showing that the metal surface can be determined as oxygen source (see SI, Figures 86-89).

Phosphanes as post-synthetic additives: Influence on the catalytic performance

The investigation on the addition of phosphanes clearly shows a coordination and a change of the metal surface. Therefore, also the influence of various phosphanes in the semi-hydrogenation catalysis of liquid alkynes with Pd@N(Octyl)$_4$Br as catalyst was tested (see Table 5).

Table 5. Additive impact on the semi-hydrogenation of 1-octyne using 1 mol% Pd@N(Octyl)$_4$Br after 2 h reaction time (0 °C, 1.0 bar H_2).

Entry	Equiv. PPh_3	Conversion [%]	Selectivity [%]
1	0.0	56	82
2	0.5	38	81
3	1.0	99	83
4	2.0	74	98
5	5.0	62	100
6	10	54	100
7	20	23	100

The reaction conditions were chosen based on the parameter optimization with pure Pd@N(Octyl)$_4$Br, using 1 mol% catalyst at 0 °C and 1.0 bar H_2. Starting with PPh_3 as additive, a variation of the phosphane amount from 0.5 equiv. to 20 equiv. with respect to Pd showed that the selectivity was strongly increased upon phosphane addition, but does not depend on the additive amount, whereas the activity is increased with decreasing PPh_3 amount, with an optimum at 1.0 equiv. PPh_3. Here, full conversion of 1-octyne was observed after 2 h reaction time with a selectivity of 83 % (see Table 5, Entry 3). The decreased activity of 0.5 equiv. PPh_3 compared to the catalytic run without any additive (see Table 5, Entry 1 and 2) can be explained by a complete oxidation of the additive to PPh_3, thus destabilizing the colloids leading to particle agglomeration. With an increasing amount of phosphane, the coordination of additional PPh_3 thus further stabilizes the particles. Based on the (simplified) concept of the model of magic number clusters, for a perfect Pd NP with icosahedral structure and a diameter of ca. 1.5 nm, it can roughly be estimated that ca. 70-75 % of all Pd atoms are located at the surface of the NPs. Therefore, by adding 1.0 equiv. of PPh_3, it can be deduced that the additive is always in a small excess and that the catalyst surface can be fully covered with phosphane. Addition of the respective phosphine oxide PPh_3O showed no influence on the catalytic performance and almost the exact results were obtained compared to the

catalysis without any additives (see Table 6 and SI, Figures 157-158). Hence, the phosphane oxide is not responsible for the increased catalytic performance and does not influence the catalyst activity or selectivity. In contrast, the phosphane is able to (a) reduce the Pd-O, (b) coordinate to the Pd(0) surface and (c) enhance the selectivity towards the olefin.

The observed activity loss with an increased PPh_3 amount from 1.0 equiv. to 20 equiv. might stem from a competitive coordination of the phosphane and the substrate. ^{31}P NMR spectra of different amounts of additive show a signal splitting for 1.0 equiv. PPh_3, whereas with higher amounts only one signal is observed. Thus, an optimum of coordinated and non-coordinated phosphane is achieved by using 1.0 equiv. additive referred to the Pd amount. Additionally, using higher amounts of PPh_3 (5.0 equiv. to 20 equiv.), yellow crystals of $[Pd(PPh_3)_4]$ were isolated and identified via NMR spectroscopy (^{31}P NMR, see SI, Figure 90) and IR spectroscopy (see Figure 13, right). This clearly points to a Pd leaching from the colloids. Catalysis control experiments with pure $[Pd(PPh_3)_4]$ as catalyst show no conversion of the respective substrate (both alkyne and alkene tested) under the standard conditions, thus also elucidating the decreased catalyst activity with higher PPh_3 amounts. It can be concluded that 1.0 equiv. phosphane represents the optimal amount for an increased catalytic performance. In detail, a distinct amount of phosphane is required to remove oxygen species from the palladium surface, resulting in an increased amount of catalytic active sites. An additional phosphane coordination to the palladium surface leads to an increased selectivity. Higher amounts of additive lead to undesired catalyst leaching.

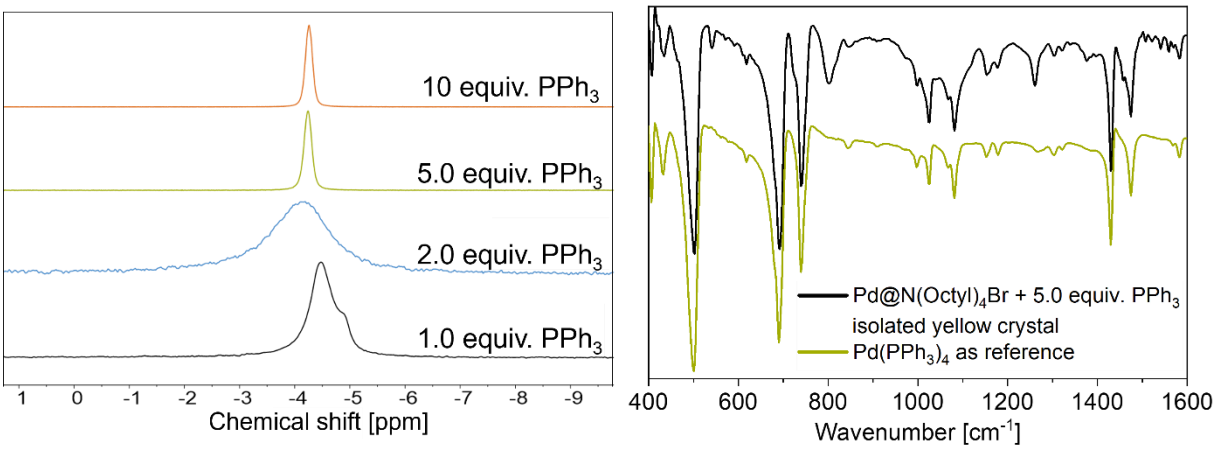

Figure 13. Left: ^{31}P-NMR study of the semi-hydrogenation of 1-octyne using 1 mol% catalyst and various amounts of PPh_3 in dry and degassed toluene-d_8. Right: IR study of an isolated yellow crystal obtained by the addition of 5.0 equiv. PPh_3 to Pd@N(Octyl)$_4$Br colloids (black trace) and pure $[Pd(PPh_3)_4]$ (green trace) as reference.

Hence, for all further investigations, 1.0 equiv. additive was used. Analysis of the colloids after catalysis runs did not show any catalyst precipitation and particle agglomeration was excluded via DLS measurement (standard conditions), thus indicating a stable catalytic

system (see SI, Figure 92). Comparison of the herein tested system with literature known monometallic Pd NPs for the semi-hydrogenation catalysis shows a rather high activity of this catalytic system (see SI, Table 40).[22,39,44,51,52] Nevertheless, a direct comparison is difficult due to different reaction conditions, substrates and measurement set-ups.

For a deeper understanding of the increased catalytic performance upon addition of PPh_3, we further studied the effect of other phosphanes bearing steric and electronic differences.

Table 6. Conversion and selectivity of 1-octyne using 1 mol% Pd@N(Octyl)$_4$Br and 1.0 equiv. additive at 0 °C and 1.0 bar H_2 after 5 h reaction time.

Entry	Additive	Conversion [%]	Selectivity [%]
1	PPh_3	100	32
2	$MePPh_2$	100	93
3	Me_2PPh	69	99
4	Me_3P	21	100
5	P(*o*-tolyl)$_3$	100	1
6	P(*p*-tolyl)$_3$	99	85
7	$P(OPh)_3$	100	89
8	P(*i*Pr)$_3$	100	33
9	$P(Cy)_3$	99	37
10	P(*p*-F-tolyl)$_3$	87	75
11	$MePPh_2O$	100	27
12	PPh_3O	100	17

Substitution of one PPh_3 phenyl group with a methyl group shows even higher selectivity after 2 h reaction time (see Table 6, Entry 2). A further consecutive substitution of the phenyl groups by sterically less demanding methyl groups, namely Me_2PPh and Me_3P, leads to an increased selectivity towards the olefin but also strongly decreased catalytic activity (see Table 6, Entries 3 and 4 and SI, Figures 158-159). The stronger interaction of these smaller phosphanes with the Pd colloids results in particle agglomeration and precipitation with a concomitant catalyst deactivation, as the stabilization effect of phosphanes is weaker than that of N(Octyl)$_4$Br. By testing a series of phosphanes with different steric demands, a relation between the Tolman cone angle[121] and the catalytic activity was found with an optimal cone angle of 145° for PPh_3 (see Figure 14). Phosphanes with a high steric demand like P(*o*-tolyl)$_3$, P(*i*Pr)$_3$ and PCy_3 do not destabilize the colloids but also show a decreased activity compared to PPh_3. This can be explained by the steric inhibition at the particle surface by the phosphane impeding substrate coordination to the catalyst. Testing various phosphanes with the same Tolman cone angle of 145° but with differences in the electronic features, namely PPh_3, P(*p*-tolyl)$_3$ and P(*p*-fluorophenyl)$_3$ gives evidence that the boost in activity is not only

influenced by the steric demand of the additive but also dependent on the electron donor ability (see Figure 14 and Table 7). The addition of both, the electron donating P(*p*-tolyl)$_3$ as well as the electron withdrawing P(*p*-fluorophenyl)$_3$, resulted in a decreased conversion of 1-octyne thus illustrating that both steric and electronic properties play a crucial role the catalyst activity and that PPh_3 combines these requirements in an optimal way.

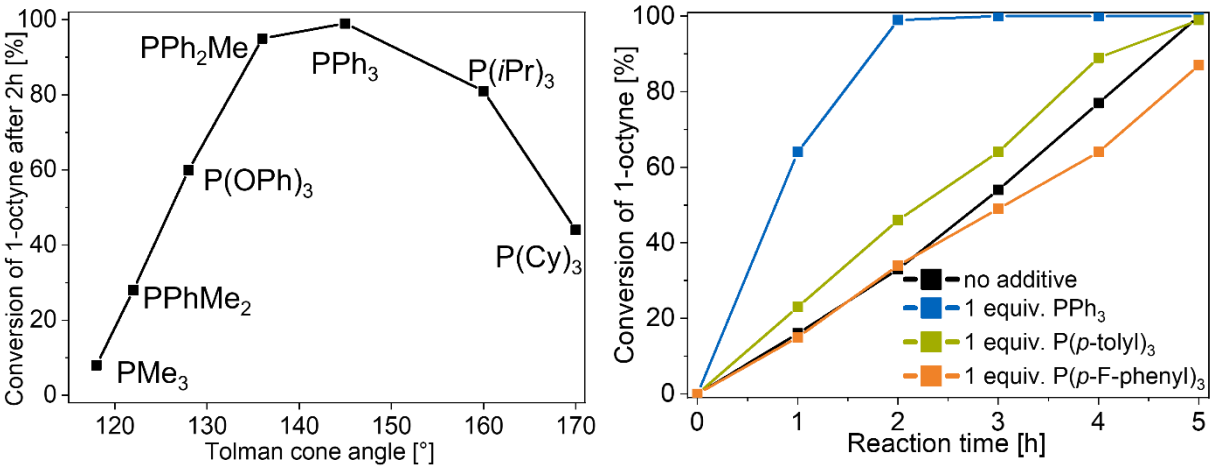

Figure 14. Substrate conversion after 2 h as a function of the phosphane cone angle (left) and the electronic properties (right). Catalysis tests were performed under standard catalytic conditions (1 mol% Pd@N(Octyl)$_4$Br, 1.0 equiv. phosphane based on the amount of Pd, 0 °C, 1.0 bar H_2).

With focus on the catalyst selectivity, a comparison of aryl phosphanes (PPh_3 and P(*o*-tolyl)$_3$) with alkyl phosphanes (P(*i*Pr)$_3$ and P(Cy)$_3$, see Table 6, Entries 1, 5, 8 and 9) indicates poorer selectivities at full conversion for the latter additives.

Table 7. Comparison of catalytic tests with 1-octyne as substrate using 1.0 equiv. phosphanes bearing the same cone angle of 145° under standard conditions (1 mol% Pd@N(Octyl)$_4$Br, 0 °C, 1.0 bar H_2).

Entry	Additive	Conversion after 2 h [%]	Selectivity at full conv. [%]	Full hydrogenation [%]	Oligomerization [%]
1	-	56	22 (5 h)	35 (5 h)	43 (5 h)
2	PPh_3	99	83 (2 h)	9 (2 h)	6 (2 h)
3	P(*p*-tolyl)$_3$	46	61 (5 h)	32 (5 h)	10 (5 h)
4	P(*p*-F-phenyl)$_3$	34	50 (6 h)	36 (6 h)	14 (6 h)

Thus, it can be concluded that in contrast to the catalyst activity, the selectivity does not underly steric but rather electronic reasons. An increased σ-donor ability might not be desirable for a high selectivity towards the olefin.

Similar to the catalytic runs of Pd@N(Octyl)$_4$Br without any post-synthetic additives, the catalytic performance using other substrates with addition of 1.0 equiv. phosphane was also tested for the colloids upon coordination of PPh_3 (see Table 8).

Table 8. Substrate variation using 1 mol% Pd@N(Octyl)$_4$Br and 1.0 equiv. PPh_3 (0 °C, 1.0 bar H_2).

Entry	Substrate	Additive	Conversion [%]	Selectivity at full conv. [%]	Oligomerization at full conv. [%]	TOF [h^{-1}]
1	1-octyne	-	56 (5 h)	22 (5 h)	8 (5 h)	330
2	1-octyne	PPh_3	99 (2 h)	83 (2 h)	4 (2 h)	840
3	1-octene	-	98 (3 h)	-	-	-
4	1-octene	PPh_3	5 (5 h)	-	-	-
5	2-octyne	-	59 (4 h)	66 (4 h)	4 (4 h)	480
6	2-octyne	PPh_3	72 (4 h)	92 (4 h)	0 (4 h)	520
7	*cis*-2-octene	-	97 (3 h)	-	-	-
8	*cis*-2-octene	PPh_3	5 (5 h)	-	-	-
9	phenylacetylene	-	66 (4 h)	41 (4 h)	9 (4 h)	760
10	phenylacetylene	PPh_3	91 (4 h)	87 (4 h)	6 (4 h)	900

In detail, 2-octyne, phenylacetylene and also the respective olefins were chosen in order to see if the conversion can be stopped at the stage of the alkene. Hydrogenation experiments of all tested olefins (1-octene and *cis*-2-octene) showed a full-hydrogenation without using any additive, while no alkene conversion is observed upon the addition of 1.0 equiv. PPh_3. This clearly shows the positive influence on the catalyst selectivity, as due to a changed electronic environment of the metal surface, the hydrogenation of the olefin does not take place. Thus, this series of catalytic experiments gives evidence that the semi-hydrogenation of alkynes by addition of phosphanes can be extended to other substrates and is not limited to 1-octyne.

The catalysis tests using phenylacetylene and 2-octyne with PPh_3 as additive exhibit similar results with a boost in both conversion and selectivity compared to the catalysis without any additives (see Table 8, Entries 5-10). A direct comparison of the conversions of 1-octyne, 2-octyne and phenyl acetylene shows that without any additives, the TOF values of 2-octyne and phenylacetylene are higher than for 1-octyne, which was also reported in literature before.[39] This trend is reversed by the addition of PPh_3, as here the conversion of the terminal alkyne is slightly higher than that of the substrates with an internal C≡C bond (see Table 8). Upon coordination of PPh_3, the hydrogenation of terminal alkynes on the metal surfaces is more favoured than that of internal ones or a terminal alkyne with a higher steric demand,

mainly due to coordination constraints at the NP surface.[122] For all substrates, PPh_3 as additive leads to an increase of the TOF values highlighting the positive effect of this additive on the catalyst activity. Furthermore, with 2-octyne as substrate, phosphane addition not only suppresses the alkane formation but selectively leads to the *cis*-isomer, pointing towards a syn-hydrogen addition.[14]

3.1.3 Conclusion

The application of monometallic, Pd-based colloids for the semi-hydrogenation reaction of liquid alkynes leads to following findings:

(a) Thiol-capped NPs suffer from catalyst poisoning, resulting in an inactive and not easily tunable colloidal system. The organic moiety of the thiol has no influence on the catalytic performance, as the strong coordination results in inactive catalysts for all tested surfactants.

(b) Colloids stabilized by an ionic surfactant, in contrast, resemble an active but not highly selective catalytic system. Nevertheless, parameter optimization allows for moderate selectivities towards the olefin.

(c) Modification of this weakly stabilized colloidal system by a post-synthetic addition of coordinating, σ-donoring agents leads to a change in reactivity due to a change of both the electronic and geometric environment of the active metal centers.

(d) NHC-bearing ligands increase the catalytic activity but also decrease the selectivity towards the olefin.

(e) Ionic liquids as post-synthetic additives lead to an increased formation of undesired oligomerization products.

(f) The herein presented study demonstrates the enormous influence of phosphane ligands on the catalytic performance of colloidal NPs, not only affecting the alkene selectivity but also the efficient conversion of the alkyne as well as the colloid stability.

Concluding from these findings, the addition of the optimal amount of phosphane ligands to ionically stabilized Pd colloids resembles an effective (desired) site-blocking strategy for an increased performance in semi-hydrogenation catalysis. For all tested additives, the removal of oxygen from the metal surface leads to an increased selectivity compared to the system without any phosphane ligands, but also a decreased particle stability. Studying a set of

phosphane ligands with electron-donating and -withdrawing substituents reveals the need of a balance of electron density on the NP surface for optimal catalysis results. Both, the selectivity as well as the activity are controlled by this class of coordinating agents. In detail, comparison of phosphanes with the same steric demand but different electronic features (PPh_3, P(*p*-tolyl)$_3$ and P(*p*-F-phenyl)$_3$) clearly shows that strongly electron-withdrawing as well as strongly electron-pushing phosphane substituents lead to a decreased activity. For this series, the catalytic activity of Pd colloids depends on the additive as follows: PPh_3 > P(*p*-tolyl)$_3$ > P(*p*-F-phenyl)$_3$. Here, the electron-donating P(*p*-tolyl)$_3$ binds more strongly to the metal surface, thus lowering the accessibility of the catalyst for substrate molecules, hence also decreasing the catalytic activity. In line with this finding, P(*p*-F-phenyl)$_3$ as weaker binding additive shows an increased activity compared to P(*p*-tolyl)$_3$. Subsequent substitution of the phenyl groups by methyl groups (PPh_3, PPh_2Me, $PPhMe_2$, PMe_3) revealed only minor differences in selectivity at full conversion within the catalytic runs using these phosphanes as additives. In contrast, by comparison of the selectivity without and with post-synthetic added ligands, for all tested phosphanes, the selectivity was strongly increased. Hence, only the activity is affected by substitutions of the organic residues at the P moiety, pointing to the binding strength of the additives as origin of the influence on the activity; the stronger the Pd-phosphane bond is, the lower the activity is.

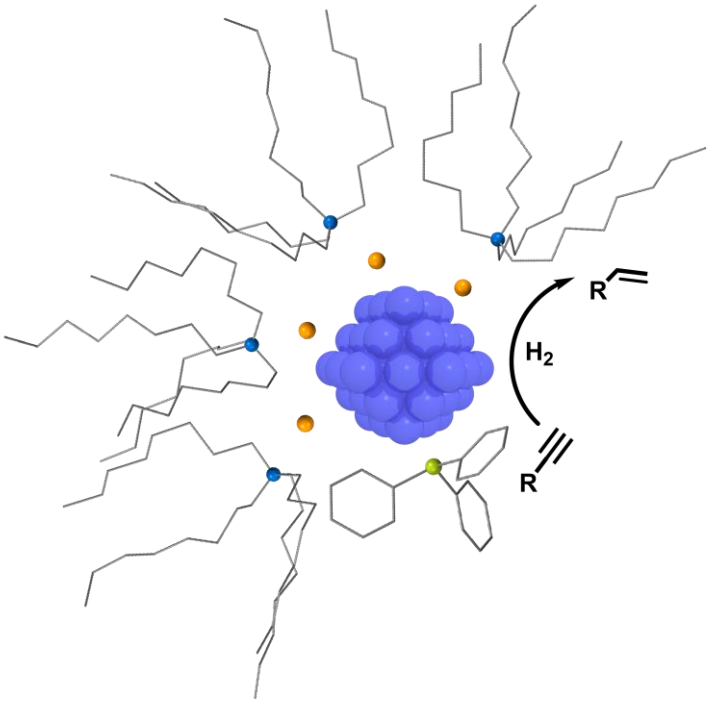

Scheme 10. Schematic representation of a Pd@N(Octyl)$_4$Br colloidal NP with PPh_3 as post-synthetic additive for the semi-hydrogenation catalysis.

Studies including phosphanes with different steric features and therefore different Tolman cone angles revealed phosphanes with smaller cone angles to lead to particle precipitation ($PPhMe_2$, PMe_3), thus decreasing the catalyst activity. In contrast, phosphane ligands with a high steric demand ($P(o\text{-tolyl})_3$, $P(i\text{Pr})_3$, $P(Cy)_3$) are able to stabilize the colloids but suffer from a decreased activity compared to PPh_3, most likely as a consequence of the shielding of the metal surface by these additives, thus lowering the substrate access to the catalyst. Summarizing, PPh_3 in co-catalytic amounts turned out to exhibit the perfect balance of steric demand and coordination strength to the metal surface.

This study emphasizes the potential of coordinating additives to have a strong influence on the catalytic performance. By adjusting the steric and electronic characteristics, a highly active and selective monometallic system can be generated. The herein gained knowledge on the interaction of ligand and catalyst surface can help to learn more about other catalytic systems. For future studies, apart from post-synthetic additives, the effect of the anion of the ionic capping agent could be investigated in detail. Using $N(Octyl)_4Cl$ and $N(Octyl)_4I$ instead of $N(Octyl)_4Br$ could give rise to the influence of the size and polarity of the anion coordinating to the Pd NP surface on the catalytic performance. In a second step, avoiding halide-containing surfactants could be beneficial for the catalysis, as this class of ligands are known catalyst poisons.

3.2 Bimetallic Systems

3.2.1 Pd/Ga colloids

Preface

Inspired by numerous reports of Schlögl, Armbrüster and co-workers on heterogeneous bulk as well as nanoparticular Pd/Ga systems for the semi-hydrogenation catalysis of acetylene,[62–64,66–68,71,108,109,123] the development of a bottom-up synthesis strategy for a colloidal Pd/Ga system is intended. The examples of literature-known heterogeneous intermetallic Pd/Ga catalysts show that the access to nano-sized alloys is restricted to high-temperature syntheses and affords powder materials with rather large crystallite sizes.[71,96] Attempts for a downsizing of such particles requires the development of alternative synthesis strategies, preferably at low temperatures in order to prevent agglomeration of the formed Pd/Ga NPs. Starting from „classical“ Pd(II) and Ga(III) salts does not fulfill this requirement. After co-precipitation of the precursors on a support, the reduction of both metals at high temperatures is an indispensable synthesis step. An elegant approach in order to work at mild conditions is to exclusively operate in solution and focusing on the development of bottom-up syntheses for colloidal Pd-Ga NPs. A simple, simultaneous reduction of the metals salts at mild temperatures is not possible since the reduction potentials of both metals are too different. Hence, alternative, organometallic metal precursors are auspicious candidates for a successful formation of (bimetallic) colloids. Consequently, the development of a synthesis strategy is based on the reaction of metal-organic precursors with labile ligands or “all hydrocarbon” ligands as they enable an easy ligand exchange and the formation of bimetallic cluster compounds.[124]

Recent studies in our group have shown that by the reaction of $[Pd_2(dvds)_3]$ (dvds=1,3-divinyl-1,1,3,3-tetramethyldisiloxane) with GaCp* (Cp* = η^5-C_5Me_5, pentamethyl cyclopentadienyl), the product formation is strongly dependent on the reaction conditions. For instance, the selective formation of multinuclear, Cp*-stabilized “$PdGa_4$”, “Pd_2Ga_5” and “Pd_3Ga_8” complexes or clusters is a function of the applied reaction conditions.[111,124] Depending on the metal precursor ratios and reaction conditions, such as temperature and solvent, the dinuclear $[Pd_2(GaCp^*)_2(\mu_2\text{-}GaCp^*)_3]$ and the trinuclear $[Pd_3(GaCp^*)_4(\mu_2\text{-}GaCp^*)_4]$ were selectively isolated (see Scheme 11).[111] This concept can principally be used to get access to even larger soluble cluster entities or NPs, which can be used as catalysts for selective hydrogenations. Therefore, under slightly modified reaction parameters, $[Pd_2(dvds)_3]$ and

GaCp* as precursors are prone for the synthesis of well-defined colloids as they are self-assembling in a broad scope of desired Pd/Ga ratios and decompose upon loss of their organic shell at elevated temperatures. These simple organometallic precursors can serve as the starting material for bimetallic colloids by a careful adjustment of reaction parameters.

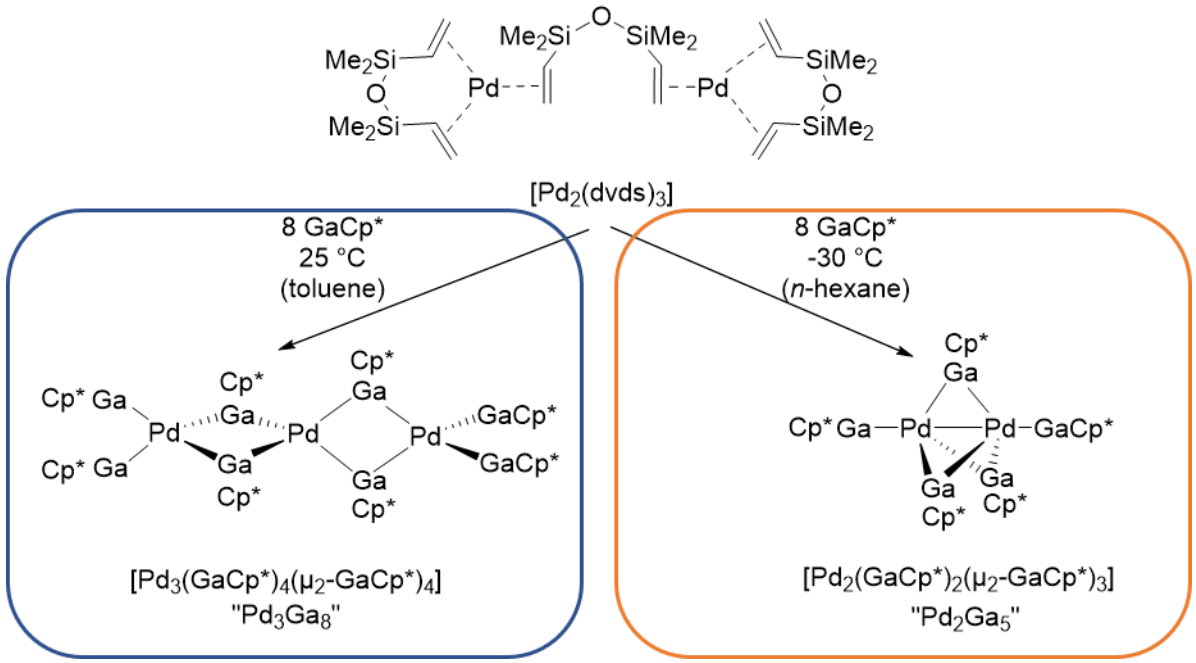

Scheme 11. Literature-reported synthesis protocols for Pd/Ga clusters starting from the metal precursors $[Pd_2(dvds)_3]$ and GaCp* yielding a "Pd_3Ga_8" (blue) or "Pd_2Ga_5" (orange) cluster compound strongly depending on the reaction conditions.[111,124]

Scientific issues

The reaction of the metal precursors $[Pd_2(dvds)_3]$ and GaCp* will be investigated with focus on the synthesis of bimetallic Pd/Ga colloids. Following questions will be addressed specifically:

a) Is it possible to obtain intermetallic Pd(0)/Ga(0) colloids with small sizes and size distributions by careful adjustment of the reaction parameters (temperature, H_2 pressure, solvent)? Can these colloids be stabilized in solution?

b) Can such Pd/Ga colloids be applied as catalysts for the semi-hydrogenation of alkynes? If yes, how is the catalytic performance (activity and selectivity) influences by the Pd/Ga ratio (site-isolation principle)?

c) Are the particles stable during catalysis runs? Here, the focus not only lies on the colloid agglomeration or precipitation, but also on the NP structure and surface.

d) How can post-synthetic additives (with different functional groups and steric demands) influence the overall performance (including stability, activity and selectivity) of the Pd/Ga colloids? Can the inactive metal not only influence the catalyst selectivity but also can serve as anchor for coordinating additives, enabling the adjustment of the catalyst stability? Here, the main focus lies on the protection against agglomeration and oxidation.

e) How do the herein discussed colloids perform compared to literature-reported intermetallic Pd/Ga catalysts? To what extent is a direct comparison reasonable?

Parts of this chapter were published in the journal *Nanoscale*. All XPS data were collected and analyzed by Tim Kratky, whereas the HR-TEM images were detected by Ondra Tomanek. ICP-MS measurements were performed by Alexander Urstöger. The XANES measurements were recorded and analyzed by Juanjuan Huang (TU Munich, Chair of Biomedical Physics).

In a collaboration with the Chair of Physical Chemistry (TU Munich), the Chair of Analytical Chemistry (TU Munich) and the Regional Center of Advanced Technologies and Materials (RCPTM, University of Olomouc), the synthesis strategy of colloidal Pd/Ga colloids including a full-characterization and the determination of the formation mechanism were reported. Catalysis studies on the semi-hydrogenation of liquid alkynes confirmed the idea of the site-isolation principle. The author list results as follows:

L. Staiger, T. Kratky, S. Günther, A. Urstoeger, M. Schuster, O. Tomanek, R. Zboril, R. W. Fischer, R. A. Fischer, M. Cokoja, *Nanoscale* **2021**, *13*, 15038-15047.

Synthesis and characterization of $Pd_{1-x}Ga_x$ colloidal NPs

The reaction of $[Pd_2(dvds)_3]$ with GaCp* in toluene was intensively investigated with the aim to obtain colloidal $Pd_{1-x}Ga_x$ NPs (x = 0.33, 0.5, 0.67) with different Pd/Ga ratios. Giving rise to the sensitivity of reactants and products towards air and moisture, all reactions were carried out under inert conditions. In detail, $[Pd_2(dvds)_3]$ was dissolved in toluene at -20 °C, giving a pale-yellow solution. In contrast, if the Pd precursor was dissolved at 25 °C, immediate precipitation of a black solid is observed. Therefore, all reactions were carried out at -20 °C. Addition of the respective amount of GaCp* (0.5, 1.0 and 2.0 molar equiv. referred to the Pd amount) lead to a bright yellow solution (see Scheme 12). Slow warming to 0 °C resulted in a color change from yellow to orange and finally to a deep red. By a further temperature increase to 25 °C, after 48 h the formation of a brown precipitate for samples of the composition $Pd_{0.67}Ga_{0.33}$ and $Pd_{0.5}Ga_{0.5}$ was observed, while all components of the sample

with the highest Ga amount ($Pd_{0.33}Ga_{0.67}$) stay in solution. Exposure of the colloids to air leads to a discoloration of the solution, as well as particle decomposition and precipitation.

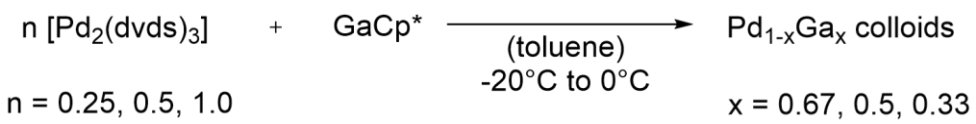

Scheme 12. Synthesis protocol of colloidal $Pd_{1-x}Ga_x$ NPs by an organometallic approach.

Structure and size determination

HR-TEM and DLS analysis of the obtained red solutions revealed small NPs for all tested Pd/Ga ratios with a narrow size distribution from 1.2±0.3 nm to 2.1±0.4 nm, depending on the metal ratios (see Figure 15). In detail, a higher Ga content resulted in smaller particle sizes. Storage of the colloidal samples (toluene solution) at -40 °C under inert conditions ensured stable colloids up to six months without any agglomeration observed. Note: the samples are stable without any additives, such as special surfactants.

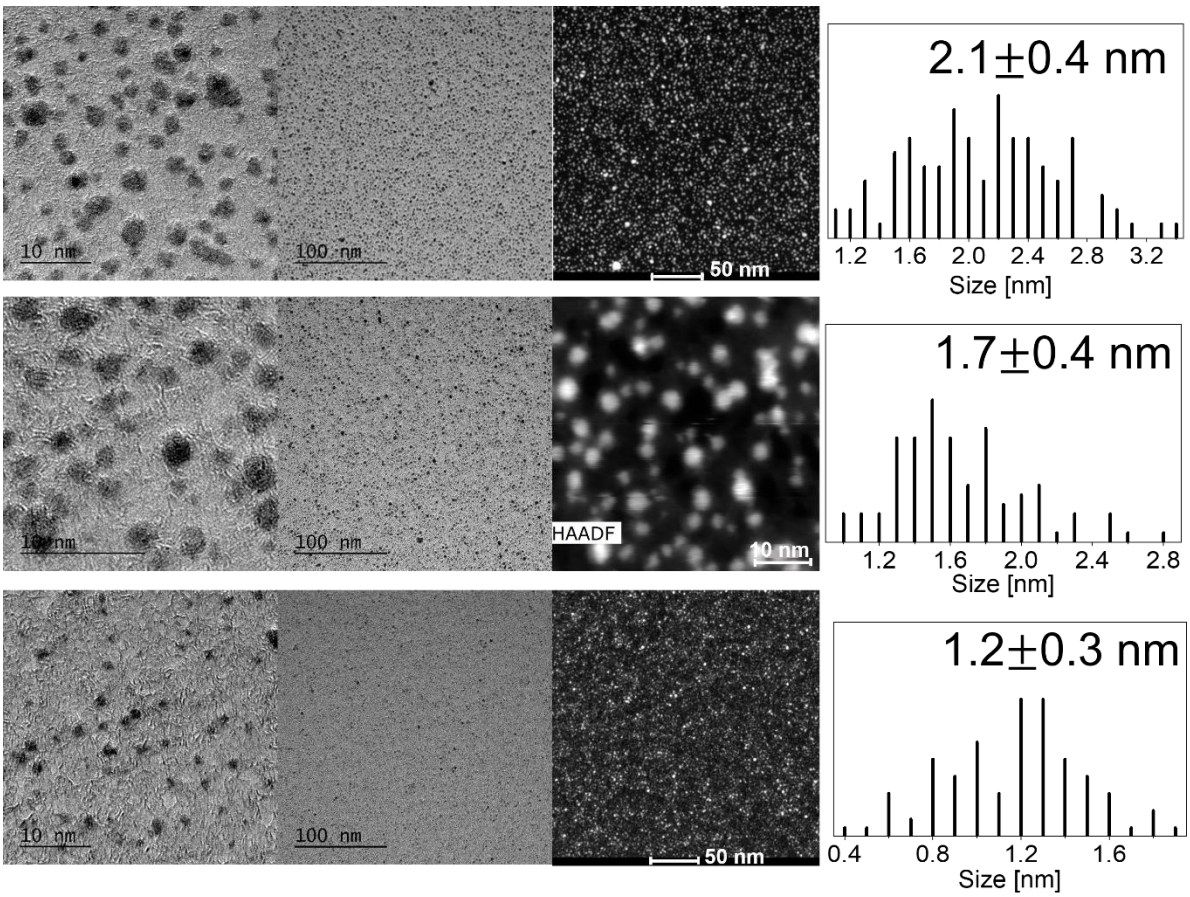

Figure 15. HR-TEM images (overview, increased magnification and HAADF) showing a narrow size distribution of $Pd_{0.67}Ga_{0.33}$ (above), $Pd_{0.5}Ga_{0.5}$ (middle) and $Pd_{0.33}Ga_{0.67}$ (bottom) nanoparticles. Particle size distribution was determined by analyzing the diameter of 100 particles.

EDX spectra confirm the NP composition of Pd and Ga, as well as Si, O, C and H stemming from the dvds ligand. The obtained Cu signal originates from the Cu mesh grid used for these measurements. Elemental mapping shows a homogeneous distribution of Pd and Ga over all particles (see Figure 16).

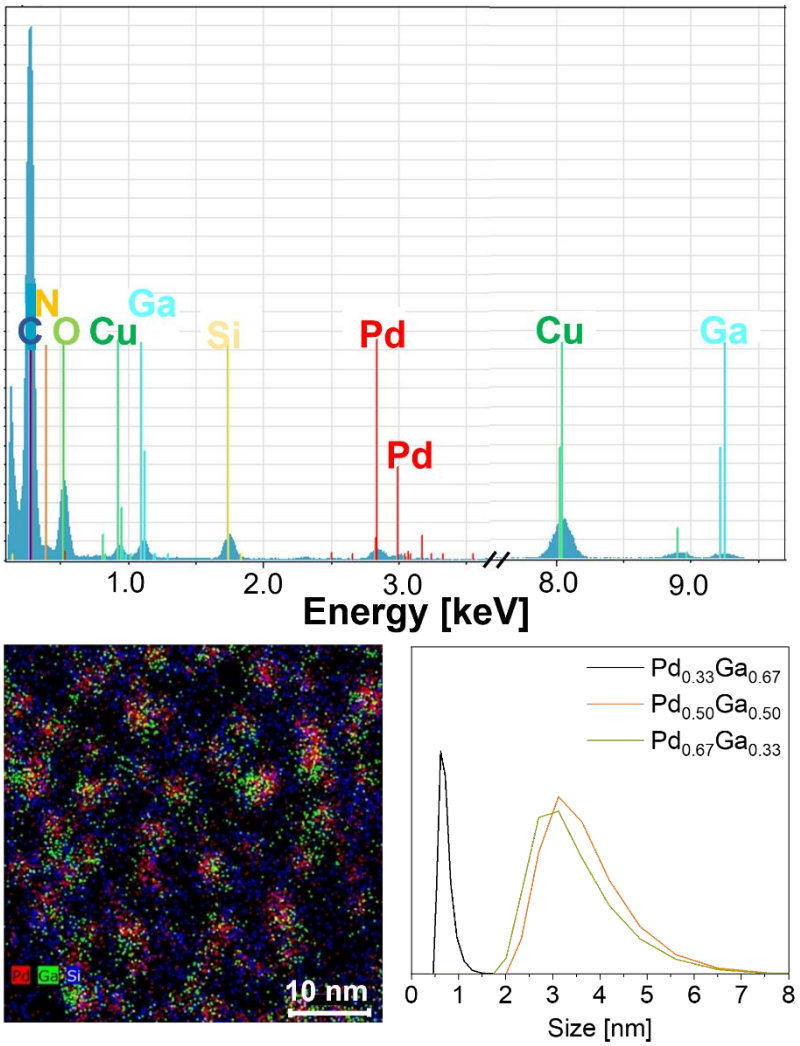

Figure 16. Representative EDX spectra (above) for all Pd/Ga colloids and elemental mapping of $Pd_{0.5}Ga_{0.5}$ NPs showing a homogeneous distribution of both metals (bottom, left). DLS measurements (bottom, right) of all samples confirm the size distribution obtained by HR-TEM analysis.

Elemental analysis was carried out in order to confirm the applied Pd/Ga ratios. Two different methods, namely induced-coupled plasma mass spectroscopy (ICP-MS) and atomic-absorption spectroscopy (AAS) measurements were performed (see Table 9) to ensure a reliable result. ICP-MS measurements show a slightly too low value of Ga for all samples. The measurement of the elemental composition *via* AAS resulted in a higher difference of the calculated Pd/Ga ratio, always with a too high Pd amount. This might be explained by the observation of insoluble white residues, which can probably be identified as Ga oxide species. Hence, the Ga content is in all samples underestimated.

Table 9. Molar Pd/Ga ratios obtained by ICP-MS and AAS analysis of the precipitated $Pd_{1-x}Ga_x$ colloids.

Sample	Pd : Ga molar (calculated)	Pd : Ga molar (measured) ICP-MS	Pd : Ga molar (measured) AAS
$Pd_{0.67}Ga_{0.33}$	2 : 1	2.52 ± 0.01 : 1	3 : 1
$Pd_{0.5}Ga_{0.5}$	1 : 1	1.13 ± 0.00 : 1	1.4 : 1
$Pd_{0.33}Ga_{0.67}$	0.5 : 1	0.60 ± 0.00 : 1	1 : 1

Beside the Pd/Ga molecular ratio, also the oxidation states of both metals are of interest, as the formation of intermetallic NPs requires both metals in the metallic state. The simple synthetic protocol for the $Pd_{1-x}Ga_x$ colloids does not include an additional reducing agent (e.g. H_2). The oxidation states of Pd and Ga in the case of the metal precursors $[Pd_2(dvds)_3]$ and GaCp* can be determined to Pd(0) and Ga(I). Hence, it has to be investigated whether these oxidation states change during colloid synthesis. The oxidation state of both metals was analyzed by XPS measurements. A detailed characterization of the oxidation states of the metals is given in Figure 17. Deconvolution of the Pd 3d core level according to literature-known binding energies evidence Pd predominately in its metallic state.[127] The Ga $2p_{3/2}$ core level shows that the main component originates from oxidized Ga species.[128]

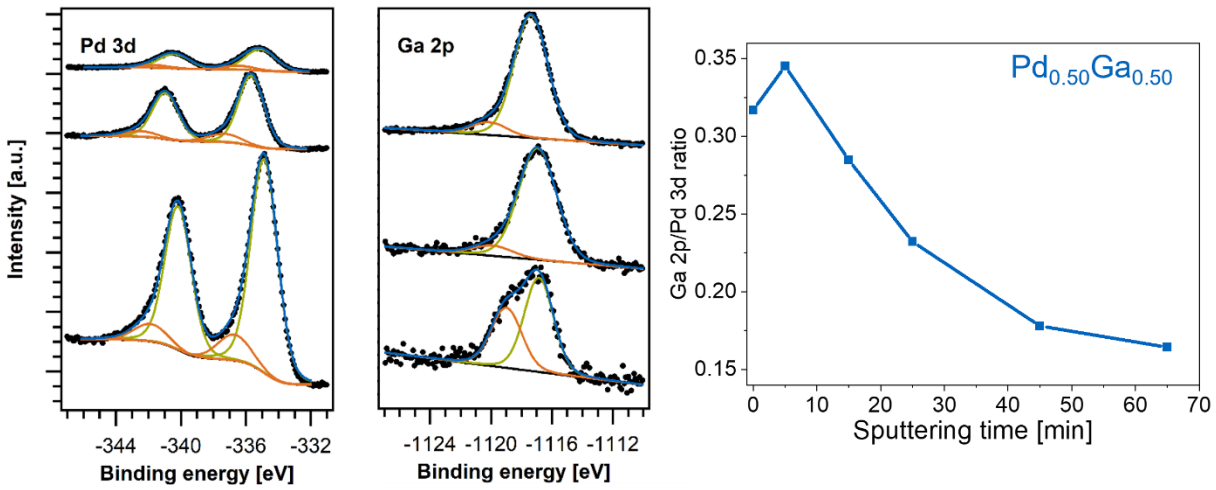

Figure 17. Left: XPS detail spectra of the Pd 3d core level showing Pd mainly in the metallic state (green component). Ga $2p_{3/2}$ detail spectra evidencing the presence of both, metallic and oxidized Ga (green and orange components, respectively). The intensity was scaled to the overall Pd 3d peak area. Right: Depth profiling by Ar^+ ion sputtering reveals a nanoparticle structure with an increasing Ga fraction from the center to the surface.

However, metallic Ga is also detected supporting the homolytically breaking of the Ga-Cp* bond. The oxidized fraction can be attributed to the highly oxophilic nature of nano-sized group 13 metals which causes the partial Ga oxidation during the XPS preparation process. Hence, the exact metallic fractions of the NPs in solution remain unknown and might be significantly higher as *ex situ* XPS sets the lower limit. Depth profiling based on repeated Ar^+

ion sputtering and subsequent XPS measurements sheds light on the structural composition of the $Pd_{0.5}Ga_{0.5}$ NPs. The decreasing Ga 2p/Pd 3d intensity ratio with proceeding sputtering time proves the NPs to consist of a nano-alloy with a Pd-rich core and a Ga-rich surface, rather than a structurally homogeneous and crystalline intermetallic Hume-Rothery phase, which is a very likely consequence of the low-temperature synthesis of the NPs. Note that the Ga 2p/Pd 3p ratio rises during the first profiling step from 0 to 5 min. As the kinetic energy of Pd 3d photoelectrons (~1150 eV) exceeds the one of Ga 2p photoelectrons (~370 eV), the latter exhibit a higher surface sensitivity than the former due to a decreased signal attenuation length. An overlayer on top of a NP, hence, attenuates the Ga 2p signal more strongly compared to Pd 3d. Due to the preparation method, it is likely that residual solvent remains on the particle surface which is removed during the first sputtering step. This causes the increase of the Ga 2p/Pd 3d intensity ratio. Concluding, the surface of the NPs can be interpreted as Pd diluted in a Ga matrix.

In order to confirm the colloid structure of a Pd-rich core and a Ga-rich shell suggested by XPS measurements, the NPs were exposed to an atmosphere of CO and analyzed the CO surface adsorption by IR spectroscopy (see Figure 18, right). The underlying adsorption properties on the surface of the $Pd_{1-x}Ga_x$ can give rise to the nature of the NP metal surface. In general, bridging and terminal bound CO adsorption modes indicate the surrounding of the Pd on the NP surface. Bridging CO is typically observed for metallic Pd, whereas terminal CO suggests a separation of the active Pd centers which indicates Pd separation by a second, non-reactive metal.[64,109,129] Therefore, the type of CO binding can serve as an indicator for the nature of the particles surface. The spectra displayed in Figure 18 exhibit characteristic bands in the carbonyl regions of 1800-1950 cm^{-1} and 1975-2100 cm^{-1}. These bands are typical for bridging and terminal CO on metallic Pd surfaces, respectively.[129] Hence, with an increasing Ga amount a Pd-poor surface is generated. Comparison of the IR spectra shows explicit differences in the adsorption behavior of CO which go in line with the literature-known site-isolation principle. The Pd-rich NPs $Pd_{0.67}Ga_{0.33}$ exclusively show bridging bound CO, whereas only terminal bound CO was detected in the case of the Ga-rich colloids $Pd_{0.33}Ga_{0.67}$ indicating an isolation of the adsorption sites.

Theoretically, based on a perfect closed packed $Pd_{0.33}Ga_{0.67}$ structure, a Pd/Ga ratio of 1:3 would be required for a complete isolation of the Pd centers indicating a higher Ga amount on the particle surface than applied, thus supporting the assumption of a Pd-rich core and a Ga-rich surface as found by XPS analysis. Regarding $Pd_{0.5}Ga_{0.5}$ with Pd/Ga = 1:1, both, bridging and terminal CO is detected. In summary, CO adsorption IR measurements highlight the presence of isolated adsorption sites by formation of intermetallic $Pd_{1-x}Ga_x$ nanoparticles.

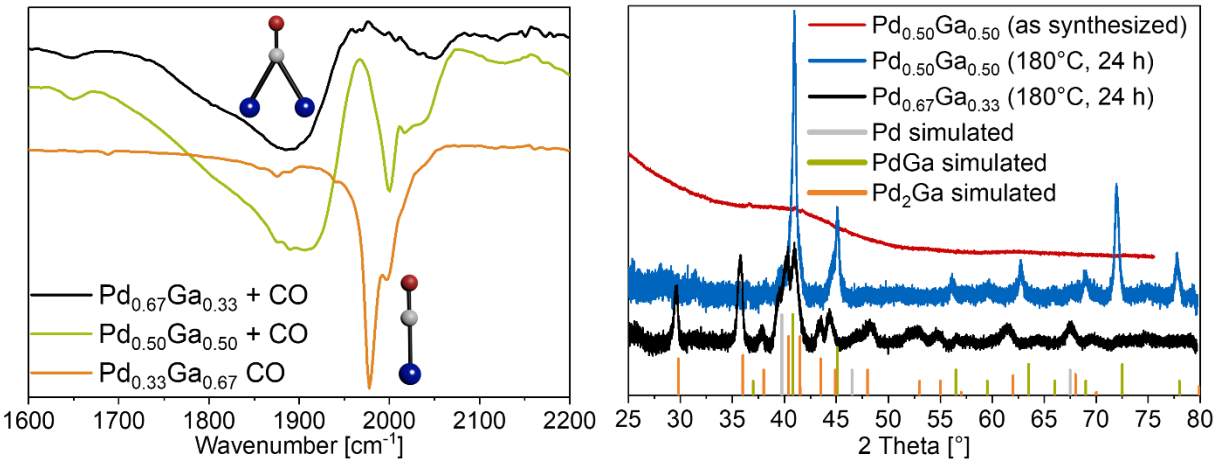

Figure 18. Left: IR spectra of CO adsorbed on $Pd_{0.67}Ga_{0.33}$ (black), $Pd_{0.5}Ga_{0.5}$ (green) and $Pd_{0.33}Ga_{0.67}$ (orange) recorded at 25 °C in the CO stretching region from 1600–2200 cm^{-1}. Right: PXRD measurements of the precipitated $Pd_{1-x}Ga_x$ colloids. For crystallinity, samples were annealed in vacuum at 180 °C for 24 h prior to measurements. Without annealing, no reflections could be detected (see red trace). For Pd/Ga = 1:2, phase determination was not successful due to the poor crystallinity of the sample.

As already mentioned before, the colloids precipitate upon long-term warming up to 25 °C (for 48 h) allowing for powder X-ray diffraction (PXRD) and elemental analysis (see Figure 18, right, and Table 9). In contrast, simple removal of all volatile compounds in the reaction mixture did not yield the NPs as powders but rather as wax-like solids with a sticky consistency. Precipitation and post-synthetic heating at 180 °C for 24 h of the $Pd_{0.67}Ga_{0.33}$ and $Pd_{0.5}Ga_{0.5}$ NPs give the respective Pd/Ga phases Pd_2Ga and PdGa, apparent by the respective reflexes (see Figure 18). This behavior supports the assumption that the partial Ga oxidation observed in XPS measurements occurs during sample preparation and is not present in the as-synthesized colloidal solution. If this would not be the case, the formation of the respective Pd/Ga phases would not take place. No reflections of pure Pd were found, indicating a quantitative alloying of both metals in the colloids.

The $Pd_{0.50}Ga_{0.50}$ colloids were further analyzed by X-Ray Near Edge Spectroscopy (XANES) with a liquid cell setup (see Figure 20).[130,131] This setup has the advantage that the particles are measured in solution and do not have to be used as a solid, thus excluding undesired agglomeration or oxidation processes during sample preparation. As the energy range of the used in-house instrument for these measurements is only tunable from 15 keV to 35 keV, the absorption edge of Ga cannot be measured.

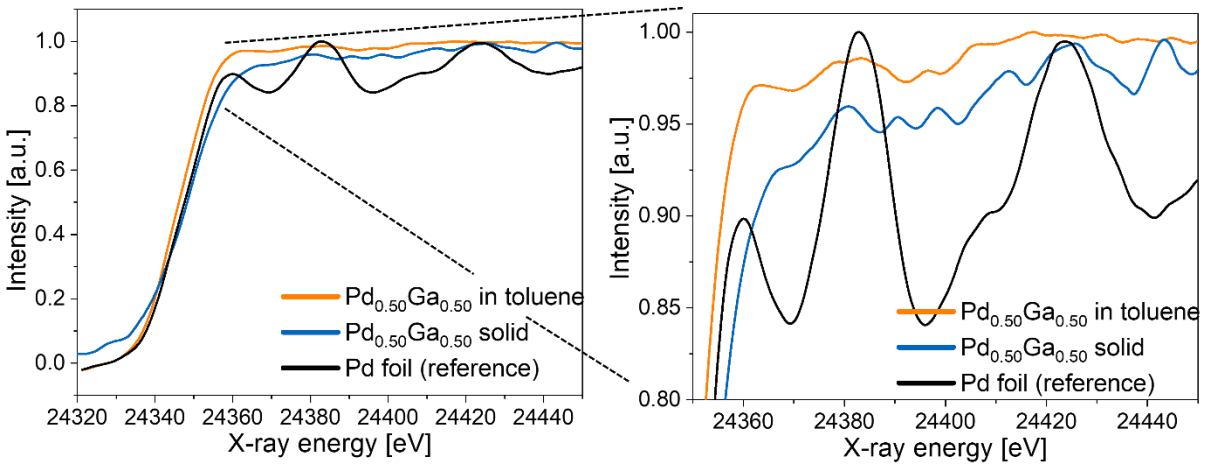

Figure 19. Pd K edge XANES spectra of $Pd_{0.5}Ga_{0.5}$ colloids in toluene and Pd foil as reference (full spectrum on the left side) showing the absorption edge of Pd(0) and zoom-in of the spectra on the right side.

The analysis of the obtained XANES data containing information about the coordination environment of Pd was used to determine the oxidation state and the nature of the metal-metal bonds. Therefore, the $Pd_{0.5}Ga_{0.5}$ NPs in toluene, precipitated $Pd_{0.5}Ga_{0.5}$ NPs (upon storage at 25 °C) and a Pd foil as reference were measured. The most notable differences between the two samples are generally lower amplitudes of the oscillations and a slight shift of the spectral features to lower energies for the bimetallic colloids compared to the Pd foil. The position of the Pd edge shifted towards lower energies, indicating the change in electron density by filling of the valence d band of Pd by covalent interactions between Pd and Ga (see Figure 20, orange and black traces). This observation is in good agreement with literature-reported XANES spectra of heterogeneous Pd/Ga NPs.[71,96] The decrease of amplitudes of the oscillations can be interpreted as the existence of many different Pd-metal distances, thus lowering the intensity of the spectral features. These findings support the idea of a mixed structure with a Pd-rich core and a Ga-rich surface rather than an ordered intermetallic PdGa structure. Comparison of the $Pd_{0.5}Ga_{0.5}$ colloids in solution and the precipitated NPs shows an increase in amplitudes of the oscillations for the solid sample, indicating the formation of more extended Pd-Pd domains which is in good agreement with the assumption of a particle growth leading to a precipitation of a Pd/Ga bimetallic material upon temperature increase.

Investigation on the $Pd_{1-x}Ga_x$ colloidal stabilization

No additional surfactants were added. Hence, the question arises how the herein obtained colloids are stabilized in solution. The ^{1}H NMR data for all $Pd_{1-x}Ga_x$ colloids are characteristic for only weakly bound, certainly not-covalently coordinated dvds, as no shift of the ligand

signal is observed (see SI, Figure 93). This becomes even more apparent by comparison with the $[Pd_2(dvds)_3]$ precursor, where all dvds signals are shifted upon coordination to the Pd centers. For a better understanding of the stabilization of the colloids, Fourier-transform-attenuated-total-reflection-infrared (ATR-FT-IR) spectra were analyzed suggesting a coordination of the dvds ligand to the $Pd_{1-x}Ga_x$ colloidal surface as a shift of all ligand signals compared to the pure dvds molecule in the region between $\tilde{\nu}$ = 650 cm^{-1} and 1300 cm^{-1} is observed (see Figure 17). Thus, dvds acts as an intrinsic surfactant of the system. This coordination is assumed to be important for a colloidal stabilization in solution. In detail, for the $Pd_{0.5}Ga_{0.5}$ colloids, the δ(C-H) out-of-plane vibration at 700 cm^{-1} and the $\delta(Si\text{-}CH_3)$ mode at 1252 cm^{-1} [125,126] split into two bands (at 694.2 cm^{-1} and 706 cm^{-1}; and 1221 cm^{-1} and 1248 cm^{-1}, respectively) upon NP formation. The symmetric and asymmetric vibration modes of Si-O-Si at 780 cm^{-1}, 834.4 cm^{-1}, 1007 cm^{-1} and 1046 cm^{-1} [125,126] are shifted to 795 cm^{-1}, 830 cm^{-1}, 1017 cm^{-1} and 1089 cm^{-1}. These finding support a weak coordination of the dvds to the metal surface (not detectable via ^1H NMR spectroscopy). Comparison of NPs with different Pd/Ga ratios suggest a stronger dvds coordination to the surface with higher Pd amount, as the asymmetric vibration modes of Si-O-Si coincide into one signal at 790 cm^{-1}.

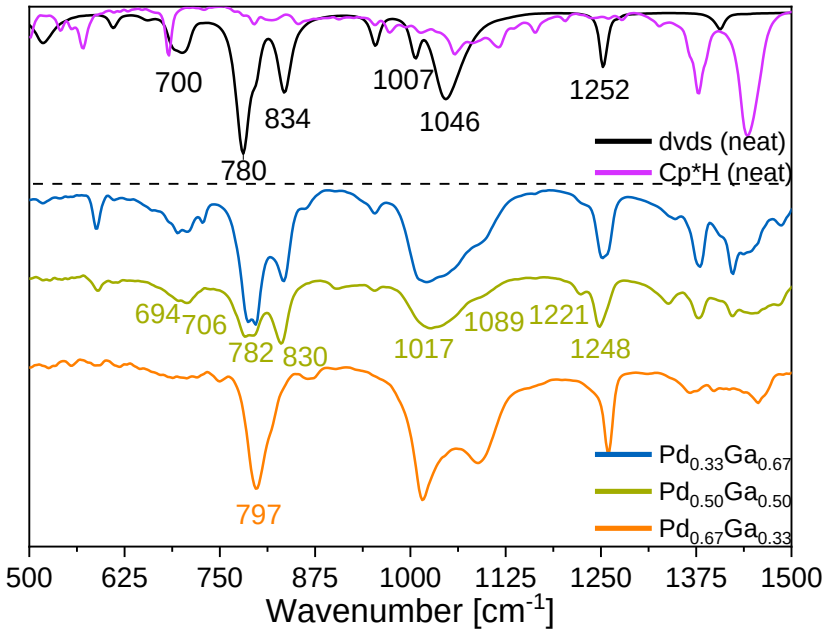

Figure 20. FT-IR spectra of $Pd_{1-x}Ga_x$ colloids (bottom traces) and pure dvds and Cp*H as reference showing a dvds signal shift suggesting a coordination to the metal surface.

This clearly shows that the $Pd_{1-x}Ga_x$ NPs are stabilized by the dvds ligand originating from the Pd precursor. Hence, this example demonstrates that such bimetallic colloids can be generated with simple and elegant synthesis protocol, where the upon reaction of the metal precursors, the “free” ligands can act as surfactant. Therefore, an additional, a post-synthetic surfactant is not necessarily required.

Investigation on the formation mechanism of $Pd_{1-x}Ga_x$ colloidal NPs

Summarizing from the so far discussed data, it can be concluded that a successful bottom-up synthesis procedure of colloidal $Pd_{1-x}Ga_x$ NPs starting from organometallic precursors exhibiting labile protecting ligands was developed. Furthermore, the dvds ligand originating from the Pd precursor $[Pd_2(dvds)_3]$ is suspected to additionally coordinate to the NP surface leading to a particle stabilization in solution. For a better understanding of the reaction between $[Pd_2(dvds)_3]$ and GaCp* in toluene at low temperatures, a combination of ^1H NMR spectroscopy, GC-MS measurements and LIFDI-MS analysis was applied to gain a deeper insight. The reaction of $[Pd_2(dvds)_3]$ with GaCp*, especially in the temperature range between -20 °C, e.g. right after addition of GaCp*, and 0 °C is analyzed in detail in order to investigate if bimetallic complexes or clusters are formed as intermediates on the way to the target NPs.

Identification of metal-organic cluster intermediates

Kinetic monitoring of the product formation was enabled by LIFDI-MS measurements. As already reported for Pd/Ga intermetallic clusters, a subsequent coordination of GaCp* to the surface and a homolytically Ga-Cp* bond breaking result in the formation of $[Pd_nGa_mCp^*_y(dvds)_z]$ clusters which can be analyzed by mass-spectrometric techniques (see Figure 21 and Table 10). Please note that a conclusion on the precise cluster composition in the reaction solution is not possible. The distinction between a “real” cluster compound and fragmentation signals would require further detailed LIFDI-MS studies. Hence, this analysis method just gives a qualitative idea of the of the nature of the cluster species which are formed in solution.

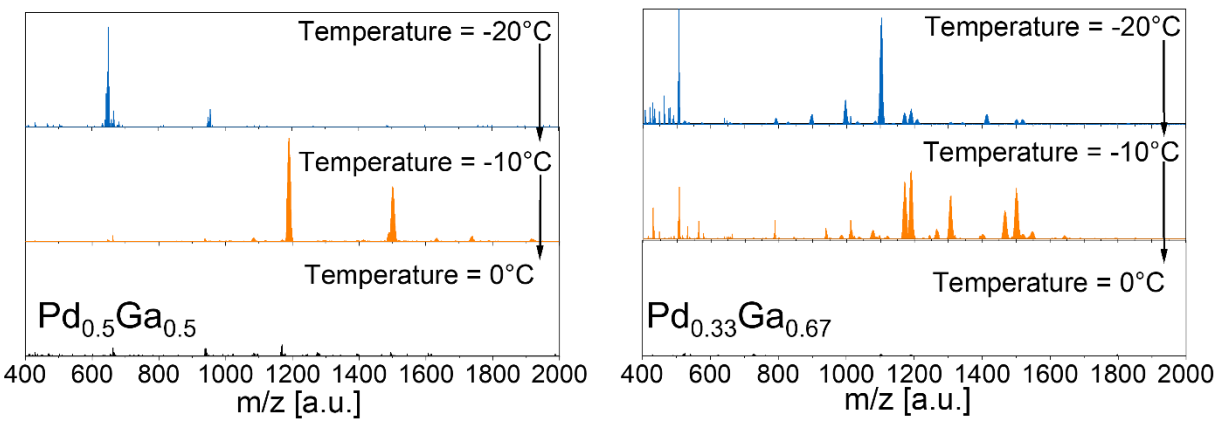

Figure 21. Representative LIFDI-MS spectra monitoring the cluster formation and deformation during synthesis of colloidal $Pd_{0.5}Ga_{0.5}$ (left) and $Pd_{0.33}Ga_{0.67}$ (right) at various temperatures (top: -20°C, middle: -10°C, bottom: 0°C) by a slow warming up of the reaction mixture.

For a Pd/Ga ratio of 1:1 ($Pd_{0.5}Ga_{0.5}$), a series of various, Cp*-deficient cluster compounds $[Pd_nGa_mCp^*_y(dvds)_z]$ with different intensities were detected (see Figure 21 left and Table 10). At -20 °C, only the two cluster compounds $[Pd_2Ga(dvds)(toluene)_2]$ (m/z = 649.3) and $[Pd_3Ga(dvds)(toluene)]$ (m/z = 665.0) were monitored. Warming up the reaction temperature to -10 °C, larger clusters were formed, namely $[Pd_3Ga_4Cp^*_3dvds]$, $[Pd_4Ga_5Cp^*_4dvds]$, $[Pd_4Ga_4Cp^*_3dvds]$, $[Pd_4Ga_5Cp^*_4(toluene)_2]$ and $[Pd_3Ga_3Cp^*_4(dvds)_3H_4]$ showing a cluster growth process by changing the temperature. Hence, the cluster compounds can be regarded as intermediates on the way to NP formation. The ionization of larger species at the emitter of the LIFDI MS instrument is strongly dependent on the nature and the thermal resistance of the sample. According to our own (qualitative) experience, organometallic species with up to a m/z of 3000 can be detected by the herein used instrument. Nevertheless, colloids with a of size 1.2 nm with a Pd:Ga ratio of 1 are calculated to exhibit 64 metal atoms (assuming a bcc structure with 74 % space filling, for a detailed calculation see experimental section), hence clearly exceed this detection limit by far (here, the m/z is calculated to 5600).

The formation of Ga-rich colloids $Pd_{0.33}Ga_{0.67}$ colloids was also analyzed by LIFDI-MS monitoring, also showing various cluster signals of the general formula $[Pd_nGa_mCp^*_y(dvds)_z]$, in which the increased Ga amount is also reflected in the detected metal clusters (see Table 10).

Table 10. Measured and calculated signals of LIFDI-MS measurements during the synthesis of $Pd_{0.5}Ga_{0.5}$ and $Pd_{0.33}Ga_{0.67}$ colloids. Most intense signals are marked in bold.

Applied Pd/Ga ratio	Chemical formula	Calculated m/z [a.u.]	Measured m/z [a.u.]	Temperature [°C]
1:1	$Pd_2Ga(dvds)(toluene)_2$	648	648.2	-20
1:1	$Pd_3Ga(dvds)(toluene)$	665	665.1	-20
1:1	**$Pd_3Ga_4Cp^*_3dvds$**	1190	1190.1	-10
1:1	$Pd_4Ga_4Cp^*_3dvds$	1296	1294.7	-10
1:1	$Pd_4Ga_5Cp^*4(toluene)_2$	1497	1496.6	-10
1:1	**$Pd_4Ga_5Cp^*_4dvds$**	1500	1501.2	-10
1:1	**$Pd_3Ga_3Cp^*_4(dvds)_3H_4$**	1632	1632.8	-10
1:1	$Pd_4Ga_3Cp^*_4(dvds)_3H_4$	1739	1738.8	-10
1:2	$PdGa_4Cp^*_3H_2$	792	792.5	-20
1:2	$PdGa_3Cp^*(dvds)_2H_3$	828	827.5	-20
1:2	$PdGa_4Cp^*(dvds)_2H_4$	897	897.5	-20
1:2	$PdGa_5Cp^*_4H_2$	998	997.9	-20
1:2	$PdGa_3Cp^*(dvds)_3H_2$	1012	1012.1	-20
1:2	$Pd_2Ga_4Cp^*_4H$	1034	1033.9	-20
1:2	$Pd_2Ga_4Cp^*_3(dvds)H_2$	1085	1085.1	-20
1:2	**$Pd_2Ga_5Cp^*_4$**	1102	1102.1	-20
1:2	$Pd_2Ga_4Cp^*_2(dvds)_2H_3$	1138	1138.7	-20
1:2	$Pd_3Ga_3Cp^*_2(dvds)_2$	1170	1170.3	-20
1:2	**$Pd_3Ga_4Cp^*_3(dvds)$**	1190	1190.0	-20

1:2	$Pd_2Ga_5Cp^*_2(dvds)_2H_4$	1209	1208.6	-20
1:2	$Pd_4Ga_5Cp^*_4$	1308	1307.9	-20
1:2	$Pd_2Ga_5Cp^*_3(dvds)_2H_3$	1344	1343.7	-20
1:2	$Pd_5Ga_{10}(dvds)$	1413	1414.1	-20
1:2	**$Pd_4Ga_5Cp^*_4(dvds)$**	1500	1500.7	-20
1:2	$Pd_4Ga_6Cp^*_5$	1520	1519.9	-20
1:2	$Pd_3Ga_3Cp^*_2(dvds)$	985	984.8	-10
1:2	$PdGa_3Cp^*(dvds)_3H_2$	1012	1012.1	-10
1:2	$Pd_3Ga_3Cp^*(dvds)_2H_3$	1038	1037.7	-10
1:2	$Pd_3Ga_3Cp^*_2$*(dvds)tol	1077	1077.9	-10
1:2	$Pd_3Ga_3Cp^*_3dvds$	1118	1118.1	-10
1:2	**$Pd_3Ga_3Cp^*_2dvds_2$**	1171	1171.5	-10
1:2	**$Pd_3Ga_4Cp^*_3dvds$**	1190	1190.3	-10
1:2	**$Pd_3Ga_3Cp^*_3(dvds)_2$**	1307	1306.8	-10
1:2	**$Pd_4Ga_{13}Cp^*$**	1467	1467.7	-10
1:2	**$Pd_4Ga_5Cp^*_4dvds$**	1501	1501.6	-10
1:2	$Ga_4Cp^*_5(dvds)_3H_4$	1513	1513.8	-10
1:2	$PdGa_8Cp^*(dvds)_4H_3$	1546	1545.9	-10
1:2	$Pd_4Ga_7Cp^*_4(dvds)H_3$	1643	1643.3	-10

In general, more cluster signals are obtained for $Pd_{0.33}Ga_{0.67}$ compared to $Pd_{0.5}Ga_{0.5}$. At a temperature of -20 °C, several cluster signals are observed, e.g. masses which can be assigned to the compounds $[Pd_2Ga_4Cp^*_3(dvds)H_2]$, $[Pd_2Ga_5Cp^*_4]$, $[Pd_4Ga_5Cp^*_4]$ and $[Pd_4Ga_5Cp^*_4(dvds)]$ were detected. Upon an increase of the temperature to -10 °C, further cluster growth leads to the detection of even higher mass signals, e.g. $[PdGa_8Cp^*(dvds)_4H_3]$ at 1545.9 m/z and $[Pd_4Ga_7Cp^*_4(dvds)H_3]$ at 1643.3 m/z. When the reaction temperature is allowed to increase to 0 °C, a continuous growth of the metal clusters to nanoparticles takes place and all the low molecular weight organometallic precursors and intermediate cluster species appear to be consumed as no cluster related signals can be detected via LIFDI MS. When applying a more Pd-rich synthesis conditions (Pd/Ga = 2:1), no cluster related signals at all temperatures could be detected indicating larger particle growth at even low temperatures. These findings indicate that the concept of the synthesis of the literature-known, defined and isolable bimetallic complexes $[Pd_2(GaCp^*)_2(\mu_2\text{-}GaCp^*)_3]$ and $[Pd_3(GaCp^*)_4(\mu_2\text{-}GaCp^*)_4$[111] can be extended to a library of various, larger clusters (of so far undefined structure). This library can be interpreted as a dynamic collection of intermediate species towards the formation of colloidal intermetallic Pd-Ga phases. At least or preliminary data based in in-situ LIFDI MS indicate options to control composition and size regime of Pd/Ga intermetallic NPs by variation of molar ratio of precursors, concentration and temperature program of the reaction.

Identification of organic byproducts

For further analysis of the formation mechanism of $Pd_{1-x}Ga_x$ colloids, ^1H NMR spectroscopy was applied. At -10 °C, for all colloidal solutions of all Pd/Ga ratios, the ^1H NMR spectrum shows the full dissociation of dvds upon formation of Pd nuclei and minor amounts of Cp*H, whereas the color of the reaction mixture changes from yellow to orange (see SI, Figure 93). Warming up the reaction mixture to 0 °C for 1 h, ^1H NMR spectroscopy shows quantitative amounts of Cp*H and toluene C-C coupling products for all Pd/Ga ratios. Additionally, no signals of organometallic cluster residues were detected giving evidence to a full conversion of organometallic compounds to bimetallic NPs. Additionally, the signals of C-C coupling products (orange marked, see Figure 22, left) were detected, which were further confirmed by GC-MS measurements. Molecule masses corresponding to these products of the C-C coupling, namely a series of toluene and Cp*-toluene coupling products, were further detected by GC-MS measurements (see Figure 22, right) supporting the herein proposed formation mechanism (see Figure 23).

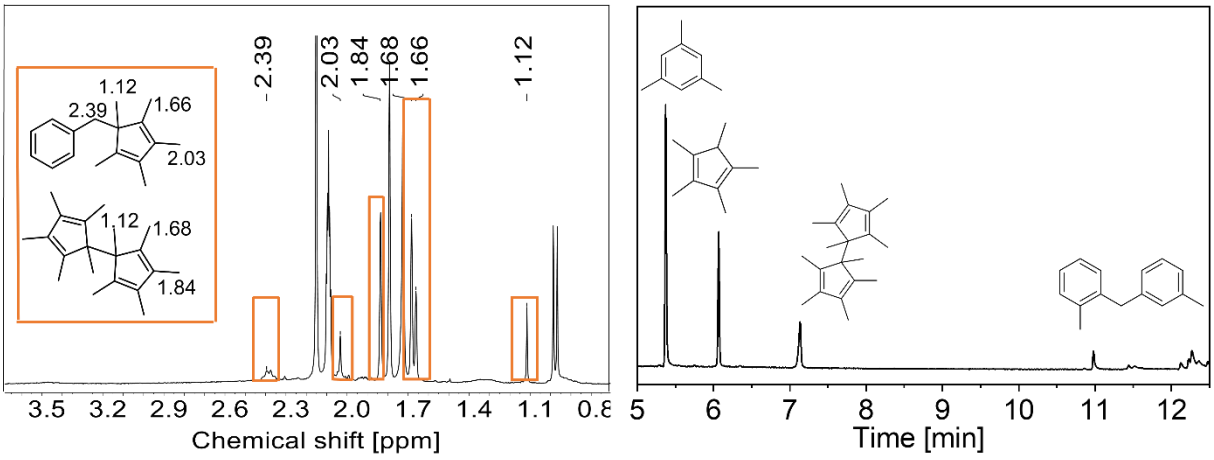

Figure 22. Left: Zoom-in of a representative ^1H NMR spectra (toluene-d_8) of colloidal $Pd_{1-x}Ga_x$ NPs showing the signals of C-C coupling products (orange marked). All other signals originate from mesitylene, toluene-d_8 and Cp*H. Note that due to overlapping signals and weak signal intensities, a distinct signal assignment is not possible. Right: Representative GC chromatogram of colloidal $Pd_{1-x}Ga_x$ NPs showing mesitylene as internal standard and products of a C-H activation reactivity.

Upon coordination of GaCp* to freshly formed Pd nuclei, a homolytic bond breaking of the Ga-Cp* bond takes place, resulting in a Pd-Ga bond and a Cp*• radical. Consequently, the reaction of the Cp*• radical with the methyl group of toluene by H• transfer results in the formation of Cp*H. The benzyl radicals then dimerize to toluene dimers. Additionally, a fraction of Cp*• dimerizes, detected by GC-MS measurements (see Figure 22). Notably, decomposition of GaCp* to Cp*H by residual traces of water in the solvent can be excluded as a targeted addition of D_2O did not yield in the respective Cp*D (see SI, Figure 106).

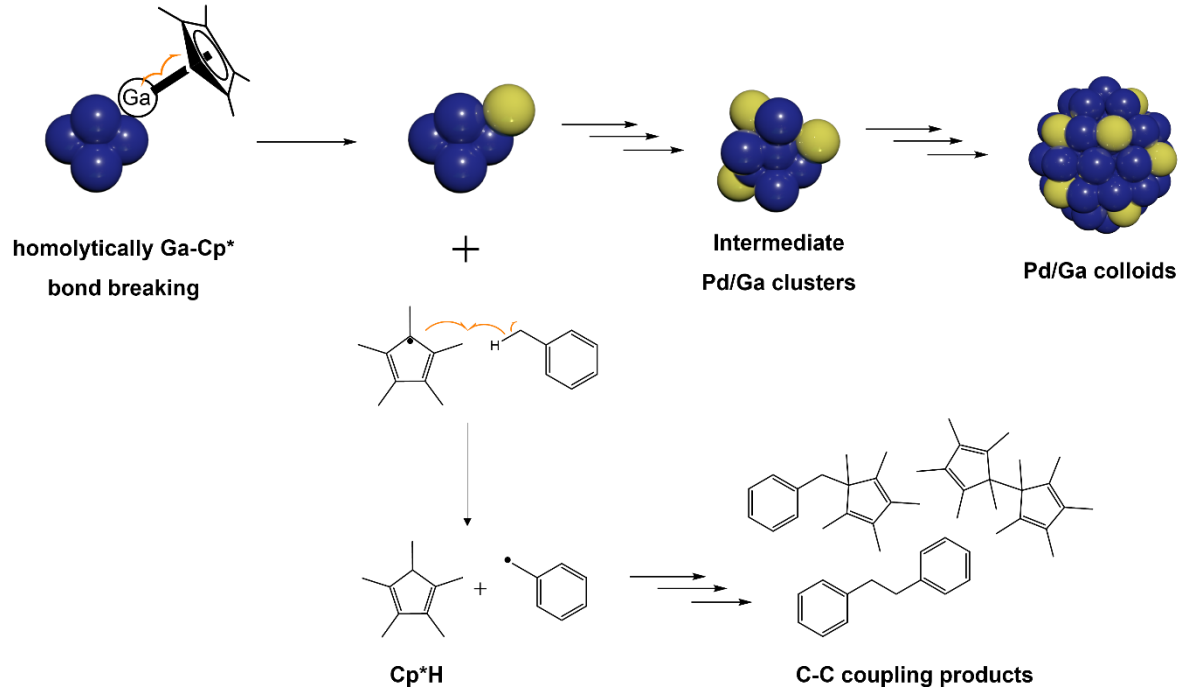

Figure 23. Proposed reaction mechanism of $Pd_{1-x}Ga_x$ NP formation by a C-C coupling mechanism leading to colloidal Pd/Ga NPs with a Pd-rich kernel and a Ga-rich shell.

Summarizing this chapter, the combination of the results of LIFDI MS, NMR spectroscopy and GC-MS measurements allow for a detailed understanding for the formation mechanism of Pd/Ga NPs by the reaction of $[Pd_2(dvds)_3]$ and GaCp* (see Figure 23). A library of various, larger clusters with undefined structures can be interpreted as intermediate species towards the formation of colloidal intermetallic Pd-Ga phases, stabilized by a weakly coordinated dvds ligand shell.

$Pd_{1-x}Ga_x$ colloids in the semi-hydrogenation catalysis of liquid alkynes

As already stated in the beginning of this chapter, the key question of the influence of the second metal Ga on the activity and selectivity in alkyne semi-hydrogenation reactions will be addressed. Therefore, the catalytic performance of $Pd_{1-x}Ga_x$ NPs was systematically tested in the semi-hydrogenation reaction of liquid alkynes. In order to get a first idea on the potential of the herein studied colloids (and to find the best reaction conditions for further catalytic tests), parameter optimization with 3-hexyne as substrate and $Pd_{0.67}Ga_{0.33}$ as catalyst (see Scheme 13) was performed. Here, not surprisingly, a dependence of the activity as well as selectivity on the temperature and the H_2 partial pressure was obtained. Note: The amount of catalyst is always referred to the Pd amount.

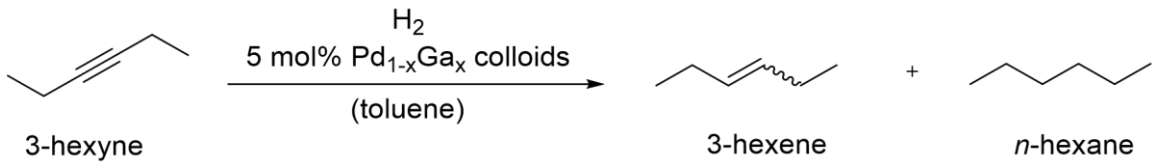

Scheme 13. Semi-hydrogenation catalysis using 5 mol% catalyst $Pd_{1-x}Ga_x$ colloids in a H_2 atmosphere.

Parameter optimization

The results of this parameter optimization are given in Table 11. As already mentioned before, partial particle precipitation for the Pd-rich NPs $Pd_{1-x}Ga_x$ (x = 0.33, 0.5) is observed at 25 °C, which results in a decreased activity (see Table 11, Entries 1 and 2 and SI, Figure 102). Additionally, at this temperature not only the substrate is hydrogenated but also the dvds ligand (up to 50 % of in 2 h), therefore competing with the alkyne and leading to an increased NP precipitation. In contrast, for the Ga-rich $Pd_{0.33}Ga_{0.67}$, no particle precipitation of dvds hydrogenation is observed at even 50 °C (see Table 11, Entry 7) showing that the Ga amount has a large influence on the particle stability.

Table 11. Catalytic tests with 3-hexyne as substrate and 5 mol% $Pd_{1-x}Ga_x$ colloids after 6 h reaction time. Conversion after 10 min were taken for TOF value calculation.

Entry	$Pd_{1-x}Ga_x$	Temperature [°C]	H_2 pressure [bar]	Conversion [%]	Selectivity [%]	TOF [h^{-1}]
1	$Pd_{0.67}Ga_{0.33}$	25	1.0	35	68	-
2	$Pd_{0.67}Ga_{0.33}$	25	2.0	79	42	-
3	$Pd_{0.67}Ga_{0.33}$	0	1.0	60	73	-
4	$Pd_{0.67}Ga_{0.33}$	0	2.0	61	69	126
5	$Pd_{0.50}Ga_{0.50}$	0	2.0	60	81	153
6	$Pd_{0.33}Ga_{0.67}$	0	2.0	4	100	40
7	$Pd_{0.33}Ga_{0.67}$	50	2.0	28	84	-

Hence, performing the catalysis tests at 0 °C, all $Pd_{1-x}Ga_x$ colloids are kept in solution with only minor ligand hydrogenation resulting in an enhanced activity (see Table 11, Entries 4-6). Increasing of the H_2 pressure from 1.0 bar to 2.0 bar showed a higher activity with comparable selectivity by suggesting no direct influence of the H_2 partial pressure on the selectivity (see Table 11, Entries 3 and 4). Therefore, a competitive coordination of the hydrogen and the alkyne to the particle surface can be excluded assuming that the rate determining step is the coordination of the alkyne to the metal surface.

Variation of the catalyst amount from 1 mol% to 20 mol% reveals almost no differences in selectivity but an optimum in activity by using 5 mol% $Pd_{1-x}Ga_x$ colloids, as with higher

catalyst amounts, particle agglomeration can be assumed (see Figure 24). These experiments show that a too high catalyst concentration is not beneficial. Hence, it is important to run the catalysis tests under optimized conditions.

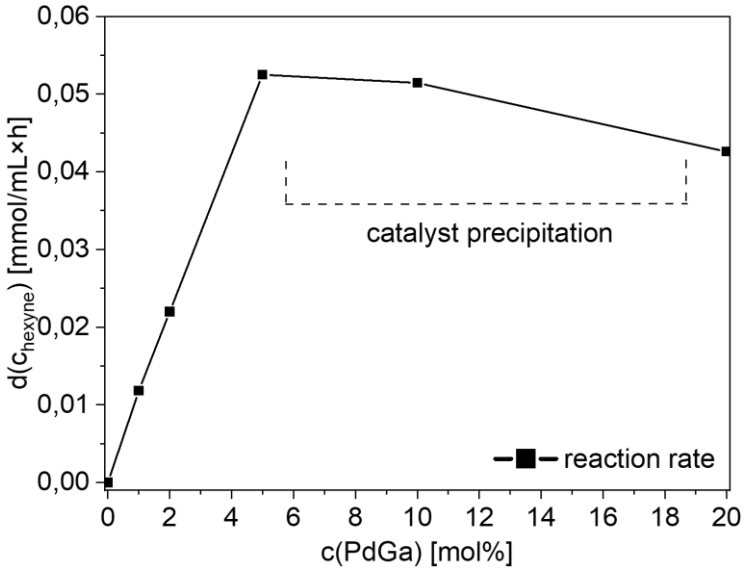

Figure 24. Variation of the catalyst amount from 0.1 mol% to 20 mol% using $Pd_{0.67}Ga_{0.33}$.

All further catalytic experiments where run under the optimized conditions with 0 °C, $p(H_2)$ = 2.0 bar and 5 mol% catalyst, if not stated otherwise. Notably, the olefin groups of the dvds are not hydrogenated upon addition of 2.0 bar H_2 and therefore is stable under catalytic conditions according to ^{1}H NMR measurements (see SI, Figure 169).

Influence of the Pd/Ga ratio

For an understanding of the influence of the Pd/Ga ratio on the catalytic performance, $Pd_{1-x}Ga_x$ NPs with different Pd/Ga ratios under the same reaction conditions were tested and directly compared with each other (see Table 11 and Figure 25). Here, a clear coherence between the Ga amount and the selectivity towards the alkene emerges, consistent with the site-isolation principle (see Table 11, Entries 4-6). In detail, the NPs with an increased molar Ga amount $Pd_{0.5}Ga_{0.5}$ show a higher selectivity of 85 % and a minimal lower activity of 60 % ($Pd_{0.67}Ga_{0.33}$: 69 % selectivity and 61 % conversion). Comparison of the TOF values (for a detailed calculation see Experimental Section) shows a decreased value for $Pd_{0.67}Ga_{0.33}$ compared to $Pd_{0.5}Ga_{0.5}$, which can be explained by particle precipitation or larger NP sizes, respectively. Note that the herein calculated TOF values are only approximate values, as for calculation a perfect icosahedral structure with a homogeneous Pd/Ga distribution was assumed (which is, according to XPS measurements, not the case). Hence, the herein introduced TOF values only allow for a comparison within the $Pd_{1-x}Gax$ colloids discussed in

this thesis. A direct comparison with literature-known intermetallic Pd/Ga catalysts is not possible, due to different measurement set-ups, substrates and catalyst structures.

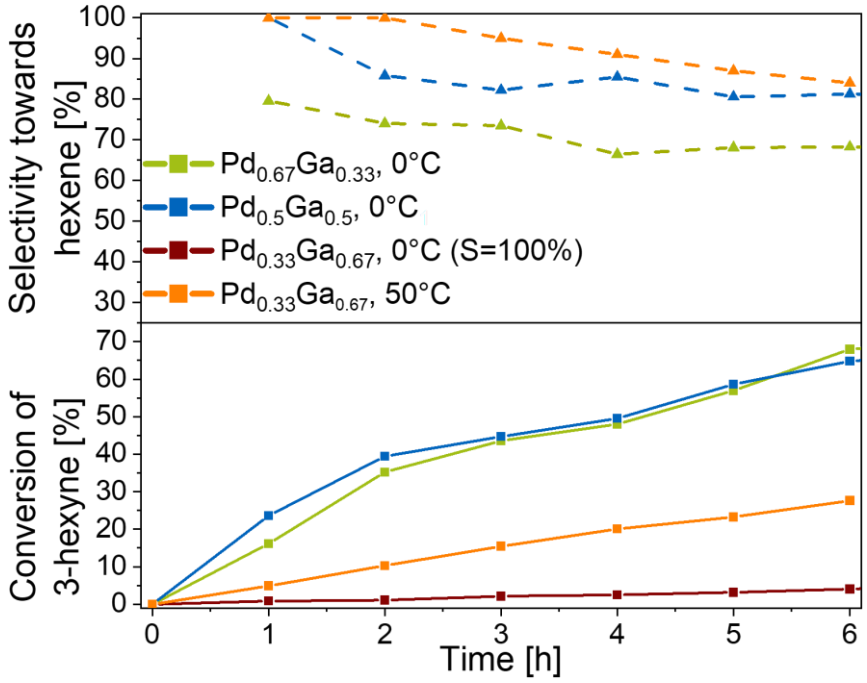

Figure 25. Catalytic performance of $Pd_{1-x}Ga_x$ (x = 0.33, 0.5. 0.67) NPs in the semi-hydrogenation of 3-hexyne with different Pd/Ga ratios using 5 mol% catalyst (referred to the Pd amount) with 2.0 bar H_2.

A further increase of the Ga amount giving $Pd_{0.33}Ga_{0.67}$ results in a highly selective but rather inactive system (4 % conversion, 100 % selectivity after 6 h catalysis time). Both, the decreased activity as well as a drastically increased selectivity can be attributed to the highly Ga-rich particle surface. This is also highlighted by a comparison of the TOF values regarding $Pd_{0.5}Ga_{0.5}$ and $Pd_{0.33}Ga_{0.67}$ colloids. An increase of the Ga amount giving $Pd_{0.33}Ga_{0.67}$ NPs leads to smaller NP sizes, but also to a strongly decreased TOF value which can be attributed to the dilution of the active metal Pd by the inactive Ga. In contrast to the Pd-rich colloids, the NPs Ga-rich $Pd_{0.33}Ga_{0.67}$ are stable up to 50 °C allowing catalysis tests at elevated temperatures, however showing drastically decreased activity but very high selectivity (Table 11, Entry 7).

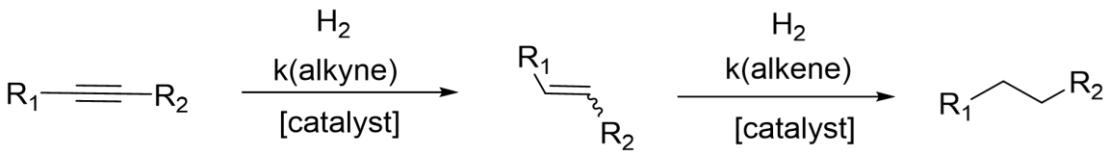

Scheme 14. Reaction scheme of successive alkyne hydrogenation to the alkene and alkane depending on the rate constants *k(alkyne)* and *k(alkene)*.

As for all $Pd_{1-x}Ga_x$ colloids, no full conversion after 5 h reaction time was observed, a more direct comparison of the catalytic performance becomes possible by a simple calculation of

the ratio between alkyne and alkene. In detail, the ratio of the rate constants $\frac{\mathrm{k(alkyne)}}{\mathrm{k(alkene)}}$ leads to a detailed kinetic study and enables a comparison of the relative selectivities of semi- and full-hydrogenation, independent on the respective conversion (see Scheme 14). The rate constants were calculated with following formula:

$$r = -\frac{dc(alkyne)}{dt} = -k(alkyne) \cdot c(alkyne)$$

Table 12. Calculated ratios of the rate constants k(alkyne) and k(alkene). Catalytic tests were performed using 5 mol% $Pd_{0.67}Ga_{0.33}$ and $Pd_{0.5}Ga_{0.5}$ as catalyst with 3-hexyne as substrate at 0°C and 2.0 bar H_2.

Reaction time [h]	$\frac{\mathrm{k(alkyne)}}{\mathrm{k(alkene)}}$ with $Pd_{0.67}Ga_{0.33}$	$\frac{\mathrm{k(alkyne)}}{\mathrm{k(alkene)}}$ with $Pd_{0.5}Ga_{0.5}$
1 → 2	2.873	3.253
2 → 3	2.932	3.193
3 → 4	2.918	3.238
4 → 5	2.635	3.162
5 → 6	2.706	2.678
6 → 7	2.062	2.348

For simplification, the H_2 partial pressure was not considered, as this reactant is always apparent in large excess during the whole period of catalysis. With preferred alkene formation over full-hydrogenation, the value of this ratio is higher than one. A ratio lower than one implies that the full-hydrogenation to the alkane is preferred over the desorption of the favoured alkene. Therefore, a high value for this constant is desired. With special regard to the different Pd/Ga ratios, a direct comparison of the obtained ratios goes in line with the site-isolation principle. With increasing Ga amount, a higher rate constant is observed, implying a preferred desorption of the alkene instead of a further hydrogenation. Increasing the amount of the ignoble metal leads to a ratio significantly higher than one illustrated by the preference towards olefin formation.

Substrate variation

In addition to 3-hexyne, other substrates with different alkyl chain lengths (4-octyne) and a terminal alkyne (1-hexyne) were tested in semi-hydrogenation catalysis. For 4-octyne, similar reactivities were found compared to 3-hexyne, therefore suggesting that the substrate's substituent in β-position does not have a great influence, electronically or sterically, on the catalysis (see Figure 26, left, and SI, Figure 167). In contrast, the hydrogenation of terminal alkynes results in a strong oligomerization, as already observed for the monometallic

Pd@N(Octyl)$_4$Br colloids, blocking the metal surface, consequently leading to a catalyst deactivation (see Figure 26, right and SI, Figure 168). This is also reflected by the calculated TOF values (ranging from 10 h^{-1} to 24 h^{-1}, depending on the Pd/Ga ratio, see SI Table 32), which are drastically decreased compared to the catalysis using 3-hexyne as substrate.

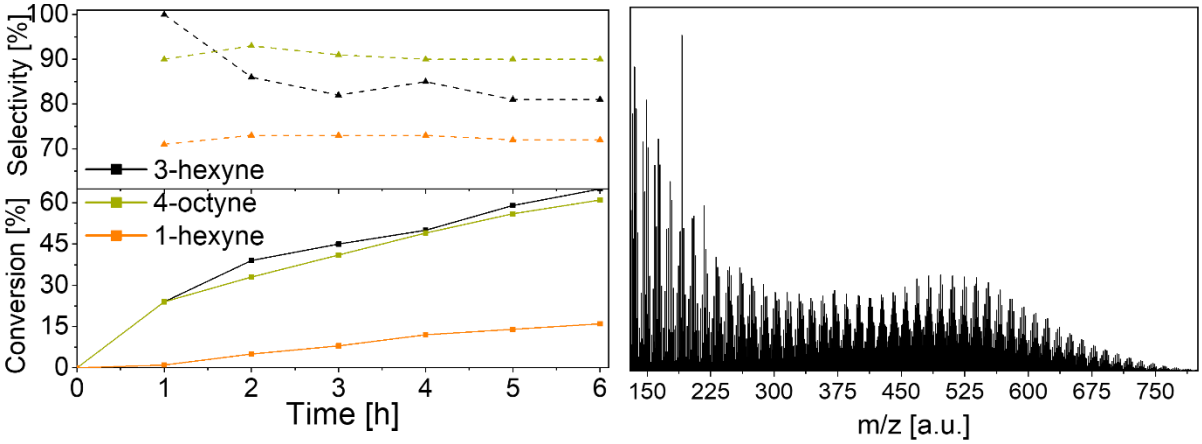

Figure 26. Left: Semi-hydrogenation of 3-hexyne, 4-octyne and 1-hexyne as substrate using 5 mol% $Pd_{0.5}Ga_{0.5}$ colloids and 2.0 bar H_2 at 0 °C. Right: LIFDI MS spectra of catalysis solution using 1-hexyne as substrate showing oligomerization products.

Summarizing the results of the herein tested $Pd_{1-x}Ga_x$ colloids in the semi-hydrogenation catalysis of liquid alkynes, the Ga amount significantly influences activity, selectivity and stability of the catalyst. Even small changes in the Pd/Ga ratios show significant differences in the catalytic performance. Additionally, the catalytic performance is strongly dependent on the chosen substrate. Highly reactive terminal alkynes tend to form oligomers blocking the catalyst active sites and hence result in a catalyst deactivation. This demonstrates that such colloidal systems are highly sensitive to various parameters, including not only the reaction conditions (e. g. temperature, H_2 pressure, catalyst amount), but also show completely different reactivities depending on the electronic features of the substrate. Hence, the high dependence on all these factors makes it more difficult to establish a high-performance catalyst system applicable for a variety of substrates.

$Pd_{1-x}Ga_x$ particle analysis after catalytic runs

Investigation on $Pd_{1-x}Ga_x$ colloids stability under catalytic conditions

The particles were further characterized after catalysis runs in order to determine the colloids´ stability under catalytic reaction conditions. Analysis of $Pd_{0.5}Ga_{0.5}$ NPs (Pd/Ga = 1:1) after catalysis by HR-TEM and DLS shows minor agglomeration ranging from 1.7-2.1 nm, which might be attributed to the absence of a strong capping agent, as the coordination of the dvds

ligand can be regarded as rather weak (see Figure 27). No precipitation or bigger agglomerates of the catalyst are observed, which is an important attribute of a colloidal catalytic system. Nevertheless, if the catalysis run is prolonged to 24 h, DLS measurements show particle agglomeration (without any precipitation) to about 40 nm highlighting the fragile structure of such systems in solution.

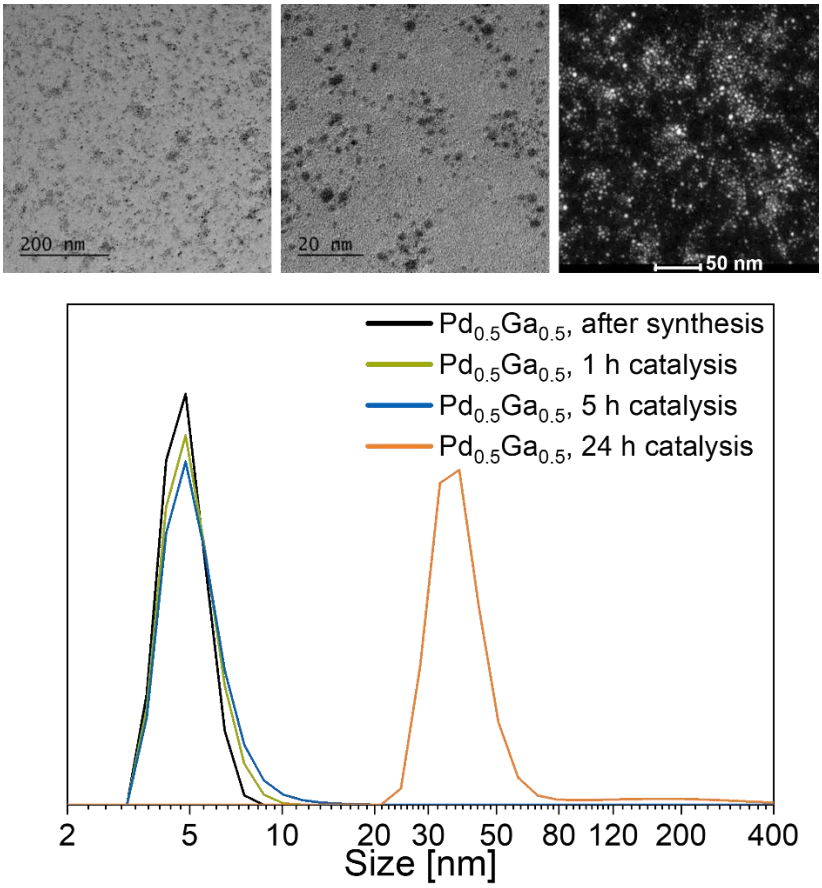

Figure 27. Top: HR-TEM images (low and high magnification) and HAADF of $Pd_{0.5}Ga_{0.5}$ colloids after semi-hydrogenation catalysis of 3-hexyne at 0°C and 2.0 bar H_2 after 5 h. Bottom: DLS monitoring of $Pd_{0.5}Ga_{0.5}$ colloids during the semi-hydrogenation of 3-hexyne at 0°C and 2.0 bar H_2.

For a better understanding of the surface dynamics under catalytic conditions, ATR-IR experiments were performed (see Figure 28). Upon addition of 3-hexyne, a partial displacement of the dvds ligand from the metal surface is observed. Alkyne addition leads to a partial displacement of the dvds ligand as a signal of the asymmetric vibration of Si-O-Si of free, not-coordinating dvds at 834 cm^{-1} is detected. Additionally, this signal is also monitored in minor amounts after catalysis runs. In the presence of an alkyne, the splitting of the dvds δ(C-H) out-of-plane vibration at 700 cm^{-1} and the δ(Si-CH_3) mode at 1252 cm^{-1} into two bands at 694 cm^{-1} and 707 cm^{-1}; and 1221 cm^{-1} and 1249 cm^{-1}, respectively upon coordination to the NP metal surface occurs. Nevertheless, a coordination of 3-hexyne or *cis*-3-hexene to the NP surface cannot be determined due to overlapping signals.

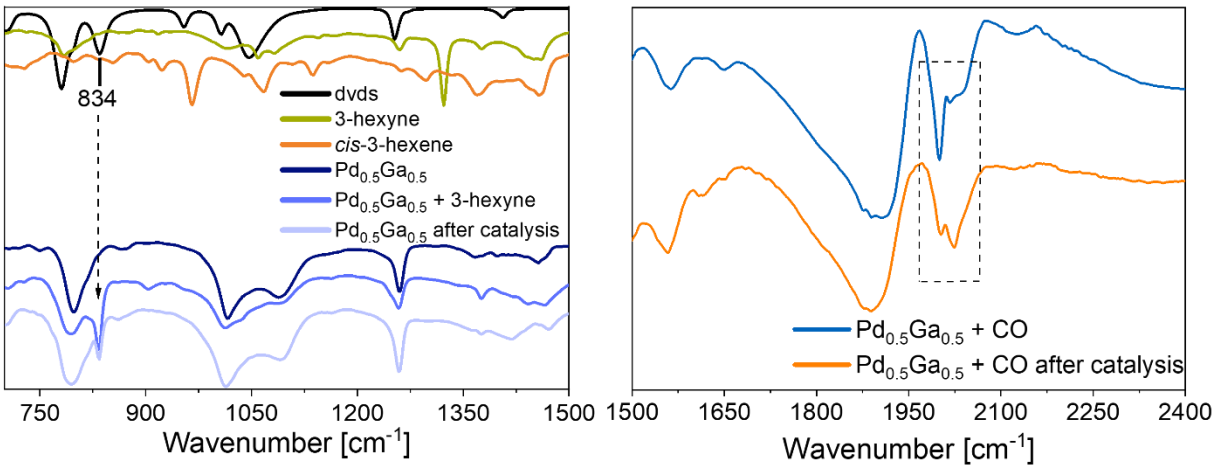

Figure 28. Left: ATR FT-IR measurement of the $Pd_{0.5}Ga_{0.5}$ colloids upon addition of 3-hexyne and after catalysis runs (bottom traces, blue) and pure dvds and Cp*H as reference (upper traces, black, green and orange). Right: ATR FT-IR measurement of the $Pd_{0.5}Ga_{0.5}$ colloids upon addition of CO before (blue trace) and after (orange trace) the catalytic semi-hydrogenation of 3-hexyne showing a change of the signal shape at 2000 cm^{-1} typical for linearly bonded CO.

Beside size determination after catalysis, also a chemical investigation of $Pd_{0.5}Ga_{0.5}$ NPs (Pd/Ga = 1:1) by XPS was performed (see Figure 29).

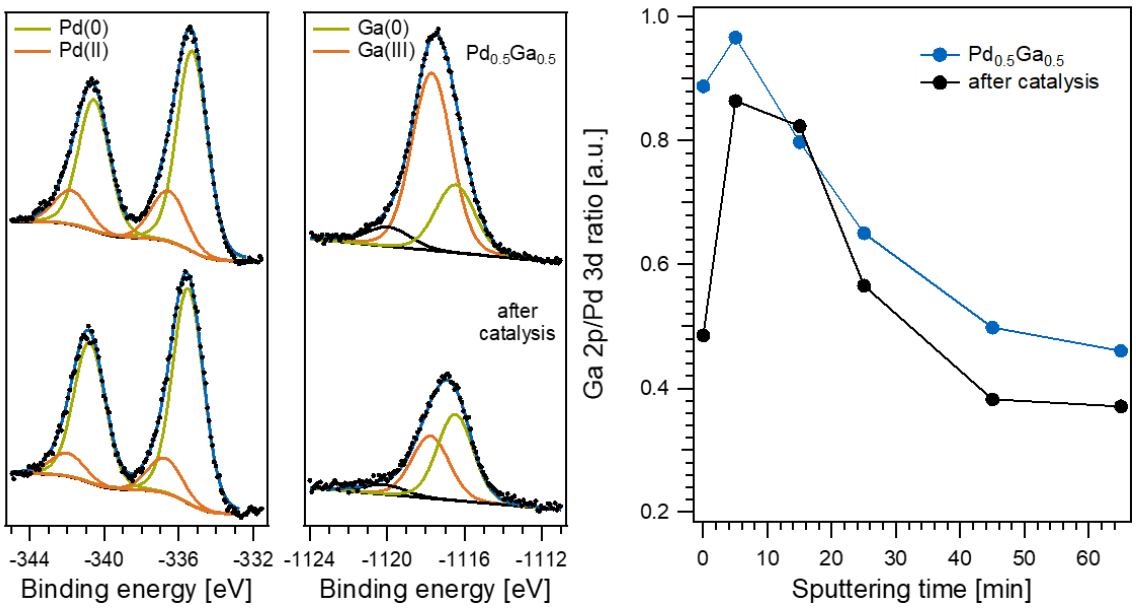

Figure 29. Left: XPS detail spectra of the Pd 3d core level before and after catalysis showing Pd mainly in the metallic state (green component). Ga $2p_{3/2}$ detail spectra evidencing the presence of both, metallic and oxidized Ga (green and orange components, respectively). The intensity was scaled to the overall Pd 3d peak area. The metallic fraction of Pd and Ga increases after the semi-hydrogenation of 3-hexyne at 0 °C and 2.0 bar H_2 for 2 h. Right: Depth profiling by Ar^+ ion sputtering reveals a nanoparticle structure with an increasing Ga fraction from the center to the surface.

Pd 3d and Ga $2p_{3/2}$ core level spectra reveal a higher fraction of both metals in their metallic oxidation state compared to the particles after synthesis. The Ga 2p signal intensity which is

scaled to the Pd 3d peak area decreases indicating a proceeding attenuation of the more surface-sensitive Ga 2p signal. This goes in line with a significantly more pronounced increase of the Ga 2p/Pd 3d intensity ratio during the first depth profiling step. The higher attenuation of the surface-sensitive signal might originate from a carbon overlayer grown during the semi-hydrogenation reaction. Kovnir et al. reported on the formation of a carbon layer on the surface of PdGa alloys during the semi-hydrogenation of acetylene which originates from hydrocarbon adsorption.[63] A similar formation mechanism can also take place in solution. Once the overlayer is formed, it might prevent the NPs from oxidation during the XPS preparation procedure, in contrast to the NPs before the catalytic reaction. It remains unclear whether the detected metallic states also reflect the situation before catalysis and are only conserved due to the carbon layer after catalysis or the reductive environment during the catalytic conversion induces a reduction of the NPs which are slightly oxidized in solution. Nonetheless, the depth profile of the NPs clearly rules out that the structure of a Pd-rich core and a Ga-rich surface is maintained.

Changes on the metal surface are additionally reflected by the CO adsorption behavior of $Pd_{0.5}Ga_{0.5}$ NPs after semi-hydrogenation catalysis. The signal for terminal bound CO at 2000 cm^{-1} (typically for isolated Pd) changes in terms of the signal shape, whereas the signal for bridging bound CO at 1800-1950 cm^{-1} is unaffected (see Figure 28, right). Thus, the overall structure of a Pd-rich core and a Ga-rich surface is maintained, but small changes at the particle surface upon catalysis runs is observed.

Investigations on structural changes during catalysis

Hence, it can be concluded that the herein tested colloidal system undergoes a small catalysis-induced structure change which remains after catalysis. This structural change is also reflected in a change of the ratio of the alkyne and alkene rate constant $\frac{k(alkyne)}{k(alkene)}$ over the time (see Table 12). A catalytic system not changing during catalysis exhibits a consistent rate constant. Comparison of the ratio over a time of 7 h shows a change during time supporting the assumption of a change of the catalyst surface. In detail, the ratio continuously decreases slightly from 3.25 to 2.35 over a period of 6 h, which is in accordance with structural changes during catalysis. Further investigation on this phenomenon was performed by monitoring of the catalytic performance regarding reusability experiments of $Pd_{0.5}Ga_{0.5}$ NPs. After 5 h of catalysis, all volatile compounds were removed, and fresh substrate was added to the colloidal catalytic system (see Figure 30). For the first hour of the reaction, the catalytic activity of the particles in run 1 was lower than in run 2. In the first catalysis run, an induction period

of ca. 40 minutes can be identified, which is not observed for the second run. Furthermore, the selectivity gradually decreases as opposed to run 2, where the selectivity towards the olefin seems more consistent and notably, higher than in the first run. These differences in both runs support the assumption of a change in the catalyst surface during the first catalysis run. XPS analysis of the colloids before and after the first catalysis run show a formation of a carbon layer on the particle surface (see Figure 28, right). As the highest activity is reached between 55 and 65 min and an induction period is only monitored in the first run, the active species is formed in situ in the beginning of the first catalysis experiment and can be described as a $Pd_{1-x}Ga_xC_n$ species. By a continuous deposition of carbon species of the surface, an activity enhancement over the time is observed. In the beginning of the second run, the particle surface is more carbon-rich resulting in a relatively higher activity. In addition, the selectivity toward the olefin is consistent giving evidence to a stable particle surface.

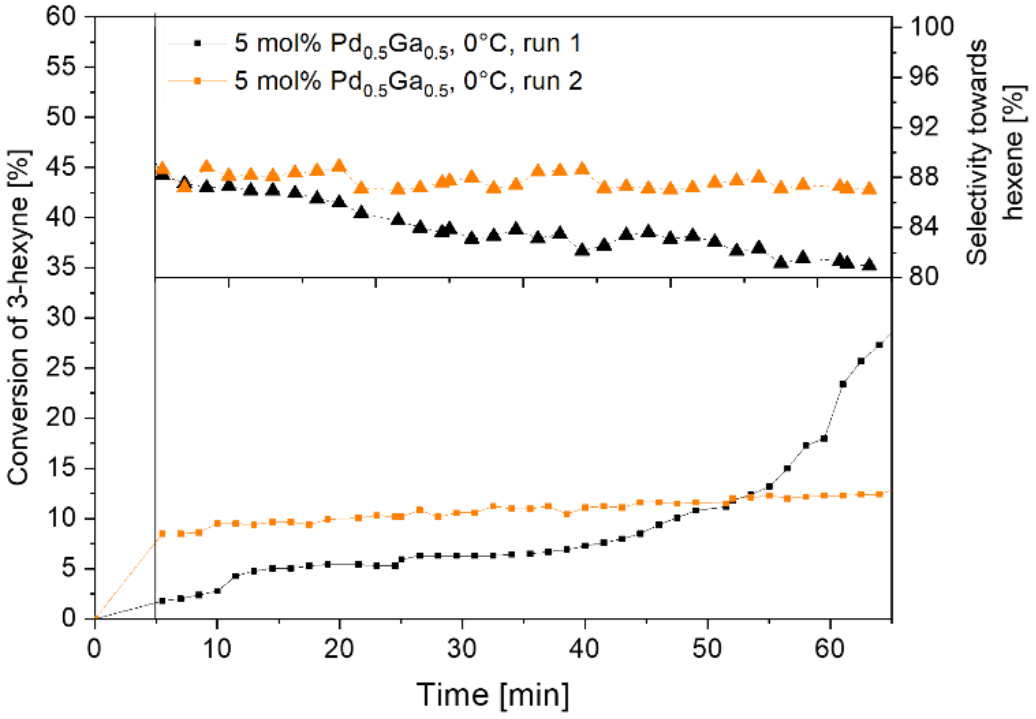

Figure 30. Catalytic reusability tests of $Pd_{0.5}Ga_{0.5}$ colloids in the semi-hydrogenation of 3-hexyne (0 °C, 2.0 bar H_2).

The herein observed behavior of the tested bimetallic colloids under catalytic conditions clearly shows that weakly stabilized NPs can be an active and highly selective system. However, such only weakly stabilized particles are prone to easily undergo structural changes under catalytic conditions. Hence, the post-synthetic addition of additives might lead to an enhanced particle stability. Therefore, in the next chapter, the effect of various ligands on the colloidal stability and also the catalytic performance will be tested.

Influence of post-synthetic additives on the stability of $Pd_{1-x}Ga_x$ colloids

The reaction of $[Pd_2(dvds)_3]$ and GaCp* at low temperatures leads to the formation of ultra-small colloidal bimetallic NPs with a long-term stability under inert conditions. However, higher temperatures (> 0 °C) result in a particle precipitation and exposure to air leads to a discoloration of the solution, particle decomposition and precipitation of the colloids. Hence, finding strategies to tackle these stability issues points to a targeted modification of the NPs' surface. This can be, as already investigated for monometallic $Pd@N(Octyl)_4Br$ colloids[37], achieved effectively by addition of surfactants, particularly by strong binding σ-donor type stabilizing agents, which prevent particle agglomeration by encapsulation of the NPs in an organic shell. Furthermore, surfactant coordination to the colloid surface changes the electronic properties and therefore positively influences the NP stability.[38,50,99,132] As already mentioned before, an adjustment of the bond strength between the NP and the σ-donor stabilizer is crucial for a compromise between colloid stability and catalytic activity. Nevertheless, all examples in literature reported on the pre-synthetic addition of the stabilizing additive. This strategy is often impossible for Group 13 metal precursors, as these are prone to react and oxidize with the surfactant. Hence, this thesis focusses on the post-synthetic addition of surfactants. Three different additives were chosen with different functional groups and steric demands. In detail, PPh_3, dodecylamine and a series of carboxylic acids with different alkyl chain lengths (C_9, C_{13}, C_{17}, and C_{17}) were tested as surfactants for $Pd_{1-x}Ga_x$ colloids (x = 0.33, 0.5, 0.67). The influence on the particles´ stability towards temperature and H_2 pressure as well as on the catalytic performance was investigated. Starting with the established colloid synthesis from the organometallic precursors $[Pd_2(dvds)_3]$ and GaCp* allows for an investigation of the post-synthetic addition of these coordinating ligands. The use of dvds and Cp*H as only weak-coordinating organic ligands enables a control over ligating additives.

Dodecylamine as post-synthetic additive

Starting with the addition of 1.0 equiv. dodecylamine as σ-donor agent to a solution of weakly dvds stabilized $Pd_{1-x}Ga_x$ colloids, first the NPs stability towards temperature and H_2 pressure was tested. Colloidal $Pd_{0.5}Ga_{0.5}$ NPs were selected (Pd/Ga = 1:1), since they exhibit an overall high stability, activity, and selectivity. As already mentioned before, the herein tested colloidal system is only stable up to 0 °C, whereas a slow particle precipitation is observed at higher temperatures. The addition of dodecylamine results in stable particles up to 50 °C without any precipitation observed. Nevertheless, upon addition of H_2, complete particle precipitation

is observed as the coordinating dvds ligand is fully hydrogenated (see Figure 31, orange marked) and the dodecylamine does not stabilize the colloids sufficiently in solution. Hence, no catalytic tests with these colloids for the semi-hydrogenation catalysis were performed as the NPs do not meet the required features for a stable, homogeneous catalytic system.

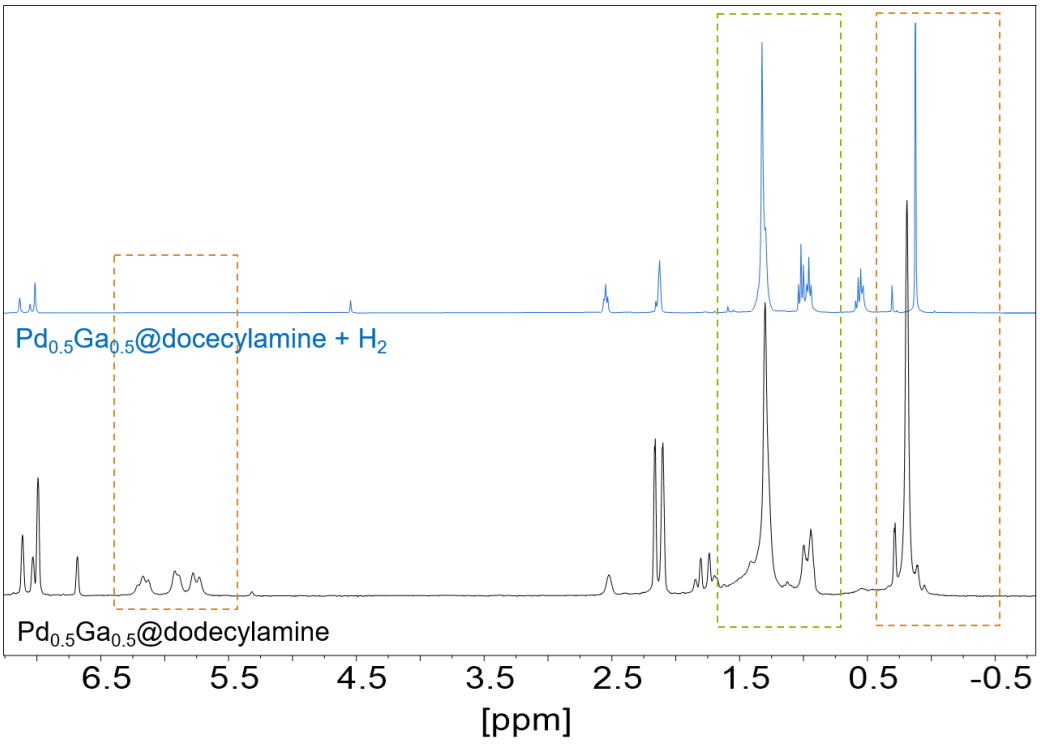

Figure 31. ^{1}H NMR spectra of $Pd_{0.5}Ga_{0.5}$ colloids upon addition of 1.0 equiv. dodecylamine (referred to the Pd amount, black trace) and under H_2 pressure (blue trace) showing a complete dvds hydrogenation (orange panel).

Triphenylphosphane as post-synthetic additive: Influence on the colloid stability

PPh_3 as σ-donating molecule was chosen to investigate the changes regarding the catalytic performance upon phosphane coordination to the particle surface. Colloidal $Pd_{0.5}Ga_{0.5}$ NPs were selected as model catalyst (Pd/Ga = 1:1).

HR-TEM images and DLS measurements show highly monodispersed colloids upon addition of 1.0 equiv. PPh_3 (phosphane amount referred to the Pd amount) with an average size of 1.59 ± 0.19 nm (see Figure 32). No agglomeration or precipitation upon phosphane addition is observed, in contrast to the above-mentioned monometallic system of Pd@N(Octyl)$_4$Br, pointing to an influence of the second metal, Ga, on the coordination behavior on the NP surface. Elemental mapping confirms a homogeneous distribution of the additive over the whole sample. The particles show a similar long-term stability in solution as the colloids without any post-synthetic additives.

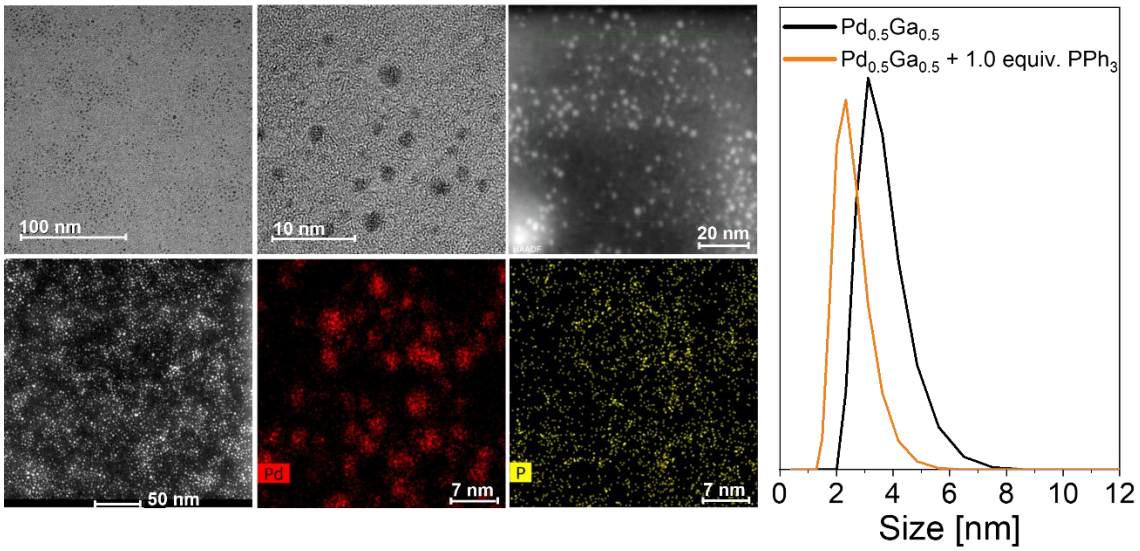

Figure 32. Left: HR-TEM images (low and high magnification, HAADF and elemental mapping of Pd and Phosphorus) of $Pd_{0.5}Ga_{0.5}$ NPs upon addition of 1.0 equiv. PPh_3. Right: DLS measurement confirming no changes in the colloid size upon phosphane addition.

The ^{31}P NMR spectrum shows a signal shift and signal broadening upon addition of 1.0 equiv. PPh_3, indicating a metal-PPh_3 coordination according to the principle of the influence of the Brownian motion of colloids on the ligand NMR signal[120] (see Figure 33, left, blue trace). The coordination of PPh_3 to the NP surface results in a shift of the signal for the phosphorus atom in the ^{31}P NMR due to the contribution of the conduction electrons of the metal particle (so-called Knight shift).[133] It must be noted that the formation of $[Pd(PPh_3)_4]$ by Pd leaching can be excluded for all experiments, as no corresponding signal in ^{31}P NMR experiments was detected.

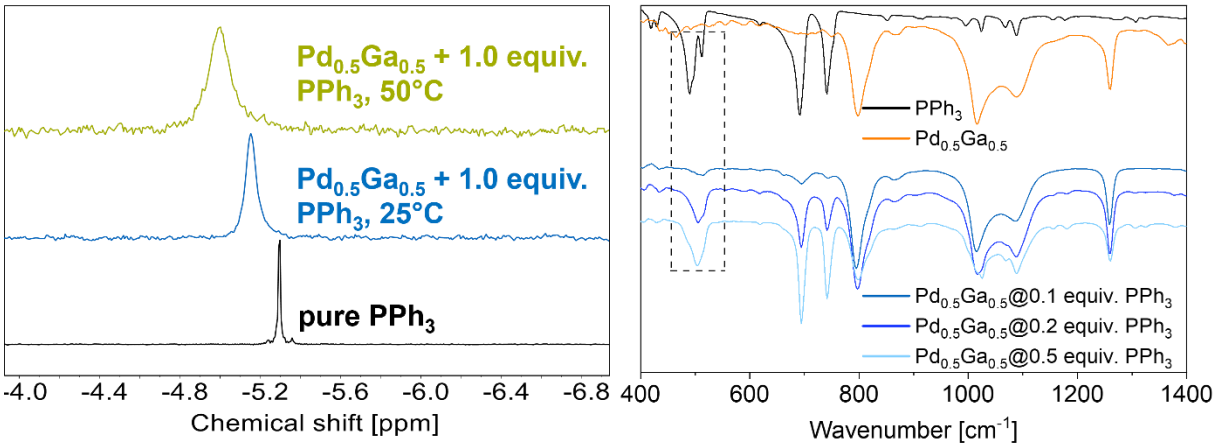

Figure 33. Left: Representative ^{31}P NMR spectra of colloidal $Pd_{0.5}Ga_{0.5}$ NPs upon addition of 1.0 equiv. PPh_3 at 50 °C (green, upper trace) and 25 °C (blue, middle trace) showing a signal shift and broadening compared to pure PPh_3 (black, bottom trace). Right: ATR-IR spectra of $Pd_{0.5}Ga_{0.5}$ colloids upon addition of PPh_3 (bottom) and spectra of pure dvds, PPh_3 and $Pd_{0.5}Ga_{0.5}$ colloids without additives as reference (above).

IR measurements further support a phosphane coordination to the metal surface, as addition of PPh_3 leads to a partial replacement of the weakly coordinating dvds, shown by a decreasing signal intensity for all dvds related vibrations (see Figure 33, right). Additionally, a shift of the PPh_3 signal at 490 cm^{-1} to 504 cm^{-1} is observed indicating a coordination of the phosphine to the metal surface. By the addition of various amounts of PPh_3 (1.0 - 0.1 equiv., based on Pd), the particle stability towards temperature was drastically increased, similar to the previous investigated dodecylamine as additive allowing for reaction temperatures up to 50 °C. The further shift to higher ppm values of the phosphane signal in the recorded ^{31}P NMR at 50 °C compared to 25 °C can be assigned to the measurement conditions and is not directly connected with a different coordination behavior at these temperatures (see Figure 33, left). In contrast to dodecylamine as additive, no particle agglomeration or precipitation is observed upon addition of 2.0 bar H_2. These conditions allow for a catalytic study for the semi-hydrogenation of liquid alkynes and therefore an investigation on the effect of PPh_3 on the catalytic performance by the comparison of the colloids without any additives.

Triphenylphosphane as post-synthetic additive: Influence on the catalytic performance

Starting with 1.0 equiv. PPh_3 referred to the total Pd amount, the semi-hydrogenation of 3-hexyne was tested with the same conditions as introduced for the $Pd_{1-x}Ga_x$ colloid without any post-synthetic additives. In detail, the catalytic tests were performed with 5 mol% catalyst, 0 °C and 2.0 bar H_2 (see Table 13, Entry 2).

Table 13. Testing of PPh_3 as additive in the semi-hydrogenation of 3-hexyne using 5 mol% $Pd_{0.5}Ga_{0.5}$ NPs and 2.0 bar H_2 after 7 h reaction time. The phosphine amount is referred to Pd. No particle precipitation is observed for all entries.

Entry	Temperature [°C]	Equiv. PPh_3	Conversion [%]	Selectivity [%]
1	0	0	67	79
2	0	1.0	9	100
3	50	1.0	22	96
4	50	0.5	35	99
5	50	0.2	38	99
6	50	0.1	90	52
7	80	1.0	79	76

Comparison of Entry 1 (no additive) with Entry 2 (1.0 equiv. PPh_3) shows a drastic change in both activity and selectivity. While the selectivity is strongly increased, the colloids show a

loss in activity, which might be the result from a rather strong coordination of the phosphane to the metal surface, competitively blocking Pd coordination sites. An increase of the reaction temperature to 50 °C leads to a slightly increased activity, whereas the selectivity stays constantly high (see Table 13, Entries 2 and 3, and SI, Figure 171). Hence, step-wise reduction of the PPh_3 amount shows an optimum of 0.2 equiv. phosphane referred to Pd to give the best results regarding stability, selectivity and activity (see Table 13, Entry 5 and SI, Figure 173). Nevertheless, also here, the activity is strongly decreased compared to the particles without any additives. A boost in selectivity to almost 100 % is observed, showing that the ligand strongly influences the catalyst reactivity. Further decrease of the phosphane amount to 0.1 equiv. PPh_3 (see Table 13, Entry 6) shows an increased activity but a decreased selectivity.

Quantification of the Pd surface atoms for $Pd_{0.5}Ga_{0.5}$ assuming a NP size of 1.6 nm with a perfect icosahedral structure and a homogeneous distribution of Pd and Ga shows that by adding > 0.3 equiv. PPh_3, an excess of ligand referred to the amount of Pd surface atoms is apparent. With 0.2 equiv. PPh_3, free coordination sites at the NP surface allow for a slightly increased substrate conversion, whereas the positive effect on the selectivity is preserved. With lower amounts (0.1 equiv. PPh_3), the influence of the ligand becomes marginal, resulting in an active but unselective catalytic system. Notably, 0.1 equiv. PPh_3 is already sufficient to keep the colloids in solution at elevated temperatures. For all tested quantities of PPh_3, a temperature of 50 °C is required for an alkyne conversion which might be explained by an equilibrium of association and dissociation regarding phosphine coordination to the particle surface. A further increase of temperature to 80 °C leads to partial particle precipitation and a decreased selectivity compared to catalytic runs at 50 °C (see Table 13, Entries 2 and 7, and SI, Figure 171). This might be attributed to partially heterogeneous catalyzed hydrogenation processes, not as selective as the catalysis in solution.

For a better understanding of the herein observed optimum of 0.2 equiv. PPh_3 as additive amount, the signal shifts in the ^{31}P-NMR spectra by addition of 1.0, 0.2 and 0.1 equiv. PPh_3 (see Figure 34) were compared with each other. Here, the highest resonance shift from -5.3 ppm (pure PPh_3) to -2.7 ppm for $Pd_{0.5}Ga_{0.5}$ colloids with 0.2 equiv. PPh_3 is observed emphasizing this amount to be an optimum regarding the phosphane-metal coordination. In addition, a signal broadening is observed with lower amounts (0.1 and 0.2 equiv.) of PPh_3, suggesting mainly coordinated ligand upon addition to the colloids. In contrast, a narrow signal width is detected adding 1.0 equiv. PPh_3, as here most of the surfactant is not coordinated to the metal surface. The signal shift upon addition of 0.1 equiv. and 1.0 equiv. is nearly identical, namely -4.9 ppm. Based on the concept of the model of

"magic number clusters", for a perfect $Pd_{0.5}Ga_{0.5}$ NP with icosahedral structure and a ratio of Pd/Ga of 1:1 (approximated, core-shell structure not considered) and a diameter of 1.6 nm, it can roughly be estimated that ca. 31% of all Pd atoms are located on surface of the NPs. Nevertheless, this number is highly overestimated as the Ga-rich surface structure is not considered.

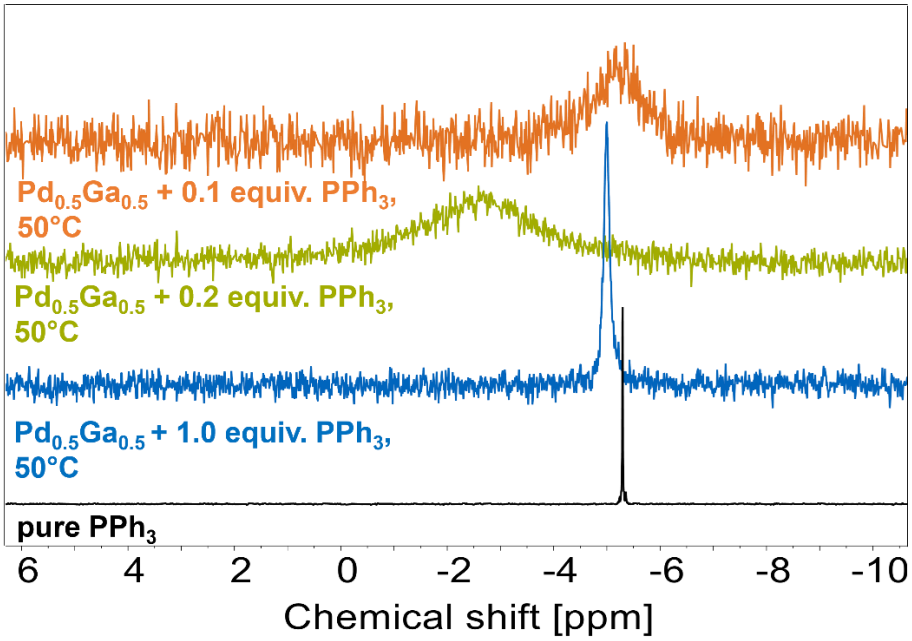

Figure 34. ^{31}P NMR spectra measured at 50 °C of $Pd_{0.5}Ga_{0.5}$ colloids upon addition of various amounts of PPh_3 (referred to the Pd amount) showing differences in the signal shift of the phosphane, with a maximum shift using 0.2 equiv. PPh_3 (green trace).

Therefore, by addition of 0.2 equiv. phosphane, it can be deduced that the additive is always in small excess and the catalyst surface can be fully coordinated with phosphane, without a complete blocking of the active sites. As already mentioned, further decrease of the PPh_3 amount to 0.1 equiv. leads to an increase in activity but also in a loss in selectivity as here, the amount of phosphane is too low for a complete saturation of the metal surface. In contrast, adding a higher amount of phosphane to the colloidal system shows only a decrease in activity (due to a blocking of the active sites) and does not affect the selectivity.

Further analysis of the colloidal NPs with PPh_3 as additive after catalysis runs by HR-TEM and DLS measurements shows a highly stable system under catalytic conditions. Minor particle growth from 1.5 ± 0.2 nm to 1.6 ± 0.3 nm is observed after 5 h reaction time at 50 °C (see Figure 35). Extension of the catalysis to 24 h, however, leads to slightly larger colloids with a size of about 9 nm, but also here, no precipitation is observed.

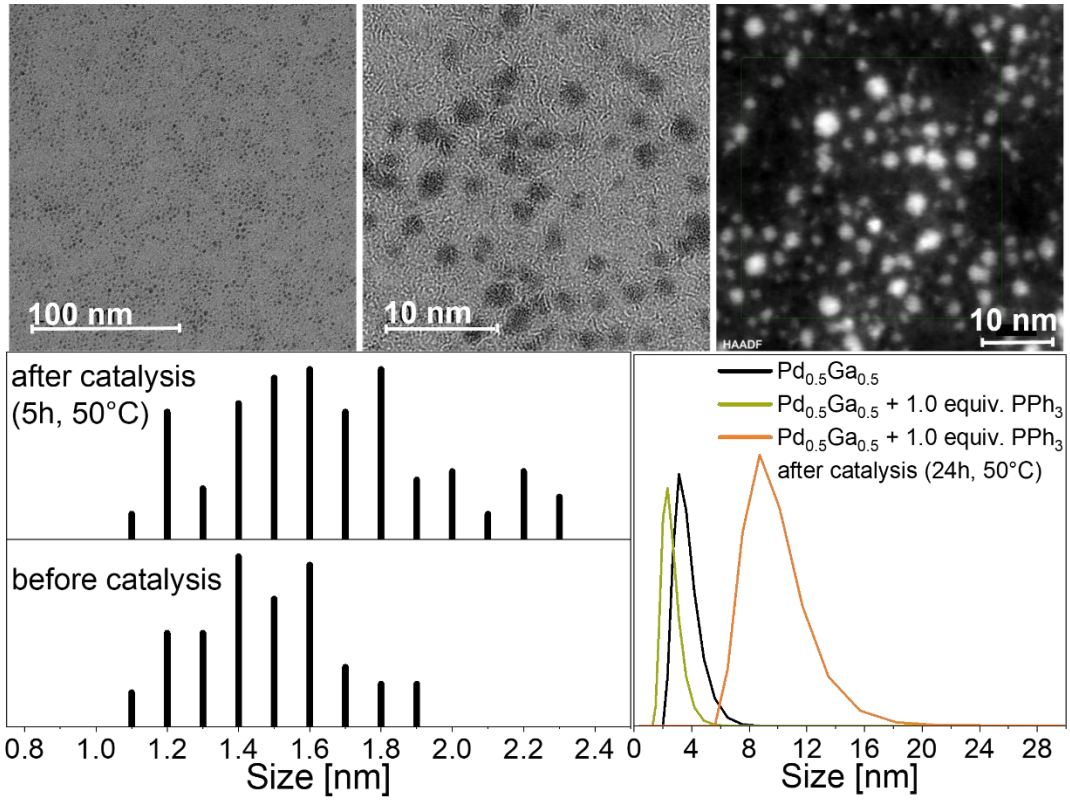

Figure 35. Above: HR-TEM images (low and high magnification and HAADF) of $Pd_{0.5}Ga_{0.5}$ colloids upon addition of 1.0 equiv. PPh_3 after catalysis runs of 5 h showing no particle growth. Bottom left: Particle size distribution was determined by analyzing the diameter of 100 particles. Bottom right: DLS measurements before and after catalysis runs showing a minor agglomeration after 24 h catalysis.

The herein shown results demonstrate that the post-synthetic addition of additives not only strongly influences the catalytic performance but also the colloidal stability. By addition of PPh_3, we succeeded in a stability increase towards both temperature and H_2 pressure. Nevertheless, colloidal $Pd_{1-x}Ga_x$ NPs are highly sensitive towards oxygen and immediately decompose upon exposure to air. Therefore, it is of high interest whether a post-synthetic additive might stabilize the colloids at ambient conditions and prevents particle decomposition and precipitation. In the next chapter, the influence of carboxylic acids on the particle stability as well as on the catalytic performance in the semi-hydrogenation of liquid alkynes will be described.

Carboxylic acids as post-synthetic additives

Synthesis and Characterization of $Pd_{1-x}Ga_x$@acid colloids

The influence of the post-synthetic addition of different carboxylic acids to $Pd_{1-x}Ga_x$ colloids (x = 0.33, 0.5, 0.67) will be discussed in the following section. After colloid synthesis, a certain amount of carboxylic acid (0.1 – 2.0 equiv. referred to the amount of Pd) was added to the colloidal NP solution at 0°C (see Scheme 15). For the synthesis of the $Pd_{1-x}Ga_x$ colloids, the Pd concentration was kept constant, whereas the Ga amount was varied. Hence, the added amount of acid for different Pd/Ga ratios was always the same allowing for a quantitative analysis on the coordination behavior.

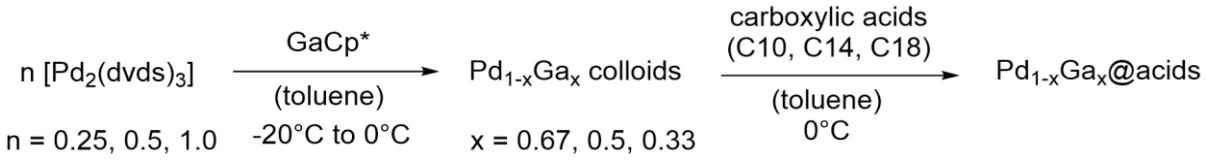

Scheme 15. Post-synthetic modification of colloidal $Pd_{1-x}Ga_x$ NPs synthesized by an organometallic approach. The amount of the additive from 0.1 – 2.0 equiv. is referred to the Pd.

Carboxylic acids with different alkyl chain lengths were tested, namely decanoic acid ($H_{19}C_9COOH$, C10), myristic acid ($H_{27}C_{13}COOH$, C14) and stearic acid ($H_{35}C_{17}COOH$, C18), as well as the isotopically labeled nonadecylic acid $H_{37}C_{18}{}^{13}COOH$. Upon separate addition of all tested carboxylic acids, a slight color change from deep red to orange is observed, without any metal precipitation. The size of the colloids slightly rises upon addition of the surfactants, independent of the amount of carboxylic acid ($Pd_{0.67}Ga_{0.33}$: 2.1±0.9 nm before surfactant addition and 2.6±1.2 nm after, $Pd_{0.5}Ga_{0.5}$: before 1.6±0.2 nm and after 2.1±0.9 nm, $Pd_{0.33}Ga_{0.67}$: before 1.2±0.2 nm and 1.4±0.8 nm after, see Figure 36 and SI, Figures 118-119). This is consistent with the behavior of other literature-reported colloidal systems upon addition of carboxylic acids.[134] Significant leaching of Pd or Ga upon the addition of the carboxylic acids (e.g. the formation of Pd/Ga complexes with the surfactant) was not detected, as DLS and HR-TEM measurements show no decrease of the NP sizes. Furthermore, the colloidal solutions (as synthesized) were investigated via LIFDI MS showing (similar to their respective colloids without any surfactants) no signals of molecular species or metal clusters. This again indicates no metal leaching with subsequent cluster formation (see SI, Figure 120).

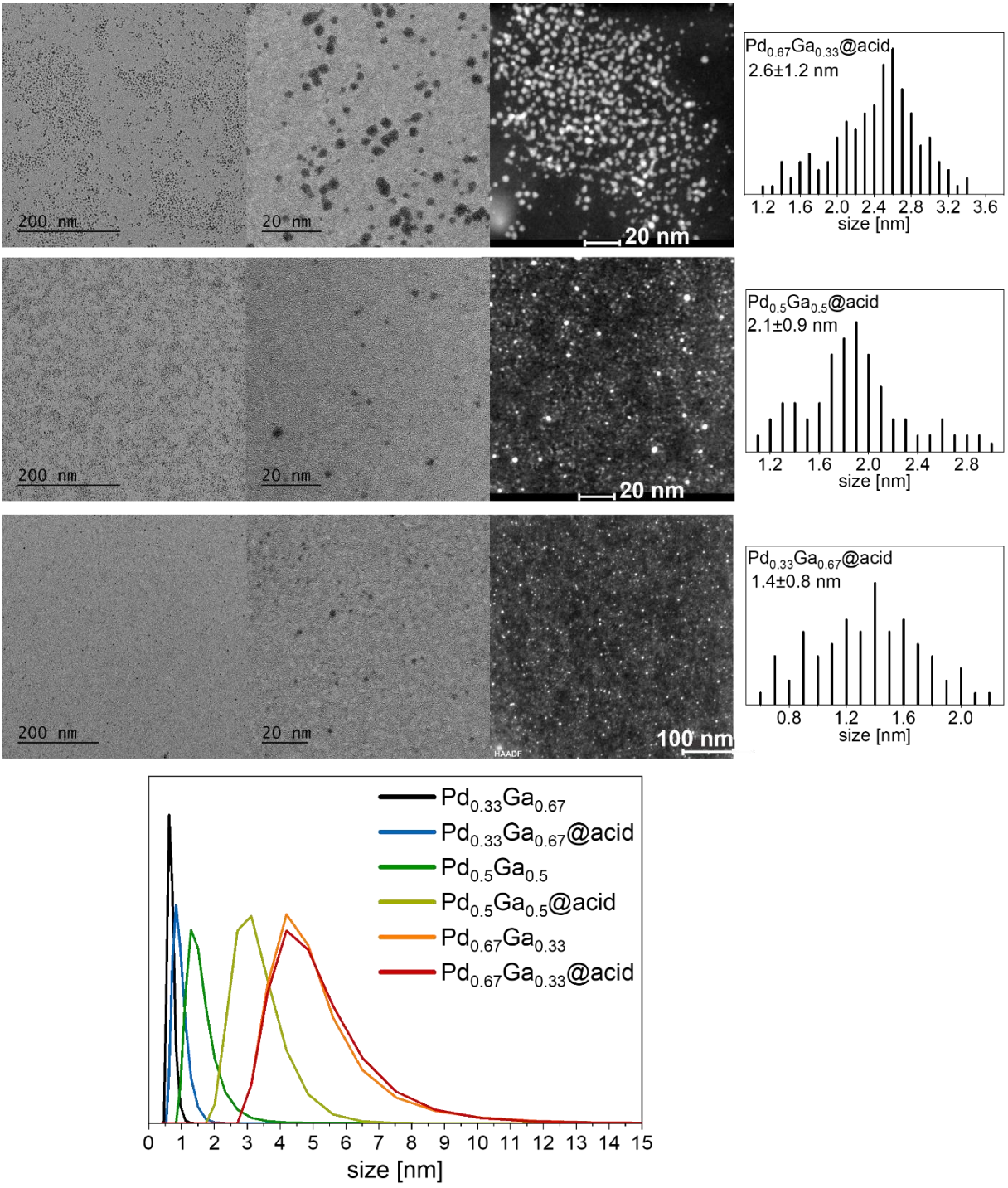

Figure 36. Left: HR-TEM images showing a narrow size distribution of $Pd_{0.67}Ga_{0.33}$ (above) $Pd_{0.5}Ga_{0.5}$ (middle) and $Pd_{0.33}Ga_{67}$ (bottom) NPs upon the addition of 1.0 equiv. stearic acid. Right: DLS measurements of all $Pd_{1-x}Ga_x$ colloids before and after addition of 1.0 equiv. stearic acid. Note: For DLS measurements, the size of the hydrodynamic radius (and not only the metal NP) is measured.

Further investigation on the interaction of the carboxylic acids with the metal NP surfaces was done to better understand the herein tested system. For all tested $Pd_{1-x}Ga_x$ colloids, FT-ATR-IR measurements with stearic acid as model additive suggest a coordination of the carboxylic

acid to the metal surface resulting in a replacement of the initially coordinated dvds ligand (see Figure 37).

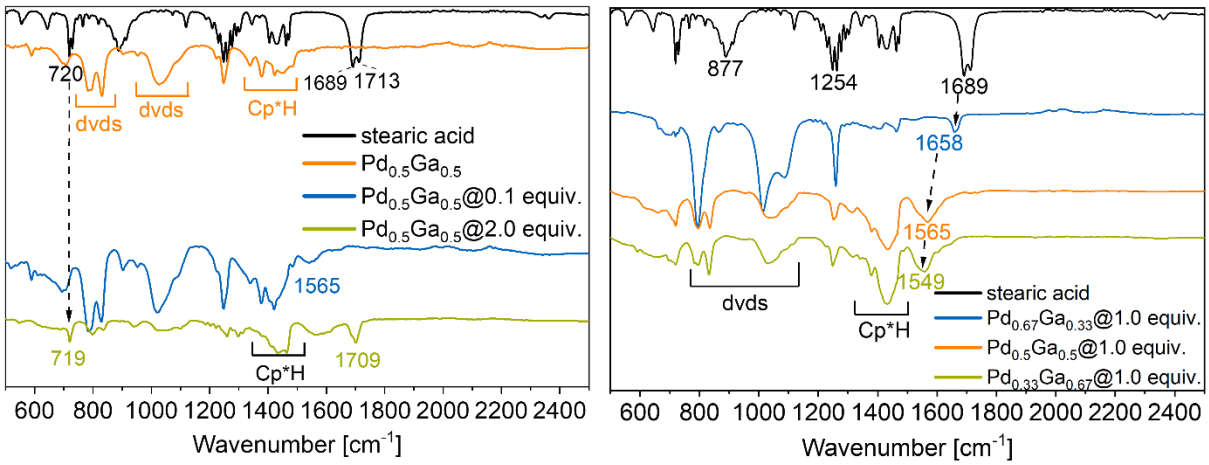

Figure 37. Left: FT-IR spectra of $Pd_{0.5}Ga_{0.5}$@stearic acid colloids with variation of the additive amount (bottom traces), stearic acid (sa, black trace) and $Pd_{0.5}Ga_{0.5}$ colloids without additives (orange trace) as reference showing a decrease of the dvds signal shift upon addition of the carboxylic acid. Right: FT-IR spectra of $Pd_{1-x}Ga_x$@1.0 equiv. stearic acid (x = 0.33, 0.5, 0.67) with various Pd/Ga ratios showing a shift of the carboxylic acid signal dependent on the Pd/Ga ratio.

As already mentioned before, colloids without any post-synthetic additives are stabilized by weakly coordinating dvds, shown by a shift of all dvds signals compared to the pure dvds molecule (see Figure 18). Upon step-wise addition of stearic acid to the bimetallic colloids, a replacement of the dvds ligand by the additive is monitored as the intensity of the δ(C-H) out-of-plane vibration at 702 cm^{-1} and the symmetric and asymmetric vibration modes of Si-O-Si at 795 cm^{-1}, 830 cm^{-1} and 1017 cm^{-1} decrease with increasing amount of stearic acid (Figure 36, left). Regarding the signals of the acid additive, a coordination to the metal surface is observed, highlighted by the strong shift of the asymmetric vibration modes of the C=O carbonyl group from 1680-1713 cm^{-1} to 1528-1557 cm^{-1} in accordance with literature.[134–137] While the weakly coordinated and volatile dvds can easily be evaporated, the non-volatile carboxylic acid binds to the metal surface more strongly. Using an excess of additive (2.0 equiv. carboxylic acid referred to Pd), an additional signal of the uncoordinated C=O vibrational mode at 1709 cm^{-1} is observed. A coordination of the carboxylic group to the colloidal surface is also supported by the missing δ(OH···O) signal at 887 cm^{-1}, since this band appears due to a dimerization observed for uncoordinated, pure carboxylic acids. With an excess of additive, this signal is detected at 937 cm^{-1}.[134–137] In addition, the intensity of the Cp*H vibrations is increased upon addition to stearic acid to the colloidal $Pd_{1-x}Ga_x$ solution (see Figure 37). This indicates that the addition of acid results not only in the displacement of the dvds ligand enables and the coordination of the acid but also a coordination of Cp*H. The

vibration *v*(O-H) of the carboxylic acid is recorded at 2851-2957 cm^{-1} for all $Pd_{1-x}Ga_x$ colloids but superimposes with *v*(C-H) vibrations of Cp*H (see SI, Figures 112-117).

Comparison of $Pd_{1-x}Ga_x$ colloids with different Pd/Ga ratios (x = 0.33, 0.5, 0.67) shows differences in the coordination sphere upon the addition of 1.0 equiv. stearic acid referred to the Pd amount (Figure 37, right). With a higher Pd amount, dvds as well as a small amount of Cp*H remains coordinated to the NPs surface. The signals of the dvds ligands strongly decrease with increasing Ga amount, accompanied by a simultaneous increase of the signals referring to coordinated carboxylic acid in particular. In addition, the strength of the coordination of the acid to the metal surface increases with higher Ga amount, as *v*(C-O) is red-shifted from 1658 cm^{-1} for the $Pd_{0.67}Ga_{0.33}$ colloids over 1565 cm^{-1} for $Pd_{0.5}Ga_{0.5}$ NPs and to 1549 cm^{-1} for $Pd_{0.33}Ga_{0.67}$, suggesting a preferred coordination of the carboxylic acid to Ga over Pd.

The coordination of the carboxylic acids to the colloidal surface was further investigated by NMR spectroscopy. ^{13}C isotopic labelling was used to enhance and resolve the ^{13}C NMR resonances at the carboxylic position. Here, various amounts of the isotopically labeled nonadecylic acid $C_{18}H_{37}{}^{13}COOH$ were added to the $Pd_{1-x}Ga_x$ colloids (see Figure 38).

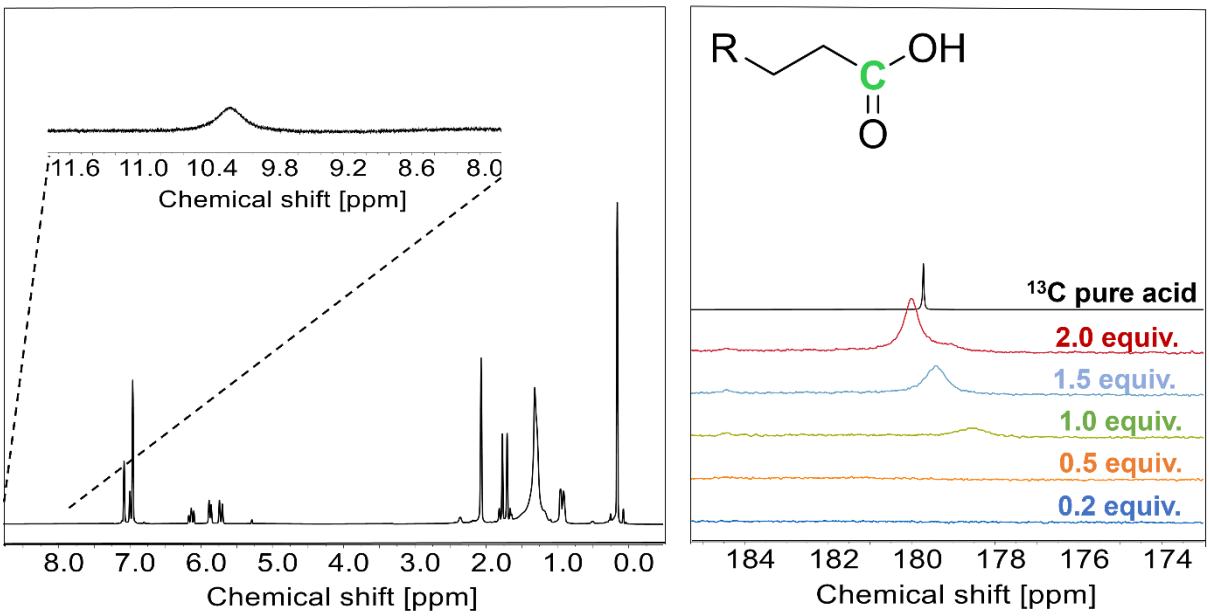

Figure 38. Left: Representative ^1H NMR spectra (toluene-d_8) of colloidal $Pd_{1-x}Ga_x$@1.0 equiv. $C_{18}H_{37}{}^{13}COOH$ (Pd/Ga = 1:1). Right: ^{13}C NMR spectra (toluene-d_8) of $Pd_{0.5}Ga_{0.5}$ colloids with various amounts of $C_{18}H_{37}{}^{13}COOH$ as additive showing a signal weakening, shifting and broadening compared to the pure carboxylic acid.

Without a ^{13}C labeling, no signal for the C atom in the carboxylic position for all tested additive amounts was observed suggesting a rather strong bond between the acid and the colloid metal surface. ^1H NMR spectroscopy confirms the intact structure of the additive for all tested

Pd/Ga ratios, independently on the amount of post-synthetic ligand added to the colloid solution (see Figure 38, right, and SI, Figures 107-108). Additionally, for all samples, the proton signal of the carboxylic group is shifted from δ = 11.4 ppm of the pure acid to δ = 10.2 ppm with a significant line broadening upon coordination to the colloids. Such signal shifting and broadening was already reported for alkanethiol-capped AuNPs with a terminal-alkyl carboxyl group.[119,138] Hence, a formation of the respective carboxylate under the chosen conditions seems unlikely. Comparison of the addition of various amounts of $C_{18}H_{37}{}^{13}COOH$ to a solution of $Pd_{0.5}Ga_{0.5}$ NPs shows that an addition of a minimum of 1.0 equiv. of the ^{13}C isotopic labeled surfactant was required to detect a signal in the ^{13}C NMR spectra of the carbon in the carboxylic position (see Figure 38, left). This suggests a rigid coordination of all R-COOH groups to the NP surface without any “free”, non-coordinating carboxylic acid.

With higher additive amounts (1.0 – 2.0 equiv. additive), a shifted signal compared to the pure $C_{18}H_{37}{}^{13}COOH$ is monitored, pointing to an equilibrium of the coordinated and “free” carboxylic acid (see Figure 38, right). Comparison of colloids with different Pd/Ga ratios clearly shows differences regarding the signal intensity and the signal shift of the carbon atom in the carboxylic position. The constant Pd concentration of all $Pd_{1-x}Ga_x$ colloids (and therefore also the constant amount of surfactant) allows for a quantitative analysis of the acid coordination behavior. $Pd_{1-x}Ga_x$ colloids with a higher Pd amount (x = 0.33), show a minor signal weakening and shift. In agreement, ^{13}C NMR spectra of colloids with a higher Ga content (x = 0.67) show a stronger coordination of the additive to the metal surface, which is highlighted by a decrease of the signal intensity in combination with a signal shift (see Figure 39, right). This effect is also monitored by a change of signal intensity of the C atoms in the C2 at 33.7 ppm and C3 position at 25.4 ppm (see Figure 39, left). As shown in Figure 38, the signal of the C2 atom splits into a duplet with $^2J_{c\text{-}c}$ = 55.0 Hz upon coordination to the metal surface (which would appear as singlet in the non-isotopic labeled carboxylic acid), due to the direct neighboring ^{13}C atom of the carboxylic group. In addition, the signals of the remaining alkyl chain at 32.8 – 29.8 ppm are significantly broadened as coordination to the particle surface limits the molecular rotation. Such effect was already reported for thiol-capped Au colloids, where the signals of the first two carbon atoms adjacent to the sulfur head group were not observable due to peak broadening, which arises from the Au-S interaction.[138,139] Also here, the ^{13}C NMR signals of the C2 and C3 carbon atoms of the stearic acid were strongly influenced by the coordination of the carboxyl group to the metal surface.

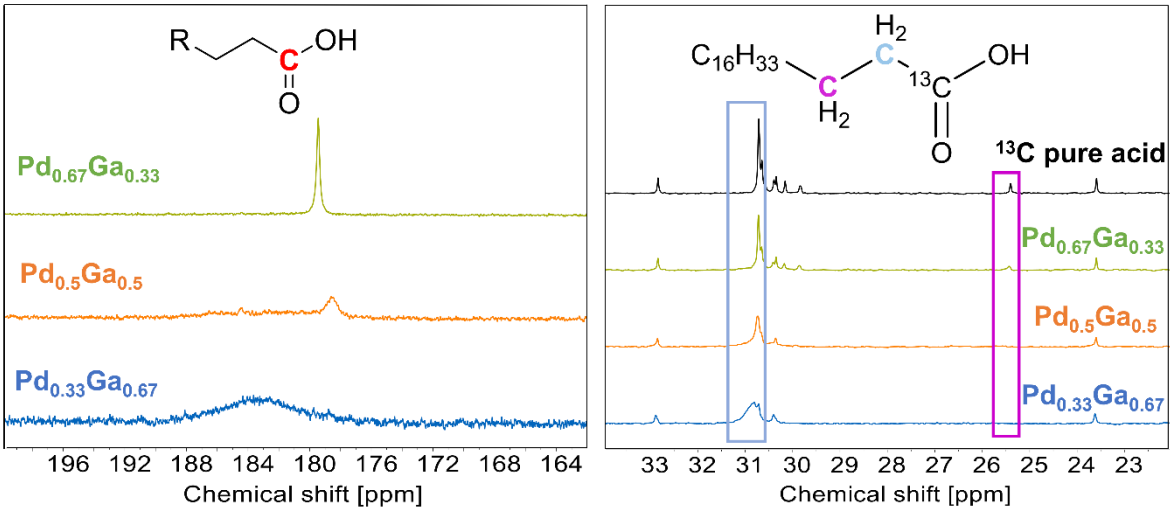

Figure 39. Left: ^{13}C NMR spectra (toluene-d_8) of colloidal $Pd_{1-x}Ga_x$@1.0 equiv. $C_{18}H_{37}{}^{13}COOH$ (x = 0.33, 0.5, 0.67) showing differences in the signal shift and broadening dependent on the Pd/Ga ratio. Right: ^{13}C NMR spectra (toluene-d_8) of $Pd_{1-x}Ga_x$@1.0 equiv. $C_{18}H_{37}{}^{13}COOH$ showing a signal broadening compared to pure $C_{18}H_{37}{}^{13}COOH$ (black trace) and differences in the signal intensity of the C2 (highlighted blue) and C3 (highlighted violet) signal of $C_{18}H_{37}{}^{13}COOH$ upon coordination of the metal surface depending on the Pd/Ga ratio.

As in all $Pd_{1-x}Ga_x$@acid solutions the amount of Pd and therefore also the amount of acid (referred to the Pd amount) is the same for all Pd/Ga ratios (for details, see the synthesis protocol of $Pd_{1-x}Ga_x$ colloids), a quantification on the coordinated additive becomes possible. Quantification of strongly bound additive to $Pd_{1-x}Ga_x$@1.0 equiv. $C_{18}H_{37}{}^{13}COOH$ based on the signal intensity of the C atom in the carboxylic position in the ^{13}C NMR spectra supports the results obtained from IR spectroscopy (toluene-d_8 was chosen as internal standard). In the case of the Pd-rich colloids $Pd_{0.67}Ga_{0.33}$, only 31 % of the additive is strongly coordinated. For $Pd_{0.5}Ga_{0.5}$, 48 % of the carboxylic acid can be assumed to have a strong interaction with the NP surface. The amount of strongly coordinated surfactant for Ga-rich colloids $Pd_{0.33}Ga_{0.67}$ can be calculated to 52 %. These findings go in line with the differences in the coordination behavior of $Pd_{1-x}Ga_x$ colloids as observed by IR measurements. With an increasing Ga amount, the interaction with the additive is enhanced supporting a coordination to Ga rather than Pd.

Apart from carboxylic acids with saturated alkyl chains, an acid with an unsaturated alkyl chain, namely oleic acid was also tested as additive. As already observed for the above discussed carboxylic acids, according to DLS measurements, upon addition of the additive the colloids show no agglomeration or precipitation (see Figure 40, left). Additionally, IR and ^{13}C NMR analysis suggest a similar coordination tendency. Nevertheless, an additional coordination of the olefinic group is monitored (see Figure 40, right). Stability tests of the colloids towards temperature and H_2 pressure revealed similar results compared to the effect of the addition of carboxylic acids with saturated alkyl chains. In detail, addition of 1.0 equiv.

oleic acid (amount referred to the Pd) leads to an increased particle stability up to 50 °C and a H_2 pressure of 2.0 bar.

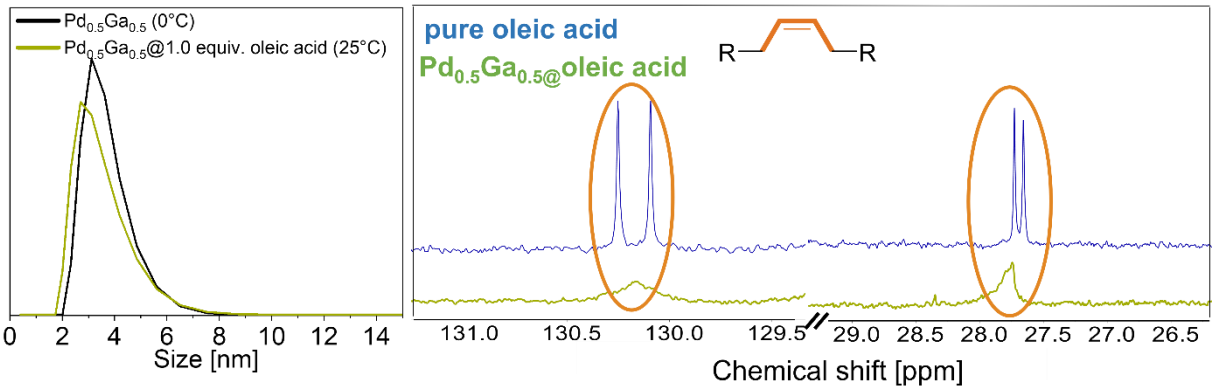

Figure 40. Left: DLS measurement of $Pd_{0.5}Ga_{0.5}$ colloids upon addition of 1.0 equiv. oleic acid showing no changes in the particle size. Right: ^{13}C NMR spectrum (toluene-d_8) of a colloidal solution of $Pd_{0.5}Ga_{0.5}$@1.0 equiv. oleic acid showing a signal broadening of the olefinic position.

The influence of the added carboxylic acids on the oxidation states and the structure of the $Pd_{1-x}Ga_x$ NPs was assessed by XPS (see Figure 41).

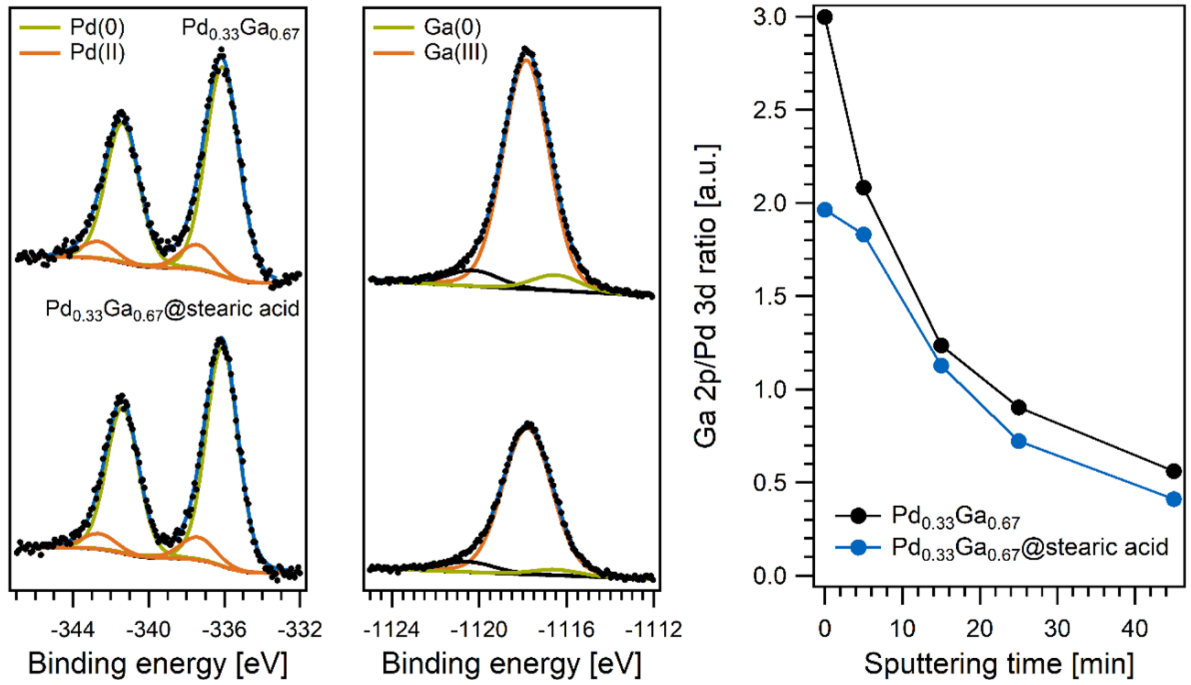

Figure 41. Pd 3d (left) and Ga2$p_{3/2}$ (middle) core level spectra of $Pd_{0.33}Ga_{0.67}$ NPs as synthesized (top) and after addition of stearic acid (bottom). Green and orange components characterize metallic and oxidized fractions, respectively. The spectra intensity is scaled to the total Pd 3d peak area. The XPS depth profile (right) based on Ar^+ ion sputtering reveals a NP structure with a decreasing Ga amount from the surface to the centre of the particles for both, the as synthesized and the modified particles.

Note that XPS measurements require ultra-high vacuum (UHV) conditions to avoid scattering of the emitted photoelectrons on a residual gas phase. As the vapour pressures of oleic acid (1.9×10^{-8} mbar) and myristic acid (7.0×10^{-7} mbar)[140] exceed the background pressure of the UHV system ($<10^{-9}$ mbar), only stearic acid was investigated to avoid evaporation of the surfactant. The Ga-rich colloids $Pd_{0.33}Ga_{0.67}$ were chosen as model catalyst for a detailed XPS investigation.

Detail spectra of the Pd 3d and Ga 2p core levels before and after addition of stearic acid (1.0 equiv.) to the $Pd_{0.33}Ga_{0.67}$ NPs are depicted in Figure 41. Deconvolution of the Pd 3d doublet reveals a main component at a binding energy of 336.1 eV (Pd $3d_{5/2}$) before and after addition, independent of the presence of carboxylic acid, which can be assigned to metallic Pd. The Pd $3d_{5/2}$ binding energy reported for bulk Pd is substantially lower (335.4 eV).[127] Rosenthal *et al.* attribute the shift of metallic Pd towards higher binding energies to an altered electronic structure of PdGa intermetallic compounds in comparison to pure Pd which is consistent to our findings.[141] A small fraction of oxidized Pd (~10 %) is found at a Pd $3d_{5/2}$ binding energy of 337.4 eV. The Ga $2p_{3/2}$ core level reveals that the main fraction of Ga is oxidized; the binding energy of 1117.8 eV corresponds to the reported value for Ga_2O_3, which was already seen for the above discussed $Pd_{1-x}Ga_x$ colloids without any post-synthetic additives.[128] The high amount of oxidized Ga species most likely relies on the XPS preparation procedure; the colloidal solutions were spin-coated on a Si wafer under inert atmosphere to remove the solvent from the NPs while avoiding particle agglomeration. This method was found to preserve isolated NPs without significant agglomeration in the case of the $Pd_{1-x}Ga_x$ colloids (as discussed in the chapter before). The dried NPs might suffer from oxidation due to the high oxophilic nature of Ga. Nevertheless, an oxidation of the colloidal NPs already in solution cannot be excluded entirely.[142] Regarding the oxidation states, no substantial changes in the Pd 3d and Ga 2p core levels are observed upon addition of the carboxylic acid. However, the Ga 2p intensity decreases significantly. Regarding the oxidation states, no substantial changes in the Pd 3d and Ga 2p core levels are observed upon addition of the carboxylic acid. However, the Ga 2p intensity decreases significantly. Besides differences in the surface composition due to structural changes of the NPs upon surfactant addition, coordination of the carboxylic acid might cause this effect as well. The photoelectrons contributing to the Ga 2p and the Pd 3d signal exhibit a different kinetic energy. As the kinetic energy of Pd 3d (~1150 eV) exceeds the one of Ga 2p (~370 eV), the inelastic mean free path of electrons in solids is larger for Pd 3d compared to Ga 2p, i.e. the Ga 2p photoelectron line is much more surface-sensitive than the Pd 3d one. Hence, coordination of carboxylic acid on the NP surface would attenuate the Ga 2p signal stronger than the Pd 3d signal resulting

in a lower Ga 2p intensity when scaling to the Pd 3d intensity (see Figure 41). Hence, the decrease of the Ga 2p/Pd 3d intensity ratio is caused either by a change in the metallic surface composition of the particles or the coordination of carboxylic acid on the particle surface. In order to disentangle both effects, a Ga 2p/Pd 3d depth profile was acquired by repeated cycles of Ar^+ ion sputtering and subsequent XPS measurements. After the first step of Ar^+ ion sputtering for 5 min, no significant difference between $Pd_{0.33}Ga_{0.67}$ with and without stearic acid is detected. It can be expected that the ligand sphere on the particle surface is removed during this first step so that all the following data points provide insight in the structure of the bimetallic NPs. As the Ga 2p/Pd 3d ratio decreases constantly throughout the depth profile, a particle structure with Ga-enriched shell and a Pd-enriched core is concluded which goes in line with the particle formation mechanisms described in the $Pd_{1-x}Ga_x$ colloids without any additives. As the only variation between $Pd_{0.33}Ga_{0.67}$ before and after addition of stearic acid is observed before sputtering, structural changes of the particles induced by the surfactant can be excluded. Thus, the higher Ga 2p/Pd 3d intensity ratio for $Pd_{0.33}Ga_{0.67}$@stearic acid proves successful coordination of the carboxylic acid to the NP surface (see Figure 40). Hence, the decrease of the Ga 2p/Pd 3d intensity ratio is caused either by a change in the metallic surface composition of the particles or the coordination of carboxylic acid on the particle surface. In order to disentangle both effects, a Ga 2p/Pd 3d depth profile was acquired by repeated cycles of Ar^+ ion sputtering and subsequent XPS measurements. After the first step of Ar^+ ion sputtering for 5 min, no significant difference between $Pd_{0.33}Ga_{0.67}$ with and without stearic acid is detected. It can be expected that the ligand sphere on the particle surface is removed during this first step so that all the following data points provide insight in the structure of the bimetallic NPs. As the Ga 2p/Pd 3d ratio decreases constantly throughout the depth profile, a particle structure with Ga-enriched shell and a Pd-enriched core is concluded which goes in line with the particle formation mechanisms described for $Pd_{0.5}Ga_{0.5}$ colloids without any post-synthetic addition of surfactants. As the only variation between $Pd_{0.33}Ga_{0.67}$ before and after addition of stearic acid is observed before sputtering, structural changes of the particles induced by the surfactant can be excluded. Thus, the higher Ga 2p/Pd 3d intensity ratio for $Pd_{0.33}Ga_{0.67}$@stearic acid proves successful coordination of the carboxylic acid to the NP surface.

Concluding, the investigation on the coordination behavior of carboxylic acids in the presence of $Pd_{1-x}Ga_x$ colloids clearly shows an interaction between the additive and the Ga metal surface, thus promising an effect on both catalytic performance and the particles´ stability.

Stabilization of $Pd_{1-x}Ga_x$@acid colloids towards oxygen

Nevertheless, the colloid sensitivity towards oxygen is still a major drawback of the herein studied $Pd_{1-x}Ga_x$ colloid system. Hence, a positive influence of a post-synthetic additive on the $Pd_{1-x}Ga_x$ colloidal stability towards ambient conditions is highly desired. Consequently, the stability of the herein studied system towards air after the addition of carboxylic acids was tested. In contrast to the $Pd_{1-x}Ga_x$ particles without any additives, the colloids stabilized by carboxylic acids show no particle precipitation or a discoloration of the solution suggesting air-stable $Pd_{1-x}Ga_x$ NPs. This observation was independent on the alkyl chain length of the additive and Pd/Ga ratio. For all cases, a minimum of 0.2 equiv. additive referred to the Pd amount is required for a stable colloidal system under ambient conditions. Analysis of the herein investigated system by HR-TEM and DLS measurements confirm a similar particle size of the $Pd_{1-x}Ga_x$@carboxylic acids upon exposure to air compared to the colloids stored under argon atmosphere (see Figure 42). Only a small increase in size is observed, which might be assigned to a proceeding oxidation of Ga species on the NP surface leading to the dissociation of the carboxylic acid, and thus, in slightly less stable NPs.

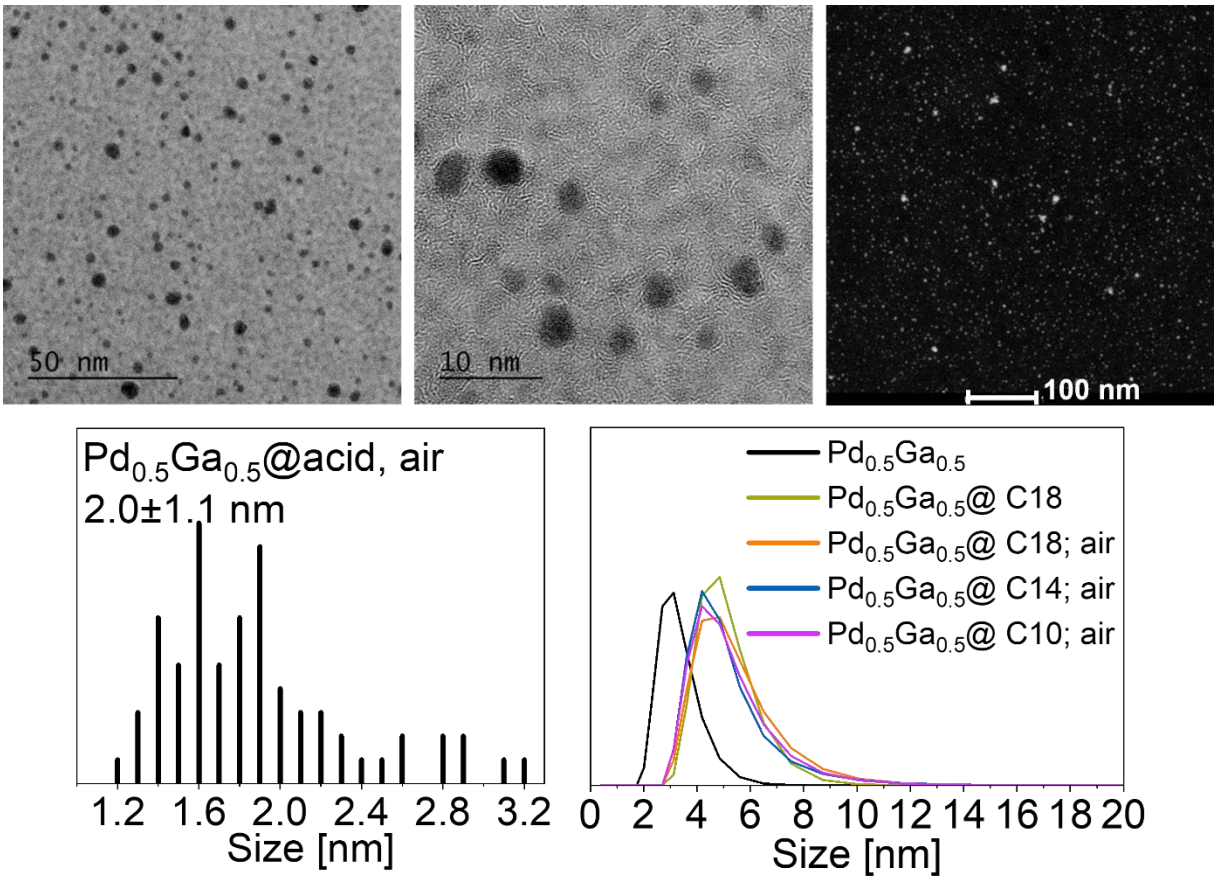

Figure 42. Above: HR-TEM measurements (low magnification and high magnification) of $Pd_{0.5}Ga_{0.5}$@1.0 equiv. stearic acid under air. Bottom: DLS measurements of 1.0 equiv. carboxylic acid stabilized $Pd_{0.5}Ga_{0.5}$ colloids upon exposure to air showing no major particle agglomeration.

For a better understanding of the changes of the NP surface and the coordination behavior of the carboxylic acid additives upon exposure to air, the herein tested colloidal system was analyzed via IR measurements (see Figure 43, left). Comparison of $Pd_{1-x}Ga_x$@stearic acid stored under inert conditions and exposed to air shows a similar coordination behavior of the carboxylic acid.

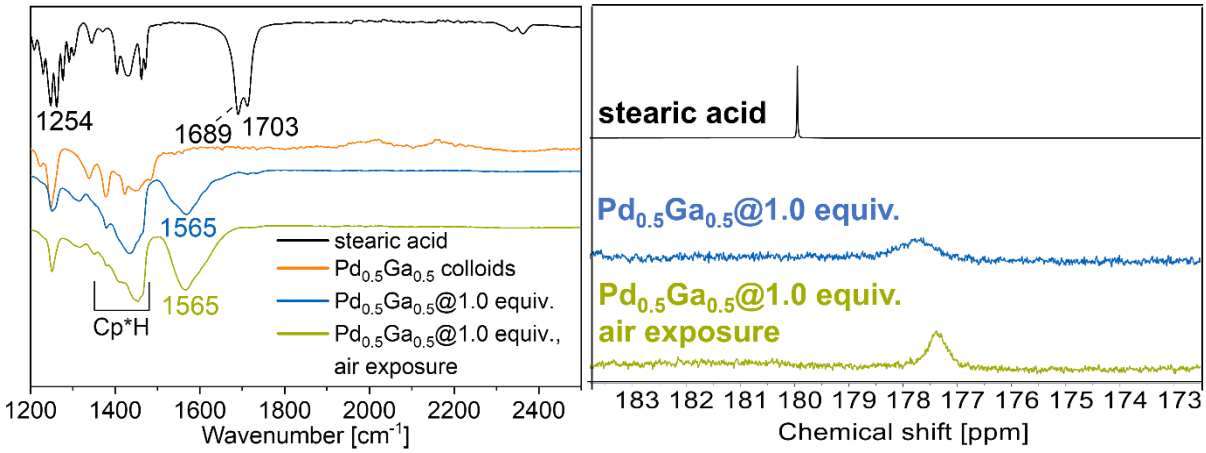

Figure 43. Left: FT-ATR-IR spectra of $Pd_{0.5}Ga_{0.5}$@stearic acid colloids stored under inert and ambient conditions (bottom traces), stearic acid (black trace) and $Pd_{0.5}Ga_{0.5}$ colloids without additives (orange trace) as reference. Right: ^{13}C NMR spectra (toluene-d_8) of $Pd_{0.5}Ga_{0.5}$@1.0 equiv. $C_{18}H_{37}{}^{13}COOH$ colloids exposed to air.

For both samples, the aforementioned shift of the asymmetric vibration modes of the carbonyl group C=O (at 1689 and 1703 cm^{-1}) is apparent. For both samples (handled under inert conditions and under air), the intensity of the Cp*H vibrations is increased compared to the colloids without any additive (see Figure 43, left). This again suggests (as already mentioned before) that upon addition of the acid, the displacement of the dvds ligand enables not only the coordination of the acid but also of Cp*H. ^{13}C NMR measurements support these findings, as no changes in the signal shift of the carboxylic carbon atom upon coordination to the NP surface is observed (see Figure 43, right) indicating an intact coordination of the acid to the colloid.

XPS analysis shows no changes in the Pd 3d and Ga 2p core levels upon exposure of $Pd_{0.33}Ga_{0.67}$@stearic acid to air (see Figure 44). Ga is predominately oxidized while Pd remains in its metallic state demonstrating the efficient prevention of the NPs from oxidation due to the protective effect of the carboxylic acid. As the Ga 2p/Pd 3d intensity ratio stays the same before and after exposure to air, significant structural changes of the NPs are excluded in accordance with HR-TEM results.

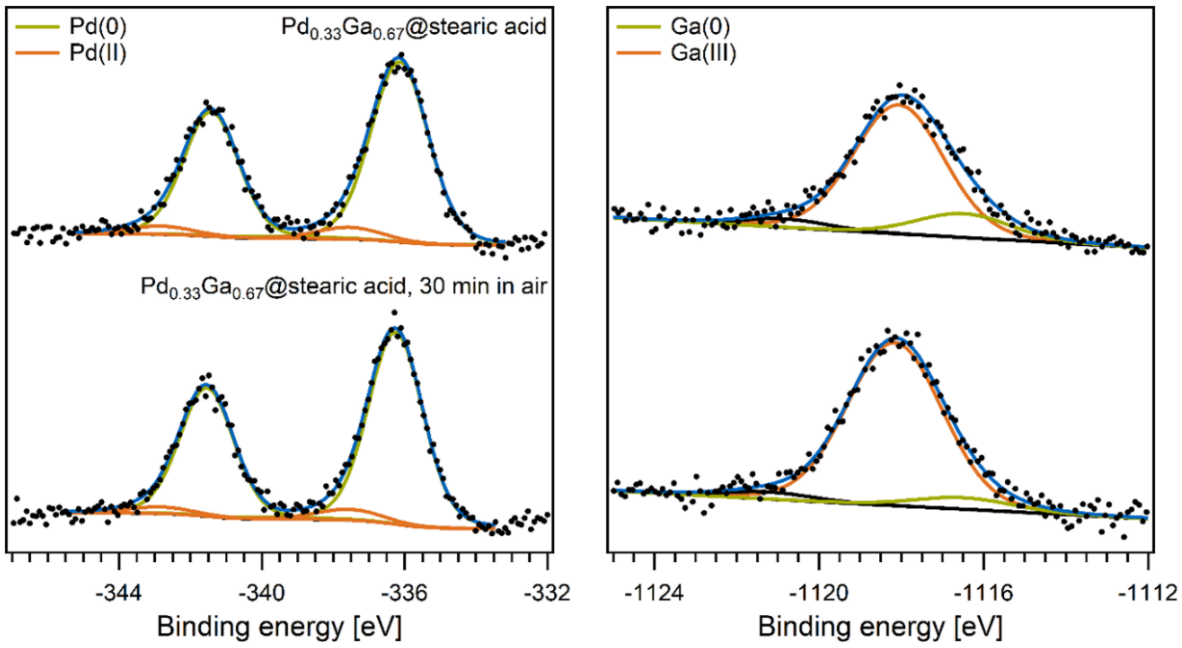

Figure 44. XPS spectra of $Pd_{0.33}Ga_{0.67}$@1.0 equiv. stearic acid colloids before and after exposure to air for 30 min. Green components indicate metallic, orange ones oxidized species. All spectra were scaled to the total Pd 3d peak area. Besides a slightly proceeding oxidation of Ga (right panel), no significant changes are observed.

Catalytic performance of $Pd_{1-x}Ga_x$@ acids in the alkyne semi-hydrogenation

The catalytic activity of $Pd_{1-x}Ga_x$ colloids after addition of carboxylic acid as well as after exposure to air were systematically tested in the semi-hydrogenation catalysis (see Scheme 16).

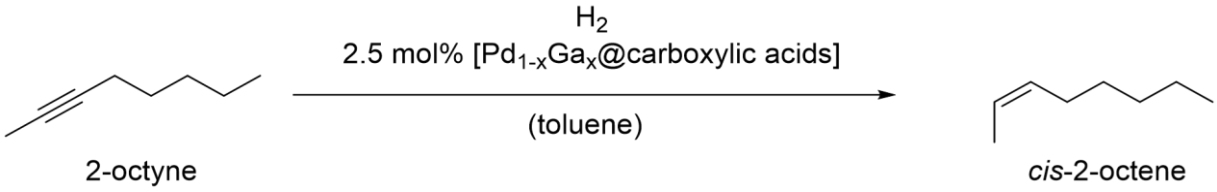

Scheme 16. Semi-hydrogenation catalysis using 2.5 mol% catalyst $Pd_{1-x}Ga_x$ colloids with the post-synthetic addition of various amounts of carboxylic acids in a H_2 atmosphere.

The effect of temperature and H_2 pressure on the colloids' stability was previously tested to catalysis runs. A similar stabilization effect of acids compared to PPh_3 was observed. In detail, the addition of 1.0 equiv. carboxylic acid (decanoic acid, mystiric acid or stearic acid) results in no NP agglomeration or precipitation up to a temperature of 50 °C for 24 h under H_2 atmosphere. Catalytic studies were carried out using 2-octyne as model substrate instead of 3-hexyne (used for the Pd/Ga catalytic studies without any post-synthetic additives) because monitoring using GC analysis and chromatographic separation of 3-hexyne and

cis/trans-3-hexene appears to be impossible. Instead, analysis via ^{1}H NMR spectroscopy (as performed for the $Pd_{1-x}Ga_x$ colloids) was not possible due to the overlapping signals of the substrate and the additive.

For a better comparison of all catalytic runs, the respective TOF values were calculated after 10 min of reaction time. The fraction of Pd surface atoms was estimated for the calculation of the TOF values assuming an idealized icosahedral NP structure and a homogeneous Pd/Ga distribution inside the NPs and not considering any inhomogeneity and surface Ga-oxo species. Nevertheless, the assumption of a homogeneous distribution of Pd and Ga is only a simplification, which is, according to XPS measurements, not the case (Ga-rich surface, Pd-rich core). Thus the amount of active Pd surface atoms is rather overestimated and therefore the TOF value underestimated. The NP size distribution obtained from HR-TEM measurements were considered, resulting in a range of "apparent" TOF values for each colloidal acid@$Pd_{1-x}Ga_x$ sample. This variation is about 10 % within the limits of our assumptions (for details, see Experimental). Hence, we use these "apparent" TOF values for a comparison between the herein discussed colloidal acid@$Pd_{1-x}Ga_x$ catalysts. Comparison with literature-known Pd/Ga intermetallic solid-state phases or any other related Pd/Ga-catalyst for semi-hydrogenation is not possible due to different measurement set-ups, condition, substrates and the less defined microstructure of our system.

In order to find the optimal reaction parameters, 2.5 mol% $Pd_{0.33}Ga_{0.67}$@1.0 equiv. stearic acid (catalyst amount referred to the Pd) was tested for the semi-hydrogenation of 2-octyne showing that both reaction temperature and hydrogen pressure significantly influences the activity and selectivity (see Table 14, Entries 1-4, and SI, Figures 174). For all catalytic runs, the *cis*-olefin was formed.

Table 14. Parameter optimization in the semi-hydrogenation catalysis of 2-octyne using 2.5 mol% $Pd_{1-x}Ga_x$@1.0 equiv. stearic acid in toluene (x = 0.33, 0.5, 0.67). Conversion after 10 min were taken for TOF value calculation.

Entry	catalyst	T [°C]	p(H_2) [bar]	Conversion [%]	Selectivity [%]	TOF [h^{-1}]
1	$Pd_{0.33}Ga_{0.67}$	25	1.0	73 (5 h)	41 (5 h)	1060
2	$Pd_{0.33}Ga_{0.67}$	0	0.5	10 (5 h)	100 (5 h)	70
3	$Pd_{0.33}Ga_{0.67}$	0	1.0	99 (3 h)	85 (3 h)	1810
4	$Pd_{0.33}Ga_{0.67}$	0	2.0	98 (2 h)	70 (2 h)	2330
5	$Pd_{0.5}Ga_{0.5}$	0	1.0	98 (3 h)	70 (3 h)	2570
6	$Pd_{0.67}Ga_{0.33}$	0	1.0	100 (3 h)	65 (3 h)	3140

Low temperatures and a relatively low hydrogen partial pressure have a positive influence on the selectivity towards the desired olefin, as already observed for the Pd/Ga colloids without any additives. At room temperature and H_2 pressure of 1.0 bar, a system with moderate activity and selectivity was observed (see Table 14, Entry 1) with a TOF value of 1060 h^{-1}. Decreasing the temperature to 0 °C leads to an improvement with full conversion after 3 h reaction time, an increased selectivity towards *cis*-2-octene of 85 % after 3 h and a TOF value of 1810 h^{-1} (see Table 14, Entry 3). This increased activity compared to the catalysis run with the same H_2 pressure at elevated temperatures can be assigned to an increased particle stability at lower temperatures and therefore less particle agglomeration, as DLS measurements show a colloidal agglomeration after catalysis runs at 25 °C (see SI, Figure 124). Such particle growth is not observed at 0 °C. A further increase of the hydrogen pressure to 2.0 bar H_2 at 0 °C leads to a further boost in activity with a TOF of 2330 h^{-1}, but a decreased selectivity of 70 % (see Table 13, Entry 4). Hence, all catalytic experiments where run under the optimized conditions with 0°C and p(H_2) = 1 bar and 2.5 mol% catalyst referred to the Pd amount, if not stated otherwise.

Comparing the catalytic activity of the different Pd/Ga ratios show a clear correlation between the Ga content and olefin selectivity (see Table 14, Entries 3, 5 and 6 and SI, Figure 178). Upon a full alkyne conversion after only 3 h reaction time for all $Pd_{1-x}Ga_x$@1.0 equiv. stearic acid, selectivities towards the alkene of 65 %, 70 % and 85 % for a Pd/Ga ratio of x = 0.33, 0.5 and 0.67 are observed. These selectivities follow the site-isolation principle,[12] as dilution of the Pd with an inactive metal results in a preferred formation of the olefin instead a full-hydrogenation to the alkane. TOF values of 3110 h^{-1} for $Pd_{0.67}Ga_{0.33}$, 2570 h^{-1} $Pd_{0.5}Ga_{0.5}$ and 1810 h^{-1} $Pd_{0.33}Ga_{0.67}$ show that the alloying with Ga does not only result in an increased selectivity but also in a decreased activity at high alkyne concentrations.

The catalytic activity with and without additional surfactants was investigated (see Table 15, Entries 1-4). The activity is slightly increased upon addition of the carboxylic acids, which is also reflected in the TOF values. The TOF of colloids without carboxylic acid was calculated to 1380 h^{-1}, whereas with additive this value ranges between 1810 – 2020 h^{-1}. This might be the result of a σ-donoring effect of the additives, hence influencing the electronic characteristics of the catalyst. Nevertheless, the overall the influence of the alkyl chain length of the carboxylic acid can be rather evaluated as low. For a better comparison, various phosphanes with different Tolman Cone angles applied in the semi-hydrogenation of 1-octyne with the monometallic Pd@$N(Octyl)_4Br$ (described in the first chapter of this thesis) showed a strongly higher influence on the catalyst performance.

Table 15. Semi-hydrogenation of 2-octyne using 2.5 mol% $Pd_{0.33}Ga_{0.67}$ colloids with different additives (1.0 equiv. referred to the Pd amount) in toluene using 1.0 bar H_2 at 0 °C after 3 h reaction time under inert and ambient conditions. Conversion after 10 min were taken for TOF value calculation.

Entry	Additive	Storage	Conversion [%]	Selectivity [%]	TOF [h^{-1}]
1	-	Inert conditions	99	90	1380
2	decanoic acid	Inert conditions	95	81	1910
3	myristic acid	Inert conditions	95	83	2020
4	stearic acid	Inert conditions	99	85	1810
5	stearic acid	air	100	82	2340

Additionally, carboxylic acid stabilized particles stored under inert conditions compared to colloids with air contact show a similar catalytic performance (see Table 15, Entry 5), with a slightly increased activity and a calculated TOF of 2340 h^{-1}. This might be explained by the partial removal of the carboxylic acid by surface oxidation, thus enabling a better access of the substrate to the particle surface. In contrast to the catalyst activity, the selectivity towards the olefin is decreased upon addition of carboxylic acids from 90 % to 85 % (see Table 15, Entries 1 and 4, and Figure 45, left). This effect is further enhanced by a colloidal storage under air, as here the selectivity is further decreased to only 71 % at full conversion (see Figure 45, left).

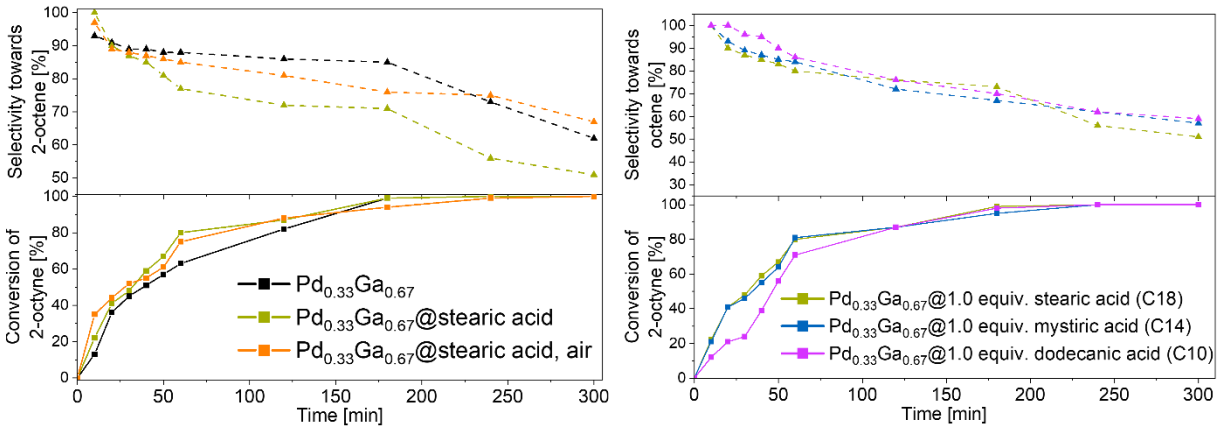

Figure 45. Left: Semi-hydrogenation catalysis of 2-octyne using 2.5 mol% $Pd_{0.33}Ga_{0.67}$ colloids without any additive and comparison with 2.5 mol% $Pd_{0.33}Ga_{0.67}$@1.0 equiv. stearic acid colloids stored under argon vs. air. Right: Semi-hydrogenation catalysis of 2-octyne using 2.5 mol% $Pd_{0.33}Ga_{0.67}$@1.0 equiv. carboxylic acids with variation of the additive alkyl chain length showing no major differences regarding activity and selectivity.

Catalytic testing of colloids with different amounts of additive as well as carboxylic acids with various alkyl chain lengths (decanoic acid, myristic acid, stearic acid) showed in each case similar results without differences in activity as well as selectivity. This suggests that these parameters do not have a great influence, electronically or sterically, on the catalysis (see Table 15, Entries 2-4 and Figure 45, right).

Other, terminal olefins such as 1-octyne and phenylacetylene with $Pd_{0.33}Ga_{0.67}$@1.0 equiv. stearic acid (2.5 mol % catalyst, 0 °C, 1.0 bar H_2) are hydrogenated at a higher rate compared to 2-octyne (6370 h^{-1} for 1-octyne and 5100 h^{-1} for phenylacetylene vs. 1810 h^{-1} for 2-octyne, see Table 16).

Table 16. Semi-hydrogenation of various substrates using 2.5 mol% $Pd_{0.33}Ga_{0.67}$@1.0 equiv. stearic acid at 0°C and 1.0 bar H_2 in toluene after 3 h reaction time. Conversion after 10 min were taken for TOF value calculation.

Entry	Substrate	Conversion [%]	Selectivity [%]	TOF [h^{-1}]
1	2-octyne	99	85	1810
2	1-octyne	70	11	6370
3	Phenylacetylene	60	5	5100

The higher activity originates from a sterically favored hydrogenation of terminal alkynes on the metal surface compared to internal ones (see Table 16). Nevertheless, the selectivity is strongly decreased to 11 % for 1-octyne and only 5 % for phenylacetylene, respectively. This clearly shows the sensitivity of the herein tested system on electronic and steric changes regarding the substrate. In these two cases oligomerization products were detected, monitored by LIFDI-MS (see Figure 46, right, and SI, Figure 180).

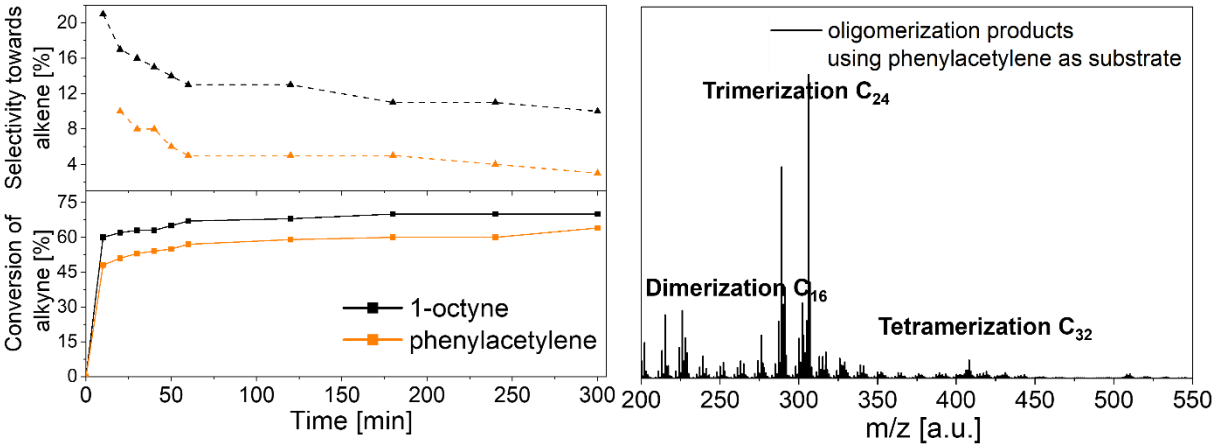

Figure 46. Left: Semi-hydrogenation catalysis of 1-octyne and phenylacetylene using 2.5 mol% $Pd_{0.67}Ga_{0.33}$@1.0 equiv. stearic acid showing a drastic loss in selectivity towards the respective alkene. Right: LIFDI-MS measurements of the reaction mixture after catalysis using 2.5mol% $Pd_{0.67}Ga_{0.33}$@1.0 equiv. stearic acid, 1.0 bar H_2 at 0°C and phenylacetylene as substrate showing oligomerization products.

For both substrates, full conversion is not observed (max. 70 %), which is most presumably a consequence of a surface “coating” by the oligomer products and hence, a blocking of the catalytically active sites polymer layer on the colloid surface (detected by LIFDI-MS analysis).The olefin oligomerization catalyzed by Group 10 metals is well-known since the early works of Wilke, Keim, Jolly and others.[15,16,116,117] Concerning colloidal catalytic systems,

this phenomenon was already discussed above for the monometallic Pd@N(Octyl)$_4$Br NPs system in the semi-hydrogenation of liquid alkynes.

$Pd_{1-x}Ga_x$@acid particle analysis after catalytic runs

Structural analysis of the colloidal $Pd_{0.33}Ga_{0.67}$@1.0 equiv. stearic acid after the catalysis run by DLS and HR-TEM measurements shows a slight particle agglomeration (see Figure 47).

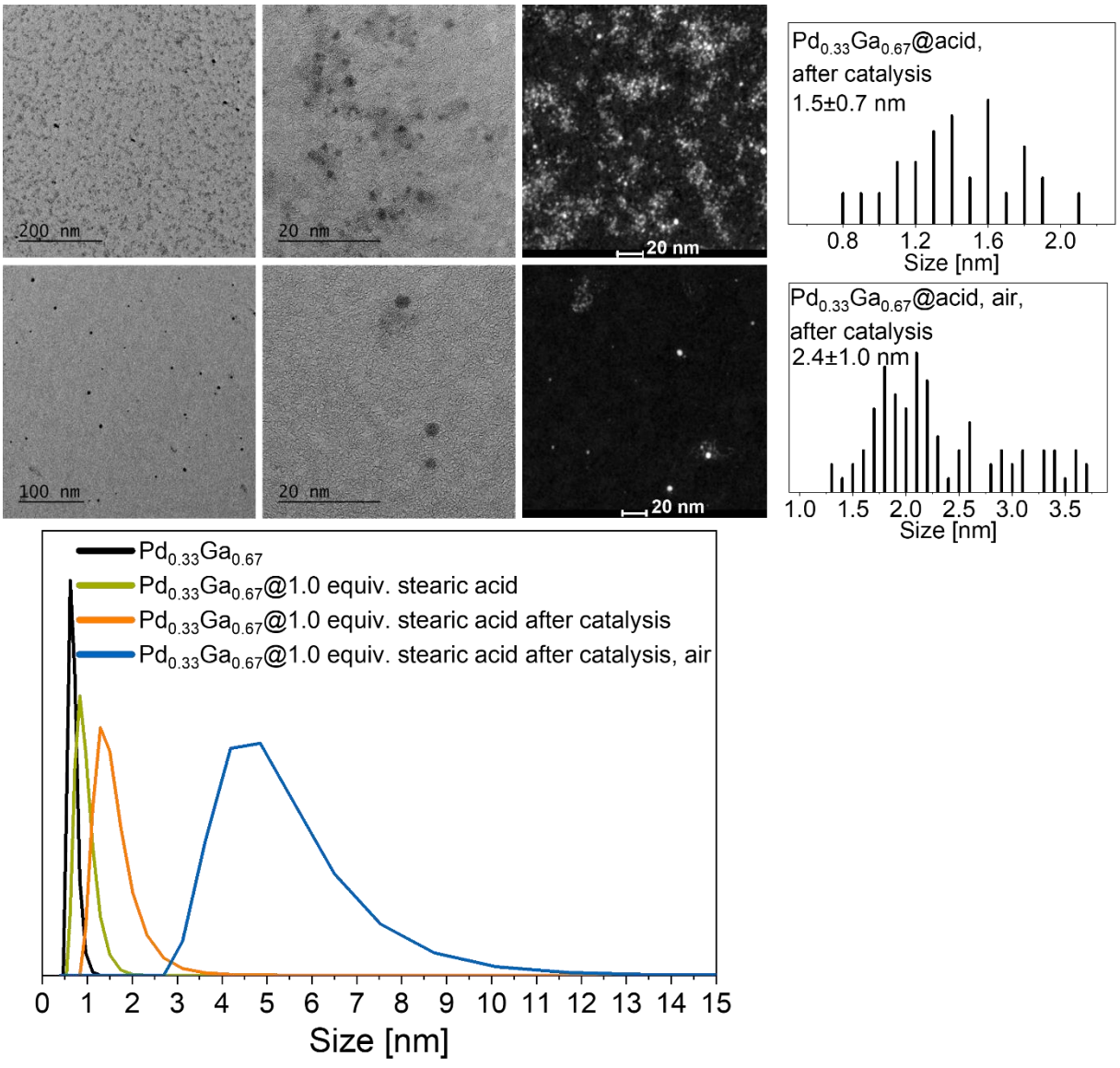

Figure 47. Left, above: HR-TEM image and HAADF of $Pd_{0.33}Ga_{0.67}$@1.0 equiv. stearic acid colloids stored under inert conditions after semi-hydrogenation catalysis of 2-octyne at 0°C and 1.0 bar H_2 after 5 h. Left, bottom: HR-TEM image and HAADF of $Pd_{0.33}Ga_{0.67}$@1.0 equiv. stearic acid colloids stored under ambient conditions (air) after semi-hydrogenation catalysis of 2-octyne at 0°C and 1.0 bar H_2 after 5 h. Bottom: DLS measurements of $Pd_{0.33}Ga_{0.67}$ colloids with and without additive stored under Argon and O_2 after the semi-hydrogenation of 2-octyne at 0°C and 1.0 bar H_2 after 5 h.

HR-TEM analysis shows that the agglomeration of the colloids stored under air is somewhat increased, namely from 2.0 ± 1.1 nm to 2.4 ± 1.1 nm compared to the NPs handled under inert conditions (1.4 ± 0.8 nm to 1.5 ± 0.7 nm, respectively). This is also confirmed by DLS measurements (see Figure 47, bottom). Nevertheless, no precipitation of the catalyst is observed. Hence, it can be concluded that the $Pd_{1-x}Ga_x$@acids (handled under inert conditions as well as under air), can be regarded as stable catalytic systems for the herein tested conditions.

Chemical analysis by XPS of $Pd_{0.33}Ga_{0.67}$@stearic acid (see Figure 48) proves that neither the Pd 3d nor the Ga 2p core level shows a significant change in oxidation states after catalytic conversion of 2-octyne, therefore, indicating no alteration of the NPs during catalytic conversion.

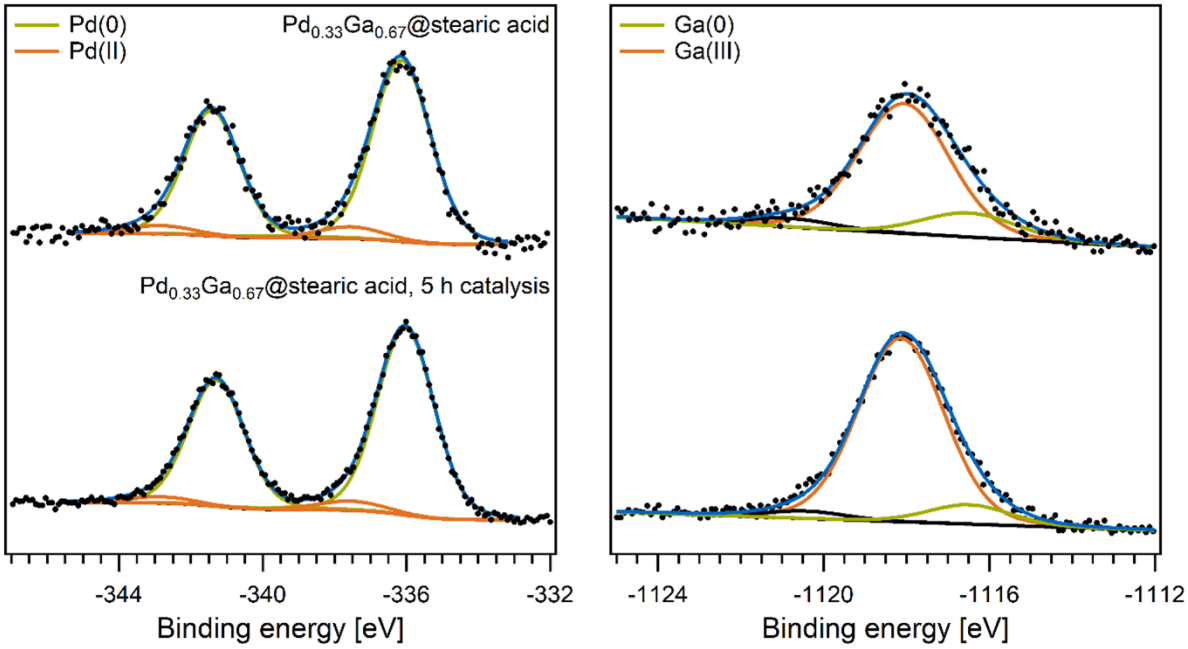

Figure 48. XPS spectra of $Pd_{0.33}Ga_{0.67}$@1.0 equiv. stearic acid before and after conversion of 2-octyne (2.5 mol% catalyst in toluene, 1 bar H_2, 0 °C, 5 h). Green components indicate metallic, orange ones oxidized species. All spectra were scaled to the total Pd 3d peak area.

Nevertheless, the Ga 2p/Pd 3d intensity ratio is slightly higher after the semi-hydrogenation of 2-octyne. As already outlined before, this does not necessarily point towards structural changes since the Ga 2p/Pd 3d ratio is also highly affected by changes in the ligand sphere around the NPs due to the different surface-sensitivity of both photoelectron lines. However, small variations in the Ga 2p/Pd 3d ratio are also observed when analysing different aliquots of the same $Pd_{1-x}Ga_x$ NPs as the unreproducible XPS preparation procedure (spin-coating on a Si wafer) leads to an undefined amount of residues, e.g. adsorbed solvent, reactants or ligands. Thus, reactivity and XPS measurements on the identical sample are essential to

address changes in either particle structure and composition or the ligands attached to their surface and to exclude effects arising from only spectating residues.

Summarizing, the herein gained information shows that upon addition of carboxylic acids, air-stable bimetallic Pd/Ga colloids can be obtained. The post-synthetic addition of these ligands provokes a coordination to the metals (probably preferred to the Ga), while the colloidal structure is maintained. The NPs with coordinated carboxylic acids show a similar catalytic performance in the semi-hydrogenation of alkynes compared to the Pd/Ga colloids without any additives. This strategy might be extended to other bimetallic, air-sensitive colloidal systems.

Conclusion

With the herein developed organometallic synthesis strategy, it is possible to generate small Pd-Ga alloys in solution, which were so far not accessible via classical, co-precipitation-based methods. Working at mild conditions, in particular at low temperatures, turned out to be the key factor for the successful synthesis of bimetallic colloids with sizes in the lower nano-regime and the prevention of their agglomeration. The successful synthesis of bimetallic colloids offers the opportunity for a study of the catalytic behavior of such systems in solution with a quasi-homogeneous nature. The herein gained expertise on the bottom-up wet-chemical synthesis of Pd/Ga colloids and their application in the semi-hydrogenation reaction of liquid alkynes lead to following findings:

a) An elegant, yet simple strategy for the generation of bimetallic systems involving metals with different redox potentials is the use of organometallic precursors with labile ligands with the metals in low oxidation states as starting material. A precise adjustment of the reaction conditions can yield colloidal Pd/Ga NPs in solution with adaptive Pd:Ga ratios. The investigation on the NP formation mechanism via a combination of NMR spectroscopy, GC-MS and LIFDI-MS analysis shows a colloid formation via various cluster intermediates, thus resulting in a deeper understanding of the herein tested system.

b) The catalytic performance of the herein studied NPs confirms the well-known selectivity-promoting effect of a second metal. With gradually increase of the Ga amount, the selectivity of the catalyst towards the olefin is enhanced, whereas the activity is lowered. This can be referred to a change from the elemental state of palladium to a diluted structure of Pd in a Ga matrix according to the literature-

reported site-isolation effect. Additionally, $Pd_{1-x}Ga_x$ colloids with higher Ga amounts show an increased stability towards temperature and H_2 pressure, resulting in minor particle agglomeration. Summarizing, the dilution of the active metal with an inactive one does not only affect the catalyst reactivity but also its stability.

c) As already investigated for monometallic Pd colloids, both the NP stability and the reactivity can significantly be influenced by the post-synthetic addition of additives. Depending on the electronic and steric features, an increased stability towards temperature, H_2 and even oxygen was observed. PPh_3 as additive results in highly selective but only poorly active colloids for the semi-hydrogenation catalysis.

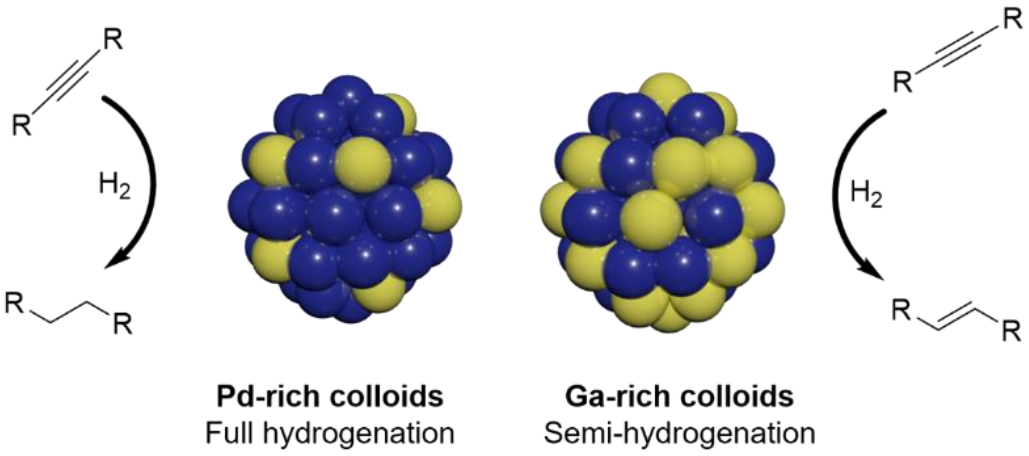

Scheme 17. Bimetallic colloids with different Pd/Ga ratios resulting in a different catalytic performance regarding activity and selectivity in the semi-hydrogenation of liquid alkynes.

d) Post-synthetic addition of substoichiometric amounts of carboxylic acids results in a coordination of these ligands to the NP surface The addition of substoichiometric quantities of carboxylic acids to the surface of bimetallic $Pd_{1-x}Ga_x$ NPs is an effective strategy to obtain air-stable colloids by coordinating surfactants to the Ga surface atoms which prevent the particles from oxidation. Additionally, the active Pd sites are not affected by coordination, which is reflected by a similar catalytic performance compared to $Pd_{1-x}Ga_x$ colloids without any post-synthetic additives. As addition of the carboxylic acids during the colloid synthesis would result in the decomposition of the metal precursors, the herein introduced method allows for the first time for the formation of (air)-stable intermetallic NPs with Group 13 metals. Remarkably, particle size and structure are preserved. This highlights the significant influence on these ligands to the characteristics of the colloids. The controlled surfactant coordination does not hamper the activity in the semi-hydrogenation reaction of liquid alkynes where $Pd_{1-x}Ga_x$ NPs are highly active and selective catalysts. The high selectivity is based on the inactive metal Ga that acts as a spacer between the active centres,

according to the well-known site isolation principle. Hence, a second, inactive metal does not only increase the catalyst selectivity but also can serve as an anchor for coordinating molecules added post-synthetically to the colloid solution. By choice of the metal system and the surfactant, the stability of the colloids can be selectively influenced, while the reactivity is not affected by the coordinating molecule. This highlights the potential of the herein introduced strategy to react metal precursors under mild conditions as a source of bimetallic materials, which are not accessible by classical bottom-up synthesis methods (e.g. by the reduction of co-impregnated metal salts).

With the herein developed synthesis strategy a simple adjustment of the metal ratios and reaction conditions as widely applicable tool enables an easy optimization of various bimetallic systems towards the required properties in terms of catalyst activity, selectivity and stability. The herein gained knowledge regarding suitable metal precursors and reaction conditions can now be exploited; future studies could focus on a systematic investigation on various, even bimetallic nanoalloys of abundant, non-precious metals only. For further optimization regarding the catalyst stability, a simple impregnation of the tailor-made colloids on a non-active support could improve the catalyst stability and hence enable the preparation of an even more robust catalytic system. The advantage over classical synthesis methods of supported bimetallic NPs is that the particles are formed under mild conditions, hence yielding ultra-small particles which are not accessible via classical co-precipitation methods. This might lead to heterogeneous catalyst with superior characteristics.

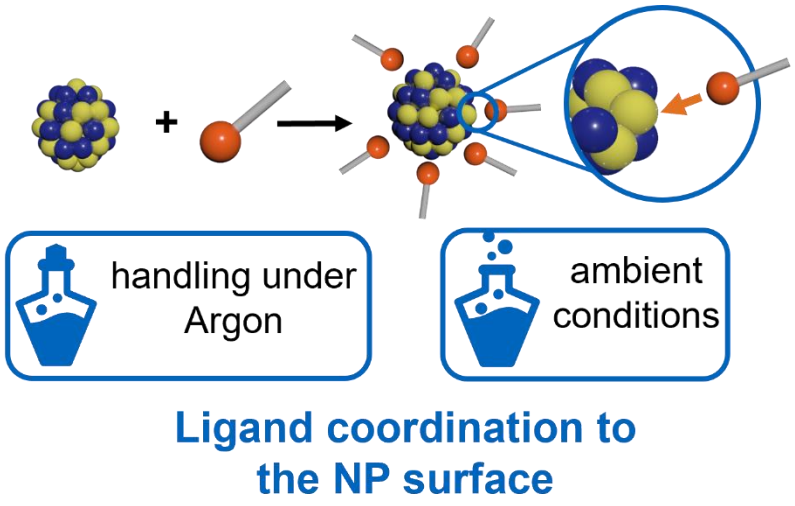

Scheme 18. Protection of $Pd_{1-x}Ga_x$ NPs (x = 0.33, 0.5, 0.67) towards oxygen-induced NP decomposition by the addition of carboxylic acids to Ga surface atoms.

3.2.2 Fe/Al catalysts

Preface

Due to the high costs, replacing noble metals usually applied as hydrogenation catalysts (e.g. Pt, Pd) by abundant, more cost-efficient metals would be beneficial. Fe-based nanoparticular materials are widely deployed for various applications, for example as magnetic fluids[143], catalysts for carbon nanotube formation[144], magnetic resonance imaging contrast agents[145] or catalysts for the C-C bond formation.[146] So far, only a few examples of both monometallic Fe NPs as well as bimetallic Fe-based systems are reported in literature. For instance, one of the first examples for the successful bottom-up synthesis of Fe NPs was achieved by the reduction of $FeCl_3$ with EtMgCl resulting in small NPs (2.7 ± 0.6 nm), which showed good activities in olefin hydrogenation catalysis.[73] In order to stabilize such NPs against agglomeration, the addition of a nitrile-functionalized IL to Fe NPs (obtained via the reduction of $FeCl_2$ with EtMgCl) allowed for the application as catalysts for the stereoselective hydrogenation of alkynes to *cis*-alkenes.[147] The coordination of the nitrile functional group of the IL to the metal surface results not only in an additional stabilization but also in the observed stereoselectivity. This demonstrates that in principle, the selectivity of a nanoparticular Fe catalyst can be tuned precisely (similar to the monometallic Pd@N(Octyl)$_4$Br colloids discussed before in this thesis). Beside the strategy of coordinating surfactants for an enhanced catalytic performance, the alloying with a second, non-active metal was also investigated. Here, a promising example of a highly selective catalyst system was reported by Armbrüster et. al in 2012.[74] The intermetallic Hume-Rothery phase Fe_4Al_{13} (synthesized by a top-down approach) showed a superior catalytic performance in the selective semi-hydrogenation of acetylene, which was assigned to the site-isolation of active Fe centers by dilution with the inactive Al.[12] This results in a decreased adsorption energy of the ethene to the metal surface leading to a preferred olefin desorption instead of a further hydrogenation to the respective alkane. With higher amounts of Al, the selectivity increases for the semi-hydrogenation of acetylene. The combination of the site-isolation of the active metal with the alteration of the electronic structure by chemical bonding demonstrated the possibility to tailor the catalytic properties of a cheap, abundant and non-toxic 3d transition metal.

Nevertheless, for industrial applications such highly sophisticated, distinct intermetallic phases with defined crystal structures made by elaborated solid-state synthesis methods may, however, not be feasible, rather than composite nano-alloys with undefined structural regimes consisting of different metal/metal ratios.[148] In this regard, Dey et al. reported on the synthesis of Fe/Al NPs via reduction of $FeCl_2$ with [$LiAlH_4$] at 600 °C yielding large particles of

ca. 20 nm.[106] Nevertheless, using halide-containing precursors may not be beneficial for catalytic applications and could lead to a decreased performance by surface-poisoning of the catalyst.[149] Another, more recent approach on the bottom-up synthesis of Fe/Al bimetallic materials with the same metal precursors ($FeCl_2$ and $[LiAlH_4]$) applied mild reaction conditions using ionic liquids as reaction medium.[107] This promising bottom-up synthesis protocol combines the reaction of two metal precursors with an IL as stabilizing agent under mild conditions (temperature, H_2 pressure), which is a good starting point for the development of more sophisticated, metal-organic based synthesis approaches. However, the authors reported on a full oxidation of both metals, which might be attributed to oxygen and/or water originating from the ionic liquid. Hence, choosing a strictly water-free and rigorous exclusion of air might be beneficial. Starting materials such as iron(II) halides, -acetates or -acetylacetonates, which most certainly lead to undesired side reactions should be avoided. Precursors with hydrocarbon-only ligands, such as $[Fe_2(mesityl)_4]$[150] are more promising candidates for a bottom-up synthesis of bimetallic Fe/Al nanoalloys. With special regard to organometallic Fe compounds, avoiding precursors with a Cp* ligand is important since the formation of stable molecular ferrocene-type complexes prevents reduction of Fe(II) to Fe(0).[112,113] Therefore, the ECp* complexes are not suitable precursors for $Fe_{1-x}E_x$ NPs. The compound $[AlH_3]{-}NMe_3$ as Al source is an alternative Al(0) source, as this precursor is able to transfer hydrogen to aryl ligands of a metal complex with a consequent reduction of the respective metal. This enables the formation of bimetallic NPs.[151] The reaction of $[Fe_2(mesityl)_4]$ with $[AlH_3]{-}NMe_3$ might result in an intramolecular reductive elimination of mesitylene, yielding active Fe(0) nuclei as starting point for the formation of intermetallic Fe/Al NPs.

Scientific Issue

The study on Pd/Ga nano-sized colloids already shed a light on the versatile stabilities, reactivities and catalytic performances of such bottom-up bimetallic systems obtained by an organometallic synthesis approach. The stabilization of small colloidal NPs by a hydrocarbon shell is crucial for a system in solution. By continuous particle agglomeration, induced by various factors like temperature or H_2 pressure, precipitation of bimetallic powders is often observed. Precisely adjusting the reaction conditions offers the opportunity to obtain a portfolio of various materials, maintained from the same starting point but with various compositions, structures and particle sizes. These factors directly influence the reactivity of

the respective material, and hence a detailed investigation on structure/property relationships with a portfolio of similar materials with distinct differences become feasible.

Hence, transferring the so-far obtained knowledge on bimetallic $Pd_{1-x}Ga_x$ colloids to the metal combination of Fe and Al leads to following questions:

a) Is it possible, analogue to the $Pd_{1-x}Ga_x$ colloids (x = 0.33, 0.5, 0.67), to obtain bimetallic $Fe_{1-x}Al_x$ colloidal NPs from the reaction of metal-organic precursors? Which reaction parameters are required (temperature, H_2 pressure, solvent) and which Fe/Al ratios are possible?

b) How can the reaction mechanism between the two precursors $[Fe_2(mesityl)_4]$ and $[AlH_3]{-}NMe_3$ be described and which species stabilize the $Fe_{1-x}Al_x$ colloids in solution (without an additional surfactant)?

c) By adjusting the reaction parameters, is it possible to precisely influence the stabilizing organic shell around the colloids, in order to obtain precipitated $Fe_{1-x}Al_x$ powders? If yes, what can we learn about the building mechanism of such bimetallic materials in general?

d) Can the reaction of $[Fe_2(mesityl)_4]$ and $[AlH_3]{-}NMe_3$ be regarded as a simple and mild bottom-up alternative for the synthesis of intermetallic Fe/Al Hume-Rothery phases compared to the classical top-down approaches?

e) How do colloidal $Fe_{1-x}Al_x$ particles and solid $Fe_{1-x}Al_x$ powders perform in the semi-hydrogenation of liquid alkynes? Can those catalysts also be applied for the acetylene semi-hydrogenation? If yes, does the catalytic performance follow the literature-reported trend of the site-isolation principle?

In the following section, the reaction of $[Fe_2(mesityl)_4]$ with $[AlH_3]{-}NMe_3$ in an apolar solvent (mesitylene or toluene) with various Fe/Al ratios, temperatures and H_2 pressures will be presented. Depending on the reaction parameters, the formation of colloidal NPs or solid powder samples will be discussed.

The XPS data were fully collected and analyzed by Tim Kratky. The HR-TEM images were recorded by Ondra Tomanek. ICP-OES measurements were done by Thomas Burger. SQUID measurements were recorded by Raphael Bühler. All TPD experiments were fully designed, performed and analyzed by Tabea Gros. The IR spectra were interpreted with the help of Prof. Janos Mink. Dr. Oksana Storcheva measured all EPR spectra, which were fully analyzed and interpreted by Dr. Benjamin J. Hofmann.

Synthesis and Characterization of $Fe_{1-x}Al_x$ colloids

In order to obtain colloidal $Fe_{1-x}Al_x$ NPs, the reaction of $[Fe_2(mesityl)_4]$ with $[AlH_3]{-}NMe_3$ was investigated. All reactions were performed under inert conditions. In detail, $[Fe_2(mesityl)_4]$ was dissolved in toluene at 25 °C, giving a deep red solution. Addition of the respective amount of $[AlH_3]{-}NMe_3$ (0.5, 1.0 and 2.0 molar equiv. referred to the Fe amount) led to an instant color change yielding a black solution (see Scheme 19). It has to be noted that the Fe amount was constant for all $Fe_{1-x}Al_x$ (x = 0.25, 0.5, 0.67), whereas the Al amount was varied. The selected Fe/Al ratios are derived by targeting the stoichiometries of the well-studied Hume-Rothery phases Fe_3Al, FeAl and $FeAl_2$.[75,103] Simple addition of $[AlH_3]{-}NMe_3$ to a mesitylene solution of $[Fe_2(mesityl)_4]$, independent on the Fe/Al ratio, leads not to a full conversion of both precursors, shown by the residual signals of $[Fe_2(mesityl)_4]$ in the ^1H NMR spectra (see SI, Figure 124).

Therefore, the obtained black solution was further pressurized with 3 bar H_2 and stirred for 20 min at 100 °C, resulting in a full conversion of both metal precursors (see SI, Figure 126). If this time was extended to 1 h, partial precipitation was observed giving a black solid and a solution with light brown color. With increasing Al amount, the time required for a complete particle precipitation increases. For instance, when no $[AlH_3]{-}NMe_3$ is used and only the Fe precursor $[Fe_2(mesityl)_4]$ is solubilized in mesitylene and pressurized with H_2, an instant precipitation of a black solid occurs. Hence, monometallic colloidal NPs consisting of only Fe are not accessible via this synthesis approach. These precipitates will not be discussed further in this section. All herein discussed $Fe_{1-x}Al_x$ colloids were obtained by the reaction of the two metal precursors at 3 bar H_2 for 20 min and are fully dissolved in solution. Exposure of the colloids (in solution) to air resulted in a discoloration of the solution, particle decomposition and precipitation.

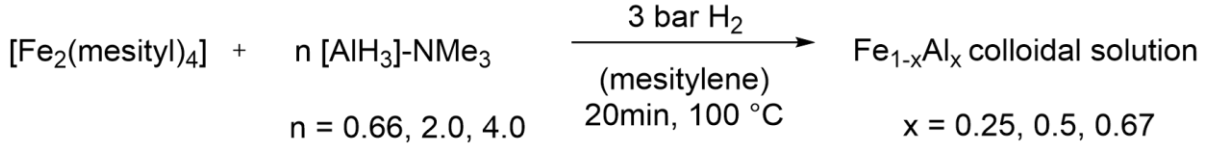

Scheme 19. Synthesis protocol of colloidal $Fe_{1-x}Al_x$ NPs by an organometallic approach.

Size and structure characterization of $Fe_{1-x}Al_x$ colloids

Elemental analysis by induced-coupled plasma optical emission spectrometry (ICP-OES) measurements were performed by evaporation of all volatile compounds of the $Fe_{1-x}Al_x$ colloidal solution with subsequent dissolution of the resulting wax-like material in

concentrated ultra-pure H_2SO_4. The analysis confirms the applied Fe/Al ratios for $Fe_{0.75}Al_{0.25}$, $Fe_{0.5}Al_{0.5}$ and $Fe_{0.33}Al_{0.67}$ colloidal NPs (see Table 17). Interestingly, after evaporation of all volatile compounds, the amount of metal in the samples is rather low with 38-46 %, depending on the Fe/Al ratio. This suggests of the formation of a stabilizing organic shell around the colloidal NPs during synthesis. Nevertheless, the decreasing metal content with increasing Al amount can be explained by the lower atomic weight of Al compared to Fe and not by an increasing amount of organic residues.

Table 17. ICP-OES analysis of $Fe_{1-x}Al_x$ colloidal solutions.

Entry	Colloid sample	Metal wt.%	Fe wt.%	Al wt.%	Fe/Al molar measured	Fe/Al molar calculated
1	$Fe_{0.75}Al_{0.25}$ colloids	45.6	39.3	6.31	3.01	3.00
2	$Fe_{0.5}Al_{0.5}$ colloids	42.7	28.9	13.7	1.01	1.00
3	$Fe_{0.33}Al_{0.67}$ colloids	38.7	20.1	18.6	0.34	0.33

HR-TEM and DLS analysis of the obtained black solutions (after 20 min at 3 bar H_2 pressure to ensure full conversion of the metal precursors without any precipitation) revealed small NPs for all tested Fe/Al ratios with a narrow size distribution from 1.9±0.5 nm to 2.4±0.6 nm, depending on the metal ratios (see Figure 49).

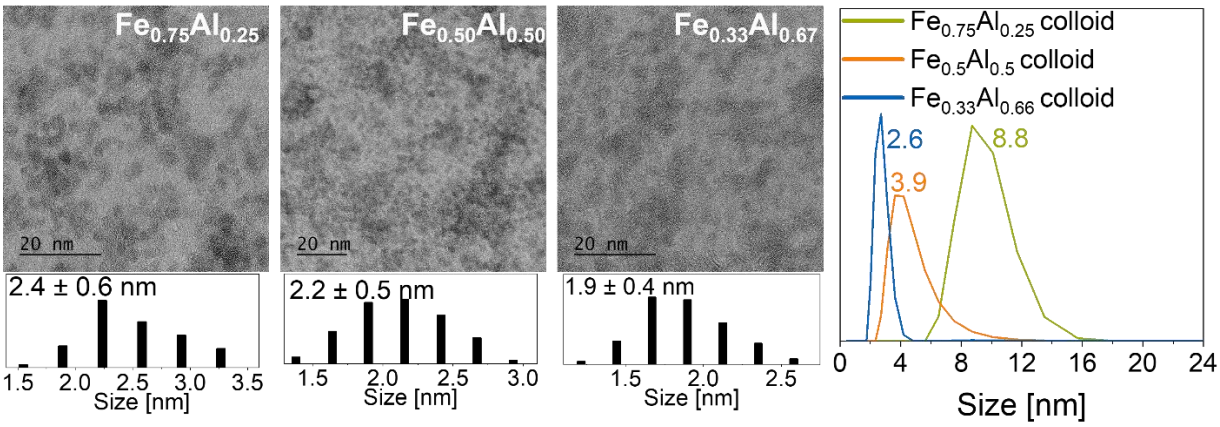

Figure 49. HR-TEM images (left side) showing a narrow size distribution of $Fe_{0.75}Al_{0.25}$ (left), $Fe_{0.5}Al_{0.5}$ (middle) and $Fe_{0.33}Al_{0.67}$ (right) NPs. Particle size distribution was determined by analyzing the diameter of 100 particles. DLS measurements (right side) of all $Fe_{1-x}Al_x$ colloids showing a decreased particle size with increasing Al amount. Note that DLS measurements detect the hydrodynamic radius (including e.g. a stabilizing shell), whereas HR-TEM images only show the metal NP.

In detail, a higher Al content resulted in smaller particle sizes. Storage at -40 °C under inert conditions ensured stable colloids up to six months without any agglomeration observed. If the synthesis procedure is slightly changed by omission of the additional hydrogen pressure, there are also colloidal NPs formed as black solution but with a decreased crystallinity (see

SI, Figure 128). The EDX spectrum confirms the NP composition of Fe and Al, as well as O, C and H. While the latter are stemming from the organic ligands, the surface oxidation during HR-TEM sample preparation could not be avoided due to the very high oxophilic nature of both metals. The small Mg signal stems from the [Fe_2(mesityl)$_4$], as this metal precursor is synthesized via a Grignard reaction and some MgX_2 residues could not be avoided in the [Fe_2(mesityl)$_4$] samples. The obtained Cu signal originates from the Cu mesh grid used for these measurements. Elemental mapping shows a homogeneous distribution of Fe and Al over all particles (see Figure 50) and hence excludes the existing of only monometallic Fe or Al particles.

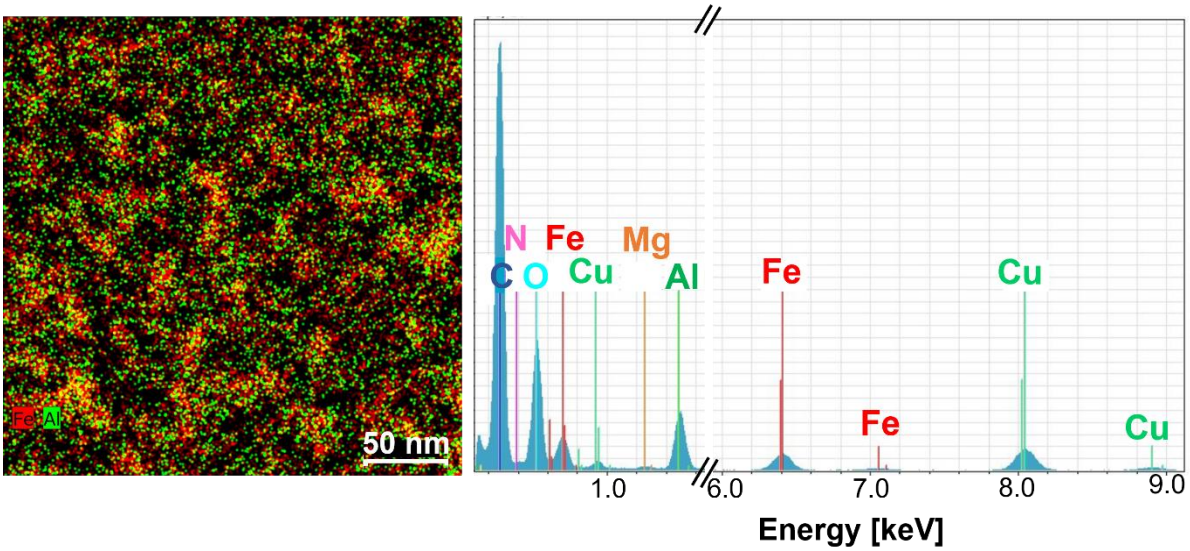

Figure 50. Left: Elemental mapping of $Fe_{1-x}Al_x$ colloids showing a homogeneous distribution of both metals over the whole sample. Right: EDX spectrum of $Fe_{1-x}Al_x$ colloids.

The bimetallic character and the inner structure of the herein studied $Fe_{1-x}Al_x$ materials was investigated by X-ray photoelectron spectroscopy (XPS). Both metals appear in their oxidized states on the surface of the nano-sized $Fe_{0.33}Al_{0.67}$ and $Fe_{0.5}Al_{0.5}$ colloids (see Figure 51). The Fe 2p core level shows the same binding energies and shapes independent of the metal composition. The satellite structure is characteristic for Fe(III) in Fe_2O_3 as described by Bagus et al.[152] The Al 2s core level at 119.0 eV indicates the presence of Al_2O_3.[153] Note that oxidation of the metallic species on the surface of the NPs is presumably caused by the XPS preparation procedure which includes evaporation of the solvent from the colloidal solution. Consequently, the “solid” particles are exposed to inert atmosphere containing ~0.1 ppm oxygen impurity for a few minutes without protection by a surrounding solvent. The traces of oxygen lead very likely to a full oxidation of both metals due to the high oxophilicity and the particularly small size of the compounds.

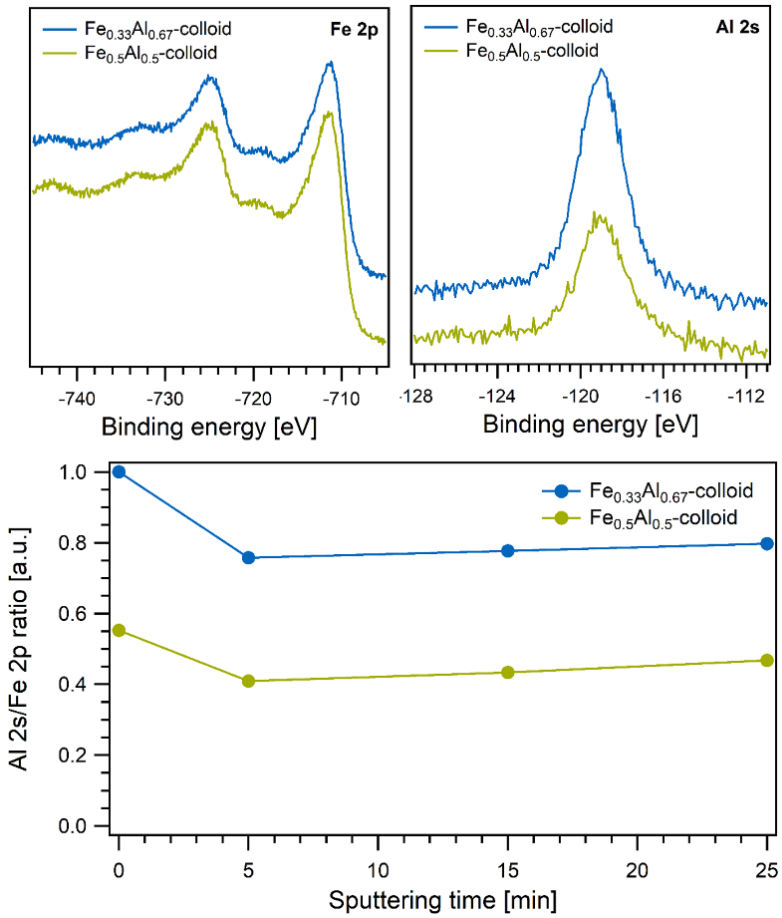

Figure 51. Fe 2p and Al 2s core level spectra (above) of $Fe_{0.33}Al_{0.67}$ colloids (blue) and $Fe_{0.5}Al_{0.5}$ colloids (green) showing Fe and Al in the oxidized states Fe(III) and Al(III), even after sputtering with Ar^+. Depth profile (bottom) revealing a random metal distribution and an organic shell around the NPs.

This phenomenon was already reported even for more noble Pd/Ga systems using the same XPS preparation method, which was already discussed in detail in this thesis. For all samples of $Fe_{1-x}Al_x$ colloidal solutions, a major signal for carbon deposits on the NP surface was detected, hence supporting the assumption of a coordinating and stabilizing organic shell around the NPs. To shed light on the overall structure of the colloids and the metal distribution within the NPs, a depth profile was acquired based on Ar^+ sputtering and subsequent XPS measurements. The obtained Al 2s/Fe 2p intensity ratios (Figure 51, bottom) show the same trend for $Fe_{0.33}Al_{0.67}$-colloid and $Fe_{0.5}Al_{0.5}$-colloid. Throughout the experiment, the Al 2s/Fe 2p ratio of $Fe_{0.33}Al_{0.67}$-colloid is roughly twice as high as the one for $Fe_{0.5}Al_{0.5}$-colloid reflecting well the metal stoichiometries proven by ICP-OES. After a decrease during the first sputtering step (5 min), the Al 2s/Fe 2p ratio remains almost constant. This behavior pinpoints a random distribution of Fe and Al within the NPs (nano-alloy). The pronounced decrease in the beginning originates from the surface sensitivity of XPS; as the kinetic energy of the Al 2s core level (~1367 eV) significantly exceeds the one of Fe 2p (~775 eV), the Fe 2p signal is more surface-sensitive in comparison to Al 2s. The surrounding organic shell attenuates the Fe 2p

signal more than Al 2s. Hence, removal of the organic shell by sputtering delivers a decreased Al 2s/Fe 2p ratio as observed. This goes in line with a C 1s signal that is reduced in intensity after the first sputtering step.

Investigation on the stabilization of $Fe_{1-x}Al_x$ colloids

For a deeper insight on the formation mechanism of the $Fe_{1-x}Al_x$ colloids and to understand the factors for a colloidal stabilization in solution, various analysis techniques were performed. A combination of LIFDI MS, GC MS and ^1H NMR analysis was applied to shed light on the reaction between $[Fe_2(mesityl)_4]$ and $[AlH_3]–NMe_3$. In contrast to the previous discussed $Pd_{1-x}Ga_x$ colloids, monitoring the course of reaction of the colloidal $Fe_{1-x}Al_x$ samples via LIFDI MS shows no detection of signals referring to mono- or bimetallic cluster species could be detected (see Figure 52). The ionization of larger species at the emitter of the LIFDI-MS instrument is strongly dependent on the nature and the thermal resistance of the sample. According to the (qualitative) experience in-house, organometallic species with up to a m/z of 3000 can be detected by the herein used instrument. For a better understanding, different molecular weights were exemplarily calculated for Fe/Al colloids with a metal ratio of 1/1, based on the concept of magic number clusters. The smallest colloids with a “perfect icosahedral” structure would exhibit a diameter of 0.8 nm with 13 metal atoms (assuming a bcc structure with 74 % space filling). Such particles with a hypothetic molecular weight of 538 g/mol would be principally detectable via LIFDI-MS measurements. Fe/Al particles with a size of 1.4 nm and 55 metal atoms and 1.9 nm with 147 metal atoms (next “magic number clusters”) would exhibit a molecular weight of 2278 g/mol and 6088 g/mol, hence already exceeding this detection limit in the case of the 1.9 nm large particles. As the observed sizes for $Fe_{0.5}Al_{0.5}$ colloids by HR-TEM with 2.2 ± 0.5 nm and hence an approximate molecular weight of 12797 g/mol, such particles will not be detectable via LIFDI MS measurements. The detection of smaller cluster species as intermediates of the colloidal NPs was, in contrast to the case of Pd/Ga colloids, not successful. This can be explained by a faster reduction of the metal precursors leading to larger metal entities and an instant growth to NPs.

Nevertheless, LIFDI MS spectra of all $Fe_{1-x}Al_x$ colloids showed some organic species, identically for all Fe/Al ratios (see Figure 52). Mass signals of mesitylene, 1-ethyl-3,5-bismethylbenzene and bis-(dimethylphenyl)ethane were detected in both the LIFDI MS and GC MS spectra for all Fe/Al ratios. For GC MS measurements, the colloidal solutions were filtrated over Celite in order to remove all metal-containing compounds. For both LIFDI-MS and GC-MS spectra, the detected m/z values indicate a C-H activation mechanism, which is

typically observed for Fe metal centers.[154] Additionally, further masses corresponding to other species (such as 1,2,3,5-tetramethylbenzene and 1,3-diethyl-5-propylbenzene) support these findings.

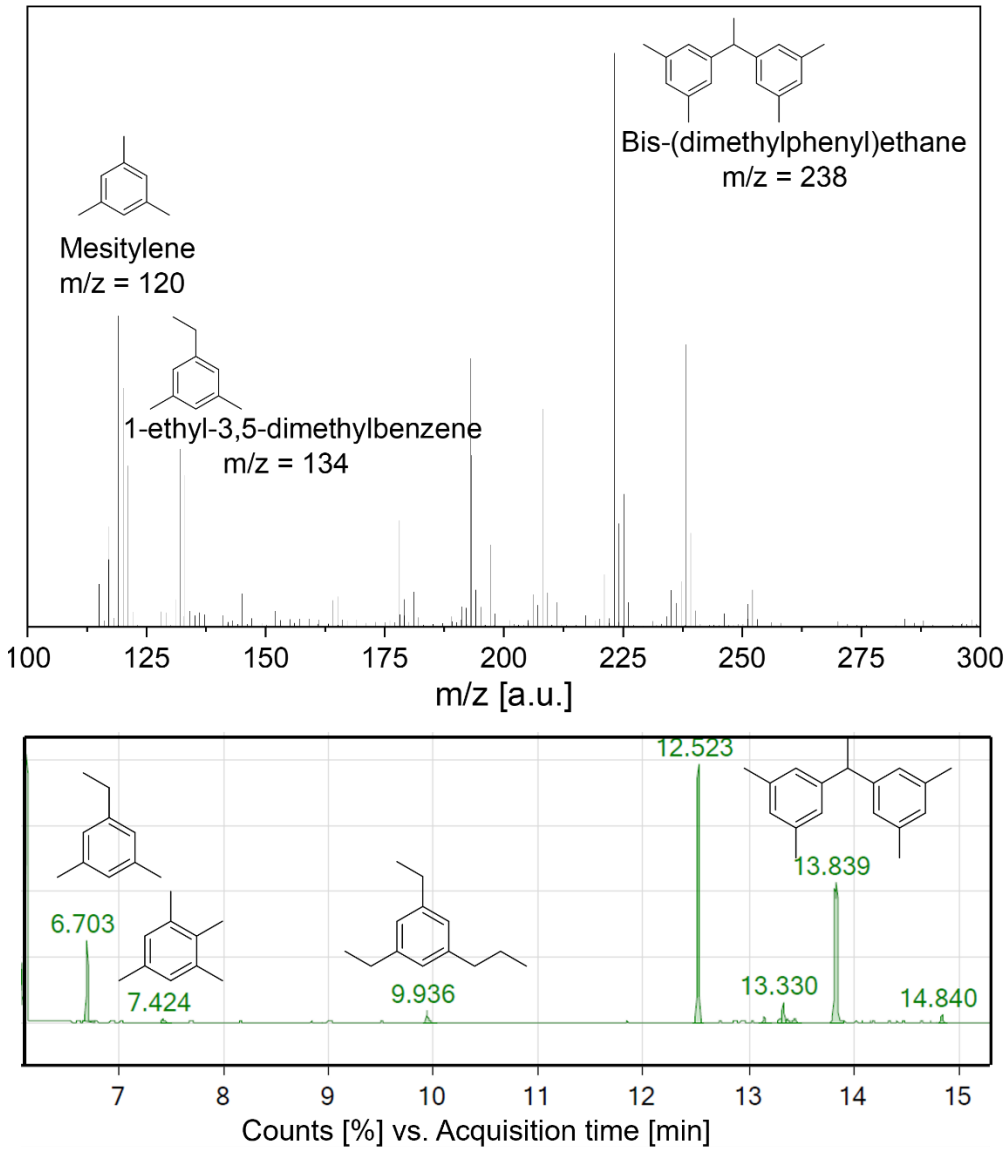

Figure 52. LIFDI MS (above) and GC-MS spectra (bottom) of the $Fe_{1-x}Al_x$ colloidal solutions (for LIFDI MS: without any further treatment; for GC-MS: after removal of all metal-containing compounds) showing the same mass signals and signal patterns.

In order to investigate whether the detected mesitylene only originates from the solvent or if it is formed in situ by the reaction of $[Fe_2(mesityl)_4]$ with $[AlH_3]{-}NMe_3$, the reaction of these two precursors was tested in toluene as solvent (see Figure 53). Here, also mesitylene was detected suggesting a reduction of $[Fe_2(mesityl)_4]$ upon addition to $[AlH_3]{-}NMe_3$ yielding the hydrogenated ligand. For a more detailed information, analysis of the reaction solution before and after addition of H_2 pressure showed that the mesitylene formation occurs immediately

after addition of the Al precursor to the solubilized Fe precursor indicating a hydride transfer from $[AlH_3]-NMe_3$ to $[Fe_2(mesityl)_4]$. The hypothesis of a C-H activation mechanism on the Fe centers is further supported by the detection of coupling products arising from both, mesitylene and toluene (see Figure 53). In detail, not only 1-ethyl-3,5-bismethylbenzene but also ethylbenzene was formed during the reaction of both metal precursors in toluene. Pressurizing the reaction mixture with H_2 does not influence the organic species detected by mass spectrometric analysis.

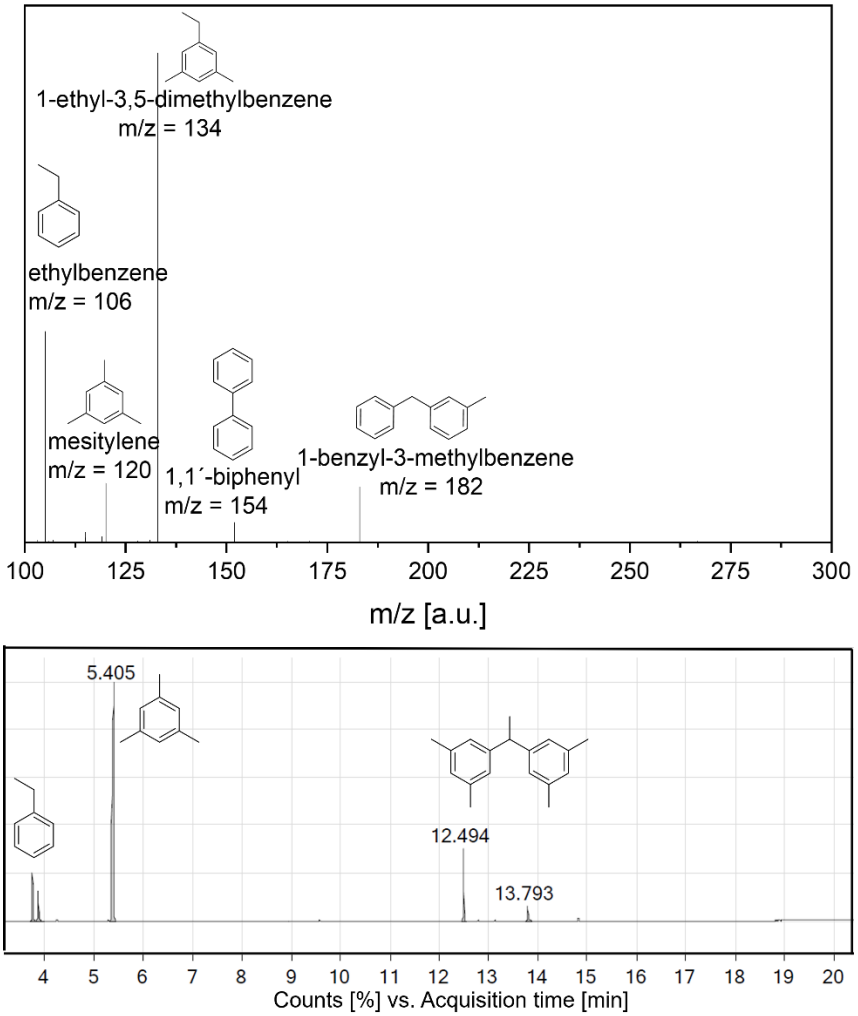

Figure 53. LIFDI MS (above) and GC-MS spectra (bottom) the $Fe_{1-x}Al_x$ colloidal solutions (for LIFDI MS: without any further treatment; for GC-MS: after removal of all metal-containing compounds) in toluene showing the same reaction products.

FT-ATR-IR analysis was performed in order to learn more about the surface characteristics of the colloids (see Figure 54 and Table 18). For these measurements, the colloidal $Fe_{1-x}Al_x$ solutions were dropped on the IR instrument under an inert atmosphere and all volatile compounds (e.g. solvent, NMe_3 originating from the Al precursor) were removed by simple evaporation. This resulted in a wax-like solid, where the organic compounds coordinating to

the metal surface are still present. Hence, this allows for an analysis of all species present on the NP surface. A detailed assignment is listed in Table 18.

Table 18. Assignment of vibration signals for $Fe_{1-x}Al_x$ colloidal solutions.

Entry	Vibration signal [cm^{-1}]	Assignment
1	1746	Metal-H stretch
2	1596	Antisymmetric C-C ring stretching
3	1468	Antisymmetric Al-H_2 stretch
4	1446	Antisymmetric CH_3 deformation + C-C ring stretching
5	1400	Antisymmetric CH_3 deformation
6	1367	Symmetric CH_3 deformation
7	1292	Asymmetric skeletal C-C stretch
8	1260	Al-alkyl deformation
9	1159	C-H in plane deformation + CH_3 rocking
10	1083	Metal-H stretch
11	1013	CH_3 deformation
12	932	Al-C-C stretch
13	884	CH out of plane deformation
14	795	Antisymmetric Al-alkyl stretching
15	749	Metal-H deformation
16	638	Al-alkyl deformation
17	595	C-C-C ring in plane deformation
18	497	C-C-C ring out of plane deformation

Hydrogen containing species can be identified as M-H vibrations (M = Fe or Al) at 1746 cm^{-1}, 1468 cm^{-1} and 749 cm^{-1} with increasing intensity with higher Al amounts.[155] Additionally, signals originating from Al-alkyl vibrations at 638 cm^{-1}, 795 cm^{-1} and 1260 cm^{-1} point towards alkyl groups binding to Al on the surface, protecting the colloid against agglomeration.[156,157] As those signals increase with increasing Al amount as well as the colloidal stability, it can be concluded that Al-alkyl groups on the surface of the bimetallic NPs are the crucial factor in order to hold the particles in solution, which is in well agreement with the found metal amounts in ICP-OES measurements. This explains also why pure Fe colloids could not be obtained by the simple reaction of $[Fe_2(mesityl)_4]$ with H_2. The vibration signals at 1596 cm^{-1} and 595 cm^{-1} further indicate the coordination of aromatic species to the NP surface. Here, the reaction of $[Fe_2(mesityl)_4]$ with $[AlH_3]$-NMe_3 could also result (beside the reduction of the Fe precursor), in an exchange of the mesityl group with a hydride, leading to $[Al(mesityl)_xH_y]$ species. Such species on the NP surface could also lead to an increased particle stabilization in solution. The stabilizing effect of Al-alkyl groups for colloidal mono- or bimetallic (alloy) systems is a

well-known phenomenon in literature.[155,156] Bönnemann et.al. reported on various colloidal systems (based on Pt and Ni), where the addition of trialkyl amines resulted in the effective stabilization of the particles in solution.[57]

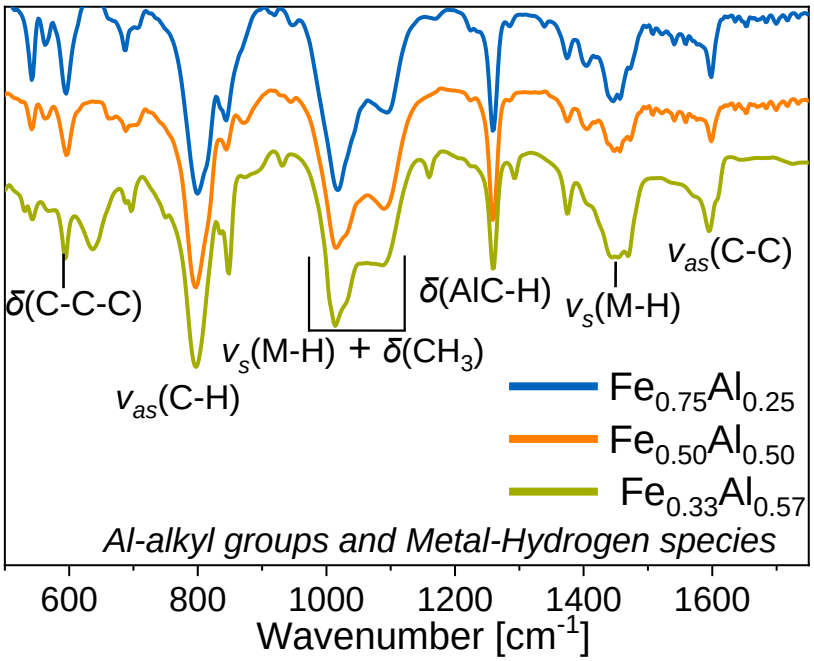

Figure 54. ATR-FT-IR spectra of the $Fe_{1-x}Al_x$ colloids showing signals for Al-H and Al-alkyl species.

Pressurizing the $Fe_{0.33}Al_{0.67}$ colloids with 1 bar H_2 for 1 h results in a broad vibration band at 1617 cm^{-1}, which can be assigned to an Al-hydride species (see Figure 55). Hence, it can be assumed that the $Fe_{1-x}Al_x$ colloids are able to bind or incorporate hydrogen, which is an interesting feature concerning their activity in hydrogenation catalysis.

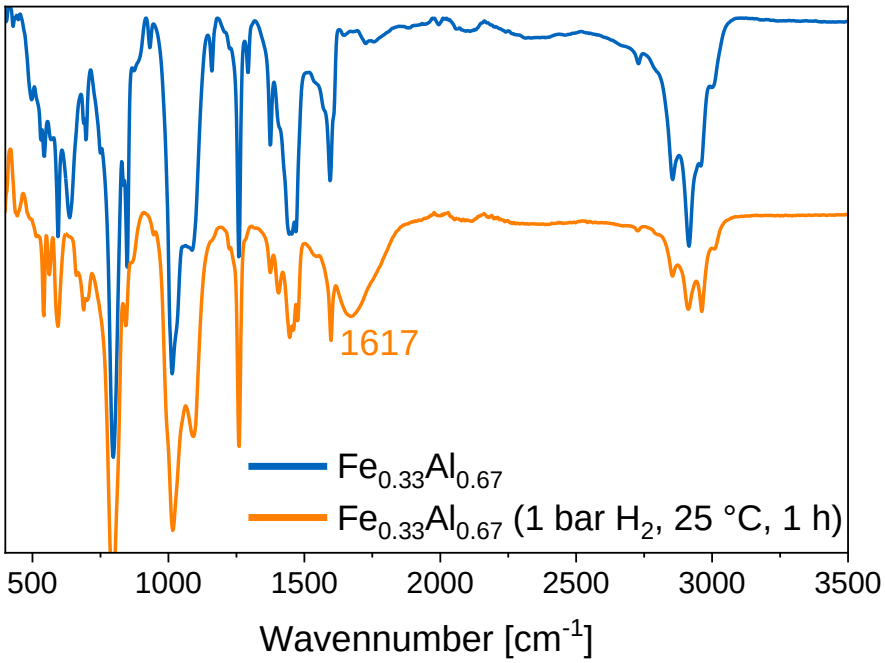

Figure 55. ATR-FT-IR spectrum of the $Fe_{0.33}Al_{0.66}$ colloids before and after pressurizing with H_2.

For a better understanding of the stabilization of the Fe/Al colloids, their decomposition by addition of aqueous HCl was investigated. Evolution of gas might indicate hydride species on the colloid surface and support the findings from ATR-FT-IR measurements. Nevertheless, the simple oxidation of the elemental metals by a reaction with HCl and water resulting in the formation of the respective metal chlorides and H_2 cannot be excluded. Analysis of the reaction solution (consisting of decomposed $Fe_{1-x}Al_x$ colloids as precipitate and the supernatant solution) by ^{1}H NMR spectroscopy shows all signals for bis-(dimethylphenyl)ethane and some additional aliphatic signals in the region between 1.5-0.2 ppm, consistent with the detected organic signals of the intact colloidal solutions (see SI, Figure 121). Analysis of the intact colloids (without any HCl addition) via ^{1}H NMR spectroscopy revealed a strong signal broadening, typical for paramagnetic samples (see SI, Figure 126). Apart from mesitylene, no other species could be identified. In contrast, for ^{13}C/^{27}Al NMR measurements, no signals were detected.

For further analysis of the NP surfaces, the colloids were exposed to an atmosphere of CO and analyzed by IR spectroscopy. The underlying adsorption properties on the surface of the $Fe_{1-x}Al_x$ can help to understand the nature of the NP metal surface. In general, bridging and terminal bound CO adsorption modes indicate the surrounding of the Fe on the NP surface. Bridging CO is typically observed for metallic Fe, while terminal CO suggests a separation of the active Fe centers which indicates Fe separation by a second, non-reactive metal.[158,159] For all samples, independent on the Fe/Al ratio, a broad signal of bonded CO is observed between 1750 cm^{-1} and 2100 cm^{-1} originating from superposed multiple single vibrations signals (see Figure 56).

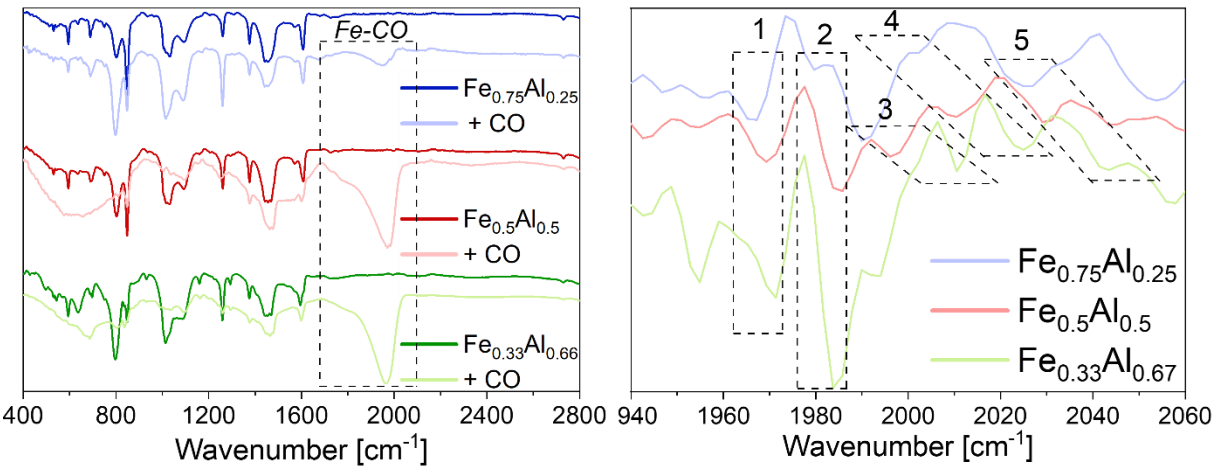

Figure 56. Left: IR spectra of CO adsorbed on $Fe_{0.75}Al_{0.25}$ (blue, above), $Fe_{0.5}Al_{0.5}$ (red, middle) and $Fe_{0.33}Al_{0.67}$ (green, bottom) colloids recorded at 25 °C in the CO stretching region from 1600–2200 cm^{-1}. Right: Second abbreviation of the IR spectra upon exposure to CO with zoom-in in the region of the Fe-CO vibrations.

Upon exposure to CO, the signals of adsorbed organic species strongly decrease suggesting a replacement of the stabilizing organic shell by CO. This is further supported by almost a full precipitation of the Fe-rich $Fe_{0.75}Al_{0.25}$ colloids by the addition of CO. Hence, the signal of CO species adsorbed on the NPs´ surface which are still in solution is also strongly decreased. Signals for oxidated Fe-O species with typical vibration peaks between 400-550 cm^{-1} are not observed.[159] For a precise determination of the band positions, the second derivative of the difference spectra were calculated showing that multiple frequency bands coincide in the original spectrum in the range of 1750-2100 cm^{-1}. This deconvolution approach is a common procedure for resolution enhancement of vibrational investigations.[160] Here, a signal maximum of the original spectrum gives a minimum in the spectrum of the second abbreviation. Five overlapping CO adsorption bands can be found for all $Fe_{1-x}Al_x$ samples (see Figure 56, right). Comparison of these signals show a shift towards higher wavenumbers with increasing Al amount, suggesting a weakening of CO adsorption with higher Al amounts. This might be attributed to a favoured terminal bound coordination mode of the CO upon dilution of the Fe with Al. With higher Fe amounts, instead, bridging bound CO leads to an increased adsorption strength and hence to lower wavenumbers.

Magnetic Properties of $Fe_{1-x}Al_x$ colloids

The paramagnetic nature of the Fe/Al colloids was further verified by EPR measurements in solution (see Figure 57). Here, all $Fe_{1-x}Al_x$ samples were diluted to a Fe concentration of 0.06 µg/mL and measured without any further treatment. For measurements, the samples were cooled down to -160 °C and the microwave power was varied from 5-20 mW showing the presence of oxidized Fe species in all three samples originating from unavoidable traces of oxygen during the preparation process. The large peak width at half-height indicates the interaction of the spins in one NP.[161] Variation of the microwave power shows that for all $Fe_{1x}Al_x$ samples, no saturation is observed between 5 and 20 mW (see SI, Figures 130-132). Hence, for a detailed analysis the spectra with 10 mW will be discussed in the following. The main species is observed as a broad signal with a g-value of ≈ 2.3 (see Figure 57).

Such a signal is indicative for interacting oxidized iron species in particles[162] and indicates a Fe(II) species with a Td symmetry.[163,164] Yet, a distinct assignment would require temperature-dependent measurements. The signal intensity increases with decreasing Al content by more than one order of magnitude from $Fe_{0.33}Al_{0.67}$ to $Fe_{0.75}Al_{0.25}$, which might indicate an oxidative protection of Fe by alloying with Al. Diminishing EPR signals of Fe^{2+} might be also attributed to strongly coupling iron centers, however, this is very unlikely due to its homogeneous

distribution (see HR-TEM-EDX, XPS) and the correlation of signal intensity with the Fe concentration.[165] Another indication for the protective character of Al is given by the second dominant signal with g ≈ 7.7 and a peak-to-peak width of 83-91 mT. It is mainly observed in the $Fe_{0.75}Al_{0.25}$ sample, whereas with higher Al content it is only marginally observable. This signal can probably be assigned to a Fe(III) cluster species,[163,165,166] whereas a bulk species can be excluded due to the large g-value. Such species would be expected at frequencies around 340 mT.[162]

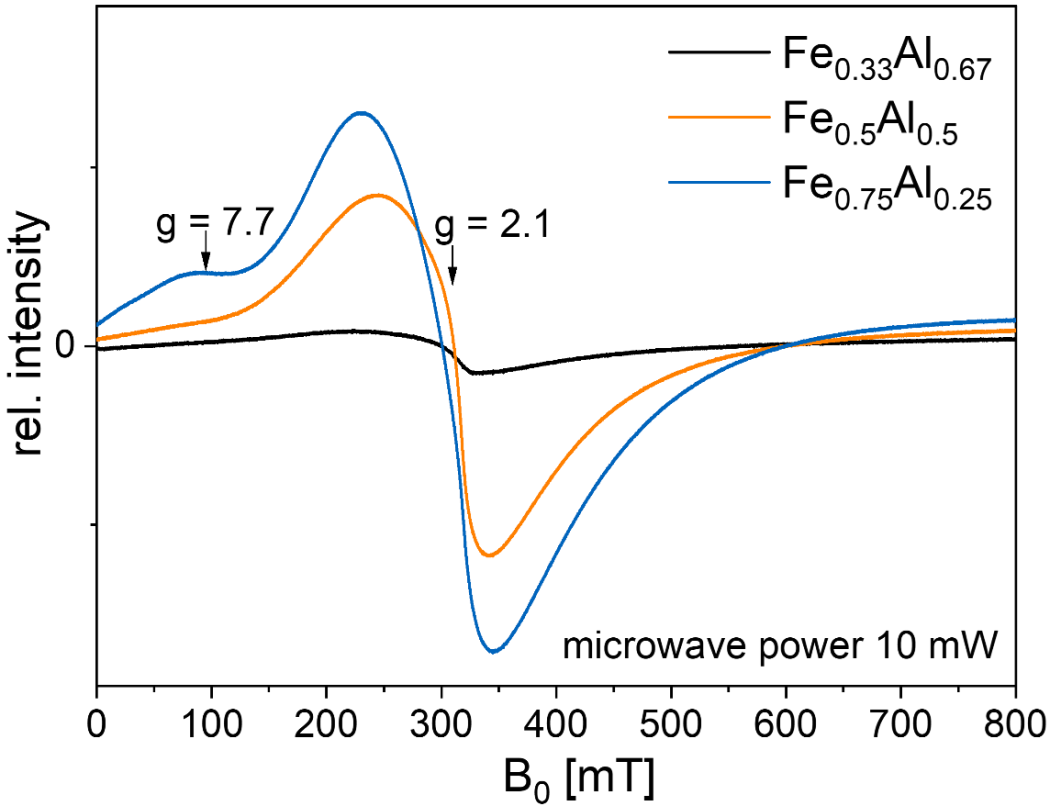

Figure 57. EPR measurements of $Fe_{1-x}Al_x$ colloids (all with the same Fe concentration) showing different signal intensities.

Comparison of intensity the herein identifies species with Fe(III)/Fe(II) = 0.07/1 points to only small amounts of the fully oxidized Fe(II) species. For the other $Fe_{1-x}Al_x$ colloids with higher Al amounts (x = 0.5, 0.67), only the Fe(II) signal can be identified. Nevertheless, due to the wide signal width of all signals over the whole range of measurement, the existence of the above discussed Fe(III) species cannot be ruled out. With increasing Al amount, the signal intensity decreases and hence the number of unpaired electrons raises. The signal can generally be assigned to the sum of oxidated Fe species, as diamagnetic Fe(0) species show no EPR signal. It has to be noted that all samples were handled under inert conditions, but the presence of oxidized Fe species in all three samples originating from unavoidable traces of oxygen during the preparation process cannot be avoided. For this, all synthesis and

preparation steps would require an ultra-high vacuum set-up. The constant concentration of Fe for all $Fe_{1-x}Al_x$ colloidal solutions in combination with a calculation of the Fe atoms in the NPs can help to understand if the differences in intensity of the observed EPR signals is a result of the different number of Fe atoms per NP (dependent on the NP size and the Fe/Al ratio) or if alloying with Al leads to a decreased number of oxidized Fe species. The number of Fe atoms in the NP was calculated assuming a perfect icosahedral structure of the NPs with the model of "magic number clusters" and the respective Fe/Al ratio with a homogeneous distribution of Fe and Al atoms (see Table 19).

Table 19. Calculation of Fe surface atoms for $Fe_{1-x}Al_x$ colloids and comparison of the observed values with the differences of the respective EPR signal intensities.

	$Fe_{0.75}Al_{0.25}$	**$Fe_{0.5}Al_{0.5}$**	**$Fe_{0.33}Al_{0.67}$**
Size of the colloids [nm]	2.41	2.16	1.9
Estimated number of atoms per NP	289	271	153
Estimated number of Fe atoms	216 (≙ 100 %)	135 (≙ 63 %)	50 (≙ 23 %)
Area of EPR signal	$4{,}73\times10^8$ (≙ 100 %)	$2{,}89\times10^8$ (≙ 61 %)	$2{,}83E\times10^7$ (≙ 6 %)

Comparison of the calculated numbers of Fe atoms for all $Fe_{1-x}Al_x$ NPs with $Fe_{0.75}Al_{0.25}$ set as maximum (100 %) shows that a NP with the composition $Fe_{0.5}Al_{0.5}$ has only 63 % and $Fe_{0.33}Al_{0.67}$ only 23 % Fe atoms compared to $Fe_{0.75}Al_{0.25}$. If the differences of the observed EPR signals matches with these values, it could be concluded that the Al has only a dilution effect. Hence, the differences of the respective areas of the EPR signals for $Fe_{1-x}Al_x$ colloids were calculated, whereas the signals of $Fe_{0.5}Al_{0.5}$ and $Fe_{0.33}Al_{0.67}$ exhibit only 61 % and 6 % of the area compared to the EPR signal of $Fe_{0.75}Al_{0.25}$. Note that this calculation is based on a simplification (perfect icosahedral structure of the colloids) and an approximation (estimated number of atoms per NP). Nevertheless, this principally shows that with an increasing Al amount, the amount of oxidized Fe species decreases suggesting that the alloying with Al prevents the colloids from oxidation.

Summarizing, from the herein discussed data it can be concluded the addition of $[AlH_3]{-}NMe_3$ to a solution of $[Fe_2(mesityl)_4]$ results in an immediate hydrogen transfer from the aluminum hydride to the iron precursor and the formation of free mesitylene (see Scheme 20). The mesitylene further reacts at the Fe centers with other components of the solution by a C-H activation yielding aromatic organic species, mainly 1-ethyl-3,5-bismethylbenzene and bis-(dimethylphenyl)ethane. Additionally, the formation of Al-alkyls such as $[Al(mesityl)_xH_y]$ species on the colloidal surface enables a NP stabilization by the coordination to the metal NP surface. XPS sputtering experiments pinpoints a random distribution of Fe and Al within

the NPs (nano-alloy) and an organic shell around the surface. The colloidal surface additionally might contain Al- or Fe-hydrogen species, indicating an intact metal NP. Beside the stabilizing effect against agglomeration (by the formation of Al-alkyl groups on the NP surface), the Al has an additional stabilizing effect in terms of the protection of Fe against oxidation. Nevertheless, this postulated mechanism should only be interpreted as a first idea of the colloid formation.

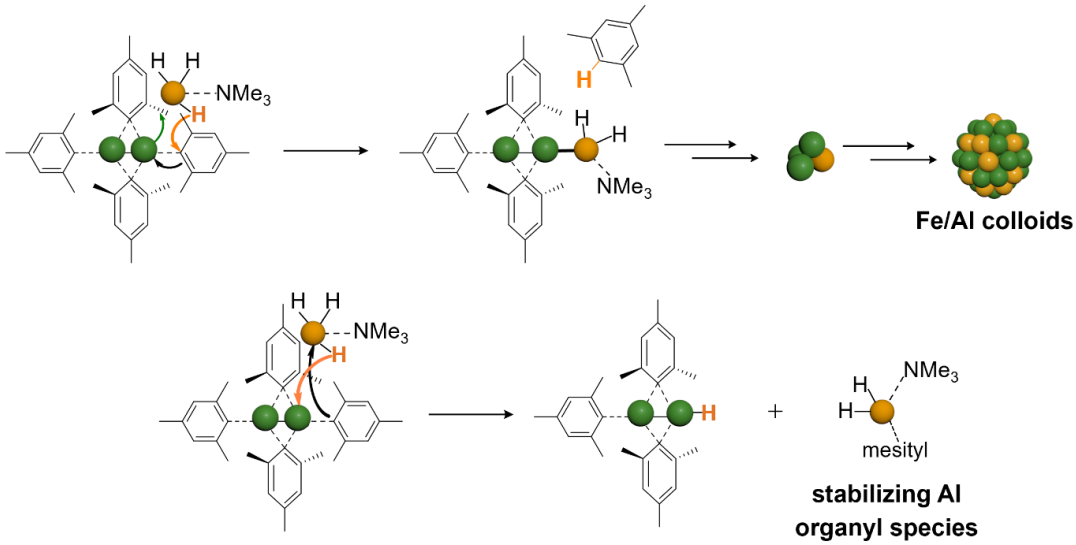

Scheme 20. Postulated mechanism of $Fe_{1-x}Al_x$ NP formation and stabilizing Al organyl species.

Catalytic performance of $Fe_{1-x}Al_x$ colloids in the alkyne semi-hydrogenation

The catalytic performance of $Fe_{1-x}Al_x$ NPs was systematically tested in the semi-hydrogenation reaction of alkynes (see Scheme 21) and will be discussed in the following section.

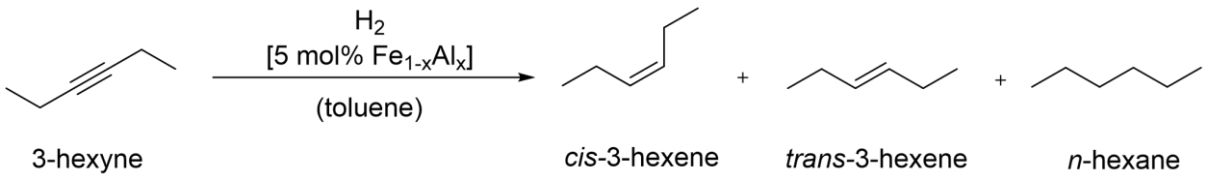

Scheme 21. Semi-hydrogenation catalysis using 5 mol% colloidal $Fe_{1-x}Al_x$ NPs as catalyst and 3-hexyne as model substrate.

The catalyst amount was calculated based on the Fe amount of the solution. All tested particles showed a strong dependence of both temperature and H_2 pressure on the activity and selectivity in the alkyne semi-hydrogenation. For all catalysis experiments, the colloidal $Fe_{1-x}Al_x$ solution was mixed with the substrate, degassed and pressurized with H_2. After 24 h reaction time, the solution was filtrated in order to separate the metal NPs and analyzed via

^{1}H NMR spectroscopy. Variation of the temperature and H_2 pressure clearly shows an influence on the catalyst performance (see Table 20).

Note that in contrast to the previously discussed $Fe_{1-x}Al_x$ NP precipitation during synthesis (precipitation is observed with 3 bar H_2 after 1 h at 25 °C), the addition of an alkyne results in an enhanced particle stability with (almost) no particle precipitation (for details, see Table 20). Such phenomenon was already observed for monometallic Pd@N(Octyl)$_4$Br colloids, which precipitated upon addition of PPh_3. This precipitation was not observed in the presence of an alkyne, hence enabling a stable system under catalytic reactions. The stability of the colloids can be assigned to the coordination of the alkyne with an additional stabilizing effect.

At relatively mild conditions with 1.0 bar H_2 and 25 °C (see Table 20, Entries 1-3), the particles only show a low activity with good selectivities (dependent on the Fe/Al ratio). With increasing Al amount, the activity decreases while the selectivity increases. Increasing the temperature to 50 °C results in a higher activity but lower selectivity towards the olefin (*cis*- and *trans*-3-hexene, see Table 20, Entries 4-6).

Table 20. Semi-hydrogenation experiments using 5 mol% $Fe_{1-x}Al_x$ colloids after 24 h reaction time and 3-hexyne as substrate.

Entry	Catalyst	Parameters	Conversion [%]	Selectivity [%]	*cis/trans* olefin	Precipitation
1	$Fe_{0.75}Al_{0.25}$	1 bar H_2, 25°C	48	87	1/0.3	No
2	$Fe_{0.5}Al_{0.5}$	1 bar H_2, 25°C	48	95	1/0.4	No
3	$Fe_{0.33}Al_{0.67}$	1 bar H_2, 25°C	42	91	1/0.5	No
4	$Fe_{0.75}Al_{0.25}$	1 bar H_2, 50°C	55	40	1/0.2	Yes
5	$Fe_{0.5}Al_{0.5}$	1 bar H_2, 50°C	39	63	1/0.9	Yes
6	$Fe_{0.33}Al_{0.67}$	1 bar H_2, 50°C	88	39	1/1	Minor
7	$Fe_{0.75}Al_{0.25}$	3 bar H_2, 25°C	50	65	1/0	Yes
8	$Fe_{0.5}Al_{0.5}$	3 bar H_2, 25°C	100	87	1/0.4	Minor
9	$Fe_{0.33}Al_{0.67}$	3 bar H_2, 25°C	52	95	1/0.4	No

For all $Fe_{1-x}Al_x$ colloids, the *cis*-alkene is preferably formed at mild reaction conditions (1 bar H_2, 25 °C, see Table 2, Entries 1-3), which is in good agreement with the literature-known *cis*-1,2-addition of hydrogen for the semi-hydrogenation of alkynes.[3] At higher temperatures, the amount of the *trans*-hexene increases indicated isomerization reactions on the catalyst surface at these conditions. The hydrogen pressure does not affect the ratio of formed *cis*- and *trans*-product. Comparison of the different $Fe_{1-x}Al_x$ colloids catalysts additionally shows that with a higher Al amount, the amount of detected *trans*-alkene is increased, pointing towards isomerization mechanisms on the catalyst surface depending on the electronic

characteristics.[167,168] At elevated reaction temperatures, a precipitation of the colloids is observed for the particles with higher Fe amounts (see Table 20, Entries 4-5). With these reaction conditions, the Al-rich colloids $Fe_{0.33}Al_{0.67}$ show the highest activity (see Table 20, Entry 6) as they are the most stable colloids under the chosen conditions showing only minor particle precipitation. Variation of the H_2 pressure from 1.0 bar to 3.0 bar does not result in a particle destabilization and precipitation for the colloids with a higher Al amount. Only the NPs with the highest Fe amount, $Fe_{0.75}Al_{0.25}$, precipitate under these conditions, which is also the reason for the decreased catalytic activity (see Table 20, Entry 7). The best catalytic performance was observed using $Fe_{0.5}Al_{0.5}$ colloids with full conversion of 100 % and a selectivity towards the olefin of 87 % (see Table 20, Entry 8). The colloids with the highest Al amount $Fe_{0.33}Al_{0.67}$ are less active (52 % after 24 h) but show a high selectivity of 95 %. Comparison of the observed selectivities using 1.0 bar H_2 and 3.0 bar H_2 suggests no strong influence, as the same trend concerning the Fe/Al ratio as described before is observed.

$Fe_{1-x}Al_x$ colloidal particle analysis after catalytic runs

Analysis of the $Fe_{1-x}Al_x$ colloids by DLS and HR-TEM measurements after catalysis shows no agglomeration during the alkyne semi-hydrogenation for all tested Fe/Al ratios (see Figure 58).

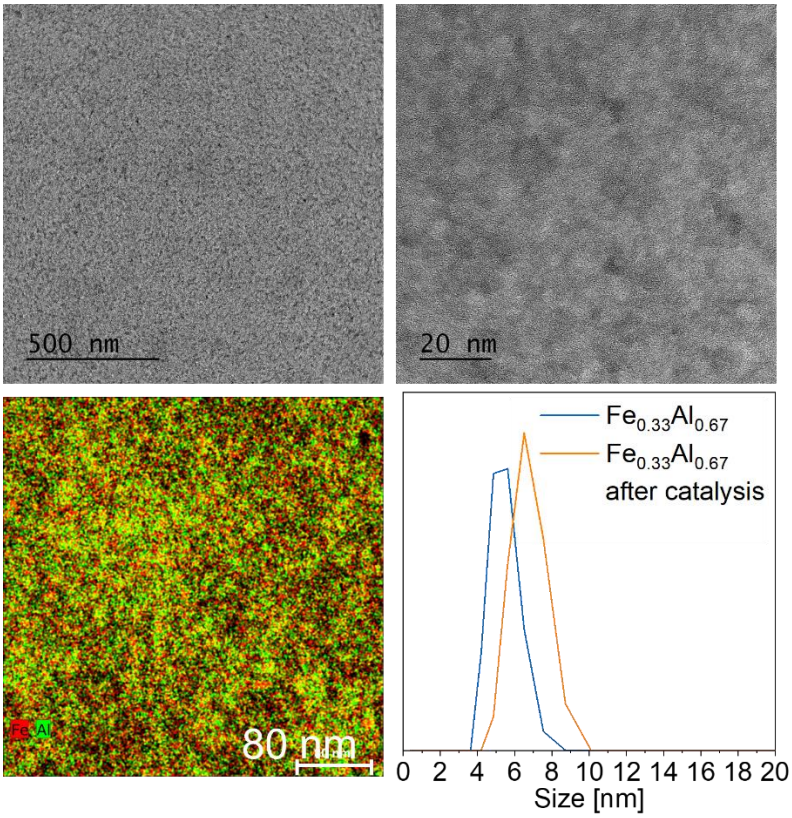

Figure 58. HR-TEM and DLS measurements of $Fe_{0.33}Al_{0.67}$ colloids after catalytic runs showing no particle agglomeration and a homogeneous distribution of Fe and Al over the whole sample.

Elemental mapping of $Fe_{0.33}Al_{0.67}$ colloids still reveals a homogeneous distribution of both metals (excluding the decomposition of the $Fe_{1-x}Al_x$ colloids by the formation of monometallic Fe or Al particles during catalysis runs). Hence, it can be concluded that the $Fe_{1-x}Al_x$ NPs are stable under catalytic conditions, without any agglomeration, precipitation of decomposition. In contrast to the Pd-based colloids, LIFDI-MS measurements of the reaction solution after catalysis runs reveal no oligomerization products of the substrate using $Fe_{1-x}Al_x$ colloids in the semi-hydrogenation of 3-hexyne. Hence, replacing Pd with Fe seems to have a positive influence on the effective suppression of the formation of undesired oligomerization products.

Concluding from the herein observed catalysis results, the $Fe_{1-x}Al_x$ colloids are active and stable in the semi-hydrogenation of liquid internal alkynes under very mild conditions. Diluting the active metal with Al results, in good accordance with the site-isolation principle, to an increased selectivity towards the olefin. These results show that principally, abundant bimetallic colloids can serve as active and selective semi-hydrogenation catalysts.

The successful synthesis of $Fe_{1-x}Al_x$ colloids in combination with their good performance in the semi-hydrogenation catalysis of alkynes shows the high potential of such materials and presents a good basis for further investigations. For example, the influence of the stabilizing organic shell as well as the size of the $Fe_{1-x}Al_x$ colloids is still appealing. Small changes in the synthesis protocol (pressurizing the colloids for an elongated time with H_2) already showed the full NP precipitation yielding a black powder. This might principally indicate the loss of the organic shell followed by a particle agglomeration and finally precipitation. Hence, these observations are a good starting point for a detailed investigation of the influence of the synthesis parameters, with special regard to the adjustment of temperature and H_2 pressure. In this way, a portfolio of solid $Fe_{1-x}Al_x$ powder materials directly related to the $Fe_{1-x}Al_x$ colloids could be obtained. This would not only allow for a comparison of the catalytic performances, but also for additional analysis techniques for solid materials (e.g. PXRD). Therefore, new insights into the material characteristics could lead to a deeper understanding of the underlying factors for the obtained catalytic performances.

Synthesis and Characterization of powder $Fe_{1-x}Al_x$ materials

Small changes in the synthesis procedure of the $Fe_{1-x}Al_x$ colloids by extension of the reaction time to 24 h and a temperature increase to 180 °C lead to full precipitation of a black solid and a colorless solution for the Fe-rich samples $Fe_{1-x}Al_x$ (x = 0, 0.25, 0.5) and to a partial precipitation and a black solution for x = 0.67 (see Scheme 21). Further elongation of the reaction time up to one week does not result in a full precipitation of the Al-rich $Fe_{0.33}Al_{0.67}$ sample. Additionally, the partial precipitated $Fe_{0.33}Al_{0.67}$ can be dissolved again in mesitylene and toluene. The higher solubility of the Al-rich material is further supported by the time required for a complete particle precipitation, as this increased with higher Al amounts. For instance, when no $[AlH_3]$—NMe_3 is used and only the Fe precursor $[Fe_2(mesityl)_4]$ is solubilized and pressurized with H_2, an instant precipitation of a black solid occurs.

$$[Fe_2(mesityl)_4] + n\ [AlH_3]\text{-}NMe_3 \xrightarrow[\text{(mesitylene)}\ 180°C,\ 24\ h]{3\ bar\ H_2} Fe_{1-x}Al_x\ powders$$

n = 0, 0.66, 2.0, 4.0 ; x = 0, 0.25, 0.5, 0.66

Scheme 22. Synthesis protocol of powder $Fe_{1-x}Al_x$ materials by an organometallic approach.

Structure and Size determination of $Fe_{1-x}Al_x$ powders

Analysis of the reaction solution via ^1H NMR, GC MS and LIFDI MS suggests the same organic species as obtained in the colloidal $Fe_{1-x}Al_x$ approach (see SI, Figures 136-137). In detail, masses corresponding to 1-ethyl-3,5-bismethylbenzene and bis-(dimethylphenyl)-ethane were detected while no other species could be identified. Elemental analysis by ICP-OES revealed the calculated Fe/Al ratios and a metal content between 38 wt.% and 68 wt.%, depending on the Fe/Al ratio (see Table 21). The same trend as already shown for the $Fe_{1-x}Al_x$ colloidal solutions was observed. The decreasing metal content with increasing Al amount can be explained by the lower atomic weight of Al compared to Fe. As already mentioned, only a partial precipitation (3 bar H_2, 180 °C, 24 h) is observed for the material with the highest Al amount, $Fe_{0.33}Al_{0.67}$. Here, a distinction between the dark reaction solution results in the definitions $Fe_{0.33}Al_{0.67}$-solution and $Fe_{0.33}Al_{0.67}$-solid for the precipitate (which is comparable to the $Fe_{1-x}Al_x$ powders). Comparison of these two samples (see Table 21, Entries 4 and 5) reveals no differences in the Fe/Al ratio but in the detected metal content. The precipitate shows a higher metal amount and hence a decreased number of organic residues, which might be responsible for the stabilization in solution. This encourages the assumption of the formation of a stabilizing Al-alkyl and/or organic shell around the colloidal

NPs during synthesis (as already discussed for the $Fe_{1-x}Al_x$ colloids). ICP-OES measurements of the colorless solutions revealed no metal content, thus indicating that both Fe and Al are fully precipitated.

Table 21. Elemental analysis with ICP-OES analysis of solid $Fe_{1-x}Al_x$ powder materials.

Entry	Sample	Metal wt.%	Fe wt.%	Al wt.%	Fe/Al molar measured	Fe/Al molar calculated
1	$Fe_{1.0}Al_{0.0}$ powder	68.7	68.7	-	-	-
2	$Fe_{0.75}Al_{0.25}$ powder	51.3	44.2	7.1	3.0	3.0
3	$Fe_{0.5}Al_{0.5}$ powder	49.4	33.1	16.3	1.0	1.0
4	$Fe_{0.33}Al_{0.67}$-solid	46.6	23.7	22.8	0.3	0.3
5	$Fe_{0.33}Al_{0.67}$-solution	38.7	19.6	19.0	0.3	0.3

Scanning-electron microscopy (SEM) measurements give an idea of the macroscopic structure of the herein investigated $Fe_{1-x}Al_x$ materials (see Figure 59), which might lead to a better understanding of the influence of the Fe/Al ratio on the size of the resulting material. In well accordance with the colloidal $Fe_{1-x}Al_x$ NPs, with increasing Al amount, the particle size decreases. This might be attributed to a decreased stabilization by organic molecules coordinating to Al on the materials´ surface. While $Fe_{1.0}Al_{0.0}$ shows big agglomerates, introduction of Al resulting in $Fe_{0.75}Al_{0.25}$, $Fe_{0.5}Al_{0.5}$ and $Fe_{0.33}Al_{0.67}$ leads to a lower particle sizes.

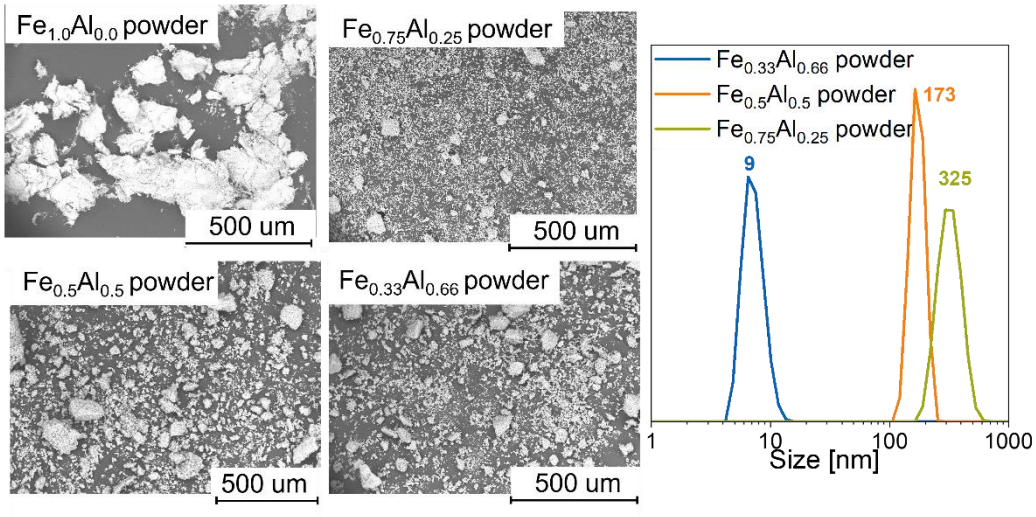

Figure 59. SEM pictures (left) and DLS measurement (right) of all tested $Fe_{1-x}Al_x$ powders showing different particle sizes depending on the Al content.

Further analysis by EDX shows a homogeneous distribution of Fe and Al over the whole material, well in accordance with the colloidal particles discussed before (see SI, Figure 139). The decreasing particle size with increasing Al amount was also verified by DLS measurements. For analysis, the insoluble samples $Fe_{0.75}Al_{0.25}$ and $Fe_{0.5}Al_{0.5}$ were

ultrasonicated in mesitylene in order to get a dispersion, which can be analyzed by DLS. The analysis revealed particle sizes of 325 nm, 173 nm, and 9 nm for $Fe_{0.75}Al_{0.25}$, $Fe_{0.5}Al_{0.5}$ and $Fe_{0.33}Al_{0.66}$, respectively. The particle sizes of the sample $Fe_{1.0}Al_{0.0}$ were too big for a DLS analysis (> 6000 nm).

The material with the highest Al amount $Fe_{0.33}Al_{0.67a}$ was further analyzed by HR-TEM analysis (see Figure 60). All other $Fe_{1-x}Al_x$ materials showed too large sizes (according to DLS), thus not suitable for this analysis technique. Here, a distinction between the (re-soluble) precipitate and the material still in solution leads again to the sample descriptions $Fe_{0.33}Al_{0.67}$-solid (which can also be regarded as a powder) and $Fe_{0.33}Al_{0.67}$-solution. The NP size measured from HR-TEM for $Fe_{0.33}Al_{0.67}$-solid is 2.7 ± 0.5 nm. The major difference is that the sample $Fe_{0.33}Al_{0.67}$-solid shows bigger agglomerates. This suggests that the colloids agglomerate under the harsher reaction conditions and finally precipitate. This is also reflected in the ICP-MS measurements, as for all three samples the same Fe/Al ratio was observed, whereas the overall metal content for the precipitated $Fe_{0.33}Al_{0.67}$-solid with 46.6 wt.% is higher than for the two soluble samples with 38.7 wt.% each. Comparison of the respective NPs by DLS measurements (giving the hydrodynamic radius) reveals sizes of 4.7 nm for $Fe_{0.33}Al_{0.67}$-solution and 8.8 nm $Fe_{0.33}Al_{0.67}$-solid (see Figure 60, right).

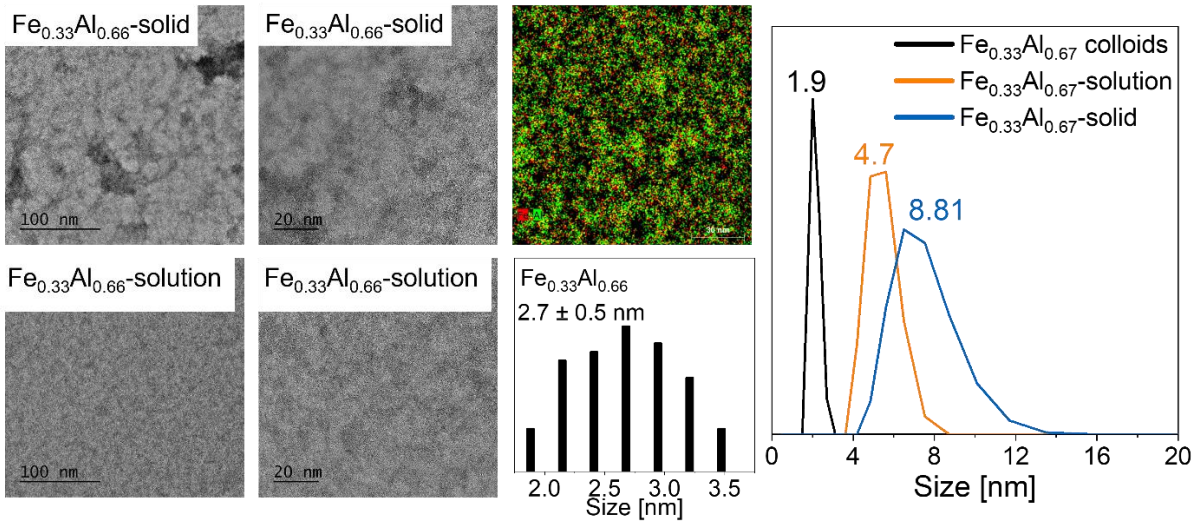

Figure 60. Left: HR-TEM images of $Fe_{0.33}Al_{0.67}$-solid (above) and $Fe_{0.33}Al_{0.67}$-solution (bottom) NPs. Particle size distribution was determined by analyzing the diameter of 100 particles. Elemental mapping shows a homogeneous distribution of both Fe and Al over the whole sample. Right: Comparison of DLS measurements of $Fe_{0.33}Al_{0.67}$-colloids, $Fe_{0.33}Al_{0.67}$-solution and $Fe_{0.33}Al_{0.67}$-solid. Please note that DLS analysis gives the hydrodynamic radius in solution, whereas HR-TEM images the radius of the metal NP.

In order to investigate the intermetallic nature of the $Fe_{1-x}Al_x$ materials, PXRD measurements of all $Fe_{1-x}Al_x$-solid samples were performed. A strong influence of the Fe/Al ratio on the material structure was observed (see Figure 61). Starting with $Fe_{1.0}Al_{0.0}$ powder, obtained by

the reaction of [Fe_2(mesityl)$_4$] with H_2, gives the diffraction pattern of the bcc-α-Fe structure. Comparison of this material with commercially available Fe powder shows broad reflections indicating a decreased crystallinity of the sample. Addition of the Al precursor results in a further decrease of the crystallite size, which appear to be "solutions" of Al in the Fe lattice rather than a distinct intermetallic Fe-Al phase, since the Fe(100) reflection of bcc-α-Fe is visible in all $Fe_{1-x}Al_x$ powders, yet slightly shifted according to the incorporation of Al atoms in the bcc-α-Fe lattice.[100,101,169] The increasing lattice strain by the incorporation of Al into the Fe lattice and the different atomic radii of Al and Fe result in increasing lattice parameters and hence to greater Fe-Fe interatomic distances.[101,104,169] This trend is observed for Fe/Al ratios with $x \leq 0.25$. With higher Al amounts ($x \geq 0.5$), broad reflections are detected, suggesting the literature-known amorphization of the respective materials by alloying of bcc-α-Fe with high amounts of Al. Concluding, the structure of the herein obtained materials can be described as a solution of Al in the bcc-α-Fe structure. Interestingly, despite targeting the formation of Fe_3Al, FeAl and $FeAl_2$ Hume-Rothery phases by the application of the respective Fe/Al ratios, no reflexes of these intermetallic phases for all $Fe_{1-x}Al_x$ powders could be detected. This suggests that the herein applied synthesis conditions facilitate rather a dilution of the bcc-α-Fe structure with Al instead of the formation of the respective intermetallic Fe/Al phase.

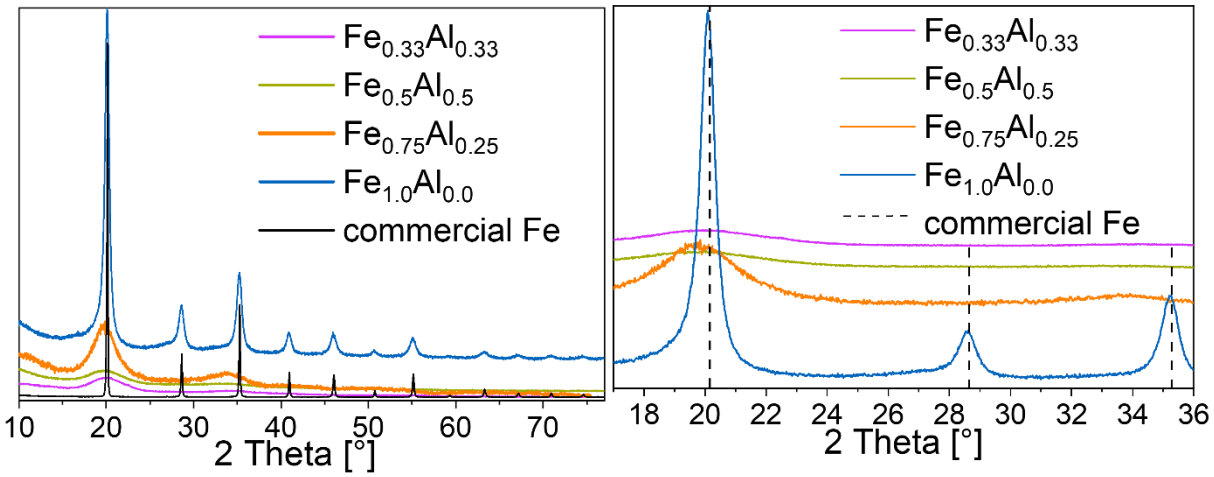

Figure 61. PXRD diffraction patterns of solid $Fe_{1-x}Al_x$ powders and commercial Fe as reference (left side: full pattern, right side: zoom-in to lower angles).

Further analysis by means of XPS measurements of $Fe_{1.0}Al_{0.0}$, $Fe_{0.5}Al_{0.5}$ and $Fe_{0.33}Al_{0.67}$ powders revealed both metals in the oxidated state (see Figure 62), similar to the $Fe_{1-x}Al_x$ colloidal solutions. In general, it can be assumed that the differences between the nano-sized colloidal $Fe_{1-x}Al_x$ and the $Fe_{1-x}Al_x$ powders can be regarded as rather weak. The only difference is the organic shell around the material (which is directly related to the C 1s signal), as with increasing H_2 pressure, hydrogenation of the coordinating ligands leads to a decreased

coordination to the surface (and hence a reduced intensity of the C 1s signal compared to the $Fe_{1-x}Al_x$ colloidal NPs). The oxidation states of the metals are assumed not to be fundamentally influenced by this process.

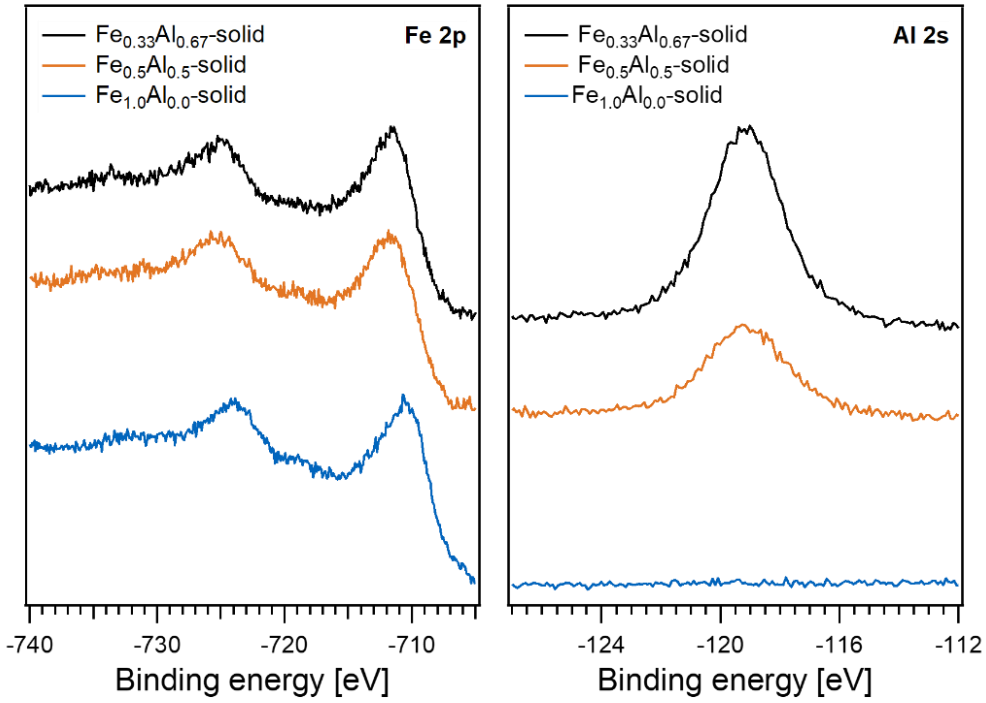

Figure 62. Fe 2p and Al 2s core level spectra of $Fe_{0.33}Al_{0.67}$ (black), $Fe_{0.5}Al_{0.5}$ (orange) and $Fe_{1.0}Al_{0.0}$ (blue) powders showing Fe and Al in the oxidized states Fe(III) and Al(III). The intensity of the Al 2s spectra is scaled to the respective Fe 2p intensity. Note that the Al 2s/Fe 2p intensity ratio reflects well the stoichiometry of the $Fe_{1-x}Al_x$-solid materials.

Correlation between $Fe_{1-x}Al_x$ particle sizes, precipitation to powders and the stabilizing organic shell

ICP-OES and XPS measurements both suggest a decreased number of organic residues for the precipitated $Fe_{1-x}Al_x$ powders compared to the colloidal solutions. Hence, the correlation between particle precipitation and a decreased organic shell stabilizing the material in solution is apparent. Additionally, this stabilizing shell is also related to the Fe/Al ratio, as a higher Al amount results in a better stabilization and hence solubility and smaller NP sizes of the resulting $Fe_{1-x}Al_x$ materials. This hypothesis applies for both the $Fe_{1-x}Al_x$ colloids and the powders demonstrating that with an increasing Al amount, $Fe_{1-x}Al_x$ NPs can be principally hold in solution. The formation of an organic shell can be regarded as crucial factor for a particle stabilization in solution (see Scheme 23). The treatment of the colloidal $Fe_{1-x}Al_x$ solutions with

H_2 pressure and high temperatures results in a decreased stabilizing organic shell and hence in a particle agglomeration and precipitation.

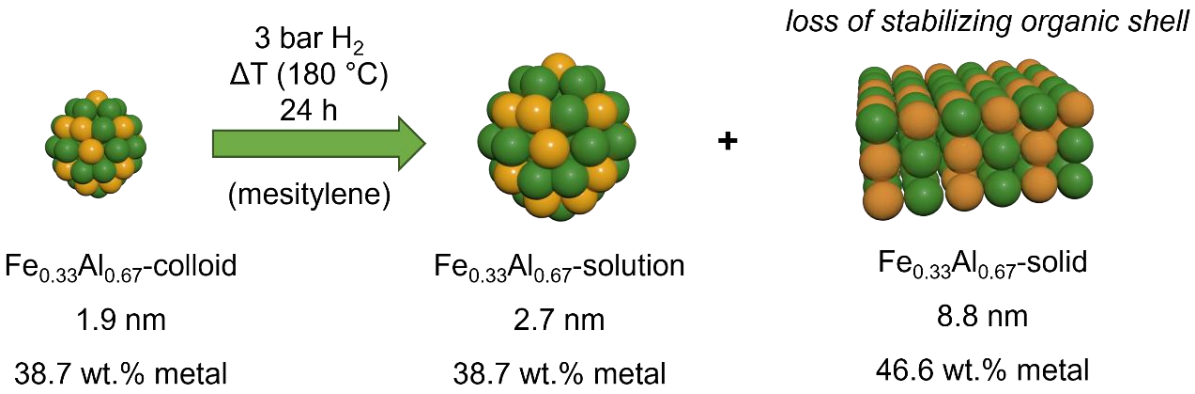

Scheme 23. Agglomeration of $Fe_{1-x}Al_x$ colloidal NPs upon heating resulting in larger colloids and a precipitate.

In order to support the herein stated hypothesis of stabilizing Al-alkyls and/or an organic shell dependent on the Fe/Al ratio, IR spectra of all $Fe_{1-x}Al_x$ powders were measured. For all samples, signals in the region from 500 cm^{-1} und 1500 cm^{-1} were detected indicating organic species on the surface of the materials (see Figure 63).

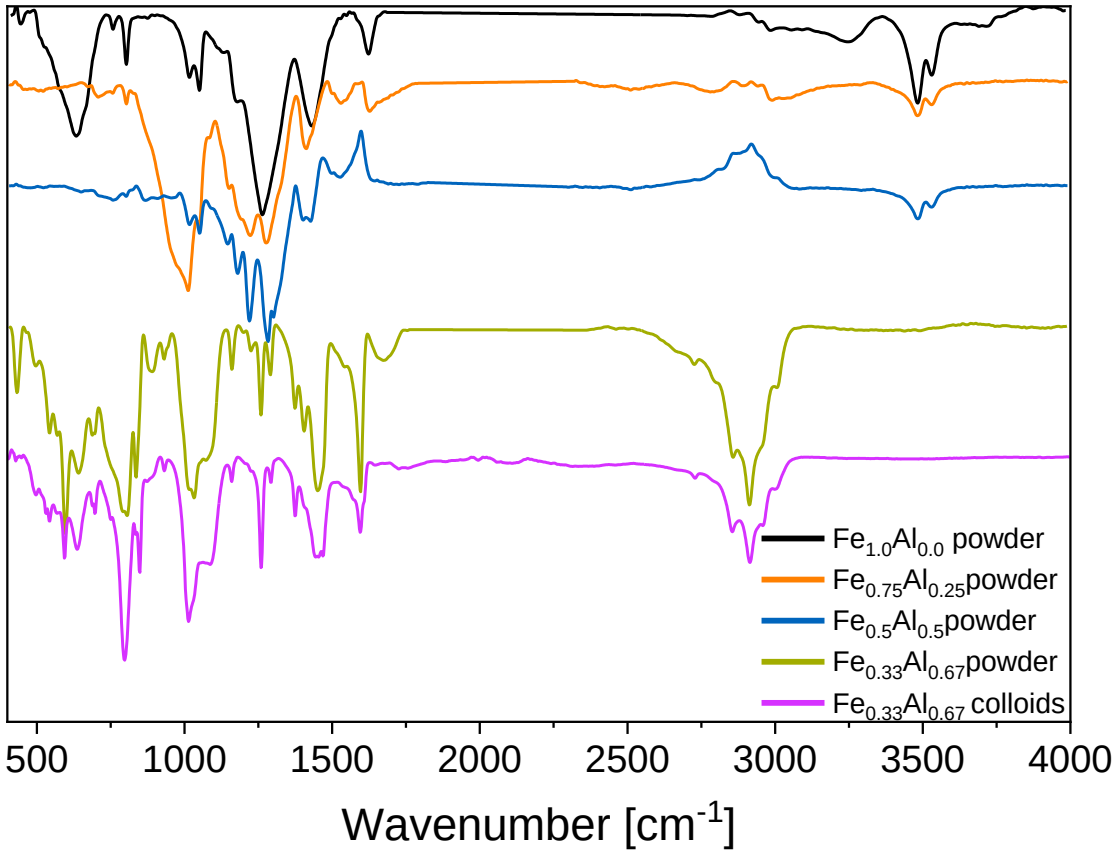

Figure 63. ATR-FT-IR spectrum of $Fe_{1-x}Al_x$ powder samples and $Fe_{0.33}Al_{0.66}$ colloids as comparison showing similar vibrations of the sample $Fe_{0.33}Al_{0.67}$ compared to the colloids.

For the Fe pure sample $Fe_{1.0}Al_{0.0}$, only C-C and C-H vibrations were detected. In detail, a broad signal at 519-712 cm^{-1} indicates symmetric, antisymmetric and out of plane C-H deformation vibrations from an aromatic species, in combination with ring vibrations at 1017 and 1050 cm^{-1}. Additionally, the strong signal at 1250 cm^{-1} can be assigned to a C-H in plane deformation, whereas the signal at 1437 cm^{-1} belongs to C-C ring stretching and CH_3 antisymmetric deformation vibrations. The signals around 3500 cm^{-1} indicate the presence of O-H bonds, which goes in line with the XPS results of an oxidized surface of the materials. As this signal decreases with increasing Al content, the assumption of a protecting effect of the Al against oxidation by EPR measurements of the $Fe_{1-x}Al_x$ colloids is supported. For the $Fe_{0.5}Al_{0.5}$ powder, an additional broad signal from M-H and $\delta(CH_3)$ signals at 867-1987 cm^{-1} were detected, whereas the rest of the spectrum is similar to that of $Fe_{1.0}Al_{0.0}$. The Al-rich (and soluble) $Fe_{0.33}Al_{0.67}$ powder sample shows similar vibrational modes compared to those detected for the colloidal $Fe_{1-x}Al_x$ NPs (see Figure 63, bottom traces). This indicates intact Al-H and Al-alkyl species on the surface of the material (for details, see chapter "*Investigation on the stabilization of $Fe_{1-x}Al_x$ colloids*"). These findings go in line with the observations for the $Fe_{1-x}Al_x$ colloidal solutions and further support the assumption of Al-alkyls and/or an organic shell (e.g. consisting of weakly coordinating organic species such as1-ethyl-3,5-dimethylbenzene) as decisive factor for a particle stabilization in solution.

Thermogravimetric (TGA) MS analysis of the powder $Fe_{0.5}Al_{0.5}$ sample was performed to detect volatile (organic) compounds on the surface of the bimetallic powder (see Figure 64).

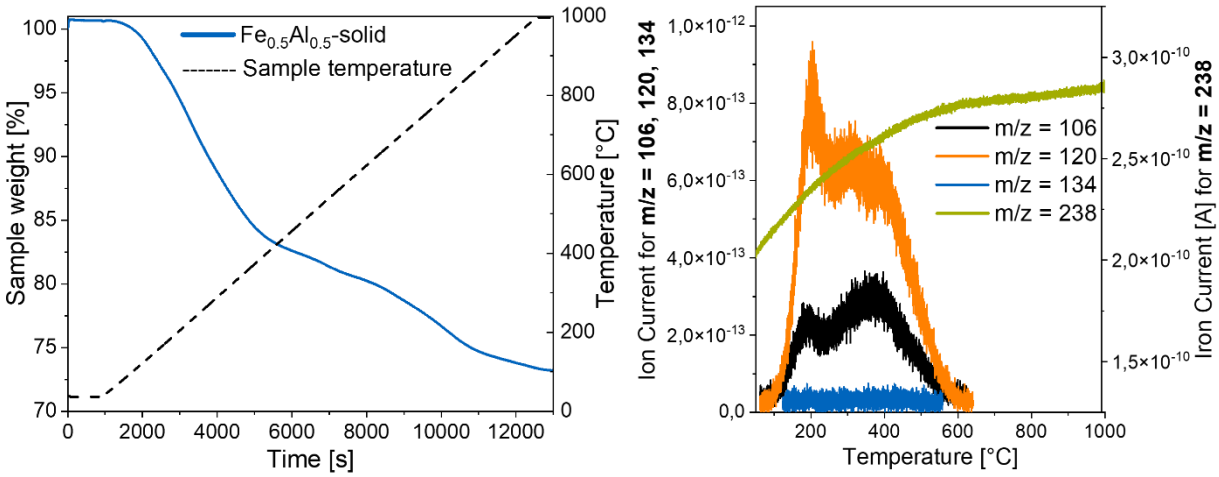

Figure 64. TGA-MS measurement of $Fe_{0.5}Al_{0.5}$ powder with the detected masses m/z = 106 (ethylbenzene), 120 (mesitylene), 134 (1-ethyl-3,5-dimethylbenzene) 238 (bis-(dimethylphenyl)-ethane).

The sample was heated to 1000 °C under an inert atmosphere revealed a weight loss of 25 %, suggesting volatile (residual) organic compounds on the surface of the alloy powder. Comparison with the ICP-OES measurement (only showing a metal content of 49 %) suggests

additional non-volatile carbon deposits or a carbon incorporation into the bulk material. With a coupled mass spectrometer, the masses of mesitylene, ethylbenzene, 1-ethyl-3,5-dimethylbenzene and bis-(dimethylphenyl) were detected during heating the sample to 1000 °C (see Figure 64).

Concluding from these observations, it can be stated that all $Fe_{1-x}Al_x$ powder materials comprise organic/C_xH_y residues on the surface or incorporated into the bulk, whereas the amount of such species is increased with higher Al amounts.

Magnetic Properties of $Fe_{1-x}Al_x$ powders

Apart from the investigation of the $Fe_{1-x}Al_x$ powder surface, also an analysis of the metallic bulk is interesting, as this can help better understand the interaction of both metals and hence the structure of the powder materials. As already shown by PXRD measurements, the structure of the $Fe_{1-x}Al_x$ powders can be regarded as a dilution of the bcc-α-Fe structure with Al. Superconducting Quantum Interference Device (SQUID) measurements can help to gain a deeper insight of the microscopic structure and the nearest neighbors of the Fe atoms in the material (see Figure 65). In principle, with increasing direct Fe-Fe interactions, the material shows an increased magnetism. Therefore, the magnetism should be directly dependent on the Fe/Al ratio, as dilution of Fe with Al results in a decreased number of direct Fe-Fe interactions. In fact, the magnetic measurements of all $Fe_{1-x}Al_x$ samples show differences in the magnetic behavior strongly dependent on the Fe/Al ratio. As reference, also commercially available Fe powder was measured (see Table 22 and Figure 65).

Table 22. Coercivity H_c, remanence R and saturation magnetism M_s values of all measured $Fe_{1-x}Al_x$ powders.

Sample	H_C [Oe]	R [emu/g]	M_S [emu/g]
Fe commercial	2.6	0.2	198
$Fe_{1.0}Al_{0.0}$ powder	53.3	4.1	109
$Fe_{0.75}Al_{0.25}$ powder	11.1	0.04	-
$Fe_{0.7}Al_{0.5}$ powder	11.	0.01	-
$Fe_{0.33}Al_{0.67}$ powder	8.23	0.003	-

Two different measurements were done for each sample. First, measurements of the material magnetism M_g at a constant external field (1000 Oe) with variation of the temperature from 4-300 K were carried out. Second, the material magnetism M_g at a constant sample temperature of 300 K with variation of the external magnetic field from -50000 Oe to 50000 Oe was measured giving the materials` hysteresis loops. For all samples, no diamagnetic

character was observed, as with variation of the temperature and a static external magnetic field of 1000 Oe, the measured magnetic susceptibility *X* is always higher than 0.

The Al-free $Fe_{1.0}Al_{0.0}$ powder shows a ferromagnetic behavior with a magnetic saturation at 109 emu/g, but with a decreased ferromagnetism compared to the reference ($M_s(Fe_{commercial})$ = 198 emu/g). This can be attributed to carbonaceous species incorporated into the material, which matches the ICP-OES analysis with only 68 wt.% Fe. The $Fe_{1.0}Al_{0.0}$ powder shows an increased coercivity H_c and magnetic remanence *R* compared to the commercial Fe powder, suggesting that this material retains a certain magnetism when no external field is applied. Comparison of the $Fe_{1-x}Al_x$ powders shows that the ferromagnetic character decreases with increasing Al amount. This is in good accordance with literature-reported SQUID analysis of Fe/Al bimetallic materials.[104,169,170] This effect can be explained by a decreased number of nearest neighbor Fe-Fe ferromagnetic exchange by the introduction of Al into the bcc-α-Fe structure. With an increasing Al amount, Fe-Al coordination sites increase with a simultaneous decreasing of Fe-Fe direct interactions. Hence, the ferromagnetic coupling between Fe atoms is weakened as a result of the reduction of the coordination number and an increase in inter-atomic distances between two Fe atoms. These findings go in line with the obtained PXRD data, as the direct ferromagnetic interaction between two Fe sites is reduced by the introduction of Al in the Fe(bcc) lattice. Hence, for $x \geq 0.25$, no saturation magnetism M_s is observed, reflecting the gradual development of an alloying process of Fe with Al.

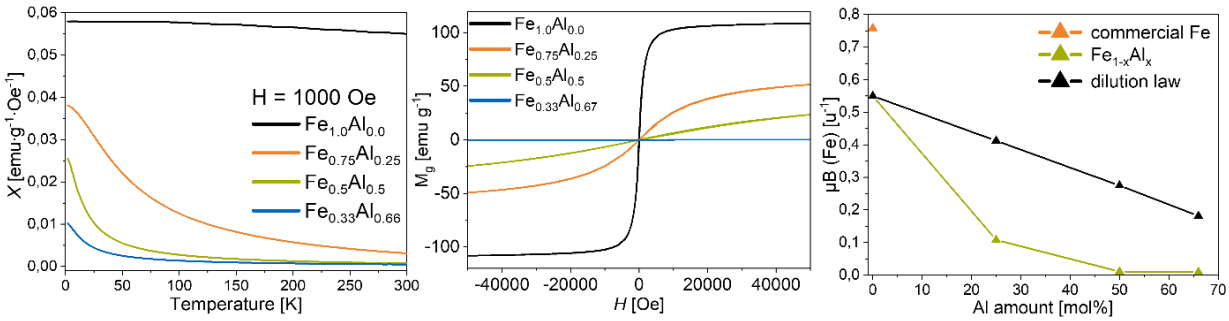

Figure 65. SQUID measurements of $Fe_{1-x}Al_x$ powders. Left: Temperature variation with a static external field of 1000 Oe. Middle: Resulting hysteresis by variation of the external magnetic field. Right: $\mu_{eff}(Fe)$ for all tested samples (300 K, 10000 Oe) with commercial Fe as comparison and the calculated $\mu_{eff}(Fe)$ values for all $Fe_{1-x}Al_x$ assuming a simple dilution of Fe with Al.

The effective Bohr magneton $\mu_{eff}(Fe)$ for all tested samples was calculated, as this value is an indication for the number of unpaired electrons (and therefore also for the paramagnetic nature) of the material. Hence, with higher $\mu_{eff}(Fe)$ values, a higher amount of unpaired electrons can be assumed. This, in turn, is an indication of the sum of oxidized Fe species, as separated Fe(0) centers exhibit a diamagnetic character. It has to be noted that the

interpretation of the herein calculated μ_{eff}(Fe) values is only of qualitative and not quantitative character, as the molecular weight of the samples is only estimated from elemental analysis. Not surprisingly, a decrease of the Bohr magneton with higher Al amounts is observed (see Figure 65, right). Nevertheless, according to a simple dilution of the magnetic Fe with Al[169], the decrease of μ_{eff}(Fe) should be consistent with the amount of Al ("simple dilution law", see Figure 65, right, black trace). In the case of the herein investigated $Fe_{1-x}Al_x$ materials, instead, a stronger decrease of μ_{eff}(Fe) than calculated for a simple dilution is observed. This indicates, in well accordance with the EPR data of the $Fe_{1-x}Al_x$ colloidal solutions, that the alloying with Al protects the Fe from oxidation as the amount of paramagnetic oxidized Fe species decreases with higher Al amounts.

Summarizing, the herein obtained information demonstrates that by alloying of Al, the Fe sites are diluted and protected from oxidation. Both of these findings make the herein investigated $Fe_{1-x}Al_x$ powders principally interesting candidates for catalytic applications.

Hydrogen adsorption capacity of $Fe_{1-x}Al_x$ powders

In order to get a first idea of the potential of the herein investigated $Fe_{1-x}Al_x$ powders as semi-hydrogenation catalysts, the ability for the adsorption of hydrogen was investigated by temperature-programmed desorption (TPD) experiments. All experiments were performed in a flow reactor equipped with a mass analyzer under inert conditions in order to examine the desorption of H_2 depending on the Fe/Al ratio (see Figure 66).

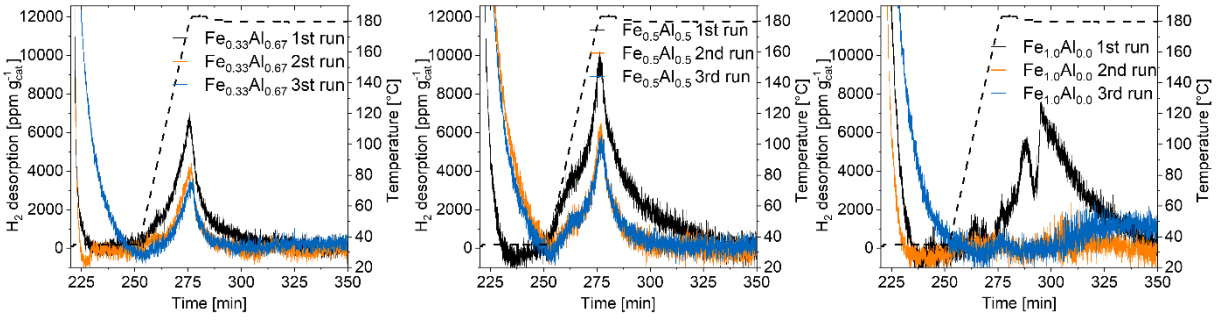

Figure 66. TPD desorption profiles of $Fe_{0.33}Al_{0.67}$ (left), $Fe_{0.5}Al_{0.5}$ (middle) and $Fe_{1.0}Al_{0.0}$ (right) powders at 180 °C for three runs. After each run, the sample was pressurized with 3 bar H_2 at 180 °C for 1 h.

Here, the solid materials were first pressurized with 3 bar H_2 at 180 °C for 1 h (similar to the synthesis conditions), cooled down to room temperature under Argon and finally heated up again to 180 °C with a heating rate of 6 °C per minute to measure the desorbed H_2. This procedure was repeated for three times. Afterwards, the powders were again pressurized with 3 bar H_2 at 180 °C for 1 h but then heated up to 300 °C and 480 °C for H_2 desorption. For all

tested powders, the m/z values for H_2O were detected during the heating step under H_2 pressure (see SI, Figures 142-144). The origin of H_2O might be assigned to an in-situ reduction of partially oxidized $Fe_{1-x}Al_x$ powders. Additionally, signals originating from mesitylene were detected for the Al-containing $Fe_{0.5}Al_{0.5}$ powder and $Fe_{0.33}Al_{0.67}$ powder, supporting the idea of adsorbed mesitylene on the Al metal surface. In contrast, the Fe-pure sample $Fe_{1.0}Al_{0.0}$ powder did not show any adsorbed mesitylene species. These findings support a stabilization by organic aromatic molecules like mesitylene or the above discussed 1-ethyl-3,5-dimethylbenzene and bis-(dimethylphenyl)ethane depended on the Fe/Al ratio, which is in good agreement with the observed particle sizes by DLS. The H_2 desorption of $Fe_{1-x}Al_x$ powders at 180 °C shows clear differences depending on the Fe/Al ratio (see Figure 66).

With increasing Al amount, the desorption of hydrogen sets on at lower temperature. This suggests the presence of weaker adsorbed H species compared to the iron-rich materials, which might also have a positive influence of the catalytic activity. For the following discussion, it has to be distinguished between hydrogen species originating from the synthesis procedure and hydrogen coming from the reducing steps in the flow reactor (3 bar H_2, 180 °C, 1 h). For all samples, the total amount of desorbed H_2 decreased for the second and third run compared to the first H_2 desorption step, indicating that a certain amount of hydrogen is incorporated into the (bulk) material during synthesis, of which desorption is irreversible. The amount of desorbed hydrogen for the second and third run is similar, showing that these materials can reversibly take up a certain amount of H_2 for the Al containing samples $Fe_{0.5}Al_{0.5}$ and $Fe_{0.33}Al_{0.67}$. For the monometallic $Fe_{1.0}Al_{0.0}$, no H_2 desorption signal is obtained for the second and third desorption run, indicating that the Al does affect the electronic characteristics of the material allowing for a reversible H_2 up take under the chosen conditions. For a better understanding of the origin of the desorbed hydrogen (incorporated into the bulk vs. adsorbed at the surface), the BET surface area of all $Fe_{1-x}Al_x$ powders was calculated from N_2 sorption experiments and compared to the calculated TPD surface area (see Table 23). Note that this comparison is only an estimation. Any determined accessible surface is limited by the diameter of the adsorptive used for probing, results from H_2 and N_2 sorption are expected to differ (H_2: 2.89 Å, N_2: 3.64 Å).[171a] Hence, the adsorption of H_2 and N_2 (and therefore TPD and BET measurement) cannot directly be compared with each other. H_2 with a smaller kinetic diameter can more easily be adsorbed, resulting in a generally higher effective surface area of the material.

With higher Al amounts, the BET as well as the TPD surface area increases, which is in well accordance with the SEM images (see SI, Figure 139). As consequence, materials with a higher Fe/Al ratio show a decreased amount of adsorbed H_2, consistent with the decreased

BET surface area. Nevertheless, it can be assumed that the hydrogen is exclusively adsorbed on the Fe and not on the Al.[171b] If the surface area calculated from H_2 desorption experiments (obtained from TPD measurements) is much higher than the one calculated from N_2 sorption experiments, it can be concluded that the material is able to not only adsorb hydrogen at the surface but also can incorporate it into the bulk system. It must be noted that the Al-rich sample $Fe_{0.33}Al_{0.67}$ shows a strongly decreased N_2 uptake, which indicates either loss of porosity or decrease of pore diameter below a for nitrogen accessible size. For all three desorption steps at 180 °C, the TPD surface area is in the same range than that calculated from BET for all tested $Fe_{1-x}Al_x$ samples. These findings point to the detection of mainly adsorbed hydrogen species rather than bulk-incorporated ones.

Table 23. Comparison of BET and calculated TPD surface area of $Fe_{1-x}Al_x$ powders. Note that for BET measurements, the $Fe_{0.33}Al_{0.67}$ powder should be compared to the other materials only on a qualitative basis. Its pore properties lead to partial He adsorption and trapping during the automated pre-measurement free space determination. The normally non-adsorbing He could not be desorbed consistently and sufficiently afterwards. Therefore, a BET surface area could not be fitted in a meaningful way and is not given.

Entry	$Fe_{1-x}Al_x$ powders	Temperature [°C]	Run	n(H_2) [µmol/g]	BET surface [m^2/g]	TPD surface [m^2/g]
1			1	480		34
2		180	2	206		15
3	$Fe_{0.33}Al_{0.67}$		3	158	54.9 ± 0.4	11
4		300	-	2092		148
5		480	-	5771		409
6			1	1009		71
7		180	2	353		25
8	$Fe_{0.5}Al_{0.5}$		3	354	145 ± 1.0	25
9		300	-	1827		129
10		480	-	1415		100
11			1	975		69
12		180	2	0		0
13	$Fe_{1.0}Al_{0.0}$		3	0	28.7 ± 0.3	0
14		300	-	606		43
15		480	-	2793		198

Apart from the desorption experiments at 180 °C, also higher temperatures of 300 °C and 480 °C were tested. It must be noted that at such high temperatures the structure of the material changes according to PXRD measurements. Interestingly, for all $Fe_{1-x}Al_x$ powders, a high amount of H_2 was detected for both temperatures (see Figure 67). This TPD signal could

not be recorded again after an additional activation step (3 bar H_2, 180 °C, 1 h, see Figure 67 right, green trace), indicating that the herein detected H_2 originates from the synthesis procedure, probably incorporated into the bulk material, and can only irreversibly desorbed. This is also reflected in the calculated TPD surface areas (at 300 °C and 480 °C), compared to the BET surface areas for all tested $Fe_{1-x}Al_x$ powders (see Table 23). The amount of hydrogen desorption at elevated temperatures (300 °C and 480°C) is significantly higher than what could reasonably be expected of the material when compared to its via nitrogen physisorption determined BET surface areas. This could be correlated to hydrogen strongly adsorbed and/or covalently bound to external surface or some for nitrogen inaccessible - and therefore in the BET surface area determination not quantifiable - internal surface area. This area might be accessible only during synthesis or at higher temperatures, leading to the observed hydrogen release at 300-480 °C in the TPD experiments.

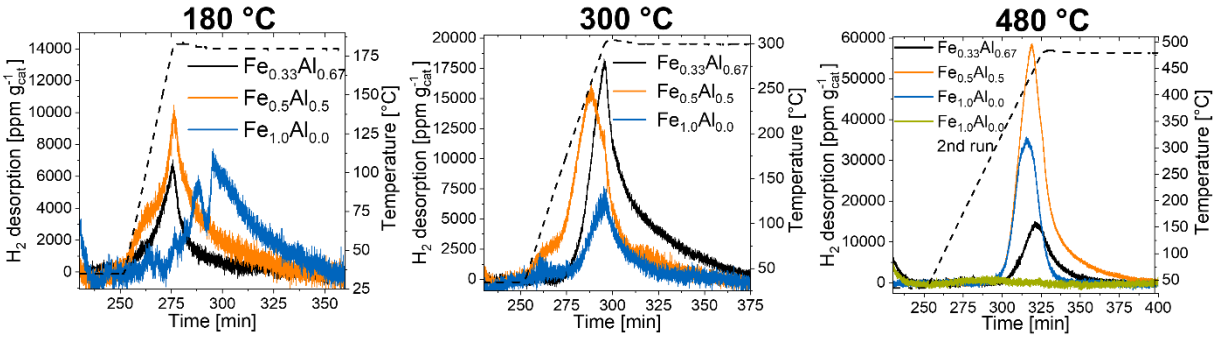

Figure 67. TPD desorption profiles of $Fe_{1-x}Al_x$ powders at 180 °C (left), 300 °C (middle) and 480 °C (right) at different temperatures.

In comparison to $Fe_{1.0}Al_{0.0}$ and $Fe_{0.5}Al_{0.5}$ powders, the Al-rich $Fe_{0.33}Al_{0.67}$ shows the highest amount of desorbed H_2 at 480 °C, thus suggesting that with higher Al amounts, higher temperatures are required to fully desorb the H_2 originating from the synthesis procedure. After heating the material to 480 °C and a following activation step at 180 °C, no additional H_2 desorption signal can be monitored (see Figure 66, blue trace). This does not only support the idea of the incorporation of hydrogen during the synthesis (which afterwards is desorbed irreversibly), but also indicates a structure change of the bimetallic powder at such high temperatures (e. g. due the formation of Fe/Al intermetallic phases).

Summarizing, it can be concluded that all $Fe_{1-x}Al_x$ powders incorporate hydrogen during the material synthesis, whereas the Al-containing samples are additionally able to reversibly ad- and desorb hydrogen under H_2 pressure at elevated temperatures (180 °C). These features highlight the potential of the $Fe_{1-x}Al_x$ powders as interesting materials for a systematic investigation in the semi-hydrogenation of alkynes. Here, a comparison between the powder materials could confirm the observed trends depending on the metal ratios for the activity and

selectivity already discussed for the $Fe_{1-x}Al_x$ colloids. Additionally, comparison of the powder samples with the colloids could give rise to the influence of the particle size and the stabilizing hydrocarbon shell on the catalytic performance.

Nevertheless, extending the portfolio of $Fe_{1-x}Al_x$ materials by the targeted synthesis of the respective intermetallic Hume-Rothery phases would allow for a direct comparison of the amorphous $Fe_{1-x}Al_x$ powders with the respective intermetallics. As already indicated by TPD measurements at 300 °C and 480 °C, a structure change of the material might indicate the formation of such intermetallic phases. Therefore, the synthesis of the intermetallic phases Fe_3Al, FeAl and $FeAl_2$ by a simple heating (annealing) of the $Fe_{0.75}Al_{0.25}$, $Fe_{0.5}A_{0.5}$ and $Fe_{0.33}Al_{0.67}$ powder samples will be discussed in the following section of this thesis.

Annealing of $Fe_{1-x}Al_x$ heterogeneous materials

Inspired by the literature-known Hume-Rothery phases Fe_3Al, FeAl and $FeAl_2$, annealing of the $Fe_{0.75}Al_{0.25}$, $Fe_{0.5}Al_{0.5}$ and $Fe_{0.33}Al_{0.67}$ powders with the same Fe/Al ratios as the respective intermetallic phases was attempted at various temperatures to obtain the specific phases. TPD experiments at high temperatures (300 °C and 480 °C) showed a first indication for a structure change of the $Fe_{1-x}Al_x$ materials, as a loss of a H_2 adsorption ability was observed. Exemplarily for all three tested samples, annealing experiments for $Fe_{0.5}Al_{0.5}$ will be discussed in the following. The obtained data for the other Fe/Al ratios can be found in the appendix.

Crystallinity and crystallite sizes of annealed $Fe_{1-x}Al_x$ powders

Heating of $Fe_{0.5}Al_{0.5}$ powder at 300 °C for 24 h under reduced (Argon) pressure in quartz ampules leads to no visible changes in the PXRD pattern (see Figure 68). The reduced pressure was necessary due to volatile organic compounds on the surface of the $Fe_{1-x}Al_x$ powders. Increasing the annealing temperature to 500 °C results in the detection of two broad reflexes at 11.7° and 20.1°, which might indicate the formation of the Fe_3Al phase. This shows that applying a certain Fe/Al ratio does not directly lead to the respective intermetallic phase. By a further increase of the temperature to 800 °C, a variety of different Fe/Al phases is formed as a result of the complex equilibrium phase diagram of Fe/Al bimetallic materials.

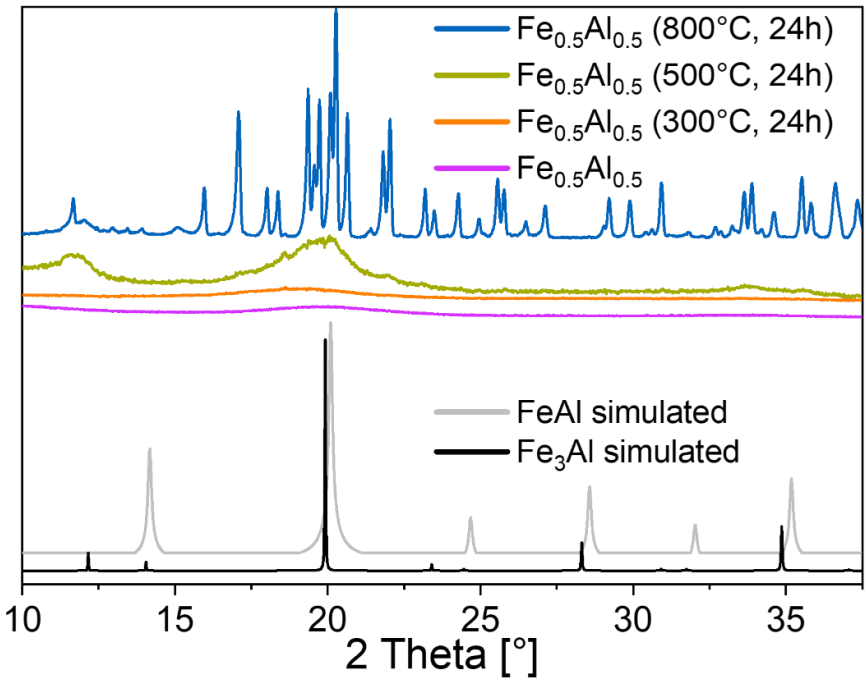

Figure 68. PXRD patters of $Fe_{0.5}Al_{0.5}$ powder before and after annealing at different temperatures and the simulated intermetallic phases FeAl and Fe_3Al as references.

The annealed samples were further analyzed by SEM measurements to see macroscopic changes upon heating (see Figure 69).

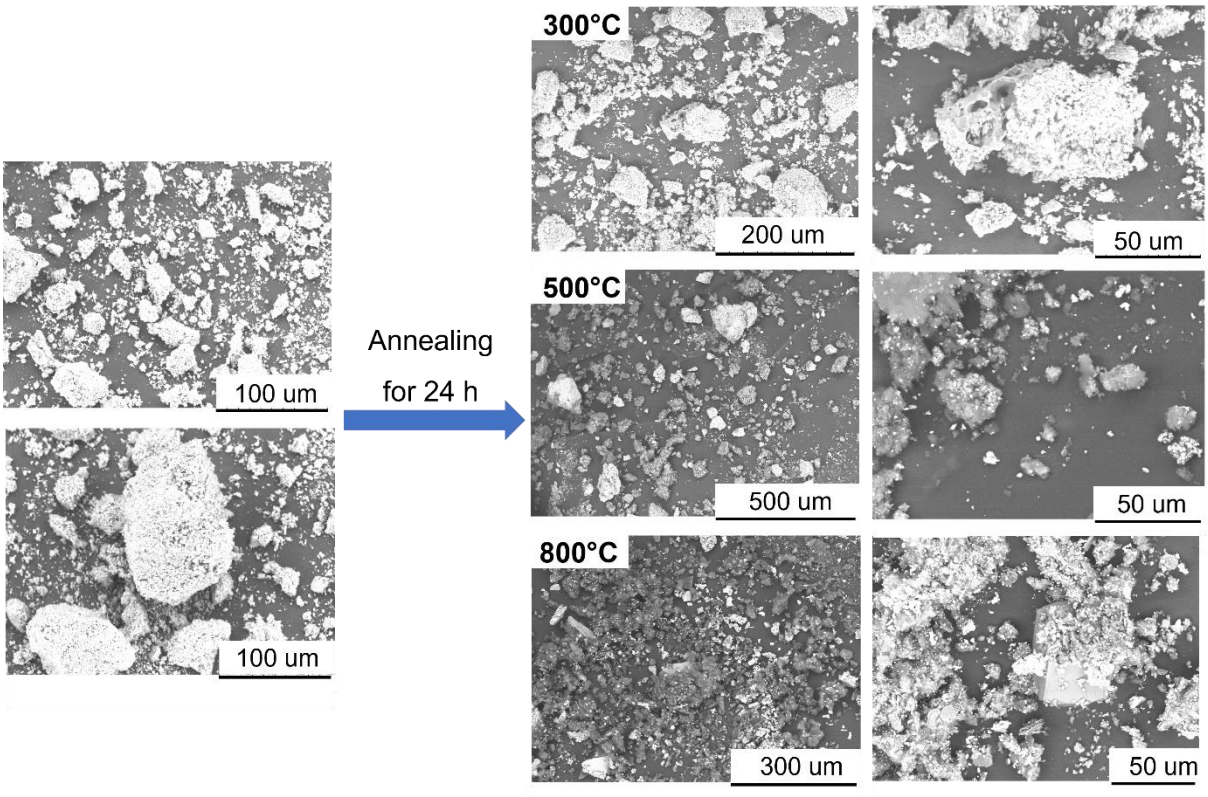

Figure 69. SEM pictures of $Fe_{0.5}Al_{0.5}$ powder before and after annealing at different temperatures with different magnification showing various crystallite sizes and surface morphologies.

The sample with a Fe/Al ratio of 1:1, $Fe_{0.5}Al_{0.5}$, will be discussed in detail. In the as-synthesized material, a structure with a homogeneous Fe/Al distribution was observed. After 24 h at 300 °C, no major differences by comparison of the SEM images could be identified. Increase of the heating temperature to 500 °C clearly shows that the sample homogeneity is decreased, indicated by darker and brighter parts. This might be attributed to the formation of Fe/Al intermetallic phases. Annealing of $Fe_{0.5}Al_{0.5}$ at 800 °C for 24 h shows the same trend, as here mainly darker sample areas were detected. Increasing the magnification further shows a partly highly crystalline material with corners and edges. This macroscopically visible crystallinity goes in line with the respective PXRD pattern.

Magnetic properties of annealed $Fe_{1-x}Al_x$ powders

SQUID measurements as indicator for Fe-Fe nearest neighbor interaction were performed. Here, the $Fe_{0.5}Al_{0.5}$ powder annealed at different temperatures reveal different magnetic characteristics (see Table 24 and Figure 70).

Table 24. Coercivity H_c, remanence R and saturation magnetism M_s values of all measured $Fe_{0.5}Al_{0.5}$ annealed at different temperatures.

Sample	H_C [Oe]	R [emu/g]	M_S [emu/g]
$Fe_{0.5}Al_{0.5}$	17.06	0.001	-
$Fe_{0.5}Al_{0.5}$-300°C	3.00	0.002	-
$Fe_{0.5}Al_{0.5}$-500°C	7.67	0.038	-
$Fe_{0.5}Al_{0.5}$-800°C	27.89	0.337	48.43

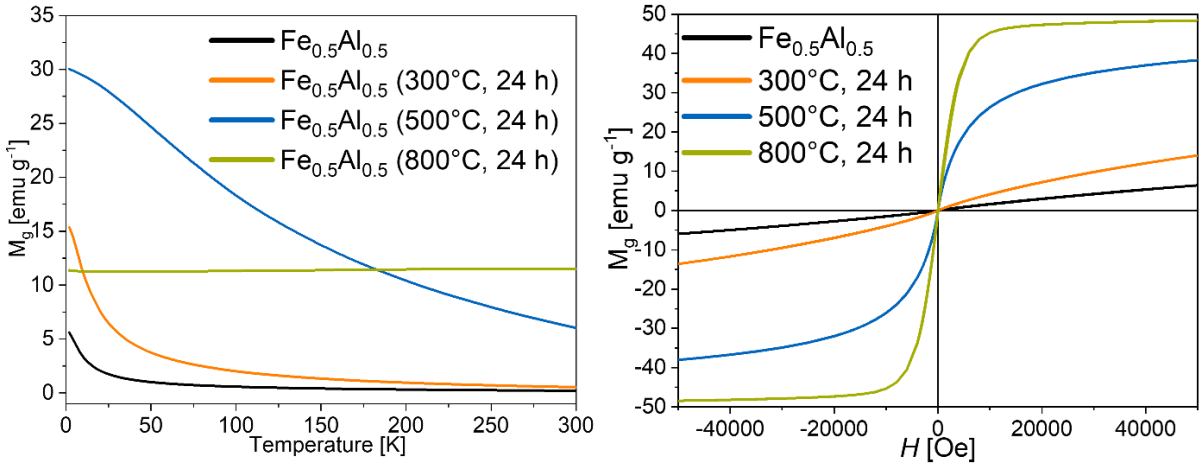

Figure 70. SQUID measurements of $Fe_{0.5}Al_{0.5}$ powders (as-synthesized and annealed at different temperatures). Above, left: Temperature variation with a static external field of 1000 Oe. Right: Resulting hysteresis by variation of the external magnetic field showing a strong increase in the magnetism with increasing annealing temperature.

With increasing annealing temperature, the ferromagnetic character of the $Fe_{0.5}Al_{0.5}$ powder increases. The formation of areas with a higher crystallinity with increasing temperature suggests an increased inhomogeneity of the samples (as indicated by SEM images). The emerge of (mixed) Fe/Al intermetallic phases, as already monitored by PXRD, results in an increased number of Fe-Fe nearest neighbors and a partial separation of Fe and Al. While the amorphous $Fe_{0.5}Al_{0.5}$ powder directly obtained from the synthesis shows a paramagnetic behavior, annealing at 800 °C leads to a ferromagnetic material with a magnetic saturation of M_s = 48.43 emu/g.

These results show that principally, crystalline intermetallic Fe/Al phases can be obtained by heating of the herein synthesized amorphous $Fe_{1-x}Al_x$ materials. Nevertheless, simple annealing at different temperatures does not lead to phase pure materials and the applied Fe/Al ratio does not exclusively lead to the respective bimetallic phase. Nevertheless, the herein annealed $Fe_{1-x}Al_x$ materials allow for a comparison of the catalytic performance with the amorphous $Fe_{1-x}Al_x$ powders and hence might help to understand the influence of the intermetallic character on the activity and selectivity in alkyne the semi-hydrogenation.

Catalytic performance of heterogeneous $Fe_{1-x}Al_x$ powders in the alkyne semi-hydrogenation

The $Fe_{1-x}Al_x$ powders (amorphous, without annealing) were tested in the semi-hydrogenation reaction of liquid alkynes (see Scheme 24). Notably, all materials with $x \leq 0.5$ were insoluble in the respective reaction solution, whereas the Al-rich $Fe_{0.33}Al_{0.66}$ could be completely dissolved in toluene. For all catalytic runs, the amount of catalyst was referred to Fe. The amount of Fe is constant for all $Fe_{1-x}Al_x$ (see the synthesis conditions of the $Fe_{1-x}Al_x$ powders; variation the Al amount).

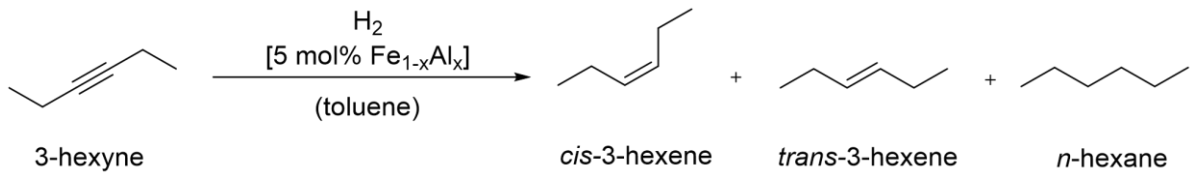

Scheme 24. Semi-hydrogenation catalysis using 5 mol% $Fe_{1-x}Al_x$ solid material as catalyst and 3-hexyne as model substrate.

Parameter optimization and comparison with $Fe_{1-x}Al_x$ colloids

Variation of the H_2 pressure and reaction temperature shows a direct influence on the catalyst activity for all $Fe_{1-x}Al_x$ powders. In detail, increasing both temperature from 25 °C to 100 °C and the H_2 pressure from 1 bar to 3 bar led to an enhanced activity.

In contrast, reaction of the substrate 3-hexyne upon addition of the $Fe_{1-x}Al_x$ powders at elevated temperatures without any additional H_2 pressure confirms the assumption of the incorporation of hydrogen of the $Fe_{1-x}Al_x$ materials during synthesis. Here, reactivity tests (without any H_2 pressure; Argon atmosphere) showed minor conversions of 3-hexyne (using 50 mol% catalyst at 100 °C for 24 h) for all tested $Fe_{1-x}Al_x$ materials. With increasing Al amount, the conversion strongly increased from 0.01 % for $Fe_{1.0}Al_{0.0}$ to 0.3 % for $Fe_{0.5}Al_{0.5}$ to 10 % for $Fe_{0.33}Al_{0.67}$. This shows the general ability of these solid materials to adsorb H_2 during the synthesis (as already suggested from TPD measurements), where the capacity of H_2 storage increases with diluting the material with Al.

Comparison of the solid $Fe_{1-x}Al_x$ materials with the above discussed colloidal $Fe_{1-x}Al_x$ NPs shows, unsurprisingly, a decreased activity of the heterogeneous approaches compared to the quasi-homogeneous catalytic tests is observed. Generally, the above discussed colloidal $Fe_{1-x}Al_x$ are already active at very mild conditions (1 bar H_2, 25 °C), while the $Fe_{1-x}Al_x$ powders require harsher conditions to show a good activity in the semi-hydrogenation reaction (see Table 25). This is not surprising as the colloidal NPs exhibit a higher surface area and are dissolved in the same phase as the substrate, whereas the agglomerated and precipitated $Fe_{1-x}Al_x$ materials are heterogeneous catalysts and hence not all active centers are equally accessible. A direct comparison of the materials with a Fe/Al ratio of 1:1, namely $Fe_{0.5}Al_{0.5}$ colloids and $Fe_{0.5}Al_{0.5}$ powder, clearly shows that the nano-sized colloids exhibit a higher catalytic activity under the same conditions. Applying 3 bar H_2 at 25 °C, 92 % of the substrate is converted after 24 h with colloidal catalyst (see Table 20, Entry 8), while for the heterogeneous catalyst, only 6 % of the alkyne is semi-hydrogenated (see Table 25, Entry 3). The activity of all tested $Fe_{1-x}Al_x$ powder catalysts is rather low at ambient temperatures with 3 bar H_2 (see Table 25, Entries 1-4). Nevertheless, even at higher temperatures and H_2 pressures, the selectivity towards the olefin is higher for the $Fe_{1-x}Al_x$ powder materials compared to the colloidal NPs. This might be attributed to the influence of the organic shell surrounding the $Fe_{1-x}Al_x$ colloids.

Table 25. Semi-hydrogenation experiments using 5 mol% $Fe_{1-x}Al_x$ powders (x = 0, 0.25, 0.5, and 0.67) after 24 h reaction time and 3-hexyne as substrate.

Entry	Reaction conditions	Catalyst	Conversion [%]	Selectivity [%]	*cis*/*trans* hexene
1	3 bar H_2, 25 °C	$Fe_{1.0}Al_{0.0}$	2	100	[a]
2	3 bar H_2, 25 °C	$Fe_{0.75}Al_{0.25}$	5	100	[a]
3	3 bar H_2, 25 °C	$Fe_{0.5}Al_{0.5}$	6	100	[a]
4	3 bar H_2, 25 °C	$Fe_{0.33}Al_{0.67}$	9	100	7.7/1
5	3 bar H_2, 50 °C	$Fe_{1.0}Al_{0.0}$	7	100	[a]
6	3 bar H_2, 50 °C	$Fe_{0.75}Al_{0.25}$	16	100	9/1
7	3 bar H_2, 50 °C	$Fe_{0.5}Al_{0.5}$	32	100	7/.7/1
8	3 bar H_2, 50 °C	$Fe_{0.33}Al_{0.67}$	45	100	4.8/1
9	3 bar H_2, 100 °C	$Fe_{1.0}Al_{0.0}$	78	100	[a]
10	3 bar H_2, 100 °C	$Fe_{0.75}Al_{0.25}$	98	100	[a]
11	3 bar H_2, 100 °C	$Fe_{0.5}Al_{0.5}$	100	96	6.3/1
12	3 bar H_2, 100 °C	$Fe_{0.33}Al_{0.67}$	100	92	3.6/1
13	1 bar H_2, 100 °C	$Fe_{1.0}Al_{0.0}$	18	100	[a]
14	1 bar H_2, 100 °C	$Fe_{0.75}Al_{0.25}$	40	100	[a]
15	1 bar H_2, 100 °C	$Fe_{0.5}Al_{0.5}$	50	100	12.5/1
16	1 bar H_2, 100 °C	$Fe_{0.33}Al_{0.67}$	67	100	3.8/1

[a] only formation of the *cis*-isomer

Influence of the Fe/Al ratio on the catalytic performance of $Fe_{1-x}Al_x$ powders

The $Fe_{1-x}Al_x$ powders (x = 0.5, 0.67) with a higher Al amount showed an increased activity compared to the Fe-rich materials. This can be explained by a smaller particle size with increasing Al amount. Additionally, the adsorption strength of the substrate is connected with the alloying of the active Fe sites with Al. Hence, the Fe-pure catalyst $Fe_{1.0}Al_{0.0}$ might exhibit a rather strong interaction of the alkyne with the catalyst surface, resulting in a blocking of the active sites by the substrate and hence a lower activity. Such an effect was already reported for Pd_1 and Pd_3 active sites in PdGa.[66]

Increasing the temperature to 50 °C shows an increased activity for all catalysts, but no full substrate conversion is observed after 24 h reaction time. Hence, catalyst runs at 3 bar H_2 and 100 °C result in an activity boost showing full conversion for $x \geq 0.25$. Only the Fe-pure sample $Fe_{1.0}Al_{0.0}$ does not show full conversion (78 %) under these conditions. The influence of the hydrogen pressure was tested applying 1 bar H_2 at 100 °C. Here, a strongly decreased catalyst activity is observed suggesting a strong dependence of the substrate conversion on

the H_2 pressure. Commercial Fe powder, as reference, did not show any activity under all tested reaction conditions. The selectivity towards the alkene is almost 100 % for all tested $Fe_{1-x}Al_x$. Nevertheless, with higher Al amounts (and hence higher activities), the selectivity slightly decreased to 96 % (x = 0.5) and 92 % (x = 0.67). The solubility and hence the existence of organic molecules coordinating to the particle surface of $Fe_{0.33}Al_{0.66}$-solid might be the reason for the decreased selectivity compared to the other $Fe_{1-x}Al_x$-solid samples, as also all $Fe_{1-x}Al_x$-colloids (with a stabilizing organic shell) show lower selectivities.

For a more detailed kinetic study, monitoring of the substrate conversion with all $Fe_{1-x}Al_x$ at optimized conditions (3 bar H_2 and 100 °C) confirmed the trend of an increased activity with higher Al amounts (see Figure 71). The shape and surface of the catalyst play a major role for its performance, including organic ligands to have a big influence on the electronic and steric features.[168] In addition, the existence of coordinating ligands (at the colloidal surfaces) vs. carbonaceous species (on the heterogeneous surfaces) might lead to a variation of the hydrocarbon adsorption strength.[172]

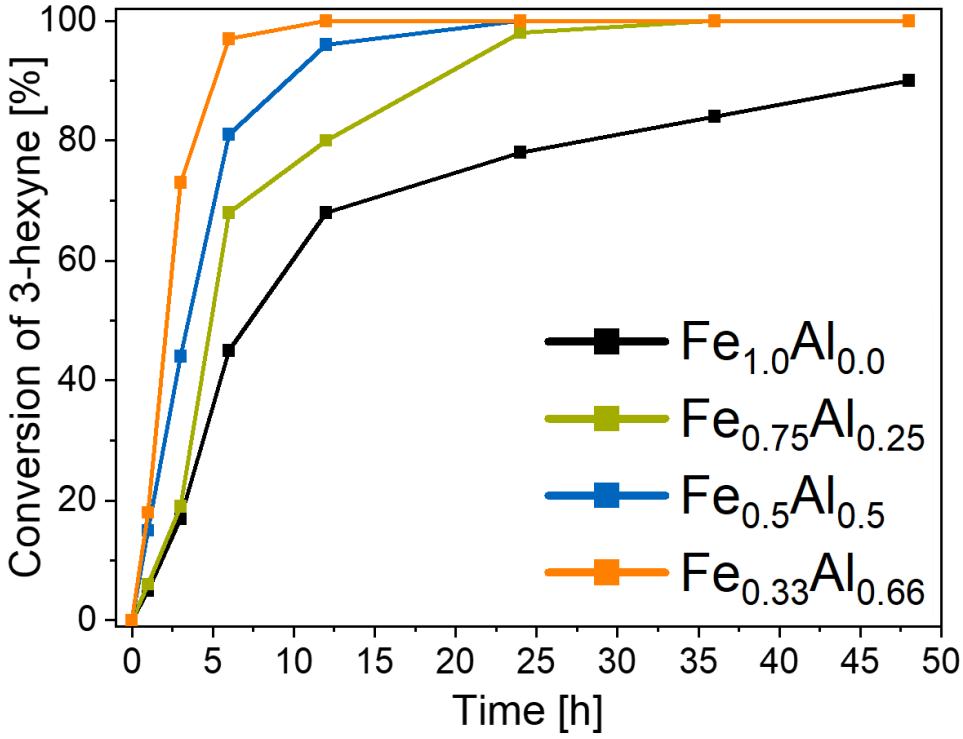

Figure 71. Kinetic monitoring of the semi-hydrogenation catalysis of 3-hexyne using 5 mol% $Fe_{1-x}Al_x$ powders as catalyst at 3 bar H_2 and 100 °C.

Comparison of the *cis*/*trans* ratio of the formed alkene shows, similar to the colloidal catalysts, a preferred formation of the *cis*-alkene for all $Fe_{1-x}Al_x$ solids. This is also reflected applying *cis*-3-hexene or *trans*-3-hexene as substrates (see Table 26). Here, surprisingly, no

isomerization of the thermodynamically unfavoured *cis*-3-hexene to the *trans*-isomer is observed.

Table 26. Time dependent *cis*/*trans* ratio of the formed 3-hexene using 5 mol% $Fe_{1-x}Al_x$ powders and 3-hexyne as substrate (3 bar H_2, 100 °C).

Entry	Time	*cis*/*trans* ratio			
	[h]	$Fe_{1.0}Al_{0.0}$ powder	$Fe_{0.75}Al_{0.25}$ powder	$Fe_{0.5}Al_{0.5}$ powder	$Fe_{0.33}Al_{0.67}$ powder
1	1	[a]	[a]	14.3/1	11.1/1
2	3	[a]	[a]	14.3/1	5.8
3	6	20/1	25/1	12.5/1	5.6/1
4	12	20/1	20/1	9.2/1	4.8/1
5	24	20/1	20/1	6.3/1	3.6/1

[a] only formation of the *cis*-isomer

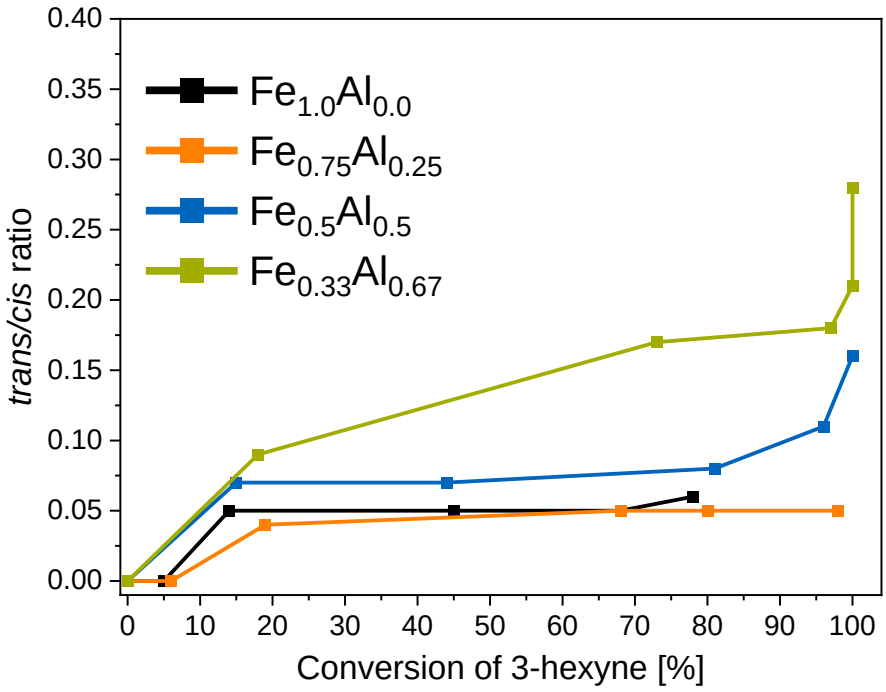

Figure 72. Conversion-dependent *trans*/*cis* ratio of the formed 3-hexene showing an increased formation of the *trans*-3-hexene with increased Al amount of the $Fe_{1-x}Al_x$ powders.

In contrast, the isomerization of the *trans*- to the *cis*-olefin was detected for all $Fe_{1-x}Al_x$ powders (see below, Table 27, Entries 13-16). This reaction occurs via a σ-bonded half-hydrogenated intermediate, where the formation of the *cis*-olefin is preferred as a result of a more favourable interaction of the respective intermediate with the catalyst surface. Similar results were reported by Zaera et. al, where the shape of Pt NPs was crucial for the stereoselectivity of the olefin isomerization. The authors suggest that the interaction of auxiliary groups of the substrate with the catalyst surface as well as the shape of the latter are the crucial factors for the *cis*/*trans* ratio.[168,173] Due to a larger adsorption energy of the *cis*-

isomer, its formation is preferred over the *trans*-olefin. Nevertheless, similar to the $Fe_{1-x}Al_x$-colloids, the amount of *trans*-alkene is increased with higher conversions. At low conversions of 3-hexyne, a high coverage of the substrate on the catalyst surface might lead to steric constraints, hence favouring the *cis*-alkene. This effect is decreased at higher conversions, hence allowing also for the formation of the *trans*-olefin.[174] The amount of detected *trans*-3-hexene is also increased with higher Al amounts (see Table 26 and Figure 72). Due to the alloy structure of the $Fe_{1-x}Al_x$ powders, a higher Al amount and hence geometrically more separated Fe active sites result in more space for the adsorbed species leading to decreased steric constraints of the substrates.[175]

Substrate variation (liquid alkynes)

Substrate variation using internal alkynes with different alkyl chain lengths and with different steric demand as well as terminal alkynes was tested using (not annealed) $Fe_{1-x}Al_x$ powders in order to evaluate those factors for the catalytic performance (see Table 27). As already seen for monometallic Pd and bimetallic Pd/Ga materials, the activity and selectivity are strongly dependent on the reactivity of the substrate, as the formation of oligomers can result in a catalyst deactivation.

In general, the conversion as well as the selectivity is strongly decreased with terminal alkynes. The semi-hydrogenation of 1-hexyne as well as 1-octyne shows no full conversion after 24 h at 3 bar H_2 and 100 °C (see Table 27, Entries 1-4 and 20). Here, $Fe_{0.5}Al_{0.5}$ as catalyst shows a slightly increased activity with the alkyne with the longer alkyl chain, 1-octyne, suggesting an influence of the electronic features of the acidic H of the triple bond. In addition, using phenylacetylene as substrate exhibiting an aromatic group shows a strongly decreased substrate conversion of only 39 % (see Table 27, Entry 22). LIFDI-MS measurements suggest an oligomerization of terminal alkynes and alkenes during semi-hydrogenation catalysis, hence blocking the metal active sites resulting in a decreased activity (see SI, Figure 182). The strongly decreased selectivity towards the olefin with terminal alkynes is further supported by a full conversion of the respective alkene, which was not monitored for internal alkenes (see Table 27, Entries 8, 21 and 23). The selectivity can be increased to 59 % and 65 % by decreasing the temperature to 50 °C and 25 °C, respectively, but with a decreased substrate conversion (see Table 27, Entries 5-6). Beside the strong influence of the position of the triple or double bond on the catalytic performance, steric effects were further tested. Therefore, cyclohexene and 1-methylcyclohexene were tested as substrates (see Table 27, Entries 24-25). While 70 % of the cyclohexene is hydrogenated into the respective alkane

after 24 h, no conversion is observed with 1-methylcylcohexene. This emphasized the steric impact of the substrate on the catalyst activity. Nevertheless, comparison of cyclohexene with *cis*-3-hexene (no conversion) shows that not only steric but also electronic effects must have an impact on the catalyst performance.

Table 27. Semi-hydrogenation experiments using 5 mol% $Fe_{1-x}Al_x$ powders after 24 h reaction time with various substrates.

Entry	Substrate	Catalyst	Reaction Parameters	Conversion [%]	Selectivity [%]	*cis*/*trans* alkene
1	1-hexyne	$Fe_{1.0}Al_{0.0}$	3 bar H_2, 100 °C	29	37	-
2	1-hexyne	$Fe_{0.75}Al_{0.25}$	3 bar H_2, 100 °C	34	52	-
3	1-hexyne	$Fe_{0.5}Al_{0.5}$	3 bar H_2, 100 °C	88	50	-
4	1-hexyne	$Fe_{0.33}Al_{0.67}$	3 bar H_2, 100 °C	56	45	-
5	1-hexyne	$Fe_{0.5}Al_{0.5}$	3 bar H_2, 50 °C	65	59	-
6	1-hexyne	$Fe_{0.5}Al_{0.5}$	3 bar H_2, 25 °C	53	65	-
7	1-hexyne	$Fe_{0.5}Al_{0.5}$	1 bar H_2, 100 °C	26	14	-
8	1-hexene	$Fe_{0.5}Al_{0.5}$	3 bar H_2, 100 °C	100	-	-
9	*cis*-3-hexene	$Fe_{1.0}Al_{0.0}$	3 bar H_2, 100 °C	0	-	[a]
10	*cis*-3-hexene	$Fe_{0.75}Al_{0.25}$	3 bar H_2, 100 °C	0	-	[a]
11	*cis*-3-hexene	$Fe_{0.5}Al_{0.5}$	3 bar H_2, 100 °C	0	-	[a]
12	*cis*-3-hexene	$Fe_{0.33}Al_{0.67}$	3 bar H_2, 100 °C	60	-	[a]
13	*trans*-3-hexene	$Fe_{1.0}Al_{0.0}$	3 bar H_2, 100 °C	0	-	0/1
14	*trans*-3-hexene	$Fe_{0.75}Al_{0.25}$	3 bar H_2, 100 °C	7	-	0.2/1
15	*trans*-3-hexene	$Fe_{0.5}Al_{0.5}$	3 bar H_2, 100 °C	16	-	0.35/1
16	*trans*-3-hexene	$Fe_{0.33}Al_{0.67}$	3 bar H_2, 100 °C	77	-	0.72/1
17	4-octyne	$Fe_{0.5}Al_{0.5}$	3 bar H_2, 100 °C	100	80	[a]
18	*cis*-4-octene	$Fe_{0.5}Al_{0.5}$	3 bar H_2, 100 °C	0	-	[a]
19	*cis*-2-octene	$Fe_{0.5}Al_{0.5}$	3 bar H_2, 100 °C	0	-	[a]
20	1-octyne	$Fe_{0.5}Al_{0.5}$	3 bar H_2, 100 °C	90	44	-
21	1-octene	$Fe_{0.5}Al_{0.5}$	3 bar H_2, 100 °C	100	-	-
22	phenylacetylene	$Fe_{0.5}Al_{0.5}$	3 bar H_2, 100 °C	39	53	-
23	styrene	$Fe_{0.5}Al_{0.5}$	3 bar H_2, 100 °C	100	-	-
24	cyclohexene	$Fe_{0.5}Al_{0.5}$	3 bar H_2, 100 °C	70	-	-
25	1-methylcyclohexene	$Fe_{0.5}Al_{0.5}$	3 bar H_2, 100 °C	0	-	-

[a] only formation of the *cis*-isomer

Additional to the amorphous as-synthesized $Fe_{1-x}Al_x$ materials, the annealed samples were also tested in catalytic semi-hydrogenation reactions under the standard conditions. All samples with an annealing temperature of 500 °C and 800 °C, giving crystalline materials,

showed no catalytic activity in the semi-hydrogenation of 3-hexyne independent on the reaction conditions. The poorly crystalline sample $Fe_{0.5}Al_{0.5}$ heated at 300 °C showed a decreased activity (conversion of 44 % compared to 100 % for the respective amorphous material). This clearly shows that with increasing crystallinity and/or the formation of intermetallic Fe/Al phases, the catalyst activity is strongly decreased.

Acetylene Semi-Hydrogenation

Apart from hydrogenation experiments of liquid alkynes, also the activity of $Fe_{1-x}Al_x$ powders for the acetylene semi-hydrogenation was tested (see Figure 73). In detail, $Fe_{0.33}Al_{0.67}$, $Fe_{0.5}Al_{0.5}$ and $Fe_{1.0}Al_{0.0}$ powders were each placed in a glass-lined tubular fixed bed flow reactor equipped with a quadrupole mass spectrometer under inert conditions. All tested $Fe_{1-x}Al_x$ powder materials showed a high acetylene conversion using a feed gas consisting of 5 % acetylene, 5 % ethene and 5 % ethane with an excess of H_2 (alkyne/H_2 = 1/60).

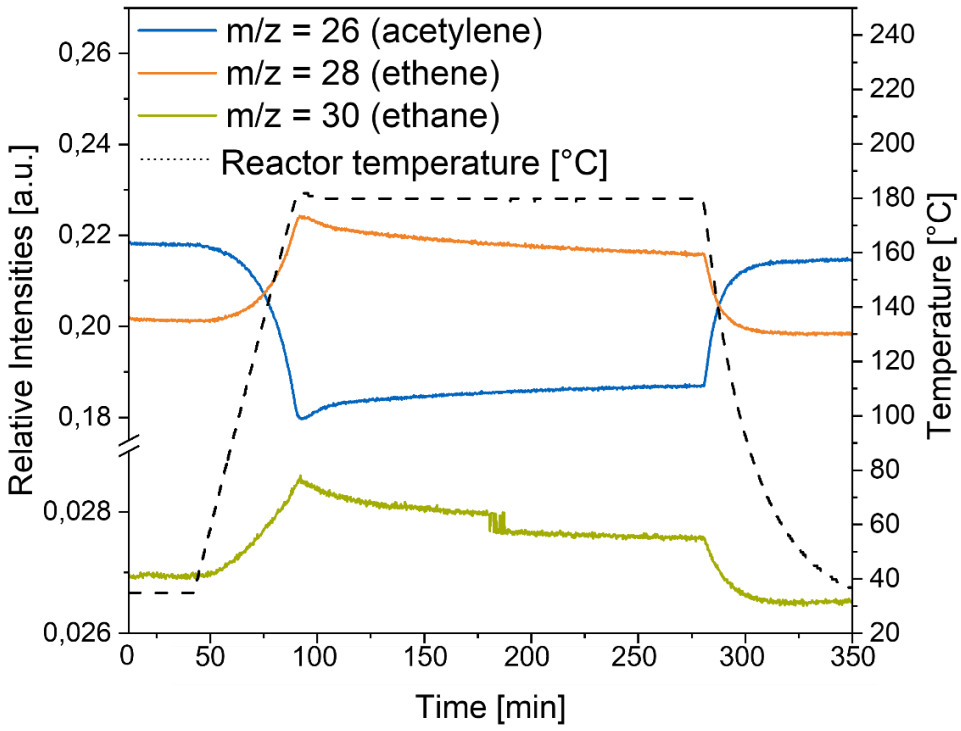

Figure 73. Acetylene (semi)-hydrogenation experiments using $Fe_{0.33}Al_{0.67}$ powder (exemplarily) as catalyst in a flow reactor set up at 180 °C and an alkyne/H_2 ratio of 1/60.

Smaller amounts of H_2 lead to a decreased catalyst activity. For all $Fe_{1-x}Al_x$ powders, a temperature of 180 °C was required to achieve an acetylene (semi)-hydrogenation (see SI, Figures 187-189). Decreasing the temperature leads to no conversion and hence to the initial gas composition of each 5 % acetylene, ethylene and ethane in argon. With a retention time

of an acetylene molecule in the reactor of approx. only 10^{-2} s, conversions of acetylene of 5.5 % for $Fe_{0.33}Al_{0.67}$, 1.9 % for $Fe_{0.5}Al_{0.5}$ and 2.2 % for $Fe_{1.0}Al_{0.0}$ powders suggest highly active catalytic systems, with a selectivity towards the alkene of 93.5 %, 92.6 % and 91.7 %, respectively (for calculation details, see Experimental). Here, the detected catalyst activity is similar to that monitored in solution; the Al-rich compound $Fe_{0.33}Al_{0.67}$ shows the highest acetylene conversion, whereas $Fe_{0.5}Al_{0.5}$ and $Fe_{1.0}Al_{0.0}$ have similar activities. The ratio between the observed conversion and the calculated TPD surface area at 180 °C strongly increases with higher Al amounts (for $Fe_{0.33}Al_{0.66}$: 0.16, $Fe_{0.5}Al_{0.5}$: 0.03, $Fe_{1.0}Al_{0.0}$: 0.02) and does not scale with the molar ratio of Al and Fe. This suggests that the Al does not only have a steric (due to an enhanced surface area) but also electronic effect on the catalytic material. The observed trend in selectivity goes in well accordance with the literature-known site isolation principle.[12,74] The dilution of the active Fe sites with Al results in a decreased adsorption energy of the alkene to the metal surface leading to a preferred alkene desorption instead of a further hydrogenation to the respective alkane. With higher amounts of Al, the selectivity increases. Nevertheless, it has to be noted that in contrast to other bimetallic systems where the second metal can be regarded as an “innocent spectator” such as Ga, Al with the ability to form hydride species might facilitate the hydride supply for the alkyne hydrogenation.

The herein obtained results show that the reactivity of $Fe_{1-x}Al_x$ powders is not only dependent on the Fe/Al ratio but also on the chosen substrate. For liquid substrates, the hydrogenation of internal alkynes results in the best conversions, with excellent selectivities towards the olefin for all $Fe_{1-x}Al_x$ powders. In contrast, the hydrogenation of terminal alkynes results in the formation an oligomer layer, blocking the catalyst active sites leading to an enormous catalyst deactivation. The semi-hydrogenation of acetylene, with a completely different measurement set-up (flow reactor, gaseous substrate) follows the literature-reported site-isolation principle with higher selectivities and lower activities for higher Al amounts. This shows the huge playground of the semi-hydrogenation catalysis, where the metal combination, metal ratio, temperature, H_2 pressure, substrate and measurement set-up all play a crucial role for the overall catalytic performance.

Recycling Experiments

In order to investigate whether the catalyst changes during catalysis, recycling experiments of the heterogeneous catalysts ($Fe_{1.0}Al_{0.0}$, $Fe_{0.75}Al_{0.25}$ and $Fe_{0.5}Al_{0.5}$ powders) with 3-hexyne as substrate over six runs were analyzed (reaction conditions: 3 bar H_2, 100 °C, 24 h; see Figure 74, left).

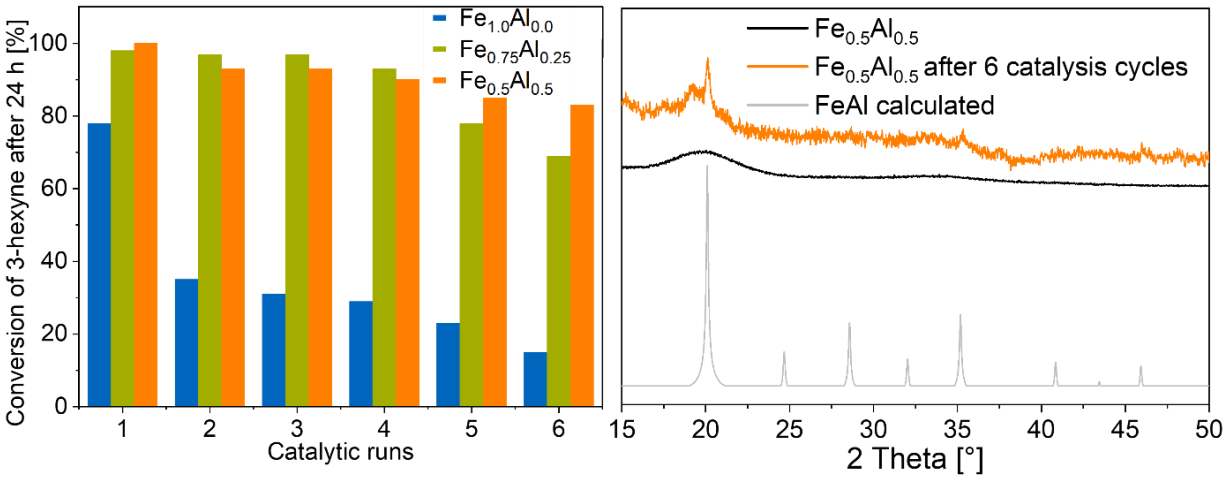

Figure 74. Left: Recycling experiments of $Fe_{1-x}Al_x$ powders (3-hexyne, 3 bar H_2, 100 °C, 24 h). Right: PXRD of $Fe_{0.5}Al_{0.5}$ powder before and after recycling experiments showing the formation of the intermetallic FeAl phase.

For all samples, a decrease in the activity was observed. Nevertheless, metal leaching can be excluded for all samples over all runs according to ICP-OES measurements. The loss in activity is strongly increased with higher Fe amount. In detail, $Fe_{1.0}Al_{0.0}$ powder already shows a strongly decreased substrate conversion in the second catalytic run, whereas this effect is not that pronounced using $Fe_{0.75}Al_{0.25}$ and $Fe_{0.5}A_{0.5}$ powders as catalyst. The selectivity is not affected by a recycling of the catalyst.

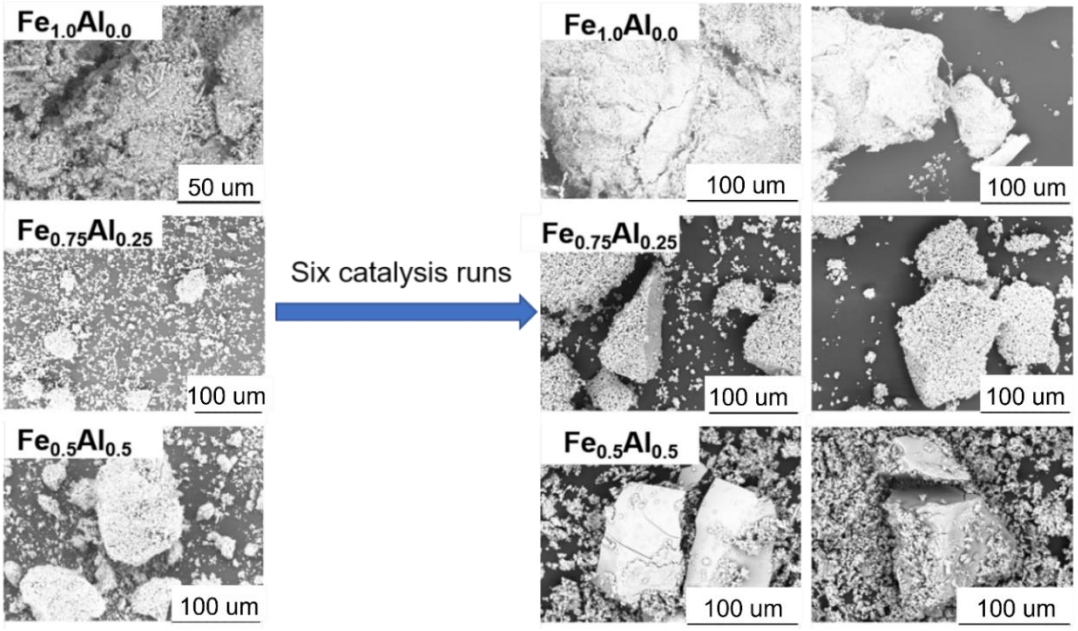

Figure 75. SEM pictures of $Fe_{1-x}Al_x$ powders before and after six catalysis runs with different magnification showing various surface morphologies and an increased crystallinity for all samples after recycling experiments.

SEM measurements of catalyst before and after recycling experiments shows a macroscopic decreased surface roughness of the material´s surface (see Figure 75). Additionally, new edges and corners are detected, suggesting an increased crystallinity of $Fe_{1-x}Al_x$ powders after

catalysis. This was further verified by PXRD measurements of $Fe_{0.5}Al_{0.5}$ before and after catalytic recycling experiments. Here, the formation of the intermetallic FeAl phase was observed suggesting the formation of bigger crystallite sizes during the catalysis, similar to a simple annealing of the sample (see Figure 74, right). As the annealed samples show no activity in the semi-hydrogenation catalysis of 3-hexyne, formation of bigger crystallite sizes and hence a decrease of the surface area over six catalysis runs might explain the strong loss in catalyst activity. The formation of the FeAl phase is further supported by SQUID analysis, as an increase in the magnetism is detected (see SI, Figure 184).

Concluding from the herein obtained catalysis data, addition of Al to the Fe-based material leads to a boost in activity as well as in selectivity. The increase in activity with higher Al amounts might be attributed to a decreasing particle size according to DLS and SEM measurements. The trend in selectivity is strongly dependent on the substrate and catalysis set-up. For the gaseous acetylene semi-hydrogenation, the observed selectivities go in well accordance with the site isolation principle (higher Al amount, higher selectivity).

Conclusion

In this section, the successful synthesis of abundant, bimetallic Fe/Al materials starting from the organometallic precursors $[AlH_3]-NMe_3$ and $[Fe_2(mesityl)_4]$ is reported. The development of a synthesis strategy of bimetallic $Fe_{1-x}Al_x$ colloids (x = 0.25, 0.5, 0.67), their respective solid precipitates, and the application in the semi-hydrogenation reaction of liquid alkynes leads to following findings:

a) Reaction of $[Fe_2(mesityl)_4]$ and $[AlH_3]-NMe_3$ is dominated by the hydride transfer from the allane to the Fe precursor and the release of "free" mesitylene, which then further reacts on the Fe center by a C-H activation with other reactants of the solution. The resulting organic products undergo further C-H activations on the Fe center forming a stabilizing shell around the bimetallic colloids by a weak coordination to the Al.

b) With increasing Al amount, the colloid particle size decreases. Furthermore, the stability of the NPs in solution is increased by the addition of Al suggesting a stabilizing effect of the inactive metal by the formation of Al-alkyl species on the NP surface. XPS sputtering experiments point, in contrast to the $Pd_{1-x}Ga_x$ colloidal system (x = 0.33, 0.5, 0.67), to a random distribution of Fe and Al within the NPs (nano-alloy) with a stabilizing organic shell around the particle surface.

c) Additional H_2 pressure and a high temperature led to (full) precipitation of the bimetallic colloids by a continuous growth of the NPs and with loss of the protecting organic shell around the material´s surface. It can be assumed that the resulting powder samples have a similar nano-alloy structure with randomly distributed Fe and Al sites as its colloidal precursors. With a higher Al amount, a decreased particle size of the precipitated material is obtained.

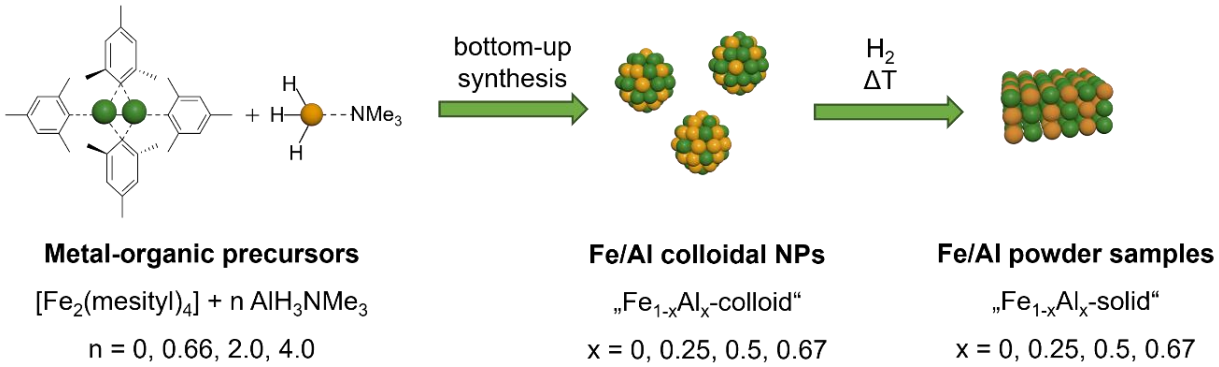

Scheme 25. Synthesis protocol of bimetallic $Fe_{1-x}Al_x$ materials by a bottom-up organometallic approach.

d) TPD measurements of solid $Fe_{1-x}Al_x$ powders allowed for a deeper insight into the (hydrogen) ad- and desorption processes of the tested materials. Simple heating of

the powder samples points to a different adsorption behavior depending on the Al amount, as for the Al-rich compounds desorbed mesitylene could be detected. This was not observed for the monometallic $Fe_{1.0}Al_{0.0}$ powder, suggesting another electronic structure. This is also important for the stabilization of the material in solution and the resulting particle size – with higher Al amount, the particles get smaller and are more easily dissolved in solution. After H_2 treatment, it could be shown that 1) all $Fe_{1-x}Al_x$ powders incorporate hydrogen during the synthesis procedure in the bulk, 2) the Al-rich samples are able to reversibly ad- and desorb H_2 at 180 °C and 3) at higher temperatures (300 °C and 480 °C), all $Fe_{1-x}Al_x$ powders irreversibly desorb H_2 (with higher Al amount, more H_2 is desorbed). At these temperatures, a simultaneous change of the sample structure is observed, most probably by crystallization processes (supported by PXRD measurements).

e) All herein investigated $Fe_{1-x}Al_x$ materials show the ability to incorporate and bind hydrogen dependent on the Fe/Al ratio, which also directs the structure and the selectivity in semi-hydrogenation catalysis. Here, the colloids are more active compared to the solids, whereas an opposite trend is observed for the selectivity. In addition, the heterogeneous materials are not stable under the catalytic conditions resulting in a sintering, loss of porosity and the formation of intermetallic phase mixtures. In contrast, the colloids are stable during catalysis runs, as due to their high activity, mild conditions can be chosen. It could be shown that the Al does not only act as spacer between the Fe active sites (according to the site-isolation principle), but also strongly influences the solubility and particle size, and protects the Fe from oxidation. Hence, the Al/Fe ratio also strongly influences the activity of the resulting material. Besides tuning the electronic features of the catalyst, the dilution of Fe with Al leads to materials with organic residues attached to the metal surface playing a major role concerning adsorption characteristics.

f) Hydrogenation experiments of a gas mixture consisting of each 5 % acetylene, ethene and ethane in Argon using the solid $Fe_{1-x}Al_x$ powders in a flow reactor set up showed a moderate selective conversion of acetylene to ethene. Here, an acetylene/H_2 ratio of 1/60 turned out to yield the highest conversion, whereas a temperature of 180 °C is required to receive an active catalyst. This clearly demonstrates that these materials are not only active in the hydrogenation of liquid alkynes, but also the potential of abundant, bimetallic Fe/Al materials as catalysts for the selective acetylene semi-hydrogenation reaction.

For the first time, the successful synthesis of an active, selective and stable semi-hydrogenation catalyst consisting of the abundantly available and low-cost metals Fe and Al was described. The easy access to those materials with a simple synthesis protocol and the better catalytic performance compared to widely investigated Pd/Ga bimetallic catalysts makes the herein presented materials interesting and promising candidates for further investigations.

Future studies could focus on a detailed investigation of the influence of the hydrogen pressure and temperature on the *cis/trans* isomerization in order to learn more about the crucial factors for a certain reactivity. Suitable surfactants for an enhanced colloid stability and their influence on activity and selectivity, e.g. via the use of crosslinking alkyl amines on the surface of the Fe/Al colloids could lead to novel, superior catalytic materials. For a more detailed investigation of the surface structure of $Fe_{1-x}Al_x$ colloids, the deuterated $[AlD_3]{-}NMe_3$ could be applied as Al source in the colloid synthesis. This would allow for detailed IR studies on the colloid surface. Additionally, pressurizing the $Fe_{1-x}Al_x$ colloids with D_2 would also help to clearly identify Al-H_2 and Al-hydride species. The structure of the heterogeneous $Fe_{1-x}Al_x$ powders could be further analyzed XANES/EXAFS or pair-distribution function (PDF) analysis could help to understand the nature of the resulting precipitates upon reaction of the herein chosen metal precursors $[Fes_2(mesityl)_4]$ and $[AlH_3]{-}NMe_3$.

4. Conclusion and Outlook

A fundamental understanding of the effects on the selectivity in the semi-hydrogenation catalysis resembles a complex field of research. In this PhD project, an investigation of selected (colloidal nano-sized) catalyst systems for the semi-hydrogenation of liquid alkynes was presented. Starting from an easy to synthesize literature-known monometallic Pd system, the focus on this study lies not on the colloid synthesis procedure but on the influence of the addition of post-synthetic additives. The collected data clearly showed the great possibilities of coordinating organic ligands to boost both, the activity as well the selectivity of a simple catalytic system. Furthermore, the investigation on a bimetallic Pd/Ga system led to first ideas how the formation of such colloids starting from organometallic precursors could occur and how the reaction parameters influence the colloidal size and stability. This knowledge was further extended to the abundant metal combination Fe/Al, where both metals are even more likely to oxidize and labile towards ambient conditions compared to the previous studied Pd/Ga. Also here, the investigation on the building formation led to a deeper understanding of the important parameters for the successful bottom-up synthesis of bimetallic NPs existing of metals with different oxidation potentials. All herein analyzed systems were further tested in the semi-hydrogenation catalysis of liquid alkynes with the goal to optimize not only the catalyst stability and activity but also the selectivity towards the olefin. Two different strategies were applied in order to gain a deeper knowledge on how to control both, the NP stability as well as the catalytic performance of the respective system: a) the post-synthetic addition of coordinating surfactants and b) the dilution of the active metal with a second, non-active one.

The post-synthetic addition of coordinating surfactants turned out to have a huge influence on the catalyst performance in terms of activity and selectivity as well as on the stability of the colloidal NPs. The effect is strongly dependent on the electronic and steric features of the surfactant as well as on the NP metal surface. In general, a coordination of the post-synthetic additive can influence the electronic features of the metal surface and hence affects the catalyst´s selectivity towards the semi-hydrogenation product. While a strong coordination to the colloid can result in a decreased activity, very small surfactants with a minor steric demand might also promote particle destabilization, agglomeration and precipitation. Hence, additives with a moderate coordination strength and a certain steric demand turned out to offer the most promising characteristics for an active, selective and stable colloidal catalyst. Using PPh_3 as post-synthetic additive demonstrated the proof of concept, as this surfactant not only showed a beneficial influence on monometallic Pd colloids, but this effect was also transferable to another, bimetallic Pd/Ga system showing its broad application potential.

The second strategy for an enhanced catalytic performance which was investigated in this PhD project was the alloying of the active metal with a second, non-active metal. In general, dilution of the active centers can lead to an enhanced selectivity towards the olefin, as the full-hydrogenation is minimized. Herein it could be shown that the so-called site-isolation principle is transferable from heterogeneous, literature-known materials to colloidal catalysts in solution. Nevertheless, the introduction of a second metal into a colloidal system requires the development of novel bottom-up synthesis strategies, as the formation of bimetallic NPs consisting out of two metals with different redox potentials evokes the necessity of starting materials with suitable metal oxidation states and weak-coordinating ligands. Hence, the use of organometallic precursors exhibiting an all-hydrocarbon ligand sphere turned out to enable the successful synthesis of bimetallic colloidal Pd/Ga and Fe/Al systems, both with the possibility to easily vary the metal-to-metal ratios and therefore the catalyst characteristics. Investigations on the building mechanism helped to understand the crucial parameters for small and stable bimetallic colloids, specifically for each system and hardly transferable to other metal combinations. Nevertheless, for all herein tested systems, it can generally be stated that for colloidal systems, a stabilization of the NPs by an organic shell seems imperative for a stable system and the prevention of particle agglomeration and precipitation. Post-synthetic additives can influence the colloid stability by displacement of the organic shell and coordination to the metal surface in both, a stabilizing or destabilizing fashion. This effect was intensively studied for the Pd/Ga system upon addition of carboxylic acids. The post-synthetic addition of those coordinating surfactants enables a stable bimetallic system towards air with an improved catalytic performance due to the existence of a second, not active metal and the resulting alloying effect.

Concerning catalysis applications, the above-mentioned organic shell of a colloidal NP can lead to a coking effect during catalysis, which might affect the catalyst activity. Yet, as mentioned earlier, a stabilizing shell is crucial for a solubilization of the NPs in solution. Colloids without such a shell will agglomerate and precipitate, resulting in a less active heterogeneous catalyst, as described for the Fe/Al system. Regarding this certain example, the targeted precipitation of bimetallic colloids by adjustment of the synthesis parameters led to a highly selective heterogeneous catalytic system with different characteristics compared to the respective colloidal NPs and the crystalline Fe/Al intermetallic phases. Hence, the development of bottom-up synthesis strategies starting from organometallic precursors might not only lead to bimetallic colloidal systems but also enables the investigation of bimetallic amorphous solid materials with different structures and catalytic performances compared to similar systems synthesized by top-down approaches. Consequently, the huge playground

of metal precursors and reaction parameters can lead to a precise design of colloidal systems in solution, but also to novel (bi)metallic heterogeneous systems by a targeted precipitation of pre-formed colloidal NPs. The growth and agglomeration of small alloy particles stabilized by an organic shell does not simply result in the respective intermetallic phase but rather in a hybrid material comprising organic residues affecting the electronic features as well as the morphology and surface. Such systems might not only exhibit innovative characteristics but also an increased stability, which is an important desirable feature of any catalyst applied in industry. Additionally, replacing noble and expensive metals like Pd with other, abundant ones is an important objective in order to get more cost-effective catalysts. In this PhD thesis, Fe and Al were selected as lower-priced metals. Nevertheless, using Ni or Ru instead of Fe might be beneficial with regard to oxophilicity and reactivity. Moreover, replacing Fe would allow for other analytic techniques like NMR measurements of both the organic shell and the respective metal leading to a better understanding of the colloid structure. First examples in literature already showed the successful synthesis of bimetallic Ni/Ga[99] and Ni/Al[176] colloids and Ru/Al intermetallics[98,177], but a detailed investigation on the semi-hydrogenation performance as well as on the coordination of stabilizing organic ligands is still lacking. Moreover, the combination of Ni and Zn was evaluated to be one of the most promising metal combinations according to DFT calculations regarding the acetylene semi-hydrogenation reaction.[12] Hence, identifying the optimal metal/metal mixture in regard to both the nature of the metals as well as their ratio resembles the first step of a successful catalyst optimization. For all these examples, changing the metal/metal ratio does not only influence the electronic but also the structural characteristics of the respective material. The precise tuning by a continuous change of the electron concentration is for example possible in the Pd/Ga/Sn system by systematically changing the Ga/Sn ratio. As Sn has with one electron more than Ga, this allows for an alteration of the electronic structure without changing the structure of the material.

Furthermore, the development of a novel, targeted synthesis strategy for such bimetallic catalysts is appealing. The co-condensation of two metals in the vapor phase resembles a promising approach to access colloids in solution with novel metal combinations, which cannot be synthesized by a simple wet-chemical route. Apart from unique metal combinations forming colloids that are only stabilized by a weakly coordinating organic shell, this synthesis technique offers many opportunities for further catalyst improvement by the post-synthetic addition of ligands. The co-condensation of two metals in vacuo does not only enable metal combinations which are not accessible *via* wet-chemical approaches but also allows for the synthesis of novel mono- and bimetallic precursors, which then again can be used for

traditional wet-chemical colloid synthesis. As such synthesis is strongly dependent on the nature of the used precursors, the development of innovative materials might be boosted by this very old but rarely used synthesis technique. Instead of focusing on bimetallic materials in the nano-regime, further downsizing the number of atoms resulting in molecular, atom-precise cluster compounds opens up a whole new pathway towards novel catalytic systems.[178] Such species exhibit completely novel characteristics, as decreasing the number of metal atoms results in entirely different electronic properties, compared to NPs or even bulk material. Hence, a direct comparison of such molecular species with colloids or heterogeneous materials as catalysts is not useful but, nevertheless, opens up a new strategy for an atom-economical way of catalysis. The huge toolbox and configuration space of such intermetalloid clusters, emerging from the choice of metals, mixing ratios as well as from the choice of the organic ligand environment implicates immense possibilities to synthesize clusters with different metal combinations, sizes and electronic features. On the other hand, the lability of such intermetalloid cluster compounds could again be used for the synthesis of bimetallic NPs. Here, a targeted decomposition, e.g. by hydrogenation and addition of stabilizing agents, could yield novel colloids with a different structure than those obtained by the direct reaction of two organometallic precursors. First examples by Janiak et. al on the targeted decomposition of Ni/Ga bimetallic compounds showed that such approaches can principally result in bimetallic materials.[99] Nevertheless, a more detailed study on optimized reaction conditions and the wise choice of the respective cluster compound is still lacking. First examples of our group on the reaction of the compound [Ni(GaCp*)$_4$] with liquid alkynes under H_2 atmosphere not only yielded the respective alkene but also the formation of very small, uniform bimetallic colloids with a small size distribution.[179] These first results show that such systems are principally active in the semi-hydrogenation catalysis, but the nature of the active species is still unknown. This could be the starting point of a more detailed investigation, not only on the semi-hydrogenation catalysis using bimetallic cluster compounds but also on the formation mechanism of colloidal NPs from such starting materials.

The size- and shape-controlled synthesis of bimetallic colloids is a challenging field of research. Nevertheless, the benefit of such NPs is questionable if they are not stable under catalytic conditions, changing their size and chape during catalysis runs. This reduces the informative value on the influence of those parameters on the catalyst performance. Hence, the stabilization of such novel, nano-sized catalyst is of utmost importance. A common, well-known method is the heterogenization of the colloids on a solid support. This could either be realized by an impregnation of the colloidal solution on a solid support or, more sophisticated

but also quite popular in the scientific community, by the incorporation of the pre-formed NPs in a 3D metal-organic framework (MOF). For the first case, metal oxides as supports are most suitable as they are robust, porous and easy to handle. Here, the introduction of anchoring functional groups on the surface mimicking the herein used coordinating additives might have a similar beneficial influence on the catalyst performance and lead to a decreased particle migration and agglomeration on the surface of the support. Most important, the preparation of the support and the reaction conditions for the heterogenization have to be optimized in order to avoid particle decomposition of labile (easy to oxidize) NPs upon impregnation on the support. Nevertheless, such hybrid materials often suffer from harsh reaction conditions during catalysis, resulting in a change of the original NP size and structure by agglomeration processes on the surface of the support. Regarding the colloid incorporation into a MOF, the most promising advantage over a simple support is an increased interaction between the NP and the host structure, thus enabling a targeted advantageous influence of the MOF on the catalytic performance of the metal particle. Additionally, such hybrid materials can also be used for tandem catalysis, where both the host and the guest are able to catalyze a certain reaction. Hence, such an intelligent design allows for the synthesis of novel catalysts with superior features. The biggest challenge is the successful incorporation of the NPs without any particle agglomeration or decomposition. Various synthesis approaches are reported in literature,[180] but there is a lack of strategies for bimetallic colloids which are not stable towards water, coordinating solvents or air. As most MOF syntheses require solvents like DMF and traces of water for the formation of a crystalline material, these basic parameters are not tolerated by sensitive, easily oxidated metal particles. Applying the literature-known wet-chemistry approaches, namely building the MOF around the colloids or impregnation of the MOF with the pre-formed NPs will come to a dead end regarding the herein investigated colloidal systems. Hence, novel synthesis strategies for the formation of hybrid materials existing of a MOF host structure with very sensitive and easily oxidizable metal NPs as guests could be obtained by the implementation of a co-condensation system, where the metals are directly and simultaneously evaporated into a pre-formed host structure.[181] With this method, the access to not only novel colloidal materials but also heterogenized bimetallic NPs might be feasible.

Beside focusing on novel synthesis strategies for bimetallic nanoparticles, also the investigation on other catalytic applications apart from the herein studies semi-hydrogenation catalysis is an interesting field of research. Enantioselective catalysis for the production of chiral molecules have widely been investigated, mostly by using homogeneous chiral metal complexes which are mostly immobilized on supports for a simplified recycling procedure.[182]

Nevertheless, due to stability issues, chiral ligand-modified metal NPs as attractive alternative forming a robust asymmetric catalyst were reported in literature. For instance, asymmetric hydrogenation reactions as well as asymmetric C-C bond formation catalysis were reported as promising strategy for constructing active and robust asymmetric catalyst systems.[182,183] Here, several examples of the post-synthetic addition of chiral ligands coordinating to the metal NP surface demonstrate the high potential of this research field. Similar to the systematic addition of additives presented in this PhD project, the influence of chiral surfactants with subtle differences in sterics, electronics and chirality could give new insights into reaction mechanisms and the crucial factors for a highly active and selective system. Inspired by the promising results of air-stable (and hence easy-to-handle) bimetallic Pd/Ga colloids in the presence of carboxylic acids, the post-synthetic addition of chiral carboxylic acids, e.g. amino acids, would be a novel and interesting topic to explore. A coordination of such chiral surfactants to a bimetallic colloidal system could combine the advantages of both approaches: a) an increased NP stability (at air and under catalytic conditions) and b) an enantioselective reactivity due to the influence of the ligand and c) as a results of the bimetallic characteristics of the NP, a certain chemoselectivity. Here, choosing a substrate with two functional groups to investigate whether only one of them can be selectively catalytically reacted would be the starting point of such a study. The combination of the herein gained knowledge about the synthesis of such colloidal systems, the impact of coordinating ligands and the right choice of the respective substrate and reaction type might lead to an enantio- and chemoselective, air stable colloidal system with superior catalytic properties and a fundamental understanding of the crucial factors for an optimized performance in catalysis.

5. Experimental Section

5.1 General Materials and Methods

All chemicals were purchased from commercial suppliers (Sigma-Aldrich, ABCR, Acros, Tokyo Chemical Industry and others) and used without further purification. Common organic solvents such as *n*-hexane, toluene, THF, diethyl ether and others, were dried using a MBraun solvent purification system (SPS), in which solvents were passed through consecutive filter columns containing suitable adsorbents by application of argon pressure gradients. All other solvents were dried using standard purification procedures e.g. by passing through a column of activated alumina under inert atmosphere or by using suitable activated molecular sieves. Such treated solvents exhibit a purity above 99 % and water contents below 5 ppm, as verified by Karl-Fischer titration. Solvents were degassed by freeze-pump-thaw cycles and subsequent saturation of argon. Deuterated solvents for NMR spectroscopy were dried over activated molecular sieves. Manipulation of air and moisture-sensitive compounds was performed under an atmosphere of purified argon using conventional Schlenk and glovebox techniques. All glassware was flame dried in vacuum prior to usage, where needed. Air and moisture sensitive chemicals were stored in a glovebox.

5.2 Analysis Techniques

Nuclear Magnetic Resonance (NMR) spectroscopy

Standard NMR spectroscopic measurements were performed on a Bruker Advance III AV400 US spectrometer operating at the appropriate frequencies. Variable temperature NMR experiments were conducted on a Bruker DRX400 spectrometer. ^{13}C and ^{31}P NMR measurements were conducted in fully proton decoupled modes. All spectra are referenced relative to the residual solvent signals (^{1}H: toluene-d_8 2.11/7.02–7.13 ppm, C_6D_6 7.16 ppm, D_2O 4.79 ppm; ^{13}C: toluene-d_8 21.10/125.68/129.33/137.91 ppm, C_6D_6 128.06 ppm). In the following chemical shifts are given in ppm (parts per million) and consecutively denoted as position, relative integral, multiplicity, coupling constant (in Hz) and assignment. Multiplicities are abbreviating as s = singlet, d = doublet, t = triplet, and m = multiplet.

Infrared Spectroscopy (IR)

IR spectra were measured on a Bruker Alpha FT-IR and a Frontier FT-IR spectrometer with an attenuated total reflection (ATR) geometry, using a diamond ATR unit under argon and on air. Spectral data were processed with the supplier software and further analysed using OriginPro 8 (OriginLab Corporation). Absorption bands are consecutively reported as position (wavenumber in cm^{-1}) and relative bands (vs = very strong, s = strong, m = medium, w = weak).

Raman Spectroscopy

Raman spectra were collected on a Renishaw inVia Raman Microscope at an excitation wavelength of 785 nm in scan range from 0 to 3200 cm^{-1} on powdered samples on air. For activated samples, the materials were filled in a capillary in a glovebox and subsequently fused under argon atmosphere. Spectral data were processed with the supplier software and further analysed using OriginPro 8 (OriginLab Corporation). Absorption bands are consecutively reported as position (wavenumber in cm^{-1}) and relative bands (vs = very strong, s = strong, m = medium, w = weak).

Elemental Analysis (EA)

Elemental analysis of all $Pd_{1-x}Ga_x$ and $Fe_{1-x}Al_x$ samples was performed by "Mikroanalytisches Laboratorium Kolbe", Mülheim an der Ruhr, Germany. Elemental analysis of all metal precursors (determination of C, H, N, Pd, Fe and Al) was conducted by Ulrike Ammari from the microanalytic laboratory of the Catalysis Research Center on a HEKAtech Euroanalysis instrument by flash combustion and subsequent chromatographic separation with an accuracy of <0.6% mass fraction. 1.5-2.5 mg of the sample are crimped into a tin foil under argon atmosphere and stored in an air-tight screw neck glass vial. For the measurement, it is transferred rapidly into the sample injector.

Powder X-Ray Diffraction (PXRD)

Powder X-ray diffraction measurements of Pd NPs and $Pd_{1-x}Ga_x$ NPs were performed on a *Panalytical* Empyrean instrument. The sample was put in a capillary under argon atmosphere and placed on a silicon wafer cut. The detection was carried out with a Pixel3D detector. All measurements were performed with Cu-K_α (λ = 1.54 Å) radiation and at 298 K. Measurements were conducted in Bragg-Brentano geometry ($\theta - \theta$ mode) or in Debye-Scherrer geometry in 2θ ranges from 5-50° or 2°- 50°, respectively 2°-90°. Grinded powders were either packed in capillaries (ϕ = 0.5 mm) or put on a silicon flatbed sample holder. Samples of dried and activated materials were packed in a glovebox under Argon atmosphere in capillaries. Silicon was employed as external standard. Patterns were normalized to the highest intensity reflection. Indexation, cell parameter refinement and Rietveld refinement have been performed with TOPAS 6 (Bruker, academic version). Powder X-Ray diffraction measurements of $Fe_{1-x}Al_x$ samples were performed using transmissions geometry with flatbed sample carriers in a *STOE STADI P* diffractometer (STOE, Darmstadt, Germany) equipped with a Ge(111) monochromator and a Mythen 1K detector (*DECTRIS*). X-ray Mo K_α (λ = 0.7093 Å) radiation operated at 50 kV (voltage) and 40 mA (intensity) was used for the measurements. For this purpose, the sample was ground to a powder and fixed in the middle between two

adhesive strips (*SCOTCH*® Magic Tape TM 810, 3M). The measurement range was from 2° to 30° (2θ).

Dynamic Light Scattering (DLS)

DLS measurements were performed on a *Malvern* Zetasizer Nano instrument using 10 mm quartz cuvettes in 173° backscattering mode. 1.4 mL of the respective sample was filtered into the cuvette through a 200 nm PTFE syringe filter. The cuvette is placed in the instrument and equilibrated at the desired temperature for 10 minutes prior to the measurement. Twelve measurement runs were averaged for one experiment to avoid statistical errors. The general-purpose method of the Malvern Zetasizer software is used for data analysis.

Mass Spectrometry (MS)

LIFDI-MS measurements were conducted on a *Thermo Scientific* Exactive Plus instrument, equipped with an Orbitrap detector and a "LIFDI 700" ionization source. All samples were prepared with dried toluene and filtered under argon atmosphere.

Quantification of 1-octyne, 1-octene and n-octane in toluene as solvent in catalytic reactions were performed on an *Agilent* Technologies 7890B GC System with a 30 m HP-5 Ultra Inert column and a flame ionization detector (FID) and referenced to the internal standard mesitylene. A seven-point calibration curve for all analytes was established.

Induced-coupled-plasma mass spectrometry (ICP-MS) measurements

ICP-MS measurements of $Pd_{1-x}Ga_x$ colloids were performed on an Agilent Technologies 7900 ICP-MS instrument. Samples were prepared by evaporating all volatile compounds and dissolution of the remaining residue in concentrated 10 mL HNO_3. The samples were then diluted 1/20.000 over two dilution steps with ultra-pure water containing 1.625 % (v/v) HNO_3. Each solvent was extra pure and checked for possible analyte contaminations before measurement. ^{69}Ga and ^{105}Pd were used as target masses, ^{115}In was used as internal standard. Analyte quantification was carried out in He-CCT mode to avoid polyatomic interferences. Calibration was performed in the range of 0 ng L^{-1}–10 ng L^{-1}. Each sample was measured with five measurement replicates. The uncertainty was calculated via Gaussian error propagation, including pipetting as well as standard deviations of the measurement replicates. The Ga and Pd concentrations were blank corrected via measurement of blank samples.

Induced-coupled-plasma optical emission spectroscopy (ICP-OES) measurements

Elemental analysis of $Fe_{1-x}Al_x$ colloids was carried out via ICP-OES on an Agilent 700. For sample preparation, 0.1 mL of the colloidal solution was added to 15 mL of 3% HNO_3 solution. The solutions were filtered using 0.45 µm syringe filters (Pall). The multi-element standard IV (Merck) was used to prepare metal standard solutions for 1, 10 and 50 ppm metal

ion concentrations. Matrix interactions and metal signal interference were excluded. The wavelengths tracked for quantification were 396.152 nm (Al) and 238.204 nm (Fe). All data were averaged over five measurements.

High-resolution Transmission-Electron-Microscopy (HR-TEM)

HR-TEM samples were prepared by dropping a solution of $Pd_{1-x}Ga_x$ in toluene on carbon-coated Cu400 TEM grids. Samples were imaged by HR-TEM FEI TITAN Themis 60-300 equipped with X-FEG type emission gun operated at 300 kV, spherical aberration Cs image corrector improving resolution limit in TEM mode below 0.7 nm, high angle annular dark field detector (HAADF) for high atomic number (Z) -contrast in scanning transmission electron microscopy (STEM) and SUPER-X energy dispersive X-ray (EDX) spectrometer with 4x30 mm^2 windowless silicon drift detectors. Particle size determination was carried out using ImageJ (version 2019).

Scanning-Electron Microscopy (SEM)

SEM images are obtained with a Jeol JSM-7500F field emission scanning electron microscope in Gentle Beam mode. Pictures are analyzed with the supplier software.

X-ray Photoelectron Spectroscopy (XPS)

X-ray photoelectron spectra were recorded on a *Leybold-Heraeus* LHS 10 spectrometer using a non-monochromatized Al K_α source (1486.7 eV). The colloidal solutions were spin-coated on a Si wafer. Sample preparation and transfer into the XPS spectrometer were carried out under argon atmosphere. All spectra were recorded in an ultra-high vacuum chamber at a pressure below 5×10^{-8} mbar. The analyzer was operated at a constant pass energy of 100 eV leading to an energy resolution with a full width at half-maximum (fwhm) of ~1.1 eV. The energy scale of the spectra was corrected for sample charging by using the C 1s main signal (284.5 eV). Core level spectra were deconvoluted by using Voigt functions and linear (Ga 2p) or Shirley (Pd 3d) background subtraction. Deconvoluted components were assigned with respect to their binding energy to literature known values (Pd $3d_{5/2}$: 335.4 eV for metallic Pd, ~336.8 eV for PdO; Ga $2p_{3/2}$: 1116.5 eV for metallic Ga, ~1117.8 eV for Ga_2O_3).Depth profiling involved cycles of Ar^+ ion sputtering (2 keV kinetic energy, 1 µA sample current) and subsequent XPS analysis.

Sorption Measurements (BET)

N_2 sorption measurements were performed on outgassed samples (120 °C for minimum 12 h in vacuo, sample mass between 20 and 100 mg) using a 3Flex Physisorption Instrument from Micromeritics Instrument Corp. The latter uses the volumetric method to determine the amount of adsorbed gas and an equilibrated gas pressure. All samples were further activated

on a SmartVacPrep sample preparation station after initial activation on a standard Schlenk line. Dead volume of sample tubes was determined prior to adsorption measurements using He. Purity of the used gases was at 99.999 vol%. The sample cells were cooled with a liquid nitrogen bath (77 K) or an isopropanol/dry ice bath (195 K). Adsorption data were processed using the 3Flex Software Version 5.01 of Micromeritics Instrument Corp.

Temperature-programmed Desorption (TPD) measurements

All reactions and TPD experiments were conducted in a single-pass setup equipped with a glass-lined tubular fixed bed reactor with an inner diameter of 4 mm. A type-K thermocouple contacting the catalyst bed is used to regulate and record the temperature inside of the reactor. For all experiments, high purity gases were used (Ar 5.0, H_2 6.0, 5 % H_2/Ar 5.0 and a gas mixture of 5 % acetylene/5 % ethene/5 % ethane/Ar 5.0 from Linde-Gas, "Prüfgasklasse 1"). The required flow rates were adjusted by calibrated mass flow controllers (model 5850TR from Brooks Instrument®). The feed gas for the reaction was obtained by mixing H_2 and the acetylene containing gas in a mixing unit connected to the setup through a manifold. A pressure regulator (ER3000 from Tescom®) is used to build the required operating pressure. All gas lines downstream of the reactor are heated in order to prevent condensation of product gases. For time resolved product gas analysis, an Omnistar GSD 301 quadrupole mass spectrometer (QMS) from Pfeiffer Vacuum® was used.

For sample preparation, samples were handled, weighed (12-18 mg) and placed inside the reactor in an inert glove box and transferred to the experimental setup under inert gas atmosphere. Afterwards, the catalyst bed was secured in the isothermal zone of the reactor between two glass wool plugs. After installation of the reactor in the experimental setup (with the absence of O_2 at all times), the catalyst was treated in H_2 ($\dot{V}$ = 60 sccm) at p = 4 bar and T = 453 K for 3 h for the reduction step. After depressurizing, the sample was flushed in Ar ($\dot{V}$ = 100 sccm) and cooled down to room temperature. For catalysis experiments, subsequently a gas mixture of H_2 and acetylene/ethene/ethane was adjusted to a molar ratio of H_2/acetylene = 60/1 and passed through the reactor ($\dot{V}$ = 40 sccm). The temperature was set to 453 K and held for 4 h before cooling down to room temperature. A constant Ar flow ($\dot{V}$ = 15 sccm) ensured an inert gas atmosphere until further experiments were carried out.

For TPD experiments, the reduction step was repeated, as H_2 was again adsorbed at 453 K and 4 bar for 1 h ($\dot{V}$ = 60 sccm). After depressurizing and cooling down to room temperature, the catalyst was flushed in Ar ($\dot{V}$ = 100 sccm) for 30 min before the TPD was carried out in Ar ($\dot{V}$ = 100 sccm). For all TPD experiments, the temperature ramp was selected to 6 K/min. After the TPD experiment was finished, the final temperature was held until the H_2 signal showed again a constant baseline. Afterwards, the system was calibrated using 5 % H_2/Ar, flushed

with Ar and cooled down to room temperature. For all tested samples, at least five TPDs were recorded in series with varying end temperatures. In detail, the order was three times 453 K, 573 K and 753 K for $Fe_{0.33}Al_{0.67}$, $Fe_{0.5}Al_{0.5}$ and $Fe_{1.0}Al_{0.0}$ powders. For the $Fe_{1.0}Al_{0.0}$ powder sample, the TPD at 753 K was repeated at the end again. For evaluation, all signals obtained by mass spectrometry were normalized to the Ar signal.

Electron Paramagnetic Resonance measurements

EPR spectra were recorded on a JEOL JES-FA 200 at X-Band frequency (approx. 9.31 GHz). The microwave frequency was measured via a microwave frequency counter Advantest R5372. The spectra were corrected using an internal Mn^{2+} (I = 5/2) standard. The fourth low field line is taken as reference signal set to g = 1.981. Temperature was controlled using an ES-DVT4 variable temperature control unit. Samples were prepared using Suprasil EPR tubes with J-Young taps. The colloids were dissolved in mesitylene and the metal concentration was calculated to n = 0.7 mmol for all tested samples. The measurements were performed at 77 K and different microwave powers between 5-20 mW.

Superconducting Quantum Interference Device (SQUID) measurements

A MPMS XL5 SQUID magnetometer (Quantum Design) was used for magnetic measurements. Zero-field cooling measurements reveal the presence of small amounts of Sn through the characteristic transition temperature for the superconducting state of Sn, no further transition was observed.

Thermogravimetric analysis coupled with mass spectrometry (TGA-MS)

A TGA/STA 409 PC apparatus from *Mettler-Toledo Intl. Inc.* was used for thermogravimetric analysis under nitrogen as specified with a continuous heating ramp of 10 °C/min. The corresponding evaluation software was *STARe 14.00.* For mass spectrometry a *Thermostar* GSD 320 T from *Pfeiffer Vacuum GmbH* was connected to the setup enabling a correlation between mass change, the fragment responsible, and the temperature. Roughly 2 mg of sample were applied per measurement.

In-house EXAFS and XANES measurements

The Munich Compact Light Source (MuCLS) is a laboratory x-ray facility with two end-stations equipped with multi-purpose X-ray experimental setups.[130,131] The ICS source of the MuCLS is manufactured by Lyncean Technologies Inc., Fremont, USA. The ICS source comprises a short linear electron accelerator (LINAC), a small electron storage ring and a laser system containing a high-finesse enhancement cavity. The electrons are generated in an RF-photocathode at a rate of 25 Hz and get accelerated to relativistic speed in the LINAC. Afterwards, the electrons are injected into a miniature storage ring, which has a circumference

of 4.62 m. At the same time, two infrared (IR) laser pulses (Nd : YAG) are stored in a high-finesse bow-tie enhancement cavity (9.2 m length) with an average power of ~300 kW. At the interaction point, x-rays with a pulse length of ~60 ps are generated in a head-on collision of the electron bunch and the laser at a repetition rate of 64.9 MHz. Both, the electron bunch and the IR laser, are tightly focused on the interaction point, giving rise to x-ray source size of 50 μm rms. The divergence of the x-ray beam is confined to ~4 mrad by an aperture. The X-ray energy on axis for a head-on collision of electron and laser pulse is given by

$$E_x \approx 4\left(\frac{E_e}{m_e c^2}\right)^2 E_L$$

As the laser wavelength is fixed at 1064 nm, the x-ray energy can be tuned flexibly by adjusting the electron energy, where E_X, E_e and E_L are the energies of X-ray, electron and laser, respectively, m_e is the electron rest mass, and c is the speed of light in vacuum. Currently, the X-ray energies available at the MuCLS range from 15 to 35 keV, corresponding to electron energies between 25 and 45 MeV.

5.3 Synthetic Procedures and Characterization Details

5.3.1 Synthesis of the catalysts

Synthesis of thiol stabilized Pd@SR colloids

The Pd NPs were obtained by reduction of $K_2[PdCl_4]$ with $NaBH_4$ and in the presence of tetraoctylammonium bromide and sodium S-alkyl thiosulfate. The method is a variation of those proposed by Shon et al.[50] In a typical synthesis, 12.5 mL of a 20 mM aqueous solution of $K_2[PdCl_4]$ (65 mg, 0.2 mmol, 1.0 equiv.) was mixed with 25 mL of a 50 mM $N(Octyl)_4Br$ solution (547 mg, 1.0 mmol, 5.0 equiv.) in toluene. After 30min, the transfer of the $[PdCl_4]^{2-}$ from the aqueous solution to the organic phase was completed as revealed by the red color of the organic phase containing the $[PdCl_4]^{2-}/N(Octyl)_4Br$ mixture. The aqueous phase was disposed. The sodium S-alkyl thiosulfate (0.4 mmol, 2.0 equiv.) was dissolved in 10 mL of a H_2O/MeOH mixture (3:1) and added to the $[PdCl_4]^{2-}/N(Octyl)_4Br$ mixture. Afterwards, additional $N(Octyl)_4Br$ (547 mg, 1.0 mmol, 5.0 equiv.) was added to the reaction mixture. Then, 7.5 mL of a freshly prepared 0.4 M $NaBH_4$ (152 mg, 4.0 mmol, 20 equiv.) aqueous solution was added at 25 °C, keeping the mixture under vigorous stirring (1400 rpm). Consequently, the solution darkened immediately, indicating the formation of NPs. The mixture was stirred for 30 min at 25 °C and after removing the aqueous phase, all volatile compounds were removed in vacuo. The obtained Pd NPs were purified three times by the addition of 25 mL Ethanol and subsequent centrifugation at 7380 rpm.

DLS measurement: 0.7 ± 0.1 nm for both colloidal samples.

Synthesis of ionic stabilized Pd@N(Octyl)$_4$Br colloids

The Pd NPs were obtained by reduction of $K_2[PdCl_4]$ with $NaBH_4$ and subsequent stabilization with the capping agent tetraoctylammonium bromide ($N(Octyl)_4Br$). The method is a variation of those proposed by the Coronado et al.[55] In a typical synthesis, 5 mL of a 30 mM aqueous solution of $K_2[PdCl_4]$ (37 mg, 0.11 mmol, 1.0 equiv.) was mixed with 20 mL of a 50 mM $N(Octyl)_4Br$ solution (602 mg, 1.1 mmol, 10 equiv.) in toluene. After 30 min, the transfer of the $[PdCl_4]^{2-}$ from the aqueous solution to the organic phase was completed as revealed by the red color of the organic phase containing the $[PdCl_4]^{2-}/N(Octyl)_4Br$ mixture. The aqueous phase was disposed. Then, 6 mL of a freshly prepared 0.1 M $NaBH_4$ (11 mg, 0.285 mmol, 2.5 equiv.) aqueous solution was added at 60 °C, keeping the mixture under vigorous stirring

(1400 rpm). Consequently, the solution darkened immediately, indicating the formation of NPs. The mixture was stirred for 30 min at 25 °C and after removing the aqueous phase, the organic phase was washed with deionized water (3x50 mL) and finally dried over anhydrous Na_2SO_4. The samples were degassed under an atmosphere of purified argon.

^{1}H-NMR (400 MHz, C_6D_6): 3.5 (m, 2 H, NCH_2), 1.7 (dt, 2 H, NCH_2CH_2), 1.4 (m, 10 H, CH_2), 1.0 (t, 3 H, CH_3).
IR (ATR, neat, cm^{-1}): 720 (s), 753 (m), 1353 (m), 1466 (s), 2850 (s), 2871 (s), 2953 (m), 3004 (w).

Synthesis of bimetallic $Pd_{1-x}Ga_x$ colloids

The precursors [$Pd_2(dvds)_3$] and GaCp* were synthesized according to literature.[111] 20.0 mg (1.00 equiv., 25.9 µmol) [$Pd_2(dvds)_3$] were dissolved in 4 mL toluene at -20 °C. GaCp* was added, whereas the amount was adjusted to the respective Pd/Ga ratio. The yellow solution was then allowed to slowly warm up to 0 °C, changing colour from orange to a dark red solution. The colloids were stored under argon at -40 °C. For nanoparticle precipitation, the colloid solution was warmed up to 25 °C for one week yielding a black precipitate. After removal of the solvent and washing with hexane, the obtained nanoparticles were annealed in vacuum at 180 °C for 24 h for PXRD measurements.
For CO adsorption experiments, 2 mL of the colloidal solutions 2 mL were placed in a Fischer-Porter-Bottle and pressurized with 0.1 bar CO for 30 min at 25°C. The reaction mixture was then dropped on the IR instrument and dried until all solvent signals disappeared.

^{1}H NMR (400 MHz, toluene-d_8): 5.92 (m, 6H, dvds, C*H*, CH_2), 1.76 (m, Cp*H, 12H, CH_3), 0.97 (d, ^3J = 7.6 Hz, Cp*H, 3H, CH_3), 0.53 (q, ^3J = 8.0 Hz, Cp*H, 1H, C*H*), 0.18 (s, dvds, 12H, CH_3).

Calculations on $Pd_{0.5}Ga_{0.5}$ colloids with a size of 1.2 nm:

Volume of a particle consisting of Pd:Ga (1:1) V(PdGa), with the atomic radii r(Pd) = 196 pm and r(Ga) = 136 pm:

$$V(PdGa) = {}^4/_3\,\pi\left(\frac{r(Pd)+r(Ga)}{2}\right)^3 = 0.01525nm^3$$

Size of the $Pd_{0.5}Ga_{0.5}$ NP is d(NP) = 1.2 nm: r(NP) = 0.6 nm

$$V(NP) = {}^4/_3\,\pi(0.6\,nm)^3 = 0.9047nm^3$$

with a simplified assumption of a bcc structure with 74% of filling leading to V($NP_{0.74}$)

$$V(NP_{0.74}) = V(NP) \times 0.74 = 0.6695nm^3$$

$$Number\ of\ atoms\ in\ this\ NP\ = \frac{V(NP_{0.74})}{V(PdGa)} = \frac{0.6695nm^3}{0.0105nm^3} \approx 64$$

Stabilization of bimetallic $Pd_{1-x}Ga_x$ colloids with carboxylic acids

The precursors [$Pd_2(dvds)_3$], GaCp* as well as the $Pd_{1-x}Ga_x$ colloids were synthesized according to the procedure explained above. A stock solution (c = 0.14 mol/L) for each tested carboxylic acid was prepared. In detail, 24.2 mg of capric acid, 32.2 mg of myristic acid, and 40 mg of stearic acid were in each case dissolved in 1 mL of dry and degassed toluene-d_8. Different amounts of these stock solutions were then added to 200 µl of the $Pd_{1-x}Ga_x$ colloids solution, depending on the acid equivalents yielding different acid@$Pd_{1-x}Ga_x$ stock solutions (see Table 4). As the Pd amount is the same for all $Pd_{1-x}Ga_x$ NP, the amount of added acid stays the same independent on the Pd/Ga ratio.

Table 28. Exact volumes of acid stock solutions added to $Pd_{1-x}Ga_x$ colloids for different equivalents.

Acid equivalents (referred to the Pd amount)	Amount of added acid stock solution [µl]
0.2	3.7
0.5	9.25
1.0	18.5
1.5	27.75
2.0	37

^{1}H NMR (400 MHz, toluene-d_8): 10.2 (s, 1 H, $C_{18}H_{37}{}^{13}COOH$, COO*H*), 5.93 (m, 6H, dvds, C*H*, CH_2), 2.09 (m, 4 H, CH_2CH_2COOH), 1.76 (m, Cp*H, 12H, CH_3), 1.51 – 1.15 (m, 30 H, $C_{18}H_{37}{}^{13}COOH$, CH_2), 0.97 (d, Cp*H, 3H, CH_3), 0.93 (s, 3 H, $C_{18}H_{37}{}^{13}COOH$, CH_3), 0.53 (q, Cp*H, 1H, C*H*), 0.18 (s, dvds, 12H, CH_3).

^{13}C{^{1}H} NMR (101 MHz, toluene-d_8): 179.4 (1 C, $C_{18}H_{37}{}^{13}COOH$, *C*OOH), 140.0 (2 C, dvds, *C*H), 134.8 (4C, Cp*H, CH*C*CH$_3$, *C*CH$_3$), 132.7 (2 C, dvds, *C*H$_2$), 52.2 (1 C, Cp*H, *C*H), 34.6 (d, $^2J_{C-C}$ = 55.0 Hz, 1 C, $C_{18}H_{37}{}^{13}COOH$, *C*H$_2{}^{13}$COOH), 34.2 (1 C, $C_{18}H_{37}{}^{13}COOH$, CH$_3$CH$_2$*C*H$_2$), 32.8-29.8 (13 C, $C_{18}H_{37}{}^{13}COOH$, *C*H$_2$), 25.4 (1 C, $C_{18}H_{37}{}^{13}COOH$, *C*H$_2$CH$_2{}^{13}$COOH), 23.6 (1 C, $C_{18}H_{37}{}^{13}COOH$, CH$_3$*C*H$_2$), 14.7 (2C, Cp*H, *C*H$_3$), 12.9 (1C, Cp*H, *C*H$_3$)14.8 (1 C, $C_{18}H_{37}{}^{13}COOH$, CH$_3$), 11.6 (2 C, Cp*H, *C*H$_3$), 2.23 (4 C, dvds, *C*H$_3$).

Synthesis of bimetallic $Fe_{1-x}Al_x$ colloids

The precursors [Fe_2(mesityl)$_4$] and [AlH_3]−NMe_3 were synthesized according to literature a literature-reported synthesis protocol.[184–186] 200 mg [Fe_2(mesityl)$_4$] (0.34 mmol, 1.0 equiv.)

was dissolved in 5 mL mesitylene to give a deep red solution. Afterwards, the respective amount of $[AlH_3]-NMe_3$ (Fe/Al molar ratio 3/1, 1/1, 1/2) was added and the reaction mixture turned immediately black for all quantities of trimethylamine allane. Next, the solution was pressurized with 3 bar H_2 at 25 °C for 20 min. No further purification was performed.

Synthesis of bimetallic $Fe_{1-x}Al_x$ powders

The precursors $[Fe_2(mesityl)_4]$ and $[AlH_3]-NMe_3$ were synthesized according to a literature-reported synthesis protocol.[184–186] 600 mg $[Fe_2(mesityl)_4]$ (1.02 mol, 1.0 equiv.) was dissolved in 5 mL mesitylene to give a deep red solution. Afterwards, the respective amount of $[AlH_3]-NMe_3$ (Fe/Al molar ratio 3/1, 1/1, 1/2) was added and the reaction mixture turned immediately black for all quantities of trimethylamine allane. Next, the solution was pressurized with 3 bar H_2 at 180 °C for 24 h resulting in a complete precipitation of a black solid and a colourless solution. The solution was removed by filtration. The precipitate was washed twice with mesitylene and dried in vacuo.

Calculation of TPD surface area of all $Fe_{1-x}Al_x$ powders[187]:

TPD surface area $S_{Fe,all}$ and S_{Fe} in m^2/g

$$S_{Fe,all} = \frac{n_{H_2} \cdot N_A \cdot \zeta}{m_{\mathrm{cat}} \cdot n_{\mathrm{H,max}}}$$

$$S_{Fe} = S_{Fe,all} \cdot x_{Fe}$$

$S_{Fe,all}$: specific surface area if sample was entirely Fe(110)

S_{Fe}: specific surface area, only considering Fe(110) [171]

n_{H_2}: molar amount of adsorbed H_2 molecules

$n_{H,max}$: overall hydrogen saturation density ($n_{H,max} = 1{,}7^{19}\ \frac{H\ atoms}{m^2}$) [188]

N_A: Avogadro's constant ($N_A = 6.023\times10^{23}\ \frac{1}{mol}$)

ζ: stoichiometry factor ($\zeta = 2$, assuming dissociative chemisorption of H_2 on Fe) [188]

x_{Fe}: molar fraction of Fe in the Fe-Al catalyst

m_{cat}: mass of catalyst

5.3.2 Synthesis of additives

Synthesis of Sodium S-Alkyl thiosulfates

The sodium S-alkyl thiosulfates were synthesized by a variation of those proposed by Shon et al.[50] The respective 1-bromoalkane (25 mmol, 1.0 equiv.) was dissolved in 50 mL EtOH. 3.95 g $Na_2S_2O_3$ (25 mmol, 1.0 equiv.) was dissolved in 50 mL H_2O and mixed with the 1-bromoalkane solution. The reaction mixture was refluxed overnight, and all volatile compounds were removed in vacuo. For purification, the obtained solid was dissolved in 20 mL of hot EtOH and Whatman filtrated. The filtrate was slowly cooled down to 8 °C. The resulting precipitate was washed twice with cold EtOH and dried under vacuo.

Sodium S-octylthiosulfate:

^{1}H NMR (400 MHz, D_2O): 3.15 (t, 2H, CH_2), 1.80 (t, 2H, CH_2), 1.47 (m, 10H, CH_2), 0.91 (d, 3H, CH_3).

Sodium S-phenylethyl thiosulfate:

^{1}H NMR (400 MHz, D_2O): 7.40 (m, 5H, aromatic C*H*), 3.41 (t, 2H, CH_2), 3.15 (t, 2H, CH_2).

Synthesis of the isotopic labeled nonadecanoic acid $C_{18}{}^{13}CH_{38}O_2$

2.5 mL of octadecylmagnesiumchloride (1 M in THF, 2.5 mmol, 783 mg) and 50 mL degassed THF were placed in a Fischer-Porter bottle. The argon atmosphere was removed, and the reaction mixture was cooled down to -78°C and purged with 1.0 bar $^{13}CO_2$. After continuous stirring for 48 h, the reaction mixture was warmed up to -20 °C and stirred for further 24 h. Then, the reaction mixture is diluted with 100 mL toluene before careful addition of 100 mL of de-ionized water and 100 mL 1M HCl. After vigorous stirring for 20 min the organic phase was washed with 1M HCl (3 × 50 mL) and de-ionized water(2 × 50 mL). All volatile compounds were removed in vacuo and the product was obtained as a white powder. Yield: 630 mg, 2.13 mmol, 85%.

^{1}H NMR (400 MHz, toluene-d_8): 11.5 (s, 1 H, COO*H*), 2.09 (m, 4 H, CH_2CH_2COOH), 1.51-1.15 (m, 30 H, CH_2), 0.93 (s, 3 H, CH_3).

^{13}C{^{1}H} NMR (101 MHz, toluene-d_8): 179 (1 C, ^{13}*C*OOH), 34.6 (d, $^2J_{C\text{-}C}$ = 55.0 Hz, 1 C, *C*H$_2{}^{13}$COOH), 34.2 (1 C, $CH_3CH_2CH_2$), 32.8-29.8 (13 C, *C*H$_2$), 25.4 (1 C, *C*H$_2$CH$_2{}^{13}$COOH), 23.6 (1 C, CH_3CH_2), 14.8 (1 C, CH_3).

Anal. Calc. for $C_{18}{}^{13}CH_{38}O_2$: C 76.5, H 12.8, O 10.7, Found: C 75.6, H 12.3.

GC-MS (toluene, m/z): 299.3 (100%, calc. 299.3), 300.3 (20 %), 301.3 (2 %).

LIFDI-MS (toluene, m/z): 299.3 (100%, calc. 299.3), 300.3 (20 %), 301.3 (2 %).

IR (ATR, neat, cm^{-1}): 678 (b, $\delta(CH_2)$), 719 (s, $\delta(CH_2)$), 729 (s, $\delta(CH_2)$), 925 (b, δ(O-OH)), 1184-1320 (s, ν(C-O)), 1413 (m, δ(C-OH)), 1462 (s, δ(C-OH)), 1472 (s, δ(C-OH)), 1656 (s, ν_{as}(C=O)), 2500 – 3266 (b, ν(OH)), 2846 (s, $\nu(CH_2/CH_3)$), 2914 (s, $\nu(CH_2/CH_3)$), 2956 (w, $\nu(CH_2/CH_3)$).

5.4 Semi-hydrogenation catalysis Procedures

5.4.1 Ionic stabilized Pd@N(Octyl)$_4$Br colloids

All catalysis experiments were carried out under inert atmosphere and n-dodecane was chosen as internal standard. For semi-hydrogenation experiments, 0.9 mL of the NP solution (1 mol% catalyst in toluene), 0.1 mL substrate (1-octyne, 2-octyne, phenyl acetylene) and 0.1 mL dodecane were placed in a 90 mL Fischer Porter bottle and cooled to 0 °C. This solution was purged with 1.0 bar H_2 and continuously stirred for 5 h. For GC measurements, aliquots were taken under a continuous argon flow. After taking of aliquots, the Fischer Porter bottle was again purged with 1.0 bar H_2.

For recycling experiments, all liquids were removed in high vacuum and fresh solvent and substrate was added. For quantification of the oligomerization products, all low-boiling components were evaporated at reduced pressure and Pd@TOAB was removed by filtration of the residue over SiO_2 in hot toluene. LIFDI-MS measurements were carried out for an exact determination of the residue components.

Error calculation

c = conversion, y = yield, s = selectivity (all denoted in %)

$$s = \frac{y}{c}$$

$$\Delta s = \sqrt{\left(\frac{\partial s}{\partial c} \cdot \Delta c\right)^2 + \left(\frac{\partial s}{\partial y} \cdot \Delta y\right)^2}$$

Table 29. Example for an error calculation for the selectivities using 1 mol% Pd@N(Octyl)$_4$Br at 0 °C and 1.0 bar H_2 without any additive assuming an instrumental GC inaccuracy of 1%.

Time [h]	c	Δc	y	Δy	s	$\left(\frac{\partial s}{\partial c} \cdot \Delta c\right)$	$\left(\frac{\partial s}{\partial y} \cdot \Delta y\right)$	Δs (percentaged)	Δs (absolute)
1	16	0.16	16	0.16	100	0.01	0.01	0.0141	1.41
2	33	0.33	30	0.33	91	0.0091	0.0091	0.0129	1.17
3	54	0.54	44	0.44	81	0.0081	0.0081	0.0115	0.93
4	77	0.77	50	0.5	65	0.0065	0.0065	0.0092	0.6
5	100	1	22	0.22	22	0.0022	0.0022	0.00311	0.068

The highest error of the selectivity of $\Delta s = \pm 1.41\%$ is too low to have an influence on the interpretation of the following catalytic test and therefore were not considered.

5.4.2 $Pd_{1-x}Ga_x$ colloids

All catalysis experiments were carried out under inert atmosphere and mesitylene was chosen as internal standard. For semi-hydrogenation experiments, 0.4 mL of the Pd NP solution (5 mol% catalyst in toluene-d_8), and 0.1 mL of a stock solution (alkyne and mesitylene in toluene-d_8) were placed in a pressure NMR tube. This solution was degassed and purged with 2.0 bar H_2 gas and continuously monitored by *in situ* ^{1}H NMR spectroscopy at 0 °C. For recycling experiments, all liquids were removed in high vacuum and fresh solvent and substrate were added. The same procedure was used for the semi-hydrogenation catalysis using $Pd_{1-x}Ga_x$ colloids and PPh_3 as post-synthetic additive.

^{1}H NMR (400 MHz, toluene-d_8): 7.11-6.98 (m, residual signal of toluene-d_8), 6.68 (s, 3H, internal standard mesitylene, CH), 5.92 (m, 6H, dvds, C*H*, CH_2), 4.97 (t, 2H, 3-hexene, C*H*), 2.15 (s, 9H, internal standard mesitylene, CH_3), 1.92 (m, 4H, 3-hexene, CH_2), 1.76 (m, Cp*H, 12H, CH_3), 1.25 (m, 8H, *n*-hexane, CH_2), 1.01 (t, 6H, 3-hexyne, CH_3), 0.91 (t, 6H, 3-hexene, CH_3), 0.79 (t, 6H, *n*-hexane, CH_3), 0.53 (q, ^3J = 8.0 Hz, Cp*H, 1H, C*H*), 0.18 (s, dvds, 12H, CH_3).

Calculation of reaction rates

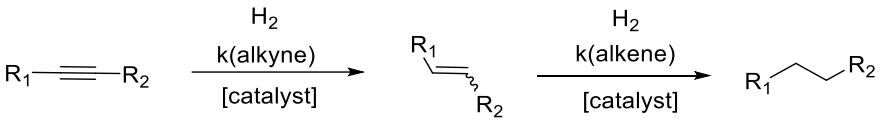

$$r = \frac{dc(alkyne)}{dt} = k(alkyne) \cdot c(alkyne)$$

Table 30. Calculated ratio of the rate constants k(alkyne) and k(alkene). Catalytic tests were performed using 5 mol% $Pd_{0.67}Ga_{0.33}$ as catalyst with 3-hexyne as substrate at 0°C and 2.0 bar H_2.

Reaction time [h]	$\frac{\mathbf{k(alkyne)}}{\mathbf{k(alkene)}}$
1 → 2	2.873
2 → 3	2.932
3 → 4	2.918
4 → 5	2.635
5 → 6	2.706
6 → 7	2.062

Table 31. Calculated ratio of the rate constants k(alkyne) and k(alkene). Catalytic tests were performed using 5 mol% $Pd_{0.5}Ga_{0.5}$ as catalyst with 3-hexyne as substrate at 0°C and 2.0 bar H_2.

Reaction time [h]	$\frac{\mathbf{k(alkyne)}}{\mathbf{k(alkene)}}$
1 → 2	3.253
2 → 3	3.193
3 → 4	3.238
4 → 5	3.162
5 → 6	2.678
6 → 7	2.348

Calculation of the TOF values

Calculation of TOF values: $\text{TOF } [h^{-1}] = \frac{\text{conversion (after 1 h)} \times n_0(\text{alkyne})}{n(\text{cat}) \times 1\ \text{h}}$

whereas $n(\text{cat}) = \frac{n(\text{all Pd}) \times 0{,}764\ (\text{Pd surface atoms})}{\text{Pd/Ga ratio}}$

The amount of Pd surface atoms was calculated based on the model of magic cluster numbers, with a Pd NP diameter of 1.5 nm. Here, in a monometallic Pd NP 76.4% of all Pd atoms are located on the surface. This value was then approximated to the corresponding Pd/Ga ratio; etc. for Pd/Ga = 1:1, the amount of active Pd atoms on the surface was divided by the factor 2. It must be mentioned that this calculation is only an approximation, as the core-shell structure of the particles was not considered, why the amount of active Pd surface atoms is rather overestimated and therefore the TOF value underestimated.

Table 32. Calculation of TOF values using 5mol% $Pd_{1-x}Ga_x$, 1 bar H_2 at 0 °C.

Entry	**Conversion**	**n_0(alkyne) [mol]**	**n(cat) [mol]**	**TOF [h^{-1}]**
$Pd_{0.67}Ga_{0.33}$, 3-hexyne	0.26	0.0000277	5.72×10^{-8}	126
$Pd_{0.5}Ga_{0.5}$, 3-hexyne	0.24	0.0000277	4.33×10^{-8}	153
$Pd_{0.33}Ga_{0.67}$, 3-hexyne	0.05	0.0000277	3.49×10^{-8}	40
$Pd_{0.67}Ga_{0.33}$, 4-octyne	0.30	0.0000277	5.72×10^{-8}	146
$Pd_{0.5}Ga_{0.5}$, 4-octyne	0.24	0.0000277	4.33×10^{-8}	155
$Pd_{0.67}Ga_{0.33}$, 1-hexyne	0.05	0.0000277	5.72×10^{-8}	24
$Pd_{0.5}Ga_{0.5}$, 1-hexyne	0.03	0.0000277	4.33×10^{-8}	19
$Pd_{0.33}Ga_{0.67}$, 1-hexyne	0.01	0.0000277	3.49×10^{-8}	10

5.4.3 $Pd_{1-x}Ga_x$@carboxylic acids

All catalysis experiments were carried out under inert atmosphere using *n*-dodecane as internal standard. For semi-hydrogenation experiments, 200 µl of the acid@$Pd_{1-x}Ga_x$ colloid solution and 50 µl of a stock solution (30 µl alkyne and 3 µl *n*-dodecane in 3 mL toluene-d_8) were mixed and out of this solution 50 µl placed in a pressure NMR tube, which was used as batch reactor, degassed and purged with 1.0 bar H_2 gas. The catalysis was stopped after a specific time (1 h – 5 h) and analyzed by GC measurements.

Error calculation

Error calculations assuming an instrumental GC inaccuracy of 1 % due to a small overlapping of substrate and product signals showed that all calculated error bars on both conversion and selectivity are too small to be considered (see error calculation for monometallic Pd@$N(Octyl)_4Br$ colloids) and have no impact on the following interpretation of the catalytic results.

c = conversion, y = yield, s = selectivity (all denoted in %)

$$s = \frac{y}{c}$$

$$\Delta s = \sqrt{\left(\frac{\partial s}{\partial c} \cdot \Delta c\right)^2 + \left(\frac{\partial s}{\partial y} \cdot \Delta y\right)^2}$$

$$\Rightarrow \frac{\Delta s}{s} = \sqrt{\left(\frac{\Delta c}{c}\right)^2 + \left(\frac{\Delta y}{y}\right)^2} = 1.4\%$$

The relative error of the selectivity of Δs/s = 1.41% is too low to have an influence on the interpretation of the following catalytic test and therefore was not considered.

Calculation of the TOF values

The amount of Pd surface atoms was calculated based on the model of magic cluster numbers assuming a perfect icosahedral NP structure. For instance, in the case of a monometallic Pd NP diameter with a diameter of 1.5 nm, 76.4% of all Pd atoms are located on the surface. In this work, for the calculation of the percentage of surface atoms, we calculated the number of surface atoms taking the Pd/Ga into account ratio (and hence the

average atomic diameter). We further assumed a homogeneous distribution of Pd and Ga, which is, according to XPS measurements, not the case (Ga-rich surface, Pd-rich core). Thus the amount of active Pd surface atoms is rather overestimated and therefore the TOF value underestimated. Further, we validated the calculated TOF values by an additional calculation based on the standard deviation of the colloid size obtained by HR-TEM measurements including the minimum and maximum size of the respective colloids. For example, in the case of $Pd_{0.5}Ga_{0.5}$@acids with a size of 2.1±0.9 nm (average TOF value: 2570 h^{-1}), TOF values for NPs with 2.0 nm (2830 h^{-1}) and 2.2 nm (2370 h^{-1}) were calculated. It turned out that the range of TOF values is ±10 % from the average value. In the discussion, only the average TOF value is therefore considered.

Table 33. Calculation of TOF values using 2.5 mol% $Pd_{1-x}Ga_x$ upon addition of various additives (1.0 equiv. additive referred to Pd). Conversion after 10 min were taken for calculation.

Sample	Conditions	Conversion	n_0(alkyne) [mol]	n(cat) [mol]	TOF [h^{-1}]
$Pd_{0.67}Ga_{0.33}$@stearic acid[a]	1.0 bar H_2, 0°C	0.48	9,2697E-06	8,5734E-09	3110
$Pd_{0.5}Ga_{0.5}$@stearic acid[a]	1.0 bar H_2, 0°C	0.3	9,2697E-06	6,495E-09	2570
$Pd_{0.33}Ga_{0.67}$@stearic acid[a]	1.0 bar H_2, 0°C	0.17	9,2697E-06	5,2371E-09	1810
$Pd_{0.33}Ga_{0.67}$@stearic acid[a]	1.0 bar H_2, 25°C	0.1	9,2697E-06	5,2371E-09	1060
$Pd_{0.33}Ga_{0.67}$@stearic acid[a]	0.5 bar H_2, 0°C	0.04	9,2697E-06	5,2371E-09	430
$Pd_{0.33}Ga_{0.67}$@stearic acid[a]	2.0 bar H_2, 0°C	0.22	9,2697E-06	5,2371E-09	2340
$Pd_{0.33}Ga_{0.67}$@stearic acid, O_2[a]	1.0 bar H_2, 0°C	0.21	9,2697E-06	5,2371E-09	2330
$Pd_{0.33}Ga_{0.67}$ [a]	1.0 bar H_2, 0°C	0.13	9,2697E-06	5,2371E-09	1380
$Pd_{0.33}Ga_{0.67}$@decanoic acid[a]	1.0 bar H_2, 0°C	0.18	9,2697E-06	5,2371E-09	1910
$Pd_{0.33}Ga_{0.67}$@mystiric acid[a]	1.0 bar H_2, 0°C	0.19	9,2697E-06	5,2371E-09	2020
$Pd_{0.33}Ga_{0.67}$@stearic acid[b]	1.0 bar H_2, 0°C	0.6	9,2697E-06	5,2371E-09	6370
$Pd_{0.33}Ga_{0.67}$@stearic acid[c]	1.0 bar H_2, 0°C	0.48	9,2697E-06	5,2371E-09	5100

[a] 2-octyne as substrate

[b] 1-octyne as substrate

[c] phenylacetylene as substrate

5.4.4 $Fe_{1-x}Al_x$ colloids

All catalysis experiments were carried out under inert atmosphere. For semi-hydrogenation experiments, 0.4 mL of a stock solution (3 mL toluene-d8, 118.5 µL 3-hexyne, 38 µL mesitylene) was added to 100 µL of the colloidal $Fe_{1-x}Al_x$ solution (as synthesized) in a pressure J-Young NMR tube, degassed and purged with H_2 gas. The catalysis was stopped after 24 h by filtration of the reaction solution under air in order to remove all metal content and analyzed by ^{1}H NMR spectroscopy.

5.4.5 $Fe_{1-x}Al_x$ powders (liquid alkynes in solution, batch reactor set up)

All catalysis experiments were carried out under inert atmosphere. For semi-hydrogenation experiments, 0.4 mL of a stock solution (3 mL toluene-d8, 306 µL 3-hexyne, 99 µL mesitylene) was added to 3 mg $Fe_{1-x}Al_x$ (as synthesized) in a pressure J-Young NMR tube, degassed and purged with H_2 gas. The catalysis was stopped after a certain time (1 - 24 h) by filtration of the reaction solution under air in order to remove all metal content and analyzed by ^{1}H NMR spectroscopy.

5.4.6 $Fe_{1-x}Al_x$ powders (acetylene, flow reactor set up)

All catalysis experiments were carried out under inert atmosphere. For catalysis experiments, subsequently a gas mixture of H_2 and acetylene/ethene/ethane was adjusted to a molar ratio of H_2/acetylene = 60/1 and passed through the reactor ($\dot{V}$ = 40 sccm). The temperature was set to 453 K and held for 4 h before cooling down to room temperature. A constant Ar flow ($\dot{V}$ = 15 sccm) ensured an inert gas atmosphere until further experiments were carried out.

Calculation of the conversions and selectivities

The signals of the detected masses m/z = 30 (ethane), 28 (ethene) and 26 (acetylene) were normalized and value for each compound before and after the catalysis was defined to be 5 %. The thereof resulting concentrations during catalysis were used for the calculation of the acetylene conversion and the selectivity towards the olefin (with the assumption of no further byproducts).

6 References

[1] A. Borodziński, G. C. Bond, *Catalysis Reviews* **2006**, *48*, 91.

[2] M. L. Derrien, *Studies in Surface Science and Technologies* **1986**, *27*, 613.

[3] Á. Molnár, A. Sárkány, M. Varga, *Journal of Molecular Catalysis A: Chemical* **2001**, *173*, 185.

[4] L. Kniel, O. Winter, K. Stork, *Chem. Industries Series* **1980**, *2*, 173.

[5] Kumar, Kaushik and Davim, J. Paulo, *Polymers and Composites Manufacturing*, Berlin, Boston: De Gruyter **2020**, 169.

[6] S. L. Aggarwal, O. J. Sweeting, *Chemical Reviews* **1957,** *57*, 665.

[7] A. Graziano, S. Jaffer, M. Sain, *Journal of Elastomers & Plastics* **2019**, *51*, 291.

[8] J. Sheridan, *Journal of Chemical Society* **1945**, 470.

[9] K. Tamaru, *Bulletin of the Chemical Society of Japan* **1950**, 23, 64.

[10] A. Borodziński, G. C. Bond, *Catalysis Reviews* **2008**, *50*, 379.

[11] A. Doyle, *Journal of Catalysis* **2004**, *223*, 444.

[12] F. Studt, F. Abild-Pedersen, T. Bligaard, R. Z. Sørensen, C. H. Christensen, J. K. Nørskov, *Science* **2008**, *320*, 1320.

[13] a) A. N. R. Bos, K. R. Westerterp, *Chemical Engineering and Processing: Process Intensification* **1993**, *32*, 1; b) A. S. Al-Amar, G. Webb, *Journal of Chemical Society, Faraday Transaction 1* **1979**, *75*, 1900.

[14] I. Horiuti, M. Polanyi, *Journal of Chemical Society, Faraday Transactions* **1934**, *30*, 1164.

[15] G. Wilke, B. Bogdanovic, P. Borner, H. Breil, P. Hardt, P. Heimbach, G. Herrmann, H.-J. Kaminsky, W. Keim, M. Kröner, H. Müller, E. W. Müller, W. Oberkirch, J. Schneider, J. Stedefeder, K. Tanaka, K. Weyer, G. Wilke, *Angewandte Chemie International Edition* **1963**, *2*, 105.

[16] B. Bogdanovlć in *Advances in Organometallic Chemistry*, Elsevier, **1979**, 105.

[17] A. Borodziński, A. Gołębiowski, *Langmuir* **1997**, *13*, 883.

[18] D. Duca, F. Arena, A. Parmaliana, G. Deganello, *Applied Catalysis A: General* **1998**, *172*, 207.

[19] M. Hu, J. Zhang, W. Zhu, Z. Chen, X. Gao, X. Du, J. Wan, K. Zhou, C. Chen, Y. Li, *Nano Research* **2018**, *11*, 905.

[20] M. M. Telkar, C. V. Rode, R. V. Chaudhari, S. S. Joshi, A. M. Nalawade, *Applied Catalysis A: General* **2004**, *273*, 11.

[21] M. Crespo-Quesada, F. Cárdenas-Lizana, A.-L. Dessimoz, L. Kiwi-Minsker, *ACS Catal.* **2012**, *2*, 1773.

[22] A. Yarulin, I. Yuranov, F. Cárdenas-Lizana, P. Abdulkin, L. Kiwi-Minsker, *J. Phys. Chem. C* **2013**, *117*, 13424.

[23] G. Vilé, D. Baudouin, I. N. Remediakis, C. Copéret, N. López, J. Pérez-Ramírez, *ChemCatChem* **2013**, *5*, 3750.

[24] N. López, C. Vargas-Fuentes, *Chemical communications* **2012**, *48*, 1379.

[25] D. Teschner, J. Borsodi, A. Wootsch, Z. Révay, M. Hävecker, A. Knop-Gericke, S. D. Jackson, R. Schlögl, *Science* **2008**, *320*, 86.

[26] D. Mei, M. Neurock, C. M. Smith, *Journal of Catalysis* **2009**, *268*, 181.

[27] D. Mei, P. Sheth, M. Neurock, C. Smith, *Journal of Catalysis* **2006**, *242*, 1.

[28] J. D. Krooswyk, I. Waluyo, M. Trenary, *ACS Catalysis* **2015**, *5*, 4725.

[29] a) A. Gosh, K. Krishnan, *Tetrahedron Letters* **1998**, *39*, 947; b) J. G. Ulan, E. Kuo, W. F. Meier, R. S. Rai, G. Thomas, *Journal of Organic Chemistry* **1987**, *52*, 3126.

[30] a) Q. Zhang, J. Li, X. Liu, Q. Zhu, *Applied Catalysis A: General* **2000**, *197*, 221; b) A. J. McCue, J. A. Anderson, *Frontiers of Chemical Science and Engineering* **2015**, *9*, 142.

[31] C. E. Gigola, H. R. Aduriz, P. Bodnariuk, *Applied Catalysis* **1986**, *27*, 133.

[32] N. K. Nag, *Journal of Physical Chemistry B* **2001**, *105*, 5945.

[33] S. B. Ziemecki, J. B. Michel, G. A. Jones, *Reactivity of Solids* **1986**, *2*, 187.

[34] a) Á. Mastalir, Z. Király, F. Berger, *Applied Catalysis A: General* **2004**, *269*, 161; b) X. Huang, Y. Xia, Y.Cao, *Nano Research* **2017**, *10*, 1302; c) G. X. Pei, X. J. Liu, A. Wang, A. F. Lee, M. A. Isaacs, L. Li, X. Pan, X. Yang, X. Wang, Z. Thai, K. Wilson, T. Zhan, *ACS Catalysis* **2015**, *5*, 3717; d) M. Jorgensen, H. Grönbeck, *Journal of American Chemical Society* **2019**, *141*, 8541.

[35] a) N. Semagina, L. Kiwi-Minsker, *Catalysis Letters* **2009**, *127*, 334; b) N. Semagina, A. Renken, D. Laub, L. Kiwi-Minsker, *Journal of Catalysis* **2007**, *246*, 308.

[36] M. Crespo-Quesada, A. Yarulin, M. Jin, Y. Xia, L. Kiwi-Minsker, *Journal of the American Chemical Society* **2011**, *133*, 12787.

[37] J. A. Delgado, O. Benkirane, C. Claver, D. Curulla-Ferré, C. Godard, *Dalton transactions* **2017**, *46*, 12381.

[38] A. Roucoux, J. Schulz, H. Patin, *Chemical reviews* **2002**, *102*, 3757.

[39] C. Evangelisti, N. Panziera, A. D'Alessio, L. Bertinetti, M. Botavina, G. Vitulli, *Journal of Catalysis* **2010**, *272*, 246.

[40] a) G. Vilé, N. Almora-Barrios, S. Mitchell, N. López, J. Pérez-Ramírez, *Chemistry* **2014**, *20*, 5926; b) P. T. Witte, P. H. Berben, S. Boland, E. H. Boymans, D. Vogt, J. W. Geus, J. G. Donkervoort, *Topics in Catalysis* **2012**, *55*, 505.

[41] D. Albani, G. Vilé, S. Mitchell, P. T. Witte, N. Almora-Barrios, R. Verel, N. López, J. Pérez-Ramírez, *Catalysis Science and Technology* **2016**, *6*, 1621.

[42] J. B. Ernst, C. Schwermann, G.-I. Yokota, M. Tada, S. Muratsugu, N. L. Doltsinis, F. Glorius, *Journal of the American Chemical Society* **2017**, *139*, 9144.

[43] C. Richter, K. Schaepe, F. Glorius, B. J. Ravoo, *Chemical communications* **2014**, *50*, 3204.

[44] R. Venkatesan, M. H. G. Prechtl, J. D. Scholten, R. P. Pezzi, G. Machado, J. Dupont, *Journal of Materials Chemistry* **2011**, *21*, 3030.

[45] B. C. Leal, C. S. Consorti, G. Machado, J. Dupont, *Catalysis Science and Technology* **2015**, *5*, 903.

[46] K. L. Luska, A. Moores, *Advanced Synthesis and Catalysis* **2011**, *353*, 3167.

[47] C. S. Consorti, G. L. P. Aydos, G. Ebeling, J. Dupont, *Organic letters* **2008**, *10*, 237.

[48] M. S. Maung, Y.-S. Shon, *The journal of physical chemistry. C, Nanomaterials and interfaces* **2017**, *121*, 20882.

[49] P. Wand, E. Kratzer, U. Heiz, M. Cokoja, M. Tschurl, *Catalysis Communications* **2017**, *100*, 85.

[50] D. J. Gavia, Y.-S. Shon, *Langmuir : the ACS journal of surfaces and colloids* **2012**, *28*, 14502.

[51] T.-A. Chen, Y.-S. Shon, *Catalysis Science and Technology* **2017**, *7*, 4823.

[52] K. A. San, V. Chen, Y.-S. Shon, *ACS Applied Materials and Interfaces* **2017**, *9*, 9823.

[53] K. Murugesan, C. B. Bheeter, P. R. Linnebank, A. Spannenberg, J. N. H. Reek, R. V. Jagadeesh, M. Beller, *ChemSusChem* **2019**, *12*, 3363.

[54] M. Guo, H. Li, Y. Ren, X. Ren, Q. Yang, C. Li, *ACS Catalysis* **2018**, *8*, 6476.

[55] a) E. Coronado, A. Ribera, J. García-Martínez, N. Linares, L. M. Liz-Marzán, *Journal of Materials Chemistry* **2008**, *18*, 5682; b) S. Buchner, J. Hormes, H. Modrow, R. Brinkmann, N. Waldöfner, H. Bönnemann, L. Beuermann, S. Krischok, W. Maus-Friedrichs, V. Kempter, *Surface Science* **2002**, *497*, 321.

[56] C. N. Thanh, B. Didillon, P. Sarrazin, C. Cameron *United States Patent No. 6054409*, **2000**.

[57] H. Bönnemann, R. M. Richards, *European Journal of Inorganic Chemistry* **2001**, *2001*, 2455.

[58] Z.-P. Liu, P. Hu, *Journal of the American Chemical Society* **2003**, *125*, 1958.

[59] M. Krajčí, J. Hafner, *Journal of Physical Chemistry C* **2014**, *118*, 12285.

[60] A. V. Yakutovich, J. Hoja, D. Passerone, A. Tkatchenko, C. A. Pignedoli, *Journal of the American Chemical Society* **2018**, *140*, 1401.

[61] J. T. Wehrli, D. J. Thomas, M. S. Wainwright, D. L. Trimm*, N. W. Cant, *Applied Catalysis* **1991**, *70*, 253.

[62] K. Kovnir, M. Armbrüster, D. Teschner, T. V. Venkov, F. C. Jentoft, A. Knop-Gericke, Y. Grin, R. Schlögl, *Science and Technology of Advanced Materials* **2007**, *8*, 420.

[63] K. Kovnir, M. Armbrüster, D. Teschner, T. V. Venkov, L. Szentmiklósi, F. C. Jentoft, A. Knop-Gericke, Y. Grin, R. Schlögl, *Surface Science* **2009**, *603*, 1784.

[64] M. Armbrüster, K. Kovnir, M. Behrens, D. Teschner, Y. Grin, R. Schlögl, *Journal of the American Chemical Society* **2010**, *132*, 14745.

[65] a) J. Osswald, R. Giedigkeit, R. Jentoft, M. Armbrüster, F. Girgsdies, K. Kovnir, T. Ressler, Y. Grin, R. Schlögl, *Journal of Catalysis* **2008**, *258*, 210; b) J. Osswald, K. Kovnir, M. Armbrüster, R. Giedigkeit, R. Jentoft, U. Wild, Y. Grin, R. Schlöfl, *Journal of Catalysis* **2008**, *258*, 219.

[66] J. Prinz, C. A. Pignedoli, Q. S. Stöckl, M. Armbrüster, H. Brune, O. Gröning, R. Widmer, D. Passerone, *Journal of the American Chemical Society* **2014**, *136*, 11792.

[67] Y. Grin, M. Armbrüster, A. I. Baranov, K. Finzel, M. Kohout, A. Ormeci, H. Rosner, F. R. Wagner, *Molecular Physics* **2016**, *114*, 1250.

[68] M. Armbrüster, G. Wowsnick, M. Friedrich, M. Heggen, R. Cardoso-Gil, *Journal of the American Chemical Society* **2011**, *133*, 9112.

[69] A. García-Trenco, E. R. White, A. Regoutz, D. J. Payne, M. S. P. Shaffer, C. K. Williams, *ACS Catal.* **2017**, *7*, 1186.

[70] A. Ota, M. Armbrüster, M. Behrens, D. Rosenthal, M. Friedrich, I. Kasatkin, F. Girgsdies, W. Zhang, R. Wagner, R. Schlögl, *Journal of Physical Chemistry C* **2011**, *115*, 1368.

[71] A. Ota, J. Kröhnert, G. Weinberg, I. Kasatkin, E. L. Kunkes, D. Ferri, F. Girgsdies, N. Hamilton, M. Armbrüster, R. Schlögl, *ACS Catalysis* **2014**, *4*, 2048.

[72] a) P. Sabatier, *Berichte der deutschen chemischen Gesellschaft* **1911**, *44* ,1984; b) Y. Nitta, S. Matsugi, T. Imanaka, *Catalysis Letters* **1990**, *5,* 67; c) S. Taira, *Bulletin of Chemical Society of Japan* **1962**, *35*, 844; d) A. F. Thompson, S. B. Wyatt, *Journal of American Chemical Society* **1940**, *62*, 2555.

[73] P.-H. Phua, L. Lefort, J. A. F. Boogers, M. Tristany, J. G. de Vries, *Chemical communications* **2009**, 3747.

[74] M. Armbrüster, K. Kovnir, M. Friedrich, D. Teschner, G. Wowsnick, M. Hahne, P. Gille, L. Szentmiklósi, M. Feuerbacher, M. Heggen, *Nature Materials* **2012**, *11*, 690.

[75] X. Li, A. Scherf, M. Heilmaier, F. Stein, *Journal of Phase Equilibria and Diffusion* **2016**, *37*, 162.

[76] J. Grin, U. Burkhardt, M. Ellner, *Zeitschrift für Kristallographie - Crystalline Materials* **1994**, *209*, 479.

[77] A. Yarulin, I. Yuranov, F. Cárdenas-Lizana, D. T. Alexander, L. Kiwi-Minsker, *Applied Catalysis A: General* **2014**, *478*, 186.

[78] C. F. Calver, P. Dash, R. W. J. Scott, *ChemCatChem* **2011**, *3*, 695.

[79] L. S. Ott, R. G. Finke, *Coordination Chemistry Reviews* **2007**, *251*, 1075.

[80] M. H. G. Prechtl, *Nanocatalysis in Ionic Liquids*, Wiley-VCH Verlag GmbH & Co. KGaA, Weinheim, Germany, **2016**.

[81] D. J. Gavia, Y.-S. Shon, *ChemCatChem* **2015**, *7*, 892.

[82] J. L. Fiorio, E. C. M. Barbosa, D. K. Kikuchi, P. H. C. Camargo, M. Rudolph, A. S. K. Hashmi, L. M. Rossi, *Catal. Sci. Technol.* **2020**, *10*, 1996.

[83] a) M. Cargnello, N. L. Wieder, T. Montini, R. J. Gorte, P. Fornasiero, *Journal of the American Chemical Society* **2010**, *132*, 1402; b) J. Simard, C. Briggs, A. K. Boal, V. M. Rotello, *Chemical Communications* **2000**, 1943; c) E. Sadeghmoghaddam, C. Lam, D. Choi, Y.-S. Shon, *Journal of Materials Chemistry* **2011**, *21*, 307.

[84] S. E. Eklund, D. E. Cliffel, *Langmuir : The ACS journal of surfaces and colloids* **2004**, *20*, 6012.

[85] A. C. Templeton, W. P. Wuelfing, R. W. Murray, *Accounts of Chemical Research* **2000**, *33*, 27.

[86] F. Mäsing, X. Wang, H. Nüsse, J. Klingauf, A. Studer, *Chemistry* **2017**, *23*, 6014.

[87] a) T. O. Ely, C. Amiens, B. Chaudret, E. Snoeck, M. Verelst, M. Respaud, J.-M. Broto, *Chemistry of Materials* **1999**, *11*, 526; b) J. S. Bradley, W. Busser, *Catalysis Letters* **1999**, *63,* 127; c) H. Hirai, Y. Nakao, N. Toshima, *Journal of Macromolecular Science: Part A - Chemistry* **1979**, *13*, 727; d) W. Yu, M. Liu, H. Liu, J. Zheng, *Journal of Colloid and Interface Science* **1999**, *210*, 218.

[88] a) Y. Huang, J. Chen, H. Chen, R. Li, Y. Li, L. Min, X. Li, *Journal of Molecular Catalsis A: Chemical* **2001**, *170*, 143. b) Y. Huang, Y. Li, J. Hu, P. Cheng, H. Chen, R. Li, X. Li, C. W. Yip, A. S. C. Chan, *Journal of Molecular Catalysis A: Chemical* **2002**, *189*, 219.

[89] a) S. Bucher, J. Hormes, H. Modrow, R. Brinkmann, N. Waldöfner, H. Bönnemann, L. Beuermann, S. Krischok, W. Maus-Friedrichs, V. Kemptner, *Surface Science* **2002**, *497,* 321; b) E. J. W. Verwey, *Journal of Physical Chemistry* **1947**, *51,* 631.

[90] K. Kusada, D. Wu, H. Kitagawa, *Chemistry* **2020**, *26*, 5105.

[91] K. Kusada, H. Kitagawa, *Advanced materials* **2016**, *28*, 1129.

[92] K. Kusada, H. Kobayashi, R. Ikeda, Y. Kubota, M. Takata, S. Toh, T. Yamamoto, S. Matsumura, N. Sumi, K. Sato et al., *Journal of the American Chemical Society* **2014**, *136*, 1864.

[93] Q. Zhang, K. Kusada, D. Wu, N. Ogiwara, T. Yamamoto, T. Toriyama, S. Matsumura, S. Kawaguchi, Y. Kubota, T. Honma et al., *Chemical science* **2019**, *10*, 5133.

[94] a) H. Kobayashi, M. Yamauchi, R. Ikeda, T. Yamamoto, S. Matsumura, H. Kitagawa, *Chemical Science* **2018**, *9*, 5536; b) S. Dekura, H. Kobayashi, K. Kusada, H. Kitagawa, *ChemPhysChem* **2019**, *20*, 1158; c) S. Dekura, H. Kobayashi, R. Ikeda, M. Maesato, H. Yoshino, M. Ohba, T. Ishimoto, S. Kawaguchi, Y. Kubota, S. Yoshioka et al., *Angewandte Chemie* **2018**, *57*, 9823.

[95] B. W. Mangum, D. D. Thornton, *Metrologia* **1979**, *15*, 201.

[96] M. Gentzen, D. E. Doronkin, T. L. Sheppard, J.-D. Grunwaldt, J. Sauer, S. Behrens, *Applied Catalysis A: General* **2018**, *562*, 206.

[97] M. Cokoja, B. R. Jagirdar, H. Parala, A. Birkner, R. A. Fischer, *European Journal of Inorganic Chemistry* **2008**, *2008*, 3330.

[98] M. Cokoja, H. Parala, A. Birkner, R. A. Fischer, O. Margeat, D. Ciuculescu, C. Amiens, B. Chaudret, A. Falqui, P. Lecante, *European Journal of Inorganic Chemistry* **2010**, *2010*, 1599.

[99] K. Schütte, A. Doddi, C. Kroll, H. Meyer, C. Wiktor, C. Gemel, G. van Tendeloo, R. A. Fischer, C. Janiak, *Nanoscale* **2014**, *6*, 5532.

[100] P. Novák, A. Michalcová, I. Marek, M. Mudrová, K. Saksl, J. Bednarčík, P. Zikmund, D. Vojtěch, *Intermetallics* **2013**, *32*, 127.

[102] a) Q. Zeng, I. Baker, *Intermetallics* **2006**, *14*, 396; b) D. S. Schmool, E. Araújo, M. M. Amado, M. Alegria Feio, D. Martín Rodríguez, J. S. Garitaonandia, F. Plazaola, *Journal of Magnetism and Magnetic Materials* **2004**, *272-276*, 1342.

[103] S. Arajs, E. E. Anderson, *Journal of Applied Physics* **1978**, *49*, 1433.

[104] E. P. Elsukov, E. V. Voronina, A. S. Shuravin, A. V. Zagainov, A. V. Korolev, S. K. Godovikov, E. A. Pechina, A. E. Elsukova, *Physics of Metals and Metallographie* **2006**, *102*, 55.

[105] a) Y. P. Pithawalla, M. S. El Shall, S. C. Deevi, *Intermetallics* **2000**, *8*, 1225; b) S. Paris, C. Pighini, E. Gaffet, Z. A. Munir, F. Bernard, *International Journal of Self-*Propagating *High-Temperature Synthesis* **2008**, *17*, 183.

[106] D. P. Dutta, G. Sharma, A. K. Rajarajan, S. M. Yusuf, G. K. Dey, *Chemistry Materials* **2007**, *19*, 1221.

[107] A. Schmitz, H. Meyer, M. Meischein, A. Garzón Manjón, L. Schmolke, B. Giesen, C. Schlüsener, P. Simon, Y. Grin, R. A. Fischer et al., *RSC Advances* **2020**, *10*, 12891.

[108] M. Armbrüster, R. Schlögl, Y. Grin, *Science and Technology of Advanced Materials* **2014**, *15*, 34803.

[109] M. Armbrüster, M. Behrens, F. Cinquini, K. Föttinger, Y. Grin, A. Haghofer, B. Klötzer, A. Knop-Gericke, H. Lorenz, A. Ota et al., *ChemCatChem* **2012**, *4*, 1048.

[110] a) C. Gemel, T. Steinke, M. Cokoja, A. Kempter, R. A. Fischer, *European Journal Inorganic Chemistry* **2004**, *2004*, 4161; b) G. Linti, H. Schnöckel, *Coordination Chemistry Reviews* **2000**, *206-207*, 285.

[111] T. Steinke, C. Gemel, M. Winter, R. A. Fischer, *Chemistry* **2005**, *11*, 1636.

[112] T. J. Kealy, P. L. Pauson, *Nature* **1951**, *168*, 1039.

[113] R. B. Woodward, M. Rosenblum, M. C. Whiting, *Journal of American Chemical Society* **1952**, *74*, 3458.

[114] J. S. Zhu, Y.-S. Shon, *Nanoscale* **2015**, *7*, 17786.

[115] a) C. Popa, T. Zhu, I. Tranca, P. Kaghazchi, T. Jacob, E. J. M. Hensen, *Physical Chemistry Chemical Physics* **2015**, *17*, 2268; b) A. Binder, M. Seipenbusch, *Applied Catalysis A: General* **2011**, *396*, 1; c) X. Yuan, N. Yan, S. A. Katsyuba, E. E. Zvereva, Y. Kou, P. J. Dyson, *Physical Chemistry Chemical Physics* **2012**, *14*, 6026.

[116] H. Breil, P. Heimbach, M. Kröner, H. Müller, G. Wilke, *Molecular Chemistry and Physics* **1969**, *69*, 18.

[117] B. R. James, *Advances in Organometallic Chemistry*, **1979**, *17*, 319.

[118] A. Borodziński, A. Cybulski, *Applied Catalysis A: General* **2000**, *198*, 51.

[119] L. E. Marbella, J. E. Millstone, *Chem. Mater.* **2015**, *27*, 2721.

[120] D. E. Woessner, *Concepts Magn. Reson.* **1996**, *8*, 397.

[121] a) T. E. Müller, D. M. P. Mingos, *Transition Metal Chemistry* **1995**, 20, 533; b) C. A. Tolman, *Chemical Reviews* **1977**, *77*, 313.

[122] a) W. F. Brown, *Physical Reviews* **1963**, 130, 1677; b) L. E. Brus, *The Journal of Chemical Physics* **1984**, *80*, 4403.

[123] a) K. Kovnir, J. Osswald, M. Armbrüster, D. Teschner, G. Weinberg, U. Wild, A. Knop-Gericke, T. Ressler, Y. Grin, R. Schlögl, *Journal of Catalysis* **2009**, *264*, 93; b) Y. Luo, S. Alarcón Villaseca, M. Friedrich, D. Teschner, A. Knop-Gericke, M. Armbrüster, *Journal of Catalysis* **2016**, *338*, 265; c) S. A. Villaseca, A. Ormeci, S. V. Levchenko, R. Schlögl, Y. Grin, M. Armbrüster, *ChemPhysChem* **2017**, *18*, 334.

[124] C. Gemel, T. Steinke, D. Weiss, M. Cokoja, M. Winter, R. A. Fischer, *Organometallics* **2003**, *22*, 2705.

[125] M. Fir, J. Vonce, A. S. Vuk, A. Vilcnik, V. Jovanosvski, G. Mali, B. Orel, B. Simoncic, *Acta Chimica Solvenica* **2007**, *54*, 144.

[126] T. Velusamy, S. Mitra, M. Macias-Montero, V. Svrcek, D. Mariotti, *ACS Applied Materials and Interfaces* **2015**, *7*, 28207.

[127] M. Brun, A. Berthet, J. Bertolini, *Journal of Electron Spectroscopy and Related Phenomena* **1999**, *104*, 55.

[128] J. L. Bourque, M. C. Biesinger, K. M. Baines, *Dalton Transactions* **2016**, *45*, 7678.

[129] K. Föttinger, *Catalysis Today* **2013**, *208*, 106.

[130] B. Günther, R. Gradl, C. Jud, E. Eggl, J. Huang, S. Kulpe, K. Achterhold, B. Gleich, M. Dierolf, F. Pfeiffer, *Journal of Synchrotron Radiation* **2020**, *27*, 1395.

[131] J. Huang, B. Günther, K. Achterhold, Y.-T. Cui, B. Gleich, M. Dierolf, F. Pfeiffer, *Scientific Reports* **2020**, *10*, 8772.

[132] D. J. Gavia, M. S. Maung, Y.-S. Shon, *ACS Applied Materials and Interfaces* **2013**, *5*, 12432.

[133] J.-P. Ansermet, C. P. Slichter, J. H. Sinfelt, *Progress in Nuclear Magnetic Resonance Spectroscopy* **1990**, *22*, 401.

[134] S. D. Pike, E. R. White, A. Regoutz, N. Sammy, D. J. Payne, C. K. Williams, M. S. P. Shaffer, *ACS Nano* **2017**, *11*, 2714.

[135] M. Klokkenburg, J. Hilhorst, B. H. Erné, *Vibrational Spectroscopy* **2007**, *43*, 243.

[136] K. B. Vu, K. V. Bukhryakov, D. H. Anjum, V. O. Rodionov, *ACS Catalysis* **2015**, *5*, 2529.

[137] N. Wu, L. Fu, M. Su, M. Aslam, K. C. Wong, V. P. Dravid, *Nano Letters* **2004**, *4*, 383.

[138] H. Schmitt, A. Badia, L. Dickinson, L. Reven, R. B. Lennox, *Advanced Materials* **1998**, *10*, 475.

[139] A. Badia, L. Demers, L. Dickinson, F. G. Morin, R. B. Lennox, L. Reven, *Journal of American Chemical Society* **1997**, *119*, 11104.

[140] C. D. Cappa, E. R. Lovejoy, A. R. Ravishankara, *The Journal of Physical Chemistry. A* **2008**, *112*, 3959.

[141] D. Rosenthal, R. Widmer, R. Wagner, P. Gille, M. Armbrüster, Y. Grin, R. Schlögl, O. Gröning, *Langmuir : the ACS journal of surfaces and colloids* **2012**, *28*, 6848.

[142] L. Staiger, T. Kratky, S. Günther, A. Urstoeger, M. Schuster, O. Tomanek, R. Zbořil, R. W. Fischer, R. A. Fischer, M. Cokoja, *Nanoscale* **2021**, *13*, 15038.

[143] J. M. MacLaren, T. C. Schulthess, W. H. Butler, R. Sutton, M. McHenry, *Journal of Applied Physics* **1999**, *85*, 4833.

[144] E. W. Wong, M. J. Bronikowski, M. E. Hoenk, R. S. Kowalczyk, B. D. Hunt, *Chem. Mater.* **2005**, *17*, 237.

[145] Y.-W. Jun, Y.-M. Huh, J.-S. Choi, J.-H. Lee, H.-T. Song, S. Kim, S. Yoon, K.-S. Kim, J.-S. Shin, J.-S. Suh et al., *Journal of the American Chemical Society* **2005**, *127*, 5732.

[146] R. B. Bedford, M. Betham, D. W. Bruce, S. A. Davis, R. M. Frost, M. Hird, *Chemical Communications* **2006**, 1398.

[147] T. N. Gieshoff, A. Welther, M. T. Kessler, M. H. G. Prechtl, A. Jacobi von Wangelin, *Chemical Communications* **2014**, *50*, 2261.

[148] C.-J. Jia, F. Schüth, *Physical Chemistry Chemical Physics* **2011**, *13*, 2457.

[149] P. Albers, J. Pietsch, S. F. Parker, *Journal of Molecular Catalysis A: Chemical* **2001**, *173*, 275.

[150] H. Müller, W. Seidel, *Journal of Organometallic Chemistry* **1993**, *445*, 133.

[151] Z. Shen, Y. Matsuki, K. Higashimine, M. Miyake, T. Shimoda, *Chemistry Letters* **2012**, *41*, 644.

[152] P. S. Bagus, C. J. Nelin, C. R. Brundle, B. V. Crist, N. Lahiri, K. M. Rosso, *The Journal of Chemical Physics* **2021**, *154*, 94709.

[153] B. R. Strohmeier, D. M. Hercules, *Journal of Catalysis* **1984**, *86*, 266.

[154] R. Shang, L. Ilies, E. Nakamura, *Chemical Reviews* **2017**, *117*, 9086.

[155] H. Bönnemann, W. Brijoux, H.-W. Hofstadt, T. Ould-Ely, W. Schmidt, B. Waßmuth, C. Weidenthaler, *Angewandte Chemie* **2002**, *114*, 628.

[156] H. Bönnemann, N. Waldöfner, H.-G. Haubold, T. Vad, *Chemistry Materials* **2002**, *14*, 1115.

[157] S. Kvisle, E. Rytter, *Spectrochimica Acta* **1984**, *40*, 939.

[158] a) D. W. Moon, S. L. Bernasek, D. J. Dwyer, J. L. Gland, *Journal of American Chemical Society* **1985**, *107*, 4363; b) C. Lemire, R. Meyer, V. E. Henrich, S. Shaikhutdinov, H.-J. Freund, *Surface Science* **2004**, *572*, 103; c) S. K. Nayak, M. Nooijen, S. L. Bernasek, P. Blaha, *J. Phys. Chem. B* **2001**, *105*, 164.

[159] A. A. Jahagirdar, N. Dhananjaya, D. L. Monika, C. R. Kesavulu, H. Nagabhushana, S. C. Sharma, B. M. Nagabhushana, C. Shivakumara, J. L. Rao, R. P. S. Chakradhar, *Spectrochimica Acta. Part A,* **2013**, *104*, 512.

[160] a) M. R. Whitbeck, *Applied Spectroscopy* **1981**, *35*, 93; b) M. A. Czarnecki, *Applied Spectroscopy* **2015**, *69*, 67.

[161] J. Michalik, D. Brown, J.-S. Yu, M. Danilczuk, J. Yeon Kim, L. Kevan, *Physical Chemistry Chemical Physics* **2001**, *3*, 1705.

[162] T. P. Gavrilova, A. R. Yagfarova, Y. Deeva, I. V. Yatsyk, I. F. Gilmutdinov, M. A. Cherosov, F. G. Vagizov, T. I. Chupakhina, R. M. Eremina, *Journal of Physics and Chemistry of Solids* **2021**, *153*, 109994.

[163] V. Q. Viet, S. Y. Adeyemi, W. H. Son, J.-S. Rhyee, N.-S. Lee, H.-J. Kim, *Crystal Growth and Design* **2018**, *18*, 3544.

[164] E. Kozlyakova, I. Danilovich, A. Volkov, K. Zakharov, O. Dimitrova, E. Belokoneva, L. Shvanskaya, E. Zvereva, D. Chareev, O. Volkova et al., *Journal of Alloys and Compounds* **2018**, *744*, 600.

[165] S. Sambasivam, I. M. Obaidat, *Materials Today: Proceedings* **2020**, *28*, 587.

[166] L. Arda, M. Acikgoz, N. Dogan, D. Akcan, O. Cakiroglu, *Journal of Superconductivity and Novel Magnetism* **2014**, *27*, 799.

[167] F. Zaera, *ACS Catalysis* **2017**, *7*, 4947.

[168] I. Lee, F. Delbecq, R. Morales, M. A. Albiter, F. Zaera, *Nature Materials* **2009**, *8*, 132.

[169] R. Brajpuriya, P. Sharma, S. Jani, S. Kaimal, T. Shripathi, N. Lakshmi, K. Venugopalan, *Applied Surface Science* **2010**, *257*, 10.

[170] a) H. Gengnagel, M. J. Besnus, H. Danan, *Physica status Solidi A* **1972**, *13*, 499; b) S. Enzo, R. Frattini, G. Mulas, F. Delogu, *Materials Science Forum* **1998**, *269-272*, 391; c) L. E. Zamora, G. A. Pérez Alcázar, G. Y. Vélez, J. D. Betancur, J. F. Marco, J. J. Romero, A. Martínez, F. J. Palomares, J. M. González, *Physical Reviews B* **2009**, *79*.

[171] a) R. van Reis, A. Zydney, *Journal of Membrane Science* **2007**, *297*, 16; b) J. Paul, *Physical Review B* **1998**, *37*, 6164.

[172] S. Hub, R. Touroude, *Journal of Catalysis* **1988**, *114*, 411.

[173] F. Delbecq, F. Zaera, *Journal of the American Chemical Society* **2008**, *130*, 14924.

[174] L. Piccolo, L. Kibis, *Journal of Catalysis* **2015**, *332*, 112.

[175] F. Zaera, *Accounts of Chemical Research* **2009**, *42*, 1152.

[176] M. Cokoja, H. Parala, A. Birkner, O. Shekhah, M. W. E. van den Berg, R. A. Fischer, *Chemistry Materials* **2007**, *19*, 5721.

[177] T. Klein, C. Pauly, F. Mücklich, G. Kickelbick, *Intermetallics* **2020**, *124*, 106851.

[178] C. Ganesamoorthy, J. Weßing, C. Kroll, R. W. Seidel, C. Gemel, R. A. Fischer, *Angewandte Chemie International Edition* **2014**, *53*, 7943.

[179] Karina Hemmer, *Master's Thesis* "*Reactivity of Intermetallic Nickel/Gallium Clusters in the Alkyne Semi-Hydrogenation*" **2019**, TU Munich.

[180] M. Meilikhov, K. Yusenko, D. Esken, S. Turner, G. van Tendeloo, R. A. Fischer, *European Journal of Inorganic Chemistry* **2010**, *2010*, 3701.

[181] a) U. Zenneck, *ChemInform* **1987**, 18, 144; b) P. Le Floch, F. Knoch, F. Kremer, F. Mathey, J. Scholz, W. Scholz, K.-H. Thiele, U. Zenneck, *European Journal of Inorganic Chemistry* **1998**, *1998*, 119.

[182] T. Yasukawa, H. Miyamura, S. Kobayashi, *Chemical Society Reviews* **2014**, *43*, 1450.

[183] a) T. Yasukawa, H. Miyamura, S. Kobayashi, *ACS Catalysis* **2016**, *6*, 7979; b) T. Yasukawa, A. Suzuki, H. Miyamura, K. Nishino, S. Kobayashi, *Journal of the American Chemical Society* **2015**, *137*, 6616.

[184] J. L. Atwood, F. R. Bennett, F. M. Elms, C. Jones, C. L. Raston, K. D. Robinson, *Journal of American Chemical Society* **1991**, *113*, 8183.

[185] T. D. Humphries, K. T. Munroe, A. Decken, G. S. McGrady, *Dalton Transactions* **2013**, *42*, 6965.

[186] W. Rüdorff, K. Brodersen, *Zeitschrift für Naturforschung* **1957**, *12b*, 595.

[187] S. Velu S. Gangwal, *Solid State Ionics* **2006**, *177*, 803.

[188] F. Boszo, G. Ertl, M. Grunze, M. Weiss, *Applications of Surface Science* **1997**, *1*, 103.

7 Supplementary Information

Pd@Sulfides

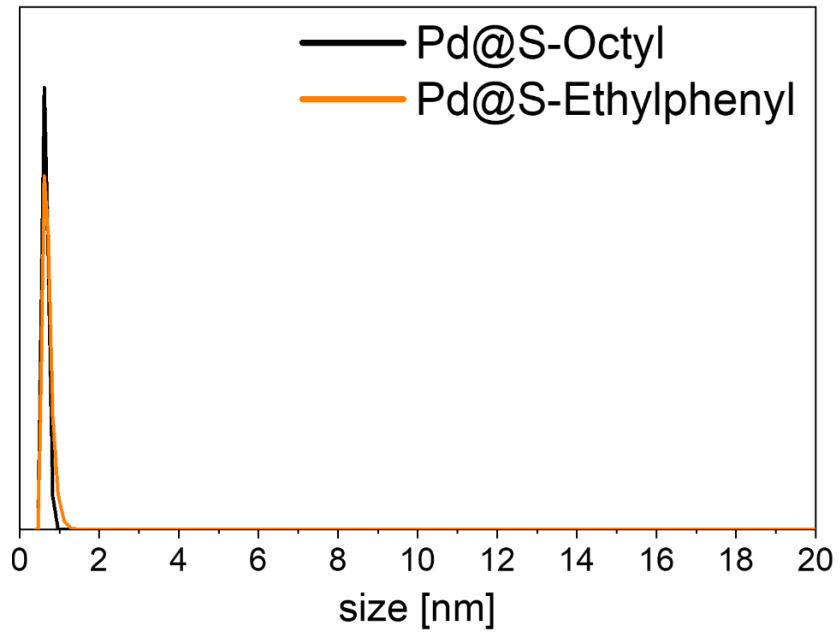

Figure 76. DLS measurement of colloidal thiol-stabilized Pd NPs.

Pd@N(Octyl)$_4$Br

Particle analysis

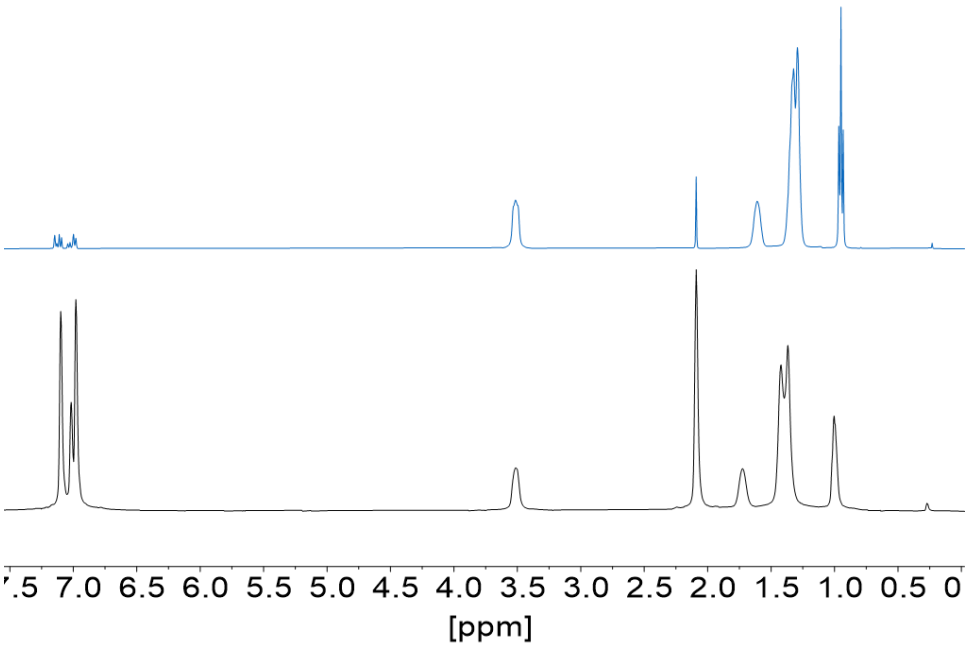

Figure 77. ^{1}H-NMR spectra (toluene-d_8) of Pd@N(Octyl)$_4$Br NPs (top) and N(Octyl)$_4$Br as reference (bottom).

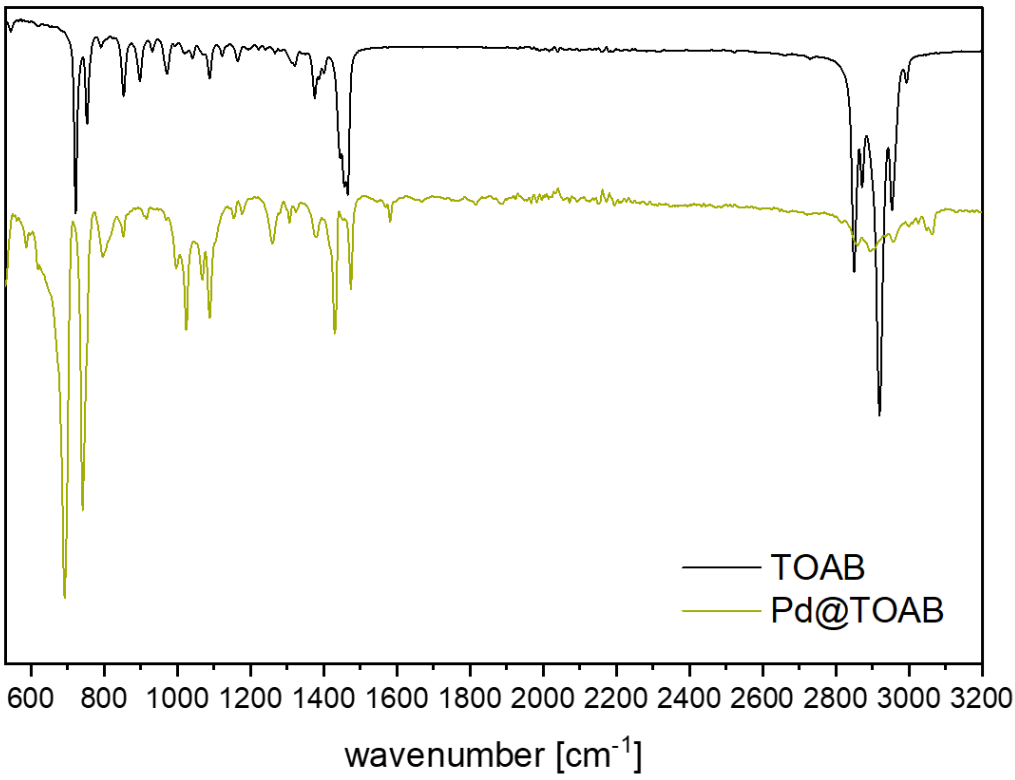

Figure 78. IR spectra (ATR-mode) of Pd@N(Octyl)$_4$Br NPs and the pure capping agent as reference.

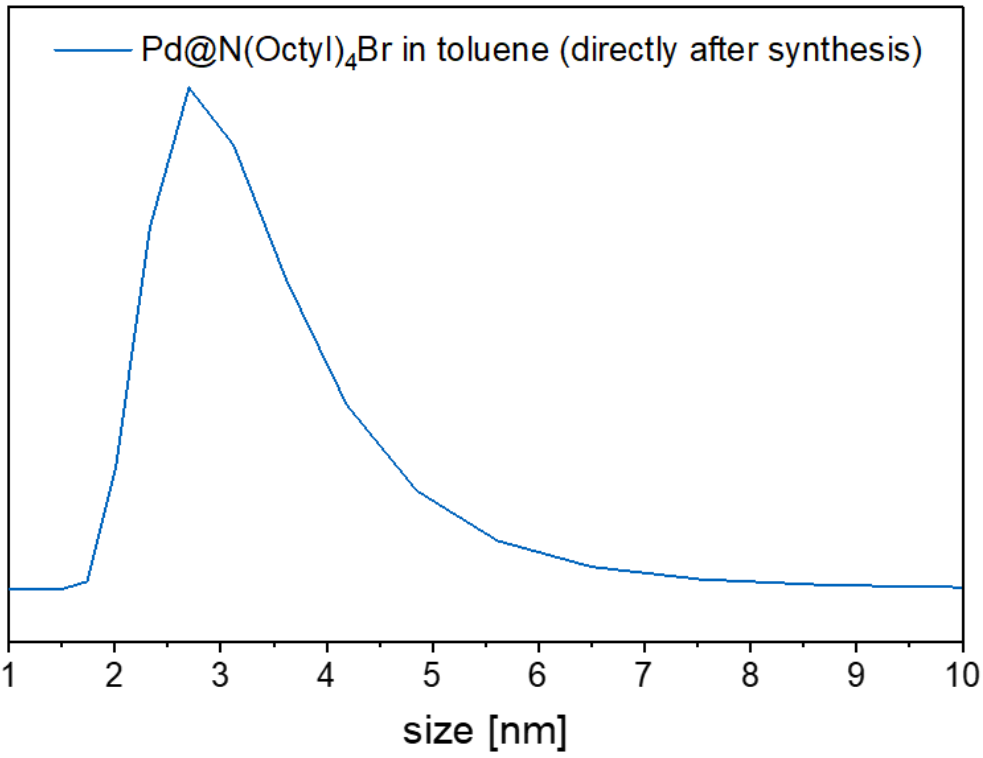

Figure 79. DLS diagram of freshly prepared colloidal Pd@N(Octyl)$_4$Br NPs (hydrodynamic radius is calculated to 2.8 nm).

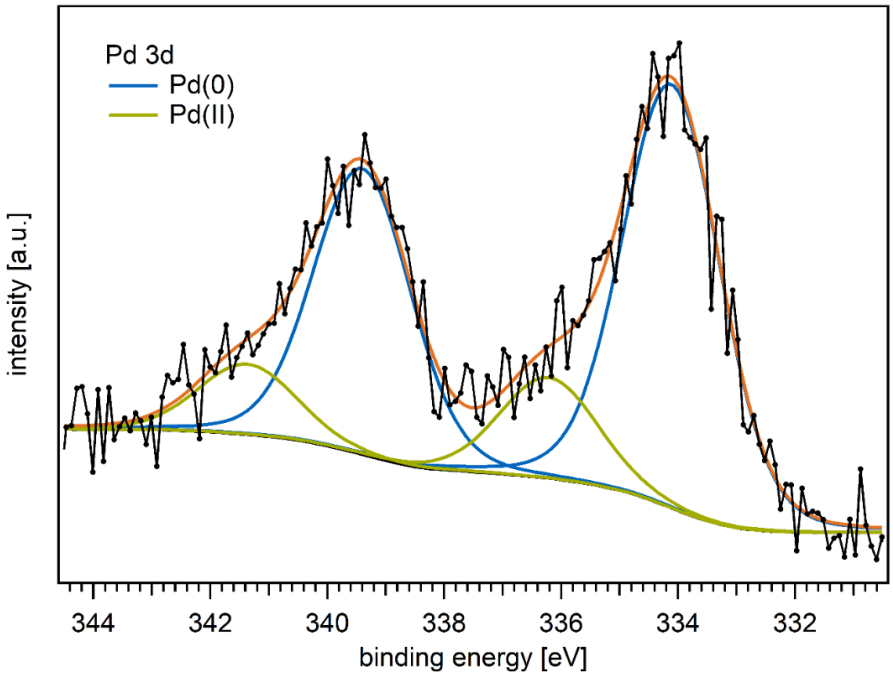

Figure 80. Pd 3d photoemission spectra obtained from Pd@N(Octyl)$_4$Br nanoparticles spin-coated on a Si-Wafer. Deconvolution into two pairs of doublets prove the presence of metallic Pd (at 334.1 eV and 339.4 eV) as well as Pd(II) (at 336.2 eV and 341.4 eV).[1] Evaluation of the integrals reveals a fraction of oxidic species (Pd(II)) of 19%.

Mechanistic Investigation

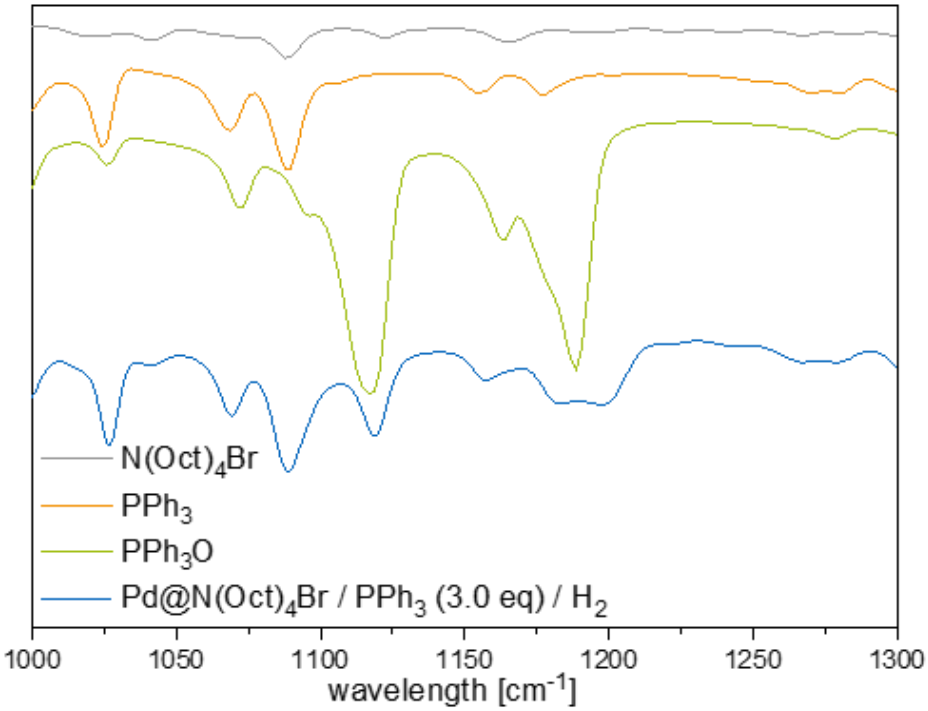

Figure 81. IR study of Pd@N(Octyl)$_4$Br NPs with an excess of PPh_3 (3.0 equiv. referred to Pd), as sensitivity with 1.0 equiv. PPh_3 was too low for showing PPh_3O formation.

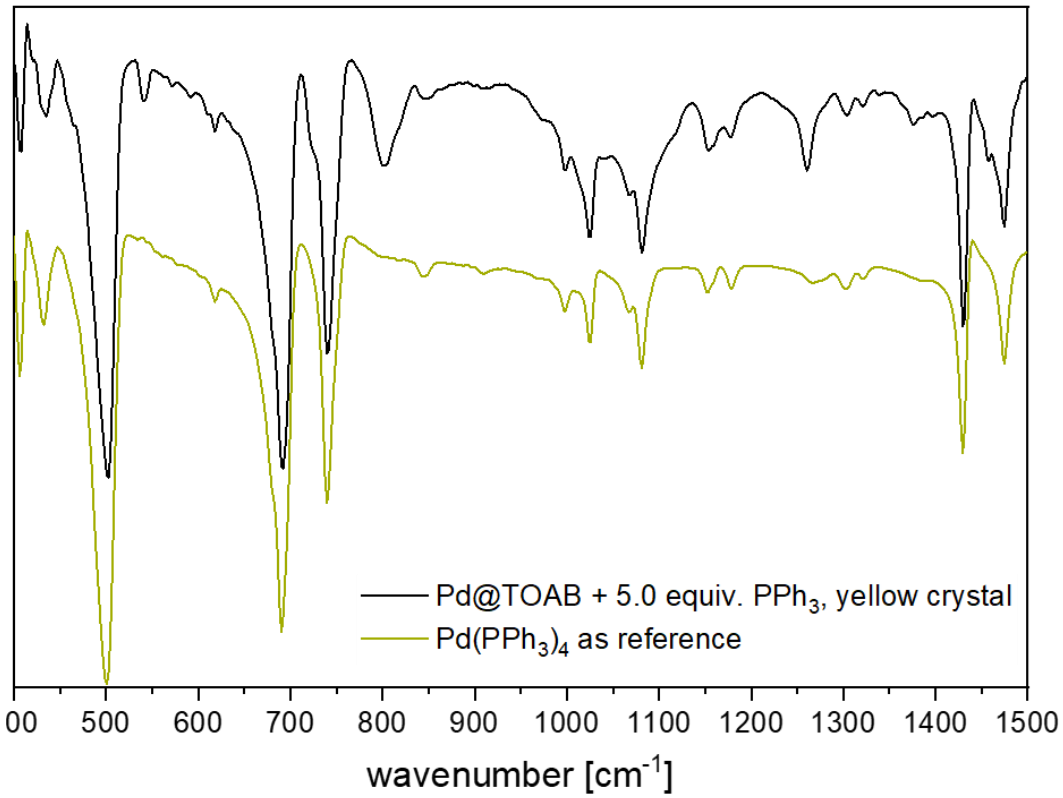

Figure 82. IR study of an isolated yellow crystal obtained by the addition of 5.0 equiv. PPh_3 to a colloidal solution of Pd@$N(Octyl)_4Br$ NPs. [$Pd(PPh_3)_4$] is shown as reference.

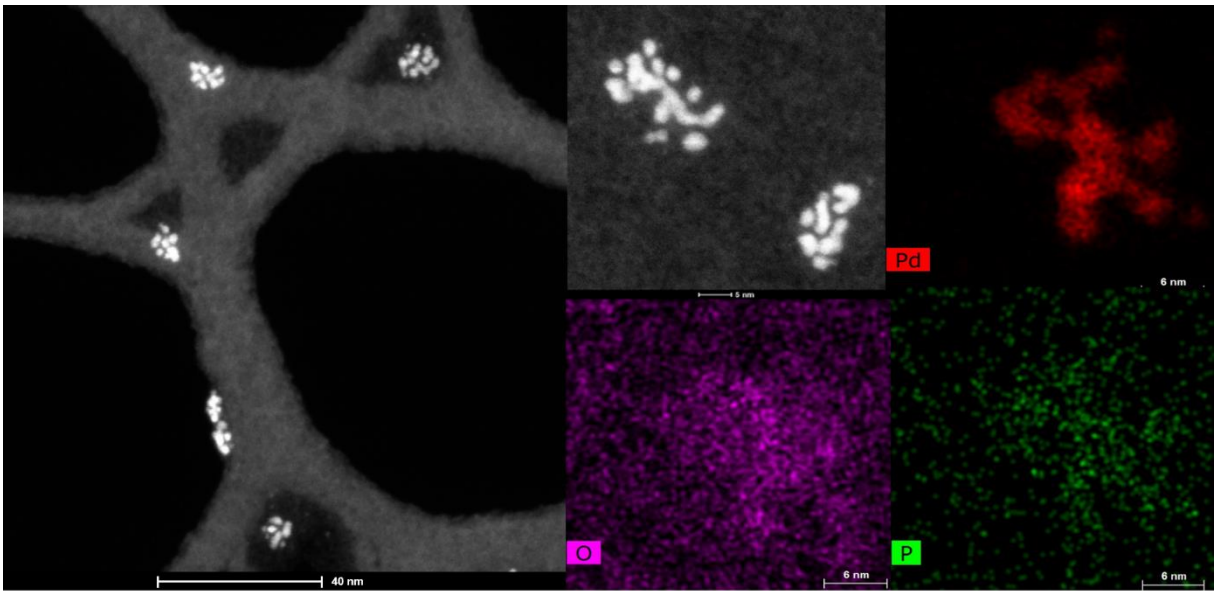

Figure 83. HR-TEM images (HAADF) and elemental mapping after phosphane addition without addition of 1-octyne showing agglomeration due to phosphane interaction with the Pd nanoparticles.

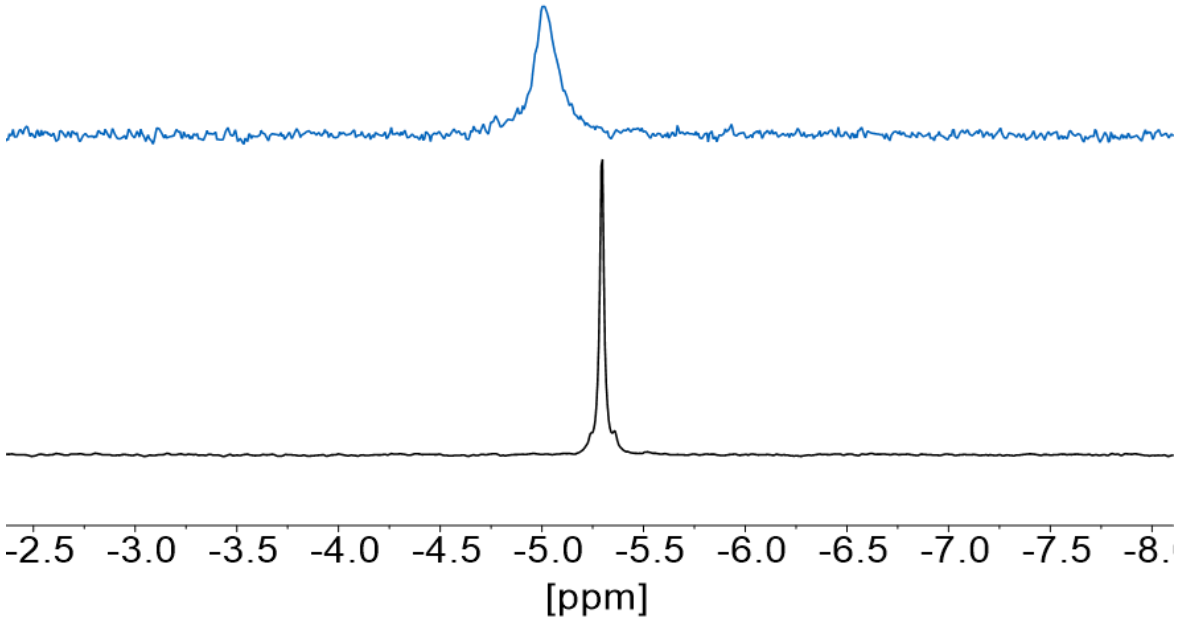

Figure 84. *In situ* ^{31}P-NMR study using 1 mol% Pd@N(Octyl)$_4$Br NPs and PPh_3 as additive in dry and degassed toluene-d_8 (top: 1.0 equiv. PPh_3 with 1-octyne, bottom: PPh_3 signal as reference, without H_2). δ [ppm]: -5.3 (PPh_3).

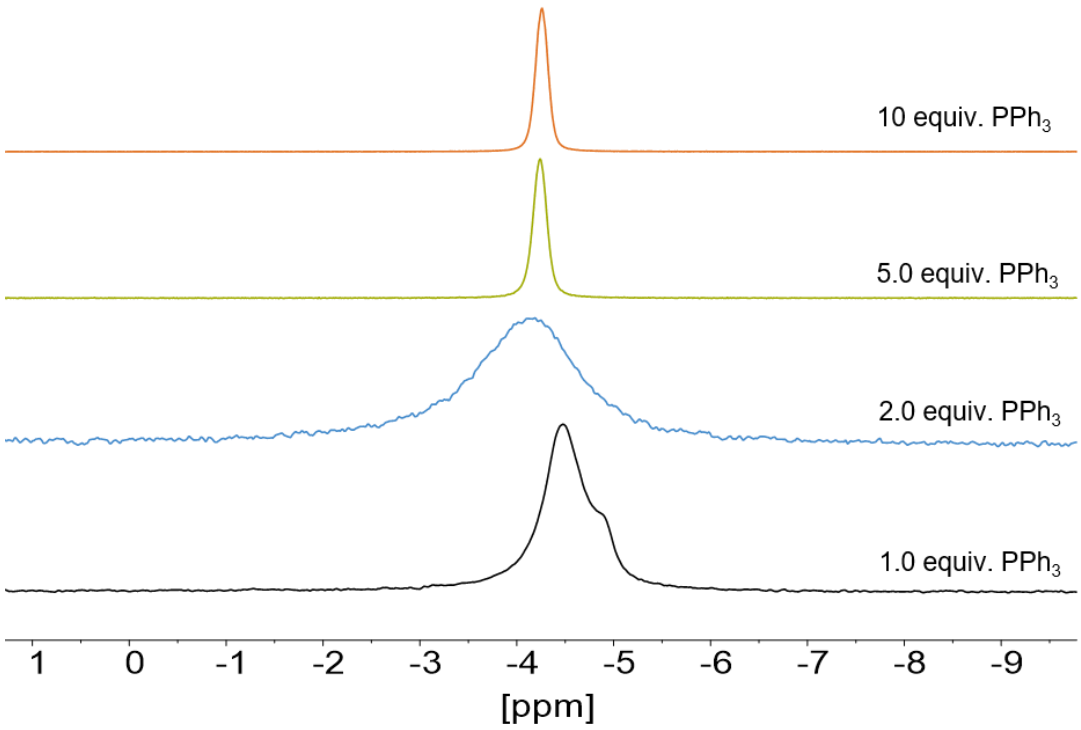

Figure 85. *In situ* ^{31}P-NMR study of the semi-hydrogenation of 1-octyne using 1 mol% catalyst and various amounts of PPh_3 as additive in dry and degassed toluene-d_8.

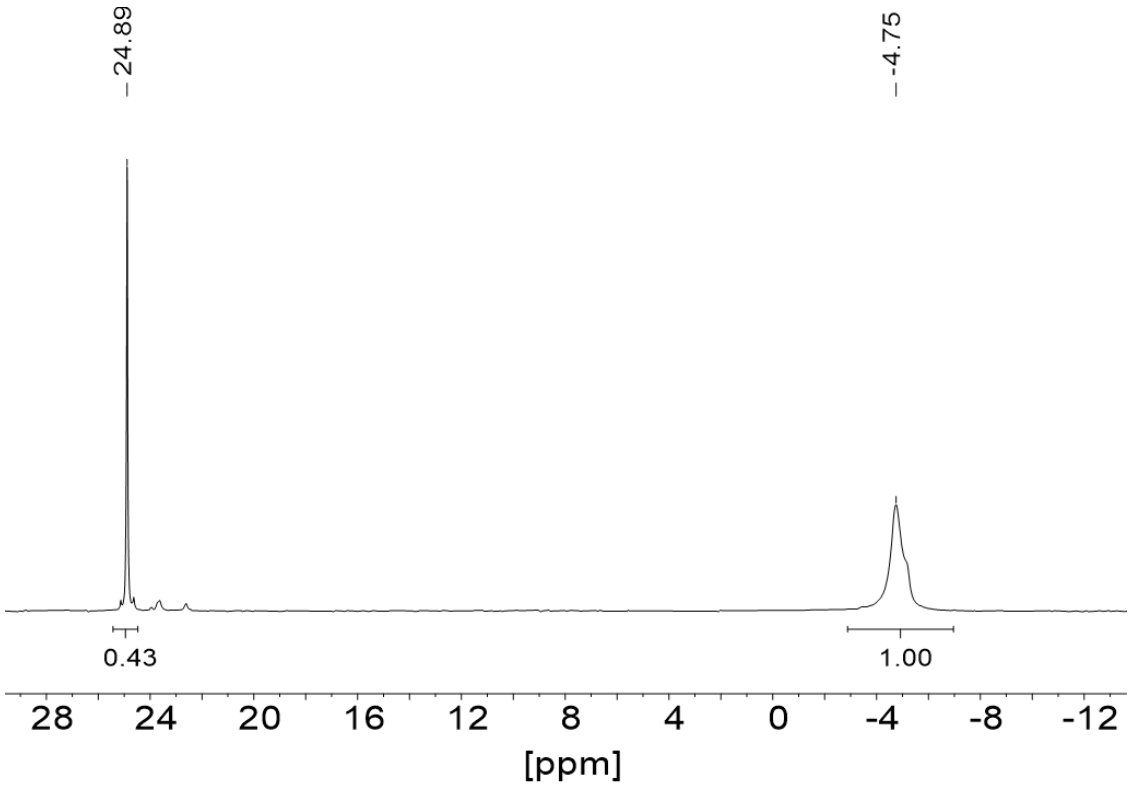

Figure 86. *In situ* ^{31}P-NMR study of the semi-hydrogenation of 1-octyne using 1 mol% catalyst and 1.0 equiv. PPh_3 as additive in dry and degassed toluene-d_8 showing partial phosphane oxidation (~30%). δ [ppm]: -4.75 (PPh_3), 24.9 (free PPh_3O).

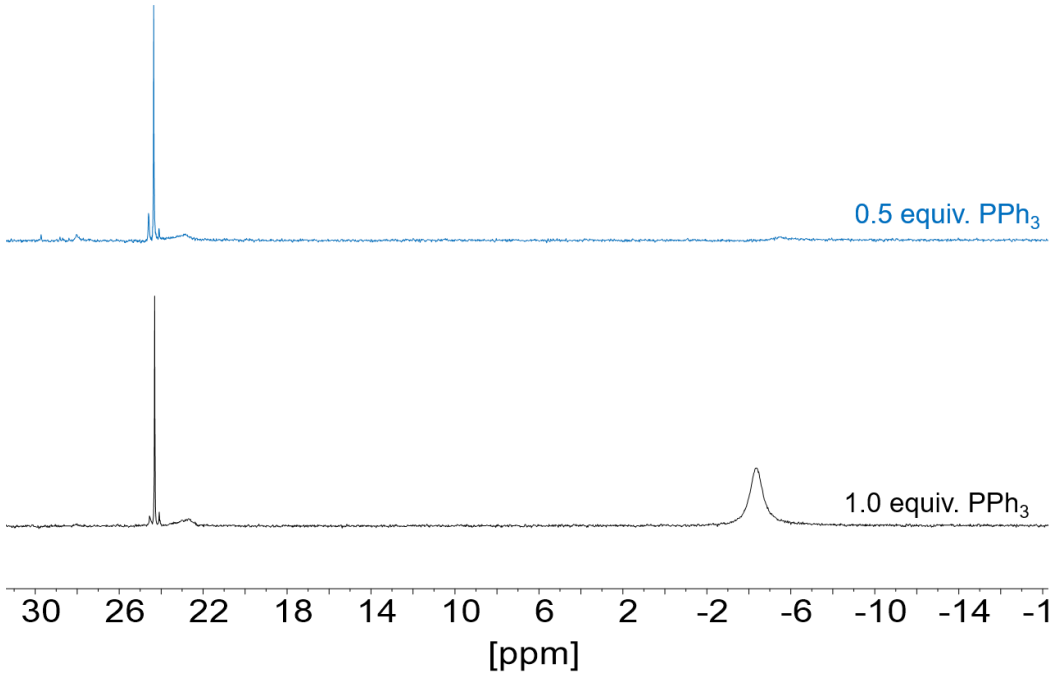

Figure 87. *In situ* ^{31}P-NMR study of PPh_3 (0.5 equiv. and 1 equiv. referred to Pd) addition to a solution of 1 mol% Pd@TOAB NPs and 1-octyne in dry and degassed toluene-d_8 under inert conditions (without H_2).

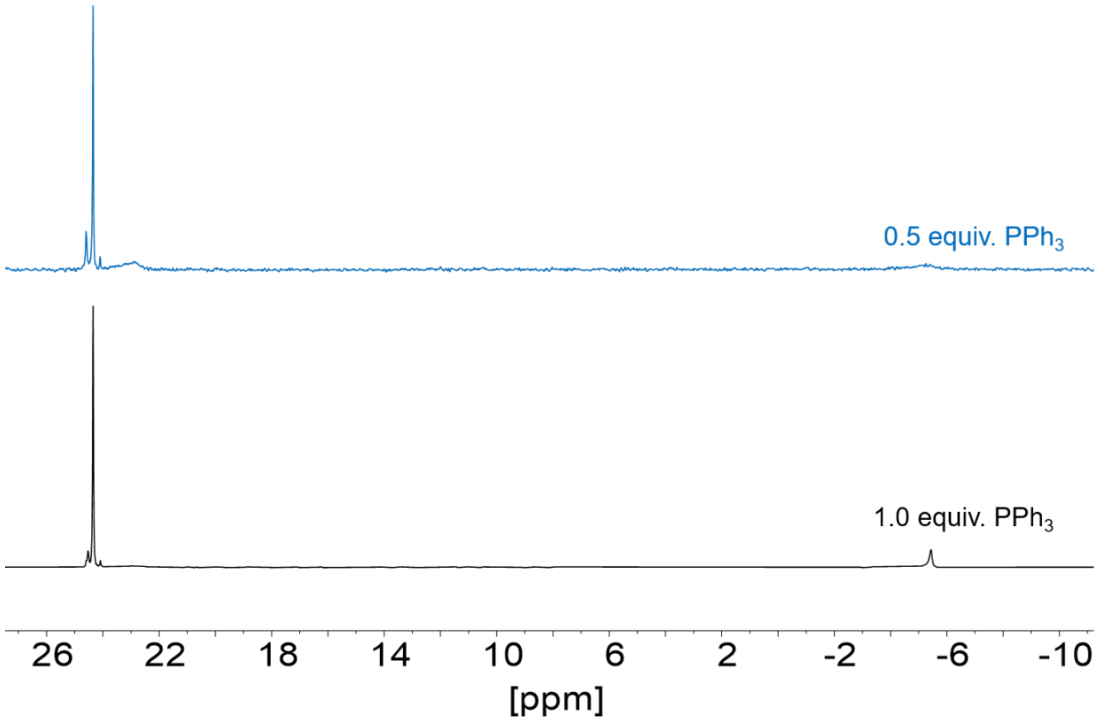

Figure 88. *In situ* ^{31}P-NMR study of PPh_3 (0.5 equiv. and 1 equiv. referred to Pd) addition to a solution of 1 mol% Pd@TOAB NPs and 1-octyne in toluene-d_8 (neither dry nor degassed) (without H_2).

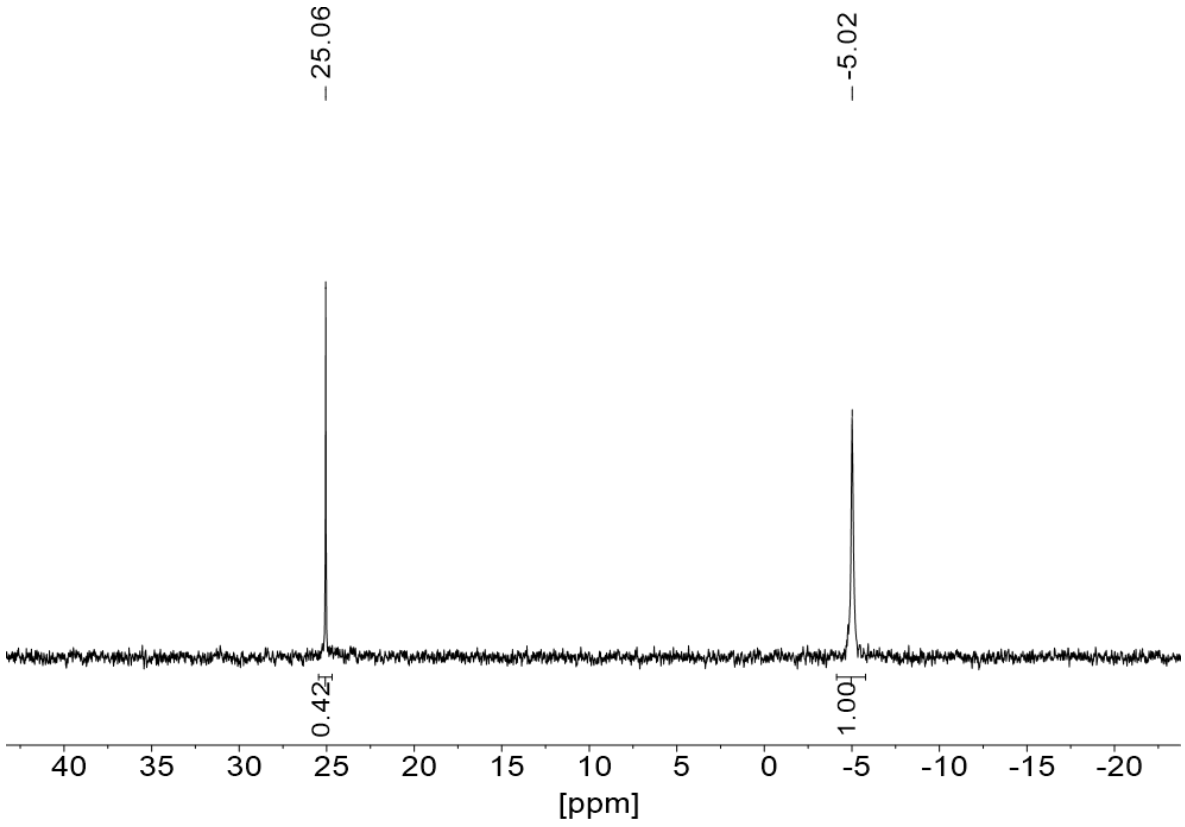

Figure 89. ^{31}P-NMR study. Addition of 1.0 equiv. PPh_3 using 1 mol% Pd@N(Octyl)$_4$Br NPs in dry and degassed toluene-d_8 under inert conditions (without 1-octyne and H_2 atmosphere).

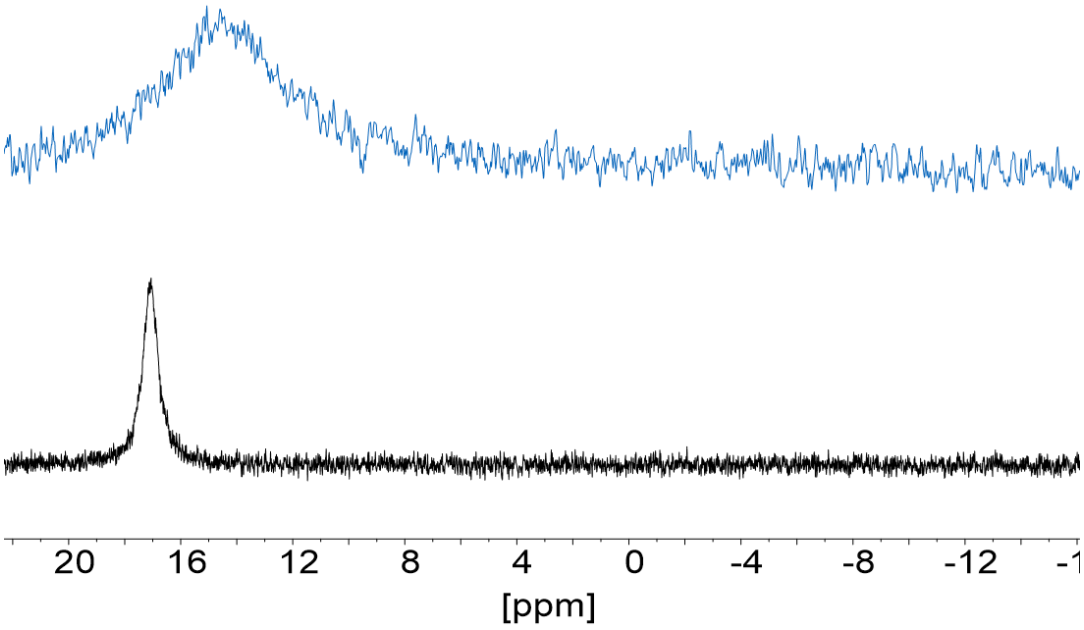

Figure 90. ^{31}P-NMR (in toluene-d_8) of an isolated yellow crystal (above) obtained by addition of 30 equiv. PPh_3 to a colloidal solution of Pd@N(Octyl)$_4$Br NPs. Those crystals were also obtained for the addition of 5.0 and 10 equiv. PPh_3. Bottom: [Pd(PPh_3)$_4$] as reference.

Particle analysis after catalysis

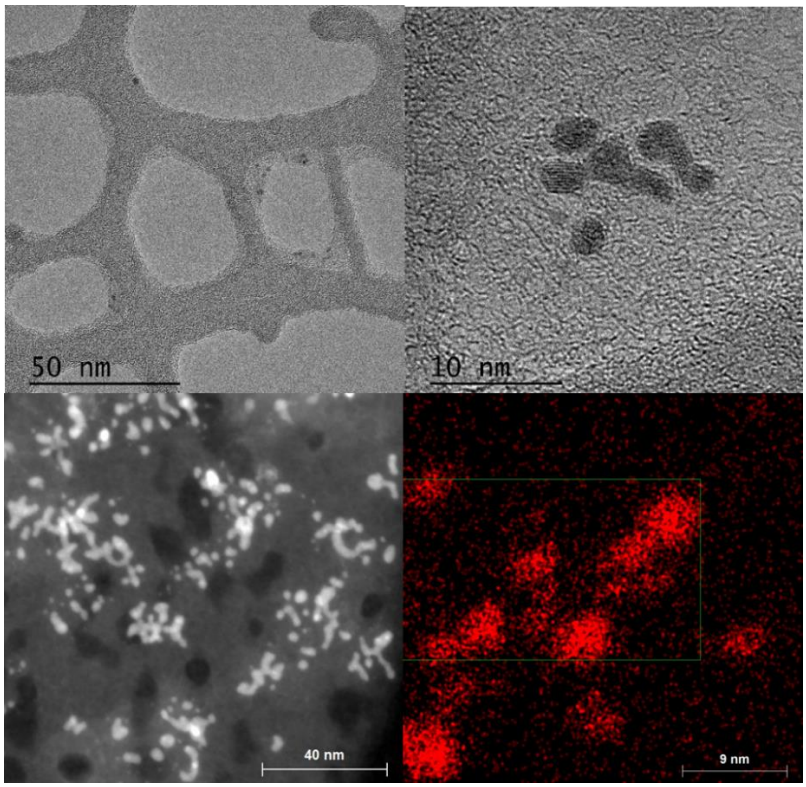

Figure 91. HRTEM measurements (including HAADF) after catalysis show slight NP agglomeration.

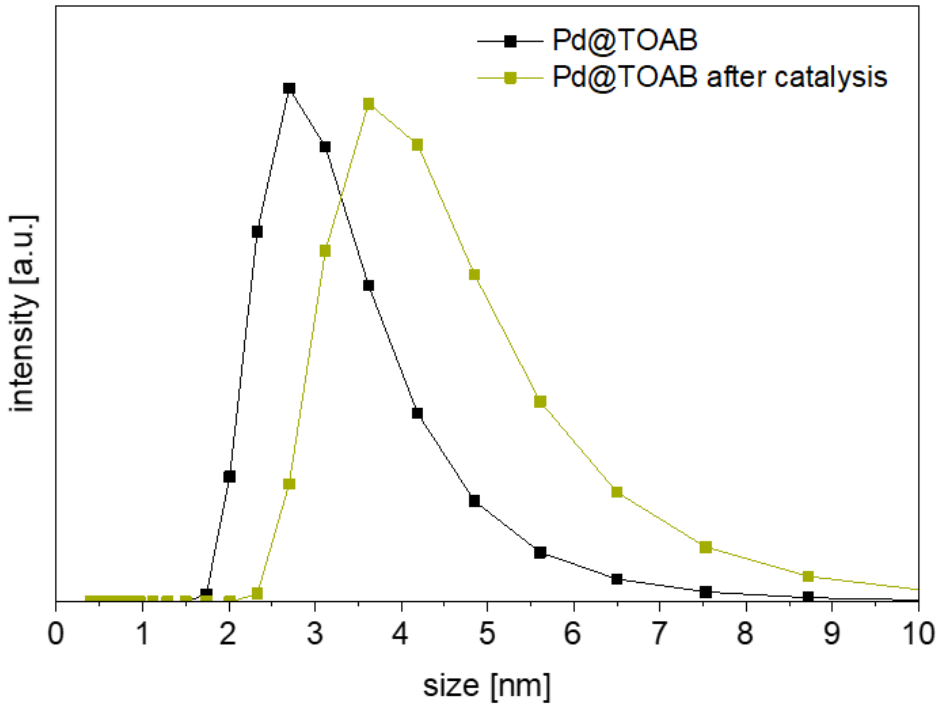

Figure 92. DLS measurements of the colloids before and after catalysis experiments at 0 °C and $p(H_2)$ = 1 bar.

$Pd_{1-x}Ga_x$ colloids

Particle analysis

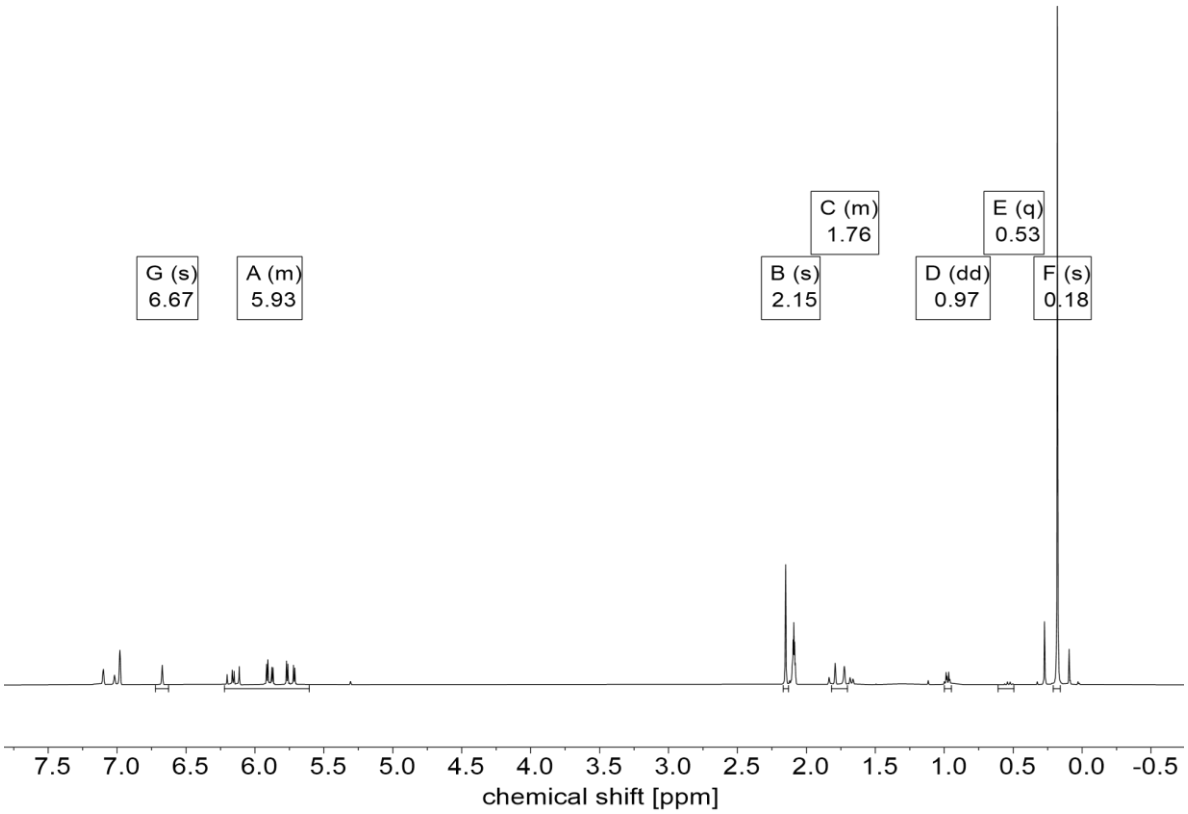

Figure 93. Representative ^{1}H NMR spectra (toluene-d_8) of colloidal $Pd_{1-x}Ga_x$ NPs. Signals of unreacted GaCp* were not detected for all samples.

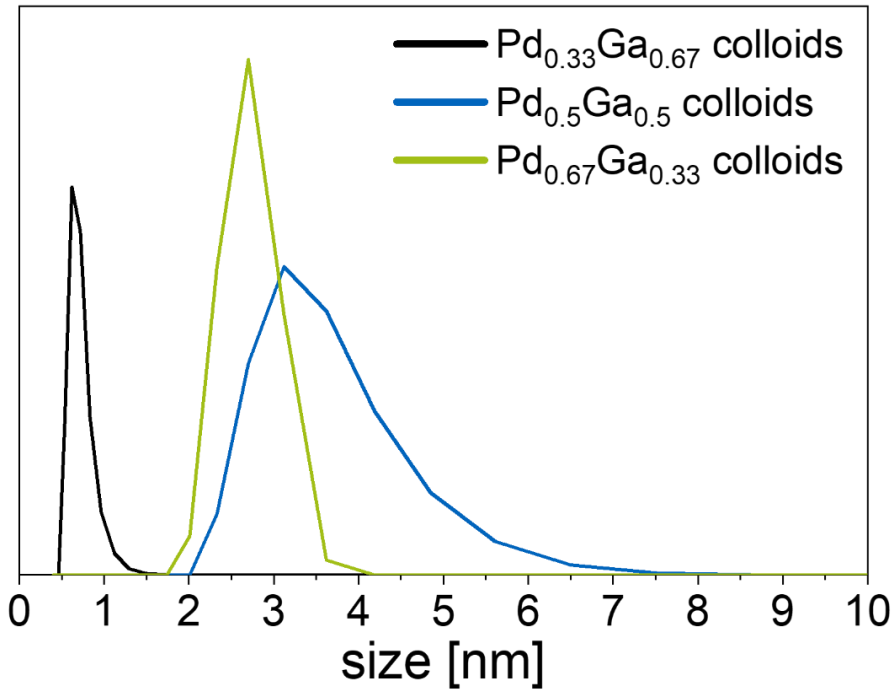

Figure 94. DLS measurements of all $Pd_{1-x}Ga_x$ samples at 0°C.

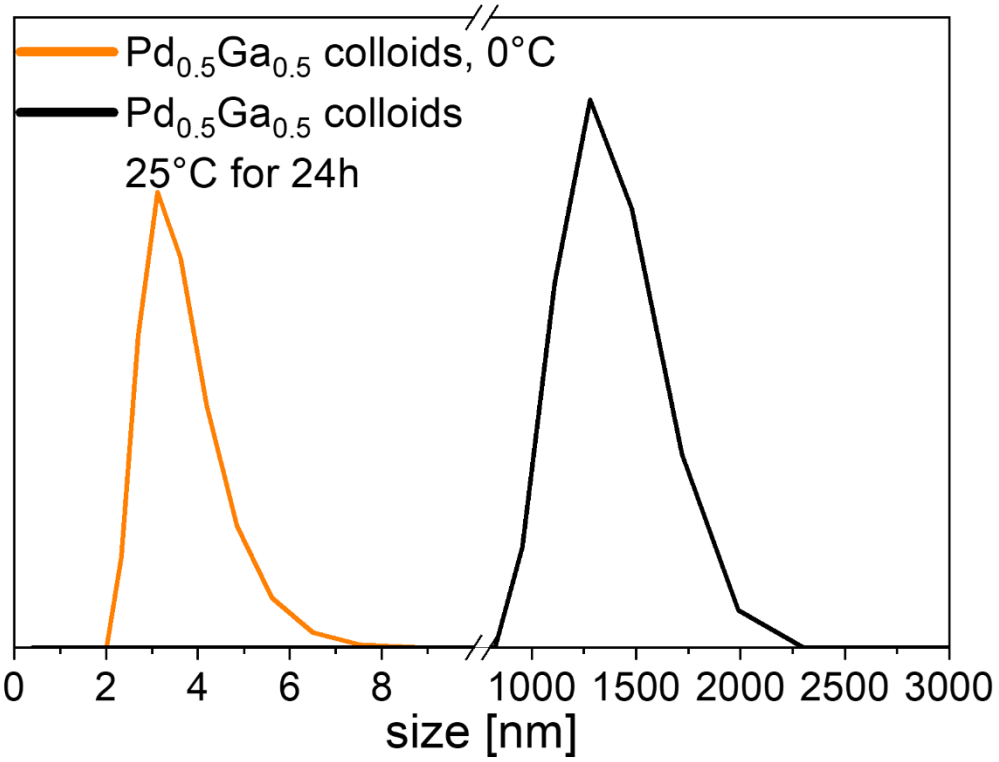

Figure 95. DLS measurements of $Pd_{0.5}Ga_{0.5}$ colloids at 0°C and after 24 h stored at 25°C showing agglomeration with concomitant precipitation.

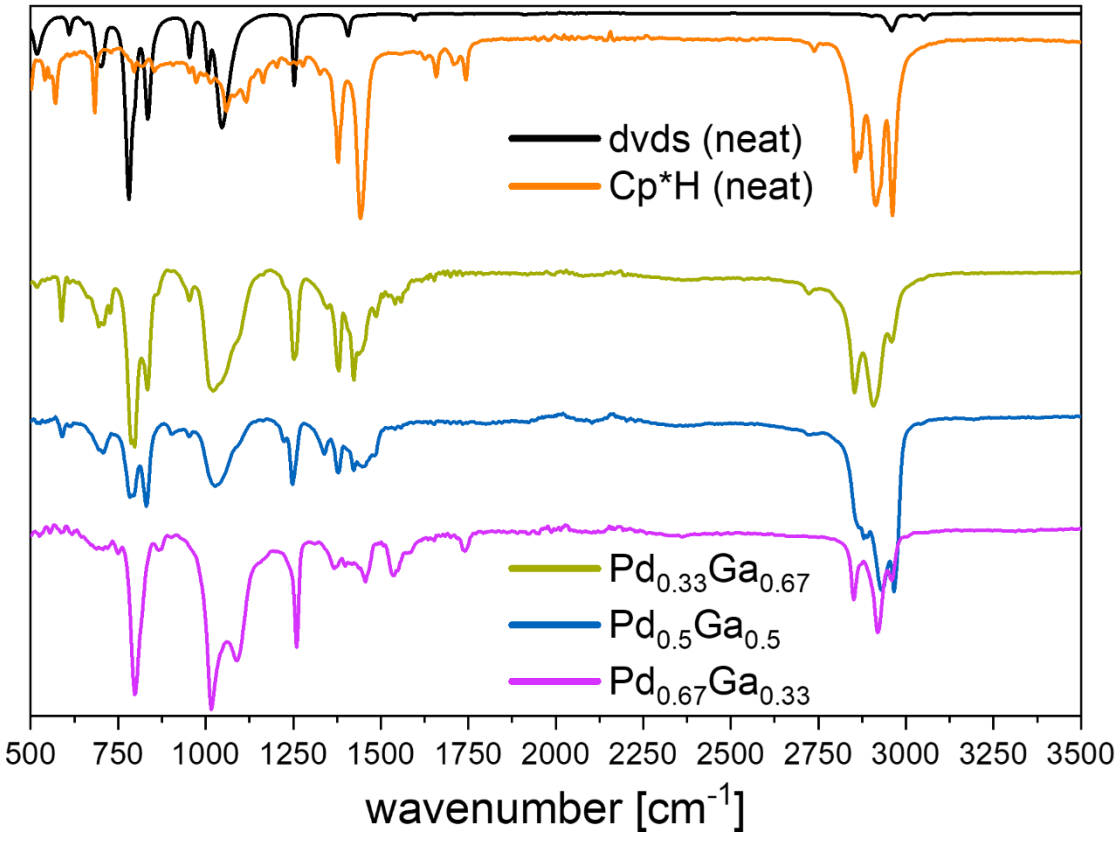

Figure 96. ATR FT-IR measurement of the $Pd_{1-x}Ga_x$ colloids (bottom traces) and pure dvds and Cp*H as reference (upper traces, black and orange).

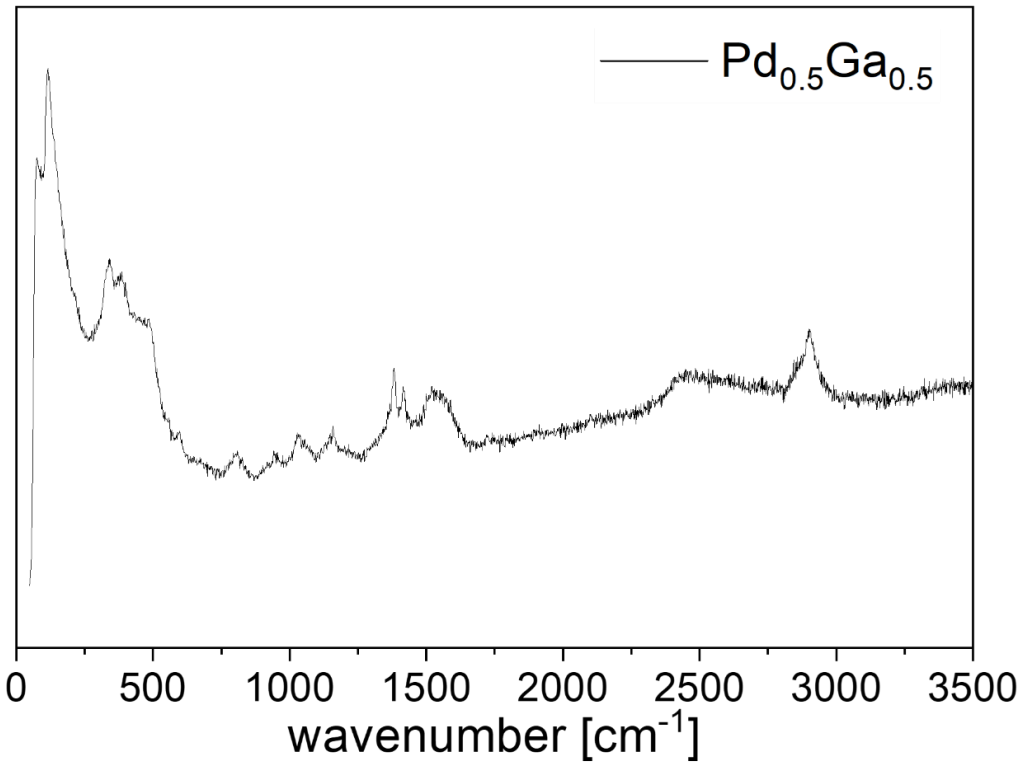

Figure 97. Raman measurement of the $Pd_{0.5}Ga_{0.5}$ colloids after precipitation at 25°C.

Mechanistic Investigation

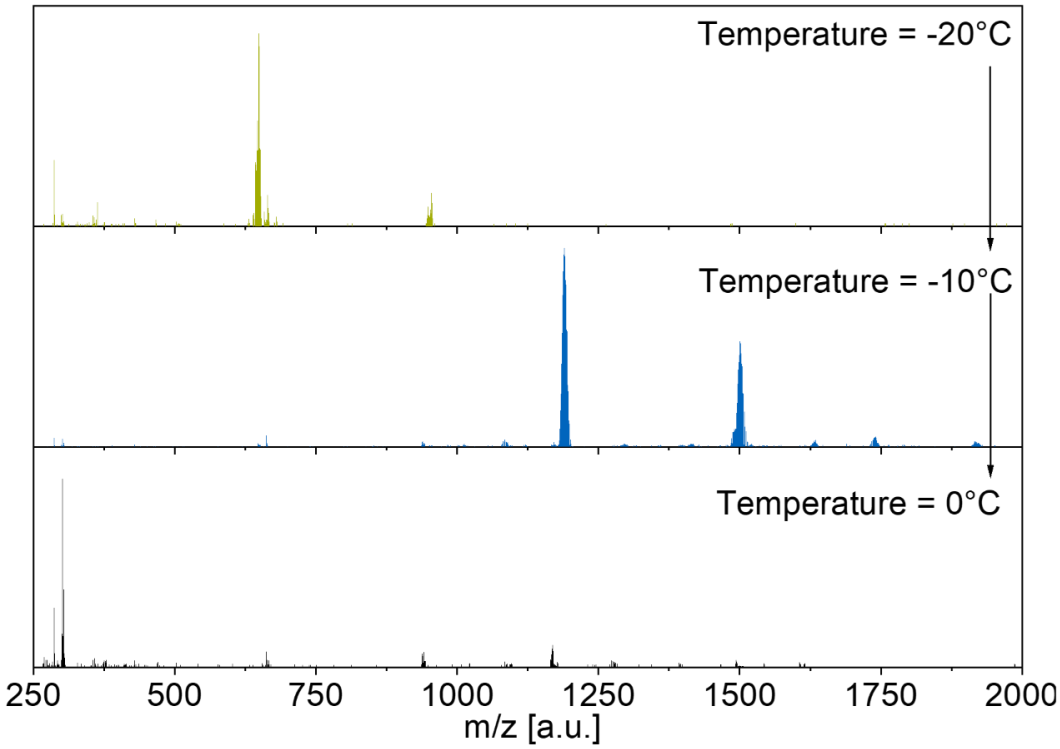

Figure 98. Representative LIFDI-MS spectra monitoring the cluster formation and deformation during synthesis of colloidal $Pd_{0.5}Ga_{0.5}$ NPs at various temperatures (top: -20°C, middle: -10°C, bottom: 0°C) by a slow warming up of the reaction mixture.

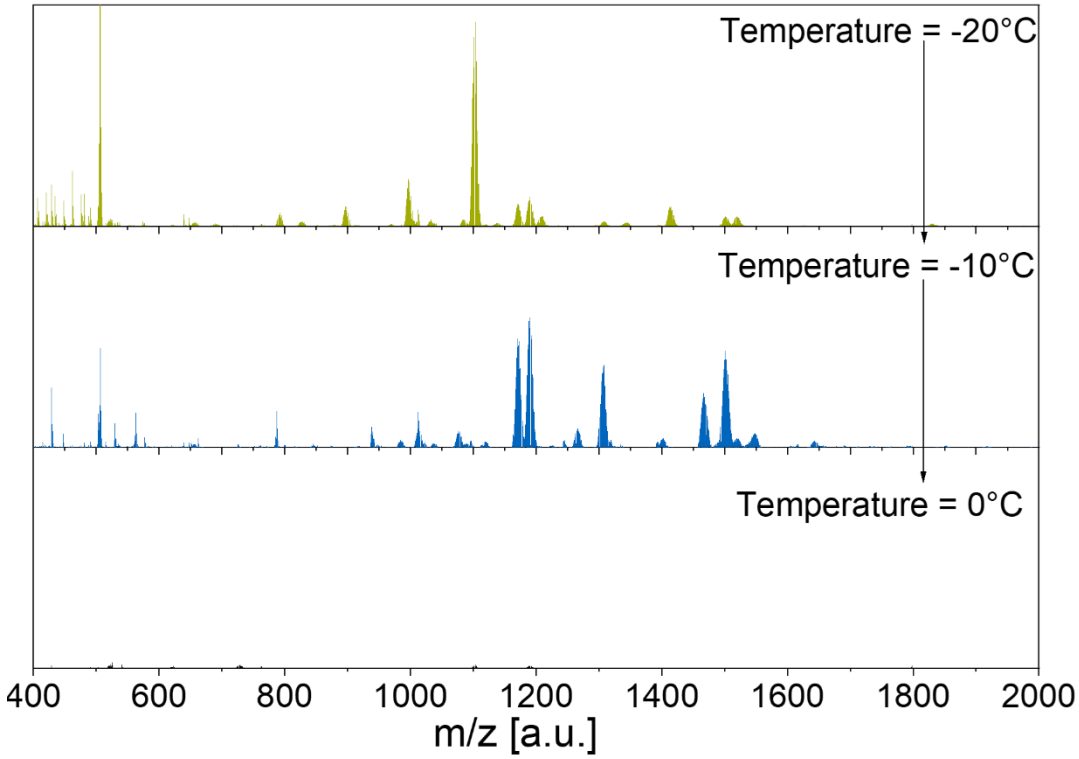

Figure 99. Representative LIFDI-MS spectra monitoring the cluster formation and deformation during synthesis of colloidal $Pd_{0.33}Ga_{0.67}$ NPs at various temperatures (top: -20°C, middle: -10°C, bottom: 0°C) by a slow warming up of the reaction mixture.

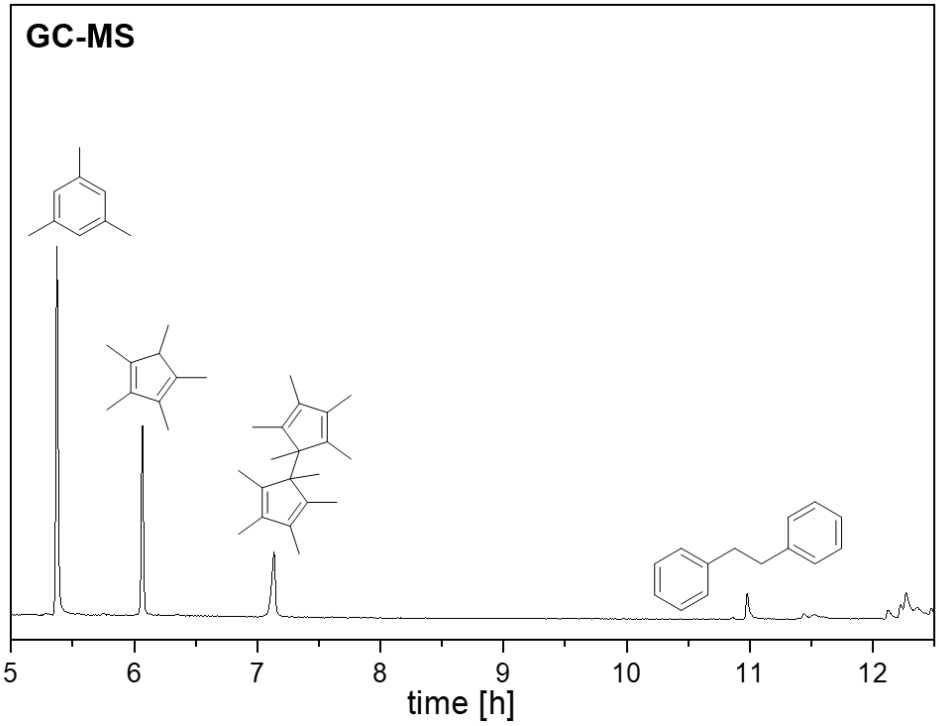

Figure 100. Representative GC chromatogram of colloidal $Pd_{1-x}Ga_x$ NPs showing mesitylene as internal standard and products of a C-H activation reactivity.

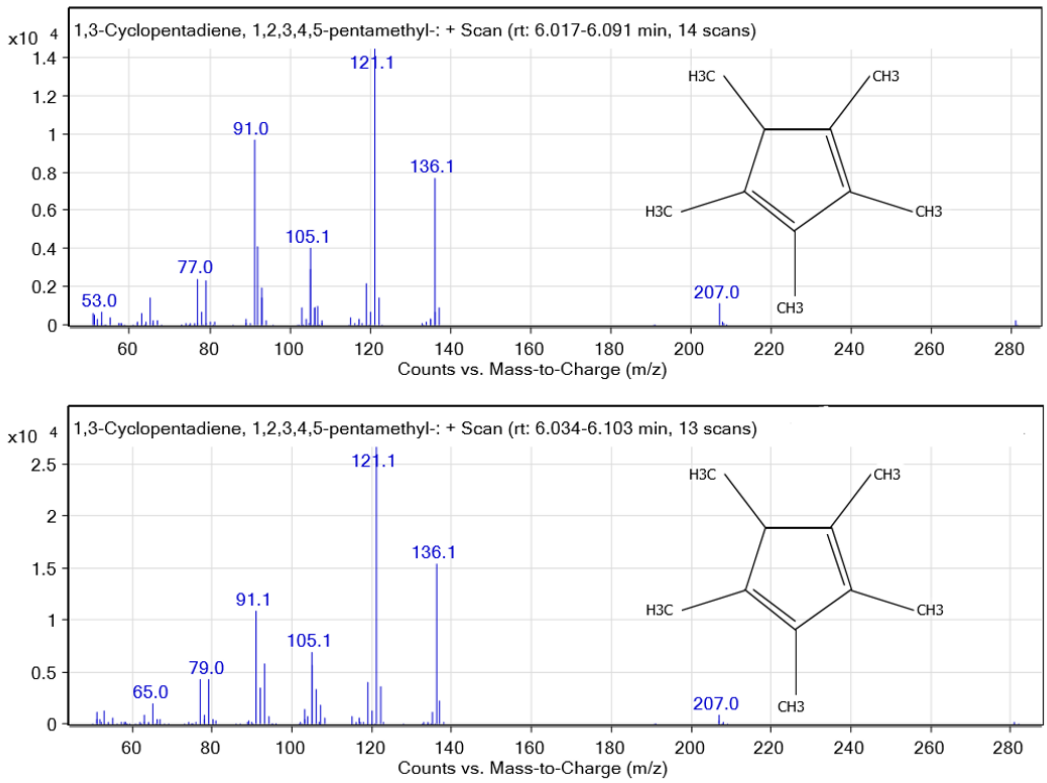

Figure 101. GC-MS mass spectra of Cp*H after the targeted decomposition experiments of $Pd_{0.5}Ga_{0.5}$ colloids with H_2O (above) and D_2O (bottom) showing no differences.

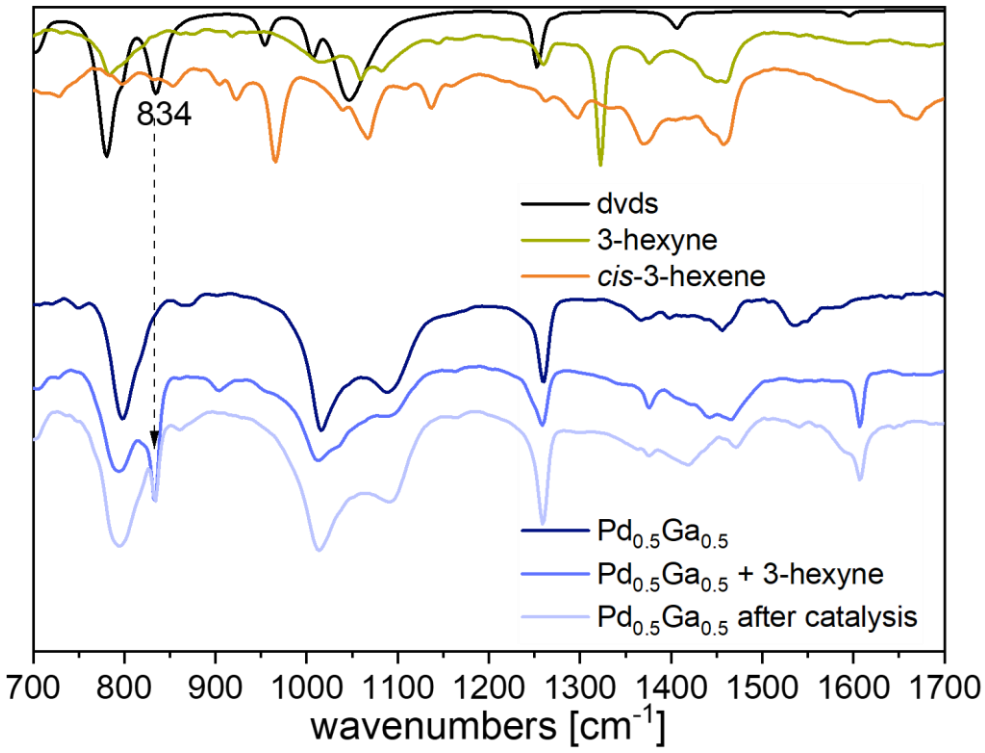

Figure 102. ATR FT-IR measurement of the $Pd_{0.5}Ga_{0.5}$ colloids upon addition of 3-hexyne and after catalysis runs (bottom traces, blue) and pure dvds and Cp*H as reference (upper traces, black, green and orange).

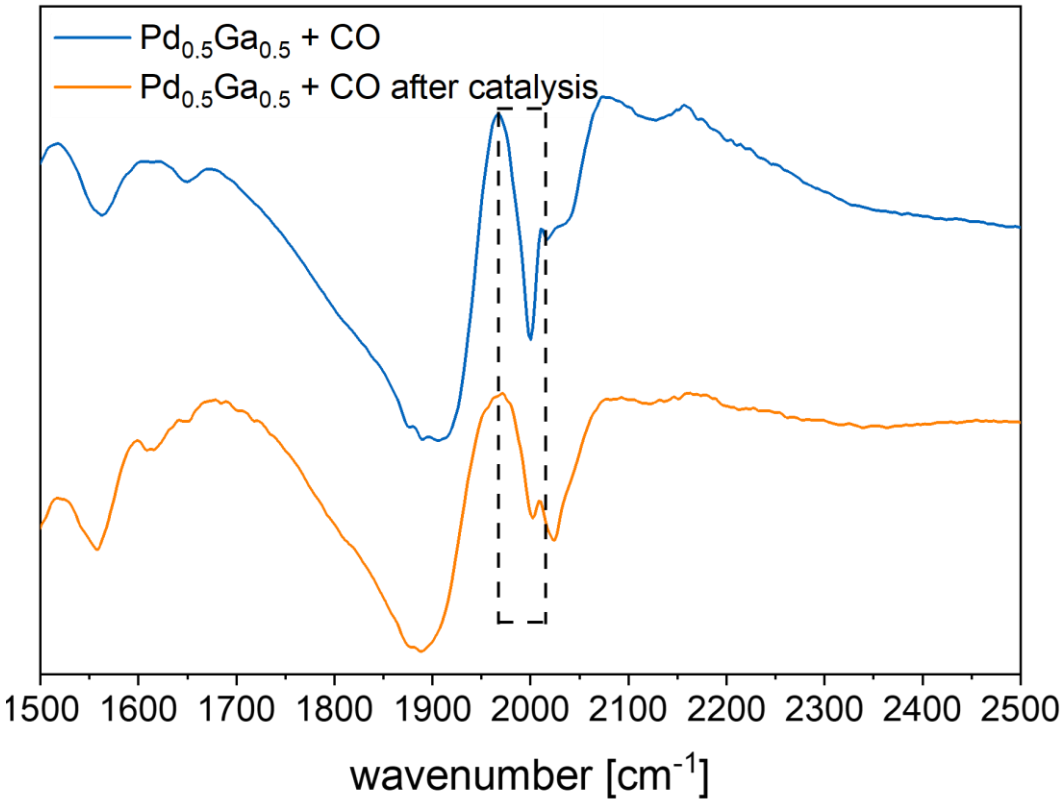

Figure 103. ATR FT-IR measurement of the $Pd_{0.5}Ga_{0.5}$ colloids upon addition of CO before (blue trace) and after (orange trace) the catalytic semi-hydrogenation of 3-hexyne showing a change of the signal at 2000 cm^{-1} typical for linearly bonded CO.

Particle analysis after catalysis

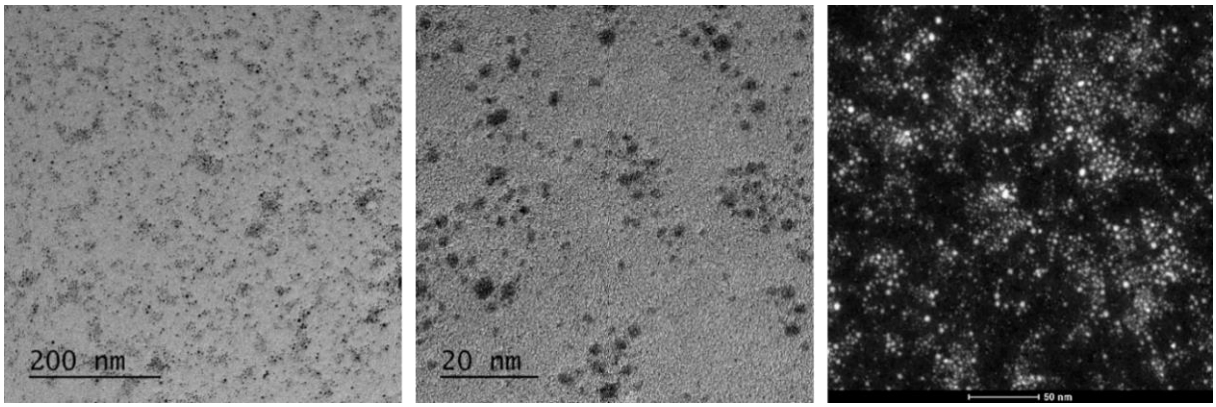

Figure 104. HR-TEM image and HAADF of $Pd_{0.5}Ga_{0.5}$ colloids after semi-hydrogenation catalysis of 3-hexyne at 0°C and 2.0 bar H_2 after 5 h.

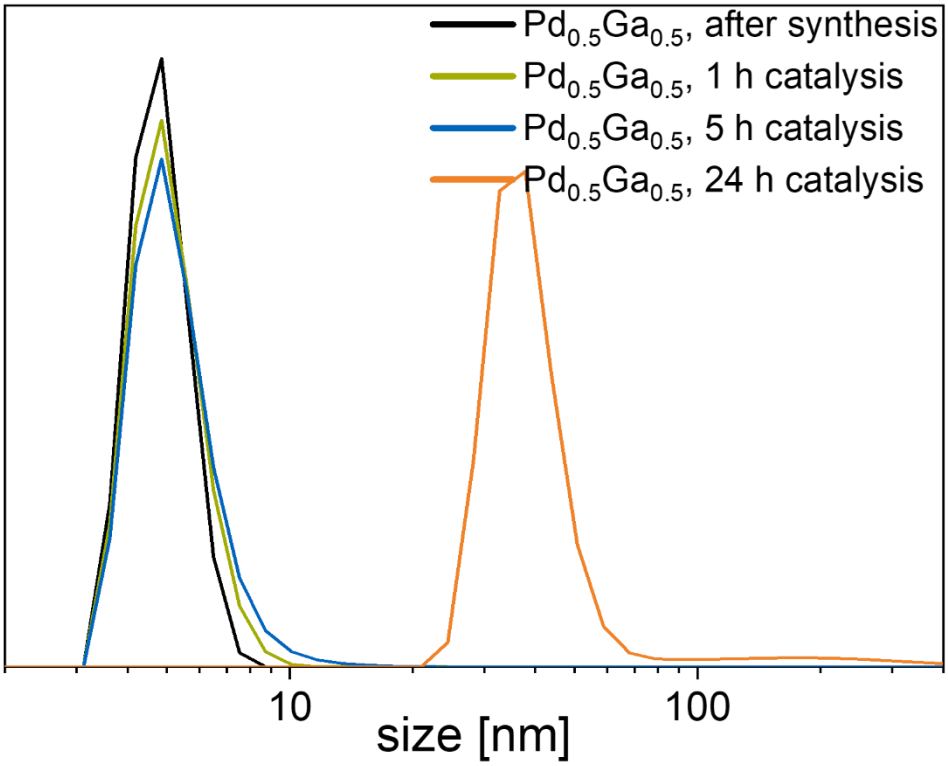

Figure 105. DLS monitoring of $Pd_{0.5}Ga_{0.5}$ colloids during the semi-hydrogenation of 3-hexyne at 0°C and 2.0 bar H_2.

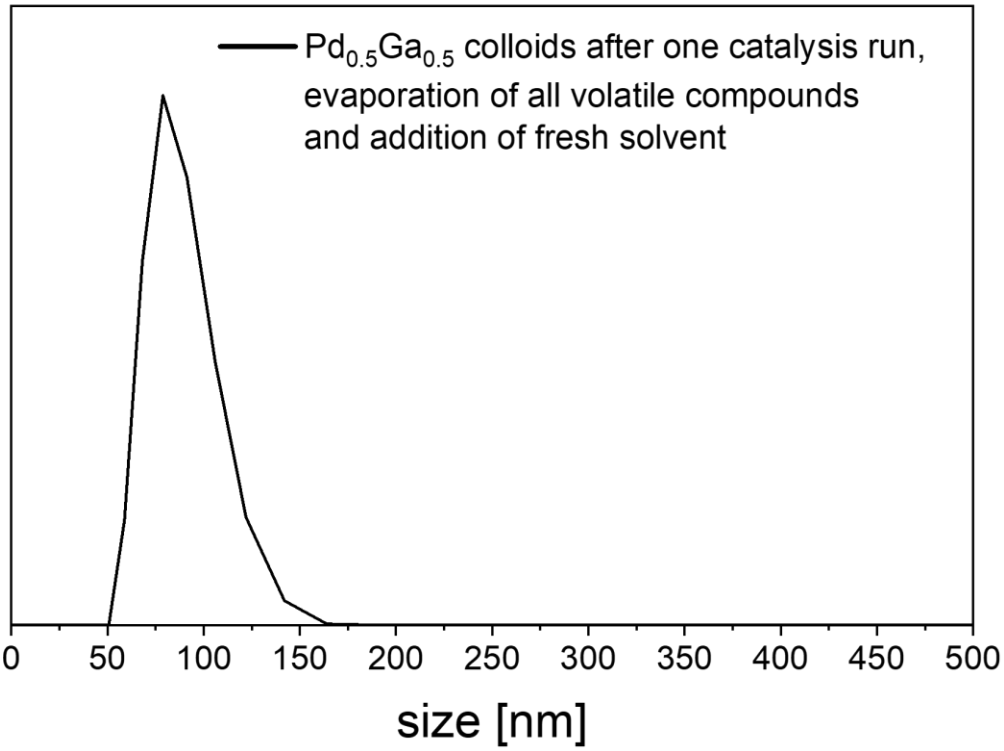

Figure 106. DLS measurements of $Pd_{0.5}Ga_{0.5}$ colloids after one catalysis run, evaporation of all volatile compounds and addition of fresh solvent and substrate showing agglomeration.

$Pd_{1-x}Ga_x$@carboxylic acids

Particle analysis

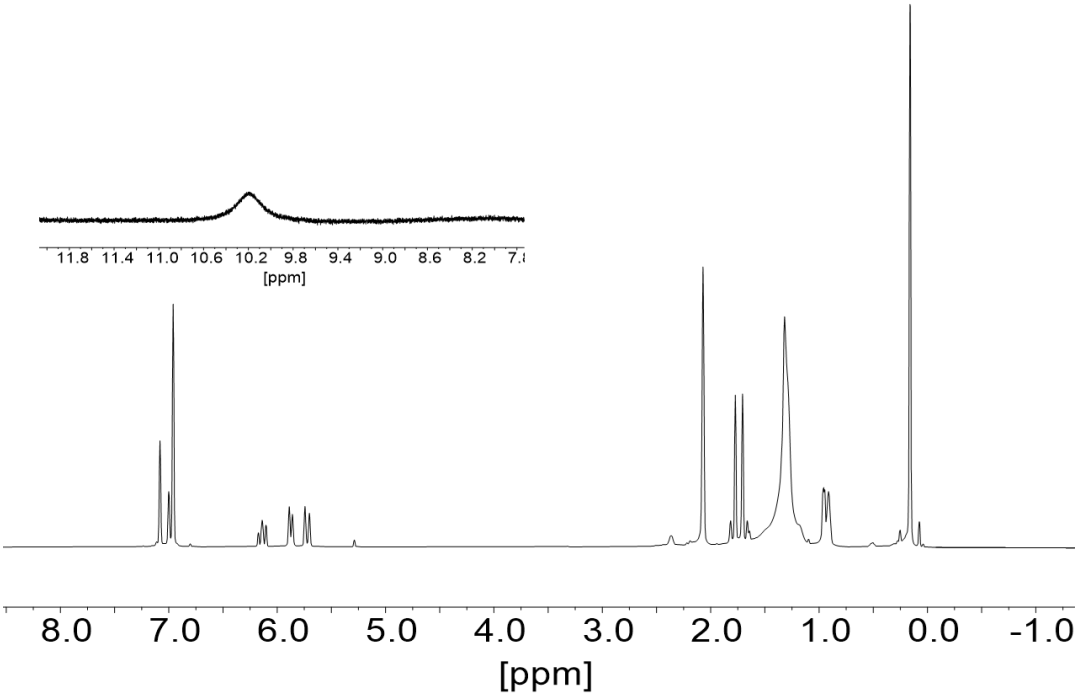

Figure 107. Representative ^{1}H NMR spectra (toluene-d_8) of colloidal $Pd_{1-x}Ga_x$@1.0 equiv. $C_{18}H_{37}{}^{13}COOH$ (Pd/Ga = 1:1).

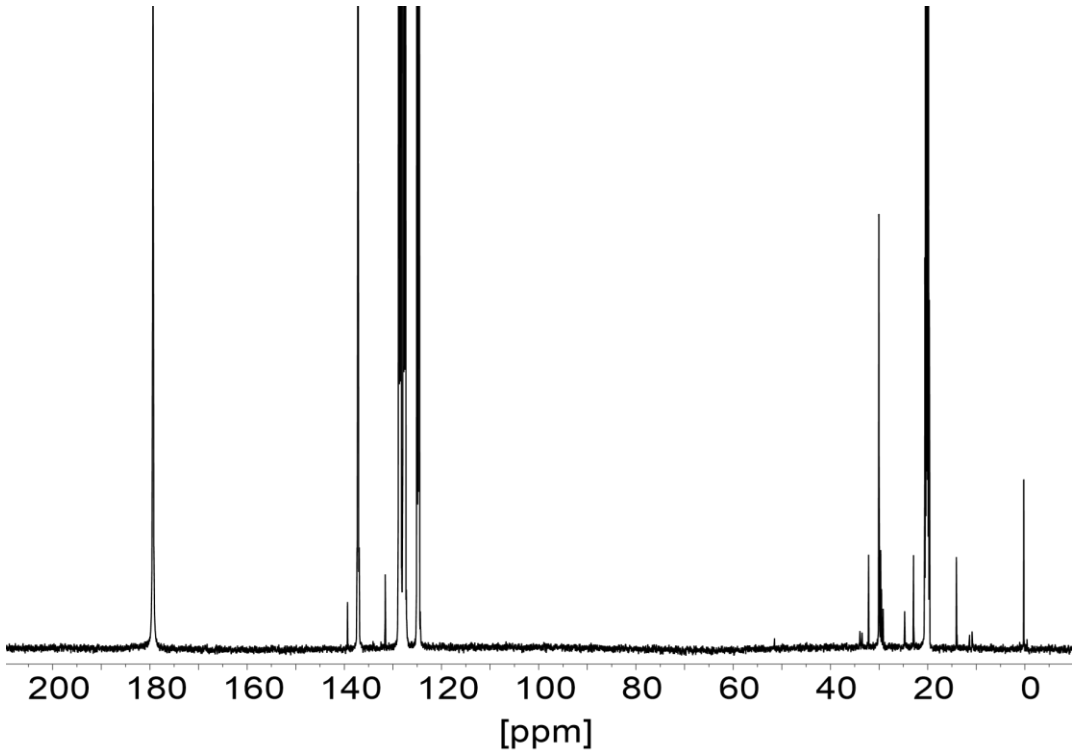

Figure 108. Representative ^{13}C NMR spectra (toluene-d_8) of colloidal $Pd_{0.5}Ga_{0.5}$@2.0 equiv. $C_{18}H_{37}{}^{13}COOH$ (Pd/Ga = 1:1).

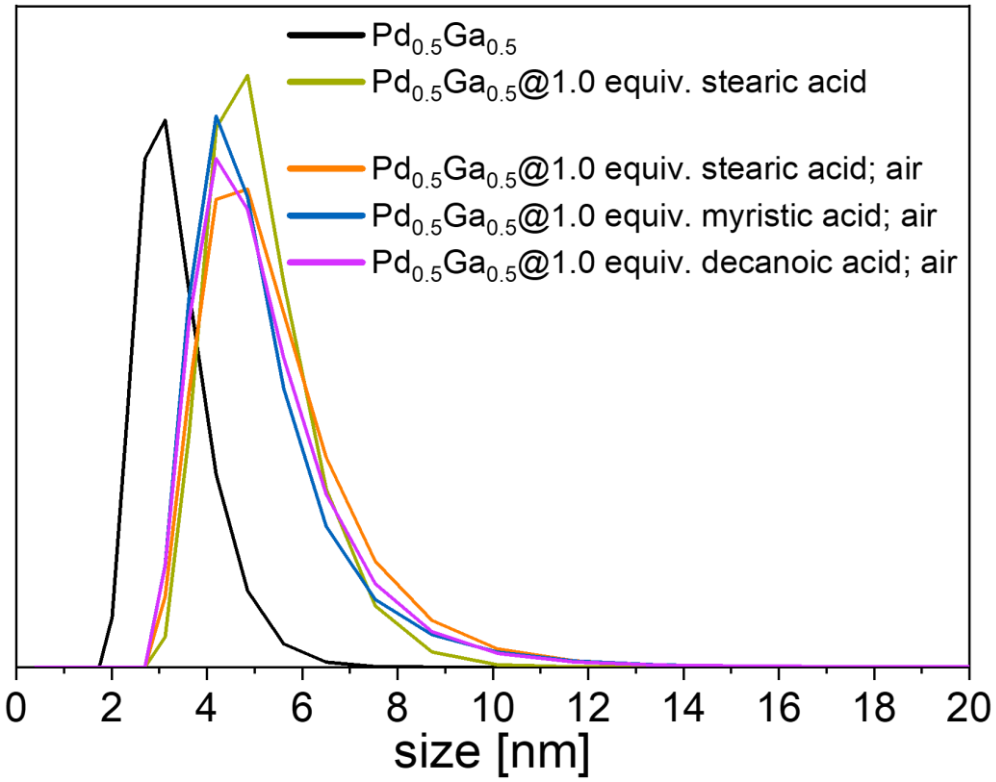

Figure 109. DLS measurements of $Pd_{0.5}Ga_{0.5}$ colloids upon addition of various carboxylic acids stored at argon and at air showing no particle agglomeration.

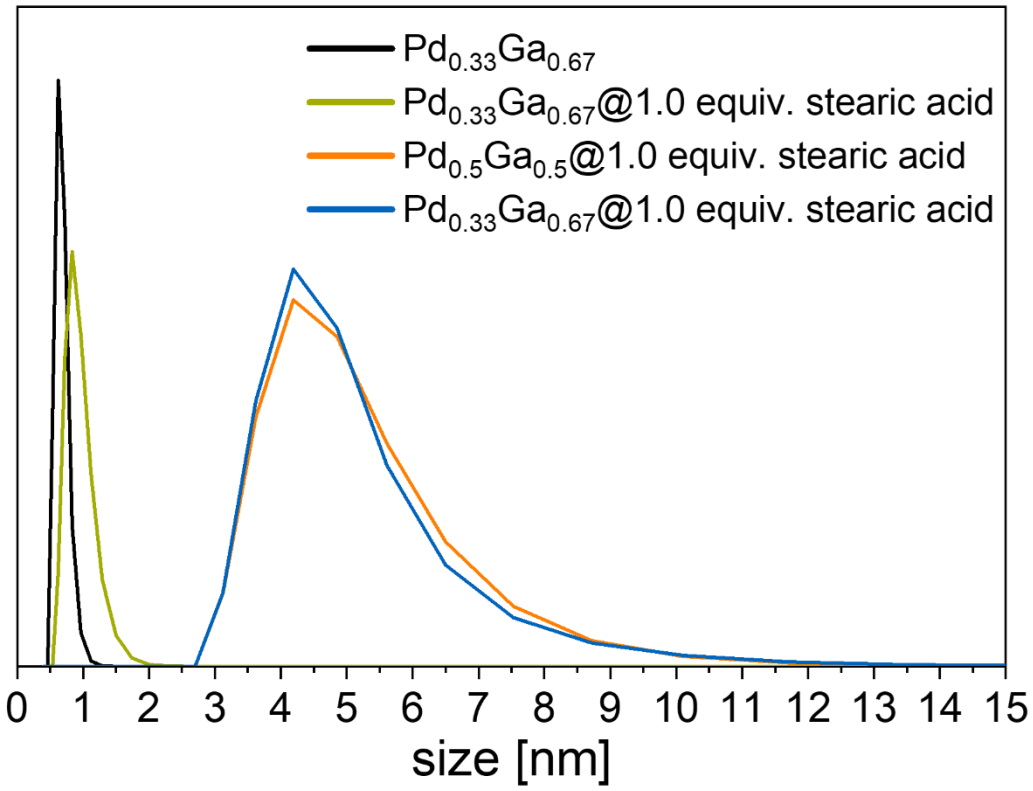

Figure 110. DLS measurements of $Pd_{1-x}Ga_x$ colloids upon addition of stearic acid.

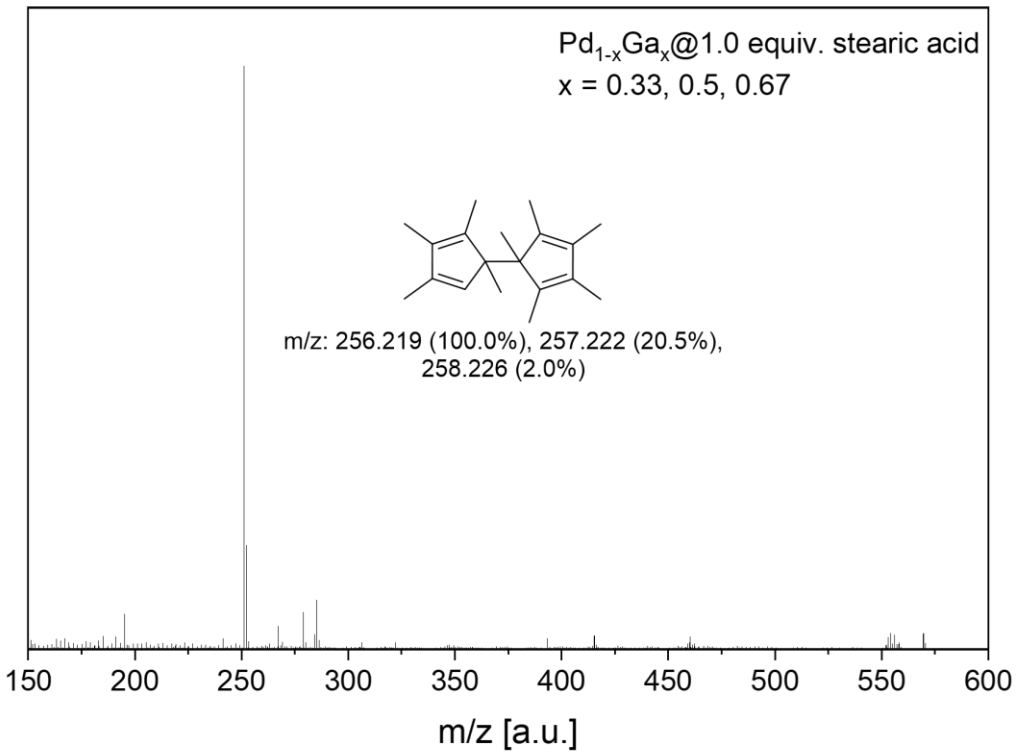

Figure 111. LIFDI-MS spectrum of $Pd_{1-x}Ga_x$@1.0 equiv. stearic acid showing only signals of organic molecules originating from the NP synthesis. Signals of metal clusters with higher m/z values (e.g. from metal leaching upon addition of the additive) were not detected.

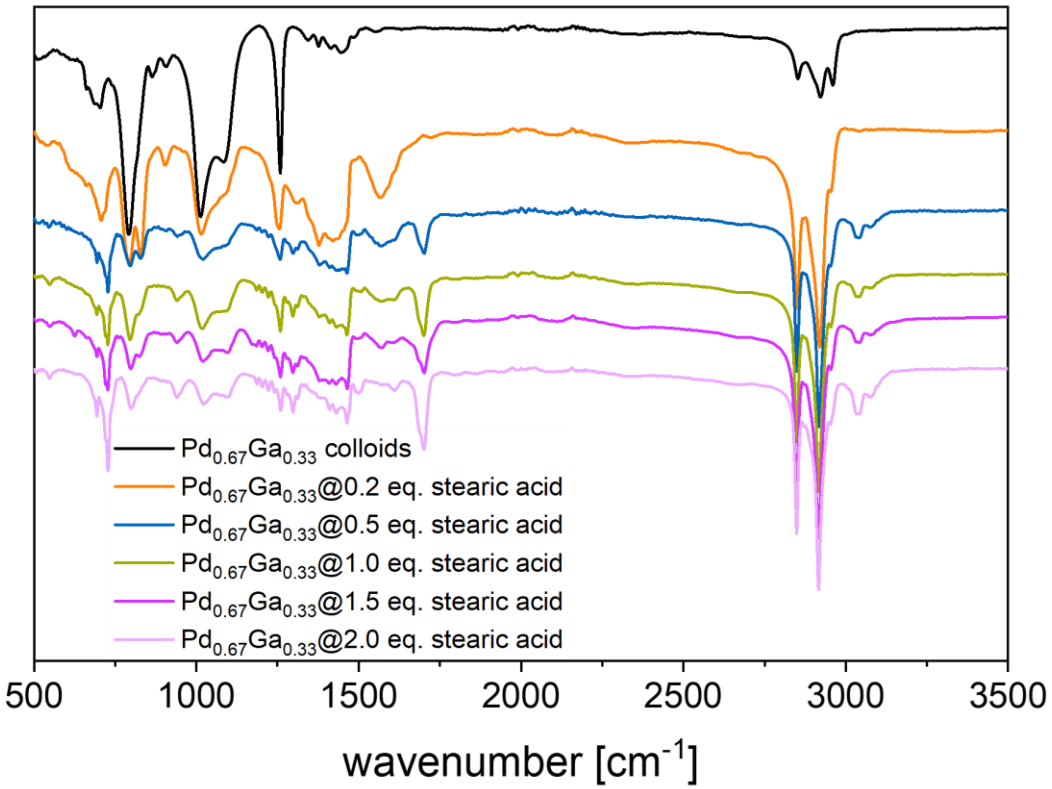

Figure 112. ATR FT-IR measurement of the $Pd_{0.67}Ga_{0.33}$@stearic acid colloids and $Pd_{0.67}Ga_{0.33}$ colloids without additives as reference.

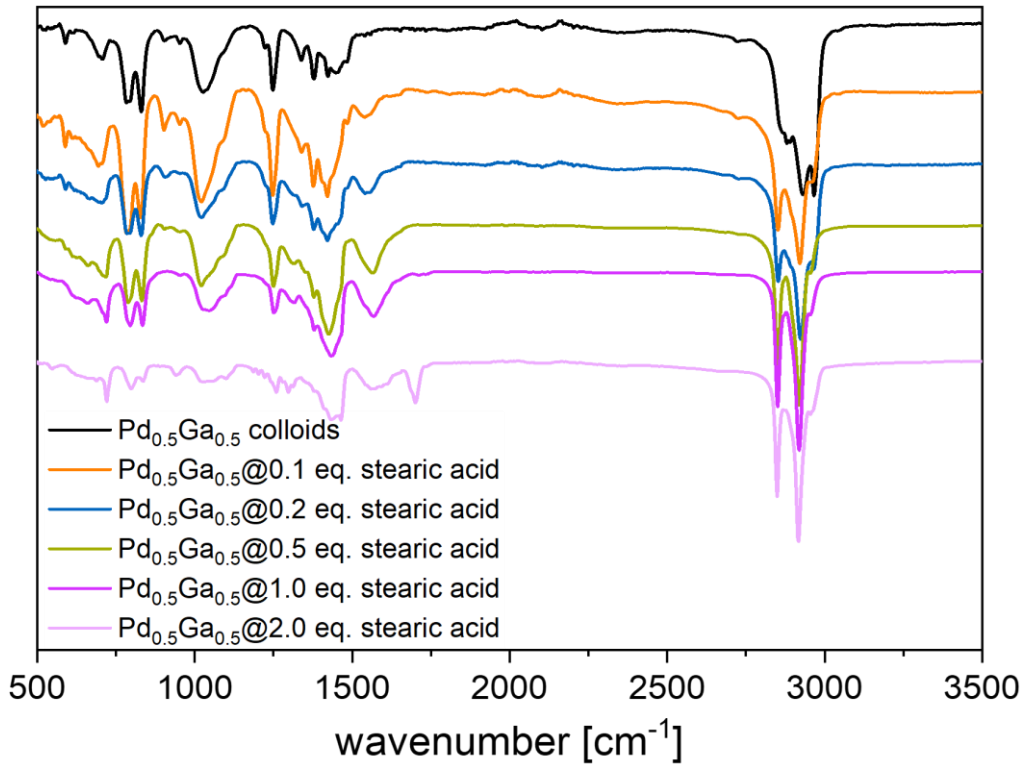

Figure 113. ATR FT-IR measurement of the $Pd_{0.5}Ga_{0.5}$@stearic acid colloids and $Pd_{0.5}Ga_{0.5}$ colloids without additives as reference.

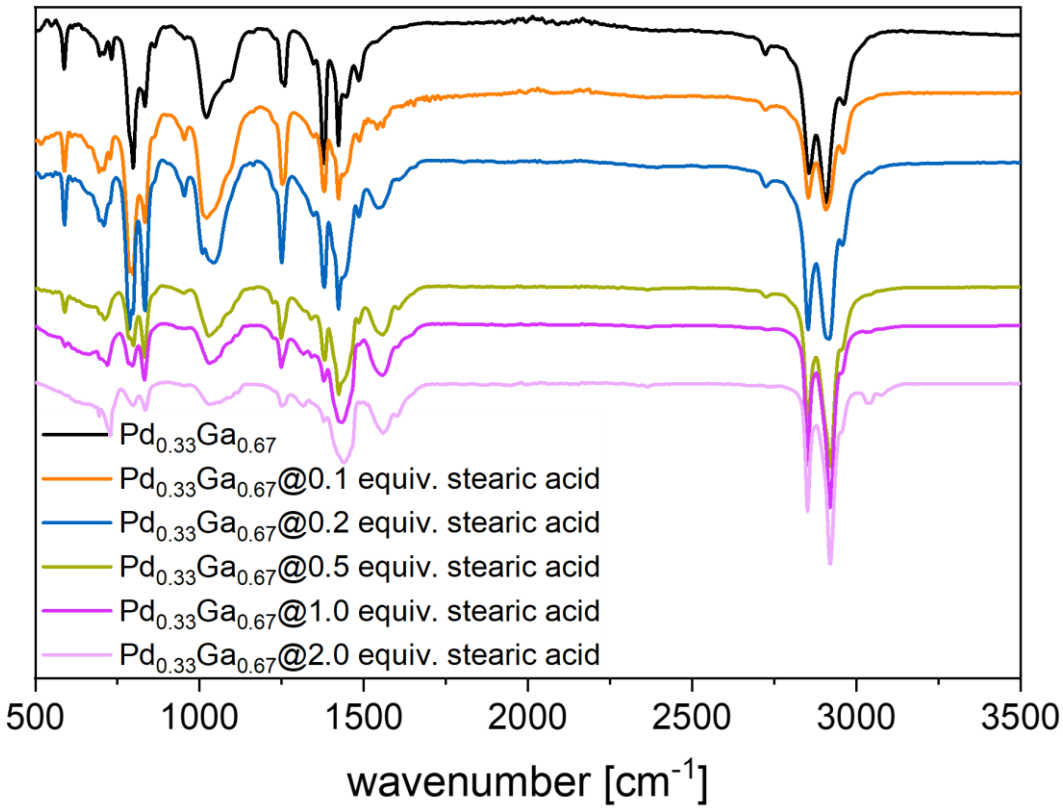

Figure 114. ATR FT-IR measurement of the $Pd_{0.33}Ga_{0.67}$@stearic acid colloids and $Pd_{0.33}Ga_{0.67}$ colloids without additives as reference.

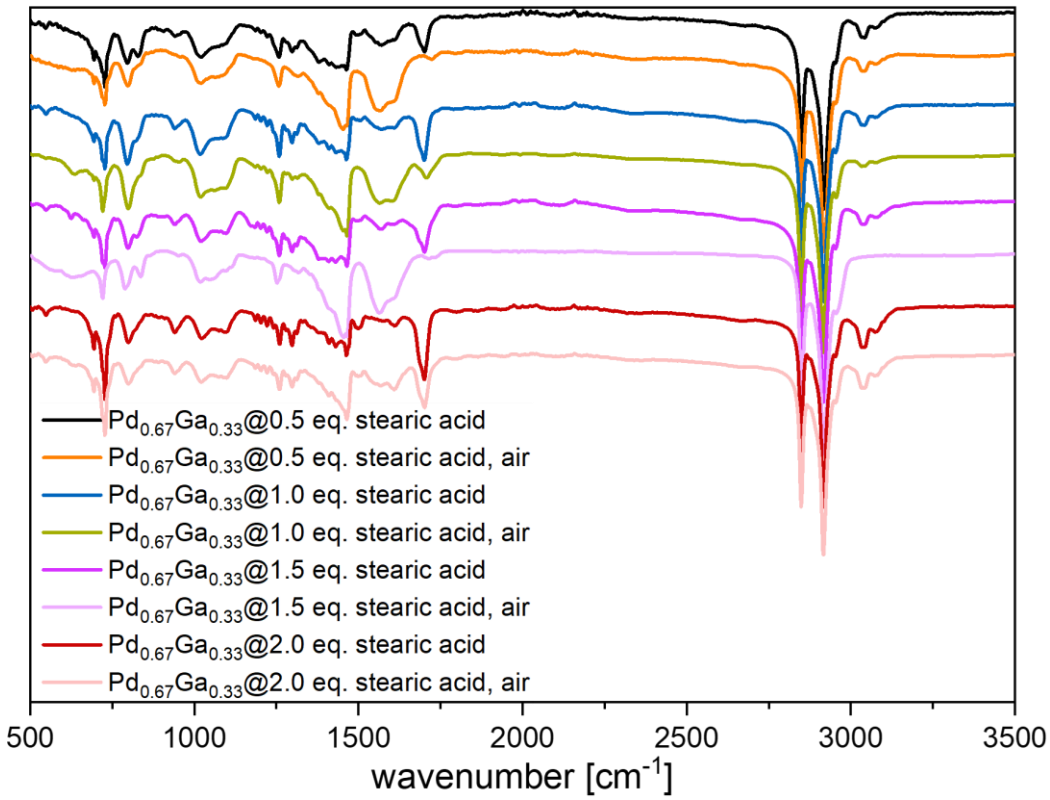

Figure 115. ATR FT-IR measurement of $Pd_{0.67}Ga_{0.33}$@stearic acid colloids stored under inert conditions and upon exposure to air.

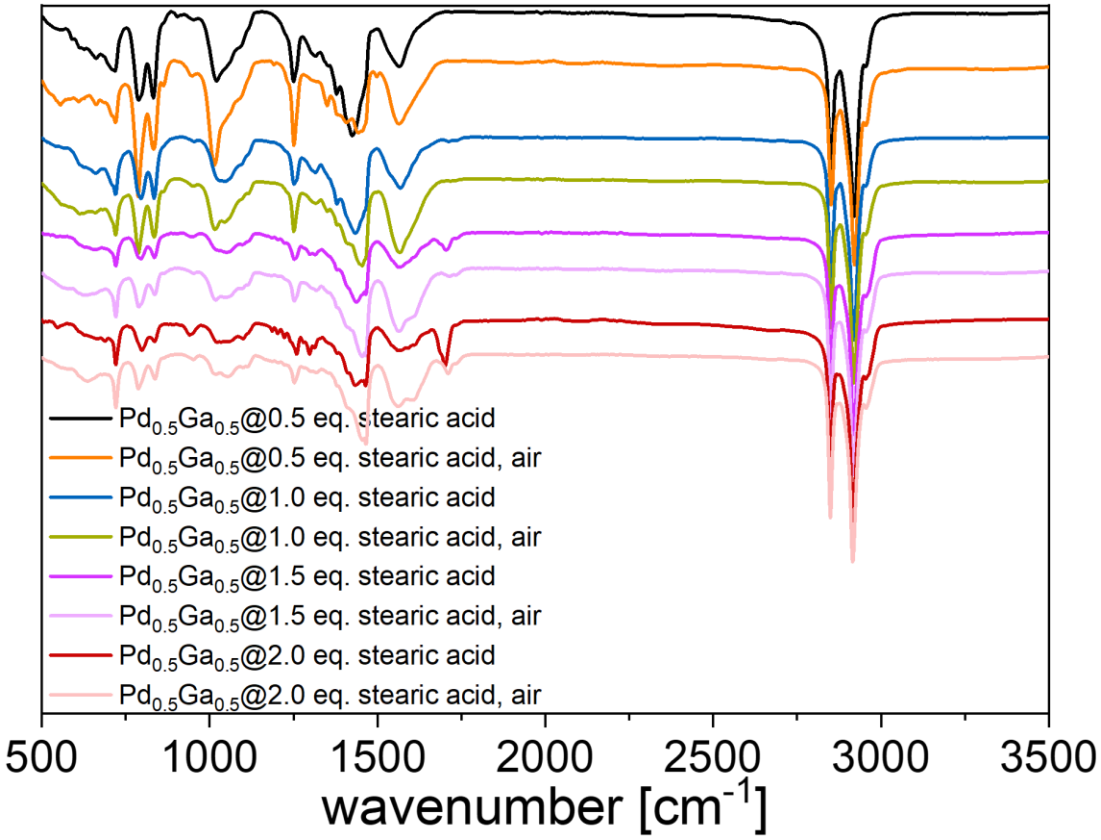

Figure 116. ATR FT-IR measurement of the $Pd_{0.5}Ga_{0.5}$@stearic acid colloids stored under inert conditions and upon exposure to air.

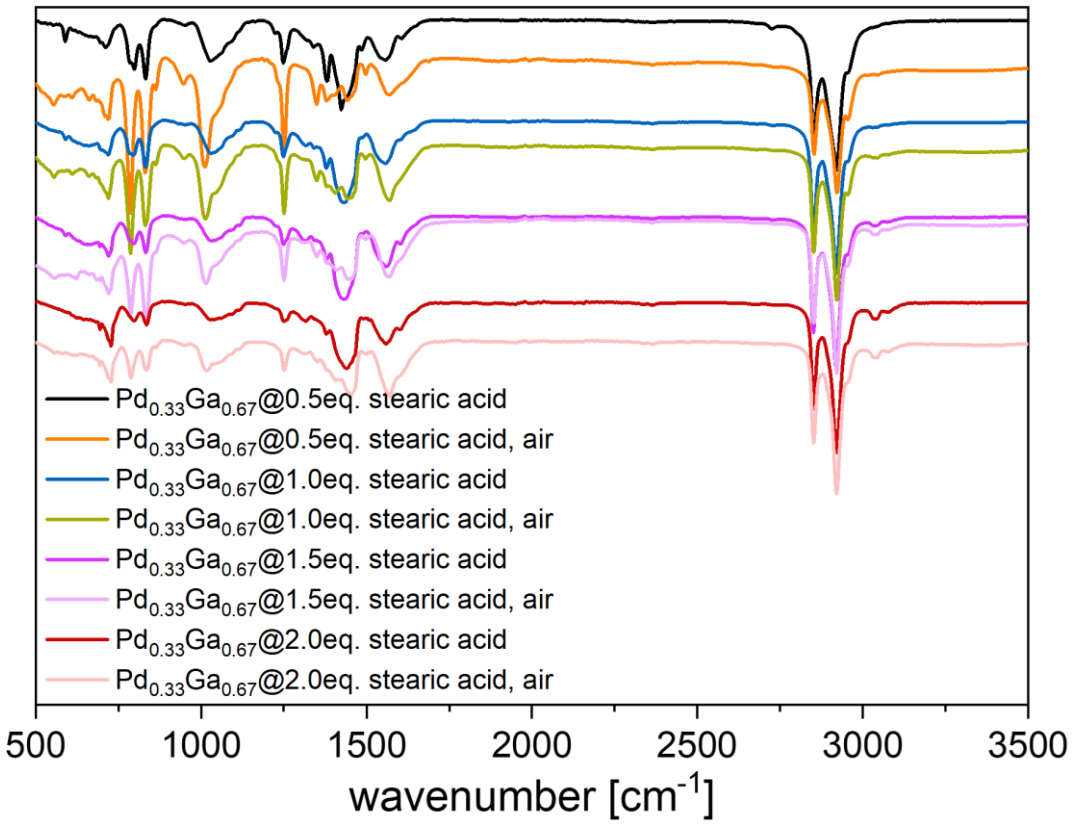

Figure 117. ATR FT-IR measurement of the $Pd_{0.33}Ga_{0.67}$@stearic acid colloids stored under inert conditions and upon exposure to air.

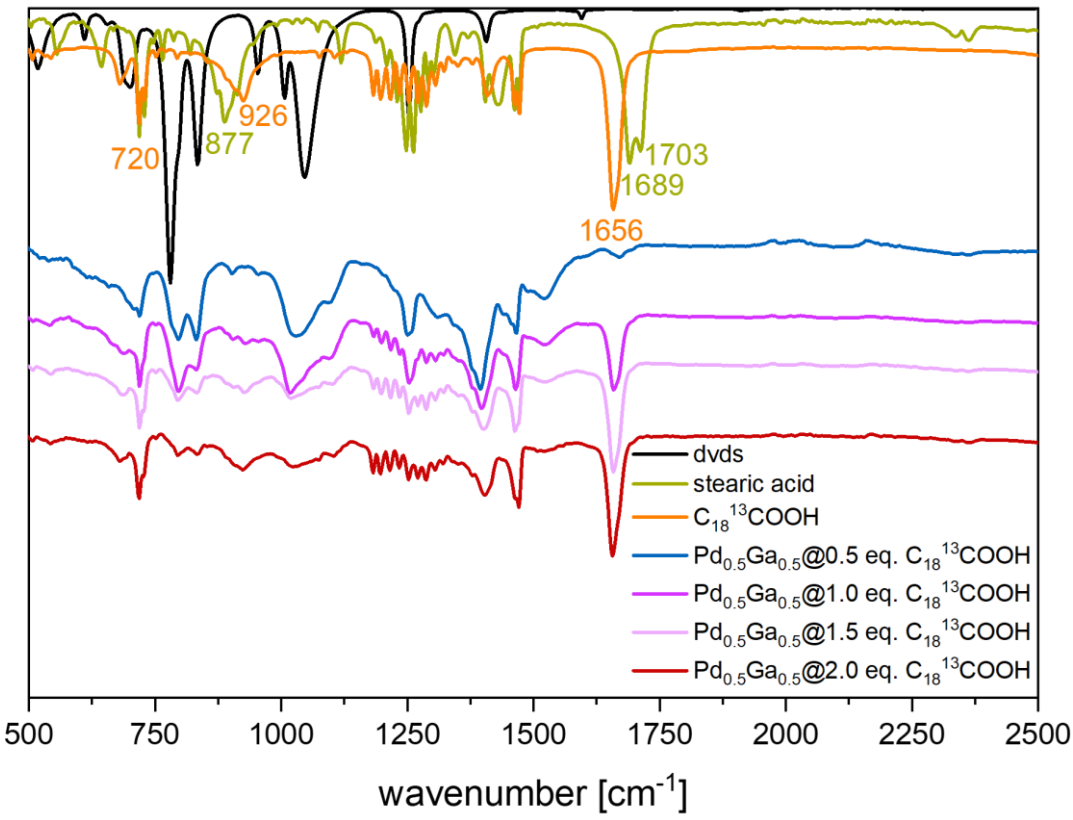

Figure 118. ATR FT-IR measurement of the $Pd_{0.5}Ga_{0.5}$@$C_{18}H_{37}{}^{13}COOH$ (bottom traces).

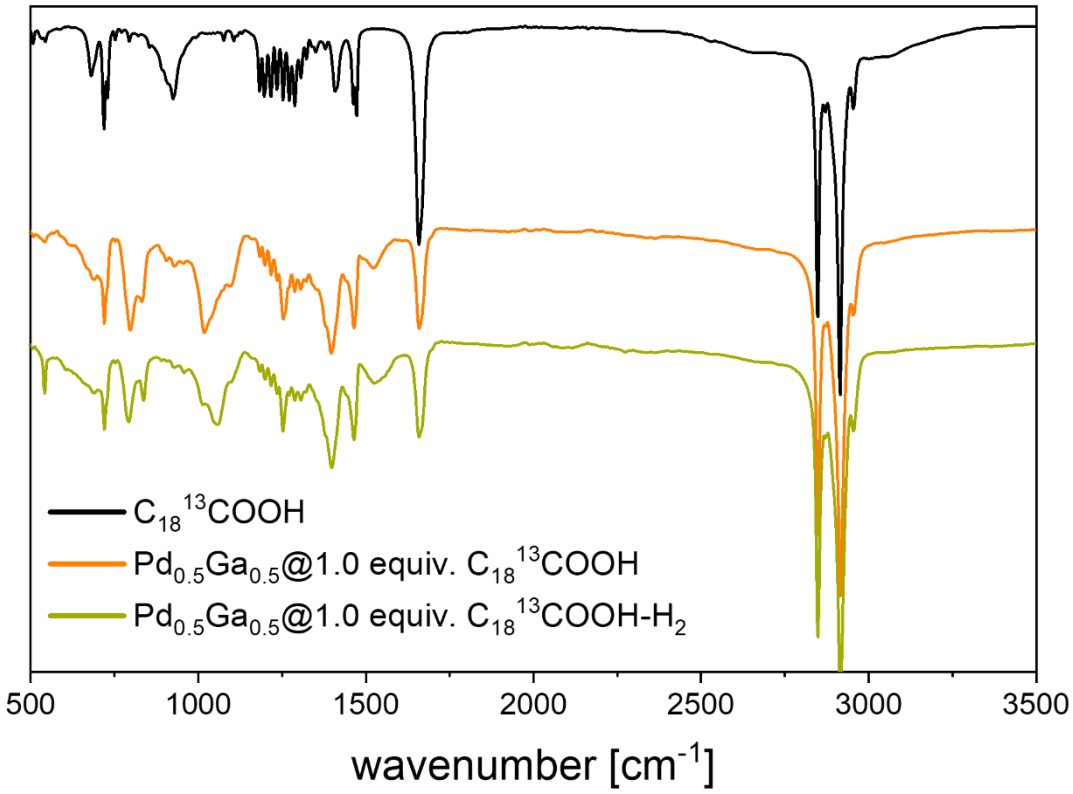

Figure 119. ATR FT-IR measurement of the $Pd_{0.5}Ga_{0.5}@C_{18}H_{37}{}^{13}COOH$ upon exposure to hydrogen showing no decomposition of the additive.

Particle analysis after catalysis

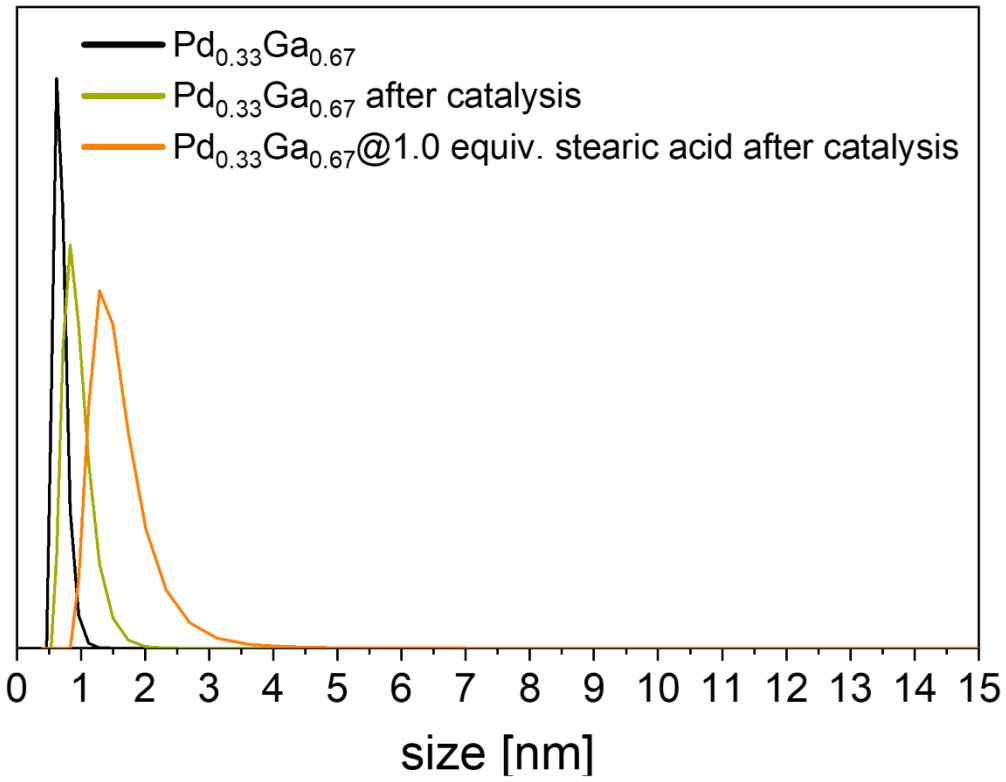

Figure 120. DLS measurements of $Pd_{0.33}Ga_{0.67}$ colloids with and without additive after the semi-hydrogenation of 2-octyne at 0°C and 1.0 bar H_2 after 5 h.

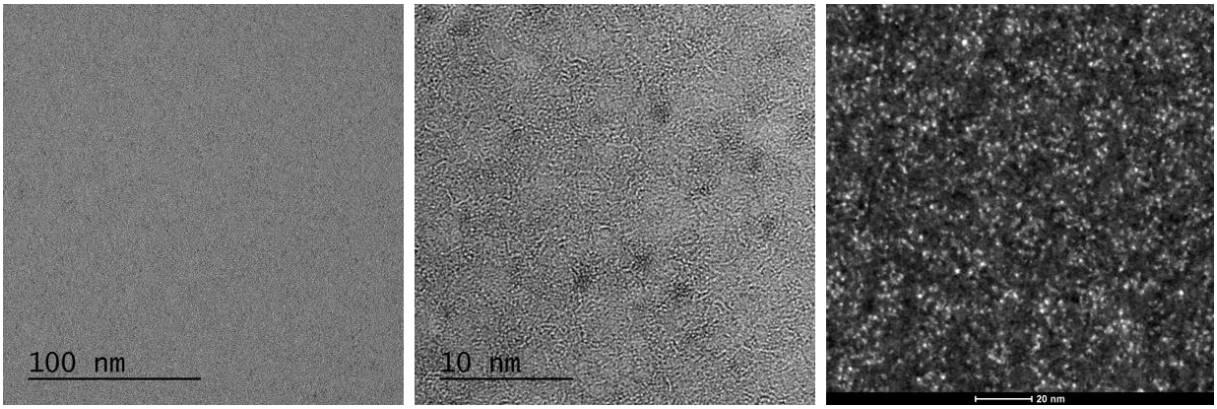

Figure 121. HR-TEM image and HAADF of $Pd_{0.33}Ga_{0.67}$ colloids without any additives after semi-hydrogenation catalysis of 2-octyne at 0°C and 1.0 bar H_2 after 5 h.

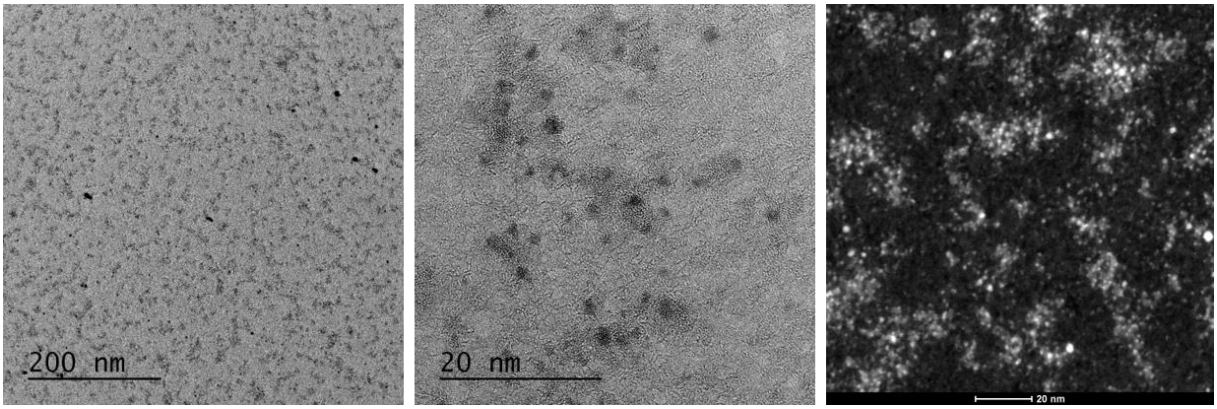

Figure 122. HR-TEM image and HAADF of $Pd_{0.33}Ga_{0.67}$@1.0 equiv. stearic acid colloids stored under inert conditions after semi-hydrogenation catalysis of 2-octyne at 0°C and 1.0 bar H_2 after 5 h.

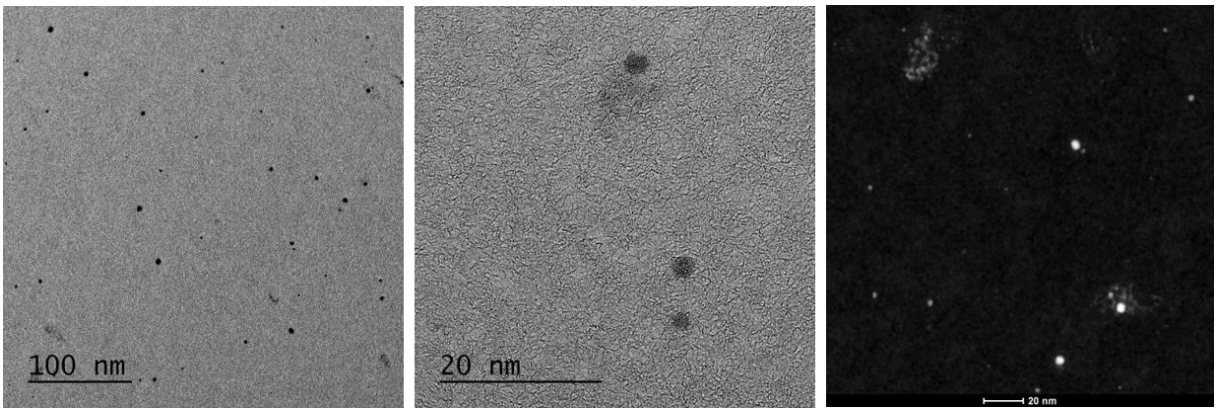

Figure 123. HR-TEM image and HAADF of $Pd_{0.33}Ga_{0.67}$@1.0 equiv. stearic acid colloids stored under ambient conditions (air) after semi-hydrogenation catalysis of 2-octyne at 0°C and 1.0 bar H_2 after 5 h.

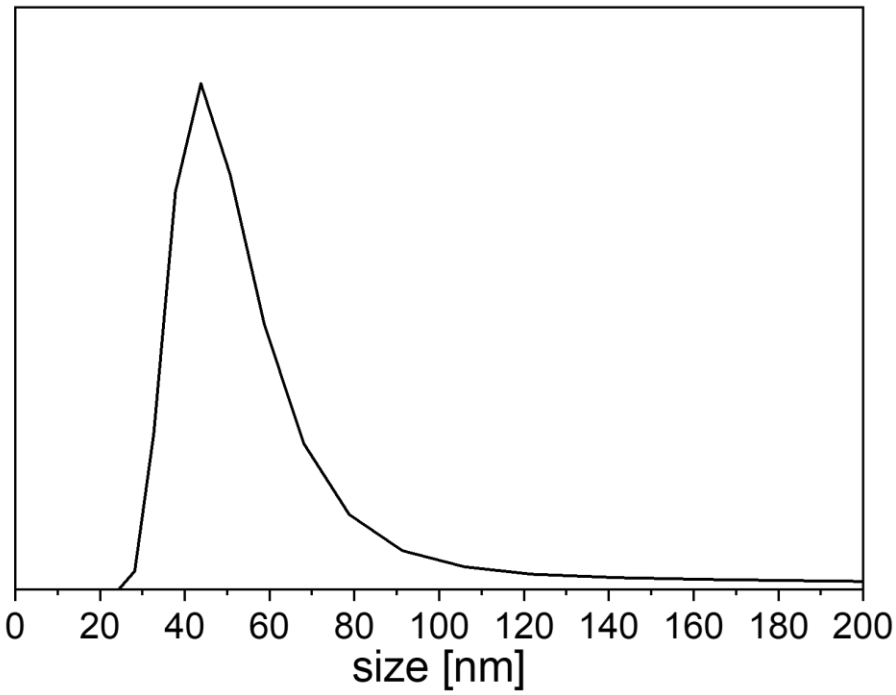

Figure 124. DLS measurements of $Pd_{0.33}Ga_{0.67}$@1.0 equiv. stearic acid after the semi-hydrogenation of 2-octyne at 25°C and 1.0 bar H_2 after 5 h showing particle agglomeration.

$Fe_{1-x}Al_x$ colloids

Particle analysis

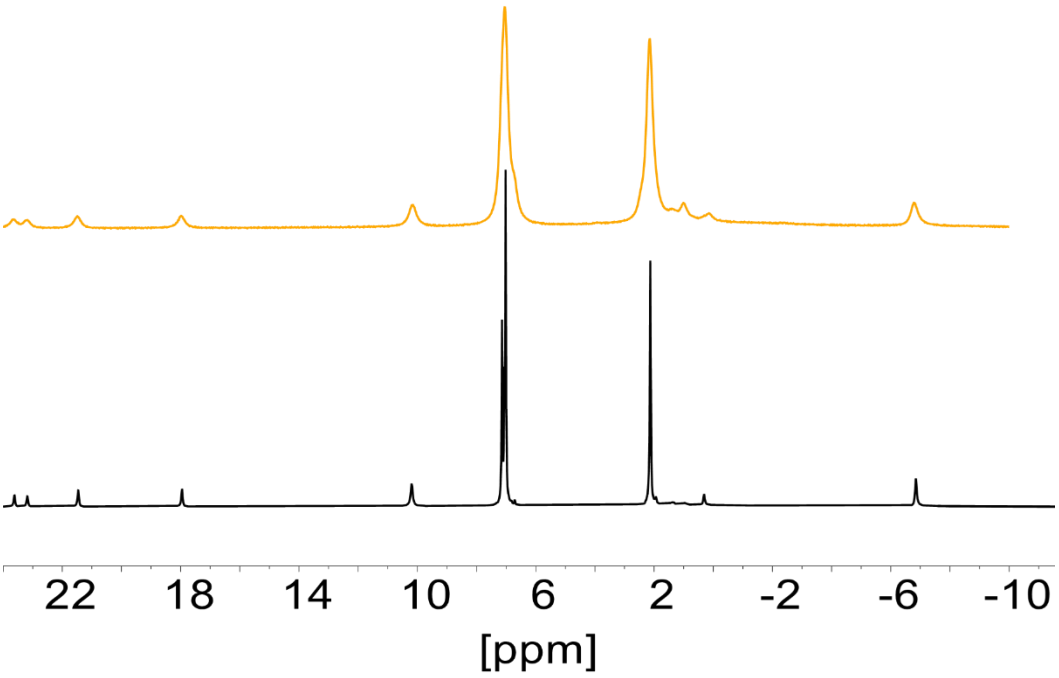

Figure 125. ^{1}H NMR spectra of [Fe_2(mesityl)$_4$] (bottom, black trace) and of the reaction solution directly after the addition of [AlH_3]-NMe_3 to [Fe_2(mesityl)$_4$] (molar ratio 1:1) showing still the characteristic signals of the metal precursor.

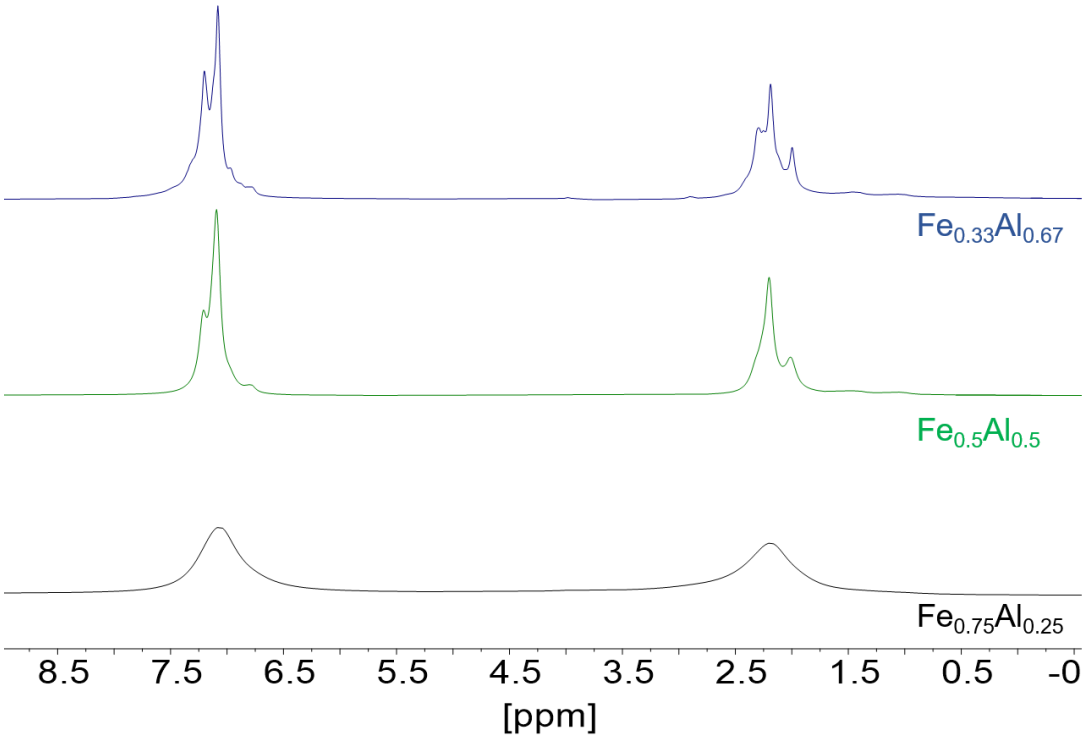

Figure 126. ^{1}H NMR spectra (in toluene-d_8) of $Fe_{1-x}Al_x$ colloidal solutions.

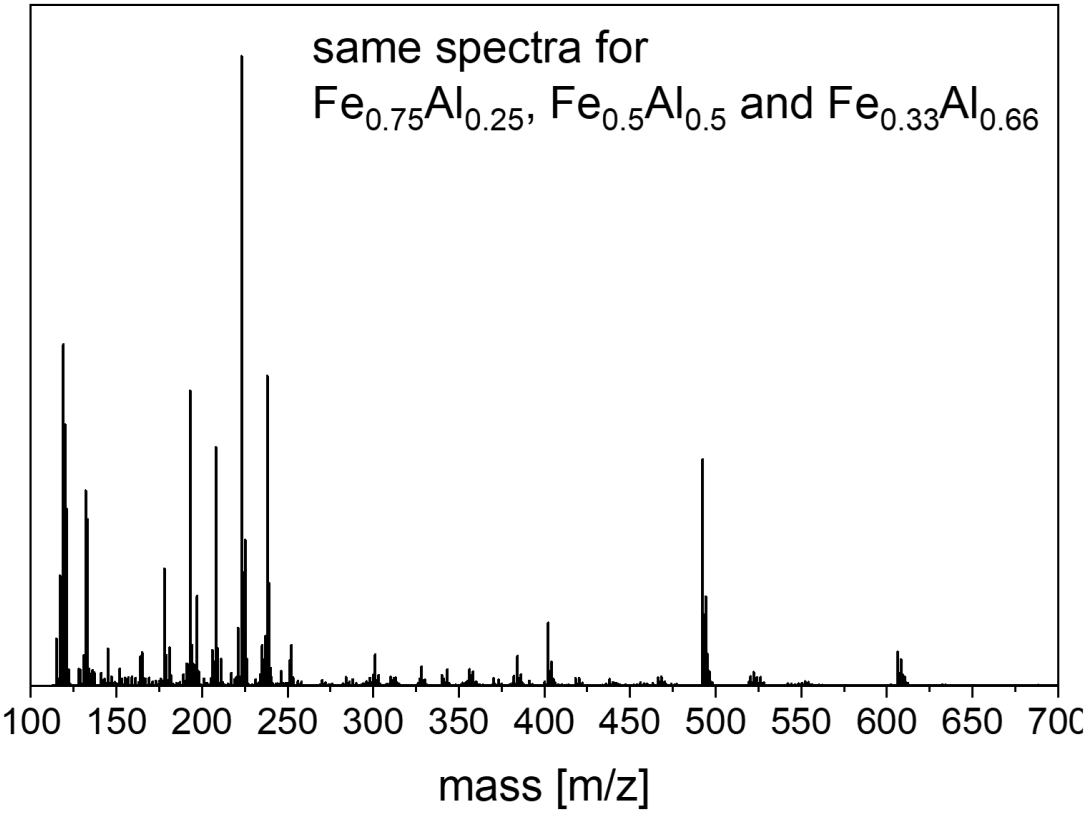

Figure 127. LIFDI-MS spectra of $Fe_{1-x}Al_x$ colloidal solutions.

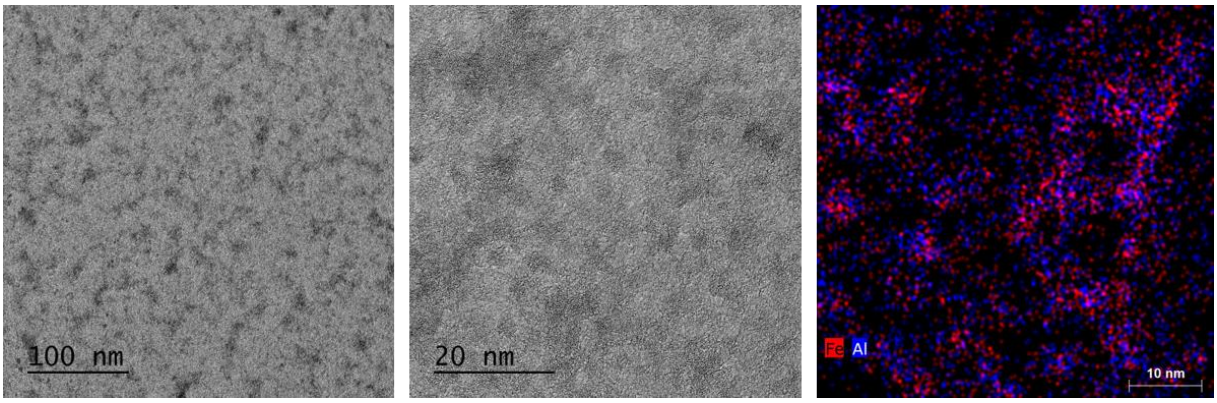

Figure 128. HR-TEM images of $Fe_{0.5}Al_{0.5}$ colloidal solutions before H_2 addition showing a decreased crystallinity compared to the colloids after 20 min under H_2 pressure.

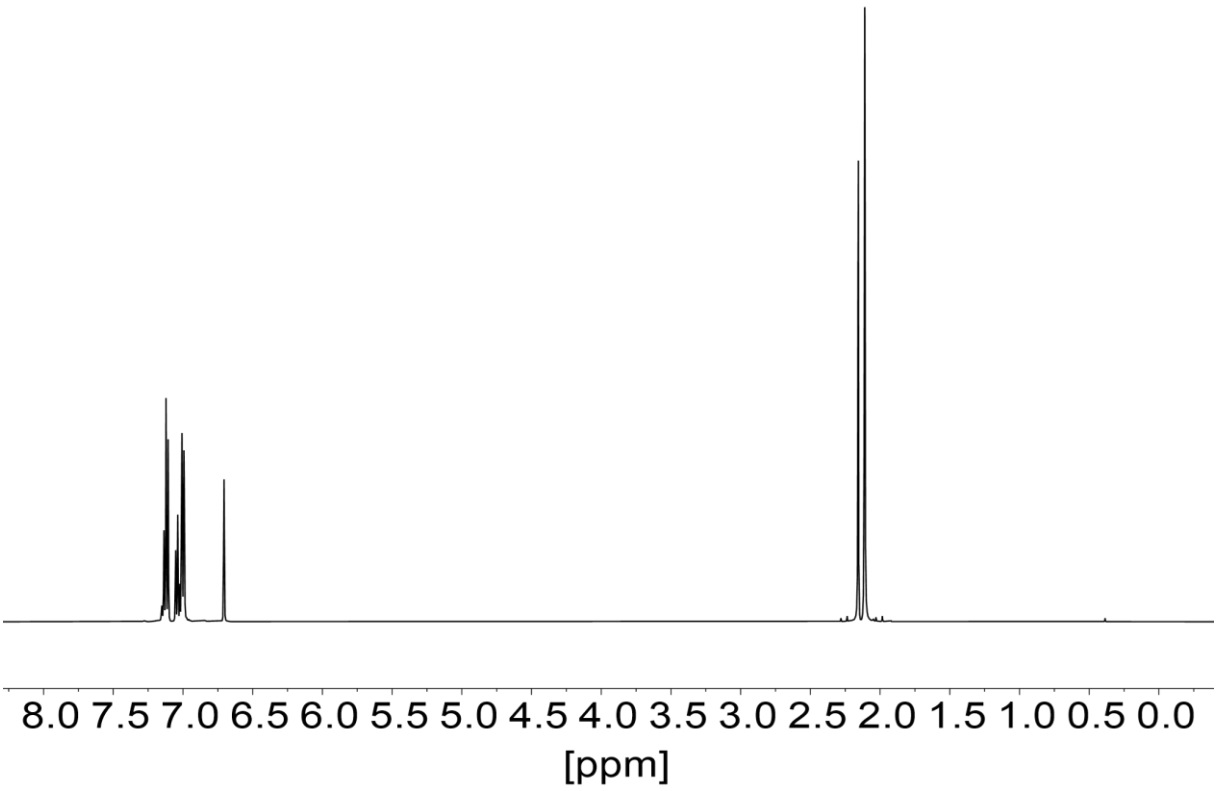

Figure 129. ^{1}H NMR spectra (in toluene-d_8) of $Fe_{1-x}Al_x$ colloidal solutions after addition of HCl.

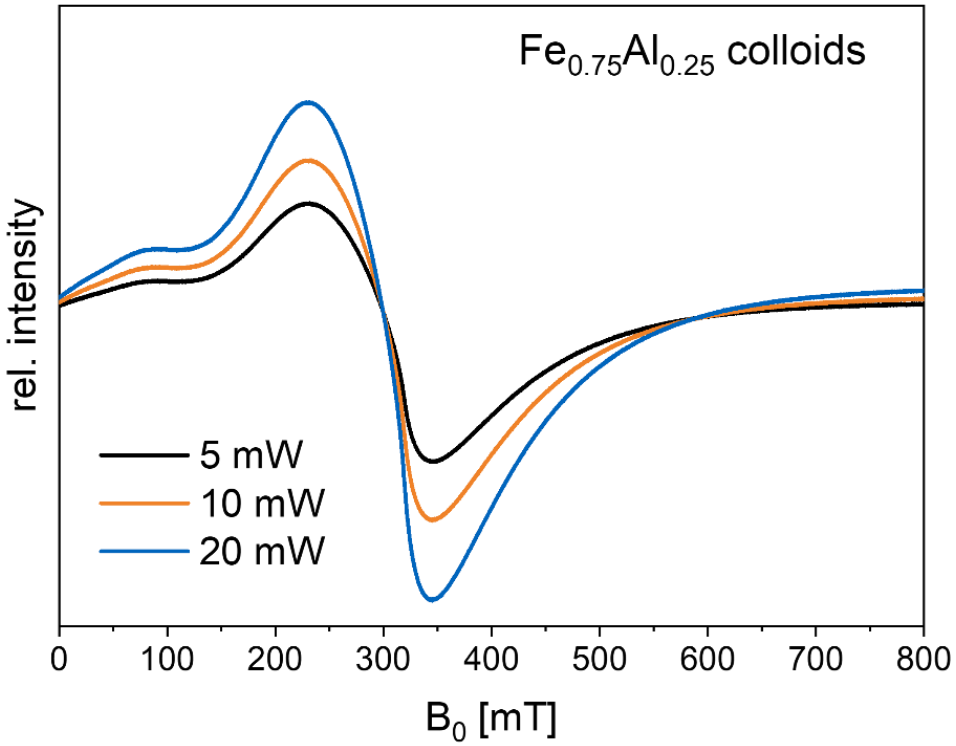

Figure 130. EPR measurement of $Fe_{0.75}Al_{0.25}$-colloids in mesitylene at -160 °C and different microwave powers.

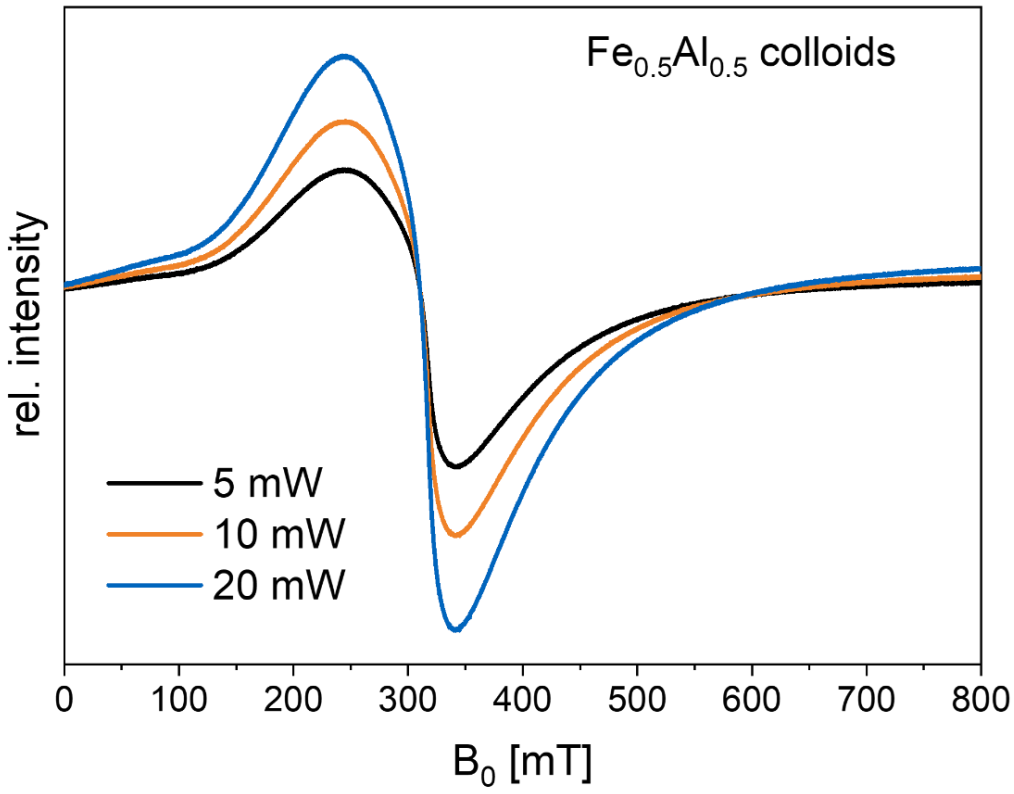

Figure 131. EPR measurement of $Fe_{0.5}Al_{0.5}$-colloids in mesitylene at -160 °C and different microwave powers.

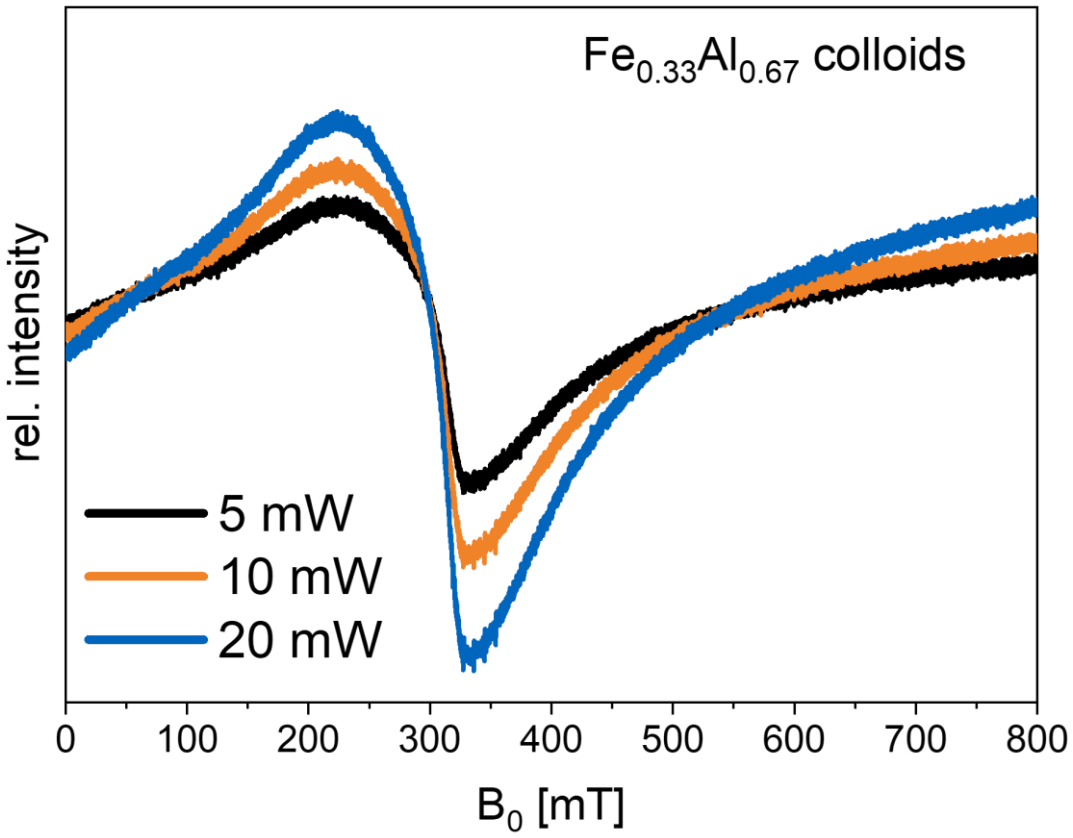

Figure 132. EPR measurement of $Fe_{0.33}Al_{0.67}$-colloids in mesitylene at -160 °C and different microwave powers.

$Fe_{1-x}Al_x$ powders

Particle analysis

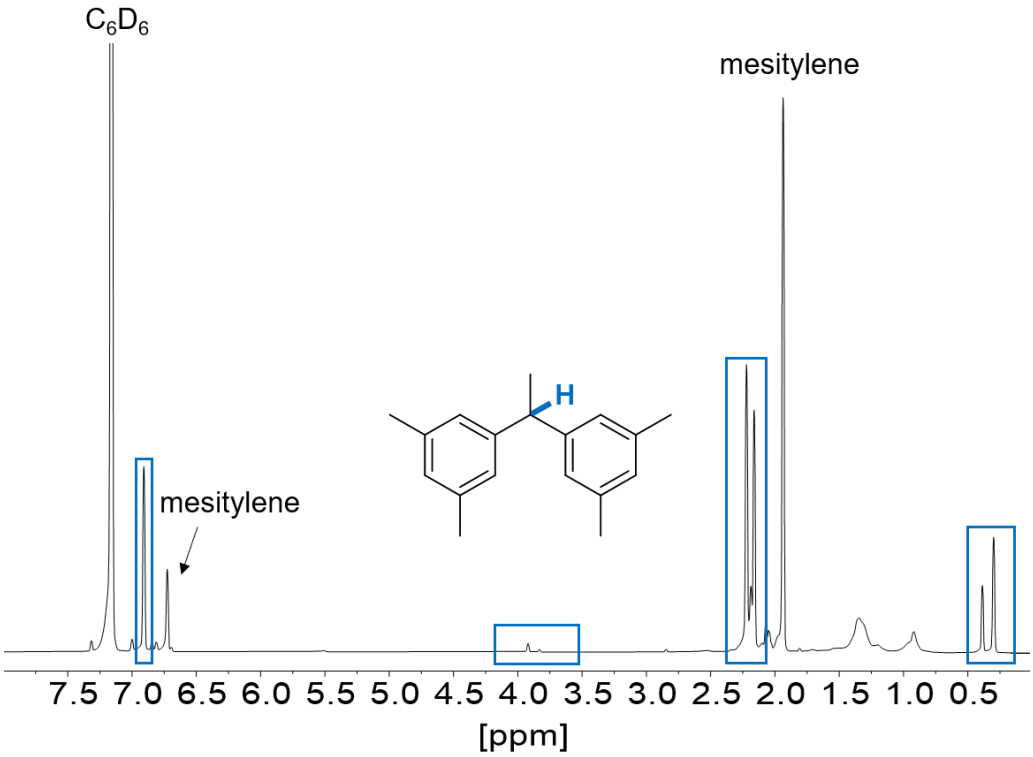

Figure 133. ^{1}H NMR spectra (in toluene-d_8) of the supernatant colourless reaction solution of the synthesis of $Fe_{1-x}Al_x$ powders.

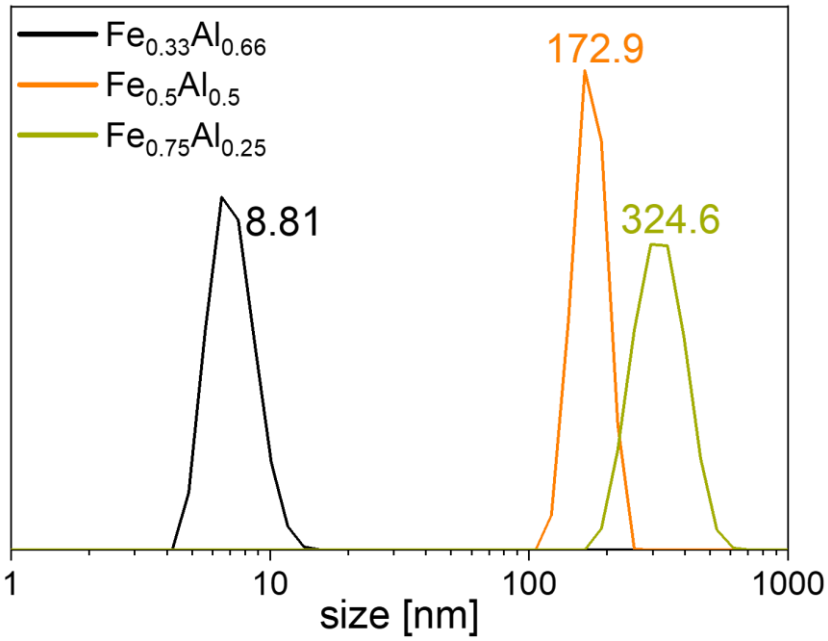

Figure 134. DLS measurement of $Fe_{1-x}Al_x$ powders. While $Fe_{0.75}Al_{0.25}$ and $Fe_{0.5}Al_{0.5}$ are only dispersed in solution, $Fe_{0.33}Al_{0.67}$ is re-dissolved in toluene.

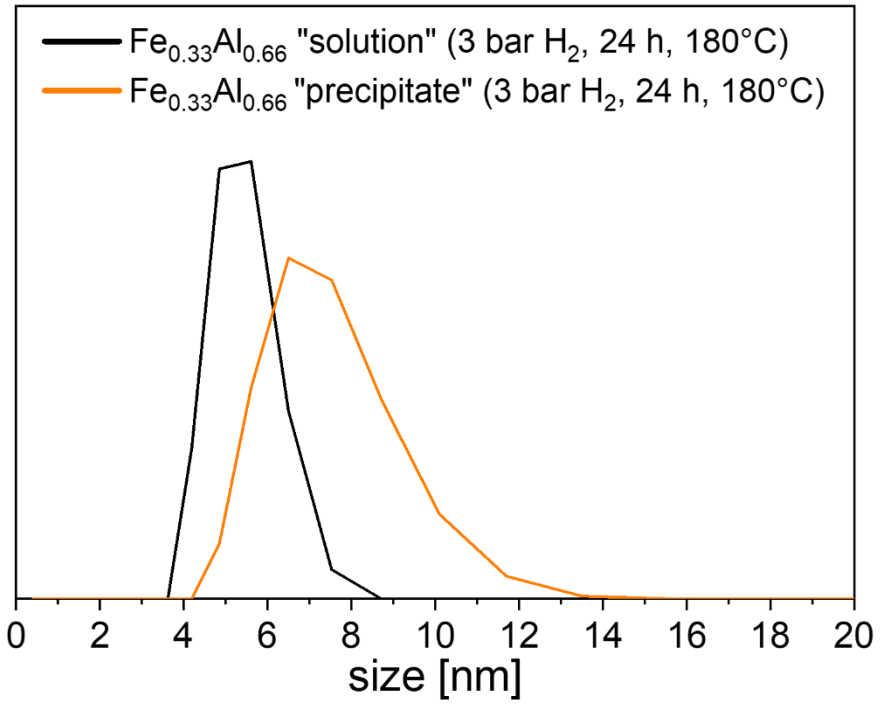

Figure 135. DLS measurement of the supernatant black solution and the precipitate of $Fe_{0.33}Al_{0.67}$ in toluene.

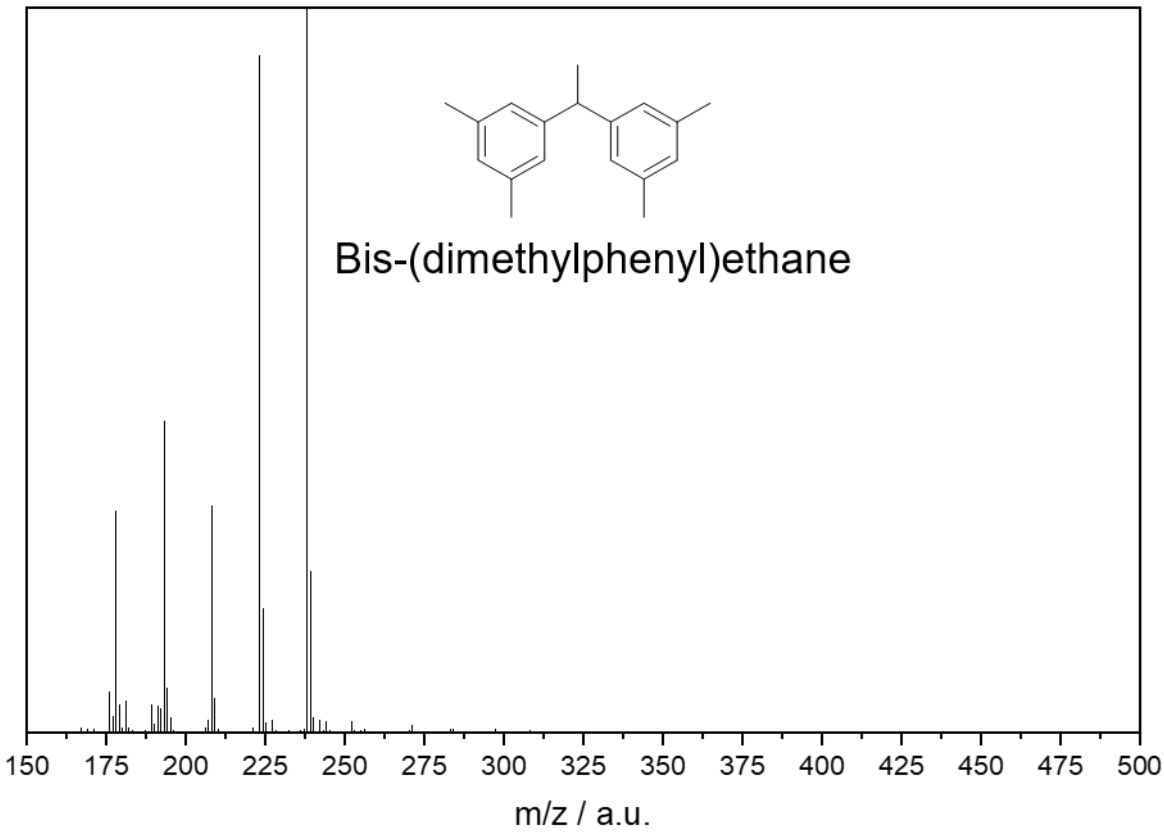

Figure 136. LIFDI-MS spectra of the supernatant colourless reaction solution of the synthesis of $Fe_{1-x}Al_x$ powders.

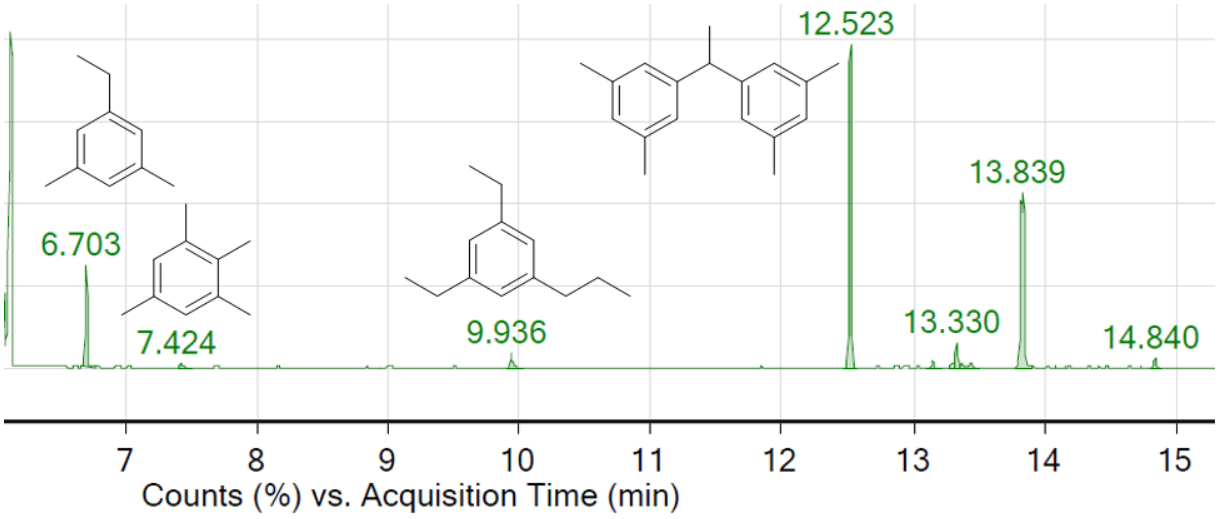

Figure 137. GC-MS spectra of the supernatant colourless reaction solution of the synthesis of $Fe_{1-x}Al_x$ powders.

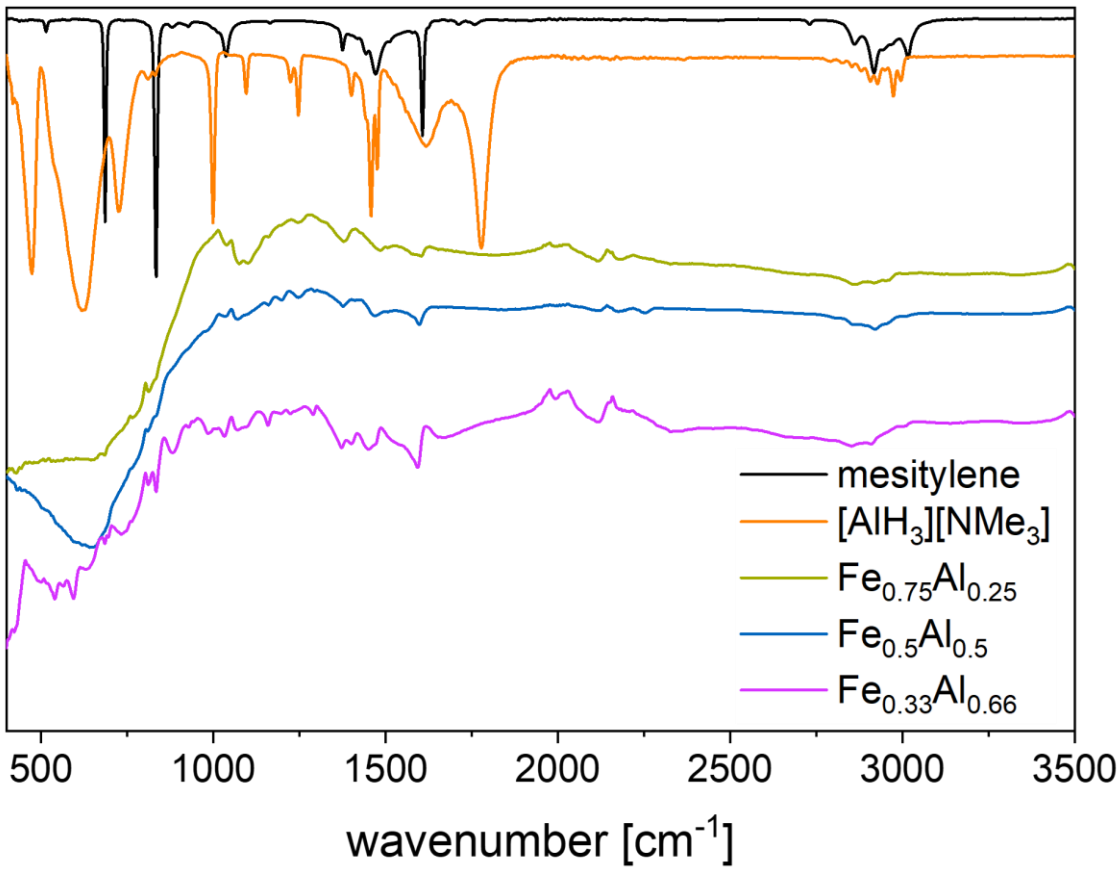

Figure 138. ATR-FT-IR spectra of $Fe_{1-x}Al_x$ powders before transformation to absorbance, baseline corrections and smoothing (with mesitylene and $[AlH_3]NMe_3$ for comparison). Due to the black colour of the powders, only a broad signal between 500-1000 cm^{-1} can be identified without further data processing.

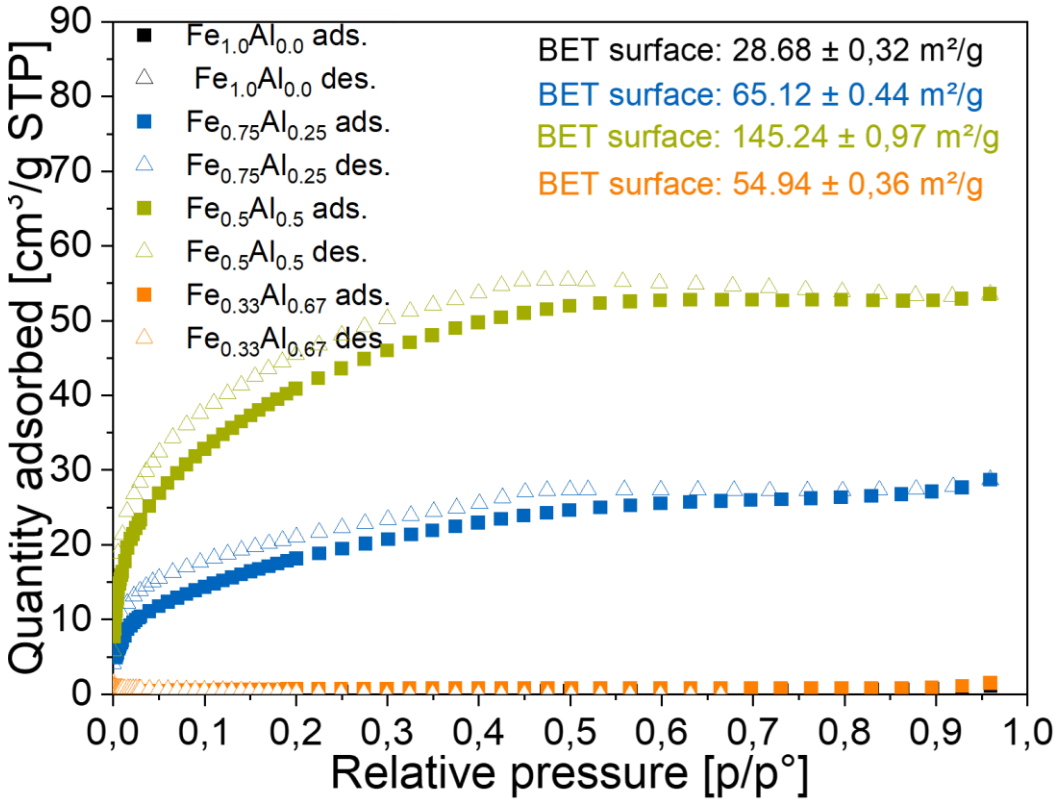

Figure 139. N_2 sorption experiments of $Fe_{1-x}Al_x$ powders with the calculation of the respective BET surface (ads. = adsorbed, des. = desorbed).

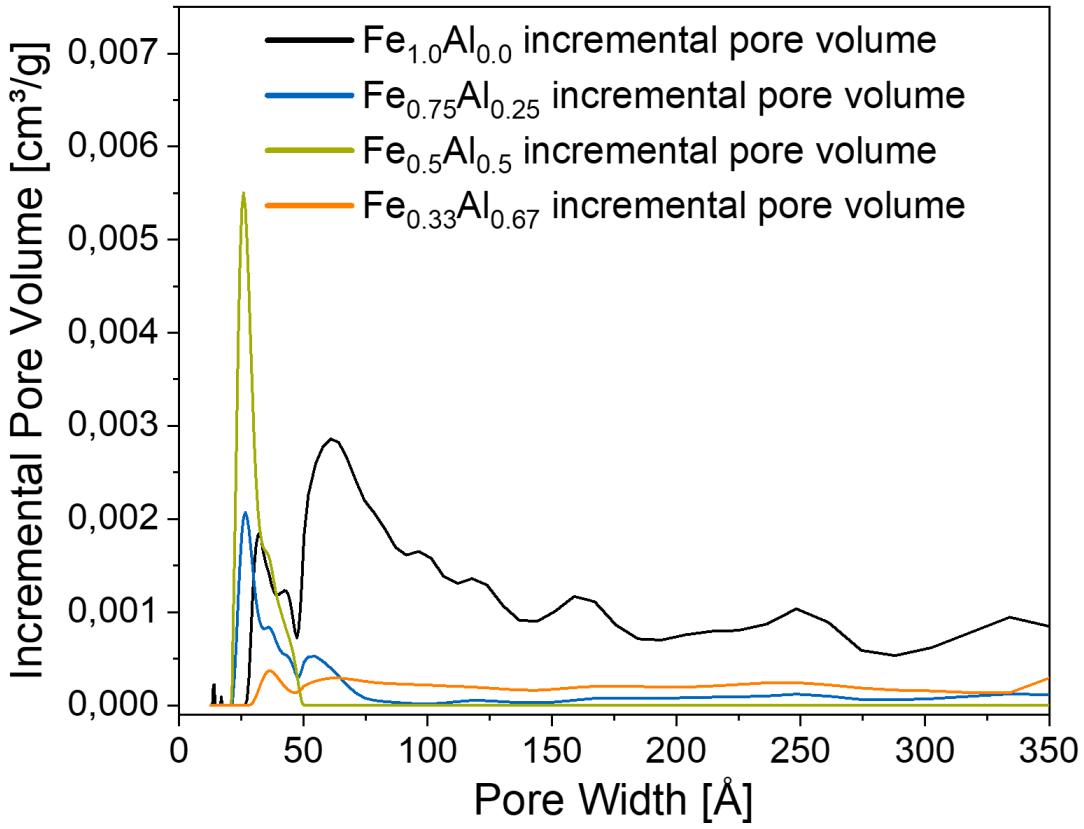

Figure 140. Calculation of the incremental pore volume of $Fe_{1-x}Al_x$ powders based on N_2 sorption experiments.

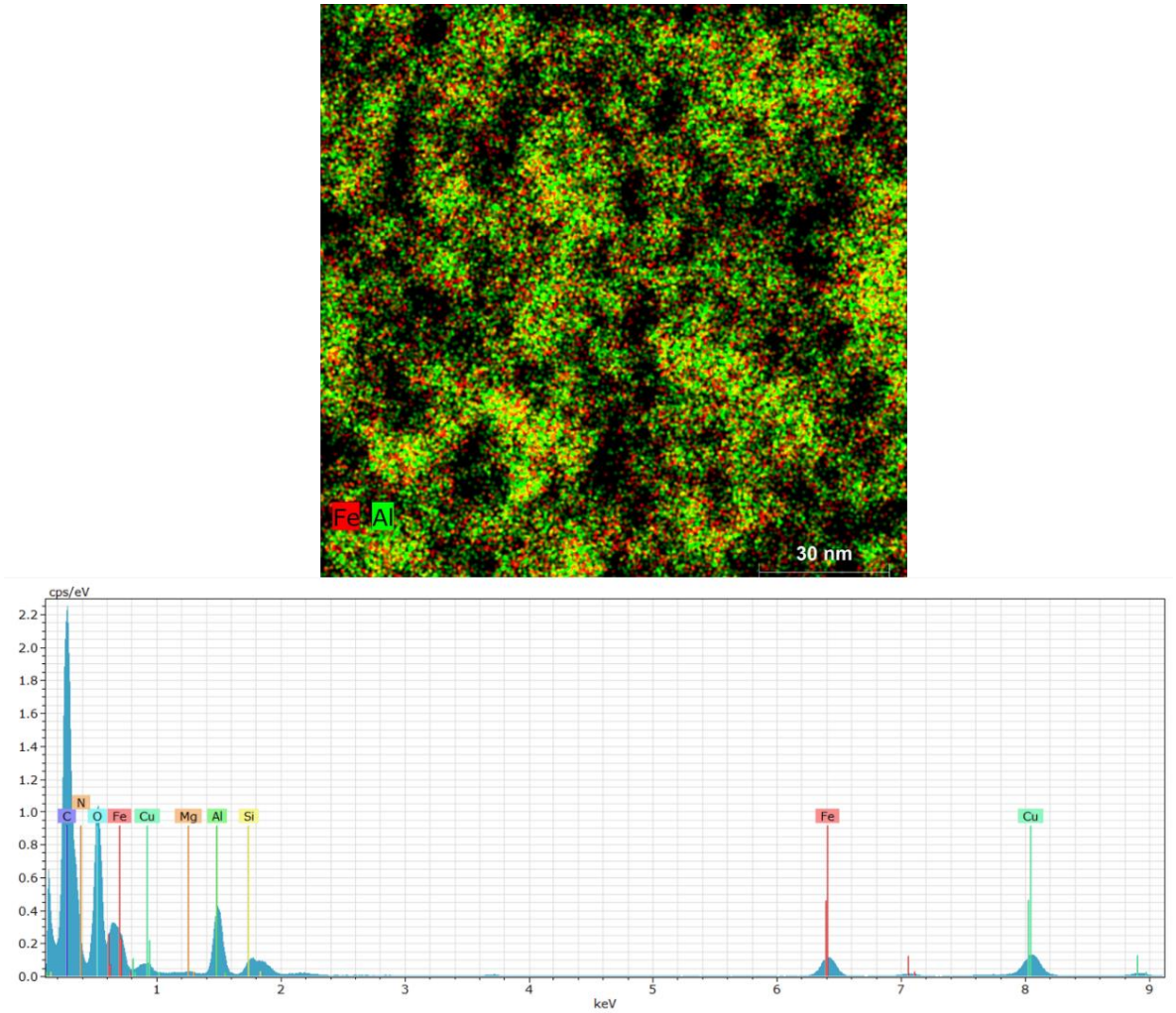

Figure 141. Elemental mapping and EDX spectra of $Fe_{1-x}Al_x$ powders.

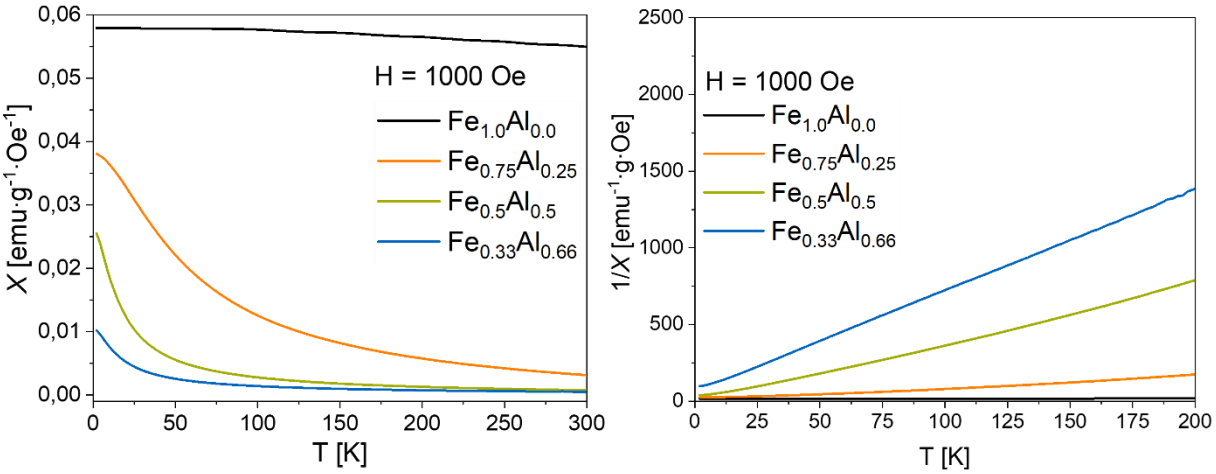

Figure 142. SQUID measurements with temperature variation with a constant external field of 1000 Oe of $Fe_{1-x}Al_x$ powder samples.

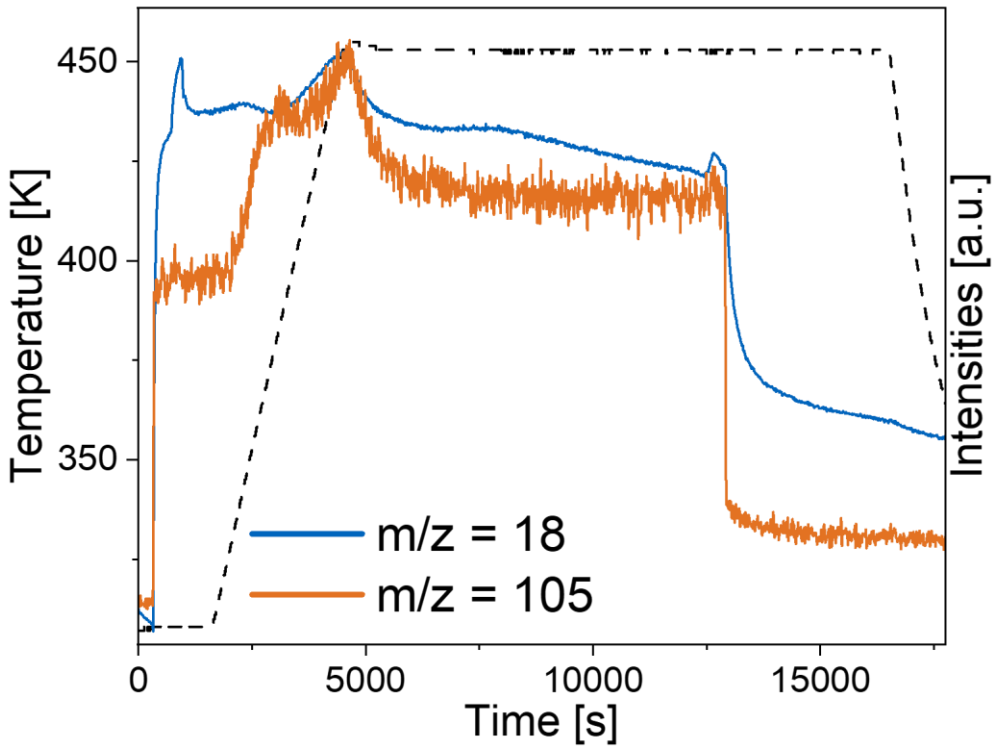

Figure 143. Mass spectrometric measurement of the gas flow upon heating $Fe_{0.33}Al_{0.67}$ powder in a H_2 atmosphere (1bar H_2, 180 °C) showing m/z values for H_2O (m/z = 18, blue trace) and a fragmentation signal of mesitylene (m/z = 105, orange trace).

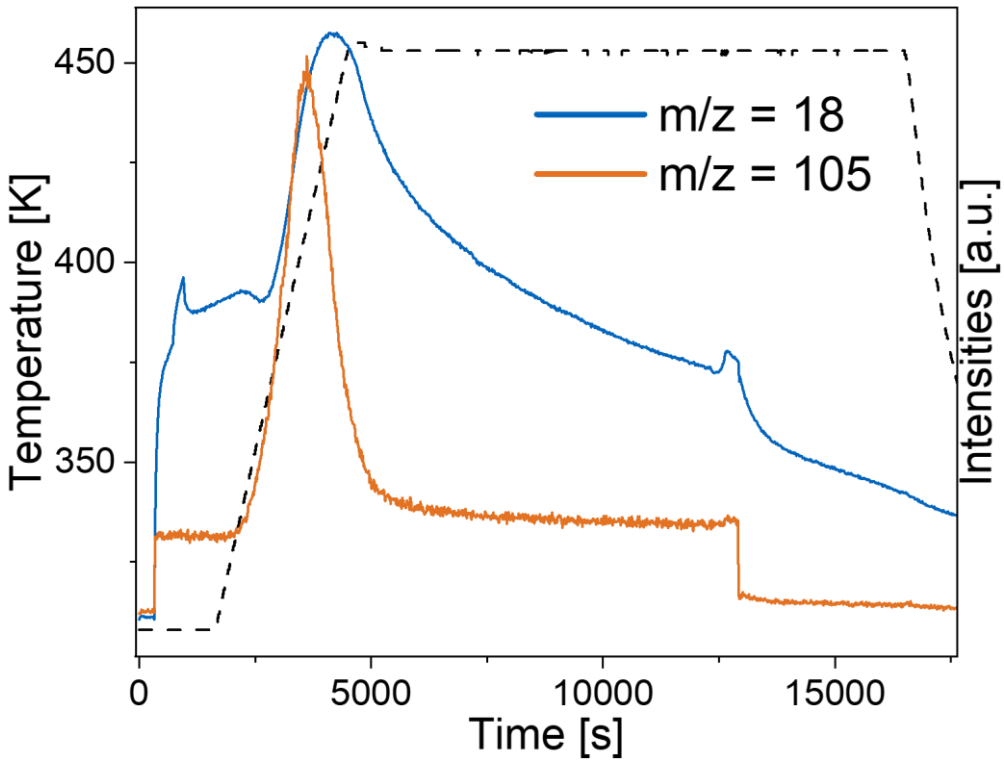

Figure 144. Mass spectrometric measurement of the gas flow upon heating $Fe_{0.5}Al_{0.5}$ powder in a H_2 atmosphere (1bar H_2, 180 °C) showing m/z values for H_2O (m/z = 18, blue trace) and a fragmentation signal of mesitylene (m/z = 105, orange trace).

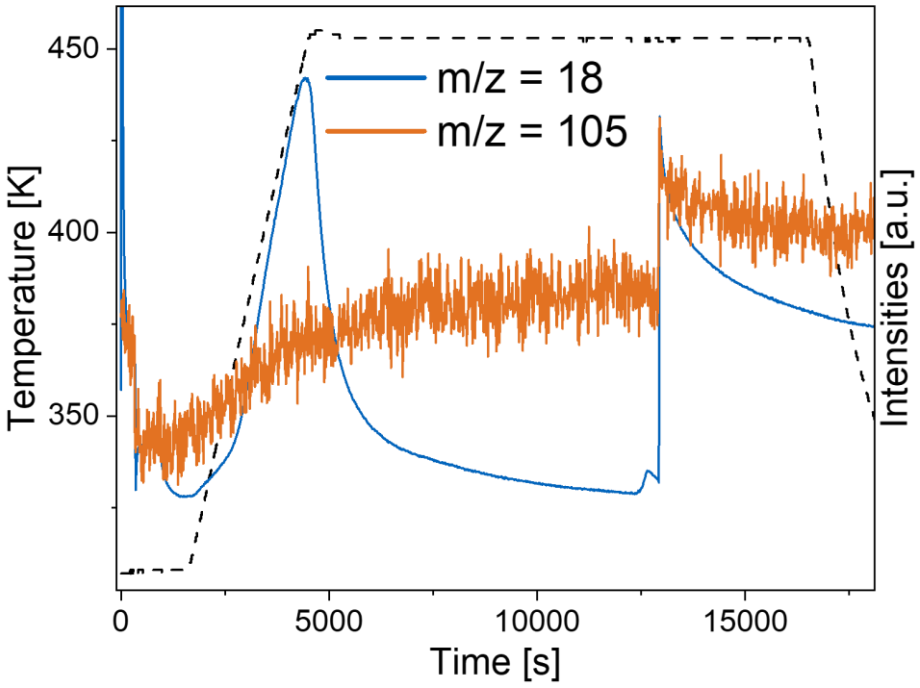

Figure 145. Mass spectrometric measurement of the gas flow upon heating $Fe_{1.0}Al_{0.0}$ powder in a H_2 atmosphere (1bar H_2, 180 °C) showing m/z values for H_2O (m/z = 18, blue trace) but no fragmentation signal of mesitylene (m/z = 105, orange trace).

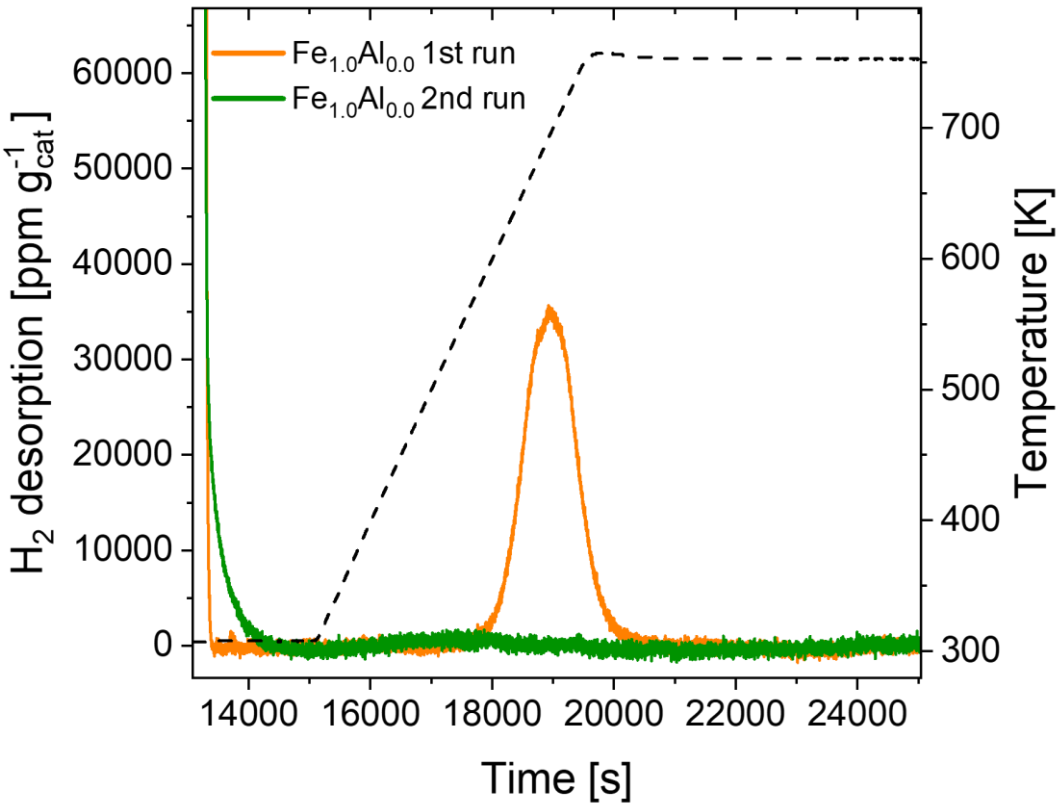

Figure 146. TPD measurement of $Fe_{1.0}Al_{0.0}$ powder of H_2 at 400 °C showing no signal for the second run after additional reducing step (180 °C at 3 bar H_2).

Particle analysis after annealing

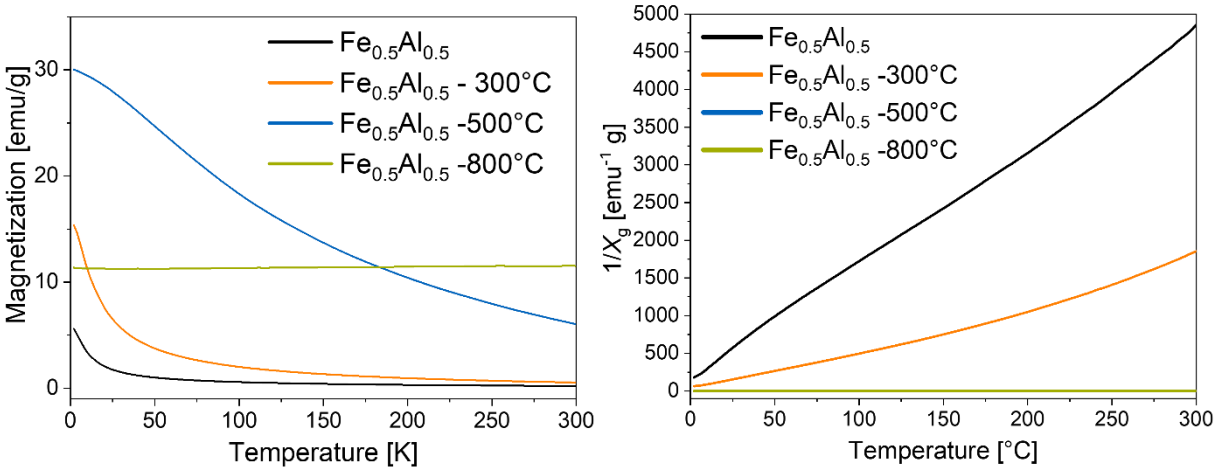

Figure 147. SQUID measurements with temperature variation with a constant external field of 1000 Oe of $Fe_{0.5}Al_{0.5}$ powder before and after post-synthetic treatment at different annealing temperatures.

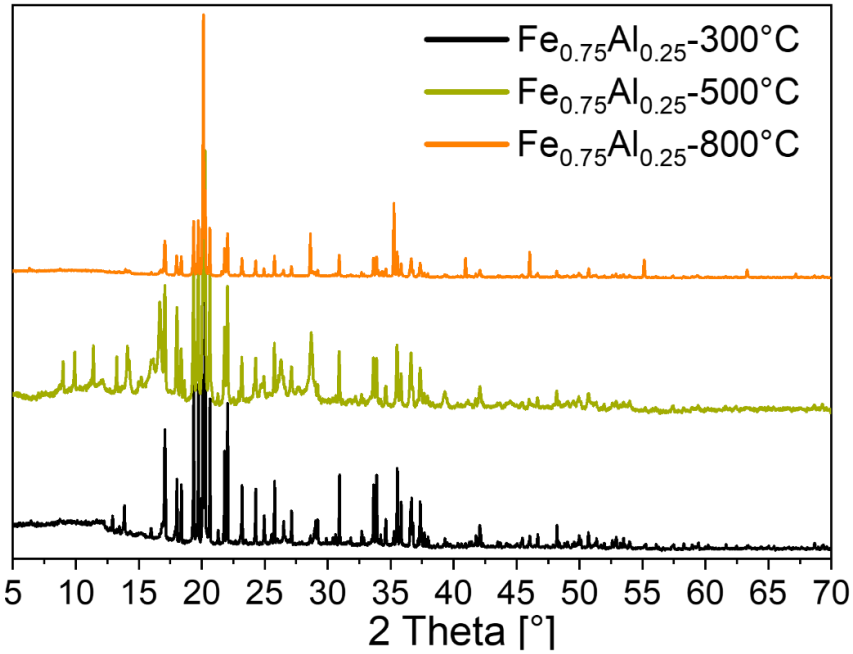

Figure 148. PXRD measurement of $Fe_{0.75}Al_{0.25}$ powder before and after post-synthetic treatment at different annealing temperatures showing crystalline phases.

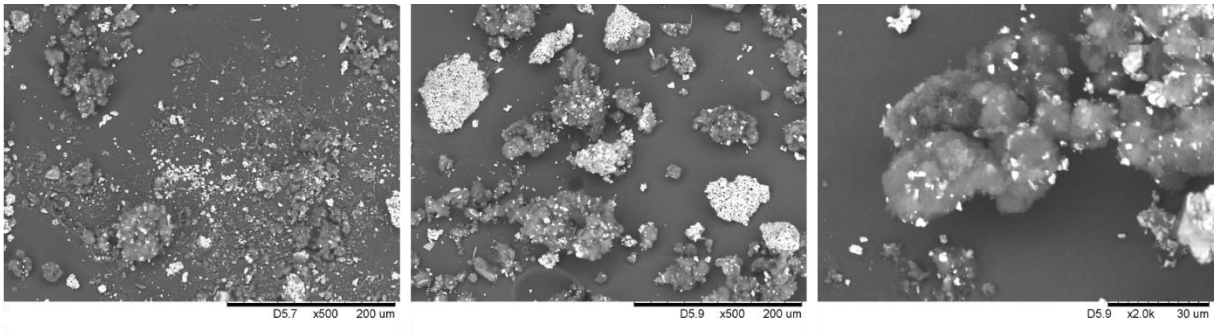

Figure 149. SEM images of $Fe_{0.33}Al_{0.67}$ powder after heating at 800 °C for 24 h.

Additive analysis

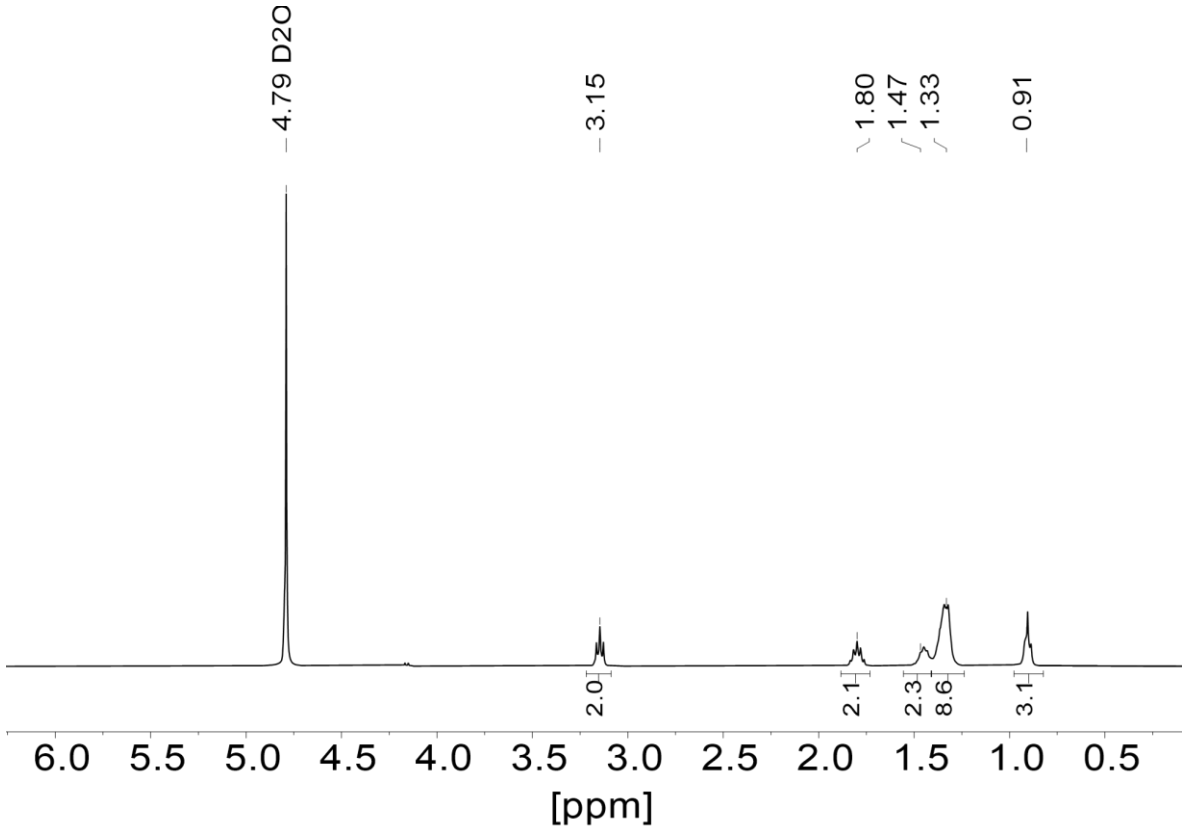

Figure 150. ^{1}H NMR spectrum of Sodium S-octylthiosulfate in D_2O.

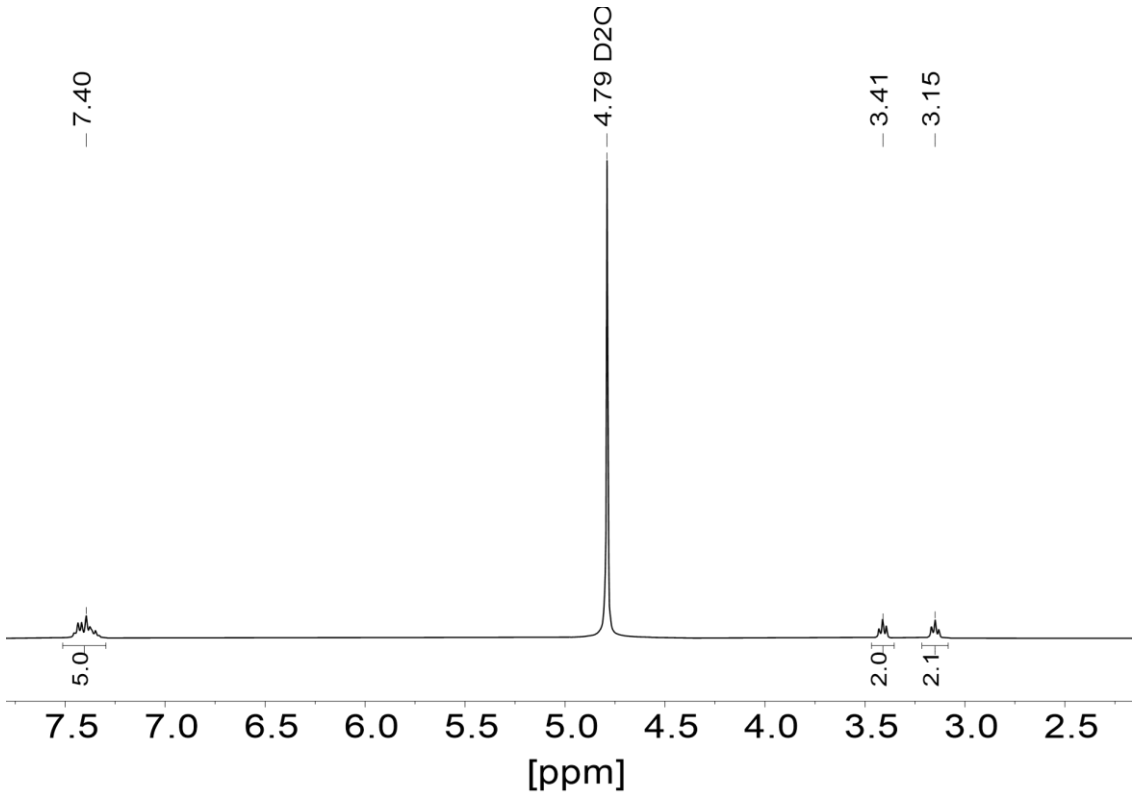

Figure 151. ^{1}H NMR spectrum of Sodium S-phenylethylthiosulfate in D_2O.

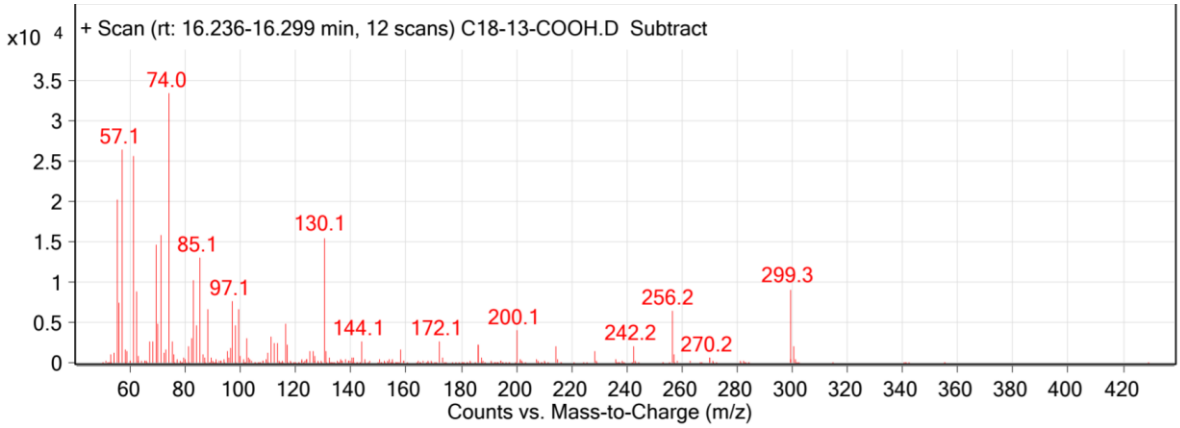

Figure 152. GC-MS spectra(in toluene) of synthesized isotopic labeled $C_{18}H_{37}{}^{13}COOH$ showing the molecule peak at 299.3 m/z.

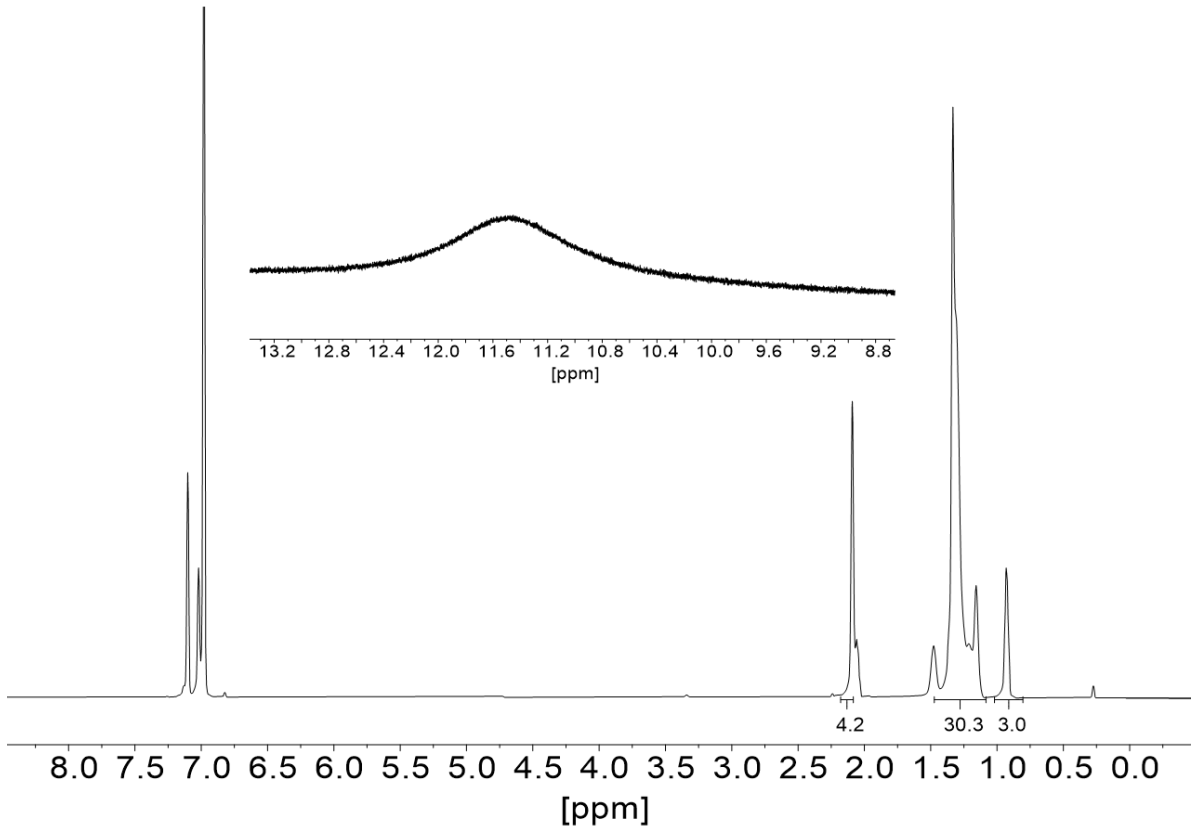

Figure 153. ^1H NMR spectra (toluene-d_8) of $C_{18}H_{37}{}^{13}COOH$.

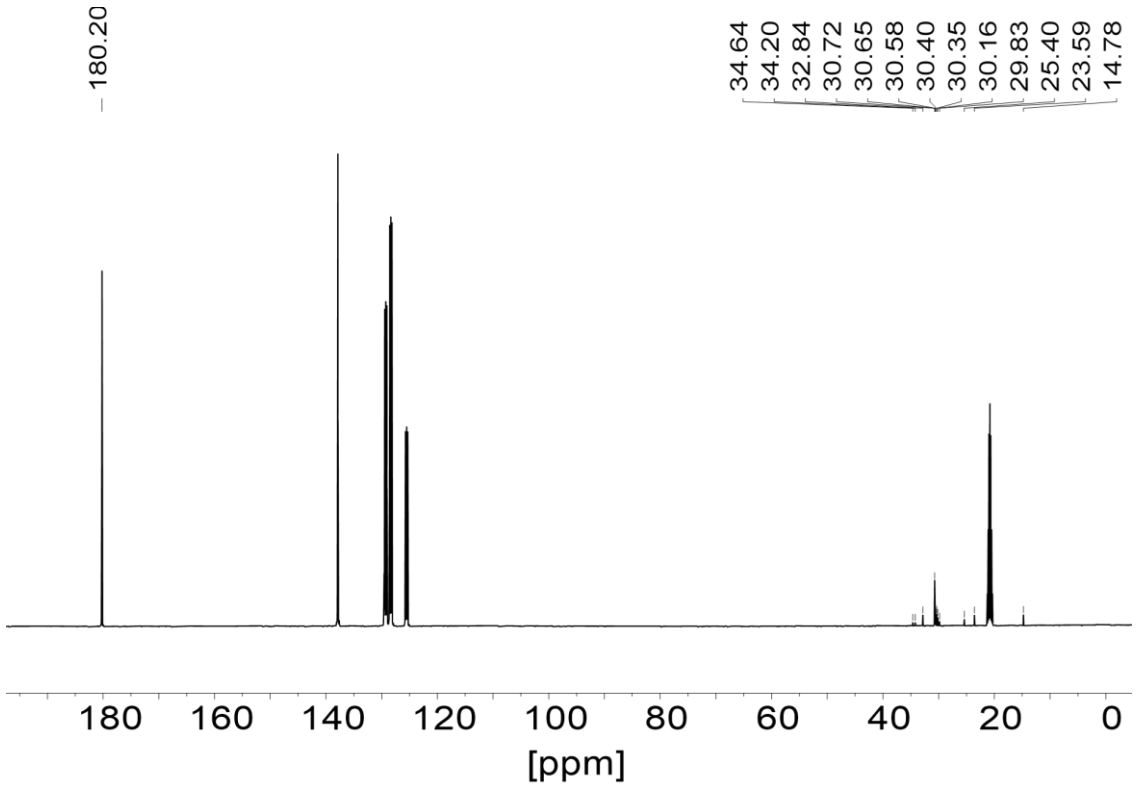

Figure 154. ^{13}C NMR spectra (toluene-d_8) of $C_{18}H_{37}{}^{13}COOH$.

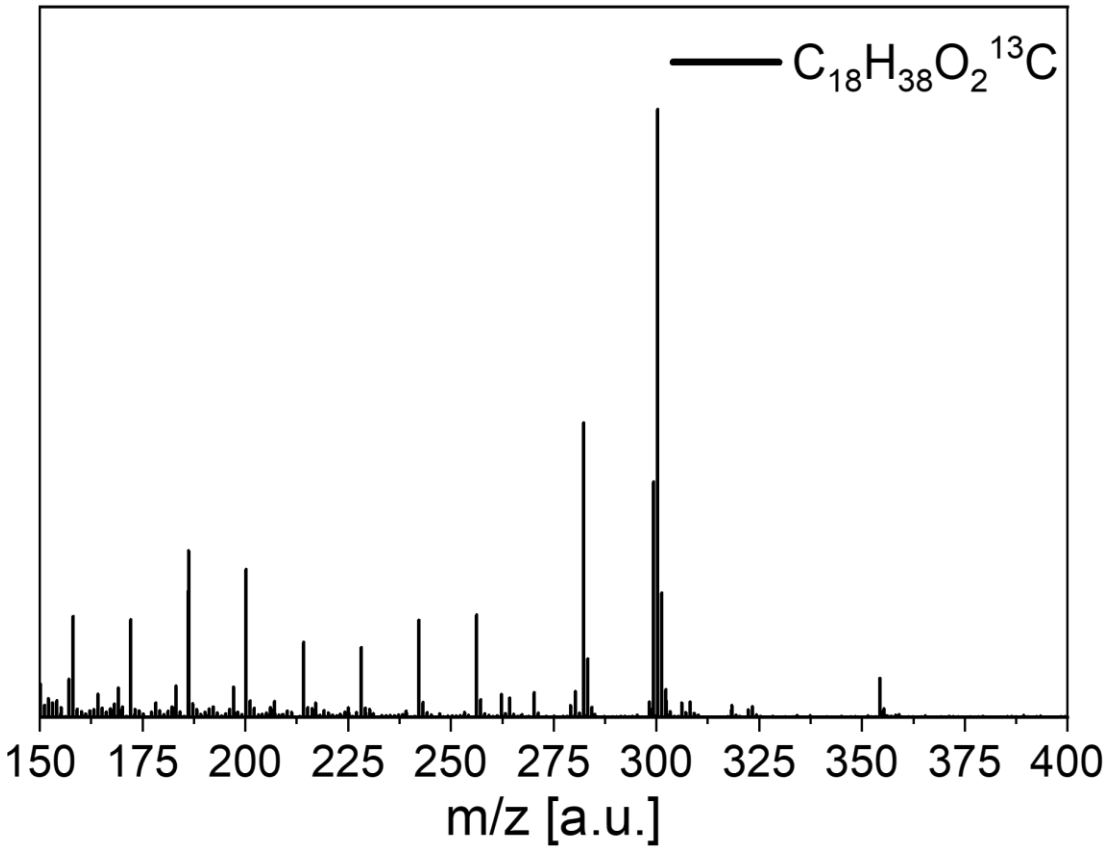

Figure 155. LIFDI-MS spectra (in toluene) of synthesized isotopic labeled $C_{18}H_{37}{}^{13}COOH$ showing the molecule peak at 299.3 m/z.

Catalysis experiments

Semi-hydrogenation experiments with Pd@N(Octyl)$_4$Br

Catalysis experiments with 1-octyne as substrate

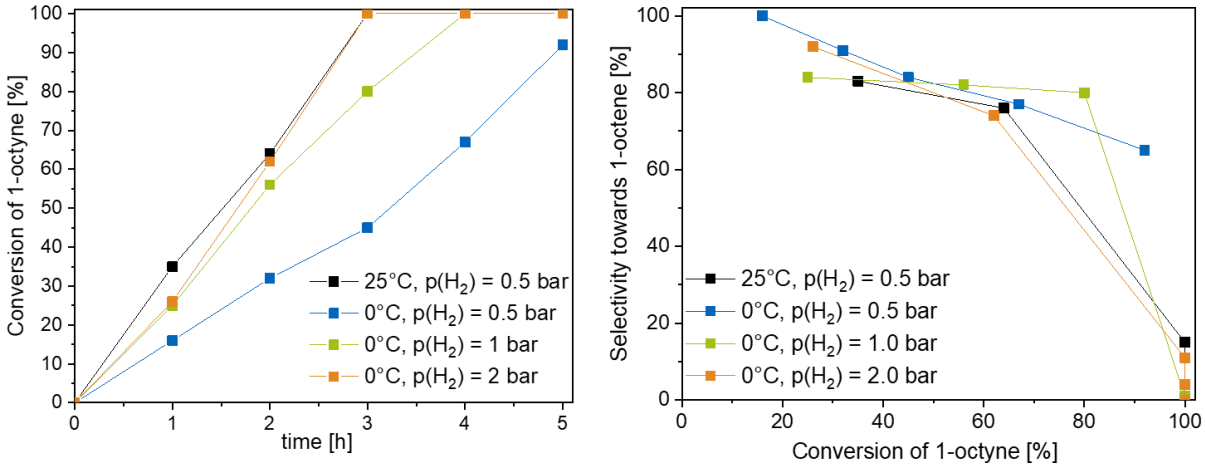

Figure 156. Testing of the catalytic performance of Pd@N(Octyl)$_4$Br NPs in the semi-hydrogenation of 1-octyne with varied reaction parameters using 1 mol% catalyst. Left graph: conversion of 1-octyne. Right graph: selectivity towards 1-octene.

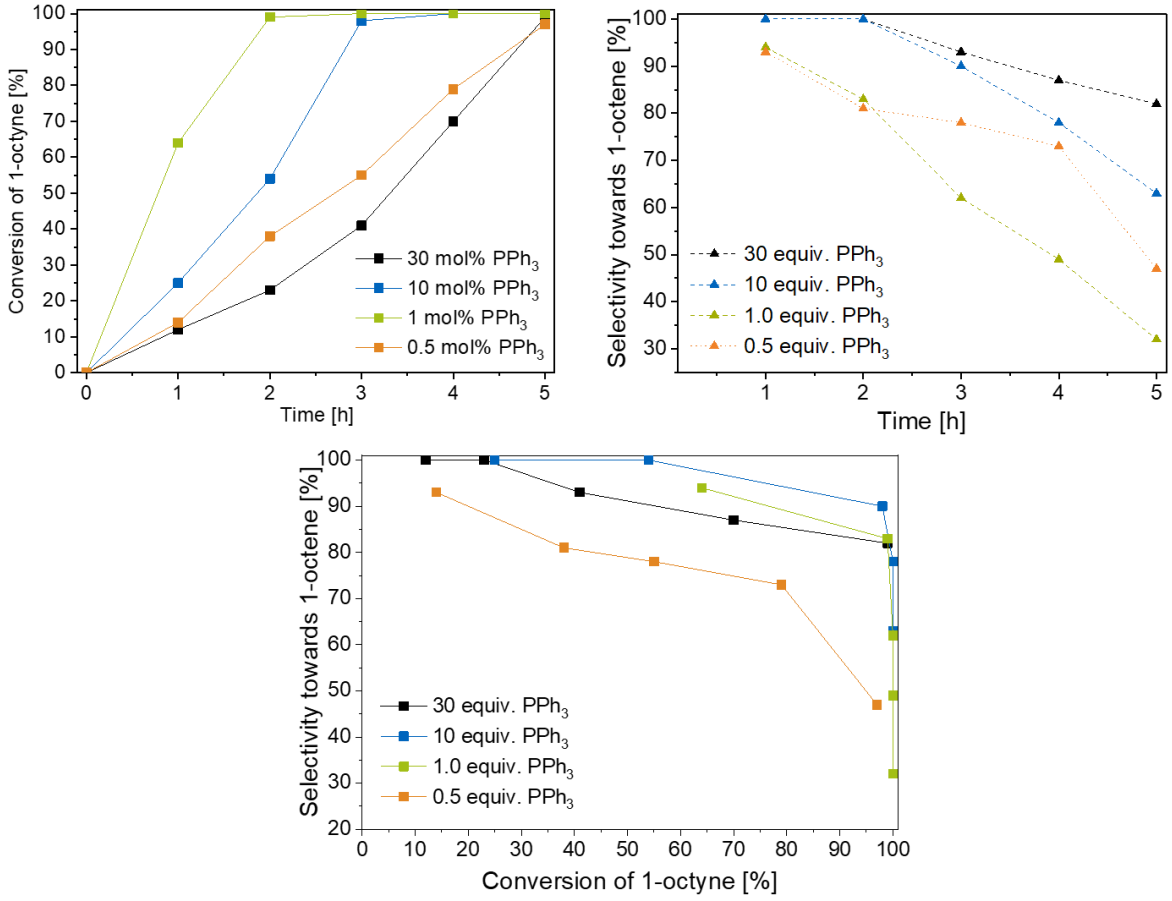

Figure 157. Conversion and selectivity of the semi-hydrogenation of 1-octyne using 1 mol% Pd@TOAB NPs and various amounts of PPh_3 as additive at 0 °C and 1 bar H_2.

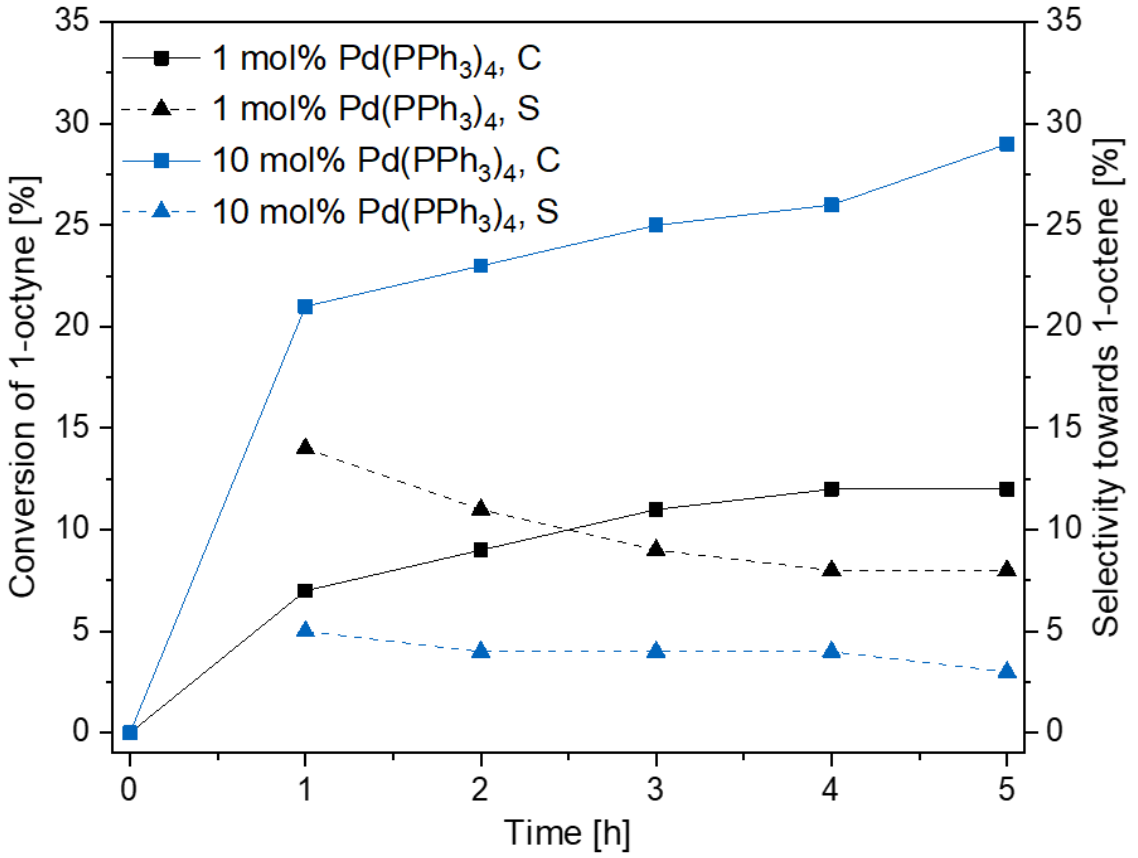

Figure 158. Conversion and selectivity of the semi-hydrogenation of 1-octyne using 1 mol% and 10 mol% $Pd(PPh_3)_4$ as catalyst at 0 °C and 1 bar H_2.

Table 34. Conversion and selectivity of 1-octyne using 1 mol% Pd@TOAB NPs and 1 equiv. additive at 0 °C and 1 bar H_2 after 5 h reaction time.

Entry	Additive	Conv. [%]	Sel. [%]
1	PPh_3	100	32
2	$MePPh_2$	100	93
3	Me_2PPh	69	99
4	Me_3P	21	100
5	$P(o\text{-tolyl})_3$	100	1
6	$P(p\text{-tolyl})_3$	99	85
7	$P(OPh)_3$	100	89
8	$P(iPr)_3$	100	33
9	PCy_3	99	37
10	$P(p\text{-F-tolyl})_3$	87	75
11	$MePPh_2O$	100	27
12	PPh_3O	100	17

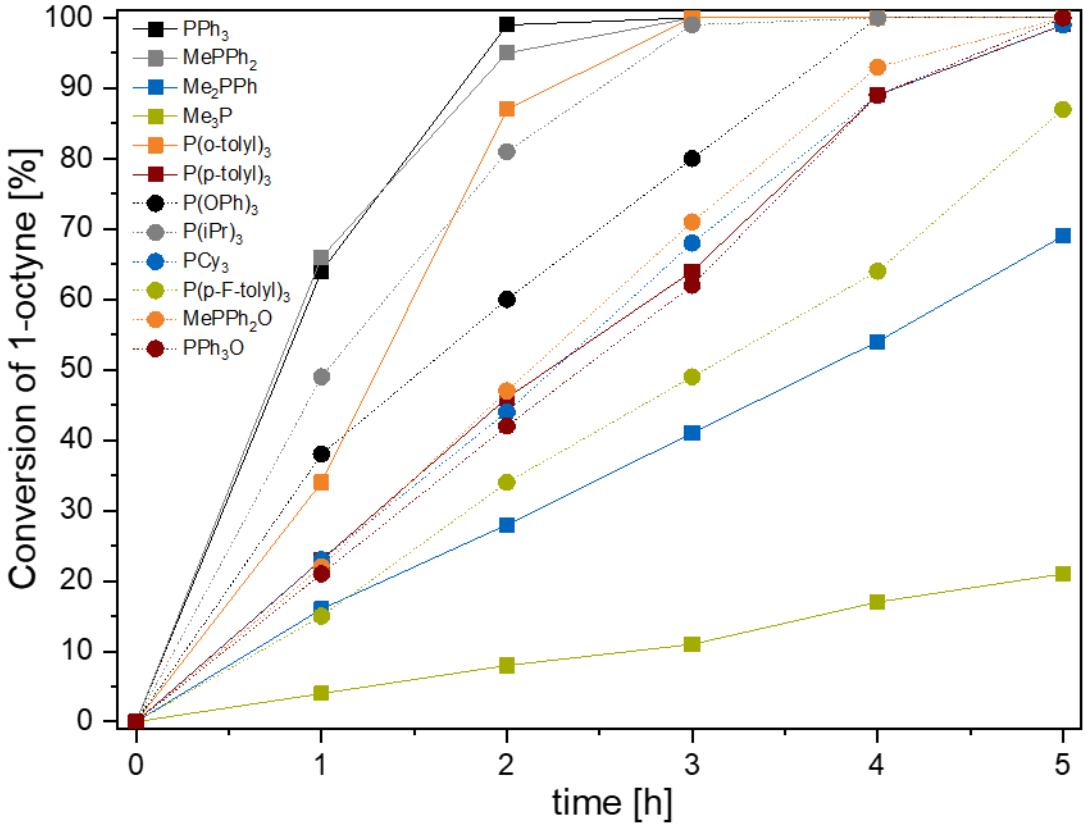

Figure 159. Conversion of 1-octyne using 1 mol% Pd@TOAB NPs and 1 mol% additive at 0 °C and 1 bar H_2.

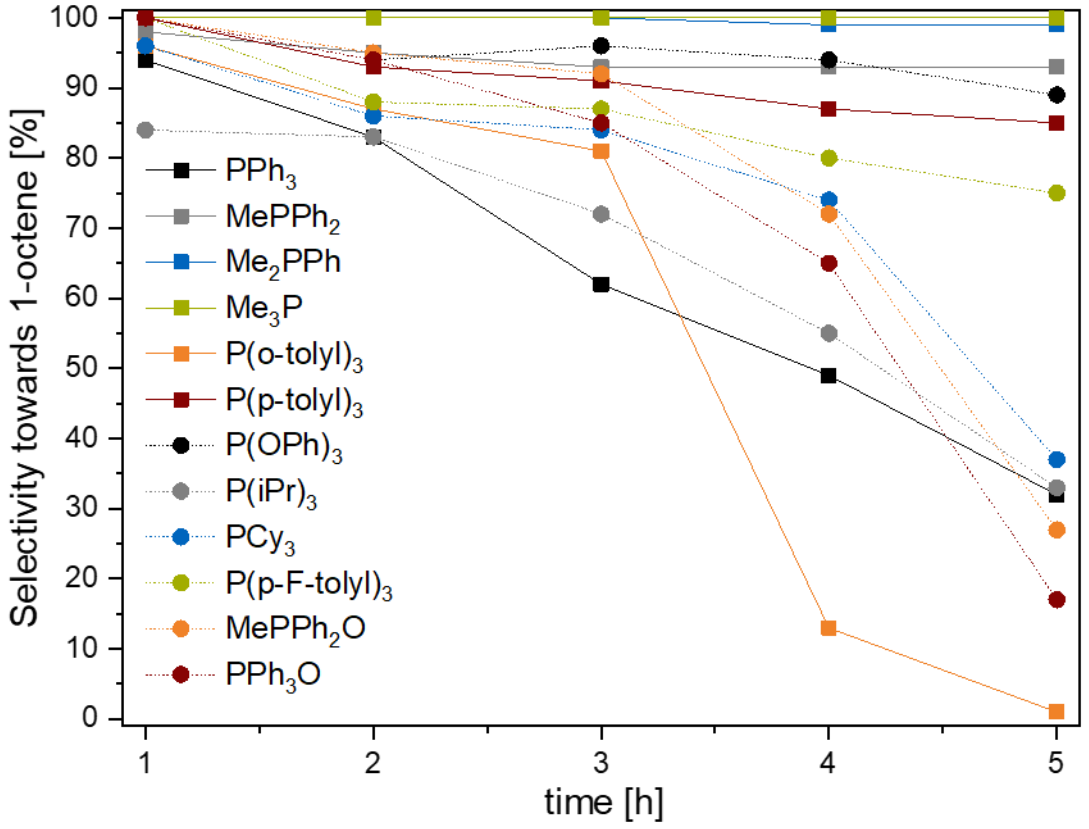

Figure 160. Selectivity towards 1-octene using 1 mol% Pd@TOAB NPs and 1 mol% additive at 0 °C and 1 bar H_2.

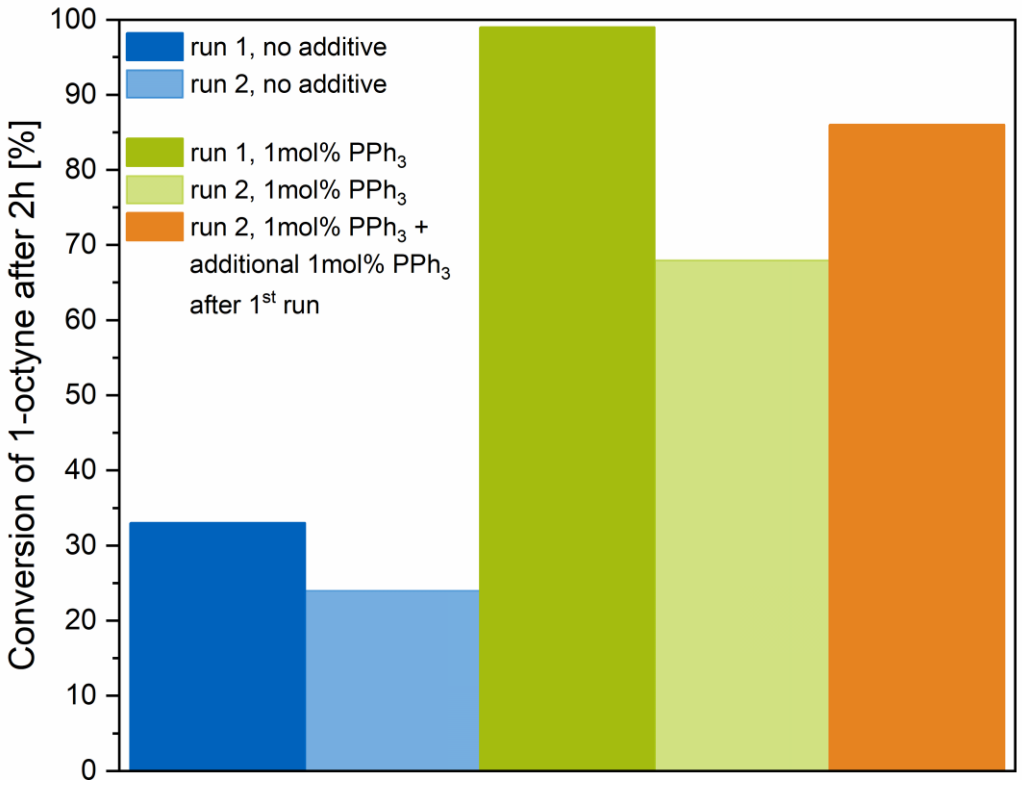

Figure 161. Catalyst deactivation experiments with and without PPh_3 as additive. Orange: After the first catalysis run, additional 1 mol% PPh_3 was added again.

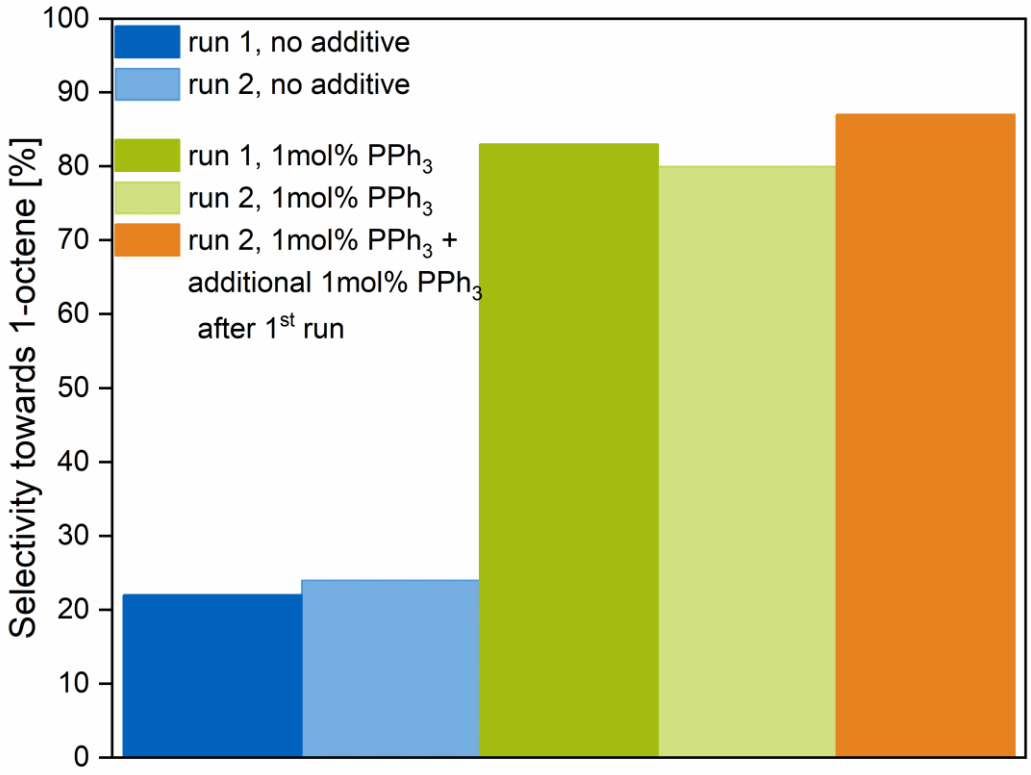

Figure 162. Catalyst deactivation experiments with and without PPh_3 as additive, selectivity towards 1-octene after full conversion. Orange: After the first catalysis run, additional 1 mol% PPh_3 was added again.

Catalysis experiments with other substrates

Table 35. Conversion of 2-octyne and selectivity (towards *cis*-2-octene) using 1 mol% Pd@TOAB NPs (0 °C, 1 bar H_2).

Time [h]	**No additive**		**1.0 equiv. PPh_3**	
	Conversion [%]	Selectivity [%]	Conversion [%]	Selectivity [%]
1	36	81	39	100
2	59	85	72	97
3	86	79	93	96
4	100	66	100	92
5	100	45	100	90

Table 36. Conversion and selectivity of phenylacetylene as substrate using 1 mol% Pd@TOAB NPs (0 °C, 1 bar H_2).

Time [h]	**No additive**		**1.0 equiv. PPh_3**	
	Conversion [%]	Selectivity [%]	Conversion [%]	Selectivity [%]
1	51	93	43	90
2	76	85	66	91
3	94	72	93	90
4	100	41	100	87
5	100	13	100	80

Table 37. Conversion of 1-octene as substrate using 1 mol% Pd@TOAB NPs (0 °C, 1 bar H_2).

Time [h]	**Conversion, no additive [%]**	**Conversion, 1.0 equiv. PPh_3 [%]**
1	85	2
2	91	3
3	98	3
4	98	4
5	99	5

Table 38. Conversion of *cis*-2-octene as substrate using 1 mol% Pd@TOAB (0 °C, 1 bar H_2).

Time [h]	**Conversion, no additive [%]**	**Conversion, 1.0 equiv. PPh_3 [%]**
1	87	0
2	95	4
3	97	5
4	97	5
5	98	5

Table 39. Comparison of literature-known TOF values for hydrogenation reactions using small monometallic Pd NPs and heterogeneous Pd/Ga systems.

Ref.	Metal/capping agent	NP size [nm]	Reaction type	Substrate	Reaction conditions	TOF [h^{-1}]	Conv.	Sel. [%]
[S1]	Pd@PVP (1:100)	1.7±0.3	Semi-hydrogenation	1-hexyne	25°C, $p(H_2)$ = 1bar	1320	100 % after 5 h	93
				2-hexyne		23400	100 % after 40 min	90
				3-hexyne		12600	100 % after 30 min	95
[S2]	Pd@PVP (1: 20)	2.1±0.1	Semi-hydrogenation	dehydroisophytol	40°C, $p(H_2)$ = 4bar	42840	100 %	96
				methylbutenol		48780	100 %	98
[S2]	Pd@PVP (1:10)	3.6±0.4	Semi-hydrogenation	dehydroisophytol	40°C, $p(H_2)$ = 4bar	69120	100 %	89
				methylbutenol		78960	100 %	98
[S3]	Pd@(BCN)MI(NTf_2)	7.3±2.2	Semi-hydrogenation	diphenylacetylene	25°C, $p(H_2)$ = 1bar	13	87 % after 6.5 h	98
				phenylacetylene		35	97 % after 2.8 h	95
				3-hexyne		231	100 % after 1.3 h	92
[S5]	Pd@SC_8	2.3	Selective hydrogenation of dienes	2,3-dimethylbuta-1,3-diene	25°C, $p(H_2)$ = 1bar	375	100 % after 24 h	100
[S5]	Pt@SC_{12}	1.5	Full-hydrogenation	Methyl propiolate	25°C, $p(H_2)$ = 1bar	30	100 % after 24 h	"high"
[S6]	Pd_2Ga	-	Semi-hydrogenation	Acetylene	200°C, flow reactor (5% H_2)	58	93 % after 20 h	76
[S6]	PdGa	-	Semi-hydrogenation	Acetylene	200°C, flow reactor (5% H_2)	1	86 % after 20 h	75
[S6]	Pd_3Ga_7	-	Semi-hydrogenation	Acetylene	200°C, flow reactor (5% H_2)	1	99 % after 20 h	71
[S6]	Pd@Al_2O_3	-	Semi-hydrogenation	Acetylene	200°C, flow reactor (5% H_2)	2452	43 % after 20 h	17
[S6]	Pd_2Ga@Al_2O_3	2-6	Semi-hydrogenation	Acetylene	200°C, flow reactor (5% H_2)	6615	88 % after 20 h	67

Semi-hydrogenation experiments with $Pd_{1-x}Ga_x$ colloids

Catalysis experiments with 3-hexyne as substrate

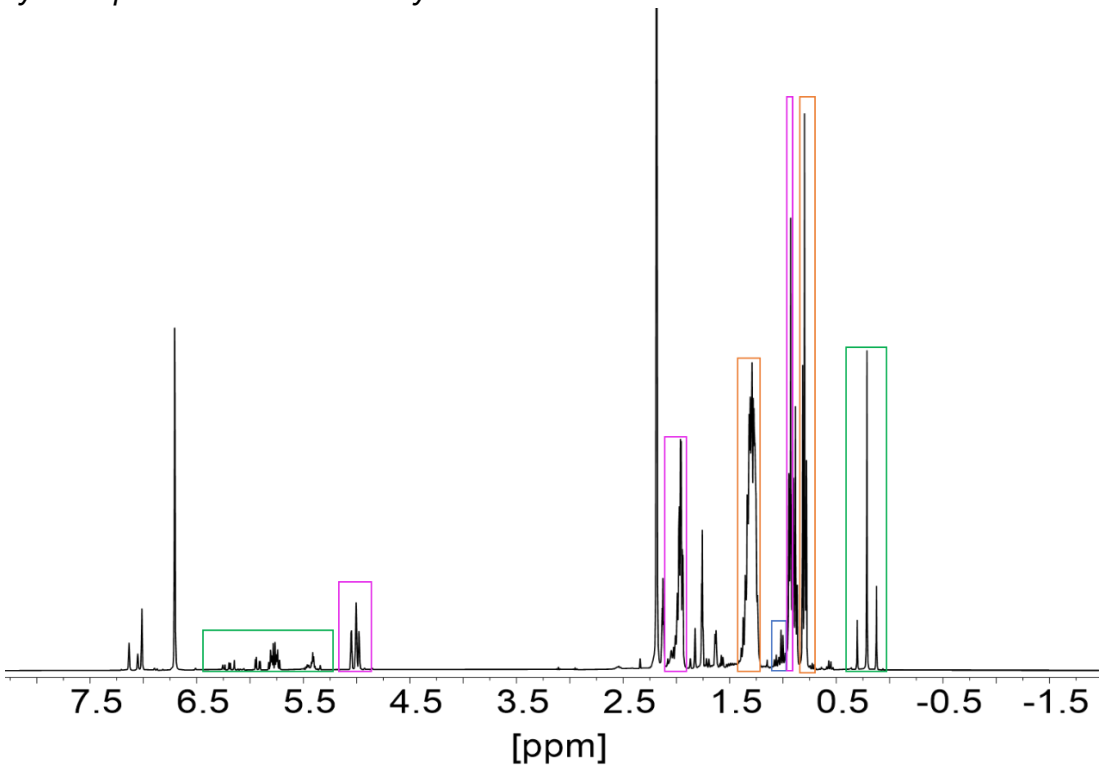

Figure 163. ^{1}H NMR study of $Pd_{0.5}Ga_{0.5}$ colloids during semi-hydrogenation catalysis of 3-hexyne (5mol% catalyst, 0°C, 1 bar H_2) after almost full conversion showing no dvds hydrogenation. Color code: Dvds in green, 3-hexyne in blue, 3-hexene in purple, *n*-hexane in orange.

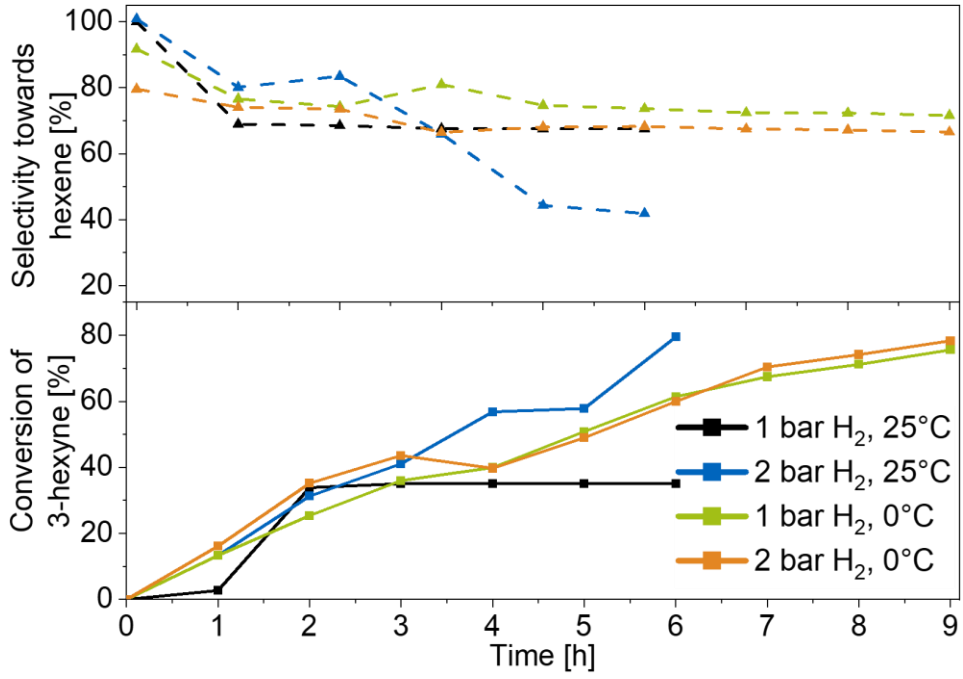

Figure 164. Parameter optimization regarding the semi-hydrogenation catalysis using 5 mol% $Pd_{0.67}Ga_{0.33}$ colloids. At 25°C (Entry 1 and 2), partial particle precipitation and dvds hydrogenation is observed. Entry 1: Complete H_2 consumption after 2 h.

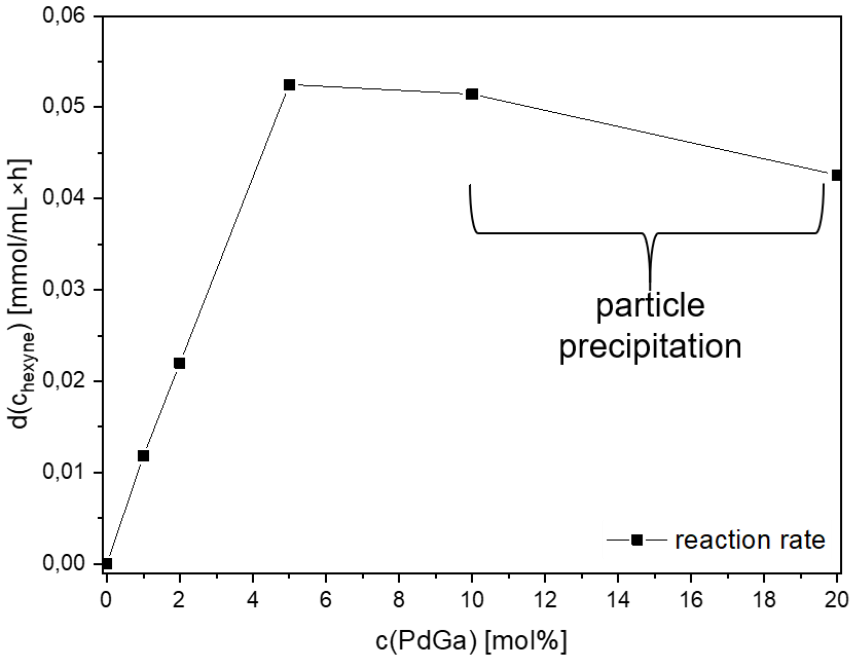

Figure 165. Variation of the catalyst amount using $Pd_{0.5}Ga_{0.5}$ colloids highlighting 5 mol% catalyst as optimum.

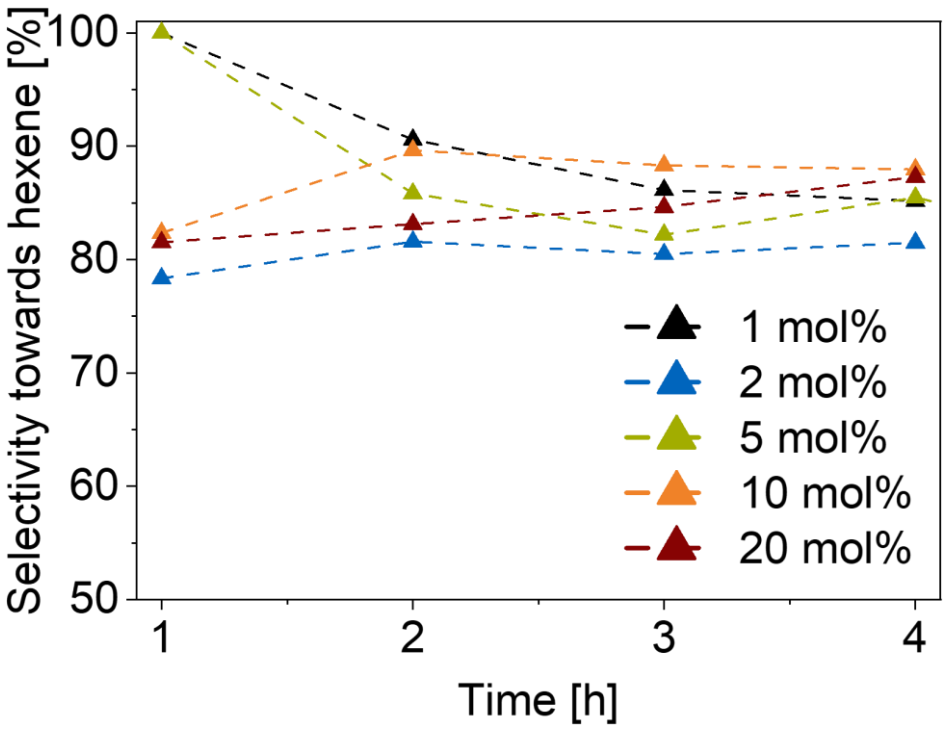

Figure 166. Influence of the loading of the colloidal $Pd_{0.5}Ga_{0.5}$ catalyst on the selectivity by variation of the catalyst amount using $Pd_{0.5}Ga_{0.5}$ colloids.

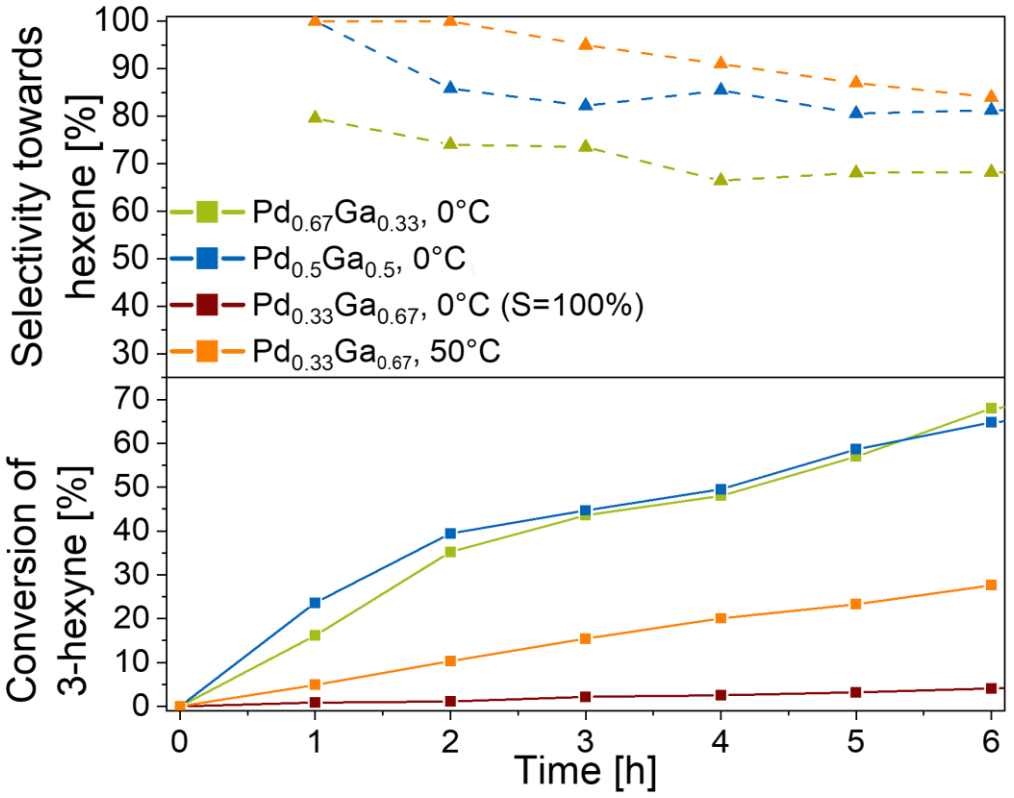

Figure 167. Testing of the catalytic performance of $Pd_{1-x}Ga_x$ colloidal NPs in the semi-hydrogenation of 3-hexyne with different Pd/Ga ratios using 5 mol% catalyst.

Catalysis experiments with other substrates

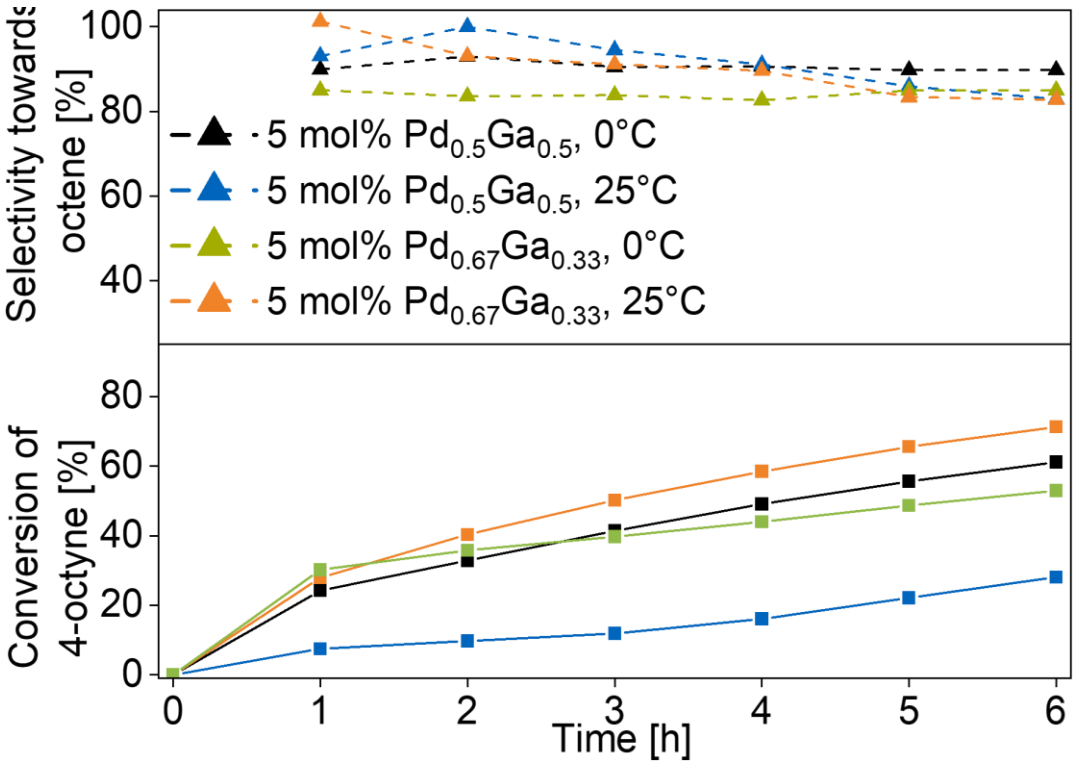

Figure 168. Semi-hydrogenation of 4-octyne as substrate using 5 mol% $Pd_{1-x}Ga_x$ colloids and 2.0 bar H_2 at various temperatures.

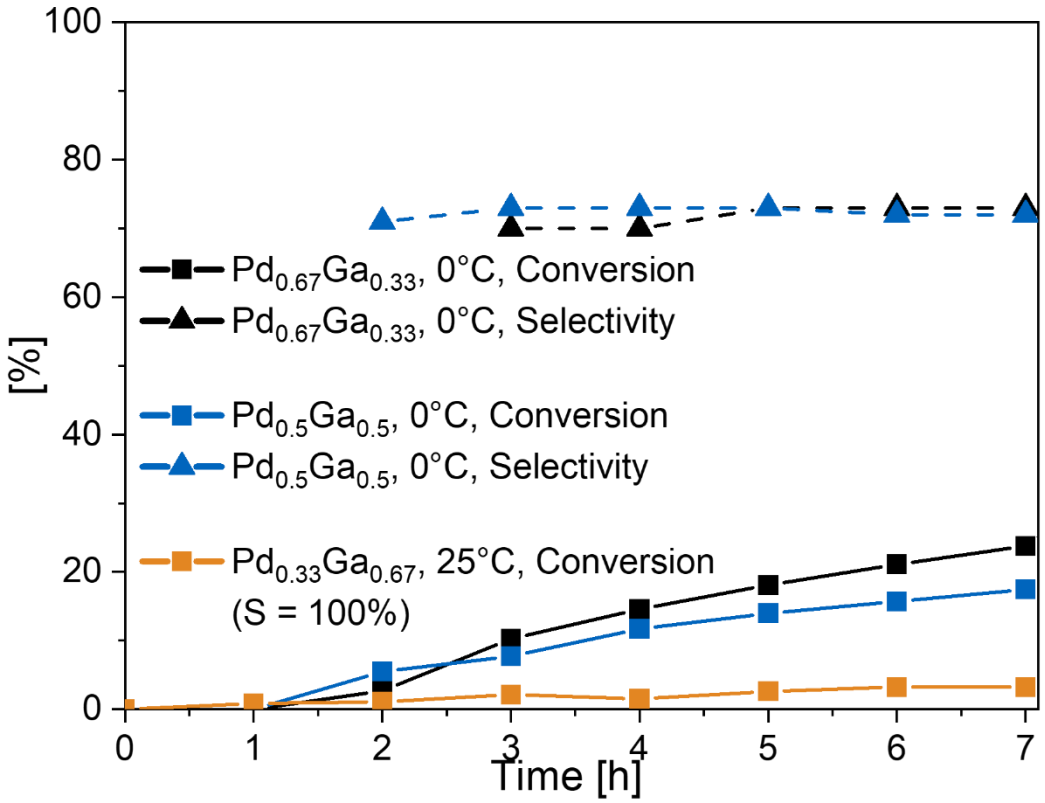

Figure 169. Catalytic tests on the semi-hydrogenation of 1-hexyne as substrate using 5 mol% $Pd_{1-x}Ga_x$ colloids and 2.0 bar H_2 showing a strong increase of the catalyst activity.

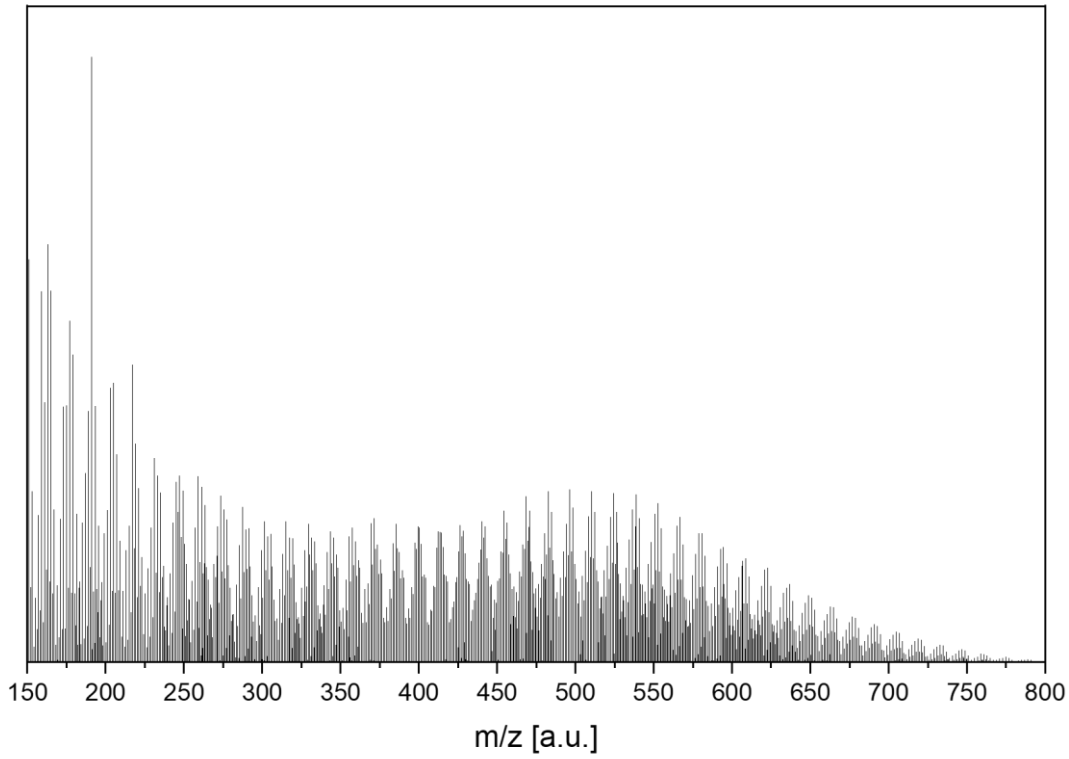

Figure 170. LIFDI-MS measurements of the reaction mixture after catalysis using 5 mol% $Pd_{0.5}Ga_{0.5}$ colloids, 2.0 bar H_2 at 0 °C and 1-hexyne as substrate showing strong oligomerization.

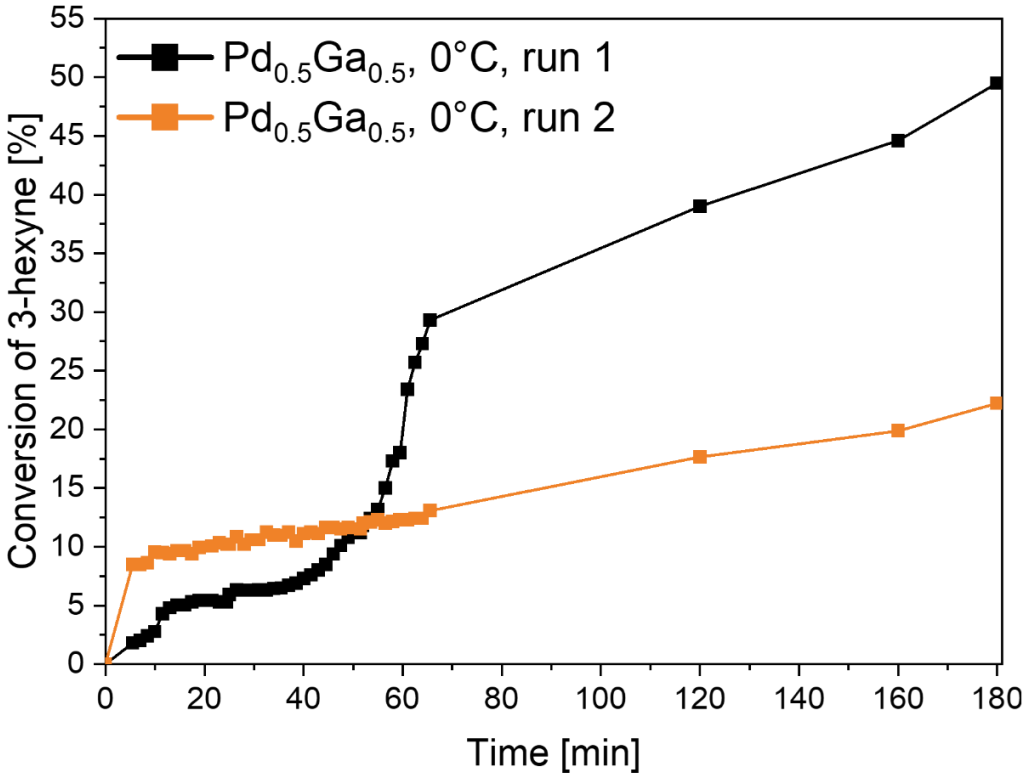

Figure 171. Recycling experiments using 5 mol% $Pd_{0.5}Ga_{0.5}$ colloids with 3-hexyne as substrate and 2.0 bar H_2 at 0°C.

Semi-hydrogenation experiments with $Pd_{0.5}Ga_{0.5}$@PPh_3

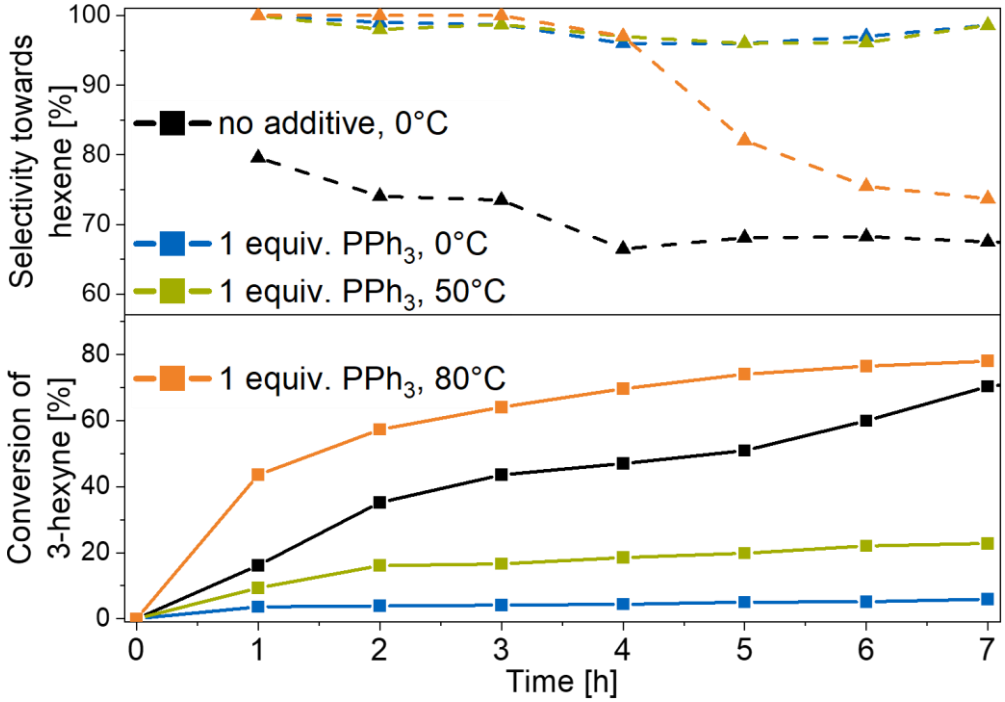

Figure 172. Semi-hydrogenation catalysis of 3-hexyne using 5 mol% $Pd_{0.5}Ga_{0.5}$@1.0 equiv. PPh_3 colloids at different temperatures. At 80°C, partial particle agglomeration is observed.

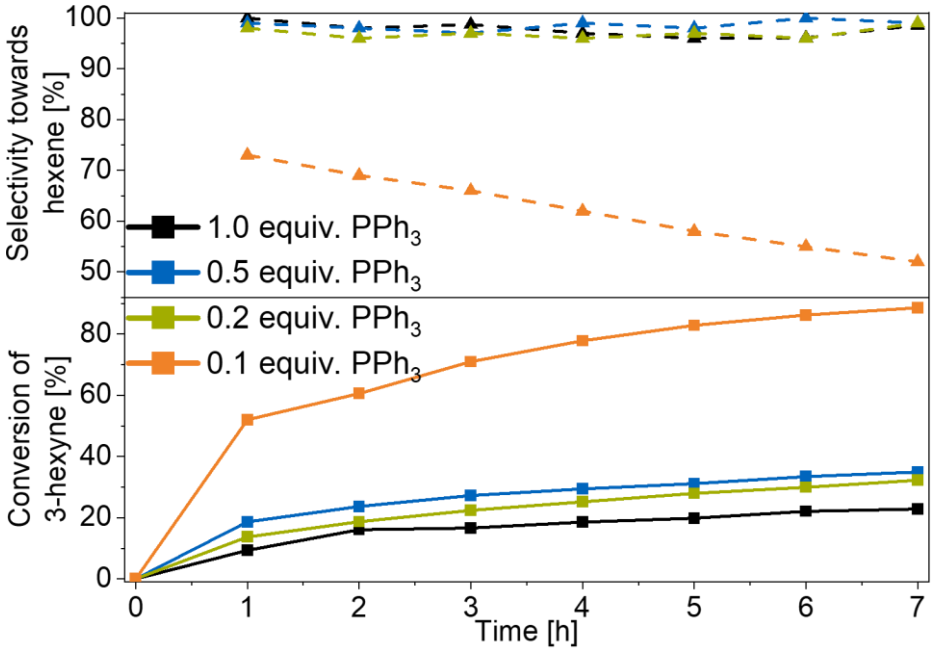

Figure 173. Semi-hydrogenation catalysis of 3-hexyne using 5 mol% $Pd_{0.5}Ga_{0.5}$ colloids with different amounts of PPh_3 colloids at 50 °C.

Semi-hydrogenation experiments with $Pd_{1-x}Ga_x$@carboxylic acids

Catalysis experiments with 2-octyne as substrate

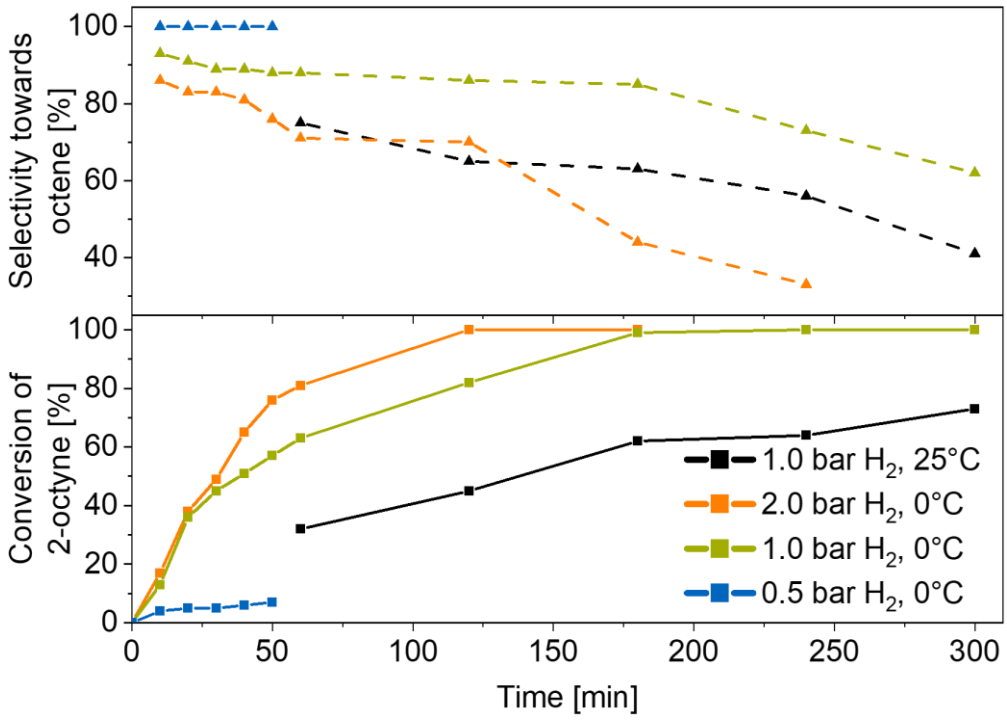

Figure 174. Parameter optimization regarding the semi-hydrogenation catalysis using 2.5 mol% $Pd_{0.33}Ga_{0.67}$@1.0 equiv. stearic acid colloids. At 25°C (Entry 1), partial particle agglomeration is observed.

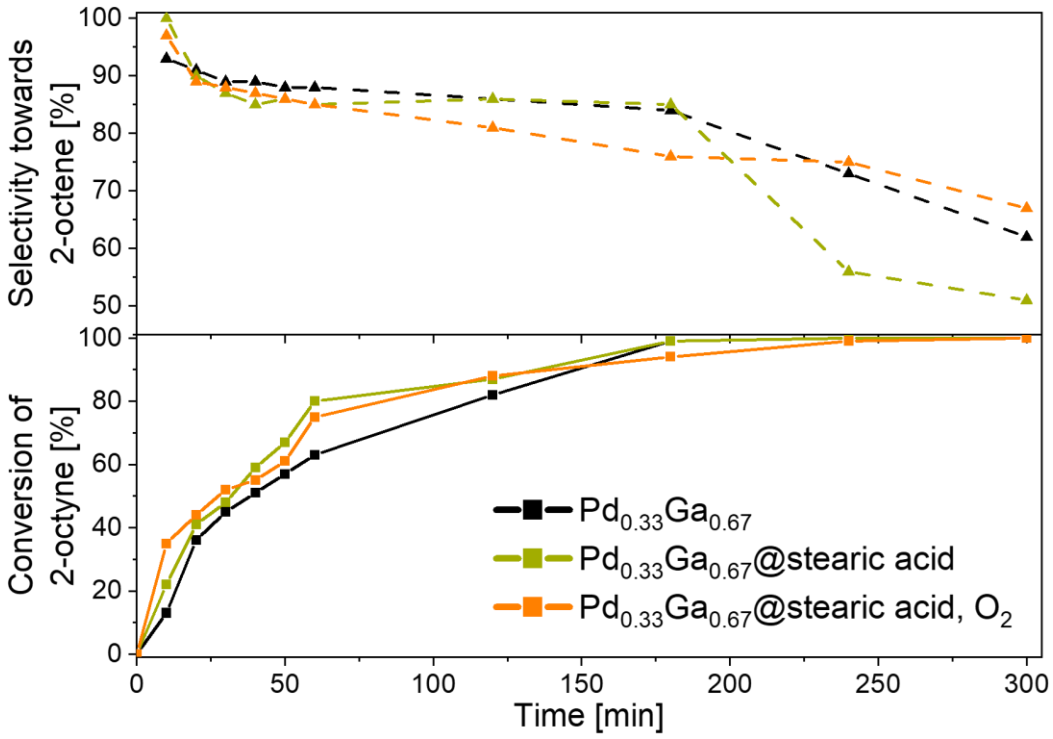

Figure 175. Semi-hydrogenation catalysis of 2-octyne using 2.5 mol% $Pd_{0.33}Ga_{0.67}$ colloids without any additive and comparison with 2.5 mol% $Pd_{0.33}Ga_{0.67}$@1.0 equiv. stearic acid colloids stored at Ar vs. air.

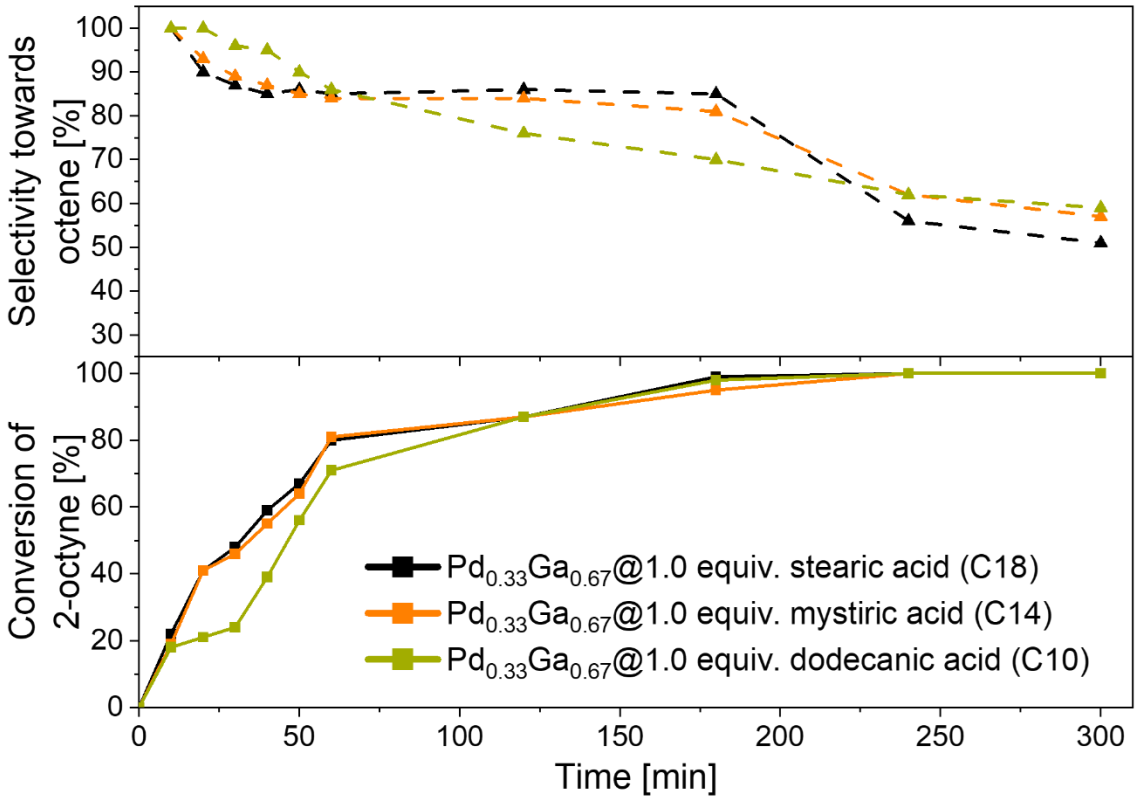

Figure 176. Semi-hydrogenation catalysis of 2-octyne using 2.5 mol% $Pd_{0.33}Ga_{0.67}$@1.0 equiv. carboxylic acids with variation of the additive alkyl chain length showing no major differences regarding activity and selectivity.

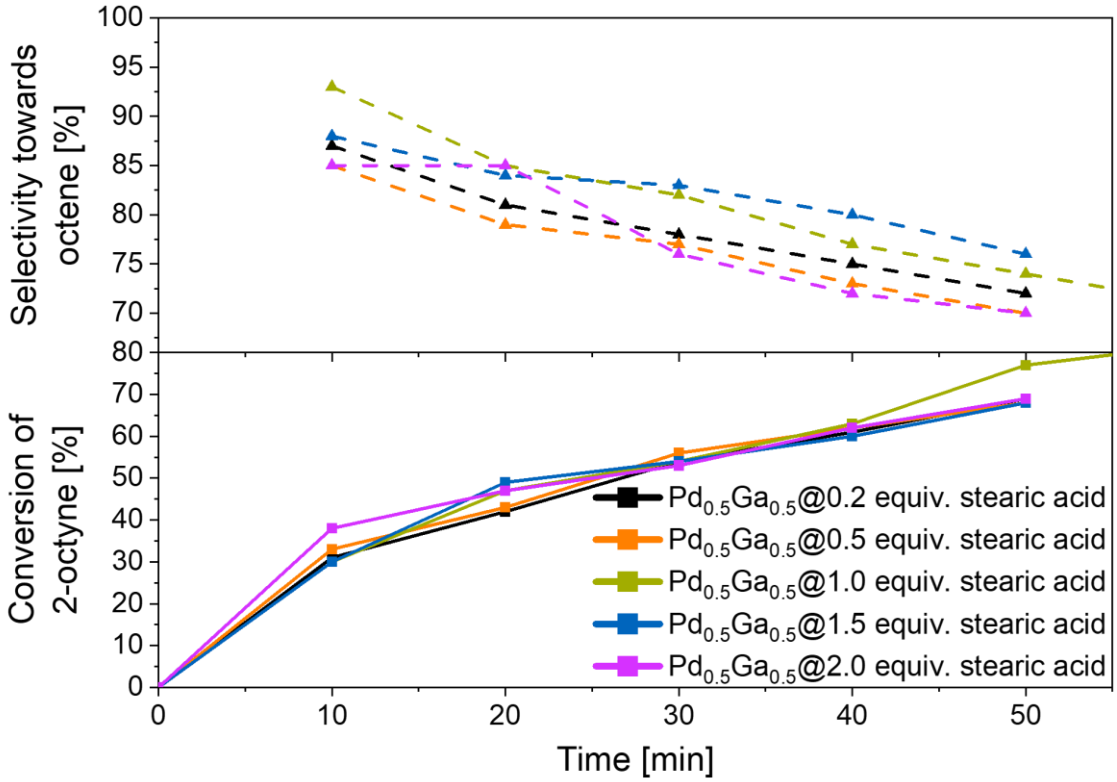

Figure 177. Semi-hydrogenation catalysis of 2-octyne using 2.5 mol% $Pd_{0.5}Ga_{0.5}$@stearic acid with variation of the additive amount showing no major differences regarding activity and selectivity.

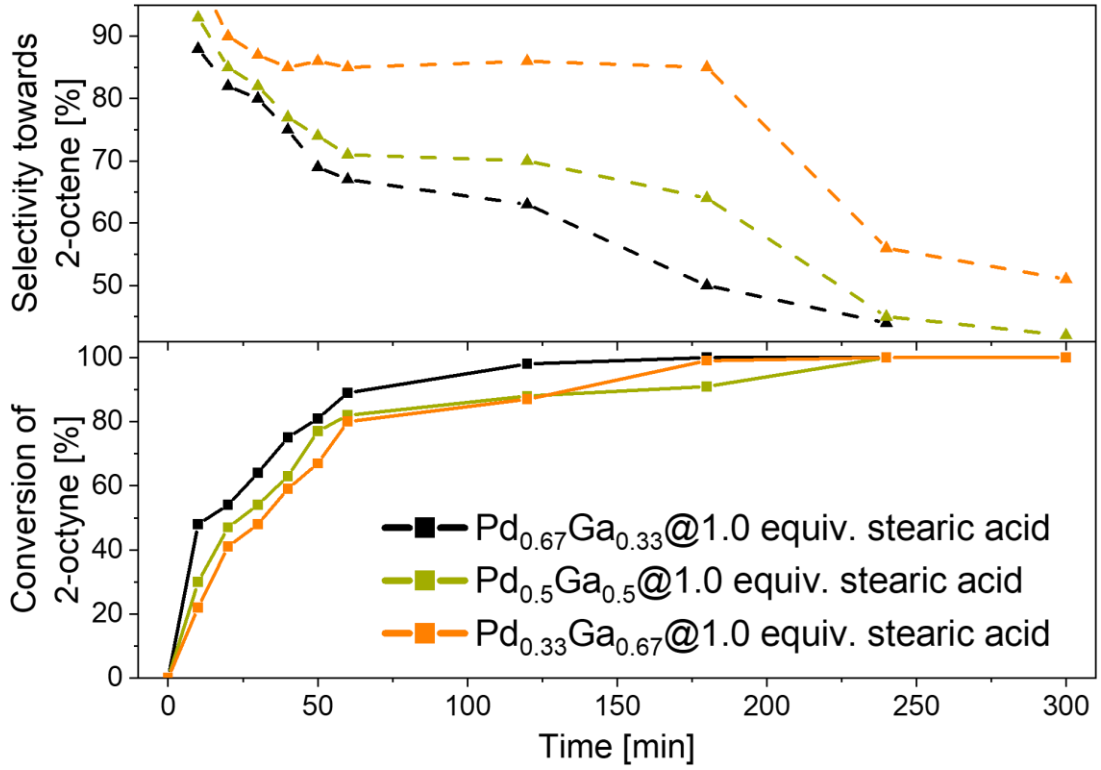

Figure 178. Semi-hydrogenation catalysis of 2-octyne using 2.5 mol% $Pd_{1-x}Ga_x$@1.0 equiv. stearic acid with variation of the Pd/Ga ratio showing a clear coherence between the Ga amount and the selectivity towards the respective alkene.

Catalysis experiments with other substrates

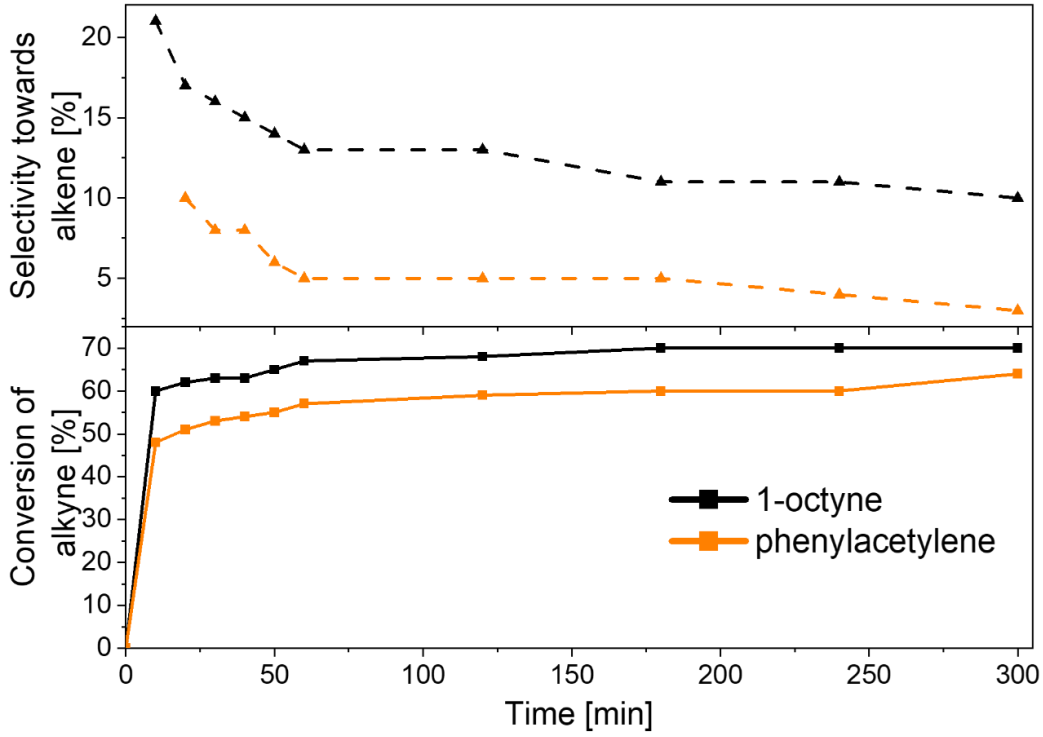

Figure 179. Semi-hydrogenation catalysis of 1-octyne and phenylacetylene using 2.5 mol% $Pd_{0.67}Ga_{0.33}$@1.0 equiv. stearic acid showing a drastic loss in selectivity towards the respective alkene. Furthermore, full conversion is not observed.

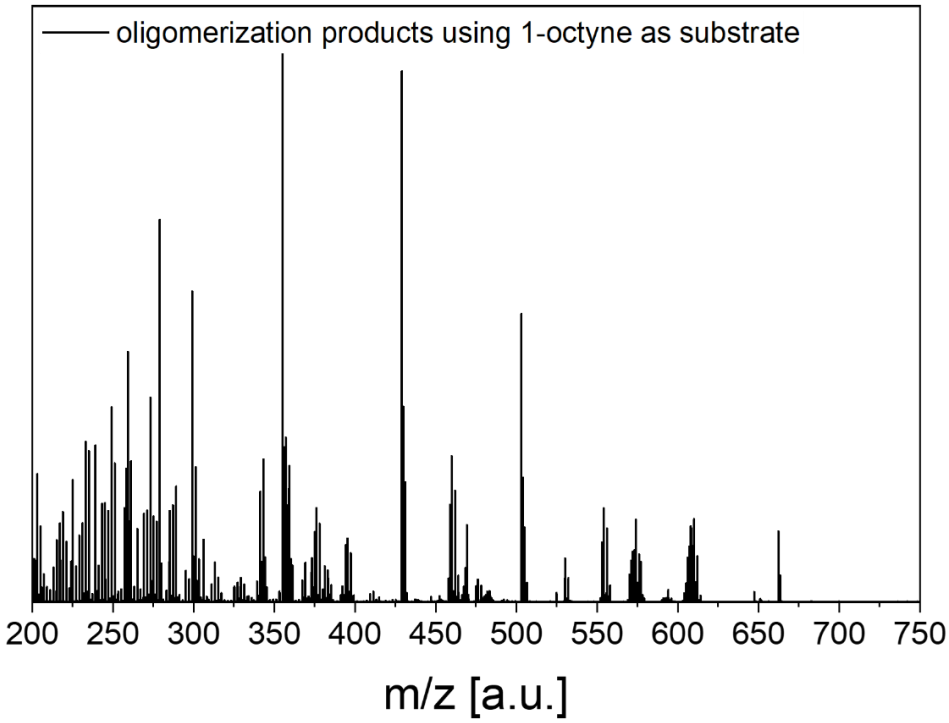

Figure 180. LIFDI-MS measurements of the reaction mixture after catalysis using 2.5 mol% $Pd_{0.67}Ga_{0.33}$@1.0 equiv. stearic acid, 1.0 bar H_2 at 0°C and 1-octyne as substrate showing oligomerization products.

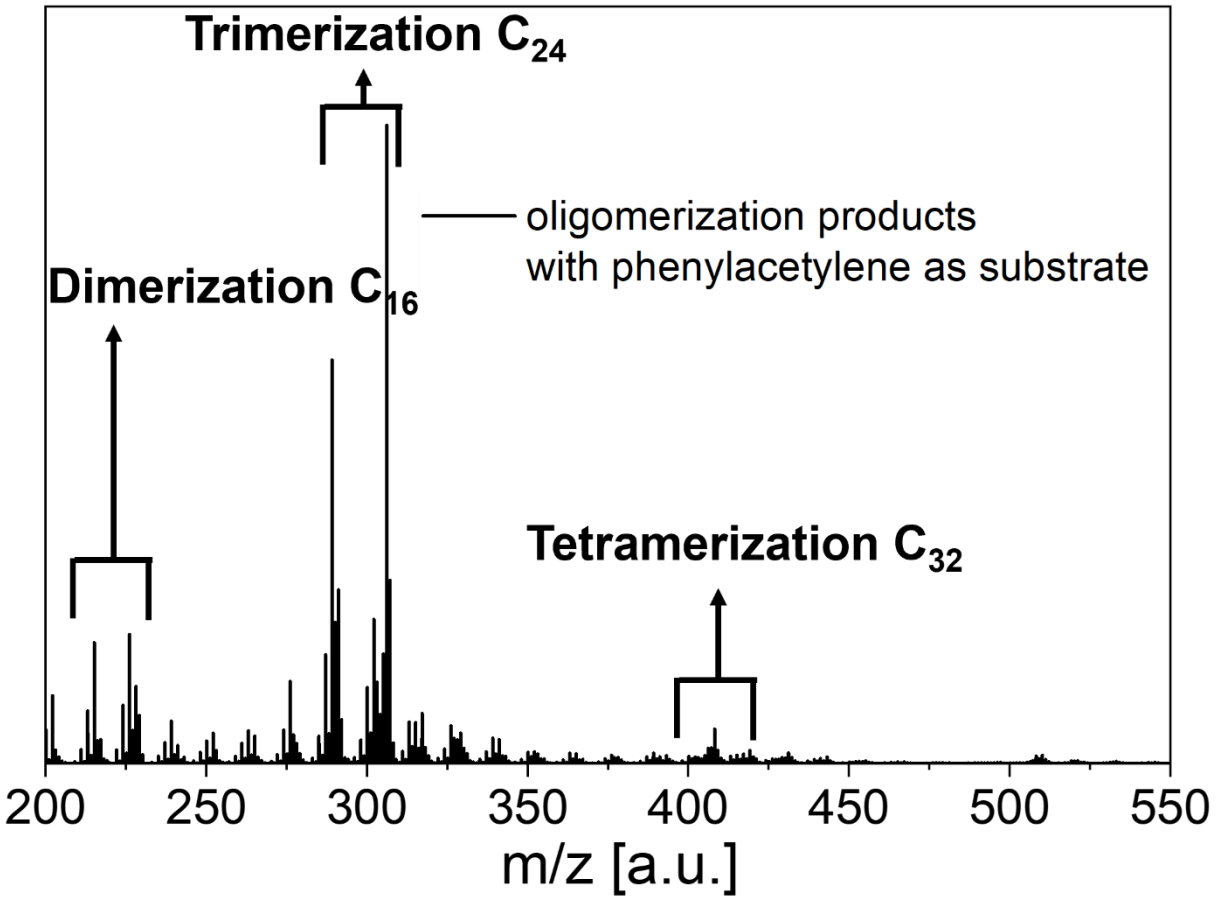

Figure 181. LIFDI-MS measurements of the reaction mixture after catalysis using 2.5mol% $Pd_{0.67}Ga_{0.33}$@1.0 equiv. stearic acid, 1.0 bar H_2 at 0°C and phenylacetylene as substrate showing oligomerization products.

Catalysis experiments with $Fe_{1-x}Al_x$ materials

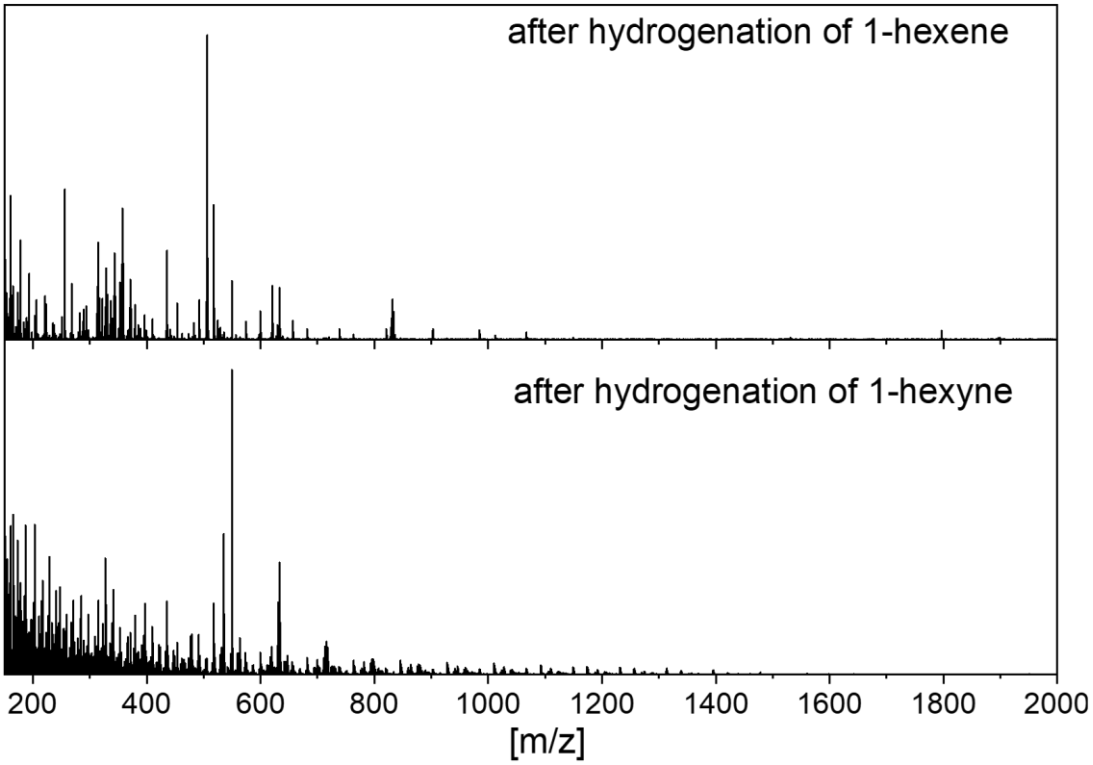

Figure 182. LIFDI-MS spectra of the reaction solution using $Fe_{0.5}Al_{0.5}$ powder in the semi-hydrogenation catalysis of 1-hexyne at 3 bar H_2 and 100 °C after 24 h.

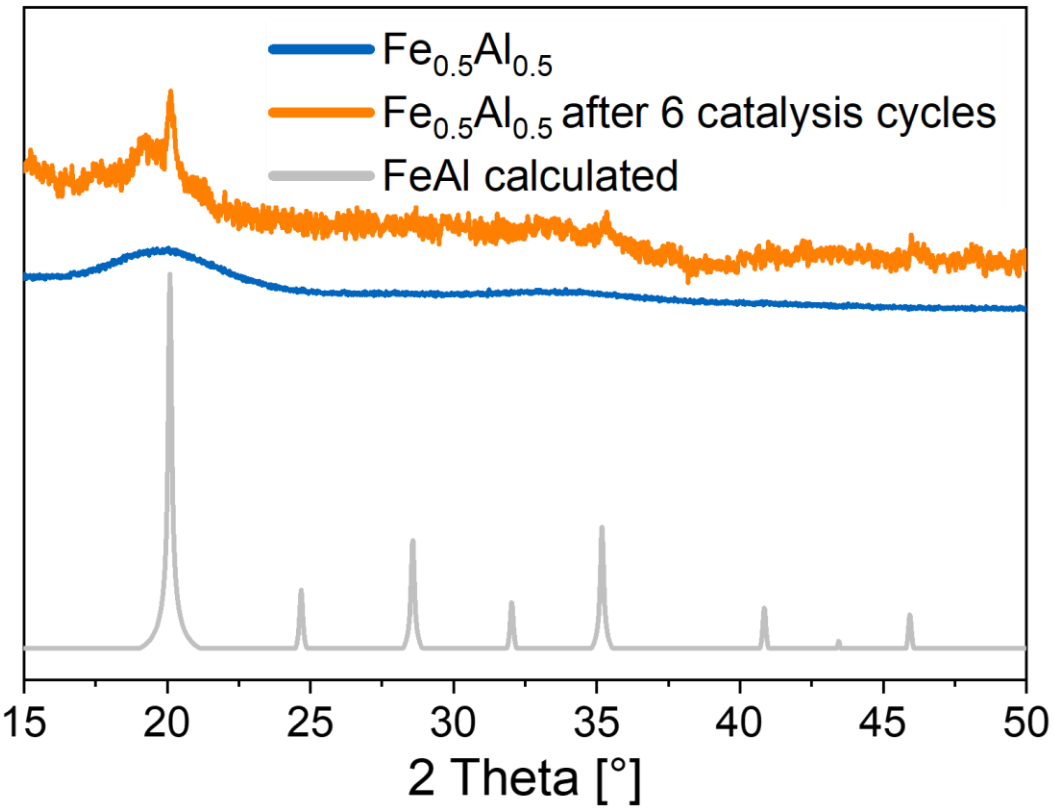

Figure 183. PXRD pattern of $Fe_{0.5}Al_{0.5}$ powder before (black trace) and after six catalysis runs (orange trace) with the calculated FeAl pattern (grey trace) as reference.

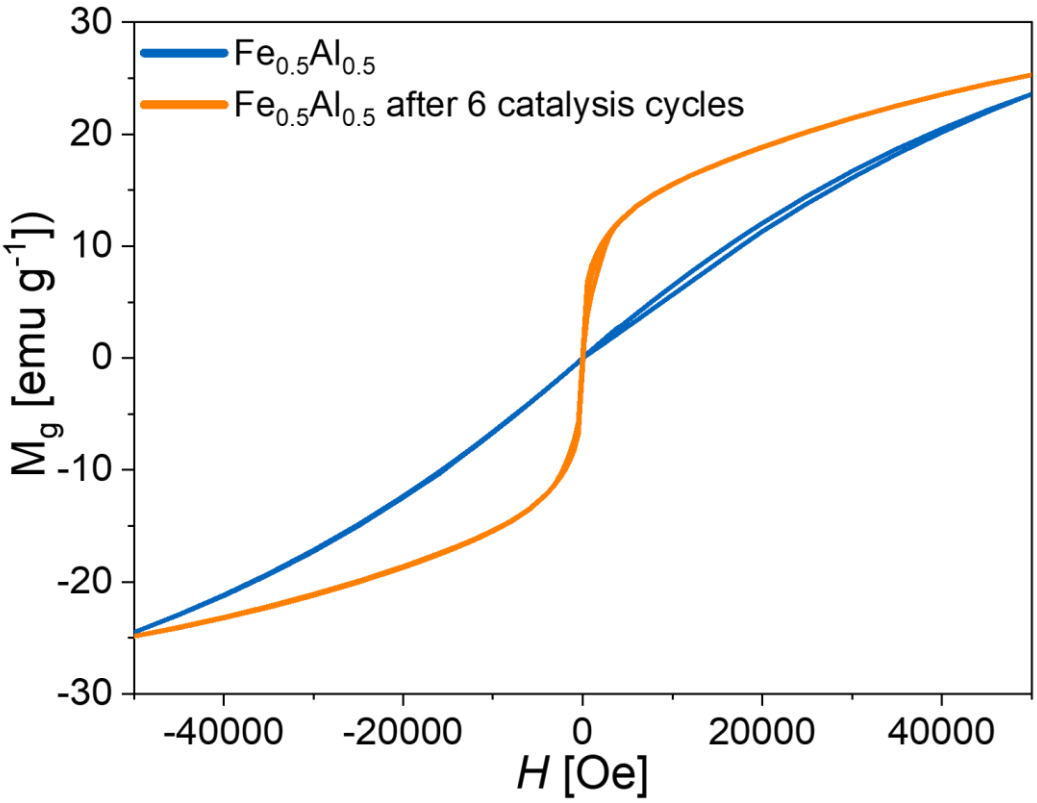

Figure 184. SQUID hysteresis measurement of $Fe_{0.5}Al_{0.5}$ powder before (black trace) and after six catalysis runs (orange trace) showing an increased ferromagnetic behaviour.

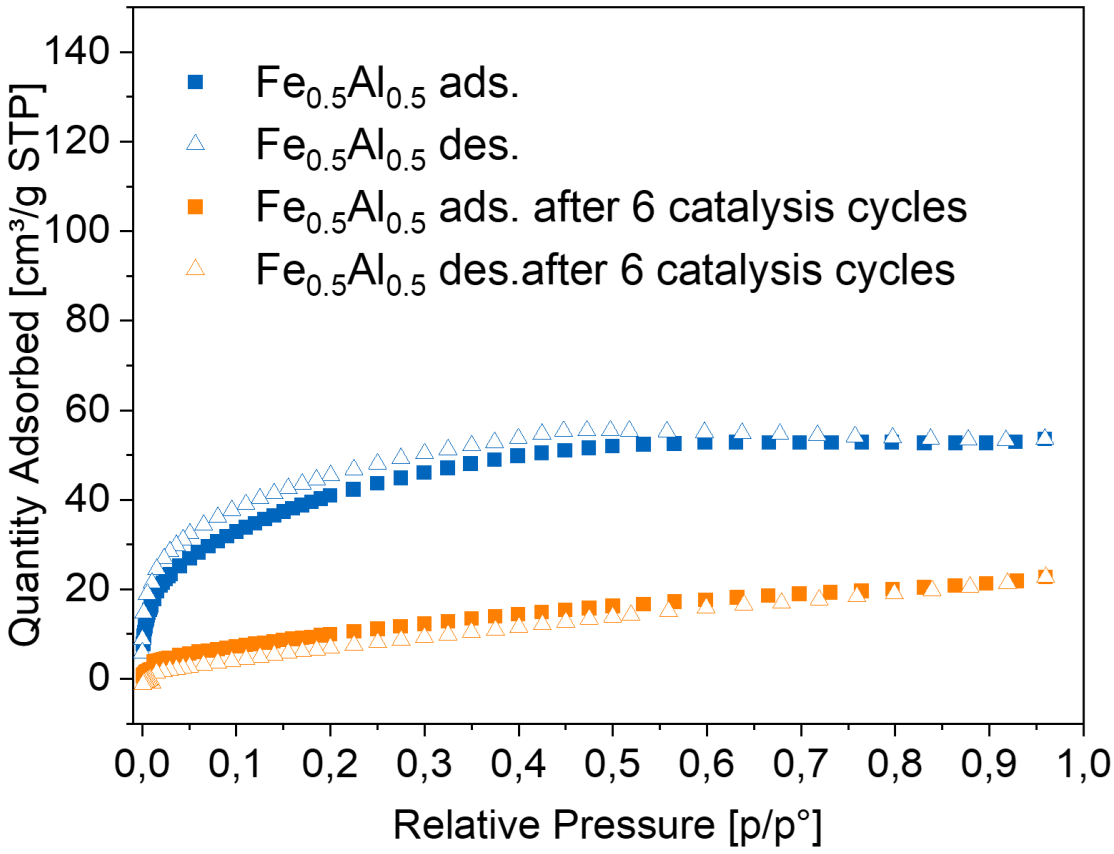

Figure 185. N_2 uptake measurement at 77 K before and after six catalysis cycles of $Fe_{0.5}Al_{0.5}$ powder.

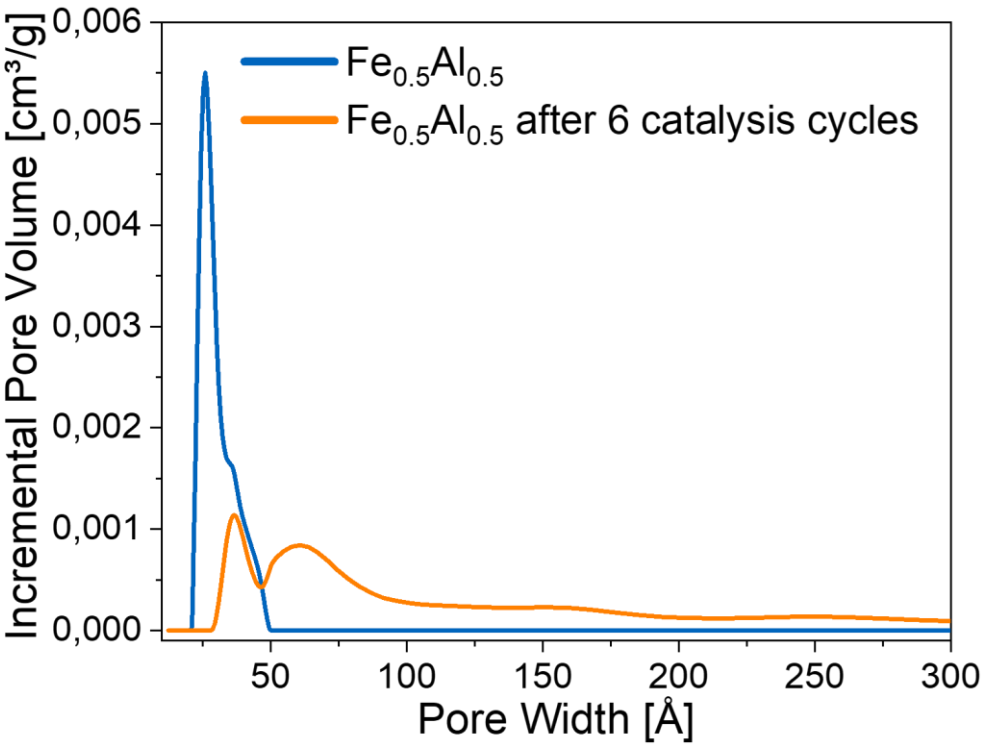

Figure 186. Pore size distribution calculated out of N_2 uptake experiments at 77 K of $Fe_{1.0}Al_{0.0}$ powder and $Fe_{0.5}Al_{0.5}$ powder before (black and green traces) and after six catalysis runs (blue and orange traces) showing bigger pore sizes after catalysis.

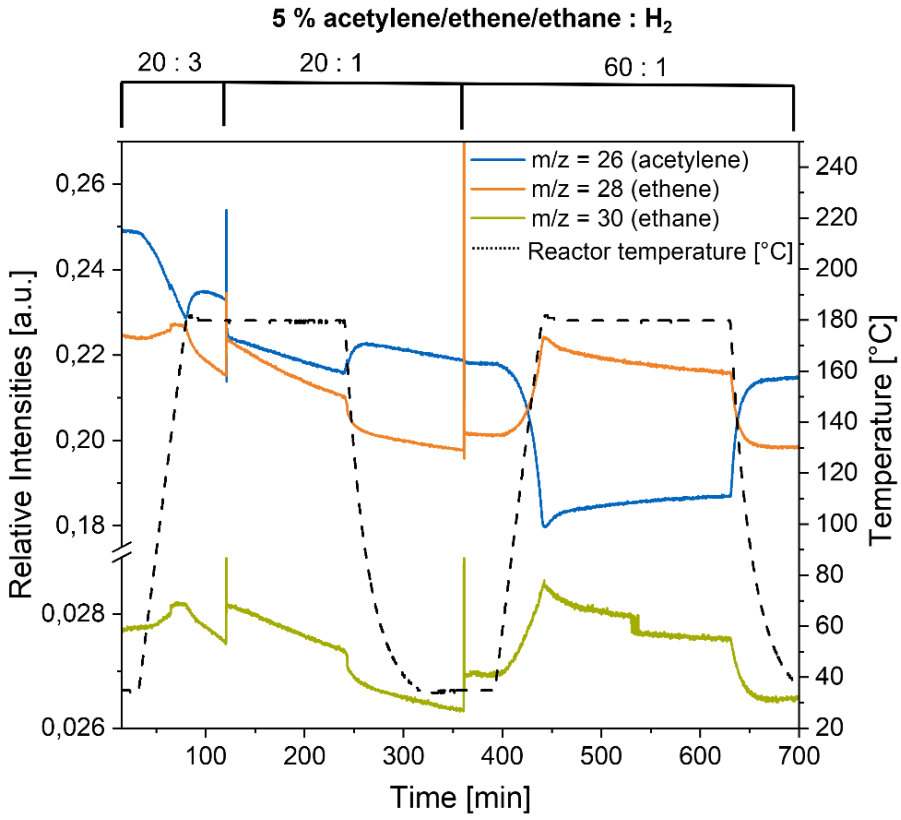

Figure 187. Acetylene (semi)-hydrogenation experiments using $Fe_{0.33}Al_{0.67}$ powder as catalyst in a flow reactor set up with different temperatures and alkyne/H_2 ratios.

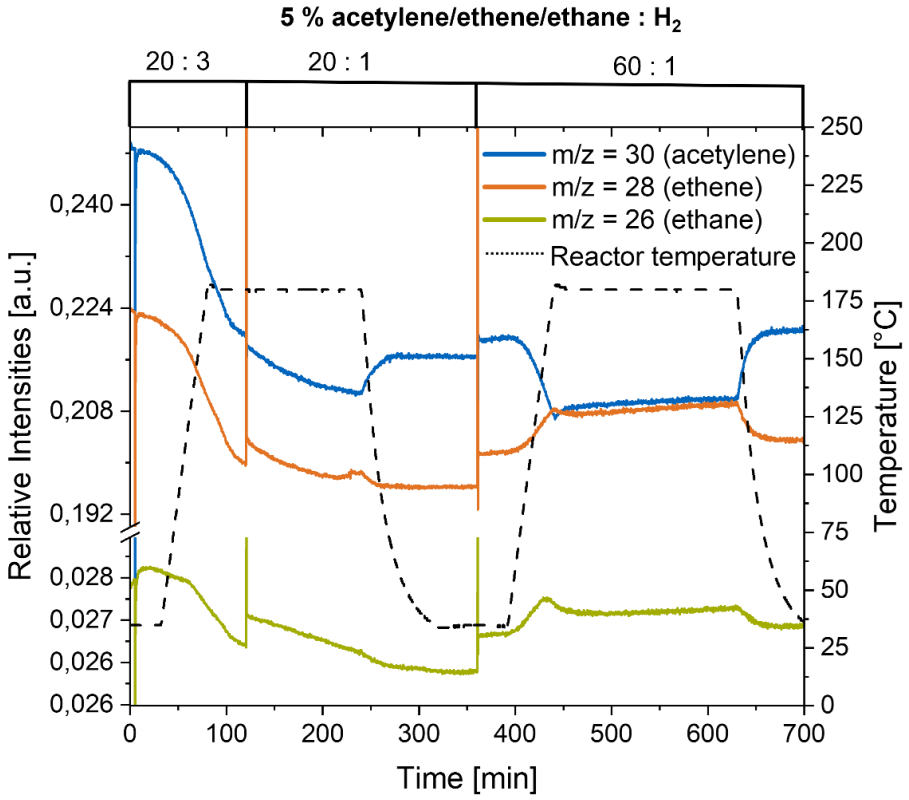

Figure 188. Acetylene (semi)-hydrogenation experiments using $Fe_{0.5}Al_{0.5}$ powder as catalyst in a flow reactor set up with different temperatures and alkyne/H_2 ratios.

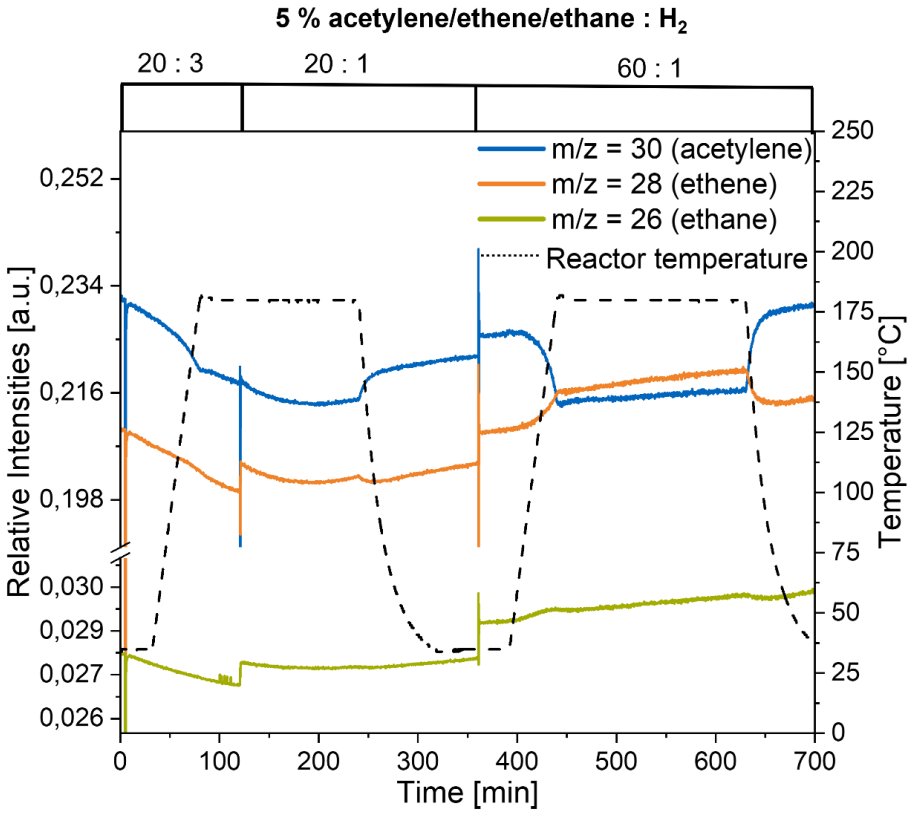

Figure 189. Acetylene (semi)-hydrogenation experiments using $Fe_{1.0}Al_{1.0}$ powder as catalyst in a flow reactor set up with different temperatures and alkyne/H_2 ratios.

List of Publications

Part of this thesis

L. Staiger, T. Kratky, S. Günther, A. Urstoeger, M. Schuster, O. Tomanek, R. Zbořil, R. W. Fischer, R. A. Fischer, M. Cokoja, *Nanoscale* **2021**, *13*, 15038–15047 (Nanometallurgy in solution: organometallic synthesis of intermetallic Pd–Ga colloids and their activity in semi-hydrogenation catalysis)

L. Staiger, T. Kratky, S. Günther, O. Tomanek, R. Zboril, R.W. Fischer, R.A. Fischer, M. Cokoja, *ChemCatChem* **2021**, *13*, 227-234 (Steric and Electronic Effects of Phosphane Additives on the Catalytic Performance of Colloidal Palladium Nanoparticles in the Semi-Hydrogenation of Alkynes)

In context with this thesis

Z. Fan, **L. Staiger**, K. Hemmer, Z. Wang, W. Wang, Q. Xie, L. Zhang, A. Urstoeger, M. Schuster, J. A. Lercher, M. Cokoja, R. A. Fischer, *Cell Rep. Phys. Sci.* **2022**, *3*, 100757 (Enhanced catalytic performance of palladium nanoparticles in MOFs by channel engineering)

S. Okazoe, **L. Staiger**, M. Cokoja, K. Kusada, T. Yamamoto, T. Toriyama, S. Matsumura, H. Kitagawa, R. A. Fischer, *Eur. J. Inorg. Chem.* **2021**, 1186–1189 (Enhanced Hydrogenation Catalytic Activity of Ruthenium Nanoparticles by Solid-solution Alloying with Molybdenum)

Intellectual Input

J. Mink, **L. Staiger**, M. Muhr, C. Gemel, M. Drees, L. Hajba, J. Mihály, C. Németh, B. V. Lokshin, K. Hemmer, M. Schütz, M. Cokoja, R. A. Fischer, *J. Raman Spectrosc.* **2021**, *52*, 2317-2337 (Structural studies of ligand stabilized Ni/Ga clusters by means of vibrational spectroscopy and theoretical calculations)

L. Schmolke, B. J. Gregori, B. Giesen, A. Schmitz, J. Barthel, **L. Staiger**, R. A. Fischer, A. Jacobi von Wangelin, C. Janiak, *New J. Chem.* **2019**, *43(42)*, 16583–16594 (Bimetallic Co/Al Nanoparticles in an Ionic Liquid: Synthesis and Application in Alkyne Hydrogenation)

Conferences and Schools

L. Staiger, T. Kratky, S. Günther, O. Tomanek, R. Zboril, R. W. Fischer, R. A. Fischer, M. Cokoja, *Poster, Sommer School „Engineering Materials for Catalysis„*, Portoroz (Slovenia) 2020.

L. Staiger, T. Kratky, S. Günther, O. Tomanek, R. Zboril, R. W. Fischer, R. A. Fischer, M. Cokoja, *Poster, Treffen Deutscher Katalytiker,* Weimar 2019.

L. Staiger, T. Kratky, S. Günther, O. Tomanek, R. Zboril, R. W. Fischer, R. A. Fischer, M. Cokoja, *Poster, Winter School „Innovative Catalysis and Sustainability„*, Bardonecchia (Italy) 2018.